Search for production of charginos and neutralinos with a small mass gap to the lightest supersymmetric particle

with ATLAS at $\sqrt{s}$ = 13 TeV

Broos Vermeulen

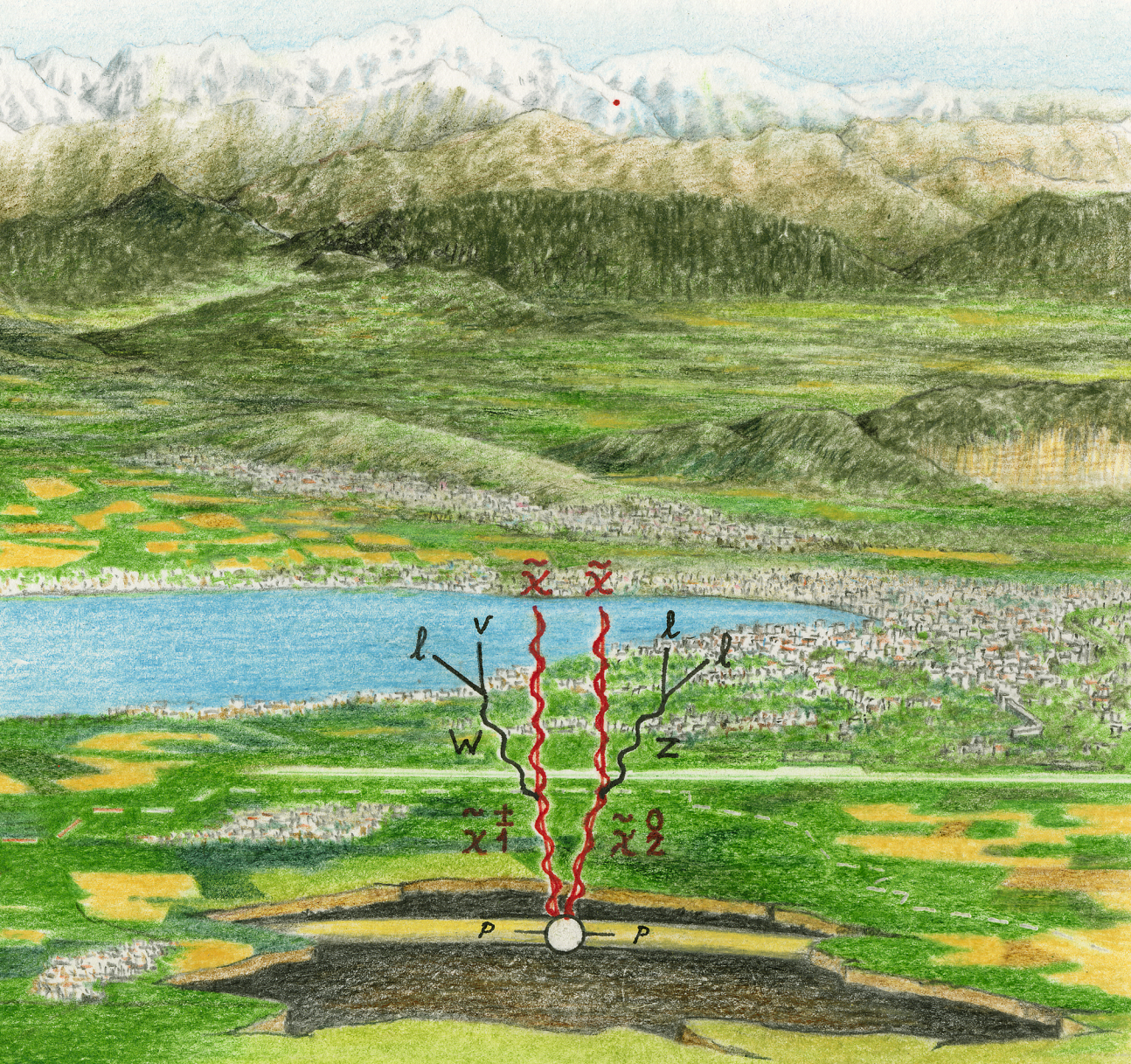

Search for production of charginos and neutralinos with a small mass gap to the lightest supersymmetric particle with ATLAS at $\sqrt{s} = 13$ TeV

Ambrosius Thomas Vermeulen

Search for production of charginos and neutralinos with a small mass gap to the lightest supersymmetric particle with ATLAS at $\sqrt{s} = 13$ TeV

ACADEMISCH PROEFSCHRIFT

ter verkrijging van de graad van doctor
aan de Universiteit van Amsterdam
op gezag van de Rector Magnificus
prof. dr. ir. K.I.J. Maex
ten overstaan van een door het College voor Promoties ingestelde commissie,
in het openbaar te verdedigen in de Aula der Universiteit
op vrijdag 27 november 2020, te 11:00 uur

door

Ambrosius Thomas Vermeulen

geboren te Bunnik

PROMOTOR	prof. dr. ir. P.J. de Jong (Universiteit van Amsterdam)
COPROMOTOR	dr. S.C. Alderweireldt (CERN)
OVERIGE LEDEN	prof. dr. M.P. Decowski (Universiteit van Amsterdam)
	prof. dr. S.C.M. Bentvelsen (Universiteit van Amsterdam)
	dr. C. Weniger (Universiteit van Amsterdam)
	prof. dr. H.G. Raven (Vrije Universiteit Amsterdam)
	prof. dr. F. Blekman (Vrije Universiteit Brussel)
	prof. dr. W.J.P. Beenakker (Universiteit van Amsterdam/Radboud Universiteit Nijmegen)
	dr. M.E.J. Postma (NWO-I Nikhef)

Faculteit der Natuurwetenschappen, Wiskunde en Informatica

Cover design by Rolf Weijburg (www.weijburg.nl)
Printed in the Netherlands by Ipskamp Drukkers

This work has been performed at the Nikhef Institute for Subatomic Physics (Nikhef), which is financed by the Netherlands Organisation for Scientific Research (NWO).

Table of contents

Introduction

The thesis in your hands is a small piece in the search to answer a bigger question; what are the fundamental building blocks of nature and which laws govern their interactions? The field of particle physics tries to answer this question. The Standard Model of particle physics (SM) [1–5], which was formulated in the mid 1970s, describes three of the four known fundamental forces, the electromagnetic, weak, and strong force. Besides describing the forces the SM classifies all discovered elementary particles. The SM has had great success over the years, the experimental confirmation of the existence of quarks came from deep inelastic scattering experiments at the Stanford Linear Accelerator Center (SLAC) in 1968 [6, 7], where the proton breaks up in the interaction and is found to be a complex dynamical system comprised of quarks, anti-quarks and gluons. The SM predicted the top quark, which was discovered in 1995 by the CDF [8] and D0 [9] experiments at Fermilab. It predicted the tau neutrino, which was discovered in 2000 by DONUT at SLAC [10]. Also the SM has predicted various properties of weak neutral currents and the W and Z bosons with great accuracy. The success of the SM was completed by the discovery of the Higgs boson at the Large Hadron Collider in 2012 by ATLAS [11] and CMS [12] as predicted by Higgs [13], Brout and Englert [14].

The SM and the confirmation of the Higgs particle, and with it its associated mechanism of electroweak symmetry breaking, are a great triumph for the principle of symmetries. So what are we after if the SM is such as success? Does it answer our big question; is it the theory that describes all observations in the universe? The main motivation for the research performed in this thesis is that the SM does not provide a complete picture of the fundamental building blocks of nature and the laws governing their interactions, as for example the SM does not provide a candidate for Dark Matter (DM).

The shortcomings of the SM can be resolved by theories which extend beyond the SM, such as supersymmetry. Supersymmetry is a symmetry that relates fermions and bosons predicting many new particles, among which a possible candidate for DM. Besides providing a DM candidate, it solves the mass hierarchy problem of the SM if supersymmetry is found at the TeV scale. Quantum corrections from the new particles can stabilise the electroweak

scale. Supersymmetry also naturally achieves the unification of the electroweak and the strong force, which has been a long held ideal for particle physics. And if supersymmetry is imposed locally, general relativity is automatically included, thus including the fourth fundamental force, gravity, and making supersymmetry a fundamental ingredient for string theory.

As a consequence supersymmetry is well motivated by theory, but unfortunately there has not been any experimental confirmation. Without experimental confirmation, a theory, no matter how many problems it solves, stays just a theory. Experiments at the Large Electron-Positron Collider (LEP), the Tevatron, and at Run-1 of the Large Hadron Collider (LHC) ruled out a large number of supersymmetric models. After Run-1 of the LHC there are strong constraints on the masses of the strongly produced supersymmetric particles called squarks and gluinos. On the other hand, the values of the masses of the weakly produced supersymmetric charginos and neutralinos are less constrained, since these particles have much smaller production cross sections.

The weakly produced charginos and neutralinos play an important role in establishing a connection between supersymmetric models and DM, where the lightest supersymmetric particle, the lightest neutralino, $\tilde{\chi}_1^0$, is the DM candidate. Since supersymmetry predicts a DM candidate, constraints from astrophysical observations can help motivate which supersymmetric models to look for. In this thesis supersymmetric models are being looked for which are motivated by the thermal relic abundance of DM in the universe. Also supersymmetric models must be coherent with the SM, and agree with measurements from b-physics, Higgs measurements and electroweak precision measurements.

The LHC and the ATLAS experiment can probe these supersymmetric models near the TeV scale. A confirmation would be a huge leap forward for particle physics and would determine the course of the field for many years to come. The alternative would be that the scale of supersymmetry is pushed to higher and higher energies and that we might have to rethink this beautiful idea, at least for now.

Outline of the thesis and author's contributions

The work presented in this thesis is divided into three main parts. The first part presents the theory, as well as the motivation for the research performed in this thesis. The second part presents the ATLAS experiment, demonstrating the detection, alignment and reconstruction techniques used by the experiment. The third part presents the analysis [15] performed by ATLAS to discover the supersymmetry signal described in the first part. For each chapter a brief summary of the content is given and the author's contribution.

Part 1 Theory

Chapter 1 provides an overview of the Standard Model of particle physics and demonstrates its shortcomings. The tension with the Lambda Cold Dark Matter model, which requires a dark matter particle, is especially highlighted.

Chapter 2 gives an introduction to supersymmetry, which is an extension to the Standard Model of particle physics. Supersymmetry can provide a candidate for Dark Matter, and thus resolve the discrepancy between the Standard Model of particle physics and the Lambda Cold Dark Matter model. Global fits performed in the supersymmetry parameter space provide the motivation for the research presented in this thesis.

Part 2 The ATLAS experiment

Chapter 3 gives a general description of the Large Hadron Collider (LHC). The chapter also provides an overview of the ATLAS experiment and all its subsystems.

Chapter 4 describes the Inner Detector Alignment procedure. It is explained that if the alignment procedure is not constrained properly, uncontrolled behaviour originates through weak modes. I have performed the alignment with first stable beams in 2016 and introduced new diagnostic figures of tracking parameters to spot weak modes introduced by the alignment procedure.

Chapter 5 provides a description of the methods used by ATLAS to reconstruct and identify particles produced in the LHC collisions. It also introduces isolation algorithms, which examine whether particles are isolated within the detector. I have contributed to improve the isolation of leptons by designing two working points using the Prompt Lepton Veto algorithm. Similar working points are now used within the whole ATLAS collaboration. I have calibrated the working point for muons, which is used in the supersymmetry analysis described in this thesis, to data.

Part 3 Analysis

Chapter 6 gives a general introduction to the supersymmetry signal searched for and provides an overview of the analysis. The analysis is published in [15].

Chapter 7 describes the Standard Model backgrounds expected in the analysis, and the methods used to estimate these backgrounds. I have validated that backgrounds estimated using Monte Carlo correctly predict the data in a loose selection region and designed control regions to normalise the largest background estimated using Monte Carlo to data. Also I have derived the fakes background for the analysis using data-driven techniques, as well as assigned the systematics to the method.

Chapter 8 presents an overview of the selection of the supersymmetry signal. I have contributed to the lepton trigger strategy by selecting which triggers to use, and studied the efficiency of these triggers. I have studied which Prompt Lepton Veto working point to use in the analysis. Also I have designed the signal regions which have low missing momentum, called the SRlow signal regions, as well as provided the expected significance of the combination with the high missing momentum signal regions, called SRhigh. I have also designed the discovery regions, which are used to possibly discover the supersymmetry signal.

Chapter 9 illustrates the validation of the methods used to predict the Standard Model backgrounds. I have designed the validation regions for all the backgrounds, as well as studied the signal contamination in the validation regions.

Chapter 10 presents the results of the analysis. The supersymmetry signal is not found, and thus an exclusion contour visualises the excluded supersymmetry phase space. I have set up the discovery fit.

Chapter 11 contains a discussion on the analysis method and results. All of the work shown in this chapter is outside of the scope of the analysis and are personal reflections on the performed analysis. Also a comparison is shown to the CMS analysis, as well as the expected sensitivity for the analysis with the High Luminosity LHC.

Part I

Theory

Chapter 1

Standard Model

As mentioned in the introduction particle physics tries to answer the questions on the fundamental building blocks of nature. The model used to describe the fundamental building blocks is the Standard Model (SM), which is successful when describing experimental data at particle colliders. However, the present situation in particle physics is contradictory. On the one hand, the SM is successful in describing experimental data, on the other hand there are contradictory predictions from the Standard Model of Cosmology, the Lambda Cold Dark Matter (Λ-CDM) model. The Λ-CDM model requires Dark Matter (DM) which is not described within the SM. The SM should also provide a description for DM if the SM were to be the theory describing all fundamental physics, it should describe the small distances as well as the physics of the large distances as illustrated in Figure 1.1. Both the SM and Λ-CDM will be described in this chapter to demonstrate the shortcomings of the SM.

1.1 Standard Model

The SM describes three of the four known fundamental forces and classifies all discovered elementary particles. The fundamental forces are mediated through gauge bosons, which have integer spin. The electromagnetic force is mediated by the massless photon γ, the weak forces are mediated by the massive $W^{\pm}$ and Z and the strong force is mediated by the massless gluons g. The matter particles are described by fermions, which are half-integer spin, and are composed of three generations of leptons and quarks. The charged leptons interact through the electromagnetic and the weak force, while the neutral leptons, neutrinos, only interact through the weak force. The quarks interact through all the forces in the SM; the electromagnetic, the weak and the strong force.

The force carriers and the three generations of matter are presented in Figure 1.2. The first generation charged particles do not decay, as a result of which atoms are able to form,

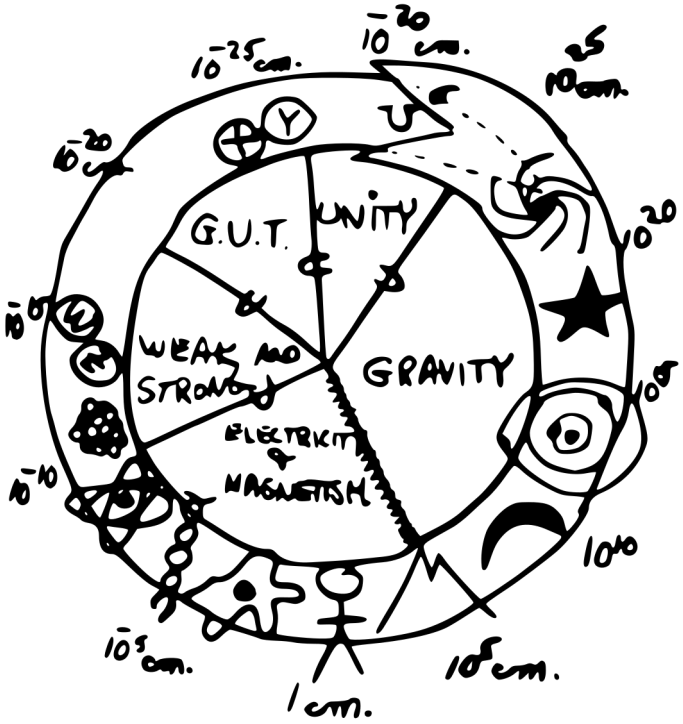

Fig. 1.1: Glashow's snake devours its tail at the point where the physics of the Planck scale meets the large-structures of galaxies [16].

which consist of electrons surrounding an atomic nucleus, made of up and down quarks. The up and down quarks in the atomic nucleus are kept together by the gluons of the strong force, and the electrons surround the nucleus through the electromagnetic force by exchanging photons. The second and third generation charged particles decay in a short amount of time and are only observed in high energy environments, such as at the energy of the collisions at the Large Hadron Collider (LHC). The high energy environment of the LHC resembles conditions of the early stage of the big bang.

1.1.1 Lagrangian and symmetries

The SM is a model within quantum field theory, in which a Lagrangian controls the dynamics and kinematics of the theory. The SM Lagrangian consists of the electroweak interactions, where the electromagnetic and weak interactions are joined together, the Higgs sector, the Yukawa terms for the fermion masses and the strong interaction,

$$\mathscr{L}_{\mathrm{SM}} = \mathscr{L}_{\mathrm{electroweak}} + \mathscr{L}_{\mathrm{Higgs}} + \mathscr{L}_{\mathrm{Yukawa}} + \mathscr{L}_{\mathrm{strong}}. \tag{1.1}$$

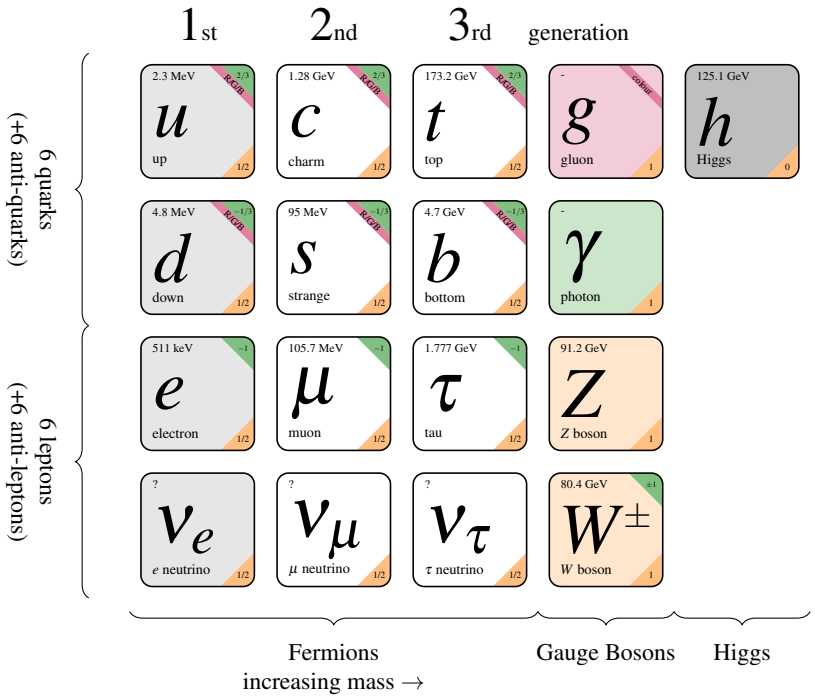

Fig. 1.2: The particles of the Standard Model. Each particle and its corresponding properties are visualised a box. At the top of each box the mass of the particle is shown. At the top right the electric charge of the particle is highlighted in green and the colour charge is highlighted in red. At the bottom right the spin of the particle is highlighted in orange.

The Lagrangian contains symmetries described by transformation groups which leave the Lagrangian invariant. Examples of such transformation groups are rotations or translations. Each of these symmetries described by a transformation group results in a conserved charge. For any symmetry transformation to be acceptable in quantum mechanics it must be unitary, since otherwise it will change the wavefunction normalisation. Also the eigenstates of the system must be unchanged by the symmetry transformation, as a consequence the symmetry transformation must commute with the Hamiltonian of the SM.

The electroweak and strong interactions are a result of such symmetries described by transformation groups in the form of unitary Lie groups.[1] The SM is a Yang-Mills theory [19], a theory based on Lie algebra to describe the behaviour of elementary particles,[2]

$$SU(3)_C \times SU(2)_L \times U(1)_Y. \tag{1.2}$$

[1] The unitary Lie group, SU(3), is for example also found in the eightfold way [17, 18], which is an ordering scheme for hadrons.

[2] U(n) is the Lie group of $n \times n$ unitary matrices. SU(n) is the Lie group of $n \times n$ unitary matrices with determinant 1.

There is a conserved charge for each symmetry transformation, which results in the fundamental forces carried by the gauge bosons.

For the fermion fields ψ there are left-handed and right-handed chirality states. The left-handed chirality states are arranged in doublets and the right-handed chirality states are arranged in singlets. The fermions fields for leptons and quarks, where i is the generation of the fermion, are given by

$$f_{\mathrm{L},i} = \begin{pmatrix} \nu_i \\ \ell_i \end{pmatrix}, \quad f_{\mathrm{R},i} = \ell_{i,\mathrm{R}}, \tag{1.3a}$$

$$f_{\mathrm{L},i} = \begin{pmatrix} u_i \\ d_i \end{pmatrix}, \quad f_{\mathrm{R},i} = u_{i,\mathrm{R}}, \quad d_{i,\mathrm{R}}. \tag{1.3b}$$

Electroweak interaction

In the Yang-Mills theory, $SU(2)_L \times U(1)_Y$ describes the electroweak interaction, containing the W_μ^a gauge boson fields, from the SU(2) symmetry, and B_μ gauge boson field from the U(1) symmetry,

$$\left(W_\mu^1, W_\mu^2, W_\mu^3\right), \quad B_\mu, \tag{1.4}$$

which interact with the fermion fields ψ through $i\bar{\psi}D^\mu\gamma_\mu\psi$, where W_μ^a only interacts with left-handed fermions. The derivative in the interaction with the fermion fields, D_μ, is given by

$$D_\mu = \partial_\mu + \frac{1}{2}ig'YB_\mu + \frac{1}{2}ig\tau^a W_\mu^a, \tag{1.5}$$

where τ^a are the SU(2) symmetry generators,[3] Y is the U(1) symmetry generator, g is the coupling constant for the W_μ^a field and g' is the coupling constant for the $B_\mu$field. The gauge bosons also have a kinetic term given by $-\frac{1}{4}B_{\mu\nu}B^{\mu\nu} - \frac{1}{4}W_{\mu\nu}^a W_a^{\mu\nu}$, where

$$\begin{aligned} B_{\mu\nu} &= \partial_\mu B_\nu - \partial_\nu B_\mu, \\ W_{\mu\nu}^a &= \partial_\mu W_\nu^a - \partial_\nu W_\mu^a + g\varepsilon^{abc}W_\mu^b W_\nu^c, \end{aligned} \tag{1.6}$$

[3]The Pauli matrices multiplied with i, $i\tau_a$, form a basis for SU(2).

and ε^{abc} is the structure constant of the SU(2) group.[4] If the substitution $\not{D} = D^\mu \gamma_\mu$ is made, the electroweak Lagrangian can be written as [19]

$$\mathscr{L}_{\text{electroweak}} = \sum_{\text{flavours}} \left(i(\bar{L}_i \not{D} L_i + \bar{Q}_i \not{D} Q_i + \bar{\ell}_{i,\text{R}} \not{D} \ell_{i,\text{R}} + \bar{u}_{i,\text{R}} \not{D} u_{i,\text{R}} + \bar{d}_{i,\text{R}} \not{D} d_{i,\text{R}}) \right) - \frac{1}{4} B_{\mu\nu} B^{\mu\nu} - \frac{1}{4} W^a_{\mu\nu} W^{\mu\nu}_a, \tag{1.7}$$

which contains the interaction of the fermion fields with the electroweak gauge bosons and the gauge field kinetic terms.

Spontaneous symmetry breaking

From experimental observations it is known that the electroweak gauge bosons have a mass, however in the Lagrangian in Equation 1.7 there is no mass term for W^a_μ and B_μ fields. Adding a mass term to solve this discrepancy in the form of $\frac{1}{2} m^2 W^a_\mu W^\mu_a + \frac{1}{2} m^2 B_\mu B^\mu$ will not leave the Lagrangian gauge invariant and is, therefore, not an option. The solution is the Higgs mechanism, where through spontaneous symmetry breaking the $W^\pm$ and Z bosons acquire mass, while conserving the gauge invariance of the Lagrangian.

The Higgs mechanism works by adding the following term to the electroweak Lagrangian,

$$\mathscr{L}_{\text{Higgs}} = |D_\mu \phi|^2 - V(\phi), \tag{1.8}$$

causing the $SU(2)_L \times U(1)_Y$ symmetry to be spontaneously broken. The potential $V(\phi)$ of the scalar Higgs field, ϕ, is given by

$$V(\phi) = \mu^2 \phi^2 - \lambda \phi^4, \tag{1.9}$$

where ϕ consists of two complex scalar fields, a charged field to generate the mass of the $W^\pm$, and a neutral field for the Z and γ,

$$\phi = \begin{pmatrix} \phi^+ \\ \phi^0 \end{pmatrix} = \frac{1}{\sqrt{2}} \begin{pmatrix} \phi_1 + i\phi_2 \\ \phi_3 + i\phi_4 \end{pmatrix}. \tag{1.10}$$

When requiring $\mu^2 < 0$ the potential of the Higgs field looks like a Mexican hat as shown in Figure 1.3, with a minimum at $|\phi|^2 = |\mu|^2/(2\lambda)$. After symmetry breaking the neutral photon is required to remain massless, therefore the minimum of the potential must correspond to a

[4] ε^{abc} is given by $[\tau^a, \tau^b] = i\varepsilon^{abc}\tau^c$, where ε^{abc} is the Levi-Civita symbol.

non-zero vacuum expectation value only of ϕ^0,

$$\langle 0|\phi|0\rangle = \frac{1}{\sqrt{2}}\begin{pmatrix}0\\ v\end{pmatrix}, \tag{1.11}$$

where v is the vacuum expectation value. The minimum of the potential lies at $|\phi|^2 = |\mu|^2/(2\lambda)$, which can now be related to v,

$$|\phi|^2 = \left(\frac{1}{\sqrt{2}}\begin{pmatrix}0\\ v\end{pmatrix}\right)^2 = \frac{1}{2}v^2, \tag{1.12}$$

resulting in an expression for the vacuum expectation value,

$$v = \sqrt{\frac{|\mu|^2}{\lambda}}. \tag{1.13}$$

The non-zero vacuum expectation value of the Higgs field, arising from spontaneous symmetry breaking, is the mechanism by which the other fields in the theory acquire mass. The photon must not experience the non-zero vacuum, since it does not have mass. The physical gauge bosons A (photon), Z and $W^{\pm}$ are a combination of the W^a_μ and B_μ bosons,

$$W^2_\mu = \frac{W^1_\mu \mp W^2_\mu}{2} \qquad M_W = \frac{1}{2}vg \tag{1.14a}$$

$$Z^0_\mu = \cos(\theta_W)W^3_\mu - \sin(\theta_W)B_\mu \qquad M_Z = \frac{v}{2}\sqrt{g^2+g'^2} \tag{1.14b}$$

$$A_\mu = \sin(\theta_W)W^3_\mu + \cos(\theta_W)B_\mu \qquad M_A = 0, \tag{1.14c}$$

where θ_W, the weak mixing angle is given by

$$\cos(\theta_W) = \frac{g}{\sqrt{g^2+g'^2}} \qquad \sin(\theta_W) = \frac{g'}{\sqrt{g^2+g'^2}}. \tag{1.15}$$

The Higgs mass is described by the Lagrangian in Equation 1.9. In a Lagrangian for a free scalar the mass term is given by $\frac{1}{2}m_h\phi^2$. The term proportional to ϕ^2, which is $\mu^2\phi^2$, can thus be interpreted as the Higgs mass,

$$m_h = \sqrt{2\lambda}v. \tag{1.16}$$

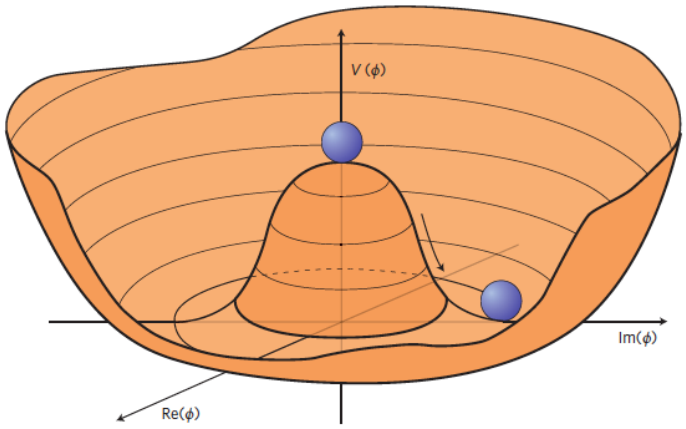

Fig. 1.3: An illustration of the Higgs potential given by $V(\phi) = \mu^2\phi^2 - \lambda\phi^4$. The potential is shown for the case that $\mu^2 < 0$. The minimum of the potential is located at $|\phi|^2 = |\mu|^2/(2\lambda)$. Choosing any of the points at the bottom of the potential spontaneously breaks the electroweak symmetry [20].

Yukawa interaction

In the electroweak Lagrangian also the matter particles, the fermions, do not have a mass term. Similar to the gauge bosons, adding a fermion mass term $-m_f(\bar{f}_\mathrm{L} f_\mathrm{R} + \mathrm{h.c.})$ will no longer leave the Lagrangian gauge invariant. The mass for fermions also arises as a consequence of spontaneous symmetry breaking through the Yukawa interaction, $-\lambda_f \bar{f}_\mathrm{L}\phi f_\mathrm{R} + \mathrm{h.c.}$,

$$\mathscr{L}_\mathrm{Yukawa} = \sum_\mathrm{generations} \left(-\lambda_e \bar{L}\phi e_\mathrm{R} - \lambda_d \bar{Q}\phi d_\mathrm{R} - \lambda_u \varepsilon^{ab}\bar{Q}_a\phi_b^\dagger u_r + \mathrm{h.c.}\right), \tag{1.17}$$

where λ_f is a dimensionless coupling constant, ϕ is the Higgs field and ε^{ab} is the two dimensional total anti-symmetric tensor with $\varepsilon^{12} = 1$. By replacing $\phi = \frac{1}{\sqrt{2}}v$ with the vacuum expectation value due to spontaneous symmetry breaking,

$$-\lambda_f \bar{f}_\mathrm{L}\phi f_\mathrm{R} + \mathrm{h.c.} = -\frac{1}{\sqrt{2}}\lambda_f v(\bar{f}_\mathrm{L} f_\mathrm{R} + \mathrm{h.c.}), \tag{1.18}$$

the following mass term for fermions is obtained,

$$m_f = \frac{1}{\sqrt{2}}\lambda_f v. \tag{1.19}$$

Cabibbo-Kobayashi-Maskawa matrix

The weak eigenstates of the quarks differ from the mass eigenstates and can be transformed into one another by using the Cabibbo-Kobayashi-Maskawa (CKM) mixing matrix [21, 22].

Mixing is chosen by convention to happen in the down quark sector. The weak eigenstates, labeled d', s' and b', are related to the mass eigenstates, d, s and b, by the complex 3×3 matrix,

$$\begin{pmatrix} d' \\ s' \\ b' \end{pmatrix} = \begin{pmatrix} V_{ud} & V_{us} & V_{ub} \\ V_{cd} & V_{cs} & V_{cb} \\ V_{td} & V_{ts} & V_{tb} \end{pmatrix} \begin{pmatrix} d \\ s \\ b \end{pmatrix}. \tag{1.20}$$

In the SM the CKM matrix is unitary, such that the experimental measurements can be interpreted as [23]

$$\begin{pmatrix} |V_{ud}| & |V_{us}| & |V_{ub}| \\ |V_{cd}| & |V_{cs}| & |V_{cb}| \\ |V_{td}| & |V_{ts}| & |V_{tb}| \end{pmatrix} \approx \begin{pmatrix} 0.974 & 0.225 & 0.004 \\ 0.225 & 0.973 & 0.041 \\ 0.009 & 0.040 & 0.999 \end{pmatrix}. \tag{1.21}$$

It can be seen that the CKM matrix is approximately diagonal. Also the mixing in the first two generations of quarks is sizeable, however the mixing between the third generation quarks and the lighter quarks is small. The CKM matrix can be reduced to three mixing angles and a complex phase.

The fact that mixing between b-quarks and the lighter quarks is small, causes b-hadrons to be uniquely identified from the hard-scatter in a proton-proton collision at the LHC, as described in Section 5.2.1.

Strong interaction

In the Yang-Mills theory, $SU(3)_C$ describes the interaction of the strong force, where the gauge boson fields are G^a_μ,

$$\left(G^1_\mu, G^2_\mu, G^4_\mu, G^5_\mu, G^6_\mu, G^7_\mu, G^8_\mu\right), \tag{1.22}$$

which interact with the quark fields ψ_q through, $i\bar{\psi}_{q,i} D^\mu \gamma_\mu \psi_{q,i}$, for which

$$D_\mu = \partial_\mu + i g_s T^a G^a_\mu, \tag{1.23}$$

where T^a are the SU(3) generators and g_s is the running strong coupling constant.[5] The gauge bosons also have a kinetic term which is written like $-\frac{1}{4} G_{\mu\nu} G^{\mu\nu}$, given by

$$G^a_{\mu\nu} = \partial_\mu G^a_\nu - \partial_\nu G^a_\mu + g_s f^{abc} G^b_\mu G^c_\nu, \tag{1.24}$$

[5]The SU(3) generators T^a can be related to the Gell-Mann matrices λ^a.

where f^{abc} is the structure constant of the SU(3) group.[6] If the substritution $\not{D} = D^{\mu}\gamma_{\mu}$ is made, the strong force lagrangian can then be written as

$$\mathscr{L}_{\text{strong}} = \sum_{\text{flavours}} \left(i(\bar{\psi}_{q,i} \not{D} \psi_{q,i}) \right) - \frac{1}{4} G^{a}_{\mu\nu} G^{\mu\nu}_{a}. \tag{1.25}$$

The strong interaction has two important properties: asymptotic freedom and confinement. Asymptotic freedom states that the strong coupling constant, g_s, becomes smaller when the interaction energy gets larger [24], which results in analytical perturbative calculations that are only possible at high energies. The second important property is confinement, which states that quarks are bound into colourless hadrons, of which there are two types, mesons and baryons. Mesons are quark anti-quark pairs and baryons are composed of three quarks or three anti-quarks.

1.1.2 Shortcomings of the Standard Model

The SM is an accurate theory describing the interaction of matter through the weak, strong and electromagnetic force. However, there are observations the SM does not describe, as well as aesthetical arguments against the SM. Observations from astrophysics experiments suggest DM, which would then require a theory beyond the SM. DM will be described in more detail in Section 1.2, where the Λ-CDM model is discussed.

In this section the observation of neutrino oscillations will be discussed, suggesting that the neutrinos have a mass, which is not described within the SM. Aesthetical arguments against the SM will be discussed as well, such as the hierarchy problem and gauge coupling unification. The hierarchy problem and gauge coupling unification suggest a theory at a higher energy scale from which the SM derives, where the parameters within the SM should be an inevitable outcome of an encompassing higher order mathematical description. Another aesthetical argument, although not discussed in this section, is the fact that the SM is not a theory of everything, as it does not contain a description of the fourth fundamental force, gravity.

Neutrino oscillations

The Super-Kamiokande Observatory [25, 26], the Sudbury Neutrino Observatory [27] and KamLAND [28] made the experimental discovery that neutrinos oscillate between flavours, ν_e, ν_μ and ν_τ. Neutrino oscillations imply that the neutrinos have mass, and the mechanism through which neutrinos can acquire mass is not described by the SM. Direct constraints on

[6] f^{abc} is given by $[T^a, T^b] = i f^{abc} T^c$.

mass of ν_e come from experiments with tritium β decay. For the electron neutrino the mass should be $m_{\nu_e} < 1.1$ eV [29]. From the CMB it is derived that the sum of all the neutrino masses is at most approximately 0.12 eV [30].

Gauge coupling unification

A grand unified theory (GUT) is a theory where the weak, strong and electromagnetic force can be described by the same force. Finding such a theory means there is just one gauge symmetry, such that the SM gauge symmetries are grouped into a higher gauge symmetry that is broken at a higher energy scale. A theory described by one single gauge symmetry is inspired by the unification of the electromagnetic and the weak forces into the electroweak interaction. The challenge is thus to unify the electroweak and the strong force. Gauge symmetries that contain the SM symmetries are Lie groups such as $SU(5)$ and $SO(10)$. Most of these symmetry groups predict the decay of the proton with a half-life below 10^{35} years [31].

The energy scale where the three forces merge is called the GUT scale, $\Lambda_{\text{GUT}} \approx 10^{16}$ GeV. In the SM the strength of couplings of the forces becomes similar at this scale, but does not completely coincide.

Hierarchy problem

The hierarchy or naturalness problem is due to quantum corrections to the Higgs mass. A spin-0 particle mass, like the Higgs mass, is not protected by any symmetry, unlike massive spin-1 and spin-$\frac{1}{2}$ particles, which are protected by broken gauge and chiral symmetries, respectively. A massive spin-0 particle couples to all virtual particles present in the vacuum, where the quantum corrections to the Higgs mass arise from its coupling to these particles, G_f,

$$\delta m_h^2 \sim -\frac{G_f^2}{16\pi^2}\Lambda^2 + \mathscr{O}\ln(\Lambda). \tag{1.26}$$

The divergencies caused by the quantum corrections have to cancel out to give the Higgs its physical mass of 125 GeV. In order to regularise the divergencies there is a cut off scale, Λ. For the SM the cut off scale can be set to the Planck scale, where $\Lambda_{\text{Planck}} \approx 10^{19}$ GeV.[7] In order for the divergencies to cancel at the Planck scale, the SM parameters would have to be fine tuned through 17 orders of magnitude, which make the SM unnatural.

[7] The Planck scale is where gravity would have the same strength as the strong and electroweak forces, and within the SM there is no new physics up to this scale.

1.2 Standard Model of Cosmology

The Λ-CDM model is a model that provides a good description of the universe assuming general relativity is correct on cosmological scales. The model consists of the big bang model, formulated in the 1920s, complemented by the theory of inflation, formulated in the early 1980s. Λ-CDM is referred to as the Standard Model of Cosmology.

In the Λ-CDM model the universe is expanding and its expansion is accelerating. The universe expands because of dark energy, which is the source of Einstein's cosmological constant Λ. Matter comes in two forms in the model, DM and baryonic matter. DM does not interact with light as the name suggests, and therefore it does not interact with the electromagnetic force. Also DM should be a stable particle to explain the DM thermal relic abundance in the universe. The thermal relic abundance is present due to a DM freeze out which occurred when the expansion of the universe became too fast for DM to annihilate. The chronology of the universe after the big bang as predicted by Λ-CDM is illustrated in Figure 1.4. The decoupling of photons is the furthest possible moment back in time to probe the early universe. Measuring the Cosmic Microwave Background (CMB) gives information on the structure of the early universe. To further explore hotter epochs will require the challenging detection of the cosmic neutrino background or gravitational waves.

The composition of the energy density in the universe is measured from the CMB by the Planck Collaboration amongst others. The measurement shows that the dark energy density is 68.5% and the matter density is 31.5%, of which 26.5% is DM and 4.93% is ordinary baryonic matter [30].[8] Although baryonic matter is described within the SM as composite particles consisting of quarks, dark energy and DM are not described within the SM. Besides the evidence for DM from the CMB, there are several more cases of evidence for DM which will be mentioned in this section.

Velocity dispersions

Dark matter was first mentioned by Zwicky in 1933 when studying the redshifts of the Coma cluster [33]. Normally the mass of the Coma cluster would be calculated from the product of the number of observed galaxies in a cluster, 800 for the Coma cluster, and the average mass of a galaxy, 10^9 solar masses as suggested by Hubble, resulting in $M_{\text{Coma}}^{\text{luminous}} \approx 1.6 \cdot 10^{42}$ kg. However, the mass of the Coma cluster can also be calculated from the virial theorem using

[8] From Planck 2018 polarisation (TE,EE+lowE) + lensing data. Planck 2018 6-parameter fit to flat Λ-CDM cosmology.

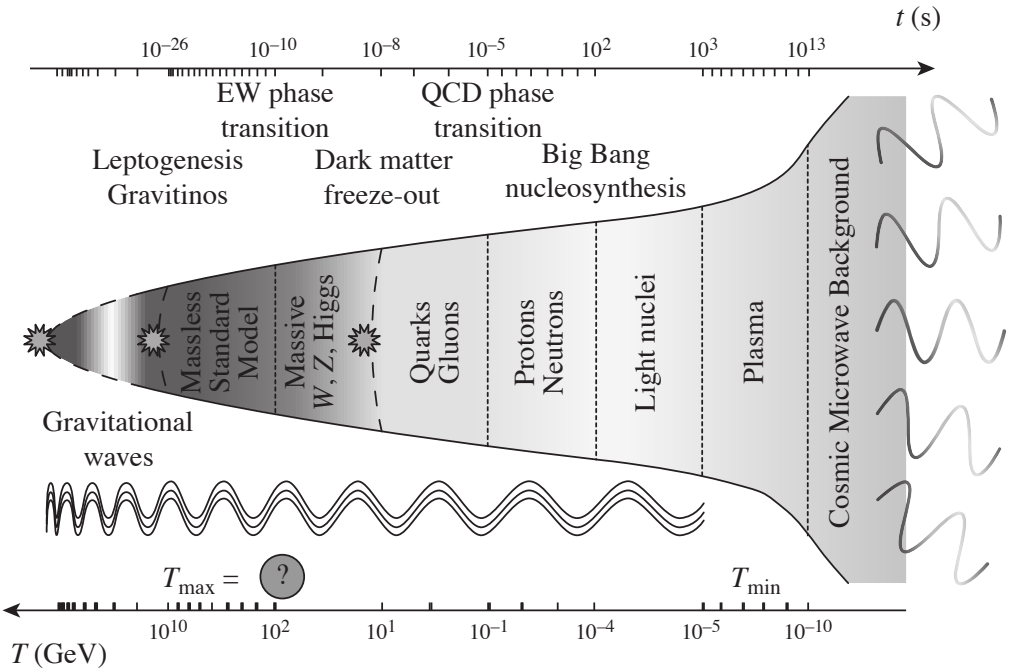

Fig. 1.4: Chronology of the early universe after the big bang [32]. The top scale illustrates the time after the big bang and the bottom scale the corresponding temperature after inflation. At $t = 0$ the electroweak symmetry of the SM is still unbroken and as a result particles are massless. The gauge bosons then acquire their mass through electroweak symmetry breaking, and the fermions acquire their mass through the Yukawa coupling with the Higgs field. DM freezes out causing a thermal relic abundance of DM when the expansion of the universe becomes too fast for DM to annihilate. The QCD phase transition occurs when quarks and gluons are bound in colourless hadrons due to confinement, after which light nuclei begin to form. The universe is then still an ionised opaque plasma due to its high temperature. When the temperature drops below the hydrogen ionisation energy, protons and electrons are combined, leading to the decoupling of baryons and photons. The decoupling of photons causes the mean free path of the photons to be equal to size of the universe, these primordial photons result in the Cosmic Microwave Background (CMB).

the velocity dispersion of the objects, σ, measured from the doppler width in the spectral lines.[9]

For a system with potential energy $V(r) = a/r$, where r is the distance between the objects, the virial theorem takes the form

$$2\langle T\rangle = -\langle V_{\mathrm{TOT}}\rangle. \tag{1.27}$$

Taking the kinetic energy per object as $T \sim \sigma^2$, and the potential energy as $V \sim \frac{GM}{R}$, the virial mass can be calculated from

$$M \approx \frac{R\sigma^2}{G}. \tag{1.28}$$

For the Coma cluster the observed average velocity dispersion is approximately 1000 km/s and R is around 10^6 light-years [34], which results in $M^{\mathrm{virial}}_{\mathrm{Coma}} \approx 1.4 \cdot 10^{44}$ kg.

The observed mass obtained through the virial theorem is in discrepancy with the mass obtained through counting the luminous objects, where $M^{\mathrm{virial}}_{\mathrm{Coma}}/M^{\mathrm{luminous}}_{\mathrm{Coma}} \approx 100$. As numerous approximations have been made, in addition to the approximate nature of the definitions, the obtained ratio is only accurate to estimate the order of magnitude. The velocity dispersions of the Coma cluster were the first evidence for DM, where extra mass was observed through the virial theorem which is not accounted for by the mass of luminous objects.

Rotational curves of galaxies

Rotation curves of galaxies are the rotational velocity of the stars and gas in a galaxy as a function of their distance from the galactic centre. The rotational velocity can be calculated from spectroscopic observations using the doppler shift to measure the relative motion of objects. In Figure 1.5 the rotational curve of the Andromeda Nebula (M31) is presented as measured by Rubin and Ford in 1970. The mass distribution of galaxies can be inferred from the rotation curves by setting the centripetal force equal to the gravitational force,

$$v = \sqrt{\frac{GM}{r}}. \tag{1.29}$$

The Andromeda Nebula is expected to have lower rotational velocities when moving further away from the galactic centre, since there is less luminous matter further away from the centre. Instead the rotation curve flattens at larger distance from the centre. The larger

[9] The virial mass and radius are generally defined for the radius at which the velocity dispersion is a maximum, where $M_{vir} \approx \frac{R_{vir}\sigma^2_{max}}{G}$.

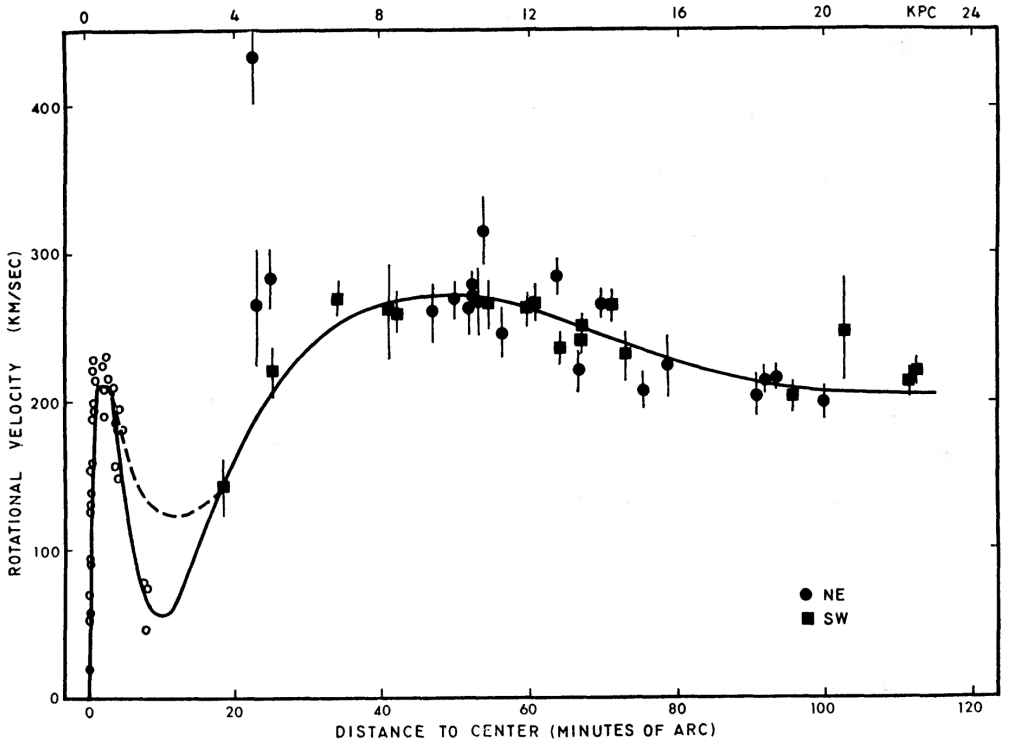

Fig. 1.5: Rotational velocity curve for the Andromeda Nebula (M31) as a function of distance from the centre. The solid curve is the adopted rotation curve, where for R < 12' the curve is fifth order polynomial and for R > 12' the curve is fourth order polynomial required to remain approximately flat near R = 120'. The dashed curve is a second rotation curve with higher inner minimum. NE refers to the north east axis and SW to the south west axis [35].

than expected rotational velocities outward from the centre of the galactic corresponds to a requirement for more mass at the boundaries of galaxies, another piece of evidence for DM.

Gravitational lensing

In general relativity space-time is curved by massive objects, causing the trajectory of photons to bend when travelling through a massive galaxy cluster. The bending of the photons resembles light getting refracted by a lens, only now the lens is a massive object, which is why the effect is known as gravitational lensing. The mass of a cluster can be determined from the amount of gravitational lensing. Again this can be compared to the mass expected from the luminous objects, where the same sort of discrepancy is found. Luminous matter is not sufficient to explain the mass of clusters [36].

Structure formation in the universe

Much of the current understanding of the influence of DM in structure formation in the universe is based on computer simulations. First results demonstrated that galaxies are found to be unstable if not surrounded by a halo of DM [37]. Later the formation and evolution of cosmological structures in an expanding universe were simulated. With the increase in computing power and the improvement of numerical techniques large simulations became possible [38, 39].

When simulating cosmological structures the initial velocity distribution of the dark matter particles requires cold DM, meaning that the velocity of the DM is slow compared to the speed of light [40–42]. When hot DM is used, with relativistic velocities, the growth of small structures is suppressed [43, 44]. Cold DM allows the formation of very low mass halos in the early universe, roughly in the range of of $\sim 10^{-3}$ to $\sim 10^{-9}\ M_{\odot}$. The low mass halos combine gradually with one another building up larger DM structures.

Another requirement for the purpose of structure formation is that the DM particles need to be collisionless, meaning the interaction cross-section is so low that collisions between particles have no significant effect on the system [34].

When comparing the simulations to measurements of structures of the actual universe, redshift surveys are used, where the redshift of astronomical objects is measured in a section of the sky. The redshift can be used to estimate the distance to the astronomical objects using Hubble's law, where a combination of the redshifts with the angular position of the measurements allows to construct a 3D map. The first CfA survey [45] is a map of around 2,200 galaxies, and revealed the first indications of the distribution of matter on the largest scales. Later this was extended to the CfA2 redshift survey [46] which contains about 15,000 galaxies. More recently the Sloan Digital Sky Survey [47] mapped approximately 800,000 galaxies.

1.2.1 Dark matter requirements

After having described the Λ-CDM model a DM particle candidate which fulfils the requirements of the model can be postulated, where DM

- is gravitationally interacting at cosmological scales,
- does not interact electromagnetically,
- has the correct relic density: $\Omega_c h^2 = 0.12$ [30],
- is cold,

- is a stable particle,
- is collisionless and
- is non-baryonic.[10]

The only SM particle that comes close to the requirements are neutrinos. Neutrinos are long-lived, non-baryonic, dissipationless and collisionless, however the problem is neutrinos are not cold. Neutrinos are light particles with a mass of $\lesssim 1.1$ eV, and travel close to the speed of light, preventing the structure formation of galaxies.

Under the assumption that a DM particle is a particle beyond the SM, and that DM interacts with the SM, the measured relic density by the Planck collaboration is a result of DM annihilation into SM particles in the early universe. The DM annihilation in the early universe is described by

$$\frac{\mathrm{d}n_\chi}{\mathrm{d}t} = -3Hn_\chi - \langle\sigma v\rangle(n_\chi^2 - n_{\chi,\mathrm{eq}}^2), \tag{1.30}$$

where $n_{\chi,\mathrm{eq}}$ is the DM density at thermal equilibrium. The DM density, n_χ, is determined by the competition of the expansion of the universe, which occurs with the rate H, and DM annihilation. The thermally averaged annihilation cross-section, $\langle\sigma v\rangle$, accounts for DM annihilation and coannihilation, where v is the relative velocity between the annihilating particles. From the DM relic density, $\Omega_c h^2 = 0.12$, the annihilation cross-section of DM can be calculated. Stable DM particles must self-annihilate with a cross-section in the order of $\langle\sigma v\rangle \sim 10^{-26}$ cm^3/s [34].[11] The annihilation cross-section suggests a DM particle with a mass in the MeV-TeV range and interactions that are mediated by the exchange of electroweak-scale particles.

The particles that fit this description are labeled Weakly Interacting Massive Particles (WIMPs). A theory beyond the SM that provides such a DM candidate is supersymmetry, providing a DM candidate in the form of the lightest neutralino $\tilde{\chi}_1^0$, which will be described in the next chapter.

[10] DM technically could be baryonic, in the form of a MACHOs, however there is a consensus today that MACHOs do not constitute a large fraction of the DM [34].

[11] Although the value can be different if the expansion rate of the universe before DM decoupling is not behaving as expected from general relativity.

Chapter 2

Supersymmetry

The Standard Model (SM) and its associated Higgs mechanism of electroweak symmetry breaking rely on the principle of symmetries, where internal symmetries are generated through the Lie groups $SU(3) \times SU(2) \times U(1)$. Supersymmetry is the combination of the internal symmetries of the SM with external spacetime symmetries [48]. In the SM there are fermionic fields and bosonic fields which behave differently due to the Pauli-exclusion principle, where two identical fermions cannot occupy the same state. The Coleman-Mandula theorem proves that combining the internal symmetries of the SM with spacetime symmetries is not possible using only the bosonic charges from the SM [49]. In order to combine the symmetries, the theory needs to be extended to also include fermionic charges [50]. Supersymmetry establishes a relationship between bosons and fermions by transforming their spin representations [51–54]. Combining the boson and fermion fields into a single algebra is done by supersymmetry through a symmetry transformation via spin-$\frac{1}{2}$ charges generated by Q_α,

$$Q_a|J>=|J\pm\frac{1}{2}> \tag{2.1}$$

where Q_α is a spinor.[1] The anticommutator of the Q_α spinors contain the Pauli spin matrices, σ, and the conserved Lorentz vector, P_μ,

$$\{Q_\alpha, Q_\beta\} = 2\sigma^\mu_{\alpha\beta} P_\mu, \tag{2.2}$$

where $\sigma_\mu = (1, \sigma)$ is a spinor. Since Q_α is the symmetry generator it commutes with the Hamiltonian, $[Q_\alpha, H] = 0$. The anticommutator also commutes with the Hamiltonian, $[\{Q_\alpha, Q_\beta\}, H] = 0$. A fermion can now be transformed into a boson and vice-versa through

[1] The spinor is actually Q^N_a. However, $N = 1$ supersymmetric theories are considered here. $N > 1$ supersymmetric theories also include a scalar charge Z in the anticommutator.

a transformation operator on supermultiplets containing the helicity states,

$$\text{Chiral}: \begin{pmatrix} \frac{1}{2} \\ 0 \end{pmatrix} \qquad \text{Higgs}: \begin{pmatrix} 0 \\ \frac{1}{2} \end{pmatrix} \qquad \text{Gauge}: \begin{pmatrix} 1 \\ \frac{1}{2} \end{pmatrix}, \tag{2.3}$$

where the SM particles are the top row, and the superpartners are the bottom row.[2]

The Lagrangian containing free fermions and bosons as well as interactions takes the form

$$\mathscr{L} = \underbrace{\partial_\mu \phi^* \partial^\mu \phi + i\psi^\dagger \bar{\sigma} \cdot \partial \psi}_{\text{Kinetic term fermions and bosons}} \underbrace{+F^\dagger F + \left(F \frac{\partial W}{\partial \phi} - \frac{1}{2} \phi^T C \phi \frac{\partial^2 W}{\partial \phi^2} + \text{h.c.} \right)}_{\text{Interactions}}, \tag{2.4}$$

where spinors are used, $\sigma_\mu = (1, \sigma)$ and $\bar{\sigma_\mu} = (1, -\sigma)$, and W is the superpotential. In many supersymmetric theories an additional symmetry called R-parity is applied in order to protect the theory from allowing the proton to decay,

$$P_R = (-1)^{2s+3B+L}, \tag{2.5}$$

where s is the spin of the particle, and B and L are the particle's baryon number and lepton number, respectively. Assuming R-parity conservation the superpotential W is given by[3]

$$W = \lambda_d Q D^C H_d + \lambda_l L E^C H_d + \lambda_u Q U^C H_u + \mu H_u H_d. \tag{2.6}$$

Corresponding to the fermion fields described in Equation 1.3, Q and L are supermultiplets of the left handed doublets, and D^C, U^C and E^C are the supermultiplets containing the right handed singlets. The coupling, λ, corresponds to the Yukawa couplings of the SM. H_u and H_d are two Higgs doublets, with opposite hypercharge in order to give masses to all the matter fermions, and μ is the Higgs mass parameter.

Higgs doublet

In a supersymmetric theory the Higgs sector needs to be extended by adding another Higgs doublet, resulting in doublets H_u and H_d. The extra Higgs doublet is needed since two types of Higgs fields are required to give mass to the up and down-type fermions. Each Higgs doublet has four degrees of freedom, as demonstrated before in Equation 1.10. As a result

[2] Local supersymmetry naturally implies gravity with two gauge fields, the graviton G and the gravitino $\tilde{G}$. The gravity supermultiplet is not included here.

[3] There is also a R-parity violating superpotential given by $W_{\text{RpV}} = \lambda L L E^C + \lambda' Q D^C L + \lambda'' U^C D^C D^C$.

of the added Higgs doublet there are now eight degrees of freedom. Due to electroweak symmetry breaking three degrees of freedom are required to give mass to the $W^{\pm}$ and Z boson, and consequently the Higgs sector needs to be extended to five observable Higgs particles. The neutral CP-even SM Higgs, h^0, a heavier CP-even Higgs, H^0, a neutral CP-odd Higgs, A^0, and two charged Higgses, $H^{\pm}$.

Just as described in Section 1.1, the neutral components of the doublet acquire a vacuum expectation value. Since there are two Higgs doublets, both ϕ_u^0 and ϕ_d^0 acquire a vacuum expectation value called v_u and v_d, which are related by $v^2 = v_u^2 + v_d^2$ and $\tan\beta = v_u/v_d$.

2.1 Soft supersymmetry breaking

Superpartners with the same mass as their SM equivalent, so for example $m_{\tilde{e}} = m_e$, have not been found. As a consequence supersymmetry must be a broken symmetry. The mechanism of supersymmetry breaking is expected to occur at an energy scale higher than the electroweak scale and perhaps as a result of a mechanism of a more complete theory that also includes gravity. However, since the origin of the supersymmetry breaking is not known, a phenomenological approach can be used to parametrise the mechanism by explicitly adding operators to the supersymmetric Lagrangian presented in Equation 2.4 [55],

$$\mathscr{L}_{\text{soft}} = \underbrace{m_{0i}^2|\phi_i|^2}_{\text{scalar masses}} + \underbrace{\frac{1}{2}M_a\tilde{V}_a^T C\tilde{V}_a}_{\text{gaugino masses}} + \underbrace{A_\lambda\lambda\phi^3 + B_\mu\mu\phi^2}_{\text{trilinear and bilinear scalar interactions}} . \tag{2.7}$$

The supersymmetric model with the added soft supersymmetry breaking terms is referred to as the Minimal Supersymmetric Standard Model (MSSM). By including $\mathscr{L}_{\text{soft}}$ the symmetry of the supersymmetric Lagrangian is broken, however a large number of unknown parameters has been introduced. The MSSM has around $\mathscr{O}(100)$ parameters, when considering that the mass terms include matrices involving all three generations. In the Constrained MSSM (CMSSM) the amount of parameters is reduced to five by assuming that the supersymmetry breaking parameters are universal at a higher energy scale such that

$$m_{0i}^2 \equiv m_0^2, \qquad M_a \equiv m_{1/2}, \qquad A_\lambda \equiv A, \qquad B_\mu \equiv B \rightarrow (\text{sign}(\mu), \tan\beta). \tag{2.8}$$

If universality is assumed squark masses are taken as degenerate, however, in the mass term of the squarks there is also a term containing the mass of the partner quark from the SM. In the calculation of the stop mass there is thus also the contribution from the SM top, which has a much larger mass than the other quarks. As a result the stop mass is often

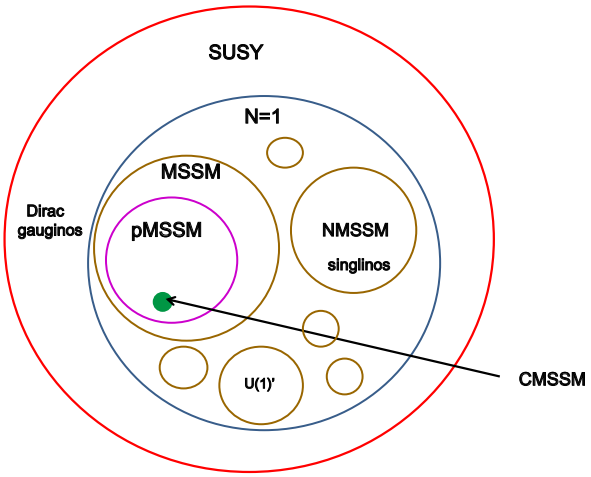

Fig. 2.1: An illustration of the parameter space of supersymmetry [58]. The models discussed in this thesis are $N = 1$ supersymmetry where the soft super symmetry breaking is described by the MSSM. The parameter space of the pMSSM is visualised with its 19 free parameters, as well as its subset, the CMSSM, with 5 free parameters.

taken as a separate parameter, while the rest of the squark masses are treated universally, and is often taken as lighter than the squarks of the first two generations [56]. The same argument holds for the sbottom mass. Still, universality for the squark mass terms m_{0i}^2 is motivated by flavour-changing neutral-current constraints (FCNC) [57], since FCNC currents are suppressed when the differences between masses of different flavour of scalar quarks and fermions, Δm_{0i}^2, are small.

In the phenomenological MSSM (pMSSM) the first and second generation of squarks are assumed degenerate, as well as the first and second generation of sleptons, whilst the third generation of squarks and sleptons are taken as separate parameters. The gaugino masses are also not assumed to be degenerate, resulting in bino (M_1), wino (M_2) and gluino (M_3) mass parameters. In the pMSSM the amount of parameters of the MSSM is reduced to 19. This is still a large parameter space making interpretation of searches within the pMSSM challenging.

2.1.1 Gaugino mixing

The superpartners of the SM electroweak bosons B, W^a and of the Higgs bosons, are the bino $\tilde{B}$, wino $\tilde{W}^a$, and higgsinos $\tilde{H}_{u,d}^{0,\pm}$. The supersymmetry breaking mass parameter M_1 corresponds to the bino, M_2 to the wino, and μ to the higgsinos. The superpartners mix into mass eigenstates called gauginos decomposed into four neutralinos $\tilde{\chi}_{1,2,3,4}^0$ and four charginos $\tilde{\chi}_{1,2}^{\pm}$. The $\tilde{B}$, $\tilde{W}^0$, $\tilde{H}_u$ and $\tilde{H}_d$ mix into the neutralinos, where mixing in the $(\tilde{W}^3, \tilde{B}, \tilde{H}_d^0, \tilde{H}_u^0)$

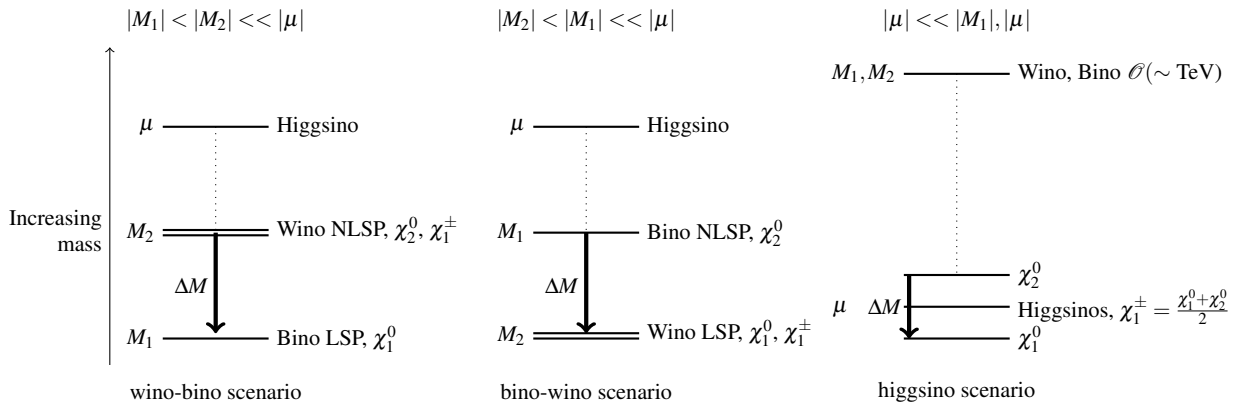

Fig. 2.2: Three possible mass spectra of the supersymmetry breaking parameters, M_1, M_2 and μ, corresponding to the bino, wino and higgsino mass respectively. The relative values of the parameters describe the gaugino mixing which result in the $\tilde{\chi}_1^0$, $\tilde{\chi}_2^0$ and $\tilde{\chi}_1^\pm$. The scenario used in this thesis is the wino-bino scenario; the next-to-lightest supersymmetric particle (NLSP) is a wino, meaning it is mostly determined by M_2. The lightest supersymmetric particle (LSP) is bino, meaning it is mostly determined by M_1.

basis is given by

$$m_{\chi^0_{1,2,3,4}} = \begin{pmatrix} M_2 & 0 & \frac{-g_2 v_2}{\sqrt{2}} & \frac{g_2 v_1}{\sqrt{2}} \\ 0 & M_1 & \frac{g' v_2}{\sqrt{2}} & \frac{-g' v_1}{\sqrt{2}} \\ \frac{-g_2 v_2}{\sqrt{2}} & \frac{g' v_2}{\sqrt{2}} & 0 & \mu \\ \frac{g_2 v_1}{\sqrt{2}} & \frac{-g' v_1}{\sqrt{2}} & \mu & 0 \end{pmatrix}. \tag{2.9}$$

The $\tilde{W^\pm}$ and $\tilde{H}^\pm$ mix into the charginos, where mixing in the $(\tilde{W}^\pm, \tilde{H}^\pm)$ basis is given by

$$m_{\chi^\pm_{1,2}} = \begin{pmatrix} M_2 & \sqrt{2} m_W \sin\beta \\ \sqrt{2} m_W \cos\beta & \mu \end{pmatrix}. \tag{2.10}$$

The mass hierarchy corresponds to different scenarios in term of mass breaking parameters M_1, M_2 and μ. The scenario used for the analysis presented in this thesis is the wino-bino scenario as can be seen in Figure 2.2, where the next-to-lightest supersymmetric particle (NLSP) is a wino and the lightest supersymmetric particle (LSP) is bino.[4] The wino-bino scenario is also used by the ATLAS Run-1 analyses described in section 2.3. The scenario is able to produce the correct DM relic density and the production cross-sections (shown in figure 2.4) are such that this scenario is accessible for searches at the LHC.[5]

[4] With $m_{\tilde{\chi}_2^0} \times m_{\tilde{\chi}_1^0} > 0$.

[5] Also other scenarios, besides the wino-bino scenario, are able to produce the correct DM relic density.

2.1.2 Particles in supersymmetry

Supersymmetry predicts many new particles by introducing a symmetry transformation between bosons and fermions. The resulting particles can be seen in Figure 2.3, where the SM particles as well as the newly predicted superpartners are shown. The additional symmetry, R-parity, introduced to protect the proton from decaying, is positive for SM particles, $P_R = 1$, while all of their superpartners have negative R-parity, $P_R = -1$.

2.2 Solving shortcomings of the Standard Model

Supersymmetry provides a DM candidate, resolving the discrepancy between the SM and the Lambda Cold Dark Matter (Λ-CDM) model described in Chapter 1. Besides providing a DM candidate supersymmetry also resolves some of the other shortcomings of the SM mentioned in Section 1.1.2. Most aesthetical shortcomings are resolved if superpartners are found at the TeV scale, allowing the unification of the gauge coupling constants and solving the hierarchy problem.

2.2.1 Dark matter candidate

DM in the universe can be explained by a particle as described in Section 1.2.1. Since R-parity is positive for SM particles and negative for superpartners, R-parity ensures that superpartners can only be created or destroyed in pairs. A heavy superpartner can decay into a lighter superpartner, along with any number of SM particles and as a consequence the LSP is stable. In this thesis the LSP is the lightest neutralino, $\tilde{\chi}_1^0$, which only interacts through the weak force and gravity, thus meeting the requirements for a DM candidate.

The remaining requirements are that DM needs to be cold and it needs to have to correct DM relic density. From the experiments performed at the Large Electron-Positron Collider (LEP) it is known that the $\tilde{\chi}_1^0$ has a mass larger than 27 GeV [59], making it massive enough to be non-relativistic and to allow for structure formation of galaxies.[6] In order to obtain supersymmetric models that provide the correct DM relic density, global fits in the supersymmetric parameter space are performed as described in Section 2.4.

Gauge coupling unification

The addition of the superpartners allows for the unification of forces at the energy scale of a Grand Unified Theory (GUT) [60], where $\Lambda_{\text{GUT}} \approx 10^{16}$ GeV. The superpartners solve one

[6] Under the assumptions of degenerate gaugino and degenerate sfermion masses at the unification scale.

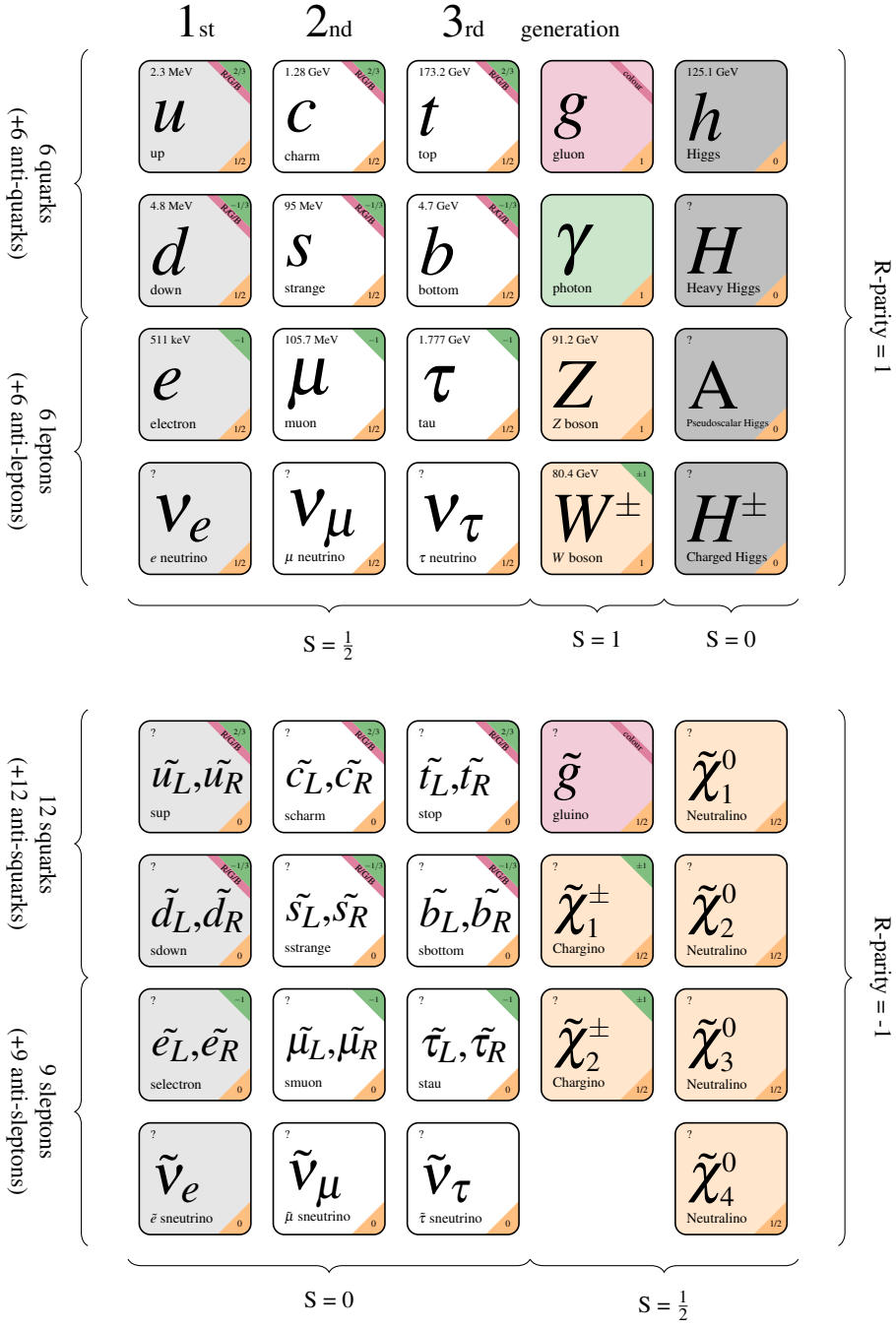

Fig. 2.3: The particle content of supersymmetry. Supersymmetry contains the SM with an additional Higgs doublet, and their superpartners. Each particle and its corresponding properties are visualised in a box. At the top of each box the mass of the particle is shown. At the top right the electric charge of the particle is highlighted in green and the colour charge is highlighted in red. At the bottom right the spin of the particle is highlighted in orange. The SM particles have positive R-parity, $P_R = 1$, and the superpartners have negative R-parity, $P_R = -1$.

of the SM problems, since the introduction of new particles alters the running of the gauge coupling constants. In order to allow for unification, if one assumes universality, the mass of the superpartners needs to be approximately between 100 GeV and 1 TeV [61].

Hierarchy problem

Quantum corrections to the Higgs mass arise from particles in the vacuum coupling to the Higgs as demonstrated in Equation 1.26. Supersymmetry is able to stabilise the weak scale by protecting the Higgs mass with new particles, resolving the hierarchy problem. The superpartners will also couple to the Higgs field and since boson and fermion loop diagrams have opposite signs, it will change the corrections to the Higgs mass to [60],

$$\delta m_h^2 \sim -\frac{G_f^2}{16\pi^2}\Lambda^2 + \frac{G_b^2}{16\pi^2}\Lambda^2 + \mathscr{O}\ln(\Lambda), \tag{2.11}$$

where G_f is the coupling of fermions and G_b is the coupling of bosons. If there are equal number of fermions and bosons and if they have equal couplings, the quadratic divergencies exactly cancel. However, since supersymmetry is a broken symmetry, the particles and superpartners do not have equal couplings. Still $|m_b^2 - m_f^2| \lesssim 1$ TeV will consequently mean that $\delta m_h^2 \lesssim m_h^2$, which will make the quantum corrections to the Higgs mass no longer unnatural.

2.3 Constraints on supersymmetry

Since there are many supersymmetry breaking parameters that determine the supersymmetric model space, there are many possible models to look for. Different experiments are slowly excluding the supersymmetry phase space by putting constraints on supersymmetry. In this section existing constraints will be discussed for supersymmetric models which have the $\tilde{\chi}_1^0$ as LSP.

In the LHC experiments it is possible to pair produce all the different supersymmetric particles depending on their production cross-section, and thus the LHC experiments are able to put constraints on all the superpartners. Since the $\tilde{\chi}_1^0$ is a DM candidate, experiments that look for DM can also put constraints on supersymmetry, through direct DM detection experiments as well as indirect DM detection experiments. Direct detection experiments look for rare interactions of DM via nuclear recoils on earth, while indirect detection experiments look for DM annihilation from areas in the universe with a high expected DM density.

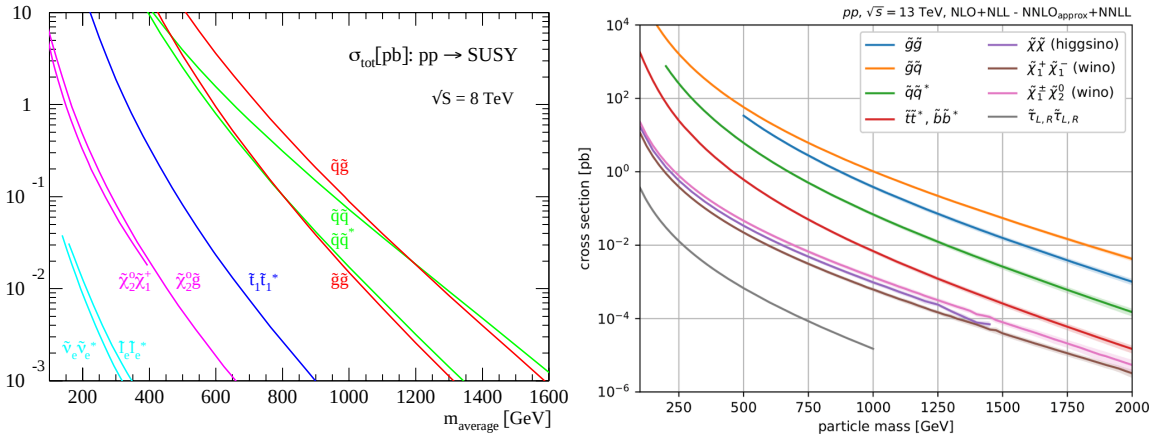

(a) **(b)**

Fig. 2.4: **(a)** Production cross-sections of the superpartners as a function of their mass in proton-proton collisions at Run-1 with a centre-of-mass energy of $\sqrt{s} = 8$ TeV [62]. **(b)** Production cross-sections of the superpartners as a function of their mass in proton-proton collisions at Run-2 with a centre-of-mass energy of $\sqrt{s} = 13$ TeV [63].

2.3.1 LHC Run-1

At the LHC supersymmetric particles are pair produced and subsequently decay into lighter supersymmetric particles and SM particles. The cross-sections for pair production of supersymmetric particles can be seen in Figure 2.4 for the LHC Run-1, with a centre-of-mass energy of $\sqrt{s} = 8$ TeV, and for the LHC Run-2, with a centre-of-mass energy of $\sqrt{s} = 13$ TeV. For Run-1 it can be seen that for a 1 TeV gluino the cross-section is given by $\sigma(\tilde{g}\tilde{g})$= 0.05 pb.[7] For the electroweak pair production of gauginos the same cross-section can be found, $\sigma(\tilde{\chi}_2^0\tilde{\chi}_1^{\pm})$ = 0.05 pb, but for a lower mass of 400 GeV [64]. For Run-2 the pair production cross-section of gauginos increases with about a factor two for a mass of 400 GeV because of the increased centre-of-mass energy. Due to the highest production cross-sections, searches for the strong production of squarks and gluinos are able to exclude up to a high superpartner mass.

Squarks and gluinos will mainly decay into quark and gluon jets and the LSP, $\tilde{\chi}_1^0$. The Run-1 searches for squarks and gluinos are therefore mainly characterised by jets, and, since the LSP does not interact with the detector, by missing energy in the detector. The result of the search performed by ATLAS can be seen in Figure 2.5(a). The interpretation is presented in the CMSSM, where $\tan\beta$, A_0 and the sign of μ are chosen to accommodate the Higgs mass, and the universal scalar and fermion masses at the GUT scale, m_0 and $m_{1/2}$, are varied. From the figure it can be seen that a limit on the gluino mass is obtained of about 1.2 TeV

[7] Resulting in about 1000 events where gluinos are pair produced.

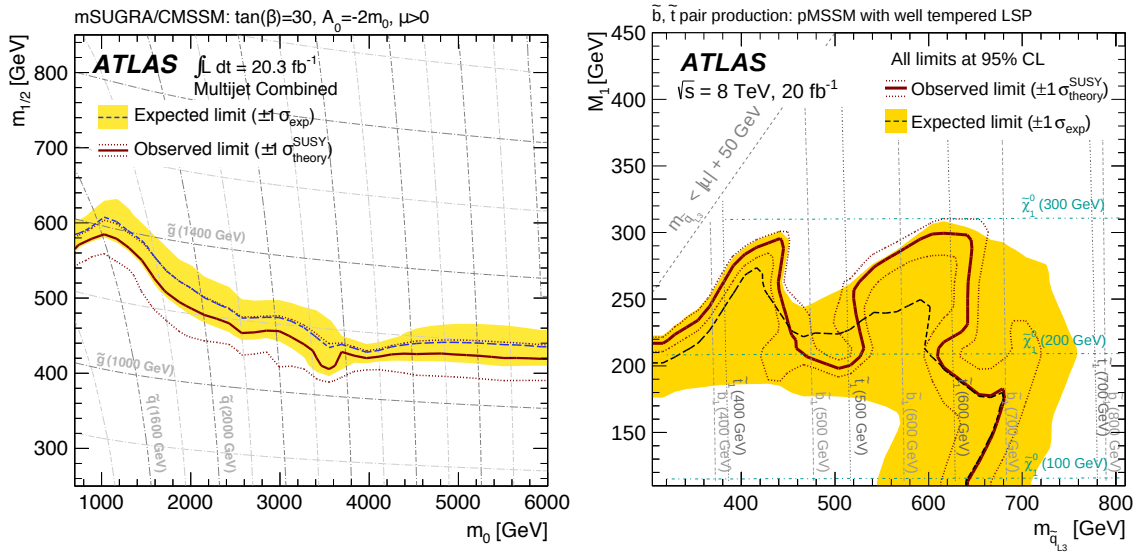

(a) **(b)**

Fig. 2.5: **(a)** The Run-1 exclusion limit at 95% CL for squarks and gluinos in the MSUGRA/CMSSM as a function of $m_{1/2}$ and m_0. The dashed black line indicates the expected limit, and the yellow band indicates the $\pm 1\sigma$ uncertainties. The dashed and dotted grey lines indicate a constant value of the squark and gluino masses [65]. **(b)** The Run-1 exclusion limit at 95% CL for stops and sbottoms in the pMSSM as a function of M_1 and $m_{\tilde{q}_L}$. The $\tilde{\chi}_1^0$ is chosen such that it is able to produce the DM relic density. The dashed black line indicates the expected limit, and the yellow band indicates the $\pm 1\sigma$ uncertainties. The dashed and dotted grey lines indicate a constant value of the stop and sbottom masses, while the dashed light-blue line indicates a constant value of the neutralino mass [67].

[65]. A high limit on the gluino mass excludes a large part of the naturalness region, where supersymmetry is able to make the quantum corrections to the Higgs mass no longer seem unnatural. The gluino mass parameter, M_3, enters in the top squark and gaugino masses through loop corrections, having the general effect to pull the whole natural superpartner mass spectrum up [66].

Still, naturalness predicts a light third-generation squark [68]. If gluinos are too heavy to be produced at the LHC, then stop and sbottom squarks will not result from gluino decay and need to be pair produced. The stop-antistop production cross-section is a 100 times smaller than the gluino pair production cross-section. In stop-antistop production there are multiple decay options, when the stop is lighter than the top there will only be the decay $\tilde{t} \to b\tilde{\chi}_1^{\pm}$, where $\tilde{\chi}_1^{\pm} \to W^{\pm}\tilde{\chi}_1^0$. When the stop is heavier than the top there will also be the decay $\tilde{t} \to t\tilde{\chi}_1^0$. For sbottom quarks a similar limit is obtained assuming $\tilde{b} \to b\tilde{\chi}_1^0$. In Figure 2.5(b) the obtained limit by ATLAS is presented, showing that stop and sbottom squarks have been excluded up to around 600 GeV for $\tilde{\chi}_1^0$ masses around 200 GeV. In both the stop and sbottom searches the assumption is made that $\tilde{\chi}_1^{\pm}$ and $\tilde{\chi}_1^0$ are the only supersymmetric

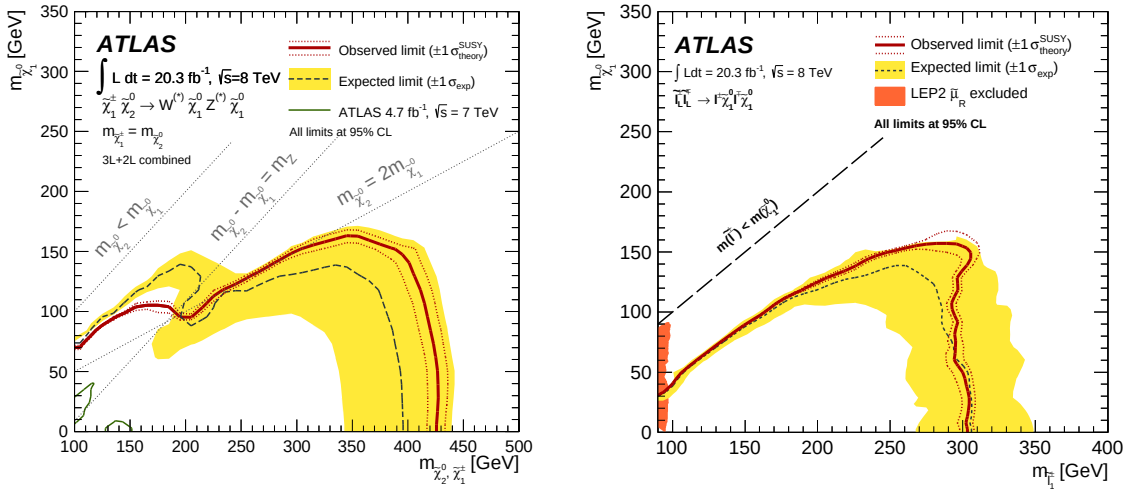

(a) **(b)**

Fig. 2.6: **(a)** The Run-1 exclusion limits at 95% CL for $\tilde{\chi}_1^{\pm}\tilde{\chi}_2^0$ production in the $(\tilde{\chi}_1^{\pm}, \tilde{\chi}_1^0)$ mass plane. The gaugino mixing scenario is the wino-bino scenario. The dashed black line indicates the expected limit and the yellow band indicates the $\pm 1\sigma$ uncertainties. **(b)** The Run-1 exclusion limits at 95% CL for slepton-slepton production in the (slepton, $\tilde{\chi}_1^0$) mass plane. The dashed black line indicates the expected limit and the yellow band indicates the $\pm 1\sigma$ uncertainties [69].

particles lighter than the $\tilde{t}$ and $\tilde{b}$. The limit is not as strong when there is a rich gaugino and slepton spectrum with masses below the $\tilde{t}$ or $\tilde{b}$ mass.

The production cross-section of gauginos, $\tilde{\chi}_2^0\tilde{\chi}_1^{\pm}$ or $\tilde{\chi}_1^{\pm}\tilde{\chi}_1^{\pm}$, is much lower than that of squarks and gluinos [64]. The produced gauginos decay into the LSP and SM particles, $\tilde{\chi}_2^0 \to Z/h\tilde{\chi}_1^0$ and $\tilde{\chi}_1^{\pm} \to W^{\pm}\tilde{\chi}_1^0$. Since the gauginos have a low production cross-section the ATLAS searches use the leptonic decay channel of W and Z in order to discriminate against the SM background, giving rise to between one and four leptons and missing energy from the LSP. In Figure 2.6(a) the limit obtained by ATLAS is presented for the wino-bino scenario. When the mass difference between the $\tilde{\chi}_2^0/\tilde{\chi}_1^{\pm}$ and $\tilde{\chi}_1^0$ is larger than 90 GeV, the W and Z are created on-shell, resulting in hard leptons. In this case the leading lepton should have $p_{\mathrm{T}} > 25$ GeV, and a limit on the $\tilde{\chi}_1^0$ mass up to 150 GeV is obtained. The search becomes more difficult in the scenario where the mass gap between $\tilde{\chi}_2^0/\tilde{\chi}_1^{\pm}$ and $\tilde{\chi}_1^0$ is smaller than 90 GeV, where off-shell W and Z bosons are created, resulting in softer leptons. When the mass gap is larger than 25 GeV, exclusion can still be obtained for a $\tilde{\chi}_1^0$ mass up to 100 GeV. In the more compressed region, where the mass gap between the $\tilde{\chi}_2^0/\tilde{\chi}_1^{\pm}$ and $\tilde{\chi}_1^0$ is less than 25 GeV, the supersymmetric models can not be excluded.

The slepton production cross-section is even smaller; a 100 times smaller than the production cross-section of gauginos of the same mass [64]. From naturalness arguments

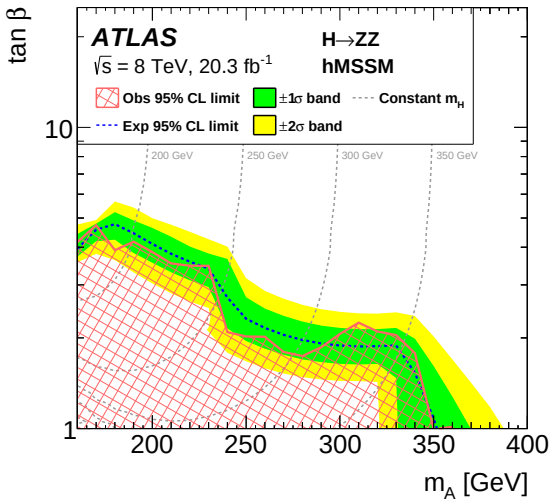

Fig. 2.7: The Run-1 exclusion limits at 95% CL for a heavier CP-even Higgs boson in the hMSSM as a function of the parameters m_A and $\tan\beta$. The value of m_A fully determines the value of m_H. The red hashed area demonstrates the observed exclusion, with the solid red line denoting the edge of the excluded region. The dashed blue line represents the expected exclusion contour and the shaded bands the 1σ and 2σ uncertainties on the expectation. The vertical dashed grey lines indicate contours of constant m_H [70].

sleptons are expected with a mass of around 1 TeV [68], however as can be seen from Figure 2.4 the production cross-section is too low in such a high mass range. As a result it is only possible to search for sleptons with a mass of around 500 GeV. The produced sleptons decay into leptons and the LSP, $\tilde{l}_L^{\pm}\tilde{l}_L^{\pm} \rightarrow l^{\pm}\chi_1^0 l^{\pm}\chi_1^0$. In Figure 2.6(b) the obtained limit by ATLAS is shown, where left handed selectrons and smuons are excluded up to 300 GeV.

Another prediction from supersymmetry is a heavier CP-even Higgs boson, H. By combining $H \rightarrow ZZ \rightarrow \ell\ell\ell\ell, \ell\ell\nu\nu, \ell\ell qq, \nu\nu qq$ the obtained limit by ATLAS is shown in Figure 2.7 [70]. The result is interpreted in the hMSSM, which takes as input the measured Higgs mass value M_h in addition to M_A and $\tan\beta$.[8] The presence of another SM Higgs-like boson is excluded up to 350 GeV for $\tan\beta < 2$.

2.3.2 Direct dark matter detection

In direct detection experiments the aim is to measure the energy released by DM particles when scattering off nuclei in a detector [72]. DM is needed for the structure formation of galaxies, requiring our galaxy, the Milky Way, to have a dark matter halo too, causing DM to

[8]The hMSSM exploits the fact that the dominant corrections to the lightest CP-even Higgs mass and the mixing parameters that enter the Higgs couplings have a common origin and that the dominant corrections stem from the top-quark and its supersymmetric partners, the stops [71].

pass through the Earth. From the expected DM density on earth and the velocity of those DM particles, a limit can be obtained on the cross-section of DM.

One of the direct detection experiments is the Xenon experiment, which looks for rare interactions via nuclear recoils in a liquid xenon target chamber. WIMPs will not interact electromagnetically with the electrons of an atom and will traverse the electron cloud in order to produce a nuclear recoil. The only other particle expected to produce a nuclear recoil is the neutron.[9] Since most of the neutron background is a product of cosmic rays interacting with the atmosphere, the experiment is built underground. The current best limit is from the XENON1T experiment, excluding a spin-independent elastic cross-section above $4.1 \cdot 10^{-47}$ cm^2 for WIMP masses of 30 GeV [73].

The obtained DM-nucleus cross-section can be interpreted in supersymmetric models. In Figure 2.8 the limits are shown for a wino-bino scenario for values of $\tan\beta = 10$ and $M_A = 500$ GeV. The squark, slepton and gluino mass parameters are chosen to be 5 TeV. For $\mu = 750$ GeV direct detection experiments rule out most of the parameter space compatible with the correct thermal relic abundance, however for larger values of $\mu = 2500$ GeV direct detection experiments become ineffective. The larger values of μ decouple the $\tilde{\chi}_1^0$ from the Higgs sector, which results in highly suppressed scattering rates for DM with nuclei [74]. As can be seen in the figure the LHC can still access these supersymmetric models with $\mu = 2500$ GeV.

2.3.3 Indirect dark matter detection

Indirect DM detection experiments look for DM annihilation in the universe. SM particles are created when DM annihilates, causing an expected increased flux of SM particles from galactic and extragalactic regions where the DM density is large. DM can annihilate into γ-rays, which propagate along geodesics and thus point to the origin of the annihilation, as well as into anti-matter, of which an increase suggests DM since anti-matter is sub-leading in space [78]. Interesting areas to look for DM annihilation are in the galactic centre, dwarf spheroidal galaxies, the galactic halo and nearby galaxy clusters.

The Fermi-LAT experiment [79, 77, 80–82] detects γ-rays and is able to provide limits on DM annihilation in the universe. The limits from searches for γ-rays from local dwarf spheroidal galaxies are included in Figure 2.8. Fermi-LAT has observed an excess of γ-rays originating from the galactic centre, which could originate from DM annihilation and can provide constraints on possible supersymmetric models as described in Section 2.4. Experiments that attempt to indirectly detect dark matter through anti-matter are the PAMELA

[9] The neutrino interaction cross-section is too small to be a background at the moment.

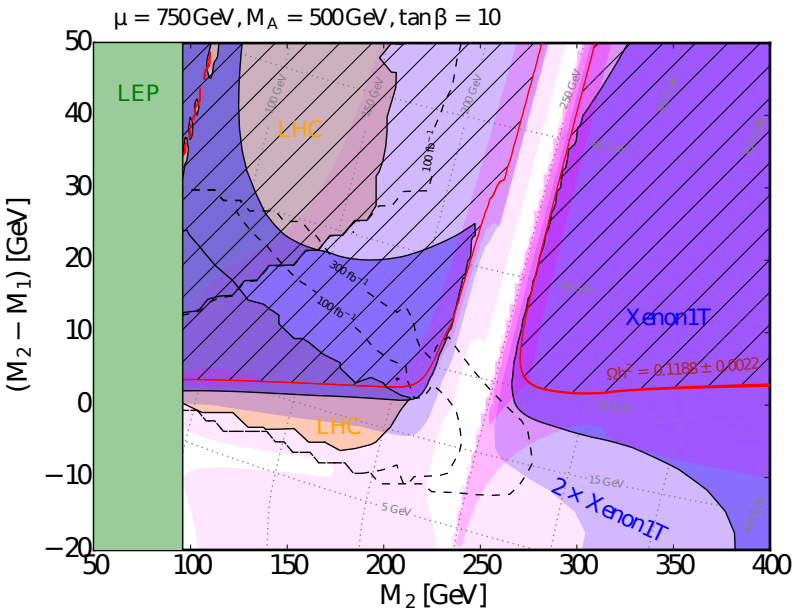

(a)

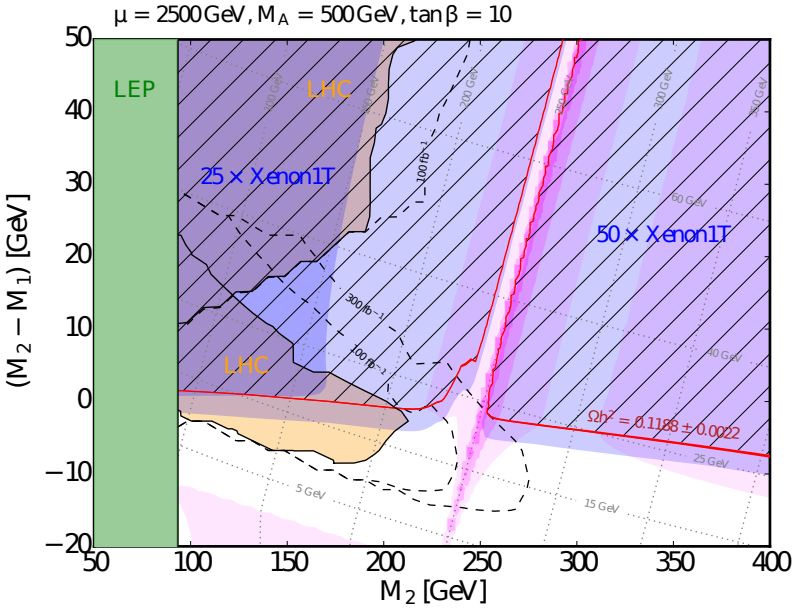

(b)

Fig. 2.8: Comparison of current and projected constraints from the LHC, direct DM detection experiments and indirect DM detection experiments. The gaugino mixing scenario is the wino-bino scenario and the constraints are presented in the (M_2, $M_2 - M_1$) mass plane for **(a)** $\mu = 750$ GeV and **(b)** $\mu = 2500$ GeV. Other chosen parameters are $\tan\beta = 10$ and $M_A = 500$ GeV. The roughly horizontal grey dotted contours give values for the mass splitting, $\delta m = m_{\tilde{\chi}_1^\pm} - m_{\tilde{\chi}_1^0}$, and the roughly vertical contours give values for the DM mass, $m_{\tilde{\chi}_1^0}$. The region that predicts the DM relic density is shown in red. The exclusion limit from the Large Electron-Positron Collider (LEP) on $m_{\tilde{\chi}_1^\pm}$ is shown in green [75]. The orange excluded regions are from the CMS Run-2 search for $\tilde{\chi}_2^0\tilde{\chi}_1^\pm \to W^\pm Z\tilde{\chi}_1^0\tilde{\chi}_1^0$ with 35.9 fb^{-1} [76] and the projected limits for 100 fb^{-1} and 300 fb^{-1} are demonstrated by dashed lines. Current and projected exclusions by the XENON1T DM direct detection experiment are shown as blue shaded regions [73]. Projected limits from DM indirect detection experiments are indicated by the magenta regions, where the current limit is scaled by factors of 10, 100 and 1000, with high to low opacity [77, 74].

satellite [83] and the AMS experiment [84]. The PAMELA and AMS-02 experiment both observed an excess in the positron fraction, which could be interpreted as DM.

Neutrino experiments like IceCube [85, 86] and ANTARES [87] can also measure DM annihilation, where gravitationally trapped DM in the sun can annihilate in the centre, producing a flux of energetic neutrinos.

2.4 Global fits

The constraints on supersymmetry can be used to determine which scenarios of supersymmetry breaking are still possible and favoured. One method to do this is to fit the supersymmetry breaking parameters to measurements from different experiments. Such a fit is called a global fit, as it combines all the global constraints according to which a favoured supersymmetric model should behave. Supersymmetric models need to be able to reproduce the thermal relic abundance of DM in the universe, be coherent with the SM, and agree with measurements from b-physics, Higgs measurements and electroweak precision measurements.

The global fit resulting from the MasterCode collaboration [88] is shown in Figure 2.9(a). The fit includes constraints from the DM density, ATLAS and CMS Run-1 supersymmetry searches, Higgs mass and rate measurements, heavy Higgs exclusion bounds, the measurements of BR($B_s \to \mu^+\mu^-$) by LHCb and CMS as well as other B-physics observables, electroweak precision observables, the anomalous magnetic moment of the muon, and the XENON100 and LUX DM searches [88, 89]. The fit is performed in the pMSSM-10, in which the following 10 parameters are considered: M_1, M_2, M_3, $m_{\tilde{q}1,2}$, $m_{\tilde{q}3}$, $m_{\tilde{l}}$, A, μ, M_A and $\tan\beta$. The region favoured by the fit is where the mass difference between the $\tilde{\chi}_1^0$ and the $\tilde{\chi}_1^\pm$ is small. In Section 2.3 it is explained that this region is difficult to analyse since the supersymmetric particles decay into off-shell W and Z bosons, which result in soft leptons. As a consequence this region is not well constrained by the LHC Run-1 searches. It can be seen in Figure 2.9(a) that nearly the same fit result is obtained when excluding the constraints from the LHC Run-1 results.

A similar result is obtained by a global fit performed by the Gambit collaboration [90], pointing to the same region as MasterCode as can be seen in Figure 2.9(b). The fit uses mostly the same constraining observables as MasterCode, but also includes observables from indirect DM experiments such as Fermi-LAT and IceCube [90]. The fit is performed in the pMSSM-7, which has 7 free parameters: M_2, A_{u3}, A_{d3}, $m^2_{\tilde{f}}$, $m^2_{H_u}$, $m^2_{H_d}$, $\tan\beta$. The sign of μ is fixed to be positive. Gambit identifies regions of the pMSSM-7 that exhibit co-annihilation with the DM candidate, $\tilde{\chi}_1^0$, to obtain the correct dark matter density. Co-annihilation of DM

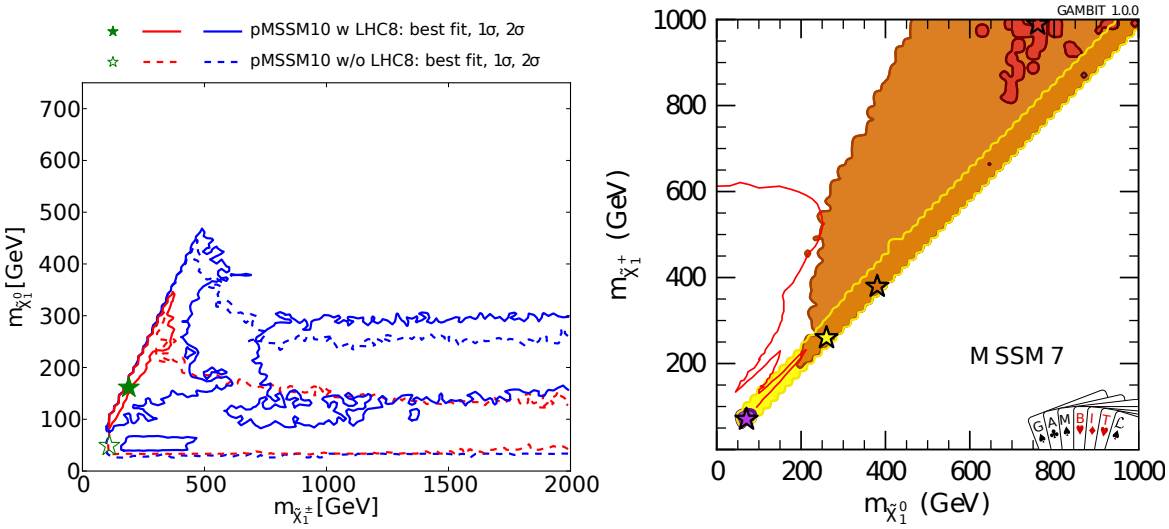

(a) **(b)**

Fig. 2.9: **(a)** The MasterCode profile likelihood region in the $(\tilde{\chi}_1^\pm, \tilde{\chi}_1^0)$ mass plane. Stars indicate the best fit. The red denote the 1σ level contours and the blue denote 2σ level contours. The solid and dashed contours indicate if the constraints from the LHC Run-1 are applied [88]. **(b)** The Gambit 95% CL profile likelihood region in the $(\tilde{\chi}_1^0, \tilde{\chi}_1^\pm)$ mass plane. Stars indicate the best fit. Superimposed in red is the CMS Run-2 search for $\tilde{\chi}_2^0\tilde{\chi}_1^\pm \to W^\pm Z\tilde{\chi}_1^0\tilde{\chi}_1^0$ with 35.9 fb^{-1} [76]. The regions are coloured according to mechanisms by which the relic density constraint is satisfied, where yellow corresponds to $\chi_1^\pm$ co-annihilation, red corresponds to $\tilde{t}_1$ co-annihalation, orange corresponds to resonant annihilation through a A/H funnel and purple corresponds to resonant annihilation through a h/Z funnel [90].

can occur with $\tilde{\chi}_1^\pm$ and $\tilde{t}_1$, as well as models that undergo resonant annihilation via both light Higgs funnels, h/Z, and heavy Higgs funnels, A/H.

A fit performed in the pMSSM-15 [91] also points in the direction of the MasterCode and Gambit global fits, where a 130 GeV bino-like $\tilde{\chi}_1^0$ is favoured. The best fit points to a supersymmetric model with a squark mass of 2.3 TeV, a gluino mass of 2.1 TeV. Another global fit of the pMSSM-19 [92, 93], in which all 19 parameters of the pMSSM are considered, is performed containing the Galactic centre excess observed by Fermi-LAT. There are supersymmetric models that provide a satisfactory explanation of the excess of γ-rays from the Galactic centre, assuming that it is produced by the annihilation of $\tilde{\chi}_1^0$. The fit also contains similar observables as MasterCode and Gambit including the DM relic density, results from accelerator searches, indirect DM detection results from IceCube, Super-Kamiokande and ANTARES, and direct DM detection results from LUX. The result of the fit corresponds to a $\tilde{\chi}_1^0$ with mass $\in [80, 100]$ GeV annihilating to WW, or mass $\in [180, 200]$ GeV annihilating to $t\bar{t}$.

As a result from the global fits, and the increased cross-section for $\tilde{\chi}_1^{\pm}\tilde{\chi}_2^0$ pair production in Run-2, as illustrated in Figure 2.4(b), a search for supersymmetric models with a $\tilde{\chi}_1^0$ in mass range [10,300] and a $\tilde{\chi}_1^{\pm}/\tilde{\chi}_2^0$ in mass range [100,350] GeV through $\tilde{\chi}_1^{\pm}\tilde{\chi}_2^0$ production is motivated for the wino-bino scenario. The analysis for this mass range is performed at the LHC with the ATLAS detector for the full Run-2 dataset of 139 fb^{-1} at a centre-of-mass energy of $\sqrt{s} = 13$ TeV. The analysis is presented in Part III of this thesis. In order to be able to interpret the results, the ATLAS detector will be discussed first in Part II.

Part II

The ATLAS experiment

Chapter 3

The LHC and the ATLAS detector

The Large Hadron Collider (LHC) is a proton-proton (p-p) accelerator and collider with a centre of mass energy of 13 TeV. Particles get created out of the collision energy, such as the heavier second and third generation fermions of the Standard Model (SM), the heavy gauge bosons $W^{\pm}$ and Z, and the recently discovered Higgs boson. The production and decays of these particles allow the SM to be studied, as well as look for physics beyond the SM, such as supersymmetry. The higher the collision energy of the collider, the more particles it is kinematically able to produce.

The schedule for the LHC is shown in Figure 3.1. During Run-1 of the LHC, from 2009 until 2013, data-taking at centre of mass energies of 7 and 8 TeV allowed the Higgs boson to be discovered. During Run-2 of the LHC, from 2015 until 2018, the centre of mass energy was 13 TeV. What is next to discover for the LHC at Run-2 and after is to be found out: in terms of actual production of new particles in an accelerator, the LHC energy frontier is the place to be.

At the LHC the protons are made to collide at four interaction points as can be seen in Figure 3.2. At each interaction point there is a detector to study the collisions. The detectors at the interaction points are ATLAS (A Toroidal LHC ApparatuS) [95], CMS (Compact Muon Solenoid) [96], LHCb (Large Hadron Collider beauty) [97] and ALICE (A Large Ion Collider Experiment) [98]. ATLAS and CMS are general purpose detectors, made to discover the Higgs boson, study the SM and look for physics beyond the SM. LHCb investigates the asymmetry between matter and antimatter by studying CP violation and rare decays of hadrons containing b and c quarks. Also extensions of the SM are studied by looking for effects of new particles in predicted processes. ALICE is optimised to study the Quark-Gluon plasma created through heavy-ion (Pb-Pb nuclei) collisions.

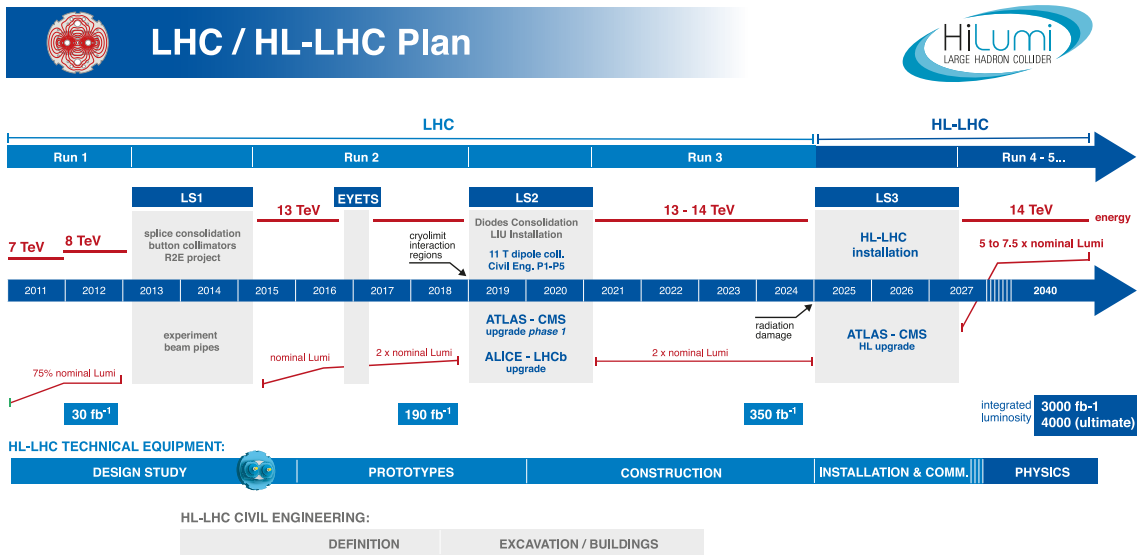

Fig. 3.1: The time schedule for the LHC. Run-1 took place from 2009 until 2013. During Run-1 the LHC was operated at centre of mass energies of 7 and 8 TeV. The analysis described in this thesis uses data from Run-2, which took place from 2015 until 2018. During Run-2 the LHC was operated at a centre of mass energy of 13 TeV and a dataset of 139 fb^{-1} was collected. In the future Run-3 will take place, which will run the LHC under similar conditions as Run-2. Around 2027 the LHC will increase its luminosity, which is referred to as the High Luminosity LHC (HL-LHC), and a dataset of 3000 fb^{-1} is expected [94]. In Figure 11.6 the expected result for the analysis of this thesis is presented for the HL-LHC.

(a) **(b)**

Fig. 3.2: **(a)** Aerial view of the LHC and its circumference of 26.7 km [99]. The locations of the four interaction points are highlighted. **(b)** Inside of the LHC tunnel, with a diameter of 3.7 m [100], the protons are accelerated up to 13 TeV. The beampipe through which the protons travel is only 5.5 cm in diameter [101, 102].

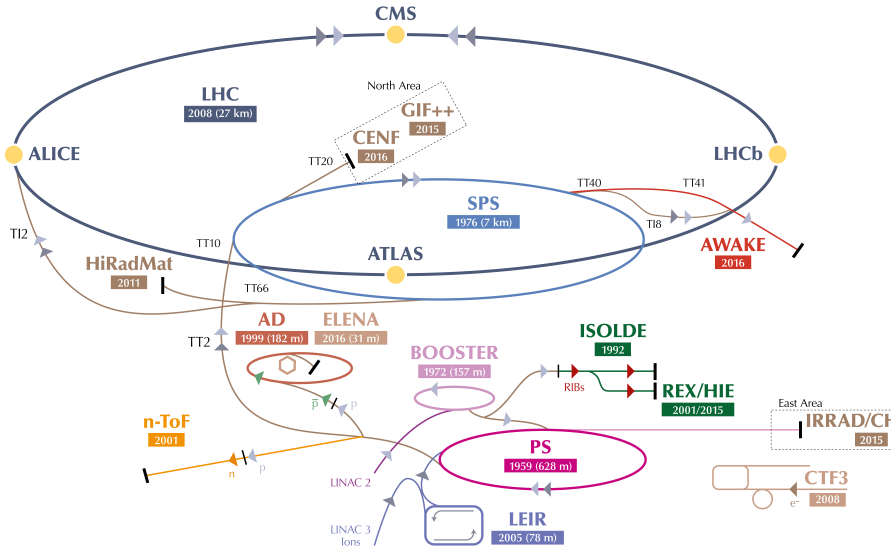

Fig. 3.3: CERN accelerator complex [105].

3.1 The LHC

For the LHC to reach an energy of 13 TeV is a great achievement, for which almost the whole CERN accelerator complex illustrated in Figure 3.3 is needed. The LHC uses about 120 megawatts of power [103] and the magnets, guiding the protons along the ring, require about 120 tonnes of liquid helium [104] to keep them cold and superconducting.

Before injection into the LHC

Before protons get injected into the LHC, they pass through a series of pre-accelerators. The pre-accelerators are mostly older accelerators that have been at the CERN site before the LHC, like the Proton Synchrotron (PS) built in 1959. The accelerators are nowadays linked in a chain to serve as pre-accelerators for the LHC. Protons originate from a bottle of hydrogen. From the hydrogen atoms the valence electrons are stripped off, leaving only protons to proceed. The protons are then sent to a series of linear and circular accelerators, increasing with energy and momentum which each step through radio frequency (RF) fields. Starting from the bottle of hydrogen, the protons get into the LINAC 2, then into the Proton Synchrotron Booster (Booster), then into the Proton Synchrotron (PS) and finally into the Super Proton Synchrotron (SPS). When arriving at the SPS the protons have already acquired

an energy of 450 GeV, before making the final step into the LHC, where the protons will be accelerated up to 6.5 TeV.

Accelerating protons

Protons are accelerated through oscillating electromagnetic fields, where the electric field needs to alternate with the revolution frequency, attracting the protons when approaching, and repulsing them once they have passed. A radio wave is a travelling electromagnetic field which can be made such that the electric field increases, decreases and finally reverses itself, in order to attract and repulse the protons.[1] At the LHC radio waves are made to resonate within a cavity. At a specific RF the resonance of a cavity creates a strong electric field. There are sixteen 400 MHz superconductive RF cavities in the LHC [106].

Keeping protons on track

The magnets in the LHC keep the protons confined and steer them along the approximately circular path of the LHC tunnel. Quadrupole magnets keep the protons confined using four magnetic poles arranged symmetrically around the beam pipe, squeezing the beam either vertically or horizontally. Dipole magnets are used to bend the paths of the protons. Dipole magnets make up the most part of the LHC, as it contains 1232 main dipole magnets, each 15 m long [107]. The dipole magnets use niobium-titanium cables: the cables enter a superconducting state when cooled at 1.9 K, through which a current of 11,080 A can run, providing a magnetic field of 8.3 T.

The dipole and quadruple magnets interact with protons through the Lorentz force, which for a proton of velocity $\vec{v}$ with charge e is given by

$$\vec{F} = e\vec{E} + e\vec{v} \times \vec{B}. \tag{3.1}$$

In the approximation that the transverse motion is dominated by the magnetic field, $\vec{B}$, a dipole magnet in a circular accelerator exerts a centripetal force on the protons given by

$$\vec{F} = \vec{v} \times \vec{B} = \frac{\gamma(v) m v^2}{\rho}, \tag{3.2}$$

where ρ is the particle's radius of curvature in the magnetic field and $\gamma(v)$ is the Lorentz factor. Increasing the velocity, $\vec{v}$, and thus $\gamma(v)$, requires increasing the magnetic field, $\vec{B}$, to maintain the radius of the accelerator. In order to achieve high energies with a circular

[1] Another option would be a high static electric field, but this is hard to make without a spark occurring.

accelerator there are thus two key aspects: the radius of the accelerator and the magnetic field, $\vec{B}$, which is why the LHC has such a large circumference, 26.7 km, and why the superconducting cables, cooled to 1.9 K, are used.[2]

3.1.1 Luminosity

At the LHC there are two beams of protons travelling in opposite direction. Both beams of protons are grouped into bunches. At the interaction points the bunches cross at discrete intervals, the bunch crossings occur every 25 ns. In a bunch there are about $1 \cdot 10^{11}$ protons. The protons in the bunches collide and interact with a cross-section σ, the interaction rate is given by $n = L \cdot \sigma$, where L is given by the instantaneous luminosity [100],

$$L = \frac{N_p^2 n_b f_{rev}}{4\varepsilon_n \beta^{IP}} F, \tag{3.3}$$

where N_p is the number of protons in a bunch, n_b is the number of bunches in one beam, f_{rev} is the frequency of bunch crossings, the beam size is expressed in terms of the transverse emittance,[3] ε_n, and the amplitude function at the interaction point,[4] β^{IP}. A luminosity reduction factor, F, due to the geometry of the beams is given by

$$F = \left(1 + \left(\frac{\theta_c \sigma_z}{2\sigma_T}\right)^2\right)^{\frac{1}{2}}, \tag{3.4}$$

where θ_c is the beams crossing angle, σ_z is the longitudinal bunch length and σ_T is the transverse size of the beam. The integrated instantaneous luminosity over time, $\int L\mathrm{d}t$, commonly expressed in fb^{-1}, multiplied with the cross-section of a given physics process leads to the total number of events for that process,

$$N = \sigma \int L\mathrm{d}t, \tag{3.5}$$

where again σ is the cross-section. In order to obtain a dataset with a large number of events for each physics process the instantaneous luminosity is maximised by adjusting parameters of the LHC such as the beam lifetime, the beam size at the collision and the crossing angle. For Run-2 ATLAS recorded a dataset which is good for physics with an integrated luminosity of 139 fb^{-1} as can be seen in Table 3.1 and Figure 3.4(a).

[2] There is also synchrotron radiation to consider, although this is more a concern for e^+e^- colliders.

[3] A low emittance particle beam is a beam where the particles are confined to a small distance and have nearly the same momentum.

[4] If β^{IP} is low, the beam is narrower, "squeezed". If β^{IP} is high, the beam is wide and straight.

Table 3.1: LHC delivered Run-2 dataset for ATLAS.

	2015	2016	2017	2018
collected data [fb^{-1}]	3.2	33.0	44.3	58.5

Pile-up

After a fill of the LHC, when there is maximum occupancy of the bunches, there are around $1 \cdot 10^{11}$ protons in a bunch. As a result of multiple protons crossing at the same time, there are multiple proton-proton collisions per bunch crossing. Pile-up, or μ, is defined as the amount of collisions per bunch crossing, which is proportional to the instantaneous luminosity L,

$$\mu = \frac{L\sigma_{\text{inel}}}{n_b f_{\text{rev}}}, \tag{3.6}$$

where σ_{inel} is the inelastic cross-section of proton-proton collisions, n_b is the number of bunches in one beam and f_{rev} is the frequency of bunch crossings [109]. The average μ over all bunch-crossings is referred to as $\langle\mu\rangle$. The pile-up profile is shown in Figure 3.4(b), where it can be seen that on average 33.7 protons collide in each bunch crossing for the full Run-2 period.

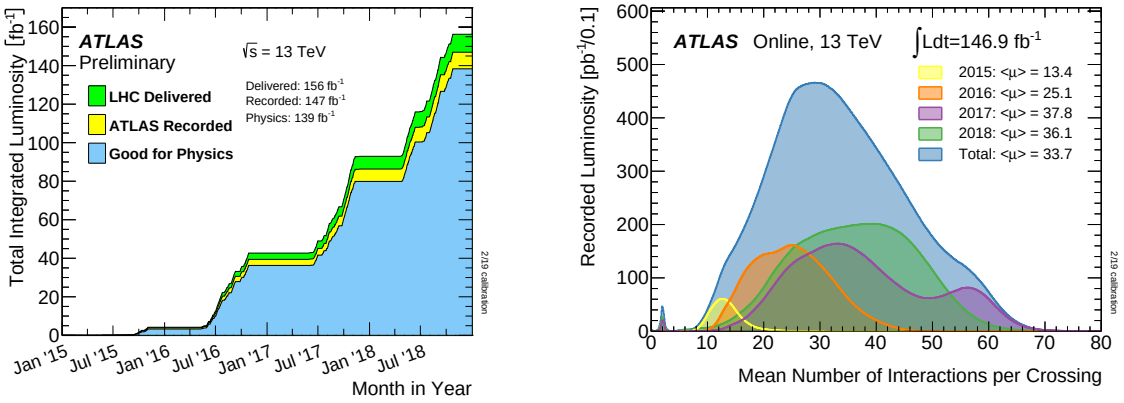

(a) **(b)**

Fig. 3.4: **(a)** Total integrated luminosity during Run-2 of the LHC. A dataset good for physics has been recorded by ATLAS with an integrated luminosity of 139 fb^{-1}. **(b)** Mean number of interactions per crossing, μ, for the full recorded dataset by ATLAS during Run-2 of the LHC. It can be seen that $\langle\mu\rangle$ increased over the years (from 2015 to 2016 and from 2016 to 2017). The increase in $\langle\mu\rangle$ is due to an increase in the instantaneous luminosity [108].

3.2 The ATLAS experiment

The ATLAS detector [95] is the largest detector at the LHC with a diameter of 25 m, a length of 44 m and a weight of ∼7000 tonnes. ATLAS consists of several subdetectors formed in a cylindrical shape around the beampipe as can be seen in Figure 3.5. Starting closest to the interaction point there is an inner tracker, called the Inner Detector (ID), surrounded by a solenoid magnet. The ID performs a position and momentum measurement on charged particles. Surrounding the ID there are the Electromagnetic (EM) and Hadronic (HAD) calorimeters that perform energy measurements. The calorimeters are surrounded by a Muon Spectrometer (MS) and toroid magnets, allowing a position and momentum measurement of muons. All of the components of the detector try to identify the types and properties of particles produced in the collision as accurately as possible. By combining the information from all subdetectors it can be inferred which particles were created at the interaction point from the hard-scatter of a proton-proton collision as can be seen in Figure 3.6.

3.2.1 Coordinate system

The ATLAS coordinate system is centred around the collision point and because of the symmetries of the detector around the beampipe described by spherical coordinates (z, ϕ, θ). The z-axis points along the beampipe. The azimuthal angle, $\phi \in [-\pi, \pi]$, is the angle rotating perpendicular to the beampipe, with $\phi = 0$ pointing to the centre of the LHC. The polar angle, $\theta \in [0, \pi]$, is the angle between the z-axis and the axis pointing upwards, where $\theta = 0$ is pointing along the beampipe. Particle production is constant under ϕ, such that $\mathrm{d}N/\mathrm{d}\phi$ is invariant, however for θ this is not the case, which is why the pseudorapidity η is introduced,

$$\eta = -\ln[\tan\left(\frac{\theta}{2}\right)], \tag{3.7}$$

under which particle production $\mathrm{d}N/\mathrm{d}\eta$ is approximately constant. The distance ΔR_{ij} is defined as

$$\Delta R_{ij} = \sqrt{(\eta_i - \eta_j)^2 + (\phi_i - \phi_j)^2}. \tag{3.8}$$

Coordinates in hadron collider physics: why do we use η and p_T?

As a function of momentum $\vec{p}$, the coordinate η can be written as

$$\eta = \frac{1}{2}\ln\left(\frac{|\vec{p}| + p_z}{|\vec{p}| - p_z}\right), \tag{3.9}$$

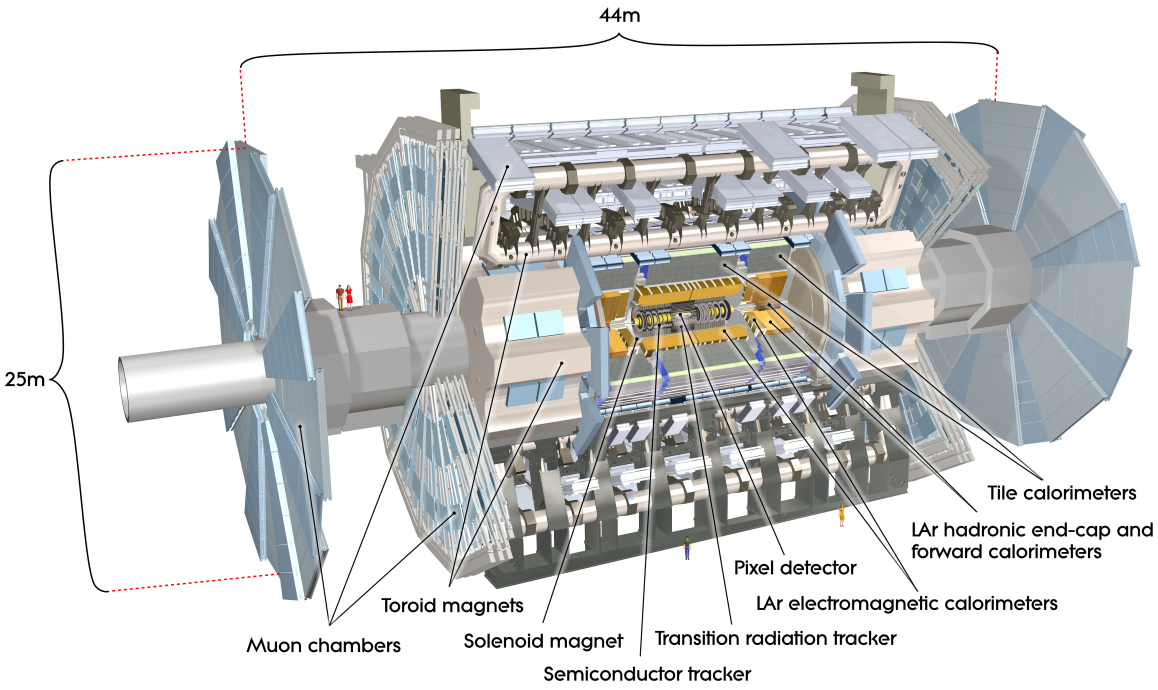

Fig. 3.5: Cut-away view of the ATLAS detector [95].

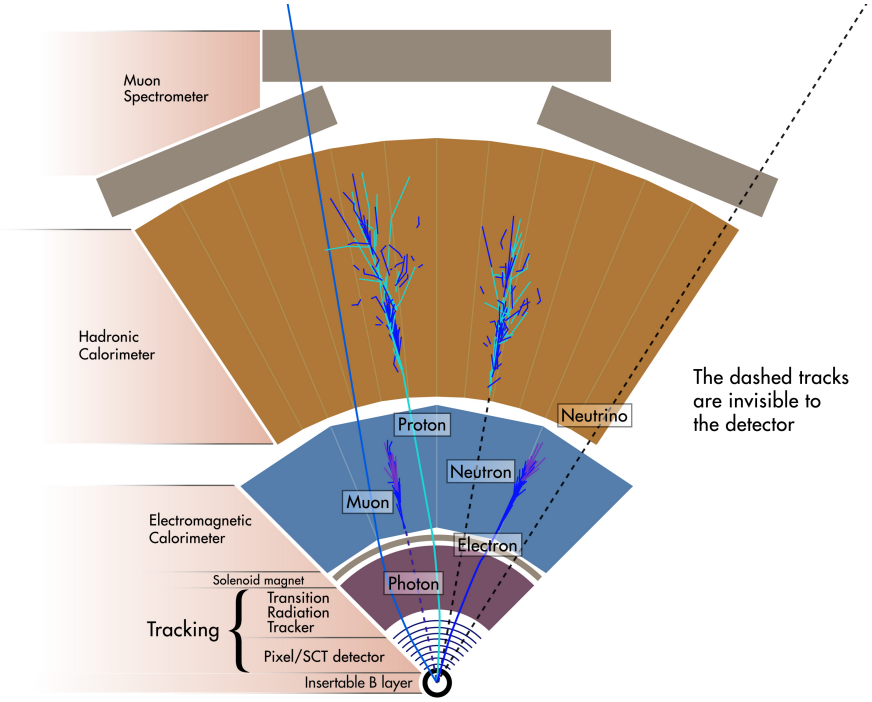

Fig. 3.6: Measurements from the subdetectors are combined in order to infer what particles are created from the hard-scatter of a proton-proton collision [110].

where p_z is the longitudinal momentum along the z-direction. Here the approximation has been made that the mass of the particle is negligible, such that the substitution $|\vec{p}| \approx E$ could be made. The actual rapidity is given by

$$y = \frac{1}{2} \ln \left(\frac{E + p_z}{E - p_z} \right), \tag{3.10}$$

for which dN/dy is invariant [111].

The transverse momentum, p_{T}, is an important conserved quantity in hadron colliders. In a hadron collider it is not the actual protons that collide, but the partons within the proton. The initial energy of the proton is known, but not of the colliding partons, which are given by a parton distribution function. The colliding partons carry different longitudinal momentum fractions x, which means that the rest frames of the parton-parton collisions will have different longitudinal boosts. The initial p_Z of the colliding parton is in principle reconstructable in a hermetic detector, but this is not the case for the ATLAS detector due to for example the beampipe. In the transverse plane the initial p_{T} is known, where $p_{\mathrm{T}} = 0$, which can thus be used as a conserved quantity.[5]

3.2.2 The Inner Detector

The goal of the Inner Detector (ID) is to measure the position and momentum of charged particles. The measurement of the position of a charged particle corresponds to hits in the detectors, these hits are then combined to form a particle track. After the position measurement the momentum can be calculated using the Lorentz force, as described in Equation 3.1. In an axial magnetic field $\vec{B}$, owing to the Lorentz Force $\vec{v} \times \vec{B}$, the track of a particle is a helix with radius of curvature R, such that the momentum can be calculated from

$$p_{\mathrm{T}} = 0.3 \cdot B \cdot R, \tag{3.11}$$

where p_{T} is transverse momentum in GeV, B magnetic flux density in tesla and R is the curvature of the track in meters. To provide the magnetic flux necessary for the momentum measurement a 2 T solenoid magnet surrounds the ID. The ID is a cylindrical shaped tracking detector around the beampipe and has a radius of around 1 m throughout which different detector techniques are used. The ID consists of four main parts, the Insertable B-Layer (IBL), the Pixel detector, Semiconductor Tracker (SCT) and the Transition Radiation Tracker (TRT). The subdetectors are organised in concentric barrels and end-caps, organised in

[5] At a e^+e^- collider the initial momentum along p_Z is known, and the momentum $\vec{p}$ can be used as a conserved quantity.

Table 3.2: Layout of the Inner Detector (ID) [95, 112].

Subdetector	$\lvert\eta\rvert$	Layout	Radius barrel layers [mm]
IBL	< 3.0	1 barrel layer	33.2
Pixel	< 2.5	3 barrel layers 3 end-cap disks each side	50.5, 88.5, 122.5
SCT	< 2.5	4 barrel layers 9 end-cap disks each side	299, 371, 443, 514
TRT	< 2.0	barrel (73 layers of length 144 cm) end-cap disks each side (160 layers of length 37 cm)	from 554 to 1082

wheels, on both sides. The layout of the ID can be seen in Table 3.2 and Figure 3.7. The ID provides full coverage in ϕ and up to $|\eta| \leq 2.0$, when excluding the TRT the ID provides coverage up to $|\eta| \leq 2.5$.

The IBL was installed in the 2013-2014 shutdown after Run-1 in order to have an additional layer closer to the beampipe. A tracking layer close to the beampipe is important for reconstruction as explained in Chapter 5, especially for vertex reconstruction and b-tagging. After the installation, bowing of the IBL was observed when varying the temperature from 15° celsius to -20° celsius, caused by materials with different thermal expansion coefficients [114]. In order to correct for this the bowing is monitored and aligned during runs as described in Section 4.2.2.

The density of tracks is higher close to the beampipe and thus a more granular detector is needed there. The IBL and pixel detector are the most granular detectors, with the highest resolution, as illustrated in Table 3.3. The IBL, the Pixel detector and the SCT use a technique where silicon is arranged between two electrodes. Silicon is a semiconductor material containing two differently doped regions. When a doped semiconductor region contains mostly free holes it is called p-type, and when it contains mostly free electrons it is known as n-type. The p-n junctions between these regions are responsible for the useful electronic behaviour. When a charged particle traverses the material it will produce electron-hole pairs and under the influence of an electric field the electrons and holes travel in opposite direction to the electrodes.

The TRT is a straw-tube tracker and uses a different technique; it tracks the trails of gaseous ionisation. A straw is a drift tube of 4 mm diameter and a length of 144 cm in the barrel (37 cm in the end-cap). Inside the straw is a 31 µm diameter gold-plated tungsten anode wire. The straw is filled with $Xe/CO_2/O_2$ gas mixture (70/27/3%). The signal on each wire is

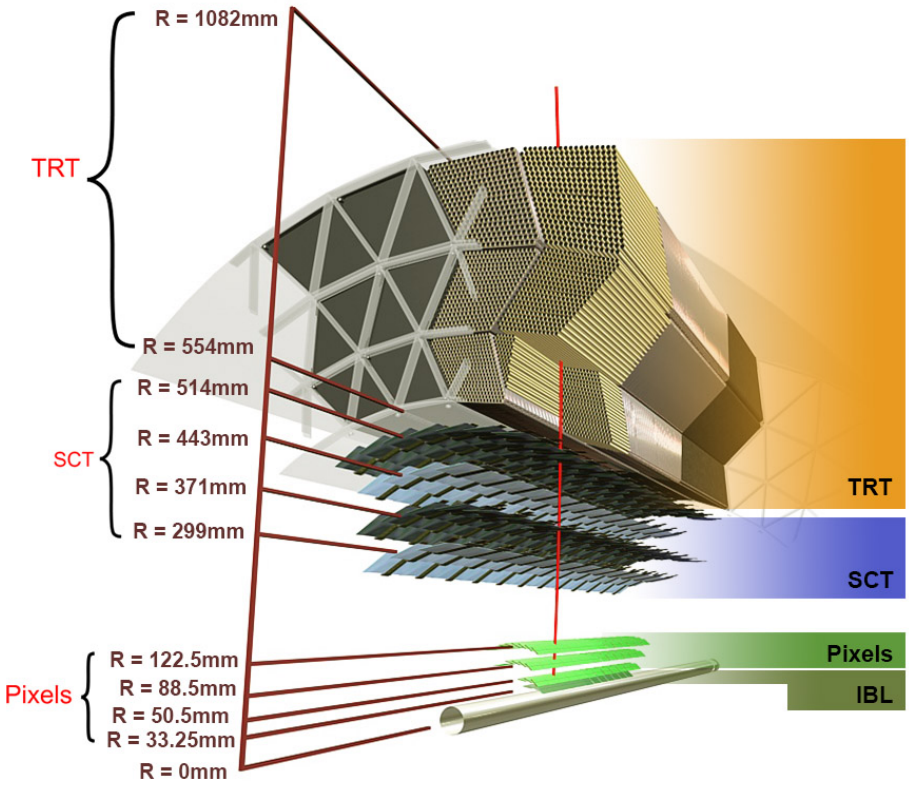

(a)

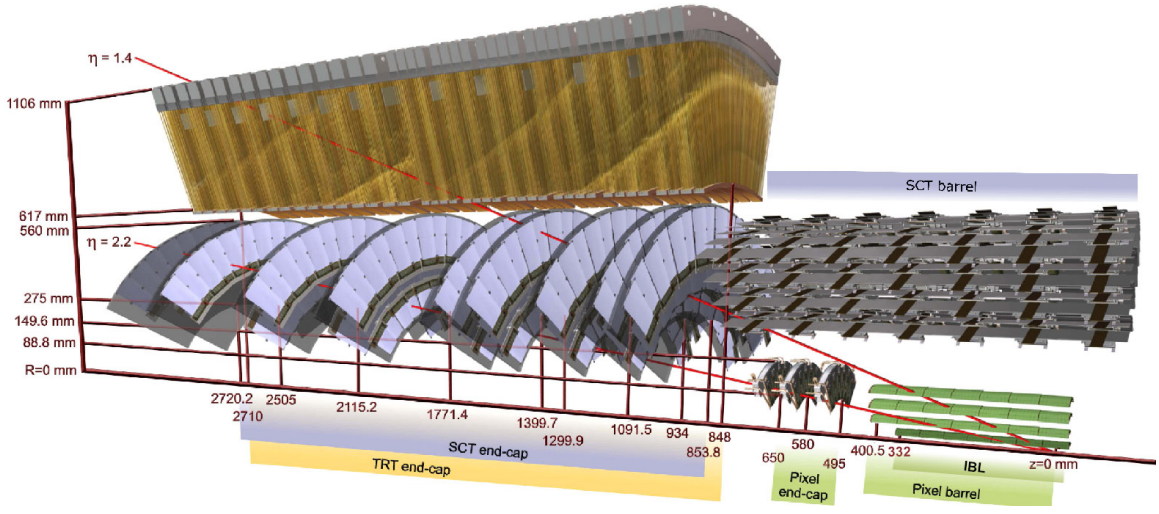

(b)

Fig. 3.7: **(a)** Cut-away view of the Inner Detector (ID) in ϕ traversed by a track with $\eta = 0$. In the picture are shown the beam pipe, the IBL, the Pixel layers, the four cylindrical layers of the SCT and the 72 straw layers of the TRT [113]. **(b)** Cut-away view of the Inner Detector (ID) in η traversed by two tracks with η =1.4, and 2.2. The TRT barrel detector is not shown [95].

Table 3.3: Techniques used in the Inner Detector (ID). The resolution shown for the IBL and pixel is $r-\phi \times z$. For the SCT and TRT the resolution shown is $r-\phi$ [95, 112].

Subdetector	Technique	Configuration	Intrinsic Resolution [μm]
IBL	Silicon	Pixels	8×40
Pixel	Silicon	Pixels	10×115
SCT	Silicon	Strips	17
TRT	Ionisation	Straws	130

discriminated against a low and a high threshold to provide tracking information as well as particle identification. For the low threshold hits the gas is simply ionised whilst particles that also produce transition radiation provide the high threshold hits. Transition radiation is emitted by charged particles as they traverse the boundaries of materials with different dielectric constants. The effect is strongest for electrons as it depends on the relativistic factor γ = E/m, which means it can be used for particle identification. In the TRT transition radiation is created by the spaces between the straws which are filled with polymer fibres in the barrel and foils in the end-caps. When a charged particle traverses the TRT, the transition radiation is created by the polymer fibres and foils, which is then absorbed by the gas inside the straws. The resulting free electrons drift towards the tungsten anode wire, where they are amplified and read out.

3.2.3 The Calorimeters

The goal of the calorimeters is to measure the energy of particles. A calorimeter consists of alternating layers of absorber material and active material. When a particle traverses a calorimeter a particle shower is produced by the absorber material and the energy of the particle shower is consequently measured in the active material. In the ATLAS experiment there are two types of calorimeters, the Electromagnetic (EM) calorimeter and the Hadronic (HAD) calorimeter. The EM calorimeter is designed to measure the energy of electrons and photons, and the HAD calorimeter is designed to measure the energy of hadrons formed by quarks and gluons in the hard-scatter process. Muons are not stopped by the calorimeters, unless they have an E_{T} smaller than 3 GeV. The calorimeters cover a range of $|\eta| < 4.9$ using different materials depending on the radiation environment, and are described in Table 3.4. In the $|\eta| < 2.5$ region matched with the ID the EM calorimeter has fine granularity for precision measurements of electrons and photons. The rest of the calorimeter has a coarser granularity designed to satisfy the requirements for jet reconstruction and $E_{\mathrm{T}}^{\mathrm{miss}}$ measurements. The calorimeters also provide information for the trigger, which will be

Table 3.4: Description of the calorimeters and the materials used in the different $|\eta|$ ranges [95].

Name	$\|\eta\|$	absorber	active material
Electromagnetic calorimeter			
LAr electromagnetic barrel	< 1.475	lead	liquid argon
LAr electromagnetic end-cap	[1.375,3.2]	lead	liquid argon
Hadronic calorimeter			
Tile barrel	< 1	steel	scintillating tile
Tile extended barrel	[0.8,1.7]	steel	scintillating tile
LAr hadronic end-cap calorimeter	[1.5,3.2]	copper	liquid argon
Forward calorimeter			
LAr forward calorimeter	[3.1,4.9]	copper (EM)	liquid argon
		tungsten (HAD)	liquid argon

described in more detail in Section 3.3. In order to provide information for the trigger, there are dedicated readout channels of the EM and HAD calorimeter with reduced granularity, called Level-1 Calorimeter (L1Calo) [95].

On the outside of the ID the EM calorimeter is located, which is then surrounded by the HAD calorimeter, as can be seen in Figure 3.8. In order to quantify the energy loss of particles interacting electromagnetically with the calorimeter the radiation length, X_0, is used, which is defined as the mean distance over which a high-energy electron loses all but 1/e of its energy through bremsstrahlung.[6] The EM calorimeter provides a depth of $> 22X_0$ in the barrel and $> 24X_0$ in the end-caps. The nuclear interaction length, λ, is used for hadronic particles and is defined as the mean distance travelled by a hadronic particle before undergoing a nuclear interaction.[6] The depth of both the calorimeters, including 1.3λ from the outer support, is 11λ at $\eta = 0$, which by measurements and simulations has been shown to be sufficient to have less hadrons punch through than the expected amount of muons from collisions. Due to the large η coverage and the large depth the calorimeters provide a good $E_{\mathrm{T}}^{\mathrm{miss}}$ measurement, which relies on measuring the total visible energy from the collision as described in Section 5.5. A good $E_{\mathrm{T}}^{\mathrm{miss}}$ measurement is important for many physics signatures, in particular for supersymmetry searches.

The EM calorimeter is a Liquid Argon (LAr) sampling detector with lead as material to produce the shower. The EM calorimeter consists of a barrel, at $|\eta| < 1.475$, called the LAr electromagnetic barrel, and two end-caps, at $1.375 < |\eta| < 3.2$, called the LAr

[6] The radiation length for a given material can be approximated by the following expression, $X_0 = \frac{716.4\ \mathrm{g\,cm^{-2}}\ A}{Z(Z+1)\ln(287/\sqrt{Z})}$, and the nuclear interaction length can be approximated using, $\lambda = 35\ \mathrm{g\,cm^{-2}} A^{1/3}$ [111].

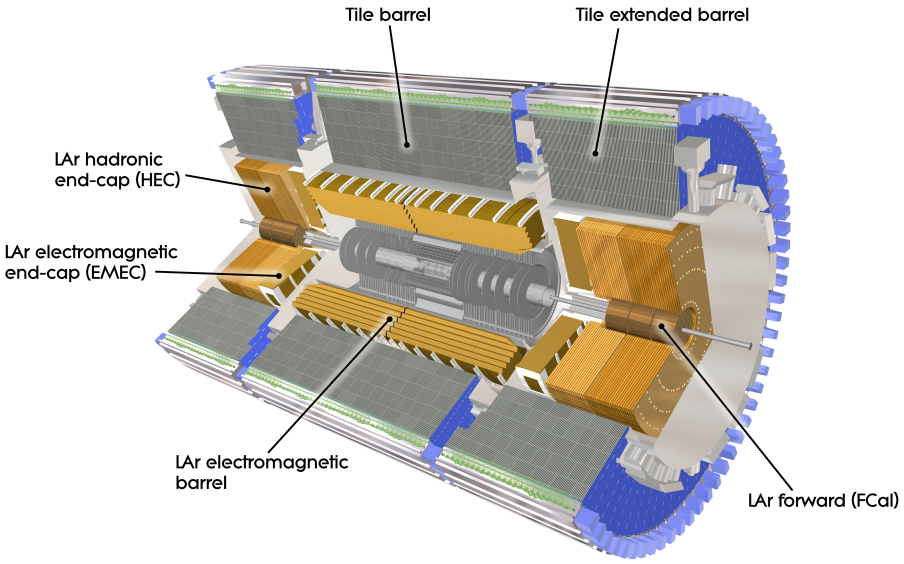

Fig. 3.8: Cut-away view of the ATLAS calorimeter system [95]. The inner most detector in grey is the Inner Detector, the orange detector in the middle is the EM calorimeter. The detector on the outside in grey and green is the HAD calorimeter.

electromagnetic end-cap (EMEC). The goal of the EM calorimeter is to stop electrons and photons and measure their energy. In materials with a high atomic number, Z, such as lead, electrons lose their energy through bremsstrahlung and photons through e^+e^- pair production. The shower is then sampled through ionisation in the liquid argon, which is measured by accordion shaped electrodes. The design energy resolution of the EM calorimeter is $\sigma_E/E = 9\%/\sqrt{E} \oplus 0.3\%$.[7]

The HAD calorimeter uses multiple materials. The tile sampling calorimeter, consisting of a barrel region, at $|\eta| < 1$, and an extended barrel region, at $0.8 < |\eta| < 1.7$, uses steel to produce a hadronic shower which is measured by scintillating tiles. The scintillating tiles radiate photons when a charged particle from the shower travels through the material; these photons are then measured by a photomultiplier tube. The LAr hadronic end-cap calorimeter (HEC), in the range $1.5 < |\eta| < 3.2$, uses copper to produce a hadronic shower which is then measured through ionisation of the liquid argon. Finally, the LAr forward calorimeter (FCal), at $3.1 < |\eta| < 4.9$, uses a layer of copper to produce an electromagnetic shower and two layers of tungsten to produce a hadronic shower, which in all layers is then measured through ionisation of the liquid argon. The design energy resolution of the tile calorimeter is $\sigma_E/E = 50\%/\sqrt{E} \oplus 3\%$ and for the forward calorimeters $\sigma_E/E = 100\%/\sqrt{E} \oplus 10\%$.[7]

[7] In the notation $[\sigma_E/E = A\%/\sqrt{E} \oplus B\%]$ A is the stochastic term and B is the constant term reflecting local non-uniformities in the response of the calorimeter. The absolute error is given by $\sigma_E = A\sqrt{E} \oplus BE$.

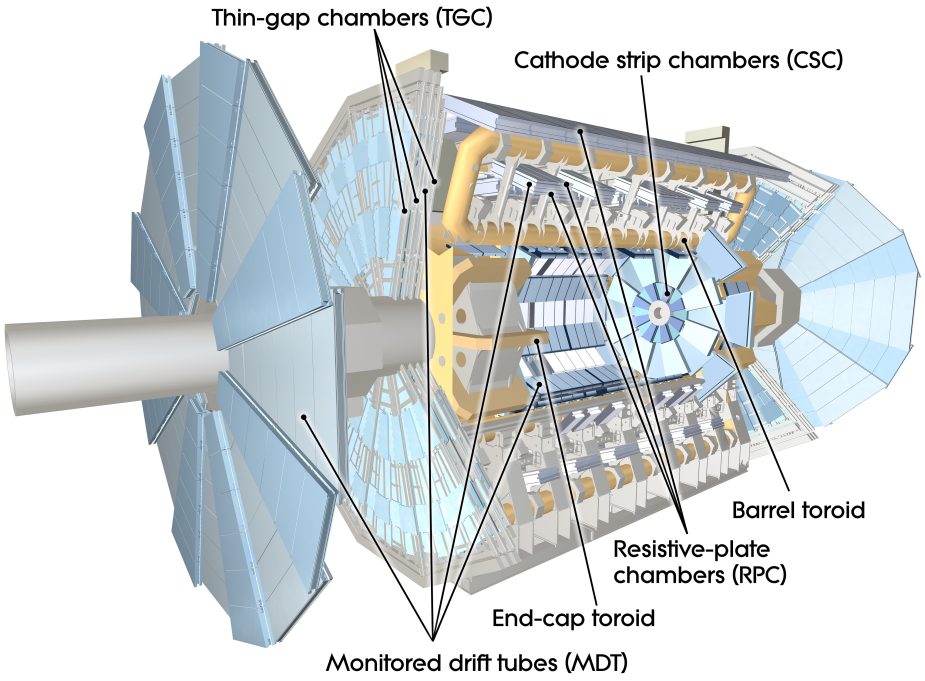

Fig. 3.9: Cut-away view of the ATLAS muon system [95].

3.2.4 The Muon Spectrometer

The goal of the Muon Spectrometer (MS) is to measure the position and momentum of muons. The MS also provides information for the trigger, which will be described in more detail in Section 3.3. The MS surrounds all other subdetectors; electrons and photons have been stopped by the EM calorimeter, hadrons have almost all been stopped by the HAD calorimeter, which leaves muons to be the only SM particle left that can interact with the detector.[8] The MS is shown in a cut-away view in Figure 3.9. In terms of kinematics only the position and momentum of muons are measured, since it is not feasible to design a calorimeter for muons to do an energy measurement. Just like the ID, the MS relies on a momentum measurement as calculated from Equation 3.11. An azimuthal magnetic field is provided by air-core toroidal magnets. Within the magnetic field, the precision tracking detectors, Monitored Drift Tubes (MDT) and Cathode Strip Chambers (CSC), are mounted to provide a position measurement from which the p_{T} can be inferred. For triggering there are Resistive Plate Chambers (RPC) and Thin-Gap Chambers (TGC). Since muons are nearly the only particles to end up in the MS, and muons are indicative of many interesting physics processes, the MS provides important information for the trigger.

[8] Neutrinos do not interact with the detector and are measured as $E_{\mathrm{T}}^{\mathrm{miss}}$.

Table 3.5: The spatial and time resolution of the muon chambers. It can be seen that the MDT and CSC have a high resolution in the z/R direction and that the RPC and TGC provide the MDT with the measurement in ϕ. The timing resolution of the trigger chambers is fast enough to keep up with the 25 ns bunch crossings [95].

Type	$\lvert\eta\rvert$	z/R resolution	ϕ resolution	time resolution
		Tracking		
MDT	< 2	35 µm (z)	-	-
CSC	[2,2.7]	40 µm (R)	5 mm	7 ns
		Trigger		
RPC	< 1.05	10 mm (z)	10 mm	1.5 ns
TGC	[1.05,2.4]	2-6 mm (R)	3-7 mm	4 ns

A system of three large air-core toroids generates the magnetic field for the MS, one in the barrel and two in the end-caps. In the barrel region, over the range $|\eta| < 1.4$, muon tracks are bent by the large barrel toroid and the field varies from 0.15 T to 2.5 T, with an average value of 0.5 T. In the end-cap regions, over the range $1.6 < |\eta| < 2.7$, muon tracks are bent by two smaller end-cap magnets, inserted into both ends of the barrel toroid. The magnetic field varies in the end-cap regions from 0.2 to 3.5 T, with an average value of 1 T. In the transition region, over the range $1.4 < |\eta| < 1.6$, muon tracks are bent by a combination of the barrel and end-cap fields [95]. The large toroids within the MS reduce the acceptance of muons measured by the MS, since in their position no detector can be placed. The loss in acceptance can be seen for example in the trigger efficiency presented in Figure 8.3(a), showing the single muon trigger reaching an efficiency of only about 80%. The RPCs have gaps in each sector, which are structure-wise inevitable due to the barrel toroid, causing an efficiency of around 70%. The efficiency from the TGCs is higher and amounts to around 90%.

The MDT and the CSC detectors perform a precision measurement of the position of the muons. The MDT tracking detectors consist of a barrel region, where there are three layers of MDTs, and four large wheels in the end-cap region, covering a pseudorapidity of $|\eta| < 2$. MDTs are pressurised aluminium drift tubes filled with Ar/CO_2 gas mixture (93/7%). A 50 µm diameter anode wire is centred within a 1.5 cm radius aluminium tube [115]. The average resolution of 80 µm per tube results in a resolution of about 35 µm per chamber. In the end-cap region the two innermost wheels contain CSCs at the centre of the wheel, at pseudorapidity range $2 < |\eta| < 2.7$. The CSCs are able to withstand the demanding rate and background conditions in the region at high pseudorapidity. CSCs are multiwire proportional chambers in a Ar/CO_2 gas mixture (80/20%) with multiple 30 µm diameter anode wires in a chamber, providing a resolution of 40 µm. Also a coarse measurement in ϕ, with a 5

mm resolution, is done by the cathode wires in the chambers [116]. Tracking relies on the two precision tracking detectors MDT and CSC, but also on the trigger chambers, RPC and TGC. The trigger chambers complement the position measurement from the MDT and CSC detectors by providing the position in ϕ, with a resolution of 10 mm for the RPCs and 3-7 mm for the TGCs.[9] From the combination of these measurements the MS is capable of doing a p_{T} measurement in the range 3 GeV to 3 TeV in the region $|\eta| < 2.7$.

Besides providing the ϕ coordinate used for tracking, the trigger detectors, RPC and TGC, provide bunch-crossing information and triggering information in the pseudorapidity range $|\eta| < 2.4$. In order to provide bunch-crossing information and triggering the detectors need to be fast enough to keep up with the 25 ns bunch crossings from the LHC. Both chamber types deliver signals with a spread of 15-25 ns. The RPCs are very fast detectors, with an excellent time resolution of 1.5 ns. The TGCs are moderately fast, with a time resolution of 4 ns, but can operate in the demanding rate and background conditions in the end-cap region. RPCs cover the barrel region with pseudorapidity range $|\eta| < 1.05$. Two resistive plates, which are 2 mm thick, are kept at 2 mm one from each other, with the gas mixture in the middle. RPCs detect the ionisation from a charged particle traversing a $C_2H_2F_4/C_4H_{10}/SF_6$ gas mixture of (94.7,10.5,0.3%) in the detector, under a strong uniform electric field applied by resistive electrodes [117]. TGCs cover the barrel region with pseudorapidity range $1.05 < |\eta| < 2.4$. TGCs also detect the ionisation caused by a charged particle traversing the gas mixture of the detector. TGCs are multiwire chambers containing 50 µm diameter gold plated tungsten wires and a very narrow gas gap [118]. The gas mixture in the TGCs is CO_2/n-C_5H_{12} (55,45%). To form a trigger signal, between 4 to 20 anode wires are grouped together [119].

3.3 The Trigger system

The trigger makes the decision which events to record and process further, and which events to discard, based on certain features of the collision [120]. The trigger is needed because when the LHC is operating with a bunch spacing of 25 ns, there are approximately 30 million events per second to record, corresponding to a rate of 30 MHz. The rate of 30 MHz is too high for the readout of the detector to handle, and in order to reduce the rate the trigger makes the decision whether to store the event or not, based on the kinematic signature of the event. When the event contains certain particles, at a defined p_{T}, E_{T} or angles, the event is stored by the trigger.

[9] By matching the MDT and RPC/TGC hits in the bending plane η.

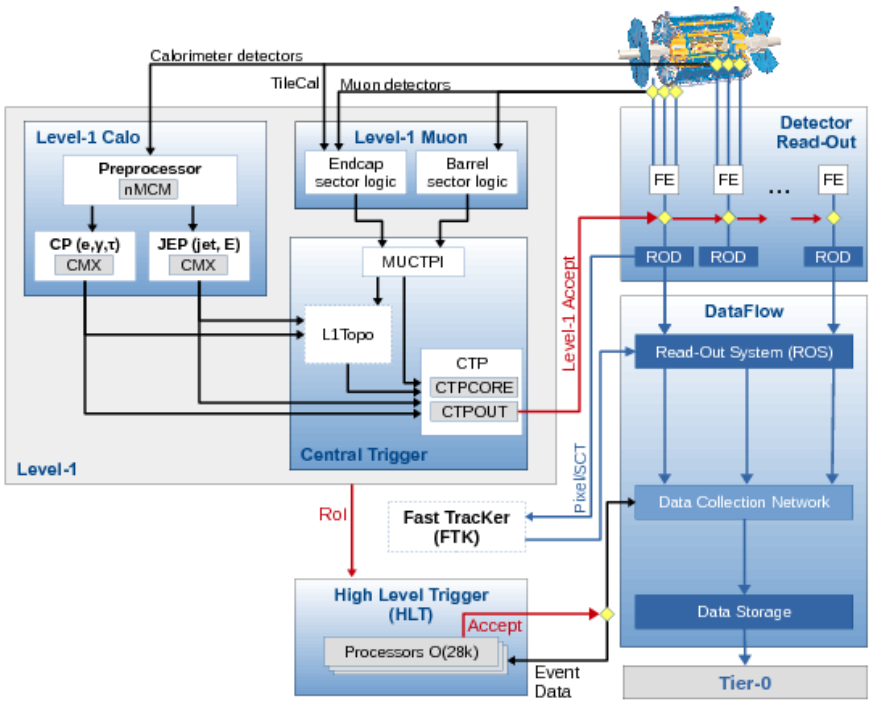

Fig. 3.10: The ATLAS Trigger and Data Acquisition (TDAQ) system [121]. The Fast TracKer (FTK) is not used for the data studied in this thesis.

The Trigger and Data Acquisition (TDAQ) system [121] operates the trigger decision on two consecutive levels, the Level 1 (L1) and the High-Level Trigger (HLT). A schematic overview of the TDAQ system is shown in Figure 3.10. The L1 trigger is hardware based and able to operate fast, reducing the initial rate of approximately 30 MHz to 100 kHz. The L1 trigger is able to make a decision to store an event within 2.5 µs. The HLT is a software based trigger and reduces the rate further from approximately 100 kHz to 1 kHz. The decision to store the event is made by the HLT in about 200 ms.

The L1 trigger makes a decision by combining limited information from the detector about the event, such as particle type and p_{T}. In order to trigger on photons, electrons, jets, taus and $E_{\mathrm{T}}^{\mathrm{miss}}$, the Level-1 Calorimeter (L1Calo) trigger system is used. L1Calo works with about 7000 analogue trigger towers of reduced granularity from the EM and HAD calorimeters. The Level-1 Muon (L1Muon) trigger system takes the data from the MS trigger chambers. The Central Trigger combines the L1Muon with the L1Calo. The Topological Processor (L1Topo) processes data from the L1Calo and L1Muon trigger systems using several algorithms, which perform geometrical cuts, correlations and calculate complex observables such as the invariant mass. The L1 trigger also determines Regions-of-Interest (RoIs) in the detector. The RoIs are sent to the HLT, in which sophisticated selection

algorithms use the full granularity event data including the Inner Detector, either in the RoI or the whole event.

While it takes 2.5 µs for the L1 to make a decision and about 200 ms for the HLT, the bunch crossings occur every 25 ns. A buffer is thus needed to store the data while waiting for the trigger decision. The trigger towers in the calorimeters and MS trigger chambers contain a buffer pipeline in order to store the data while waiting for the L1 trigger decision. After the L1 decision the data is read out from the detectors and digitised. The TDAQ system stores the digitised data in local buffers while waiting for the HLT decision. If the HLT decides to store the event it will be recorded on a central storage system. The data is then subjected to calibration procedures, including the alignment procedure described in Chapter 4, after which the data is subjected to the reconstruction procedure as described in Chapter 5.

Chapter 4

Inner Detector Alignment

In the Inner Detector (ID) the goal is to measure charged particle tracks as accurately as possible. The ID consists of four main parts, the Insertable B-Layer (IBL), the Pixel detector, the Semiconductor Tracker (SCT) and the Transition Radiation Tracker (TRT) as described in Section 3.2.2. All of the layers combined form a collection of more than 350,000 sensitive elements, and all sensitive elements perform independent measurements, called hits, of charged particles that travel through the detector. Each of these sensitive elements has a position, and the positions of all the hits on the sensitive elements are used to reconstruct the path of the charged particle, called a track. A track is the trajectory of a charged particle in the ID and is reconstructed as described in Section 5.1. In order to do precise track reconstruction the position of the sensitive elements needs to be known with high precision.

The better the exact position of the sensitive elements is known, the more accurately tracks can be reconstructed. As is illustrated on the left of Figure 4.1, a not aligned geometry causes tracks to have abrupt movements or unphysical kinks. In order to know the position of the sensitive elements as accurately as possible track-based alignment is used. Track-based alignment corrects the assumed ATLAS geometry to the actual relative positions of all sensitive elements in the ID as is shown in Figure 4.2. Track-based alignment has uncontrolled behaviour if not constrained properly: the alignment procedure is invariant to so-called weak modes. Weak modes affect the track parameters and thus distort our ability to reconstruct tracks properly. The method of track-based alignment is described in Section 4.1. The alignment procedure is reported in Section 4.2. Finally, monitoring of weak-modes is discussed in Section 4.3, where new diagnostic figures allow to spot problems in the alignment.

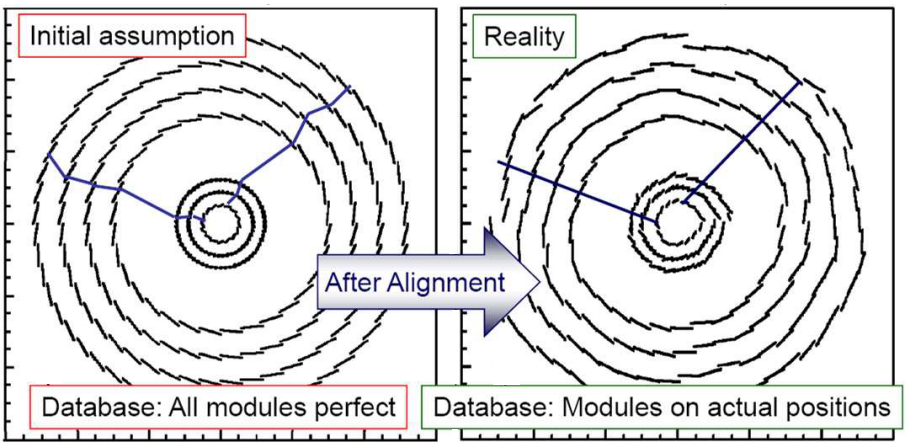

Fig. 4.1: Cross-section of the Inner Detector (ID) without (left) and with (right) track-based alignment. The real positions of the modules will be kept in an updated geometry database [122].

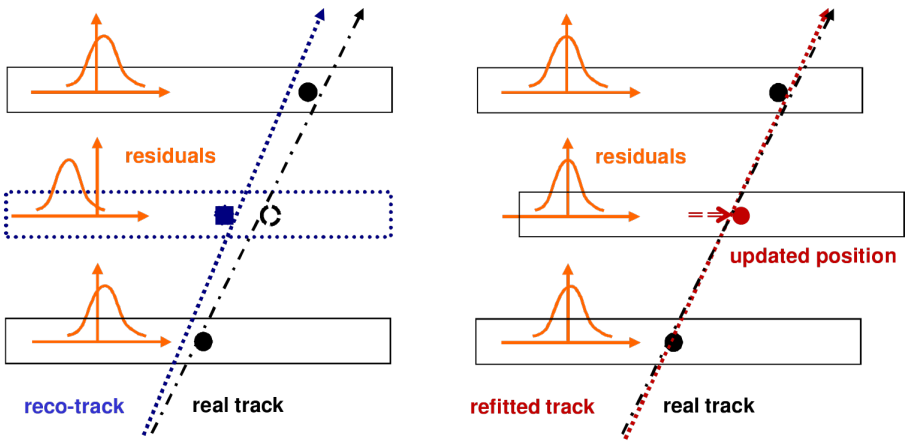

Fig. 4.2: Track fit with three silicon hits. Left: As the actual displacement of the module is unknown, the hit is reconstructed in a wrong place and the track fit is pulled to the left. Right: With an updated geometry, the hit is reconstructed at its true position and the reconstructed track agrees with the true track [122].

4.1 Alignment method

The ID alignment uses track-based alignment to improve our knowledge on the position of sensitive elements. A particle track in the ID is described by the following parameters,

$$\vec{\tau} = (d_0, z_0, \phi_0, \theta, q/p), \tag{4.1}$$

where d_0 is the distance to the point of closest approach between the track candidate and the vertex in the transverse plane, z_0 is the z-coordinate where d_0 is measured, ϕ_0 is the azimuthal angle, θ is the polar angle and q/p is the ratio of the particle charge and momentum.

Track-based alignment relies on tracks to correct the detector geometry by χ^2 minimisation and this procedure is closely related to how track fitting is done. A global track fit, described in Section 4.1.1, minimises χ^2 with respect to track parameters, while track-based alignment, described in Section 4.1.2, minimises χ^2 with respect to alignment parameters summing over all reconstructed tracks. When correcting the detector geometry using χ^2 minimisation there are weak modes, which are changes of the detector geometry that do not change the χ^2. Track-based alignment is not able to correct for these weak modes, as they are invariant to the procedure of minimising χ^2. Weak modes are alternative detector configurations, with respect to the true detector configuration, which are thus equally correct to the alignment procedure. Weak modes are described in Section 4.1.3.

4.1.1 Global track fit

The quality of a track is measured by its χ^2, a goodness of fit, and is thus a measure for how well the detector is aligned. The χ^2 of a set of measurement is defined as

$$\chi^2 = \sum_i \frac{r_i^2}{\sigma_i^2}, \tag{4.2}$$

where r are the residuals and σ are the errors associated with the measurement. Residuals are the distance of the measurement to the assumed position and are defined as following,

$$r_i = m_i - h_i(\vec{\tau}, \vec{a}), \tag{4.3}$$

where m_i is the measurement and h_i is the estimated value from the track fit for datapoint i. The track hypothesis h depends on $\vec{\tau}$, the track parameters, and $\vec{a}$, the alignment parameters.

The errors of the measurements m_i are correlated so the covariance matrix V is introduced, a matrix containing the detector measurement errors with all correlations. An example source of correlation is the contribution of Multiple Coulomb scattering, which has an effect on subsequent measurements. In order to include the covariance matrix, Equation 4.2 is rewritten in matrix notation,

$$\chi^2 = \vec{r}(\vec{\tau}, \vec{a})^T V^{-1} \vec{r}(\vec{\tau}, \vec{a}). \tag{4.4}$$

Before describing the alignment procedure, it is important to understand how tracks are reconstructed. Track fitting is done by minimising the χ^2 for an initial assumed geometry

$\vec{a}_0$. The method that minimises the χ^2 with respect to all track parameters simultaneously is called a global track fit. By minimising Equation 4.4 the smallest residuals for the track fit are found,

$$\begin{aligned} \frac{d\chi^2}{d\vec{\tau}} = \frac{d}{d\vec{\tau}}\left(\vec{r}(\vec{\tau},\vec{a}_0)^T V^{-1}\vec{r}(\vec{\tau},\vec{a}_0)\right) = \\ \left(\frac{d\vec{r}(\vec{\tau},\vec{a}_0)}{d\vec{\tau}}\right)^T V^{-1}\vec{r}(\vec{\tau},\vec{a}_0)) + \vec{r}(\vec{\tau},\vec{a}_0)^T V^{-1}\left(\frac{d\vec{r}(\vec{\tau},\vec{a}_0)}{d\vec{\tau}}\right) = \\ 2\cdot\left(\frac{d\vec{r}(\vec{\tau},\vec{a}_0)}{d\vec{\tau}}\right)^T V^{-1}\vec{r}(\vec{\tau},\vec{a}_0))) = 0, \end{aligned} \tag{4.5}$$

which means that this gives the best estimate for the track parameters $\vec{\tau}$.

In a simple geometry and a limited number of hits, Equation 4.5 without any modifications can be used. However, when a more complex scenario is considered, Equation 4.5 becomes a large set of non-trivial equations. The ATLAS detector has complex detector shapes and events can contain a large amount of vertices. A Taylor series is performed expanding to the first derivative of Equation 4.5 around initial track parameters τ_0, which are assumed to be close to the final solution of the track parameters $\tilde{\tau}$,

$$\frac{d\chi^2}{d\vec{\tau}} \approx \left.\frac{d\chi^2}{d\vec{\tau}}\right|_{\vec{\tau}=\vec{\tau}_0} + \left.\frac{d^2\chi^2}{d\vec{\tau}^2}\right|_{\vec{\tau}=\vec{\tau}_0}(\vec{\tau}-\vec{\tau}_0). \tag{4.6}$$

A Taylor series to the first derivate is a linear approximation, which means that in case τ_0 is close to our final solution $\tilde{\tau}$, the approximation is valid. The track parameter τ results from the equation as follows,

$$\vec{\tau} = \vec{\tau}_0 - \left(\left.\frac{d^2\chi^2}{d\vec{\tau}^2}\right|_{\vec{\tau}=\vec{\tau}_0}\right)^{-1}\left.\frac{d\chi^2}{d\vec{\tau}}\right|_{\vec{\tau}=\vec{\tau}_0}. \tag{4.7}$$

By iterating Equation 4.7, successively better results for τ are obtained; this is called the Newton-Raphson method. The process is repeated as

$$\vec{\tau}_{n+1} = \vec{\tau}_n - \left(\left.\frac{d^2\chi^2}{d\vec{\tau}^2}\right|_{\vec{\tau}=\vec{\tau}_n}\right)^{-1}\left.\frac{d\chi^2}{d\vec{\tau}}\right|_{\vec{\tau}=\vec{\tau}_n}, \tag{4.8}$$

until a convergence criterion value is reached, defined by a minimum change in χ^2.

4.1.2 Track-based alignment

Track-based alignment [123, 124] minimises track-to-hit residuals from Equation 4.3 by correcting the alignment parameters a, where they were set constant to a_0, the assumed geometry, before. As a is common to all reconstructed tracks [125], track-based alignment derives the alignment parameters a by minimising the χ^2 of the sum of all tracks with respect to a,

$$\frac{d\chi^2}{da} = 2 \cdot \sum_{tracks} \left(\frac{dr(\tau,a)}{da} \right)^T V^{-1} r(\tau,a))) = 0. \tag{4.9}$$

Minimising with respect to a will give us the detector geometry for which the goodness of fit is best for all the tracks considered in the alignment procedure. When using a large set of tracks inaccurate hits or statistical fluctuations get averaged out resulting in an estimate of the true geometry a.

A similar linear approximation is made as in the previous Section 4.1.1, but here the approximation is done around the assumed geometry a_0,

$$\frac{d\chi^2}{da} \approx \left. \frac{d\chi^2}{da} \right|_{a=a_0} + \left. \frac{d^2\chi^2}{da^2} \right|_{a=a_0} (a - a_0), \tag{4.10}$$

which again means that in case a_0 is close to our final solution $\tilde{a}$, the approximation is valid. Alignment constants then follow from

$$a = a_0 - \left(\left. \frac{d^2\chi^2}{da^2} \right|_{a=a_0} \right)^{-1} \left. \frac{d\chi^2}{da} \right|_{a=a_0}. \tag{4.11}$$

By iterating Equation 4.11, successively better results for a are obtained. Analogous to the global tack fit the process is repeated as

$$a_{n+1} = a_n - \left(\left. \frac{d^2\chi^2}{da^2} \right|_{a=a_n} \right)^{-1} \left. \frac{d\chi^2}{da} \right|_{a=a_n}. \tag{4.12}$$

In order to simplify notation and make Equation 4.11 more understandable, the equation can be rewritten as

$$\vec{a_n} = \vec{a_{n,0}} - M_{n,n}^{-1} \vec{v}_n, \tag{4.13}$$

where $\vec{a_n}$ denotes the obtained n-dimensional vector of alignment constants. The n-dimensional vector $\vec{a_{n,0}}$ contains the initial assumed alignment. The n×n matrix $M_{n,n}^{-1}$ is

given by

$$M_{n,n}^{-1} = \left(\frac{d^2\chi^2}{da^2}\bigg|_{a=a_n} \right)^{-1} \tag{4.14}$$

and needs to be inverted. The matrix contains the second derivative of χ^2 to the alignment constants. The n-dimensional vector $\vec{v}_n$ is given by

$$\vec{v}_n = \frac{d\chi^2}{da}\bigg|_{a=a_n}, \tag{4.15}$$

which contains the first derivative of χ^2 to the alignment constants.

4.1.3 Weak modes

In track-based alignment there are certain modes in the matrix $M_{n,n}$, from Equation 4.14, to which fitted tracks have little sensitivity to correct the alignment parameters. Weak modes are alternative descriptions of the detector geometry and are different from the true detector description. Weak modes preserve the helical trajectory of tracks and therefore do not affect the χ^2. The different configurations provide us with the same quality of track fits, and are the main source of systematic uncertainties associated with the alignment procedure [126].

They are called weak modes because they correspond to near-singular modes of the solution to the alignment problem. One can try to understand this by looking into $M_{n,n}$,

$$M_{n,n} = \frac{d^2\chi^2}{d\vec{a}^2}\bigg|_{a=a_n} = 2 \cdot \sum_{tracks} \left(\frac{d\vec{r}(\tau,a)}{d\vec{a}} \right)^T V^{-1} \left(\frac{d\vec{r}(\tau,a)}{d\vec{a}} \right), \tag{4.16}$$

which is a symmetrical matrix where all off-diagonal entries contain the correlations between detector elements. It can be imagined that there are many configurations in which this matrix can produce similar results with different alignment parameters, due to correlations. A weak mode is a set of such alignment parameters which leaves $M_{n,n}$ invariant, and thus is invariant to the alignment procedure.

4.2 Alignment procedure

Track-based alignment is used to correct the assumed detector geometry to the actual relative positions of all sensitive elements in the ID. The new geometry is stored in a database and subsequently used by the reconstruction [127]. Again, there are more than 350,000 sensitive elements within the ID, corresponding to a large number of free parameters. Due to

computation time and limited amount of tracks the alignment procedure can be split up into different groupings of alignable structures. These grouping are called alignment levels and are described in Section 4.2.1. Once the alignment levels have been established the frequency of the alignment is discussed in Section 4.2.2. For each data taking period there are different alignment campaigns, as well as run-by-run alignment. The alignment with first stable beams in 2016 is also discussed in this section.

4.2.1 Alignment levels

The alignment levels form a hierarchal structure, where the number of alignment parameters increases per level. The main compromise for choosing between the levels is the number of tracks that are available and the computation time. With each increment in alignment level more tracks are needed and computation time will be longer. The number of tracks is important to have a good amount of statistics. Computation time to obtain the alignment constants mainly depends on the inversion of $M_{n,n}$. As $M_{n,n}$ contains all the alignable structures, its size increases with each level. A larger $M_{n,n}$ to invert means longer computation time.

There are three main alignment levels, Level 1, Level 2 and Level 3. They are defined as Level 1 for large structures, Level 2 for separate layer and end-cap disk alignment, and Level 3 for alignment of separate modules. A more detailed description of the alignment levels and the corresponding number of alignable structures is given in Table 4.1. The orientation and positioning of an alignable structure in space is determined by six degrees of freedom, three translations T_x, T_y and T_z, and three rotations R_x, R_y and R_z. The IBL has one extra degree of freedom for bowing as discussed in Section 3.2.2.

4.2.2 Frequency of alignment

For Run-2 alignment campaigns are done for each data taking period: 2015, 2016, 2017 and 2018. There can be movements at the beginning of a data taking campaign and several changes in detector conditions, but within a data taking period it is assumed that the detector stays more or less the same. Only global movements and IBL bowing are corrected per run.

At the beginning of a data taking campaign there is no data yet to perform the alignment procedure; so before a data taking period starts, alignment can be done using calibration runs which consist of cosmic ray data and initial collisions runs. At this point alignment constants will be calculated at Level 2 and Level 3 if statistics allow to do so. The number of tracks will be limited in this case, making the alignment less precise. After the initial alignment constants have been derived, alignment can be done with the first stable beams of that data

Table 4.1: Alignment levels as defined in the software for each of the subdetectors. Naming and number of structures to be aligned at each level are given [128].

Alignment level	Detector	Alignable structures
Level 1	IBL: layer	1
	Pixel: barrel and end-caps	1
	SCT: barrel and 2 end-caps	3
	TRT: barrel and 2 end-caps	3
	Total	8
Level 2	IBL: layer	1
	Pixel: barrel layers	3
	Pixel: end-caps	6
	SCT: barrel layers	4
	SCT: end-caps	18
	TRT: barrel modules	96
	TRT: end-caps wheels	80
	Total	208
Level 3	IBL: modules	280
	Pixel: barrel modules	1456
	Pixel: end-caps modules	288
	SCT: barrel modules	2112
	SCT: end-caps modules	1976
	TRT: barrel wires	105088
	TRT: end-cap wires	245760
	Total	356960

taking period. The results of the first stable beam alignment in 2016, which has been worked on during this thesis, is described later in this section. When more data becomes available in a data taking period, alignment constants at Level 2 and Level 3 are recalculated, typically during a technical stop.

For each run alignment constants are calculated at Level 1 during the Calibration Loop. These corrections are calculated on top of the baseline alignment constants derived at the start of a data taking period or during a technical stop. Alignment is done at Level 1 because a run has a limited amount of tracks and because the frequency of this computation is about once a day, since there is a run every $\sim$ 12 hours. The Level 1 alignment in the Calibration Loop is described in Table 4.2, showing that global movements and IBL bowing are corrected. The alignment levels shown in the table are labeled Level 11 and Level 16, which correspond to specific configurations of Level 1 corrections. Level 11 corrects global movements, as

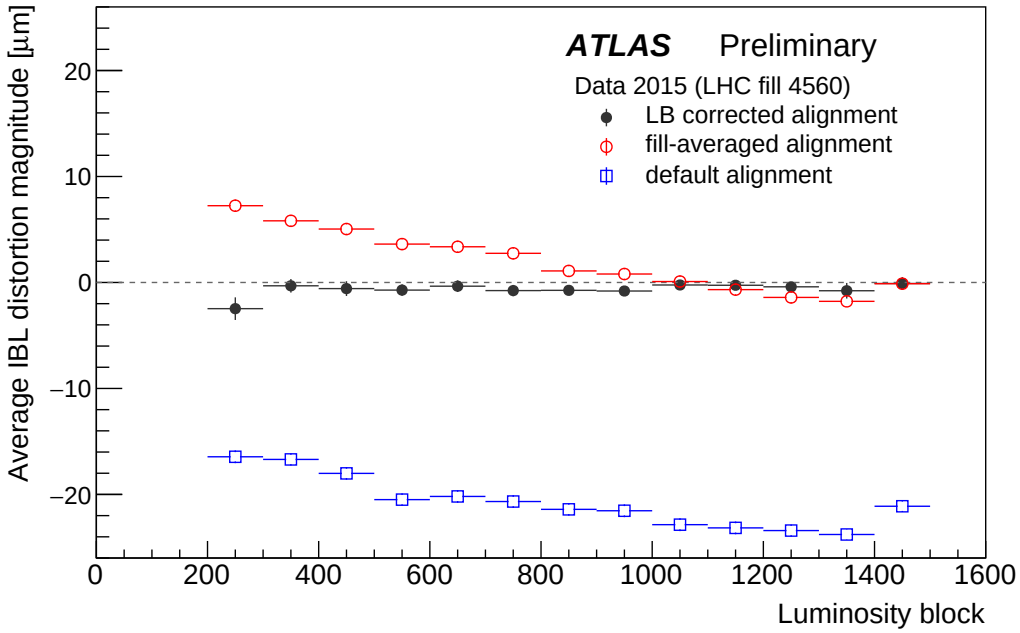

Fig. 4.3: IBL distortion magnitude in the transverse plane per luminosity block (LB) range for LHC fill 4560 averaged over all 14 IBL staves. The 'default' data (open blue squares) shows the average IBL distortion in the transverse plane after the default Inner Detector (ID) alignment. The 'LB corrected alignment' includes an additional time dependent alignment correction (solid black circles) [129].

well as the IBL bowing magnitude, M, averaged over the 14 staves. Level 16 corrects for the bowing in each stave independently, while keeping the rest of the ID fixed.

One set of Level 11 alignment constants is calculated for each run. Level 16 alignment is performed multiple times during a run, because the magnitude of IBL bowing can change over the course of a run as demonstrated in Figure 4.3. A run is divided into luminosity blocks (LB), an interval of constant luminosity and stable detector conditions, which have a length of the order of one minute. The Level 16 alignment intervals correspond to 100 LBs, for each of which a separate set of alignment constants is obtained. For both Level 11 and Level 16 the first 60 LBs are not considered in the alignment, to remove the effect at the start of a run where there can be a bias due to pixel movement of a few µm because of the detector temperature.

At the end of a data-taking period the whole alignment procedure is performed again in a reprocessing campaign. Here the alignment constants at Level 2 and Level 3 are recalculated. For each run new Level 1 alignment constants are calculated on top of these new alignment base constants, similar to the Calibration Loop during the data taking period.

Table 4.2: Alignment levels in Calibration Loop. At Level 11 the IBL bowing magnitude, M, is averaged over the 14 staves. At Level 16 each of 14 staves in IBL has a separate bowing magnitude [130].

Level 11							
Structure	T_x	T_y	T_z	R_x	R_y	R_z	M
IBL	✓	✓	✓	✓	✓	✓	✓ (1 d.o.f.)
Pixel	✓	✓	✓	✓	✓	✓	×
SCT: barrel	Kept fixed as reference						
SCT: end-caps	✓	✓	×	×	×	✓	×
TRT: barrel	✓	✓	×	✓	✓	✓	×
TRT: end-caps	✓	✓	×	×	×	✓	×
Level 16							
IBL	×	×	×	×	×	×	✓ (14 d.o.f.)
Pixel	Kept fixed as reference						
SCT	Kept fixed as reference						
TRT	Kept fixed as reference						

Alignment with first stable beams in 2016

During this thesis the alignment with the first stable beams in 2016 was performed. The alignment was performed starting from previously derived aligned constants obtained during calibration weeks before the start of data taking. In Table 4.3 the steps that were undertaken for each alignment level are presented. The number of iterations done at each level is determined by the convergence of the alignment parameters, an example is illustrated for step 2 in Figure 4.4. The goal of the alignment procedure was to obtain alignment constants at Level 3, which have been derived for the IBL, Pixel and SCT barrel, and the Pixel end-caps. Level 3 alignment for SCT end-caps and TRT have not been derived as both subdetectors contain a lot of alignable structures as can be seen from Table 4.1; for such a granularity more statistics are needed.

The performance of the alignment is measured using unbiased track-to-hit residuals. Unbiased means that the hit under consideration will be taken out of the track fit when the track-to-hit residual is calculated. The mean of the residuals is expected to be at zero in case of correct alignment, and the smaller the full width at half maximum (FWHM), the smaller the residuals. The aim is a FWHM of the order of 10 µm for the Pixel and SCT detectors, and of the order of 100 µm for the TRT [131]. In Figure 4.5 the performance of the IBL and Pixel alignment is presented. The mean of the residuals for the IBL and Pixel barrel, and Pixel end-caps is within $1-2$ µm after alignment. In Figure 4.6 the alignment of the

Table 4.3: Steps that were undertaken for in the alignment with first stable beams in 2016.

Step	Alignment level	Iterations	Goal
1	Level 11	6	**Correct global movements**
	Comments: Old constants are used and Pixel barrel is kept as reference IBL aligned with 6 d.o.f. (there was no apparent bowing shape after quiet beam alignment)		
2	Level 2	4	**Pixel and SCT barrel+end-caps**
	Comments: IBL and TRT fixed as reference		
3	Level 16	4	**IBL staves**
	Comments: Rest of ID fixed as reference		
4	Level 3	8	**IBL modules**
	Comments: Rest of ID fixed as reference		
5	Level 3	4	**Pixel and SCT barrel**
	Comments: Additional constraints on d_0, z_0 and momentum TRT is fixed as reference		
6	Level 3	3	**Pixel and SCT barrel and Pixel end-caps**
	Comments: Additional constraints on d_0, z_0 and momentum TRT is fixed as reference		
7	Level 2	4	**TRT barrel+end-caps**
	Comments: Rest of ID fixed as reference		

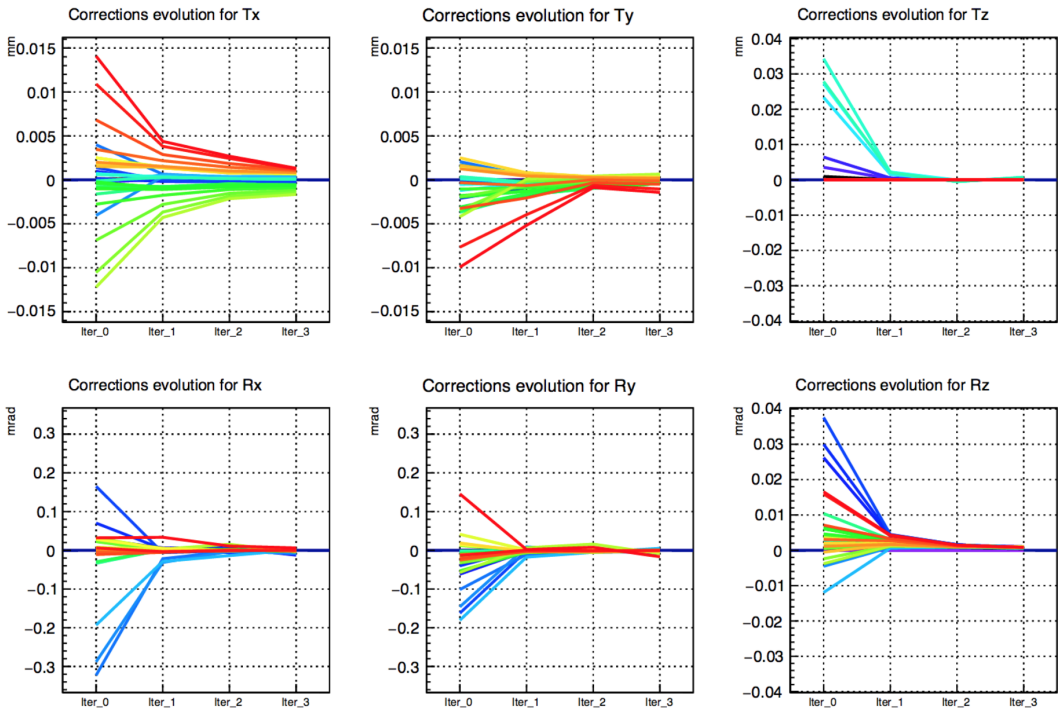

Fig. 4.4: Convergence for alignment Level 2. In this case the IBL and the TRT are held fixed. The convergence is seen for the Pixel barrel layers and end-caps, and SCT barrel layers and end-caps.

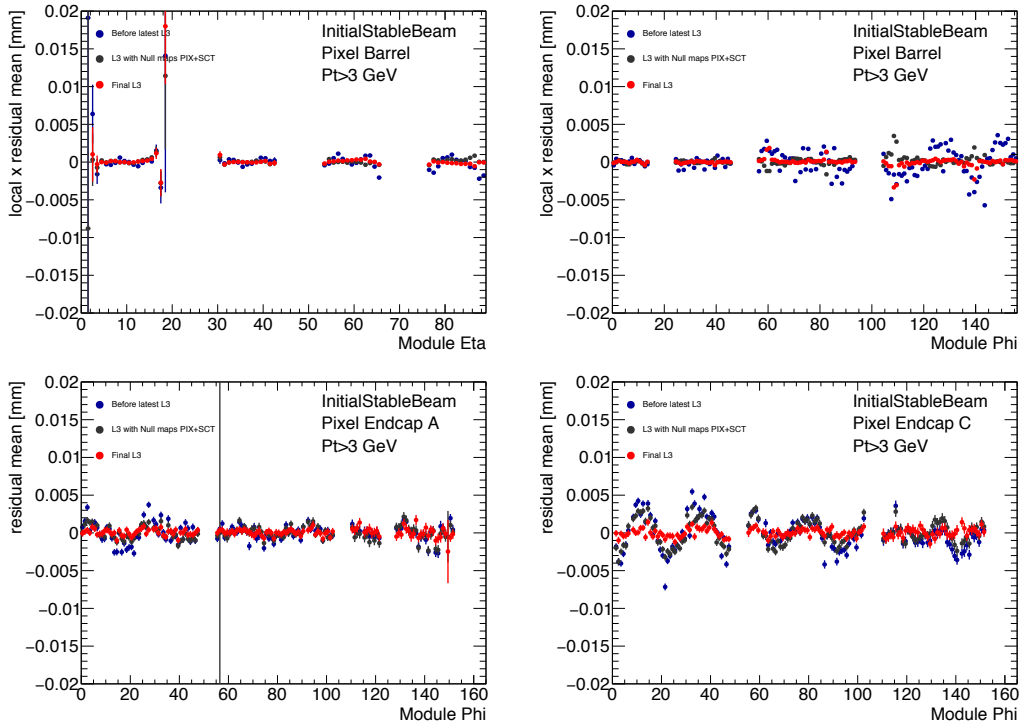

Fig. 4.5: Mean of the residuals in IBL, Pixel barrel and Pixel end-cap modules as a function of η and ϕ. The mean of the residuals for the IBL, Pixel barrel and Pixel end-caps is within $1-2\,\mu$m.

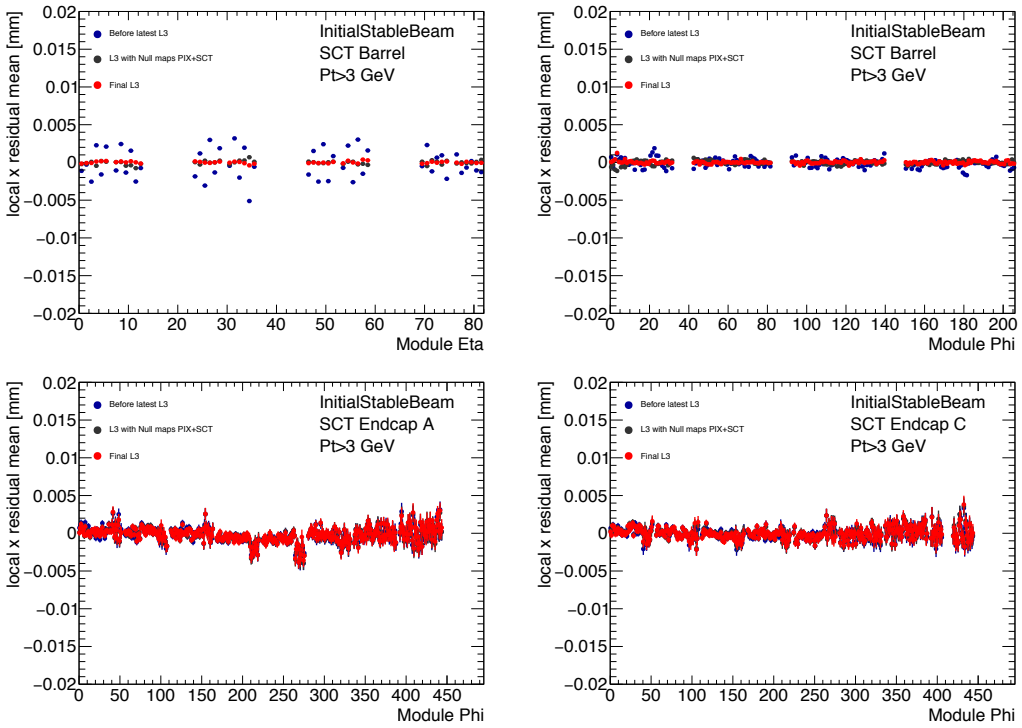

Fig. 4.6: Mean of the residuals in SCT modules in barrel and end-cap as a function of η and ϕ. The mean of the residuals in the SCT barrel is within $1-2\,\mu$m, and for the SCT end-caps within $5\,\mu$m.

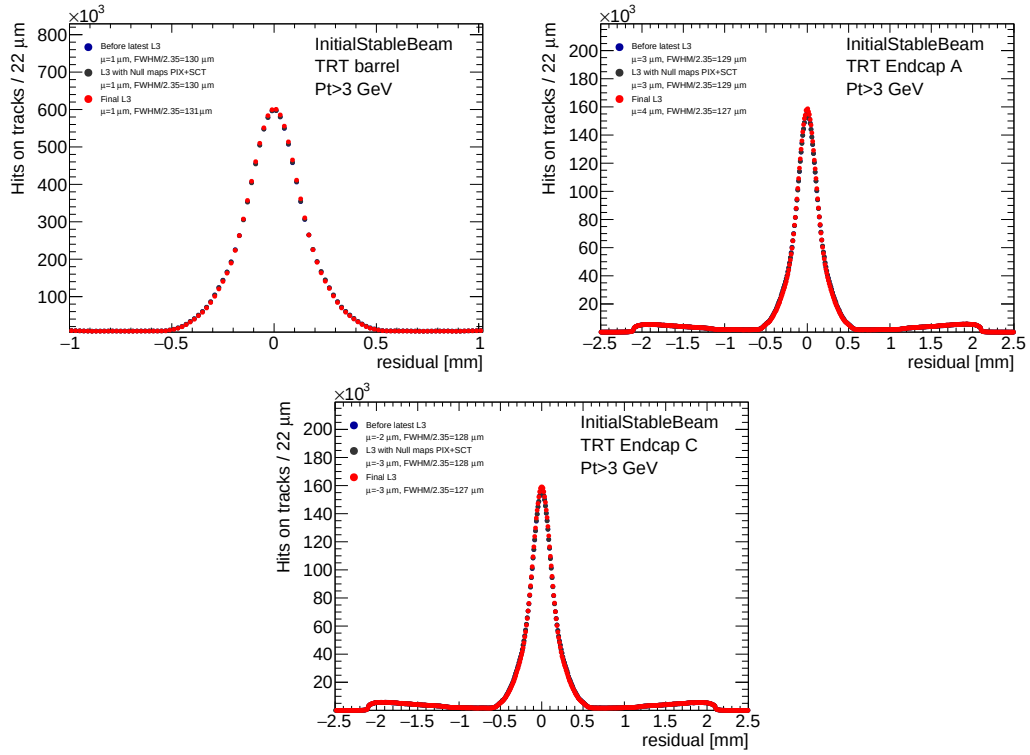

Fig. 4.7: Residuals of the TRT barrel, end-cap A and end-cap C. The mean of the residuals for the TRT barrel is 1 µm, 4 µm for end-cap A and 3 µm for end-cap C.

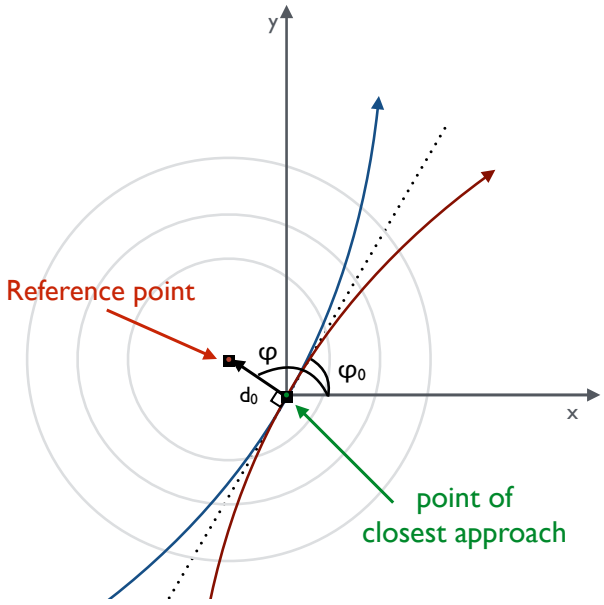

Fig. 4.8: Definition of the transverse impact parameter d_0 [132].

SCT is demonstrated. The mean of the residuals for the SCT barrel is within $1-2\,\mu$m, and for the SCT end-caps within $5\,\mu$m. The SCT barrel displayed an oscillatory pattern in η of its modules after the shutdown, this happened before after a shutdown. The track-to-hit residuals for the TRT alignment can be seen in Figure 4.7. The mean of the residuals for the barrel is $1\,\mu$m, $4\,\mu$m for end-cap A and $3\,\mu$m for end-cap C.

4.3 Alignment monitoring

The alignment procedure is invariant to weak modes as described in Section 4.1.3. While the weak modes provide the same quality of track fits, they do affect the track parameters highlighted in Equation 4.1, of which the most important ones are d_0 and q/p. Measurements related to beam-spot reconstruction, primary and secondary vertex fitting, and b-tagging performance all rely on a good estimation of d_0, while q/p is important for the invariant mass of resonances.

Track parameters d_0 and z_0 are the distances from the point of closest approach of a chosen reference in the transverse plane and along the z-axis, respectively. The definition of d_0 can be seen in Figure 4.8. The reference point of the d_0 parameter is free to choose. Generically the reference point for d_0 is defined to be the primary vertex (PV) or the beamspot; for example in a $Z \to \mu\mu$ decay it is defined as the vertex of the Z. When looking at a large

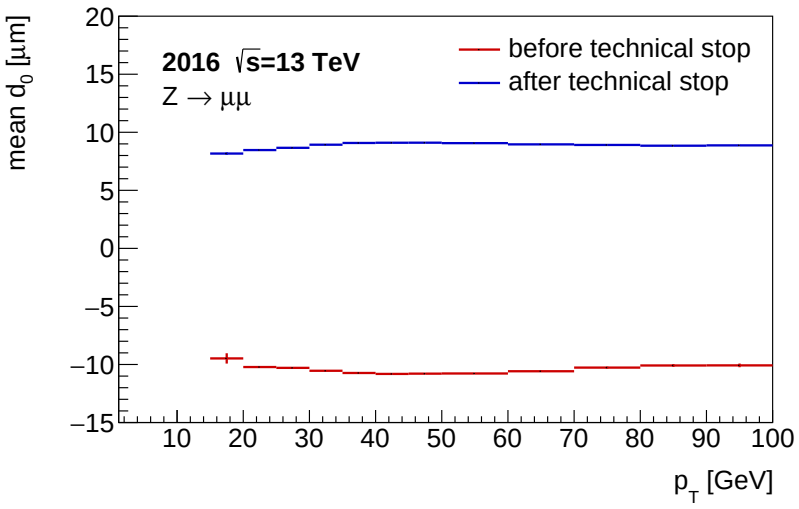

Fig. 4.9: Mean d_0 as a function of p_T. A bias in d_0 was introduced by the alignment procedure during the first technical stop in 2016.

number of tracks, d_0 is expected to be centred around zero, since particle production is uniform in the transverse plane. If the mean d_0 deviates from zero, a bias is observed.

As mentioned, a weak mode introduced by the alignment procedure affects the track parameters. When the alignment procedure was performed during the first technical stop in 2016, a bias in track parameter d_0 was introduced as a consequence of a weak mode as can be seen in Figure 4.9. The two types of weak modes that could be responsible for this are: a radial expansion, discussed in Section 4.3.1 and illustrated in Figure 4.10(a), or a curl as presented in Figure 4.10(b).

4.3.1 Radial expansion

A bias in d_0 can be explained as a a global radial expansion of all layers of the ID. Figure 4.11 demonstrates how a radial expansion, denoted by the dotted lines, of the true detector, denoted by the solid line, causes a bias in d_0. The alignment parameter, R_{Layer}, the radius of curvature of the track, R_{Trk}, and d_0 are highlighted. For ease of illustration, it is assumed that the track is tangential to the first measurement plane. It can be seen that the following formula can be constructed [132],

$$R_{\text{Trk}} + d_0 = \sqrt{R_{\text{Layer}}^2 + R_{\text{Trk}}^2}. \tag{4.17}$$

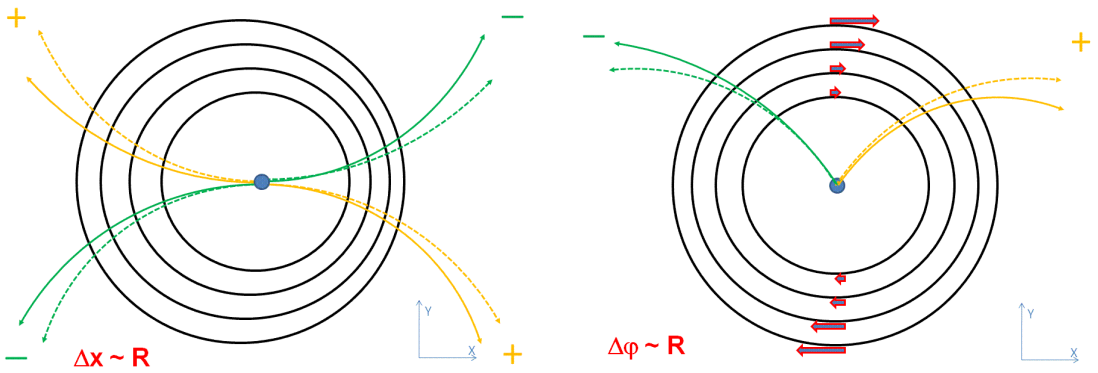

(a) Radial expansion. **(b)** Curl distortion.

Fig. 4.10: Example of weak modes affecting the measured particle. The detector deformation as well as the impact on the reconstructed particle momenta are illustrated. The true particle trajectories are shown as dashed lines, and the reconstructed trajectories as solid lines [126].

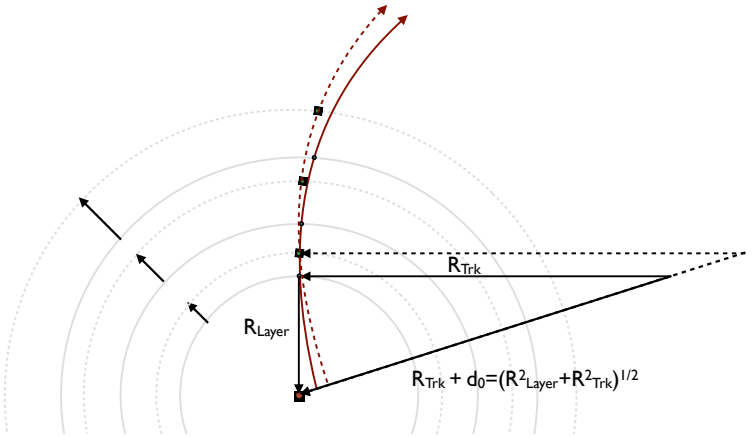

Fig. 4.11: Schematic diagram of global expansion of the detector and its impact on the measurement of the transverse impact parameter, d_0 [132]. The radial expansion is denoted by the dotted lines and the true detector is denoted by the solid line.

Assuming a global radial expansion of all layers of the detector by a factor $1+dr$, the alignment parameter would then change by

$$R_{\text{Layer}} \rightarrow R_{\text{Layer}}(1+dr). \tag{4.18}$$

Also the radius of curvature of the track, R_{Trk}, of all tracks will be scaled by a factor $1+dr$,

$$R_{\text{Trk}} \rightarrow R_{\text{Trk}}(1+dr). \tag{4.19}$$

The measured d_0 then also moves by a factor of $1+dr$,

$$d_0 \to d_0(1+dr). \tag{4.20}$$

Reorganising this equation an observed bias in the impact parameter, Δd_0, of tracks can be interpreted as an expansion of the detector,

$$\delta_r = \frac{\Delta d_0}{\sqrt{R^2_{\text{Layer}} + R^2_{\text{Trk}}} - R_{\text{Trk}}}. \tag{4.21}$$

Assuming a radial expansion of about 0.1% this corresponds to an observed d_0 bias of around 2.5 µm, which is a bias that can easily be introduced by alignment.

There are a few things to note about the effect of a radial expansion on the measured impact parameter. The first is that positive and negative tracks will be biased in opposite directions, because when the detector expands the measured d_0 will move in the direction of the point of curvature of the track. The second is that if there are an equal number of positive and negative tracks, the change on the average d_0 should be zero as the effects cancel out, but, the resolution will be degraded. The third aspect to note is that tracks with a lower momentum will be more sensitive to radial biases, due to the smaller radius of curvature.

4.3.2 Monitoring of d_0 and z_0

The alignment procedure can cause a bias in d_0 or z_0 due to weak modes, and such a bias has a negative effect on the ability to reconstruct tracks. In order to prevent such a bias being introduced by the alignment as happened after the first technical stop in 2016, new diagnostic figures for d_0 and z_0 are introduced. The figures allow to spot problems in the alignment during data taking and allow to correct the bias before the data is used by the collaboration.

For the diagnostic figures of d_0 or z_0, the chosen reference point is the PV of the event.[1] The monitoring is split up into several different categories of track charge and p_{T}. Tracks with different charge are monitored because they follow an opposite helical trajectory from one another, and the p_{T} of the track is monitored because the accuracy to reconstruct a track depends on the track's radius of curvature in the detector. The different categories that are monitored are demonstrated in Table 4.4.

The different categories are further split up into η and ϕ bins to monitor the different detector areas. For each η and ϕ bin an iterative gaussian fit is performed as highlighted in Figure 4.12. The previous fit parameters are used as input until the mean converges, to extract

[1] The PV should have at least 10 tracks associated to it.

Table 4.4: Monitoring is split up into different categories of and p_T in order to monitor a bias in d_0 or z_0.

Charge	p_T
Positive tracks	$400-600$ MeV
	600 MeV -1 GeV
	$1-2$ GeV
	$2-5$ GeV
	$5-10$ GeV
	>10 GeV
Negative tracks	$400-600$ MeV
	600 MeV -1 GeV
	$1-2$ GeV
	$2-5$ GeV
	$5-10$ GeV
	>10 GeV

the mean of the d_0 and z_0 distribution. After the η and ϕ bins have been fitted, they are combined into η and ϕ maps as shown in Figure 4.13. A selection of the diagnostic figures can be seen from the 600 MeV-1 GeV p_{T} category. Besides creating maps, also profiles in ϕ and η have been made as presented in Figure 4.14.

The monitoring plots are used in the Data Quality (DQ) webmonitoring, as displayed in Figure 4.15. The monitoring assigns a flag to indicate the severity of the bias in d_0 and z_0, of which the values are presented in Table 4.5. Using this new procedure the bias in d_0 or z_0 can be observed for every run. It allows to assess whether a bias in d_0 or z_0 is being introduced, such that unlike in the first technical stop of 2016, such a bias will be noticed in advance.

Table 4.5: Flags for the webmonitoring that will indicate if a bias in d_0 or z_0 is present in the data.

Flag	average d_0 and z_0 bias
Green	$1-2\,\mu$m
Yellow	$2-4\,\mu$m
Red	$>4\,\mu$m

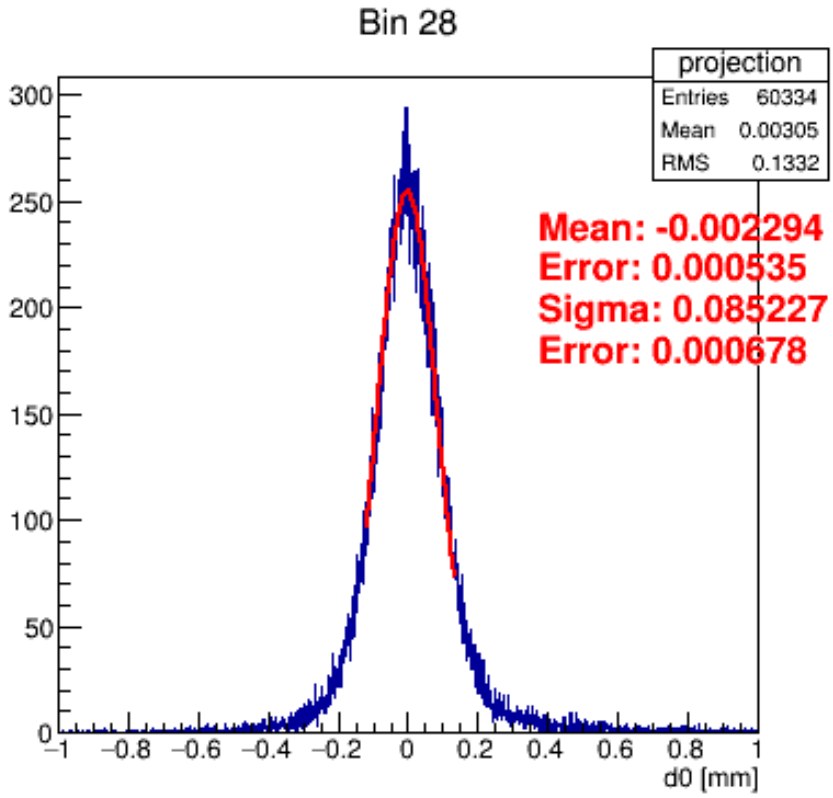

Fig. 4.12: Fit in one of the η and ϕ bins. The mean of the iterative gauss fit is -0.002294, where the arithmetic mean is 0.00305. The tails of the d_0 and z_0 distribution affect the mean and the fit on the core of the gauss makes sure the correct result is obtained.

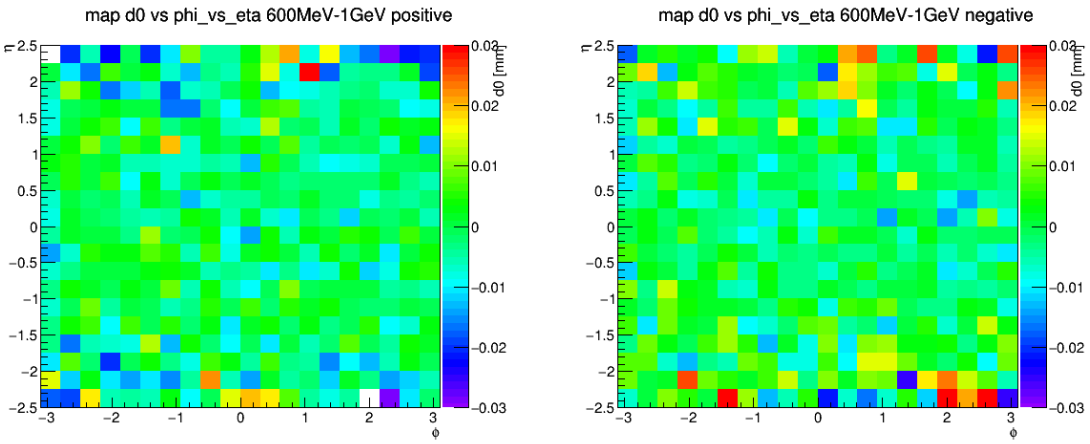

(a) Positive tracks. **(b)** Negative tracks.

Fig. 4.13: Monitoring of d_0 using maps of η and ϕ for tracks of p_{T} between 600 MeV-1GeV.

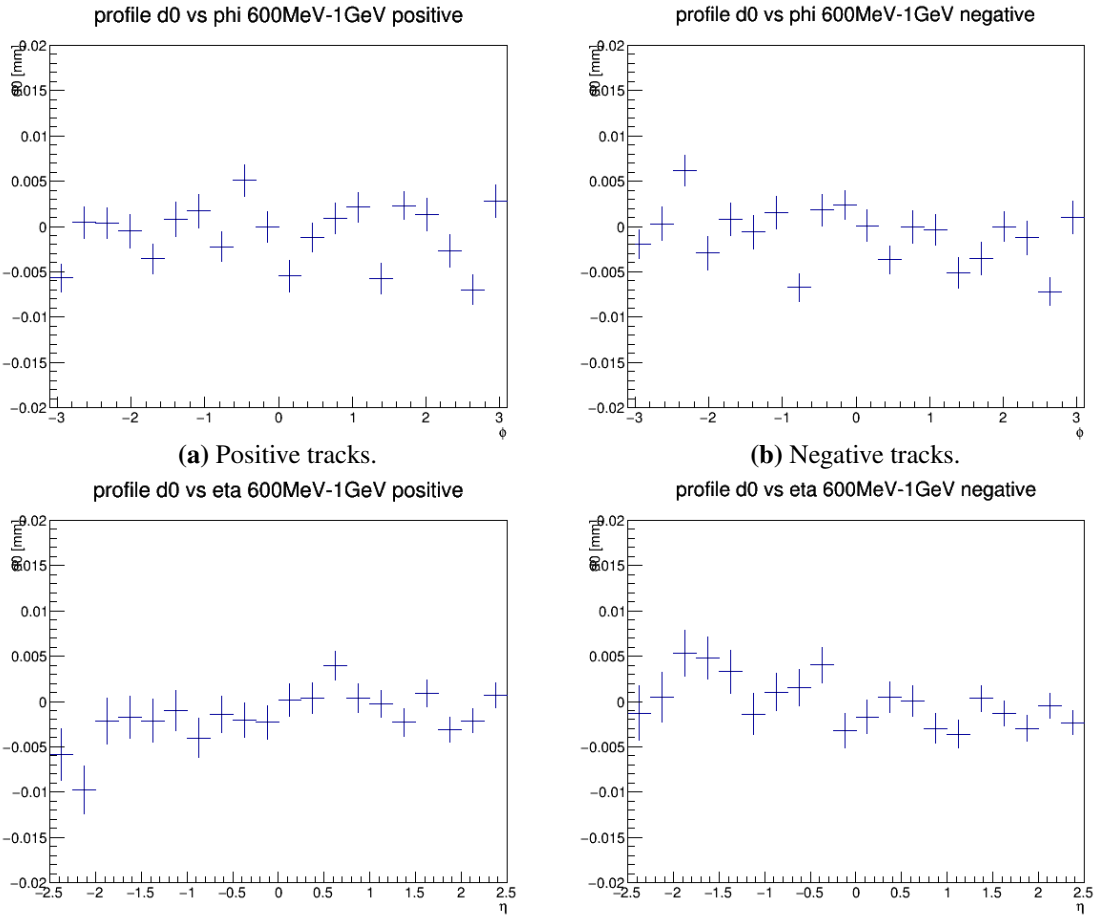

(a) Positive tracks. **(b)** Negative tracks.

(c) Positive tracks. **(d)** Negative tracks.

Fig. 4.14: Monitoring of d_0 using a profile versus (**a-b**) ϕ and (**c-d**) η for tracks of p_{T} between 600 MeV-1GeV.

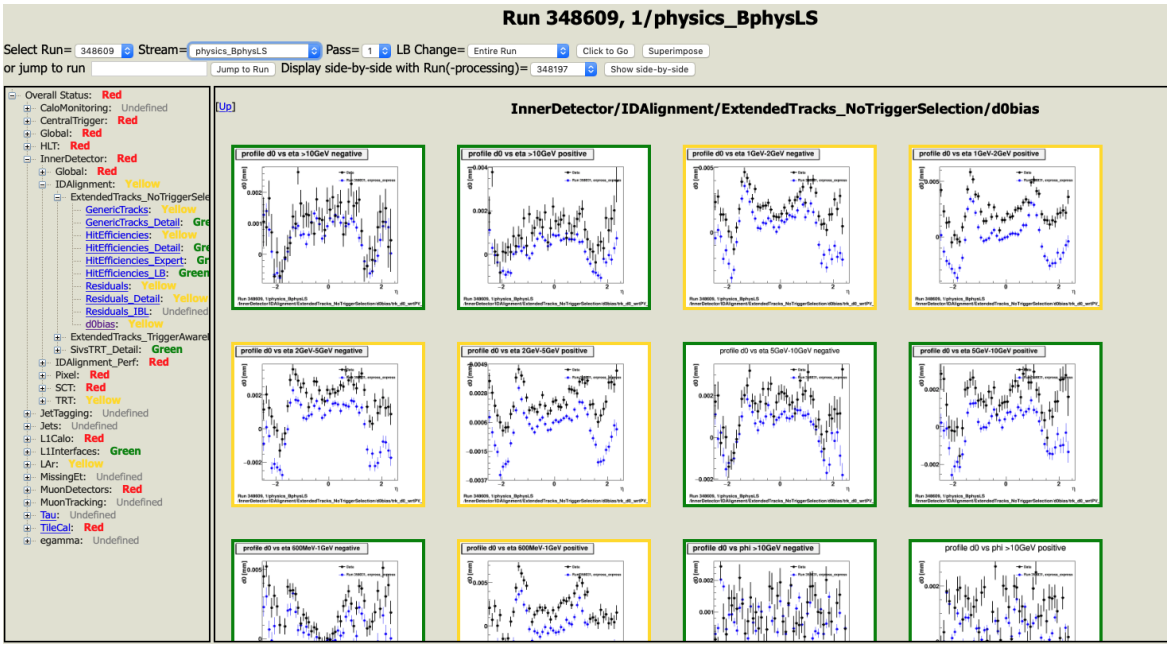

Fig. 4.15: A screenshot of the Data Quality web monitoring of run 348609, showing the physics_BphysLS stream. The green and yellow flags indicate if a bias in d_0 or z_0 is present in the data.

Chapter 5

Event reconstruction

In the ATLAS detector particles are produced in proton-proton (p-p) collisions. The particles travel through the detector and are measured by the various subdetectors as described in Section 3.2. The measurements from these subdetectors provide us with raw data, the digitised detector response. However, not the digitised detector response, but the created particles and their physical properties are required to study p-p collisions. The event reconstruction is done starting from the digitised detector response of the ATLAS detector to see which particles were created in the p-p collision.

The event reconstruction first combines hits in the Inner Detector (ID) to form particle tracks. These tracks are then combined to reconstruct the spatial position of the p-p interaction, the vertex. The reconstruction of tracks and vertices is described in Section 5.1. Tracks are then combined with measurements in the Electromagnetic (EM) and Hadronic (HAD) calorimeters and the Muon Spectrometer (MS) to reconstruct particles and their physical properties. The reconstruction of jets is discussed in Section 5.2, of leptons in Section 5.3 and 5.4, and of missing transverse momentum, $E_{\mathrm{T}}^{\mathrm{miss}}$, in Section 5.5.

5.1 Track and vertex reconstruction

Charged particles originating from the p-p collision create hits in the ID. The event reconstruction in the ID combines these hits to form particle tracks, where the geometry of the ID obtained from the alignment procedure described in Chapter 4 is used. Particle tracks are combined to find the vertex of the particle. The vertex with the highest $\sum_i^{N_{trk}} p_T^2$ is called the primary vertex (PV), the other vertices are labeled as pile-up vertices.

5.1.1 Track reconstruction in the Inner Detector

Hits in the ID are combined into tracks corresponding to a charged particle. Charged particles follow a helical trajectory due to the axial magnetic field in the ID and are identified using the New Tracking Algorithm [133]. Tracks can originate from the p-p hard scatter, which are labeled as primary tracks, from the decay of a long-lived particle, which are labeled as secondary tracks, or from interaction of the particle with the material, which are labeled as conversion.

For primary tracks an inside-out track reconstruction algorithm is used. The algorithm is referred to as inside-out because it seeds at the inside of the ID, starting from three hits in separate layers of the innermost part of the ID: the IBL, Pixel and SCT detectors. A Kalman filter is then used to decide which hits in the Pixel and SCT layers outward from the seed are added to form the track [134, 135]. After having identified the potential tracks a scoring algorithm decides which tracks to keep by resolving track ambiguities [136]; an example of a track ambiguity is when a hit is shared by two different tracks.

For secondary and conversion tracks an outside-in track reconstruction algorithm is applied. In this algorithm the seed starts from the outside part of the ID: the TRT segments. Starting from the outside TRT seed, hits are added from the innermost part of the ID, the SCT, Pixel and IBL.

After having identified hits that belong to a track, a global track fit is performed to obtain the particle track from the combined hits, as described in more detail in Section 4.1.1. Tracks are described by the following parameters: d_0 is the distance to the point of closest approach between the track candidate and the vertex in the transverse plane, z_0 is the z-coordinate where d_0 is measured, ϕ_0 is the azimuthal angle, θ is the polar angle and q/p is the ratio of the particle charge and momentum.

Since the particle follows a helical trajectory because of the axial magnetic field, the momentum can be determined by

$$p_T = 0.3 \cdot B \cdot R, \tag{5.1}$$

where B is the magnetic flux density and R is the curvature of the track. The magnetic flux density in the ID is 2 T, causing tracks with a $p_{\mathrm{T}} \lesssim 400$ MeV to bend away from the calorimeter by the solenoid magnetic field in the ID cavity [95]. As a consequence tracks are reconstructed with a $p_{\mathrm{T}} > 400$ MeV.

The track reconstruction efficiency can be measured using MC as demonstrated in Figure 5.1. It can be seen that different selections have been used, `Loose` and `Tight Primary`, corresponding to different quality cuts. The `Loose` selection allows for holes in the Pixel

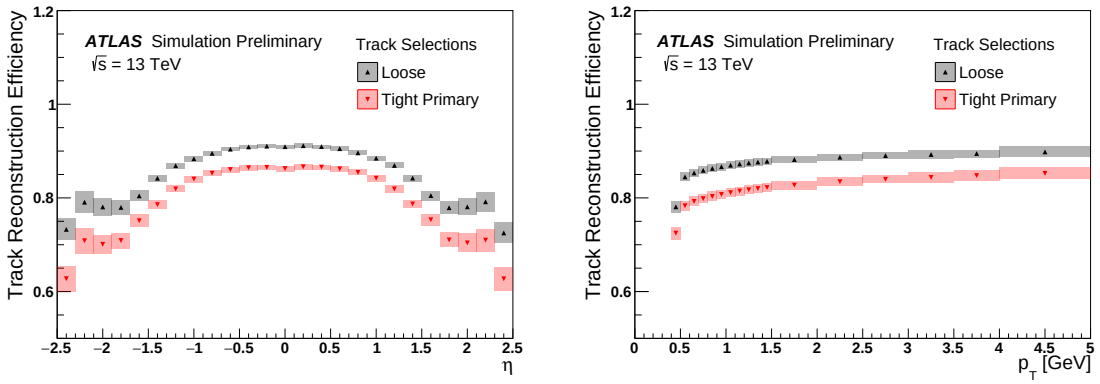

(a) **(b)**

Fig. 5.1: Track reconstruction efficiency **(a)** as a function of η for $p_{\mathrm{T}} > 400$ MeV and **(b)** as a function of p_{T} for $|\eta| < 2.5$. The efficiency is evaluated by using minimum bias simulated events for `Loose` and `Tight Primary` track selections. The coloured bands indicate the total systematic uncertainty [137].

layer and requires at least 7 hits in the Pixel and SCT layers, while the `Tight Primary` selection does not allow holes in the Pixel layer and requires 9 or 11 hits in Pixel and SCT layers depending on η.[1] It can be seen that, as a consequence of the tighter quality cuts, the `Tight Primary` selection has a lower track reconstruction efficiency.

There is the possibility that a reconstructed track does not correspond to a particle from the p-p collision, but instead is a random combination of hits that forms a helical trajectory, such a track is called a fake track. As is shown in Figure 5.2(a) the number of tracks in an event increases with increasing pile-up, μ, as described in Section 3.1.1, meaning there will be more hits in the ID. If there are more hits in the ID the number of random combinations that forms a helical trajectory, and thus fake tracks, will increase. Figure 5.2(b) illustrates that the `Tight Primary` selection is more effective at reducing the fake tracks at high pile-up compared to the `Loose` selection. Using the `Tight primary` selection the fake rate is below 1% at higher μ.

5.1.2 Primary vertex reconstruction

To reconstruct the PV it is required to assign particle tracks to the correct vertex. Due to pile-up there are multiple vertices in an event as presented in Figure 5.3. An algorithm assigns particle tracks to the correct vertex. The tracks selected for the vertex reconstruction are `Tight Primary`. Tracks are combined to find their common origin: the spatial position of the p-p interaction vertex. An algorithm applying an iterative procedure starts with a seed

[1] A hole is a missing hit on one of the layers the track traverses.

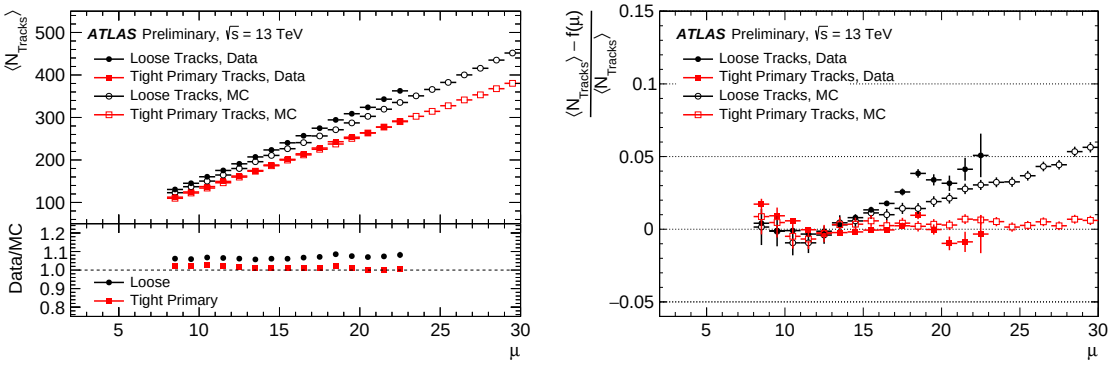

(a) **(b)**

Fig. 5.2: **(a)** Average number of reconstructed tracks as a function of μ for data and minimum bias simulation. The statistical uncertainty on the mean number of tracks is considered, but is too small to be seen. **(b)** Estimation of the tracking fake rate, derived from the deviation from linearity of a fit to $\langle N_{\text{Tracks}} \rangle$ as a function of μ. The fit is denoted as $f(\mu)$. The displayed μ range for data, in contrast to simulation, is limited by the available μ values in the data sample [137].

for a vertex and then measures a track's compatibility with that particular vertex [138]. The global maximum of z_0 over all combined tracks, with respect to a fixed reference point, is taken as the seed. Using a χ^2 adaptive vertex fitter the compatibility of each track with the vertex is assessed [139] and tracks that match the vertex are assigned to the seed. The next iteration then starts analysing the tracks that were not assigned to the previous vertex in order to find the next vertex. The procedure is iterated until no additional vertices can be found.

Once all the vertices are found the vertex which has the highest $\sum_i^{N_{trk}} p_T^2$ is assigned to be the PV. The remaining vertices are pile-up vertices. This criterion is based on the assumption that the charged particles produced in p-p collisions have on average a harder transverse momentum spectrum than those produced in pile-up collisions [143]. Figure 5.4(a) highlights the performance of the vertex reconstruction. The figure shows that with four tracks the efficiency for vertex reconstruction is above 99% in a low-μ run. Figure 5.4(b) shows that even though the vertex reconstruction is fully efficient at four tracks, the z resolution still increases with more tracks. An increased z resolution helps to assess whether a track corresponds to the PV.

5.2 Jets

Quarks and gluons are produced by the p-p interactions and since they are colour charged particles they are not observable as free particles. Quarks and gluons created in the collision undergo a fragmentation and a hadronisation process, eventually forming colourless hadrons.

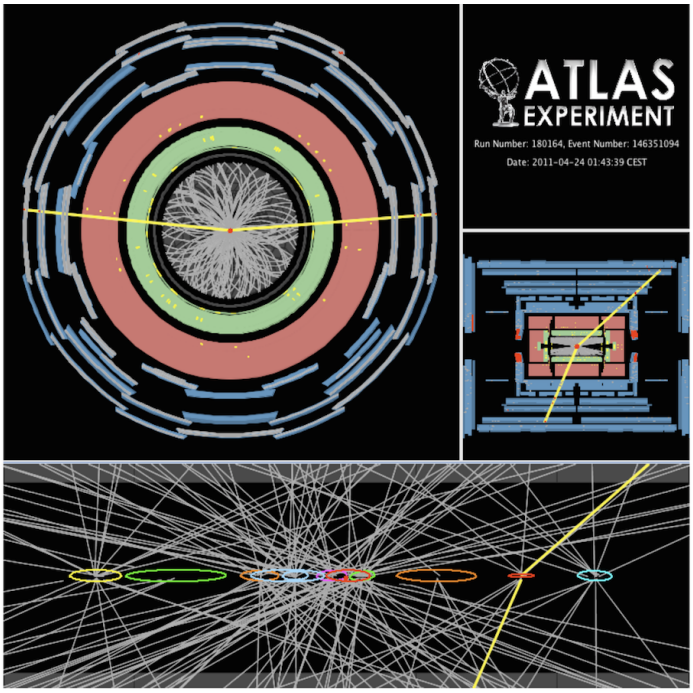

Fig. 5.3: Event display showing a Z boson decaying into two muons with 11 reconstructed vertices [140].

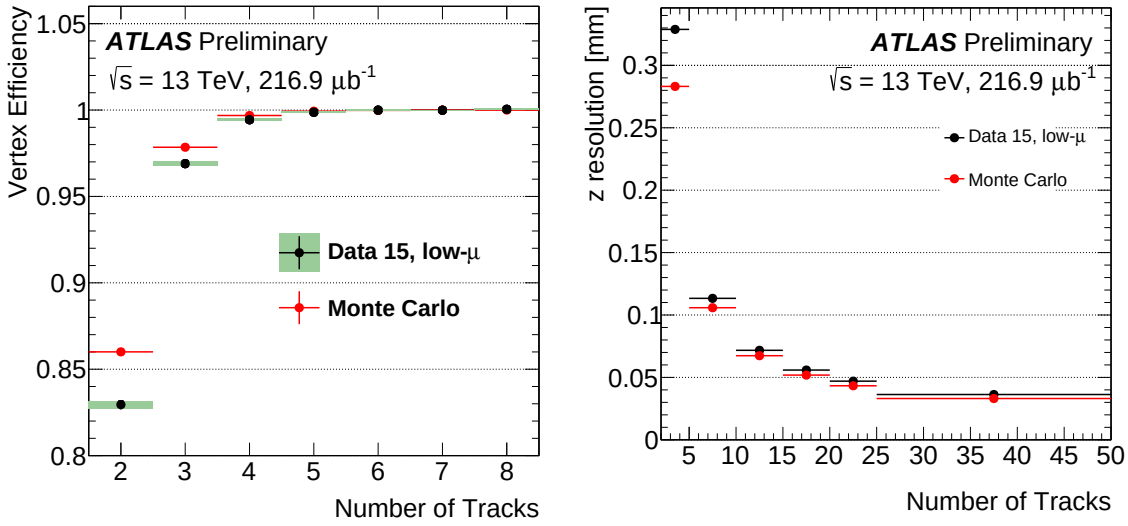

(a) **(b)**

Fig. 5.4: **(a)** Efficiency of vertex reconstruction as a function of the number of tracks in low-μ data [141, 142]. **(b)** Primary vertex (PV) z resolution as a function of the average number of tracks used in the Split-Vertex method. The Split-Vertex method works by randomly splitting the reconstructed vertices in two, each part conserving approximately half the original number of tracks with approximately the same $\sum p_{\mathrm{T}}$, such that two independent vertices can be reconstructed. It is possible to use their separation to get an estimate of their combined intrinsic resolution.

The colourless hadrons form a narrow cone originating from the original quark or gluon. This collimated spray of hadrons is called a jet. The HAD calorimeter stops the jets and measures their energy deposition and position. The signature of a jet is a large energy deposit in the EM and HAD calorimeter and collimated charged particle tracks in the ID.

Reconstruction

Jets typically leave a large energy deposit in the calorimeter. Calorimeter clusters are built from neighbouring calorimeter cells [144] and jets are then reconstructed using the anti-k_t algorithm [145] if they pass a p_{T} threshold of 7 GeV. The algorithm merges calorimeter clusters together using,

$$d_i = E_{\mathrm{T},i}^{2p}, \tag{5.2}$$

and,

$$d_{ij} = min(E_{\mathrm{T},i}^{2p}, E_{\mathrm{T},j}^{2p}) \frac{\Delta R_{ij}^2}{R^2}, \tag{5.3}$$

where E_T is the transverse energy, R defines the size of the jet cone, and ΔR_{ij}^2 the distance between two un-merged jets. The algorithm finds the smallest of all the d_i and d_{ij} and labels it d_{min}. If the d_{min} that is found is originally calculated from d_{ij}, the algorithm merges clusters i and j into a new cluster k, and the algorithm continues. If the found d_{min} is calculated from d_i, it means the corresponding cluster i is not mergable and i is removed from the list of clusters and added to the list of jets [146]. The case of $p = -1$ corresponds to the anti-k_t algorithm; it ensures that soft radiation will be clustered together to the hard object before being merged between themselves. Jets are clustered using $R = 0.4$. Jets also leave collimated sets of charged particle tracks in the ID. The particle tracks that can be associated to the jet must be within full acceptance of the ID ($|\eta| < 2.5$), need to have a minimum p_{T} of 500 MeV and need to be associated to the hard-scatter vertex. A neural network clustering algorithm [147] groups the tracks that belong to the jet.

After the jet has been reconstructed the energy is calibrated. The Jet Energy Scale (JES) calibration [144] calibrates the reconstructed jet energy with a series of simulation-based corrections and in situ techniques. Also muon track segments are used in the jet calibration to capture the jet energy carried by energetic particles not stopped by the calorimeter. The calibration stages are summarised in Figure 5.5 for jets that are reconstructed with the anti-k_t algorithm and radius parameter $R = 0.4$ at the electromagnetic energy scale (EM scale), corresponding to $0.2 < p_{\mathrm{T}}^{\mathrm{jet}} < 2$ TeV. The uncertainty for the different steps in the JES calibration versus p_{T} and η is visualised in Figure 5.6.

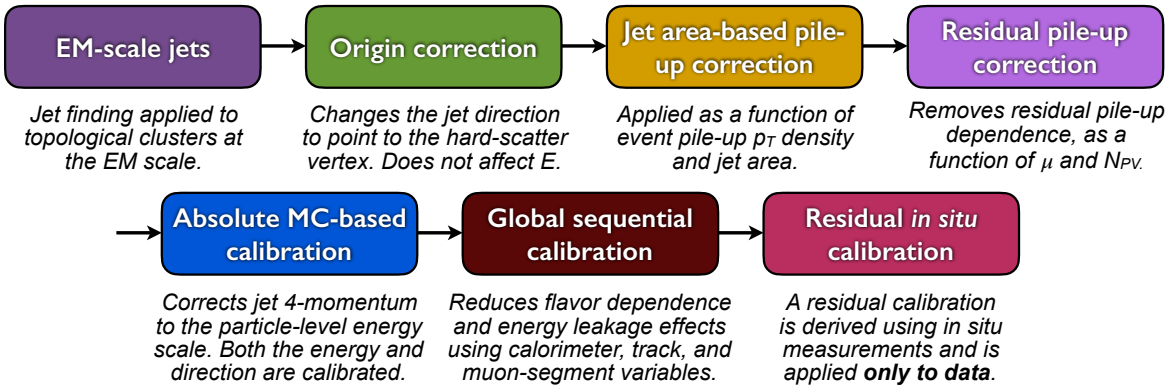

Fig. 5.5: Calibration stages for jets at the EM scale reconstructed with the anti-k_t algorithm and radius parameter $R = 0.4$. Each stage of the calibration corrects the full four-momentum of the jet [144].

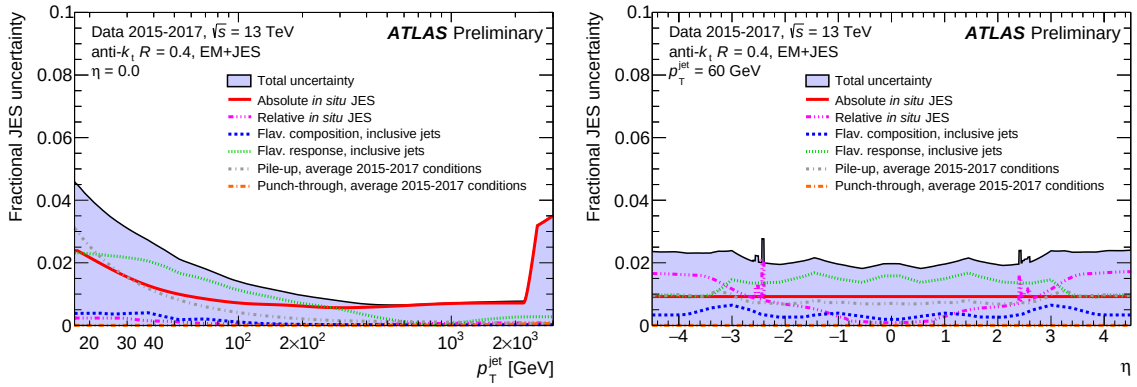

Fig. 5.6: **(a)** Fractional jet energy scale systematic uncertainty components as a function of p_{T}^{jet} at $\eta = 0.0$. **(b)** Fractional jet energy scale systematic uncertainty components as a function of η for $p_{\mathrm{T}}^{jet} = 60$ GeV. The uncertainties are fairly constant with respect to η, and a dedicated uncertainty is introduced for $2.0 < |\eta| < 2.6$ to account for details in the calorimeter energy reconstruction, where a sharp feature can be seen. The effect is due to details of the jet reconstruction in calorimeter transition regions, primarily due to the LAr pulse reconstruction effects. The total uncertainty (all components summed in quadrature) is shown as a filled region topped by a solid black line. The flavour composition and response uncertainties assume a quark and gluon composition taken from Pythia dijet MC simulation (inclusive jets) [148].

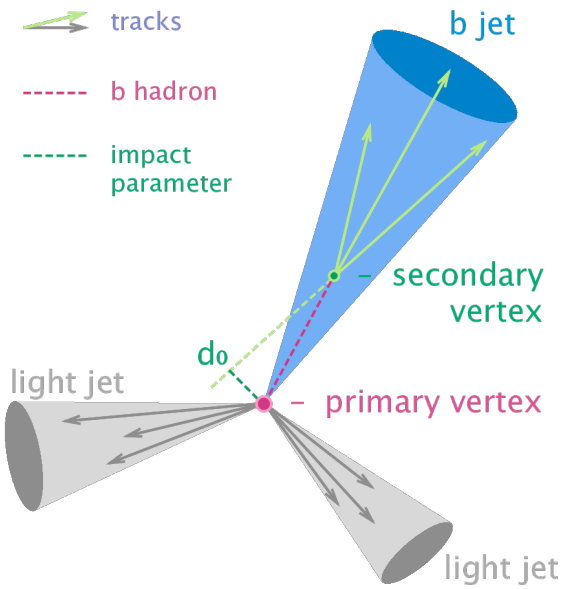

Fig. 5.7: Sketch showing the displaced secondary vertex which is used to tag a b-jet [150].

The Jet Vertex Tagger (JVT) [149] classifies which jets originate from the hard scatter and which from pile-up. The JVT is a multivariate combination of two variables: pile-up corrected Jet Vertex Fraction (corrJVF), which is designed to suppress jets not originating from the PV, and $R_{p_{\mathrm{T}}}$, which combines both calorimeter and tracking information. The JVF variable is the ratio of $\sum_i^{N_{trk}} p_T$ assigned to the jet which are also assigned to the PV. In case all the assigned tracks to the jet originate from the PV, the JVF equals one. The corrJVF is the JVF variable corrected for the N_{Vtx} dependent average scalar sum p_{T} from pile-up tracks, $\langle p_{\mathrm{T}}^{\mathrm{PU}} \rangle$, associated with a jet. The $R_{p_{\mathrm{T}}}$ variable is defined as the ratio between $\sum_i^{N_{trk}} p_T$ assigned to the jet and the fully JES calibrated jet, which includes pile-up subtraction.

5.2.1 Tagging b-jets

Quarks and gluons hadronise to particles that are collectively reconstructed as jets. However, ideally the reconstruction distinguishes between the different quarks and gluons from which a jet can originate. Flavour tagging algorithms centre around the identification of heavy flavour hadrons in the substructures of jets originating from quarks. In the case of b-quarks, b-tagging algorithms exploit the lifetime, flight length and secondary vertices to distinguish b-hadrons from c-hadrons and light flavour hadrons. Due to the CKM suppression in Equation 1.21 for b-quark decays, b-hadrons have a longer lifetime than c-hadrons and a flight length of approximately 3 mm in the transverse direction, depending on the Lorentz factor γ, before decaying. A sketch of a b-jet is illustrated in Figure 5.7. The Insertable B-Layer (IBL)

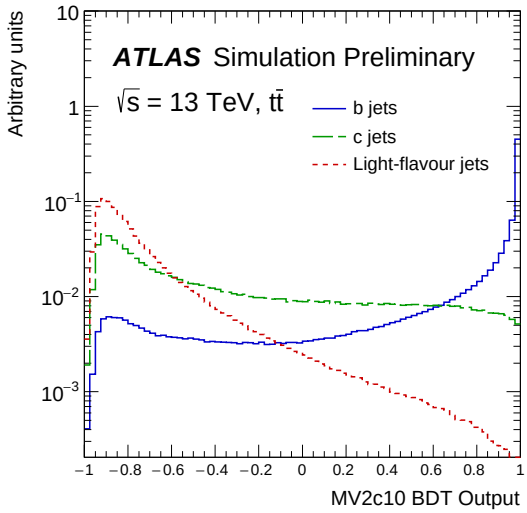

Fig. 5.8: MV2c10 BDT output for b-jets (solid blue), c-jets (dashed green) and light-flavour jets (dotted red) evaluated with $t\bar{t}$ events. Since c-jets have a longer lifetime than light jets, but smaller than b-jets, c-jets are harder to distinguish from b-jets [151].

described in Section 3.2.2, at a close distance of 33.2 mm to the beam-line, especially helps to reconstruct the secondary vertex and the impact parameters, crucial for b-tagging. Due to the ID pseudo-rapidity coverage, described in Section 3.2.2, a jet can be identified as originating from a b-hadron only up to $|\eta| < 2.5$.

A b-tagging algorithm, based on a Boosted Decision Tree (BDT), called the MV2c10 algorithm [151], determines if jets originate from a b-hadron by using a number of different input variables such as impact parameters and secondary vertex finding algorithms. The MV2c10 algorithm is trained on a $t\bar{t}$ sample, where the signal is defined as b-jets, and the background is composed of 10% c-jets and 90% light flavour jets. The output of the BDT is shown in Figure 5.8. A cut on the BDT score is placed corresponding to a specific b-jet identification efficiency. The fixed efficiency cut b-tagging working points that have been calibrated correspond to an efficiency of 85%, 77%, 70% and 60%, as determined from a $t\bar{t}$ sample.

5.3 Leptons

There are three types of charged leptons: electrons, muons and taus. Electrons and muons are stable within the ATLAS detector and thus can be detected as free particles. Taus, however, do decay, causing a different signature than electrons and muons in the detector. Since taus are not used in the analysis presented in this thesis, they are not described here. For electrons,

measurements in the calorimeter are combined with reconstructed tracks, and for muons there is also the additional measurement from the MS. The reconstruction for leptons is performed in three consecutive steps, reconstruction, identification and then isolation.

5.3.1 Electrons

To reconstruct electrons, measurements from the EM calorimeter are combined with charged particle tracks. Electrons are reconstructed down to an E_{T} of 4.5 GeV, using topologically formed clusters in the EM calorimeter and dedicated Bremstrahlung correction. Electron identification reduces background from jets, heavy flavour decays and photon-conversion and has three different working points: `Loose`, `Medium` and `Tight`. The electron isolation depends on two variables, one for the isolation in the ID, and the other for isolation in the calorimeter.

Reconstruction

An electron leaves a shower in the EM calorimeter, which needs to be combined with a reconstructed track. Since it is not possible to distinguish whether the particle is an electron or a photon in the absence of a track in the ID, a reconstructed electron should have always traversed the ID. The ID covers up to $|\eta| < 2.5$, and electrons are reconstructed for $|\eta| < 2.47$.

The reconstruction in the EM calorimeter starts with a seed, then forms a cluster, and afterwards tracks can be associated to the calorimeter cluster. Figure 5.9 summarises the efficiency from the combination of these steps for a simulated single-electron sample. A sliding window algorithm, that takes calorimetric towers as input, obtains the seed of the electron in the calorimeter. The $\eta \times \phi$ space of the EM calorimeter is divided into a grid of 200×256 elements, called towers, of size $\Delta\eta \times \Delta\phi = 0.025 \times 0.025$. The sliding window algorithm clusters 3×5 towers until a threshold energy of 2.5 GeV is found, and a calorimeter cluster is formed. The calorimeter cluster defines a region of interest in the ID. The ATLAS Global χ^2 fit [125] associates the calorimeter cluster with tracks, which should have a p_{T} above 1 GeV in the region of interest. Successfully matched tracks are then re-fitted using an optimised fit procedure for electrons. Electrons follow a helical trajectory in the ID and consequently experience bremsstrahlung. The Gaussian Sum Filter [152] takes into account the non-linear energy losses due to bremsstrahlung and improves the track fit.

Identification

There are signatures in the detector that also pass the electron reconstruction that do not originate from prompt electrons; electron identification aims to reduce this background. The

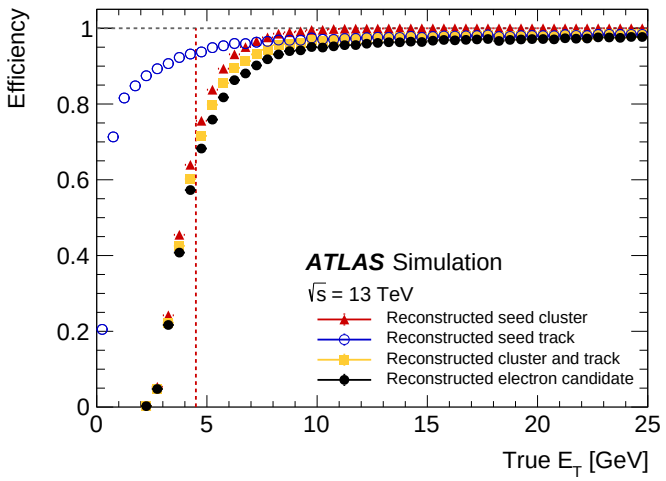

Fig. 5.9: The reconstruction efficiency for electrons in a simulated single-electron sample as a function of the true E_{T} for each step of the electron reconstruction. Seed-cluster reconstruction using 3×5 towers (red triangles), seed-track reconstruction using the Global χ^2 Track Fitter (blue open circles), and the track-to-cluster matching which is the final reconstructed electron candidate (black closed circles). As the cluster reconstruction requires uncalibrated cluster seeds with $E_{\mathrm{T}} > 2.5$ GeV, the total reconstruction efficiency is less than 60% below 4.5 GeV(dashed line) [153].

fake electron background arises from misidentification of light-flavour jets, semi-leptonic decays from heavy flavour and photon-conversion. Electron identification uses a method based on the likelihood approach [154] in combination with a multivariate analysis of several properties of the electron. Probability density functions are used for the discriminating variables for signal electrons and fake background electrons. Finally, the overall probability of a signal lepton is given.

There are three different levels of identification: `Loose`, `Medium` and `Tight`. The working points are constructed in such a way that the tighter working points are inclusive of the looser points. In Figure 5.10 the efficiencies of the working points are presented as a function of E_{T} and η in $Z \rightarrow$ ee events. The working points have been optimised in bins of E_{T}, to account for the shower shape, and in $|\eta|$, to account for the material the electron traverses in the detector. As can be seen the efficiency decreases when the working points become tighter, but the rejection of fake electron background is significantly stronger for a tighter working point. This is illustrated in Figure 5.11, which shows the efficiency of a jet getting reconstructed as an electron.

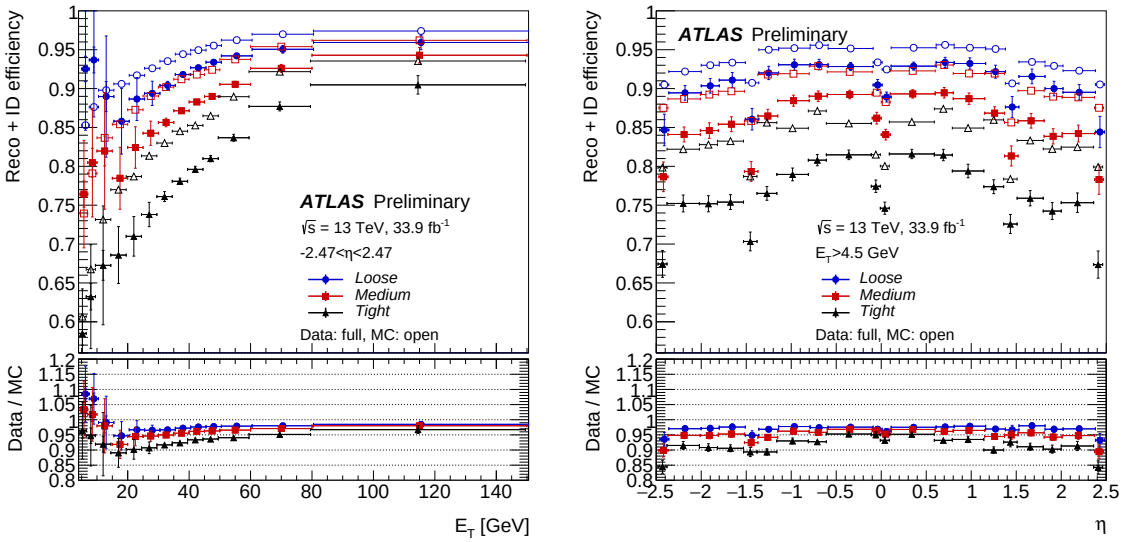

(a) **(b)**

Fig. 5.10: Electron reconstruction and identification efficiencies in $Z \to$ ee events **(a)** as a function of E_{T} for $|\eta| < 2.47$ and **(b)** as a function of η for $E_{\mathrm{T}} > 4.5$ GeV. The efficiencies are shown in data and MC for the three working points, `Loose`, `Medium` and `Tight`.[2] The used dataset corresponds to an integrated luminosity of 33.9 fb^{-1}, recorded in 2016 at a centre-of-mass energy of $\sqrt{s} = 13$ TeV [155].

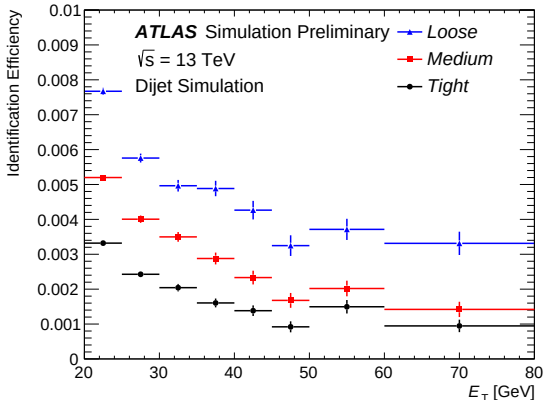

Fig. 5.11: The efficiency to identify hadrons as electrons (background rejection) estimated using simulated dijet samples. The efficiencies are obtained using Monte Carlo simulations, and are measured with respect to reconstructed electrons. The candidates are matched to true electron candidates for $Z \to$ ee events [154].

Table 5.1: Definition of the electron isolation working point `Gradient` [153]. The units of p_{T} are GeV.

Working point	$p^{\mathrm{isol}}_{\mathrm{T,\,var}}$ ($R_{\mathrm{max}} = 0.2$)	$E^{\mathrm{isol}}_{\mathrm{T,\,cone}}$ ($\Delta R = 0.2$)	Total $\varepsilon_{\mathrm{iso}}$ ($\varepsilon_{\mathrm{iso,track}} \cdot \varepsilon_{\mathrm{iso,calo}}$)
`Gradient`	$\varepsilon_{\mathrm{iso,track}} = (0.1143 \times p_{\mathrm{T}})\% + 92.14\%$	$\varepsilon_{\mathrm{iso,calo}} = (0.1143 \times E_{\mathrm{T}})\% + 92.14\%$	90(99)% at 25(65) GeV

Isolation

After having identified the electron, isolation makes it possible to further discriminate real leptons against the fake electron background. Isolation quantifies the amount of energy in a cone of radius ΔR around the direction of the electron candidate, excluding the candidate itself, in order to check if the electron is isolated, and that it is not for example part of the decay of a jet [153]. Separate isolation variables exist for tracks in the ID and energy deposits in the EM calorimeter: $p^{\mathrm{isol}}_{\mathrm{T,\,var}}$ for track isolation and $E^{\mathrm{isol}}_{\mathrm{T,\,cone}}$ for calorimeter isolation. Figure 5.12(a) presents a schematic figure of the isolation cone for track isolation, and in Figure 5.12(b) a schematic figure shows the isolation cone for calorimeter isolation. Calorimeter isolation uses a fixed size of the isolation cone given by ΔR = 0.2. Track isolation uses a variable isolation cone size depending on the p_{T} of the electron, it decreases in size as a function of the p_{T} of the electron candidate such that,

$$\Delta R = min\left(\frac{10\ \mathrm{GeV}}{p_{\mathrm{T}}\ [\ \mathrm{GeV}]}, R_{\mathrm{max}}\right), \tag{5.4}$$

where $R_{\mathrm{max}} = 0.2$.[3]

A cut is placed on $p^{\mathrm{isol}}_{\mathrm{T,\,var}}$ and $E^{\mathrm{isol}}_{\mathrm{T,\,cone}}$ to make sure that the electron is isolated in both the ID and calorimeter. The `Gradient` isolation working point for electrons used in this thesis is clarified in Table 5.1. The isolation working point targets a value of the isolation efficiency, $\varepsilon_{\mathrm{iso}}$, dependent on the E_{T} of the electron.[4] The efficiency $\varepsilon_{\mathrm{iso}}$ increases linearly as a function of E_{T}, starting at 90% at an E_{T} of 25 GeV until it reaches a maximum efficiency of 99% at an E_{T} of 65 GeV.

[2]The lower efficiency in data than in MC arises from the fact that the MC does not properly represent the 2016 TRT conditions, in addition to the known mismodelling of calorimeter shower shapes in the GEANT4 detector simulation.

[3]The value of 10 GeV in the argument is derived with a simulated $t\bar{t}$ sample and designed to maximise the rejection of background. From electron candidates with $p_{\mathrm{T}} > 50$ GeV onwards the isolation cone size will decrease.

[4]The isolation efficiency is given by $\varepsilon_{\mathrm{iso}} = N_{\mathrm{passes\ isolation}}/N_{\mathrm{passes\ identification}}$.

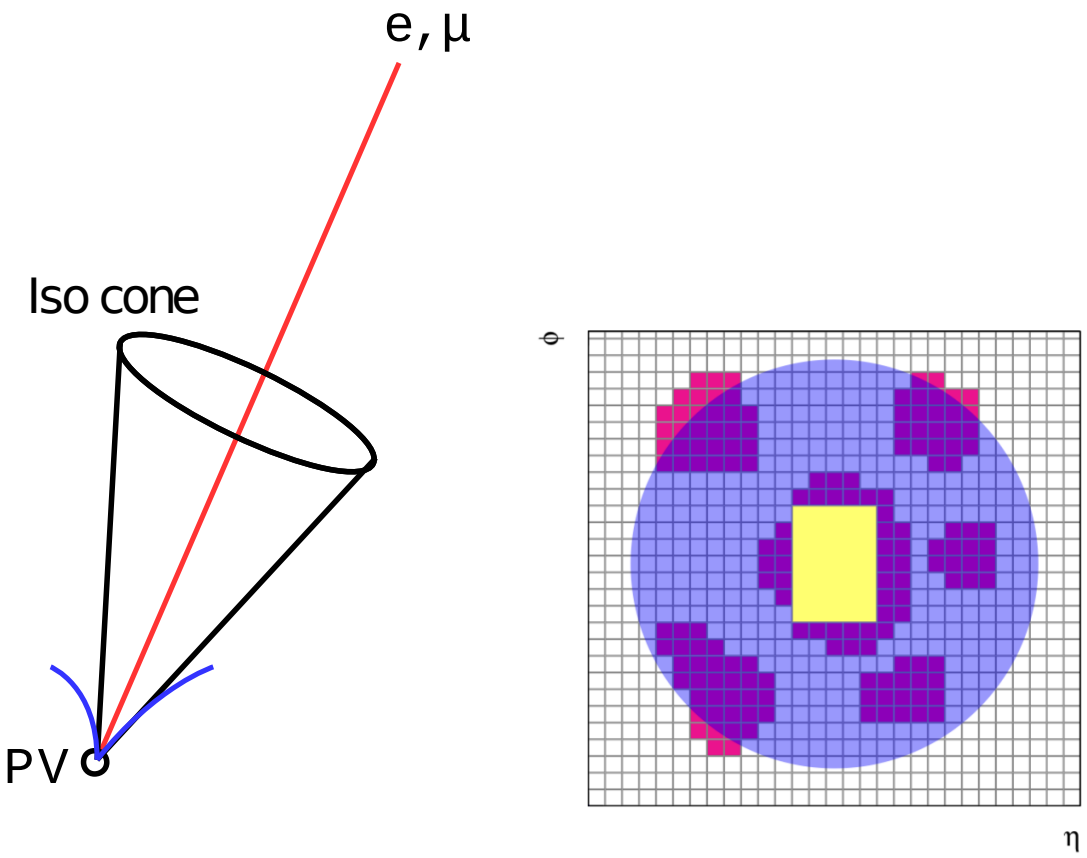

(a) **(b)**

Fig. 5.12: **(a)** A schematic figure of the ID isolation. The red line indicates the electron/muon track. The blue lines are tracks that are close-by, but in this case not in the isolation cone, meaning this is an isolated electron/muon. If the blue tracks would be high p_{T} and inside the isolation cone the electron/muon would not be isolated depending on the electron/muon-isolation working point [156]. **(b)** A schematic figure of the calorimeter isolation. The candidate electron/muon is located in the centre of the purple circle representing the isolation cone. All topological clusters, represented in red, within the isolation cone are included in the computation of the isolation variable. The yellow rectangle corresponds to the excluded cells which contain the electron/muon candidate itself [153].

5.3.2 Muons

For muons, measurements from the MS and calorimeters are combined with reconstructed ID tracks. Unlike electrons, muons are not stopped in the EM calorimeter, or even in the HAD calorimeter.[5] For this reason the MS surrounds the ATLAS detector. Muons are reconstructed for momenta down to 3 GeV, as the average energy loss in the calorimeter is 3 GeV. Four different reconstruction algorithms are applied, depending on muon p_{T} and η. For identification there are three working points to reduce background from jets and heavy flavour decays: `Loose`, `Medium` and `Tight`, but there are also the `Low-`p_T and `High-`p_T working points. Isolation depends on two variables, one for the track isolation in the ID, and one for isolation of the energy deposit in the calorimeter.

Reconstruction

In the MS, muon tracks are reconstructed in two consecutive steps: track segments are reconstructed in the individual MDT and CSC detector chambers in the first step, and in the next step these track segments are then combined to form track candidates [157].

The track segments are reconstructed from the MDT, at $|\eta| < 2$, and CSC chambers, at $2 < |\eta| < 2.7$, which provide 4 to 8 measurements in η per chamber. Once the track segments are formed from the MDT and CSC measurements in η, they are associated to measurements from the trigger chambers, RPC and TGC.

To form track candidates seeds are taken from the track segments generated in the middle layers of the detector, where more trigger hits are available. Segments from the outer and inner layers are then added to extend the track candidate. A global χ^2 track fit is done to combine the track segments into a track candidate, taking into account multiple scattering and energy loss in the calorimeter. A track candidate is accepted if the χ^2 of the fit satisfies the selection criteria. The momentum of tracks in the MS is calculated from the deviation of the muon trajectory from a straight line, where the deviation is caused by the toroidal magnetic field. The deviation of the muon trajectory is inversely proportional to the momentum of the muon. In the end-caps, in the absence of a position measurement inside the toroid, a point-angle measurement is conducted.

As mentioned four reconstruction algorithms are applied for muons, depending on the muon p_{T} and η. A `Combined muon` is the most straightforward case, when there is a track in the MS and a track in the ID. The track from the MS is then associated with a track from the ID and calorimeter measurements. In the case where $|\eta| > 2.5$ however, there is no track from the ID, though there can still be a track in the MS, and this measurement can be used

[5] For muons with an average energy larger than 3 GeV.

to form an `Extrapolated muon`. When there is no complete muon track reconstructed in the MS, but there is a track segment reconstructed, this track segment can be associated to the a measurement in the ID to form a `Segment-tagged muon`. Finally, when there is no track or track segment in the MS, for example due to poor coverage around $\eta = 0$ (as displayed in the reconstruction efficiency Figure 5.13(a)), a track from the ID is combined with measurements from the calorimeter to form a `Calorimeter-tagged muon`. Although muons are minimum-ionising in the calorimeter, leaving only small amount of energy in the calorimeter, it is still beneficial to regain efficiency in regions of poor coverage of the MS.

Identification

Muon identification identifies muons that originate from the hard scatter process and reduces muons from the background of light jets and heavy flavour decays. Five muon identification working points exist: `Loose`, `Medium`, `Tight`, `High-`p_{T} [157] and `Low-`p_{T} [158]. The identification procedure discriminates against the fake muon background using parameters such as the quality of the combined MS and ID fit, and the difference of the muon p_{T} from the MS and ID divided by the p_{T} of the muon using the combined detector information. In Figure 5.13(a) the efficiencies for `Loose` and `Medium` identification are demonstrated as a function of η, for muons with $p_{\mathrm{T}} > 10$ GeV measured in $Z \to \mu\mu$ events. At low p_{T} improvements in efficiency and fake rate reduction are possible with the `low-`p_{T} working point, as illustrated in Figure 5.13(b) for simulated $t\bar{t}$ events .

Isolation

After having identified the muon it is possible to further reduce the fake muon background through isolation. The isolation procedure for muons is similar to that of electrons; the same schematic figure presented in Figure 5.12 applies. Again there is a variable for track isolation $p^{\mathrm{isol}}_{\mathrm{T,\,var}}$, containing the p_{T} of tracks other than the track of the muon itself in the isolation cone, and a variable for calorimeter isolation $E^{\mathrm{isol}}_{\mathrm{T,\,cone}}$, containing the E_{T} of energy deposits other than the energy deposit of the muon itself in the isolation cone. The isolation cone for muon tracks is also given by Equation 5.4, with $R_{max} = 0.3$, while the isolation cone for calorimeter isolation given by $\Delta R = 0.2$. The $p^{isol}_{T,var}$ and $E^{isol}_{T,cone}$ variables for medium identification are shown in Figure 5.14, which have been measured in $Z \to \mu\mu$ events. A cut is placed on these variables to ensure that the muon is isolated. The muon isolation working point Fixed Cut Loose (`FCLoose`) as used in this thesis is presented in Table 5.2.

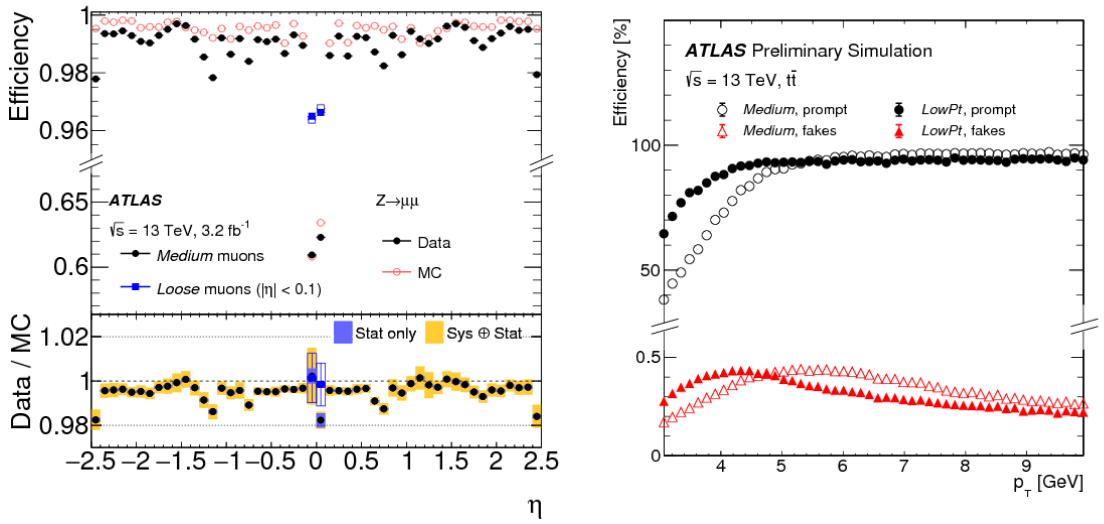

Fig. 5.13: **(a)** Muon reconstruction efficiency as a function of η measured in $Z \to \mu\mu$ events for muons with $p_{\mathrm{T}} > 10$ GeV shown for `Loose` and `Medium` identification. In the region $|\eta| < 0.1$ the poor coverage of the MS can be observed. The error bars on the efficiencies indicate the statistical uncertainty [157]. **(b)** Expected efficiency and fake rate as a function of p_{T} for muons fulfilling the LowPt (filled markers) and Medium (empty markers) requirements in simulated $t\bar{t}$ events [158].

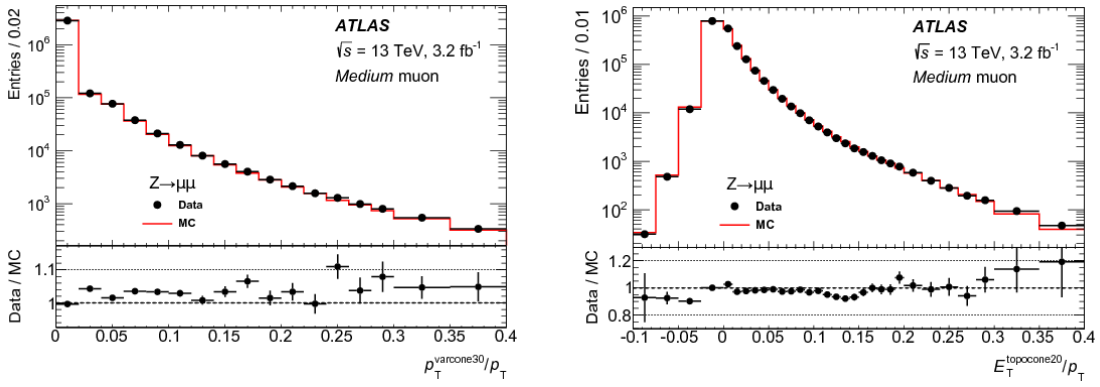

Fig. 5.14: Distributions of **(a)** the track-based $p^{\mathrm{isol}}_{\mathrm{T,\,var}}/p_{\mathrm{T}}$ and **(b)** the calorimeter-based $E^{isol}_{T,cone}/p_{\mathrm{T}}$ isolation variables measured in $Z \to \mu\mu$ events. Muons are selected using the Medium identification. The dots show the distribution for data while the histograms show the distribution from simulation. The bottom panels show the ratio of data to simulation with the corresponding statistical uncertainty [157].

Table 5.2: Definition of the muon isolation working point Fixed Cut Loose (`FCLoose`) [157].

Working point	$p^{\mathrm{isol}}_{\mathrm{T,\,var}}$ ($R_{max} = 0.3$)	$E^{\mathrm{isol}}_{\mathrm{T,\,cone}}$ ($\Delta R = 0.2$)
`FCLoose`	$p^{\mathrm{isol}}_{\mathrm{T,\,var}}/p_{\mathrm{T}} < 0.15$	$E^{\mathrm{isol}}_{\mathrm{T,\,cone}}/p_{\mathrm{T}} < 0.30$

Table 5.3: Prompt Lepton Veto (PLV) BDT input variables [156].

Variable	Description
N_{track} in track jet	Number of tracks collected by the track jet
RNNIP	Impact parameter tagger[7] (using a recurring neural network)
DL1mu	B-tagging algorithm[8] (using a deep neural network)
p_T^{rel}	Lepton p_{T} relative to matched track jet direction, $p\cdot$ sin(<lepton, track jet>)
$p_T^{\text{lepton track}}/p_T^{\text{track jet}}$	The ratio of the lepton track p_{T} and the track jet p_{T}
ΔR(lepton, track jet)	ΔR between the lepton and track jet axis
$p_{\mathrm{T,\,var}}^{\mathrm{isol}}/p_{\mathrm{T}}$	Lepton track isolation, with track collecting radius of $R_{\mathrm{max}} = 0.3$
$E_{\mathrm{T,\,cone}}^{\mathrm{isol}}/p_{\mathrm{T}}$	Lepton calorimeter isolation, with topological cluster radius of $\Delta R < 0.3$

5.4 Prompt Lepton Veto

Prompt leptons are leptons that originate from the hard scatter, whereas non-prompt leptons can originate from misidentification of light-flavour jets, semi-leptonic decays from heavy flavour and photon-conversion. Typically, prompt leptons are selected by the identification and isolation working points, however, non-prompt leptons may still pass these criteria. Besides the identification and isolation working points an additional algorithm is used called the Prompt Lepton Veto (PLV) [156]. The PLV is a Boosted Discussion Tree (BDT) based algorithm that selects prompt leptons and discriminates against non-prompt leptons.[6] More features on top of the standard cone-based isolation variables described in Sections 5.3.1 and 5.3.2 are exploited, by looking for a track jet nearby the lepton, and using the associated b-tagging score and momentum information. The input variables for the BDT are listed in Table 5.3. Since even isolated single leptons are also reconstructed as track-jets, a track-jet is almost always present. Prompt leptons tend to have nearby track-jets with momenta consistent with the lepton, low track multiplicity and a low b-tagging score. This is not the case for non-prompt leptons, where the nearby track-jets most likely correspond to the decay of a parent heavy flavour.

The training of the BDT is done using a $t\bar{t}$ sample, which contains prompt and non-prompt leptons with $p_{\mathrm{T}} > 10$ GeV. Figure 5.15 shows the output BDT score distribution for a selection of p_{T} slices for both electrons and muons. The figure reveals that the PLV BDT score changes with p_{T}, especially in p_{T} range of 10-20 GeV, and therefore, a fixed cut in

[6] Technically, the PLV selects non-prompt leptons and discriminates against prompt leptons, hence the name of the algorithm.

[7] Using low level input variables based on impact parameters described in Section 5.1.

[8] Using same inputs as the b-tagging BDT algorithm, MV2c10, described in Section 5.2.1, including an additional soft muon tagger to help separate from light jets due to the semi-leptonic heavy flavour decay (MV2c10 calibration is treated as uncorrelated from the PLV BDT calibration because the real jets around the fake lepton are almost always removed by overlap removal).

Table 5.4: Upper cut values of the PLV score for `PLVLoose` and `PLVTight` working points. For electrons `Gradient` isolation is applied in addition, for muons `FCLoose` isolation is applied in addition.

Electrons										
p_T [GeV]	<6	6-8	8-10	10-15	15-20	20-25	25-30	30-40	40-50	>50
`PLVLoose`	0.95	0.90	0.91	0.83	0.70	0.69	0.57	0.60	-0.16	-0.50
`PLVTight`	0.71	0.70	0.69	0.48	0.41	0.23	0.29	0.60	-0.16	-0.50
Muons										
p_T [GeV]	<6	6-8	8-10	10-15	15-20	20-25	25-30	30-40	40-50	>50
`PLVLoose`	0.91	0.78	0.66	0.80	0.50	0.50	0.46	0.20	-0.20	-0.50
`PLVTight`	0.63	0.41	0.24	0.20	-0.16	-0.34	-0.40	-0.42	-0.50	-0.50

BDT score leads to too low efficiency for leptons in the low p_T regime. Two p_T dependent working points have been created to regain efficiency. Working points called `PLVLoose` and `PLVTight` are defined as in Table 5.4. To make sure leptons that fail isolation are not selected, also standard isolation is required as part of the working point definition. For electrons the `Gradient` isolation working point is required and for muons the `FCLoose` isolation working point is required.

In Figure 5.16 the real/prompt lepton efficiency and fake/non-prompt lepton rejection as function of p_T is highlighted, for the standard isolation working points as well as `PLVLoose` and `PLVTight` working points (including the standard isolation). `PLVTight` typically outperforms standard isolation by $40-80\%$ in fake/non-prompt rejection at the same real/prompt efficiency in the range of $p_T > 20$ GeV. Also at lower p_T it maintains nearly optimal performance down to $p_T \sim 6$ GeV, and as good as a performance compared to the standard isolation for $p_T < 6$ GeV.

5.4.1 PLVTight calibration

The accuracy of the MC detector simulation in modelling the efficiency of the `PLVTight` working point is important to quantify when using MC simulation to predict the data. In order to achieve reliable results, the simulated events are corrected with a scale factor to reproduce as closely as possible the efficiency measured in data,

$$\mathrm{SF}_{\mathrm{PLVTight}} = \frac{\varepsilon^{\mathrm{data}}_{\mathrm{PLVTight}}}{\varepsilon^{\mathrm{MC}}_{\mathrm{PLVTight}}}, \tag{5.5}$$

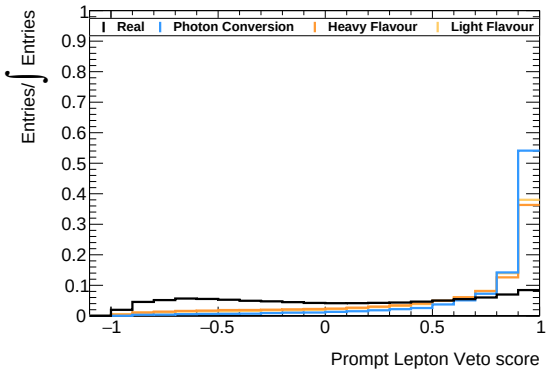

(a) Electron (4.5-6 GeV)

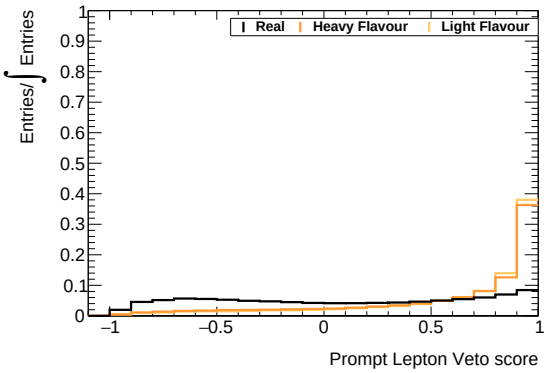

(b) Muon (4-6 GeV)

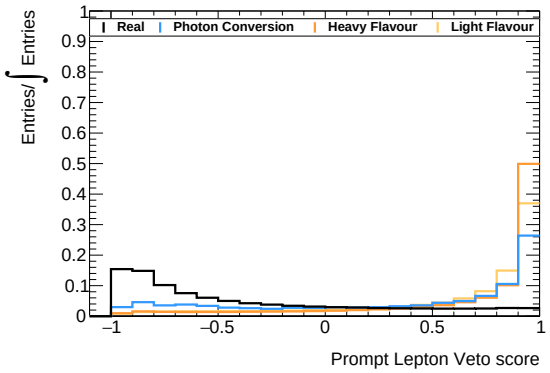

(c) Electron (10-15 GeV)

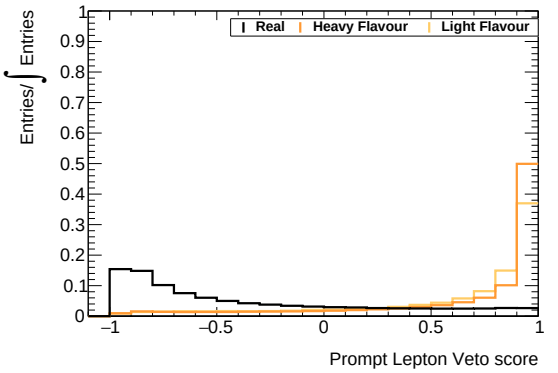

(d) Muon (10-15 GeV)

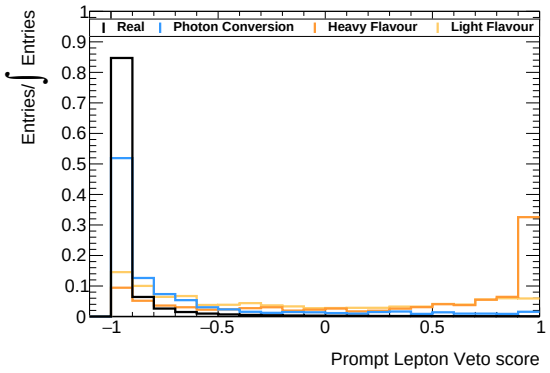

(e) Electron (>30 GeV)

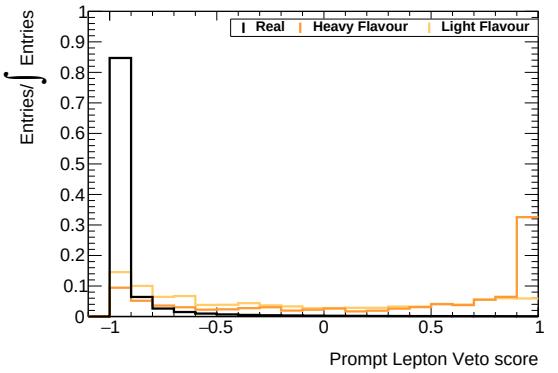

(f) Muon (>30 GeV)

Fig. 5.15: Normalised PLV score distributions for real/prompt (black) and fake/non-prompt leptons in various p_{T} ranges. The real/prompt efficiencies are evaluated by WZ MC, while Z+jets MC is used for the fake efficiencies. The valid range is $[-1, 1]$ while the entries in -1.1 correspond to lepton candidates with no track jets found around $\Delta R < 0.4$. This typically happens for light-flavour fakes from pile-up jets since track jets are formed only by tracks originating from the primary vertex (PV).

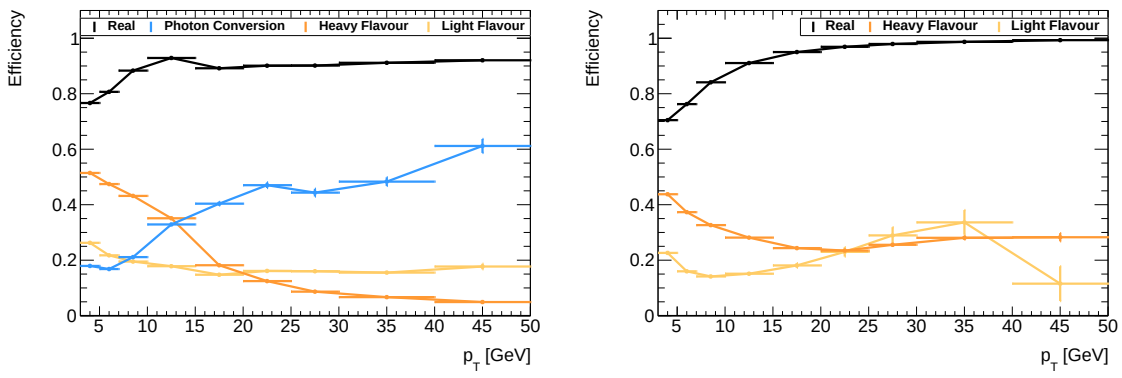

(a) Electron - `Gradient`

(b) Muon - `FCLoose`

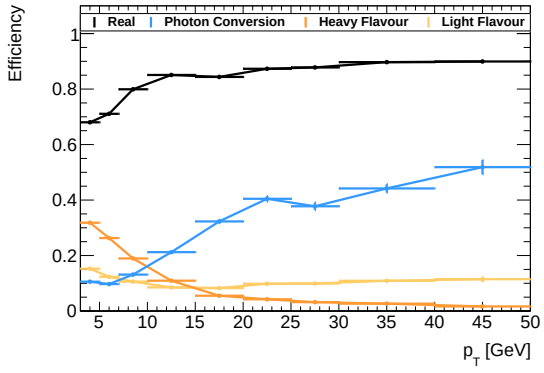

(c) Electron - `PLVLoose`

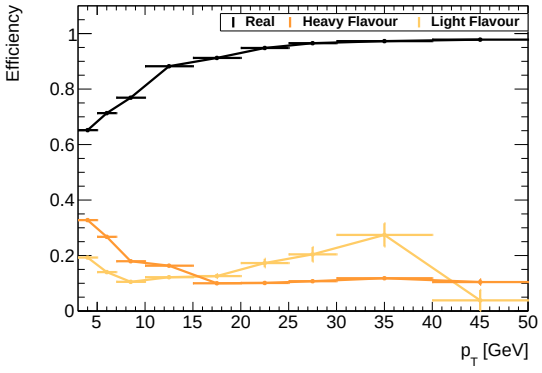

(d) Muon - `PLVLoose`

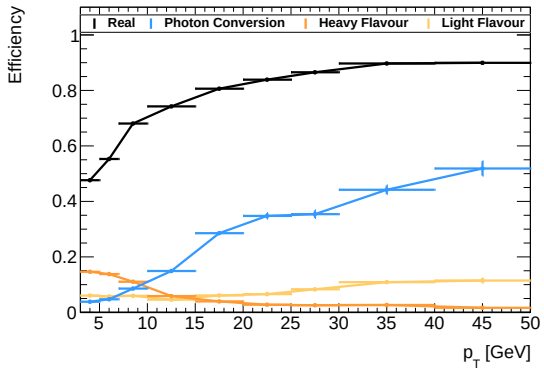

(e) Electron - `PLVTight`

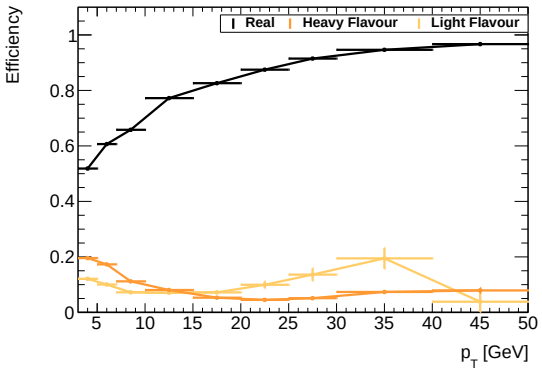

(f) Muon - `PLVTight`

Fig. 5.16: Efficiency for real/prompt (black) and fake/non-prompt leptons for for the **(a-b)** standard isolation working points as well as **(c-d)** `PLVLoose` (including the standard isolation) and **(e-f)** `PLVTight` (including the standard isolation) working points. In the efficiency, the denominator includes all leptons passing signal requirements (except isolation), while the numerator includes the subset which additionally passes isolation or PLV (including the standard isolation). *WZ* MC is used for evaluating the real/prompt lepton efficiency, while the *Z*+jets MC is used for the fake/non-prompt leptons.

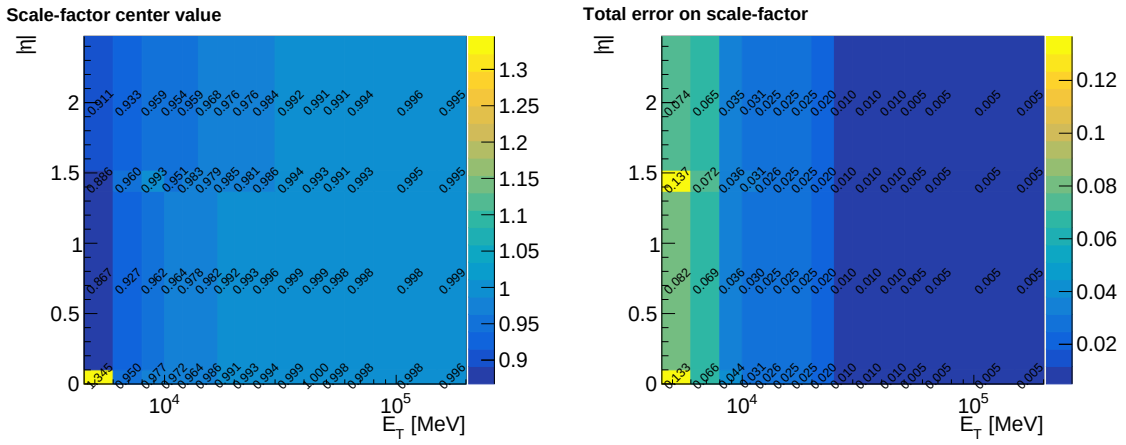

Fig. 5.17: **(a)** Scale factor and **(b)** associated uncertainties on the `PLVTight` working point for electrons in each (p_{T}, η) bin.

where $\varepsilon^{\mathrm{data}}_{\mathrm{PLVTight}}$ is the efficiency measured in data and $\varepsilon^{\mathrm{MC}}_{\mathrm{PLVTight}}$ is the efficiency determined from MC simulation.

The efficiencies for the `PLVTight` working point are estimated using tag-and-probe methods [157, 153]. In such a method electrons and muons are selected from a known resonance such as $Z \to \ell\ell$ or $J/\psi \to \ell\ell$. For the calibration of isolation working points only the Z decay is chosen. As a result of the $Z \to \ell\ell$ process there are two leptons in the final state, one of which will be the tag and one of which will be the probe.[9] The tag lepton has strict selection requirements. The probe lepton is used to calculate the efficiency,

$$\varepsilon_{\mathrm{PLV}} = \frac{N_{\mathrm{PLVTight}}}{N_{\mathrm{id}}}, \tag{5.6}$$

where in the numerator, N_{PLVTight}, leptons pass the `PLVTight` isolation criteria and in the denominator, N_{id}, leptons are only required to pass the identification criteria.

For electrons, the definition of the tag and probe is clarified in Table 5.5. The $\mathrm{SF}_{\mathrm{PLVTight}}$ is computed for a range of $p_{\mathrm{T}} \in [4, 200]$ GeV and for four separate $|\eta|$ bins, [0,0.1], [0.1,1.37], [1.37,1.51] and [1.51,2.47]. The scale factor extraction from the data takes place after a background template subtraction. A background template in the measurement region is obtained by using leptons failing identification criteria. The leptons failing the identification criteria are normalised in a side-band region with respect to the measurement region at the m_Z resonance, chosen to be $m_{\ell\ell} \in [120, 250]$ GeV. Efficiency extraction using simulated events is performed in a very similar fashion, except that background subtraction is not performed.

[9] If both leptons pass the tag requirements, the event will provide two probes.

Table 5.5: Electron PLV calibration selection region and the definition of the tag and probe electron. The tag electron has to be identified as tight because the online single electron trigger indication criterion is `Tight`. Requirements on the impact parameter $|z_0 \sin\theta| < 0.5$ mm and $|d_0/\sigma_{d_0}| < 5$ are applied, as well as track-to-vertex association.

Electron selection region		
$m_{e^+e^-}$	$\in [80, 100]$ GeV	
$\Delta R(j, e)$	> 0.4	
Tag electron		
Trigger	Matches single-electron trigger	
Identification	`Tight`	
Isolation	$p_{\mathrm{T}}^{\mathrm{cone20}}/p_{\mathrm{T}} < 0.1$	
E_{T}	> 27 GeV	
Probe electron		
	N_{id}	N_{PLVTight}
Identification	`Medium`	`Medium`
Isolation	-	`Gradient` + `PLVTight`

Table 5.6: Muon PLV calibration selection region and the definition of the tag and probe muons. Requirements on the impact parameter $|z_0 \sin\theta| < 0.5$ mm and $|d_0/\sigma_{d_0}| < 5$ are applied, as well as track-to-vertex association.

Muon selection region		
$m_{\mu^+\mu^-}$	$\in [86, 96]$ GeV	
Identification	Medium	
$\Delta R(\mu, \mu)$	> 0.3	
$\Delta R(j, \mu)$	> 0.4	
Tag muon		
Trigger	Matches single-muon trigger	
Isolation	`FCLoose`	
p_{T}	> 24 GeV	
Probe muon		
	N_{id}	N_{PLVTight}
Isolation	-	`FCLoose` + `PLVTight`

Systematic uncertainties in the correction factors are evaluated by varying the requirements on the selection of both the tag and the probe electron candidates as well as varying the details of the background-subtraction method. Also the envelope of the variation against pile-up is found to be $\leq 0.5\%$ and thus an extra systematic of 0.5% is applied on the scale factor. The electron scale factors for $\mathrm{SF}_{\mathrm{PLVTight}}$ and uncertainties are shown in Figure 5.17.

For muons, the definition of the tag and probe appears in Table 5.6. The $\mathrm{SF}_{\mathrm{PLVTight}}$ is computed for a range of $p_{\mathrm{T}} \in [3,500]$ GeV, separately for the years 2015, 2016, 2017 and 2018, and is shown in Figure 5.18(a-d). The scale factor extraction from the data also occurs after a background template subtraction using leptons failing identification criteria, where again the side-band region is chosen to be $m_{\ell\ell} \in [120,250]$ GeV. Systematics have been implemented including the variation in probe identification working points, $m_{\mu\mu}$ window size of the measurement region, isolation against jets, the contribution of which being summarised in Figure 5.18(g) in various p_{T}-ranges. A 2% systematics to account for the dependency on η is applied as derived from Figure 5.18(e). The dependancy on pile-up was found negligible as perceived in Figure 5.18(f).

5.5 $E_{\mathrm{T}}^{\mathrm{miss}}$

Standard Model particles such as neutrinos or some hypothetical supersymmetry particles will not interact with the ATLAS detector and will escape the detector undetected. This would mean that it is not possible to directly detect one of the particles of interest, the neutralino, $\tilde{\chi}_1^0$, in the final state of the analysis described in this thesis. However, by using momentum conservation it is possible to still indirectly detect these particles. By adding the momentum of all visible reconstructed particles it can be inferred whether a particle escaped the detector as missing momentum, which is denoted as $E_{\mathrm{T}}^{\mathrm{miss}}$.

Since the p-p collision takes place along the z-axis, there is zero initial momentum in the transverse plane. In the final state, due to conservation of momentum, the added momentum of all reconstructed particles from the same hard-scatter vertex should remain zero in the transverse plane. As a consequence the negative total vectorial sum determines the missing transverse momentum [159],

$$E_{\mathrm{T}}^{\mathrm{miss}} = -\sum_{\mathrm{jets}} p_{\mathrm{T}}^{\mathrm{jets}} - \sum_{\mathrm{e}} p_{\mathrm{T}}^{\mathrm{e}} - \sum_{\mu} p_{\mathrm{T}}^{\mu} - \sum_{\gamma} p_{\mathrm{T}}^{\gamma} - \sum_{\mathrm{tracks}} p_{\mathrm{T}}^{\mathrm{tracks}}, \tag{5.7}$$

which corresponds to the momentum of our invisible particles. The component $\sum_{\mathrm{tracks}} p_{\mathrm{T}}^{\mathrm{tracks}}$ corresponds to the soft term in the $E_{\mathrm{T}}^{\mathrm{miss}}$. The soft term contains all contributions arising

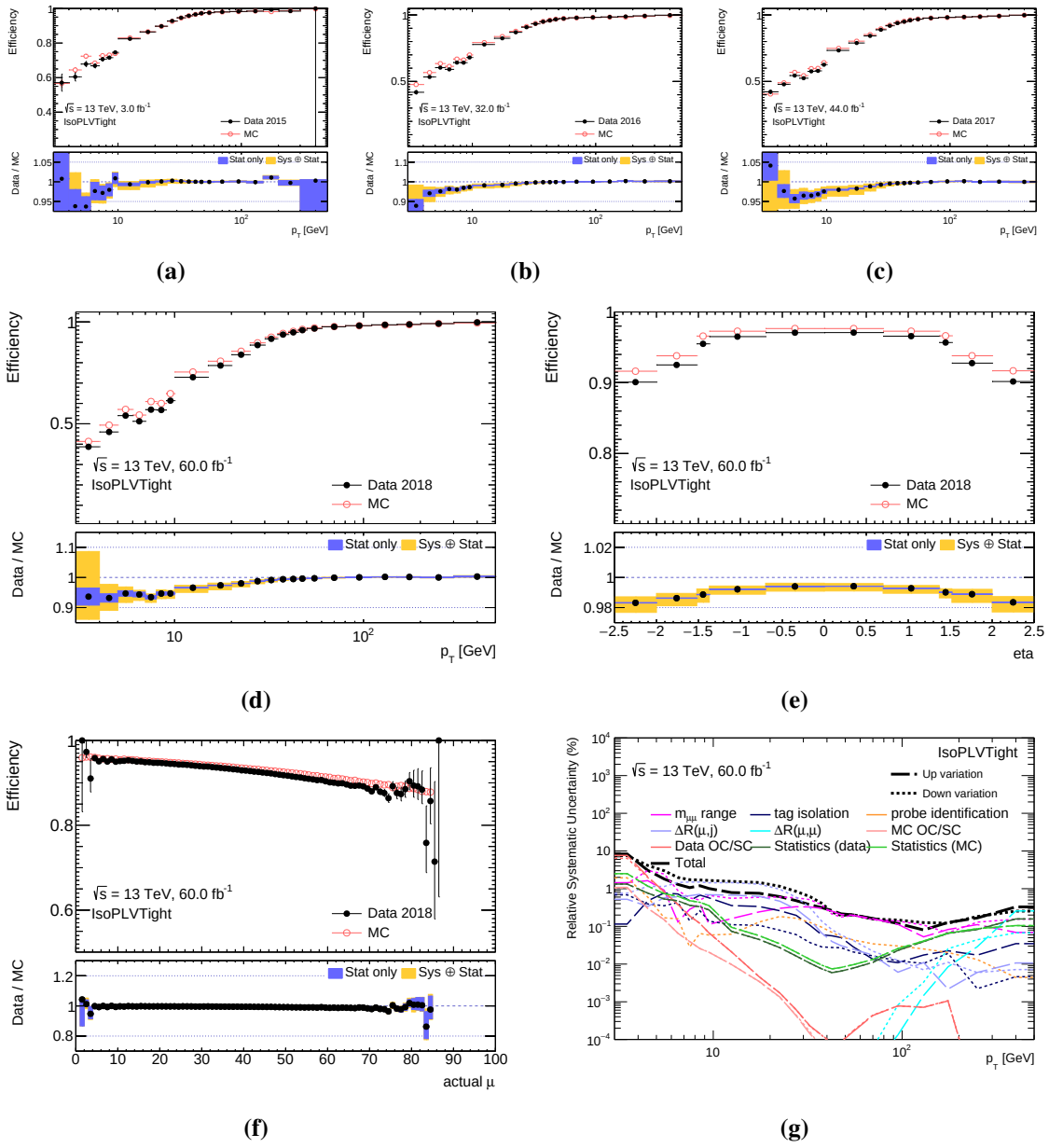

Fig. 5.18: Measured data/MC `PLVTight` efficiency for muons for the **(a)** 2015, **(b)** 2016, **(c)** 2017, and **(d)** 2018 period. The efficiency dependency on **(e)** η and **(f)** pile-up, μ, for the 2018 period. **(g)** Breakdown of scale factor systematics for the 2018 period. The solid line indicates the up variation and the dotted line is down variation.

from soft charged particles, for which tracks not associated to any reconstructed particle but associated to the hard-scatter vertex are added up.[10] Uncertainties from all the reconstructed particles and the soft term are combined to an overall systematic uncertainty on $E_{\mathrm{T}}^{\mathrm{miss}}$. Pile-up has a significant impact on the $\sum_{\mathrm{jets}} p_{\mathrm{T}}^{\mathrm{jets}}$ and $\sum_{\mathrm{tracks}} p_{\mathrm{T}}^{\mathrm{tracks}}$ terms. In order to reduce the pile-up dependence on tracks the `Tight Primary` selection is used as described in Section 5.1.1. For jets dedicated algorithms reduce pile-up dependence, as described in the jet reconstruction Section 5.2.

5.5.1 Photons

Photons are reconstructed in order to compute the $E_{\mathrm{T}}^{\mathrm{miss}}$. Photon reconstruction is similar to electron reconstruction, because both particles deposit their energy in the EM calorimeter. The photon reconstruction algorithm determines a seed in the EM calorimeter according to the same method as the electron reconstruction, forming a calorimeter cluster. The difference between electrons and photons is that photons typically do not leave a track in the ID, since photons are not charged. In the occurrence of a photon-conversion (into an electron), the resulting electron will leave a track in the ID. Photons that do not leave a track in the ID are classified as unconverted photons, while photons that do leave a track in the ID are classified as converted photons. In the reconstruction, when no track is associated to the calorimeter cluster, an unconverted photon is reconstructed, while when a track can be associated to the calorimeter cluster, a converted photon is reconstructed. The identification efficiency increases from $45-60\%$ at $E_{\mathrm{T}} = 10$ GeV to $95-98\%$ for $E_{\mathrm{T}} > 100$ GeV, depending on pseudorapidity and on the photon-conversion status [160].

5.5.2 $E_{\mathrm{T}}^{\mathrm{miss}}$ significance

The precision of the reconstructed $E_{\mathrm{T}}^{\mathrm{miss}}$ depends on the precision with which the particles in Equation 5.7 are reconstructed. Fake $E_{\mathrm{T}}^{\mathrm{miss}}$ can arise due to particles which escape the acceptance of the detector, are inaccurately reconstructed, or fail to be reconstructed all together [161]. In order to have a handle on the precision with which the $E_{\mathrm{T}}^{\mathrm{miss}}$ is reconstructed, $E_{\mathrm{T}}^{\mathrm{miss}}$ significance is defined by using the energy resolution in the calorimeter. The energy resolution in the calorimeter can be estimated using $\sqrt{\sum E_{\mathrm{T}}}$, where $\sum E_{\mathrm{T}}$ is the measured energy in the collision, from which an event-based $E_{\mathrm{T}}^{\mathrm{miss}}$ significance can be

[10] Calorimeter clusters could be used as well but are unreliable mostly due to a large dependence on pile-up.

defined by the following equation,

$$\mathscr{S} = \frac{E_{\mathrm{T}}^{miss}}{\sqrt{\sum E_{\mathrm{T}}}}. \tag{5.8}$$

However, this definition is based on the assumption that the $E_{\mathrm{T}}^{\mathrm{miss}}$ is purely calculated from the calorimeter and also puts the same weight on the resolution of all the reconstructed particles, while for example leptons can be reconstructed with much higher resolution than jets. In order to use all the sub-detectors and the individual resolution of the reconstructed particles the approach needs to be reconsidered. Resolution effects from all sub-detectors can be taken into account by using the object-based $E_{\mathrm{T}}^{\mathrm{miss}}$ significance. The object-based $E_{\mathrm{T}}^{\mathrm{miss}}$ significance indicates the degree to which the reconstructed $E_{\mathrm{T}}^{\mathrm{miss}}$ agrees with momentum resolution and particle identification efficiencies given the full event composition [162].[11] A high value of the $E_{\mathrm{T}}^{\mathrm{miss}}$ significance is an indication that the $E_{\mathrm{T}}^{\mathrm{miss}}$ observed in the event is not well explained by resolution smearing alone, implying that the event is more likely to contain unseen objects such as neutrinos or hypothetical supersymmetry particles. The comparison between the $E_{\mathrm{T}}^{\mathrm{miss}}$, event-based $E_{\mathrm{T}}^{\mathrm{miss}}$ significance and object-based $E_{\mathrm{T}}^{\mathrm{miss}}$ significance is shown in Figure 5.19. From this figure it can be concluded that the performance of the object-based $E_{\mathrm{T}}^{\mathrm{miss}}$ significance improves the ability to reject backgrounds with fake $E_{\mathrm{T}}^{\mathrm{miss}}$.

[11] By evaluating the p-value whether the observed $E_{\mathrm{T}}^{\mathrm{miss}}$ is consistent with a null hypothesis of zero real $E_{\mathrm{T}}^{\mathrm{miss}}$ in the event.

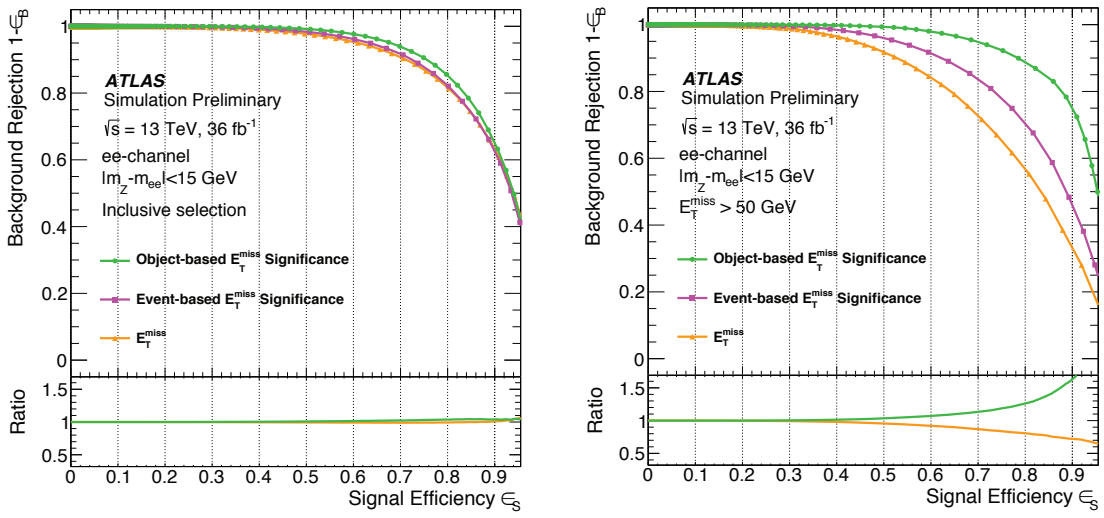

(a) **(b)**

Fig. 5.19: Background rejection versus signal efficiency for $E_{\mathrm{T}}^{\mathrm{miss}}$, event-based $E_{\mathrm{T}}^{\mathrm{miss}}$ significance, and object-based $E_{\mathrm{T}}^{\mathrm{miss}}$ significance. In the following a simulated $Z \to ee$ sample is considered as background, and a simulated $ZZ \to ee\nu\nu$ sample is considered as signal. A $Z \to ee$ selection is used in **(a)** an inclusive region and **(b)** a region with $E_{\mathrm{T}}^{\mathrm{miss}} > 50$ GeV. In the inclusive region the bulk of the events have little hard activity and the object-based $E_{\mathrm{T}}^{\mathrm{miss}}$ significance is dominated by the variance of the soft-term. A clear improvement is observed for events with higher $E_{\mathrm{T}}^{\mathrm{miss}}$ [162].

Part III

Analysis

Chapter 6

Introduction

The analysis presented in this thesis focuses on the pair production of $\tilde{\chi}_1^{\pm}$ and $\tilde{\chi}_2^0$ decaying into $W^{\pm}\tilde{\chi}_1^0$ and $Z\tilde{\chi}_1^0$, respectively,

$$\tilde{\chi}_1^{\pm}\tilde{\chi}_2^0 \rightarrow WZ\tilde{\chi}_1^0\tilde{\chi}_1^0 \rightarrow \ell\ell\ell\nu\tilde{\chi}_1^0\tilde{\chi}_1^0, \tag{6.1}$$

where the $W^{\pm}$ and Z decay leptonically. This process is illustrated in the Feynman diagram in Figure 6.1. The process leads to a reconstructed final state with three leptons, and $E_{\mathrm{T}}^{\mathrm{miss}}$ from the $\tilde{\chi}_1^0$ and ν. Initial state radiation and final state radiation can lead to quarks or gluons being radiated in the process as well, leading to the possibility of also having jets in the final state. Throughout the analysis the considered leptons in the final state are electrons and muons, thus not including taus. The analysis focuses on the simplified supersymmetric model where the masses of the $\tilde{\chi}_1^{\pm}$ and $\tilde{\chi}_2^0$ are degenerate and the $\tilde{\chi}_1^0$ is the lightest supersymmetric particle (LSP). The $\tilde{\chi}_1^{\pm}$ and $\tilde{\chi}_2^0$ are assumed to be wino like and the $\tilde{\chi}_1^0$ is assumed to be bino like, as explained in Section 2.1.1. Furthermore, the remainder of the supersymmetric particles, thus supersymmetric particles besides the $\tilde{\chi}_1^{\pm}$, $\tilde{\chi}_2^0$ and the $\tilde{\chi}_1^0$, are assumed to have a much higher mass and as a consequence are decoupled in the simplified model.

In this thesis the intermediate compressed regime is considered, where the mass difference (Δm) corresponds to $m_{\tilde{\chi}_1^{\pm}/\tilde{\chi}_2^0} - m_{\tilde{\chi}_1^0} < m_Z$. The range of Δm is motivated by global fits in the supersymmetry parameter space, as described in Section 2.4. The kinematics of the process are mainly determined by the Δm between the $\tilde{\chi}_1^{\pm}/\tilde{\chi}_2^0$ and the $\tilde{\chi}_1^0$. In the compressed regime the $W^{\pm}$ and Z will be created off-shell. The more the spectrum of the $\tilde{\chi}_1^{\pm}/\tilde{\chi}_2^0$ and the $\tilde{\chi}_1^0$ particles is compressed, the more the resulting amount of energy available to the $W^{\pm}$ and Z decreases. With decreasing energy available to the $W^{\pm}$ and Z, the available p_{T} for the resulting leptons will decrease as well. The most compressed scenarios thus correspond to the lowest p_{T} leptons. Since the final state leptons have lower p_{T}, they recoil less against the $\tilde{\chi}_1^0$,

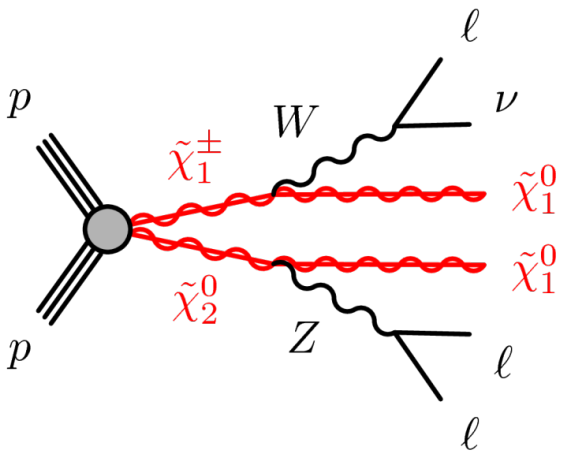

Fig. 6.1: Feynman diagram showing the process $\tilde{\chi}_1^{\pm}\tilde{\chi}_2^0 \rightarrow WZ\tilde{\chi}_1^0\tilde{\chi}_1^0$ decaying into a final state of three leptons and $E_{\mathrm{T}}^{\mathrm{miss}}$. Initial state radiation and final state radiation can lead to quarks or gluons being radiated in the process as well, causing the possibility of also having jets in the final state.

and as a result the two $\tilde{\chi}_1^0$ are often produced back to back. When the two $\tilde{\chi}_1^0$ are produced back to back there will be a similar amount of $E_{\mathrm{T}}^{\mathrm{miss}}$ in opposite sides of the detector, thus canceling out and resulting in low total $E_{\mathrm{T}}^{\mathrm{miss}}$.

The goal of this analysis is to search for this process in the compressed regime. However, obtaining an experimental outcome from which a significant statistical statement can be inferred is challenging, as described in Section 2.3.1. The previous Run-1 analysis from ATLAS on the same supersymmetric phase space [69] concluded that when Δm between the $\tilde{\chi}_2^0/\tilde{\chi}_1^{\pm}$ and $\tilde{\chi}_1^0$ was larger than 25 GeV, a lower limit on the mass of $\tilde{\chi}_1^0$ could be set at 100 GeV. However, in the more compressed region, where the Δm between the $\tilde{\chi}_2^0/\tilde{\chi}_1^{\pm}$ and $\tilde{\chi}_1^0$ is less than 25 GeV, the supersymmetric models could not be excluded. The process is difficult to detect at small Δm due to the kinematics of the process: the low p_{T} leptons and low $E_{\mathrm{T}}^{\mathrm{miss}}$. Low p_{T} leptons are arduous to reconstruct and trigger, and at low $E_{\mathrm{T}}^{\mathrm{miss}}$ there is a lot of Standard Model (SM) background. In this thesis a dedicated analysis for Run-2 is presented to target the process and improve the Run-1 analysis with better analysis techniques and a larger dataset.

6.1 Search overview

The analysis considers the full ATLAS Run-2 dataset highlighted in Table 6.1, corresponding to a total integrated luminosity of 139.0 fb^{-1}, collected by the ATLAS detector during 13 TeV proton-proton (p-p) collisions in the period 2015-2018. Only data recorded while the LHC

Table 6.1: ATLAS Run 2 dataset used in the analysis.

	2015	2016	2017	2018
collected data [fb^{-1}]	3.2	33.0	44.3	58.5

Table 6.2: Signal regions phase space is divided into four regions SRlow-0j, SRlow-nj, SRhigh-0j and SRhigh-nj. In the 0j region, the $E_{\mathrm{T}}^{\mathrm{miss}}$ is softer since it recoils against the WZ system, while in the nj region, $E_{\mathrm{T}}^{\mathrm{miss}}$ recoils against the jet, resulting in a harder $E_{\mathrm{T}}^{\mathrm{miss}}$.

	SRlow-0j	SRlow-nj	SRhigh-0j	SRhigh-nj
$N_{\mathrm{jets}}^{30\ \mathrm{GeV}}$	$=0$	≥ 1	$=0$	≥ 1
$E_{\mathrm{T}}^{\mathrm{miss}}$ [GeV]	<50	<200	>50	>200

declared stable beams, the ATLAS detector was properly operating, and both the solenoid and toroid fields were at nominal conditions is selected.

In the analysis, regions called Signal Regions (SRs) are designed where the supersymmetric signal is enhanced and the SM contributions are reduced. The regions are constructed by combining event selection criteria. The SR phase space is divided into four parts, with a different SM background composition in each region: SRlow-0j, SRlow-nj, SRhigh-0j and SRhigh-nj, as reflected in Table 6.2. The SRs will be further explained in Chapter 8. The first division is by the number of jets with $p_{\mathrm{T}} > 30$ GeV, $N_{\mathrm{jets}}^{30\ \mathrm{GeV}}$; into jet-veto regions called 0j, and regions with jets, where at least one jet is required, called nj. The second division is in $E_{\mathrm{T}}^{\mathrm{miss}}$, with the exact threshold dependent on whether the region is a 0j or an nj region. The low $E_{\mathrm{T}}^{\mathrm{miss}}$ SRs, SRlow-0j and SRlow-nj, target a phase space never explored by ATLAS before.[1] The low $E_{\mathrm{T}}^{\mathrm{miss}}$ SRs are worth exploring in the spirit of an inclusive search and closing the uncovered phase space, in an era where it is important to care more for unintended and untargeted signatures.

The analysis strategy is presented in the following steps. In Chapter 7 SM backgrounds that enter the kinematic regime of the signal model are estimated and the systematic uncertainties on the estimate of the backgrounds are calculated. Control regions for some backgrounds are designed in which our estimate of the background is scaled to the data. In Chapter 8 the estimate for the signal is generated, triggers are selected that optimise the trigger efficiency for the signal process. Cuts on kinematic variables, such as the invariant mass of the leptons, are optimised for the SRs until a significant statistical statement can be made about the process. In Chapter 9 validation regions are defined to validate the SM background estimate in the SR-like phase space. In Chapter 10 a statistical analysis is presented, where hypothesis

[1] It has typically been part of control and validation regions in Run-1.

testing is used to interpret the experimental outcome. In Chapter 11 the interpretation of the results as well as potential improvements to the analysis are discussed.

6.2 Particle selection

A selection of reconstructed particles, using the methods as described in Chapter 5, is made to select the supersymmetric signal shown in the Feynman diagram in Figure 6.1. The reconstructed particles in the analysis are electrons, muons and jets. Jets are not necessary to reconstruct the supersymmetric signal, however initial state radiation and final state radiation can lead to quarks or gluons being radiated. For the reconstructed electrons, muons and jets there is a baseline selection and a signal selection. The reconstructed particles need to pass the baseline selection consisting of loose identification criteria and the signal selection consisting of a tighter selection of identification criteria. Since all particles are reconstructed simultaneously, there is the possibility that the same tracks or calorimeter deposits are used in multiple particle objects, to resolve these ambiguities an algorithm called overlap removal (OR) is applied. After performing OR, the reconstructed electrons, muons, jets and photons are used for computing the $E_{\mathrm{T}}^{\mathrm{miss}}$.

Electrons The analysis encompasses electrons reconstructed, identified and with isolation criteria as described in Section 5.3.1. The impact parameters are defined in Section 5.1.1 and σ_{d_0} is the standard deviation of d_0 obtained from the track fit. The electron selection criteria are summarised in Table 6.3.

In the Z+jets/$Z+\gamma$ background estimation for electrons as described in Section 7.2, the baseline and signal selection definitions define ID and anti-ID electrons. The ID electrons are signal electrons and the anti-ID electrons are electrons that pass the baseline selection but fail the signal selection.

Muons The analysis uses muons reconstructed, identified, and with isolation criteria as described in Section 5.3.2. The impact parameters are defined in Section 5.1.1 and σ_{d_0} is the standard deviation of d_0 obtained from the track fit. The muon selection criteria are summarised in Table 6.4.

Also in the Z+jets/$Z+\gamma$ background estimation for muons, the baseline and signal selection definitions define ID and anti-ID muons. The ID muons are signal muons and the anti-ID muons are muons that pass the baseline selection but fail the signal selection.

Table 6.3: Summary of the electron selection criteria. The signal selection requirements are applied on top of the baseline selection requirements.

Cut	Value/description
Baseline Electron	
Acceptance	$p_{\mathrm{T}} > 4.5$ GeV, $\lvert\eta\rvert < 2.47$
Identification	`Loose` + hit in the innermost pixel layer
Impact parameter	$\lvert z_0 \sin\theta\rvert < 0.5$ mm
Signal Electron	
Identification	`Medium`
Isolation	`Gradient`
Isolation of 3$^{\mathrm{rd}}$ leading electron in p_{T}	`Gradient` + `PLVTight`
Impact parameter	$\lvert d_0/\sigma_{d_0}\rvert < 5$

Table 6.4: Summary of the muon selection criteria. The signal selection requirements are applied on top of the baseline selection requirements.

Cut	Value/description
Baseline Muon	
Acceptance	$p_{\mathrm{T}} > 3$ GeV, $\lvert\eta\rvert < 2.5$
Identification	`Medium`
Impact parameter	$\lvert z_0 \sin\theta\rvert < 0.5$ mm
Signal Muon	
Identification	`Medium`
Isolation	`FCLoose`
Isolation of 3$^{\mathrm{rd}}$ leading muon in p_{T}	`FCLoose` + `PLVTight`
Impact parameter	$\lvert d_0/\sigma_{d_0}\rvert < 3$

Table 6.5: Summary of the jet and b-jet selection criteria. The signal selection requirements are applied on top of the baseline requirements.

Cut	Value/description
Baseline jet	
Acceptance	$p_{\mathrm{T}} > 20$ GeV , $\lvert\eta\rvert < 4.5$
Signal jet	
Acceptance JVT	$p_{\mathrm{T}} > 20$ GeV , $\lvert\eta\rvert < 2.8$ $\lvert\mathrm{JVT}\rvert > 0.59$ for jets with $p_{\mathrm{T}} < 120$ GeV and $\lvert\eta\rvert < 2.5$
Signal b-jet	
Acceptance b-tagger Algorithm Efficiency	$p_{\mathrm{T}} > 20$ GeV , $\lvert\eta\rvert < 2.5$ MV2c10 85 %

Jets The analysis uses jets reconstructed with the anti-k_t algorithm [145] with $R = 0.4$ calibrated with the Jet Energy Scale (JES) calibration [144] as described in Section 5.2. Since the Jet Vertex Tagger (JVT) algorithm [149] and MV2c10 b-tagging algorithm [151], which are also described in Section 5.2, rely on particle tracks from the Inner Detector (ID), which only covers up to $|\eta| < 2.5$ as described in Section 3.2.2, these algorithms can only be applied to jets up to $|\eta| < 2.5$. The jet selection criteria are summarised in Table 6.5.

Overlap removal As particles are reconstructed simultaneously, it is possible that the same tracks or calorimeter deposits are used in multiple particle objects. OR is performed with reconstructed particles considered in the analysis, electrons, muons and jets, in order to assign tracks or calorimeter deposit to a single particle hypothesis. The following procedure is applied:

- Any calorimeter-tagged muons, as described in Section 5.3.2, sharing an ID track with an electron are removed.
- Any electrons sharing an ID track with remaining muons are removed.
- Jets within $\Delta\mathrm{R} < 0.2$ of a lepton are discarded as they most often result from calorimeter energy deposits of the electron shower or muon bremsstrahlung. For the overlap with muons, the jet is only discarded if it is associated to less than three tracks with p_{T} above 500 MeV, or if the jet p_{T} is less than half of the muon p_{T} and the relative fraction of associated track p_{T} to jet p_{T} is above 70%.

- Electrons and muons with $p_{\mathrm{T}} < 50$ GeV that are close to a remaining jet are discarded to reject non-prompt or fake leptons originating from hadron decays. These are discarded if situated within a distance of $\Delta\mathrm{R} < 0.4$ for leptons of $p_{\mathrm{T}} \leq 25$ GeV, decreasing inversely with lepton p_{T} down to $\Delta\mathrm{R} < 0.2$ for leptons of $p_{\mathrm{T}} = 50$ GeV.

In addition, a selection is applied on the the minimum ΔR for all possible combinations of leptons in the event, $\min \Delta R^{3\ell} > 0.4$. This cut ensures that leptons are isolated from each other.[2]

$\mathbf{E_T^{miss}}$ $E_{\mathrm{T}}^{\mathrm{miss}}$ is computed as described in Section 5.5. Reconstructed particles used in the analysis are taken as input, as well as photons. Also all tracks matched to the primary vertex that are not associated with reconstructed particles are taken as input. The reconstructed particles considered in the analysis (electrons, muons and jets) entering the $E_{\mathrm{T}}^{\mathrm{miss}}$ calculation are required to satisfy the baseline selection criteria defined above, and have to pass the OR criteria as well. While photons are not used as signal objects in this analysis, they provide input to the $E_{\mathrm{T}}^{\mathrm{miss}}$ calculation. Photons are required to have a $p_{\mathrm{T}} > 25$ GeV and $|\eta| < 2.37$, with a veto for photons that fall in the calorimeter crack region, corresponding to $1.37 < |\eta| < 1.52$.

6.3 Variables used in the analysis

In order to discriminate the SM background from the signal, several variables are used in the analysis. The variables are constructed after an explicit requirement of exactly three leptons. All variables are listed in this section, which can be used as a reference throughout the analysis part of this thesis.

$E_{\mathrm{T}}^{\mathrm{miss}}$ significance The object-based $E_{\mathrm{T}}^{\mathrm{miss}}$ significance indicating the degree to which the reconstructed $E_{\mathrm{T}}^{\mathrm{miss}}$ agrees with momentum resolution and particle identification efficiencies as described in Section 5.5.2.

$\mathbf{N_{jets}^{30\ GeV}}$ The number of jets with $p_{\mathrm{T}} > 30$ GeV.

$\mathbf{N_{b\text{-}jets}^{20\ GeV}}$ The number of b-jets with $p_{\mathrm{T}} > 20$ GeV. Jets are tagged as b-jets as explained in Section 5.2.1. The working point chosen for the analysis corresponds to a b-jet tagging efficiency of 85%.

[2] Since the isolation used is mostly with a $\Delta R = 0.2$ cone, $\min \Delta R^{3\ell} > 0.4$ $(0.2 \cdot 2)$ is found to be enough.

OSSF The presence of an opposite-sign same-flavour (OSSF) lepton pair in the event. Since the leptonic decay of a Z results in an OSSF lepton pair, OSSF leptons are assigned to the Z boson in the event reconstruction.

$\mathbf{m_{\ell\ell}}$ The invariant mass of the OSSF lepton pair. If there are two OSSF pairs in the event there are multiple ways to assign the leptons to the Z:

1. $m_{\ell\ell}$: the invariant mass of the OSSF lepton pair closest to m_Z
2. $m_{\ell\ell}^{\text{min}}$: minimises the invariant mass of the OSSF lepton pair
3. $m_{\ell\ell}^{\text{max}}$: maximises the invariant mass of the OSSF lepton pair

In the analysis, assignment of leptons to the Z can be achieved taking the lepton pair corresponding to the $m_{\ell\ell}$, $m_{\ell\ell}^{\text{min}}$, or $m_{\ell\ell}^{\text{max}}$ assignment. The remaining lepton is then assigned to the W.

$\mathbf{m_{3\ell}}$ The invariant mass of the three leptons.

$\mathbf{m_T}$ The transverse mass of the $W^{\pm}$ boson. The W boson decays into a visible particle, a charged lepton, and an invisible particle, a neutrino. In a hadron collider, only the transverse components of an invisible particle momentum can be inferred, so it is useful to define the transverse mass. The transverse mass describes a system of one visible particle, and one invisible particle, ν,

$$m_{\text{T}}^2 = m_{\text{vis}}^2 + m_{\nu}^2 + 2(E_{\text{T}}^{\text{vis}} E_{\text{T}}^{\nu} - p_{\text{T}}^{\text{vis}} p_{\text{T}}^{\nu}). \tag{6.2}$$

The charged lepton from the W decay can be assigned in multiple ways:

1. m_{T}: W-lepton assigned according to $m_{\ell\ell}$
2. $m_{\text{T}}^{\text{minmll}}$: W-lepton assigned according to $m_{\ell\ell}^{\text{min}}$

$\mathbf{m_{T2}^{100}}$ The stransverse mass. In the supersymmetric signal there is not one $\tilde{\chi}_1^0$ escaping the detector, but there are two $\tilde{\chi}_1^0$ simultaneously escaping the detector. However, only one quantity capturing their energy can be reconstructed, which is $E_{\text{T}}^{\text{miss}}$. The m_{T2} algorithm tries to disentangle the $E_{\text{T}}^{\text{miss}}$ and find out which part belongs to each of the $\tilde{\chi}_1^0$ [163]. Since only the sum of the missing transverse momentum of the invisible particles in the event is

known, the best that can be done is to evaluate the quantity, m_{T2} which is a lower bound on the maximum of the transverse mass, m_{T},

$$m^2_{\mathrm{T2}}(m_{\tilde{\chi}^0_1}) = \min_{E^{\mathrm{miss},1}_{\mathrm{T}}+E^{\mathrm{miss},2}_{\mathrm{T}}=E^{\mathrm{miss}}_{\mathrm{T}}} [\max\{m^2_{\mathrm{T}}(p^{\mathrm{vis},1}_{\mathrm{T}}, E^{\mathrm{miss},1}_{\mathrm{T}}; m_{\tilde{\chi}^0_1}), m^2_{\mathrm{T}}(p^{\mathrm{vis},2}_{\mathrm{T}}, E^{\mathrm{miss},2}_{\mathrm{T}}; m_{\tilde{\chi}^0_1})\}]. \tag{6.3}$$

Taking as input an assumption for the $\tilde{\chi}^0_1$ mass, the algorithm divides the event topology into two legs, each containing a visible part, $p^{\mathrm{vis}}_{\mathrm{T}}$, and an invisible part $E^{\mathrm{miss}}_{\mathrm{T}}$.

In case of the signal illustrated in Figure 6.1, the two legs are $\tilde{\chi}^0_2 \to Z\tilde{\chi}^0_1$ and $\tilde{\chi}^\pm_1 \to W\tilde{\chi}^0_1$. The two leptons assigned to the Z, through $m^{\mathrm{min}}_{\ell\ell}$, correspond to $p^{\mathrm{vis},1}_{\mathrm{T}}$ and the remaining lepton specifies $p^{\mathrm{vis},2}_{\mathrm{T}}$. The $\tilde{\chi}^0_1$ from the $\tilde{\chi}^0_2$ decay represents $E^{\mathrm{miss},1}_{\mathrm{T}}$. The $\tilde{\chi}^0_1$ and ν from the $\tilde{\chi}^\pm_1$ decay are regarded as one particle, which can be labeled as Y, and together proportionate to $E^{\mathrm{miss},2}_{\mathrm{T}}$. The particle Y has an invariant mass bound by $m_{\tilde{\chi}^0_1} + m_\nu$, which can numerically be considered as $m_{\tilde{\chi}^0_1}$.

An assumption for the $\tilde{\chi}^0_1$ mass has to be made. Studies have been carried out comparing different values of $\tilde{\chi}^0_1$. The performance of the variable does not change much by the choice of $m_{\tilde{\chi}^0_1}$, except for a massless $\tilde{\chi}^0_1$, and thus a sufficiently high $\tilde{\chi}^0_1$ mass is chosen. The mass of the $\tilde{\chi}^0_1$ is set to 100 GeV, and this variable is labeled m^{100}_{T2} .

min ΔR The minimum ΔR between all OSSF lepton pairs in the event.

$\mathbf{p^{leptons}_T/E^{miss}_T}$ The ratio of the vector sum p_{T} of the three leptons and the $E^{\mathrm{miss}}_{\mathrm{T}}$.

$\mathbf{m^{p^{balance}_Z}_W}$ The reconstructed W-boson mass assuming the WZ topology and balanced longitudinal momenta of the W and Z boson.

$\Delta\mathbf{R(W-lepton, E^{miss}_T)}$ The ΔR between the W-lepton and the $E^{\mathrm{miss}}_{\mathrm{T}}$ is defined by $\sqrt{\eta^2_{W\text{-lepton}} + (\phi_{W\text{-lepton}} - \phi_{E^{\mathrm{miss}}_{\mathrm{T}}})^2}$. The W-lepton is assigned according to $m^{\mathrm{min}}_{\ell\ell}$.

Chapter 7

Modelling of the background

Proton-proton (p-p) collisions at the Large Hadron Collider (LHC) will create Standard Model (SM) particles, through SM processes. Since this thesis presents a search for supersymmetry, which is beyond the SM, these SM processes are called the background. SM backgrounds which result in a 3-lepton final state, comparable to our supersymmetry signal, are identified in order to form the estimate of the background. All the different backgrounds and how they have been grouped are shown in Table 7.1. In order to have an efficient bookkeeping and focus on the larger backgrounds, contributions from backgrounds with a small cross-section have been grouped into Others.

Table 7.1 contains backgrounds with a 3-lepton final state, however, backgrounds with other lepton multiplicity in the final states are also considered. Also backgrounds with a 1- or 2-lepton final state are included, in order to incorporate the possibility that the second or third lepton is being faked in the form of leptons that arise from heavy flavour decays, are misidentified jets, or are photon-conversions. Also backgrounds with more than three leptons in the final state are included. These backgrounds look like a 3-lepton final state when some of the leptons are not reconstructed, either because these fall outside the range of acceptance, are too low p_{T}, fail the lepton identification, or are a tau that decays hadronically.

A 3-lepton final state is produced by WZ, some of the triboson processes, some $t\bar{t}W$, $t\bar{t}Z$ or $t\bar{t}h$ ($t\bar{t}$+X) processes, and some rare t processes (topOther). Fake backgrounds with a 1- or 2-lepton final state are Z+jets/Z+γ, $t\bar{t}$, WW (diboson2ℓ) and t (singleTop). The backgrounds with more than three leptons are ZZ, some of the triboson processes, some $t\bar{t}$+X processes, and some of the topOther processes.

For estimating the backgrounds different techniques are applied. It is possible to estimate a background either through Monte Carlo (MC) simulations or by using a data-driven approach. For Z+jets/Z+γ a data-driven approach is selected and for the rest of the backgrounds MC is used. All the simulated events are reconstructed the same way as the data events.

Table 7.1: The backgrounds included in the analysis. The smaller backgrounds have been grouped into Others. All the backgrounds are estimated using MC, except Z+jets/$Z+\gamma$ which is estimated using a data-driven technique.

Group name	Background	Estimation method
Fakes	Z+jets/$Z+\gamma$	Data-driven
WZ	WZ	MC
ZZ	ZZ	MC
$t\bar{t}$	$t\bar{t}$	MC
$t\bar{t}$+X	$t\bar{t}$+X	MC
Others	topOther	MC
	singleTop	MC
	diboson2ℓ	MC
	triboson	MC
	Higgs	MC

For the largest background estimated using MC, WZ, a normalisation factor is derived with respect to data in order to improve the estimate.

7.1 Monte Carlo background samples

In order to model SM background processes MC simulations are used. The MC method makes use of pseudorandom numbers to simulate the event-to-event fluctuations due to quantum physics in the processes and the fluctuations in the interactions with detector material. Generating events using MC follow a number of steps. First the matrix element of the given process needs to be generated in order to model what took place in the hard-scatter of the p-p interaction. Afterwards the particles that arise from the hard-scatter need to shower and hadronise to the point of forming individual stable particles in the detector. As a final step, the interaction of the showered event with the detector is modelled in the detector simulation. The processes that are generated to model the SM backgrounds are described in Table 7.2.

To generate the matrix element different generators are available. The selected generators in this analysis are Sherpa [164], Powheg [165] and Madgraph [166]. Each generator relies on different techniques, so certain generators are more suitable for certain processes [167]. From the p-p interaction, the generator determines which particles take part in the hard-scatter and subsequently calculates the corresponding Feynman diagrams. The generator uses a Parton Density Function (PDF) to describe the constituents of the colliding protons, the

Table 7.2: Processes simulated by the MC generators comprising the WZ, ZZ, $t\bar{t}$, $t\bar{t}$+X, topOther, singleTop, diboson2ℓ, triboson and Higgs backgrounds. When a W or Z decay is fixed in the setup of the generator, the decay product is written between brackets, where $\ell\ell$ corresponds to a leptonic decay, and qq to a hadronic decay. VBS stands for vector-boson scattering.

background	process	σ [pb]
WZ [1]	$WZ \to \ell\ell\ell\nu$	7.54
	$jjWZ \to \ell\ell\ell\nu jj$ (VBS)	0.05
ZZ [1]	$ZZ \to \ell\ell\ell\ell$	2.72
	$jjZZ \to \ell\ell\ell\ell jj$ (VBS)	0.01
$t\bar{t}$	$t\bar{t} \to W(\ell\nu)W(\ell\nu)bb$	87.7
$t\bar{t}$+X	$t\bar{t}W \to WWWbb$	0.60
	$t\bar{t}Z \to WWZ(qq)bb$	0.59
	$t\bar{t} \to WWbb\ell\ell$	0.44
	$t\bar{t}h \to W(qq)bW(qq)bh$	0.24
	$t\bar{t}h \to W(\ell\nu)bW(qq)bh$	0.23
	$t\bar{t}Z \to WWZ(\ell\ell)bb$	0.17
	$t\bar{t}Z \to WWZ(\nu\nu)bb$	0.17
	$t\bar{t}h \to W(\ell\nu)bW(\ell\nu)bh$	0.05
topOther	$tqZ \to WbqZ(\ell\ell)$	0.03
	$tWZ \to WWbZ(\ell\ell)$	0.02
	$t\bar{t}WW \to WWWWbb$	0.01
	$t\bar{t}t\bar{t} \to WWWWbbbb$	0.01
	$t\bar{t}t \to WWWbbb$	0.002
singleTop	$tq \to W(\ell\nu)bq$	73.85
	$tW \to W(\ell\nu)W(\ell\nu)b$	7.56
diboson2ℓ [1]	$WW \to \ell\ell\nu\nu$	13.43
	$WZ \to \ell\ell qq$	3.43
	$ZZ \to \ell\ell qq$	2.20
	$jjWW \to \ell\ell\nu\nu jj$ (VBS)	0.12
triboson [1]	$WWW \to \ell\ell\ell\nu\nu\nu$	0.016
	$ZWW \to \ell\ell\nu\nu\nu\nu$	0.006
	$ZWW \to \ell\ell\ell\ell\nu\nu$	0.004
	$ZZW \to \ell\ell\ell\ell\ell\nu$	0.0006
	$ZZZ \to \ell\ell\ell\ell\ell\ell$	0.0001
Higgs	$h \to \tau\tau$	14.46

[1] Sherpa does not generate pp$\to Z \to \ell\ell$, but pp$\to \ell\ell$, which includes off-shell and non-Z diagrams (including h).

Table 7.3: The backgrounds that are generated using MC simulations and the choice of generator and parton shower.

Background name	Generator	Parton Shower
WZ	SHERPA v2.2.2	
ZZ	SHERPA v2.2.2	
$t\bar{t}$	Powheg	Pythia8
$t\bar{t}$+X (excl. $t\bar{t}h$)	MadGraph5_aMC@NLO	Pythia8
$t\bar{t}h$	Powheg	Pythia8
topOther	MadGraph5_aMC@NLO	Pythia8
singletop	Powheg	Pythia8
diboson2ℓ	SHERPA v2.2.2	
triboson	SHERPA v2.2.2	
Higgs	Powheg	Pythia8

quarks and gluons, at the energy of the collision. The PDF describes the probability of each quark or gluon in the proton to undergo an interaction in the p-p collision. The predominant PDF used in this analysis is NNPDF3.0 [168], which uses a neural network to perform a dataset combination of HERA and LHC experiments.

The matrix element is calculated using perturbation theory. Perturbation theory leads to an expression for the solution in terms of a power series, an ordered sequence of numbers in terms of α_s, where an approximate solution is obtained by truncating the series. The simplest case is the simulation of leading-order (LO) matrix elements. A problem with LO matrix elements is that the results in many cases are only reliable for the shape of the kinematic distributions, while the absolute normalisation is often poorly described, due to corrections in the matrix element at higher order. However, at each higher-order matrix element calculation, such as next-to-leading-order (NLO) and next-to-next-to-leading order (NNLO), many more possible diagrams are to be taken into account, and it is technically difficult to compute them all. There are also certain logarithms that appear in the perturbation theory, and not just at NLO or NNLO, but in all orders of α_s. How many logarithms at each order in α_s are resummed is determined by whether the calculation is leading logarithm (LL), next-to-leading logarithm (NLL), or next-to-next-to-leading logarithm (NNLL) accurate. Most matrix element calculations in this analysis are done at NLO and are then normalised to NNLO and NNLL.

After having generated the matrix element, the particles from the hard-scatter need to shower in order to acquire the final state from the p-p collision to the level of individual stable particles. The created particles from the matrix element can have colour charge and

thus radiate virtual gluons, which can further emit gluons or produce quark-antiquark pairs, leading to a parton shower. When the strong interaction coupling increases in magnitude, due to colour confinement, hadronisation starts, and the created coloured particles will turn into colourless hadrons. In a hadron-hadron collider the constituents of the incoming hadrons will also undergo interactions with the produced particles in the hard-scatter; this is called the underlying event. The parton shower, hadronisation and underlying event are all referred to as showering. In the case where the matrix element is generated by Powheg or Madgraph, showering is done by Pythia [169]. Pythia is tuned to better match the ATLAS data using the A14 tune [170]. In the case of Sherpa, the showering is done by Sherpa itself. The SM backgrounds and the generator and parton shower choices for each of them are summarised in Table 7.3.

After the stable particles from the event have been generated, the detector simulation describes the interaction of the particles with the material of the detector. The detector simulation is achieved using GEANT4 [171], which simulates the interaction of particles with matter using MC. The detector simulation for the background MC samples is carried out with the full ATLAS detector simulation [172].

7.1.1 Treatment of uncertainties

A systematic uncertainty is connected to the way the MC simulation has been performed. The systematic uncertainties can be divided into two classes. The first are uncertainties from experimental conditions and reconstructed particles, called instrumental uncertainties. The second are uncertainties from the theoretical modelling in MC, called theoretical uncertainties. Both the instrumental and theoretical uncertainties are discussed in this section.

Instrumental uncertainties

The reconstruction, as described in Chapter 5, relies on measurements performed by the ATLAS detector to reconstruct the experimental conditions and particles in the p-p collisions. Instrumental uncertainties arise from the precision with which the detector is able to perform these measurements. Instrumental uncertainties affect all MC samples used to model the background (and signal) processes, but not the data-driven Z+jets/$Z+\gamma$ sample. The instrumental uncertainties attached to the experimental conditions and the reconstructed particles will be summarised in this section.

a) Luminosity The absolute luminosity scale is determined using van der Meer scans [173] during dedicated running periods in each year. The luminosity scale is then extrapolated to

normal data taking periods incorperating measurements from several luminosity sensitive detectors. The primary bunch-by-bunch luminosity measurement is provided by the LUCID2 Cherenkov detector. The ATLAS calorimeters then provide bunch-integrated measurements [95]. On the measurement of the luminosity of the combined Run-2 dataset it has been found that the relative uncertainty is equal to 1.7% [174].

b) Pile-up Pile-up, or μ, as described in Section 3.1.1, is defined as the amount of collisions per bunch crossing. Differences between MC and data are corrected by means of μ scaling to data. Simulated samples are generated with a pile-up profile $\langle\mu\rangle$ overall scaled to data, where the profile is approximately equal to the profile observed in data, however only after data taking the real μ profile is known. After data taking the pile-up profile is reweighed in MC in each μ bin to match data. The uncertainty on this reweighing procedure is taken into account.

c) Electron-related uncertainties The electron energy scale and resolution are calibrated using $Z \to e^+e^-$ and $J/\psi \to e^+e^-$ data events [175]. The calibration procedure adjusts the calorimeter response in data and compares data to MC to produce correction factors to account for differences between data and MC. The uncertainty on the electron energy scale and resolution is taken into account.

Further sources of uncertainties are related to the electron reconstruction, identification and isolation as described in Section 5.3.1. Correction factors are measured with a tag-and-probe approach on $Z \to e^+e^-$ events in both data and MC [153] and applied to MC events. The uncertainty on the reconstruction, identification and isolation is taken into account.

The PromptLeptonVeto isolation algorithm is calibrated for electrons as is described in Section 5.4.1. The uncertainty attached to the calibration of the PLV is taken into account.

d) Muon-related uncertainties The muon momentum scale and resolution are calibrated using $Z \to \mu^+\mu^-$ and $J/\psi \to \mu^+\mu^-$ data events [157]. Uncertainties are associated to the muon momentum scale, the momentum resolution as measured in the Muon Spectrometer and Inner Detector, as well as sagitta distortions caused by small detector mis-alignment.

Further sources of uncertainties are related to the muon reconstruction, identification and isolation as described in 5.3.2. Correction factors are measured with a tag-and-probe approach on $Z \to \mu^+\mu^-$ events in both data and MC and applied to MC events. The uncertainty on the reconstruction, identification and isolation is taken into account.

The PromptLeptonVeto isolation algorithm is calibrated for muons as is described in Section 5.4.1. The uncertainty attached to the calibration of the PLV is taken into account.

e) Jet energy scale, resolution and Jet vertex tagger Jets are reconstructed as described in Section 5.2. Jet energy scale (JES) uncertainties originate from the calibration process consisting of a combination of MC-based methods and in situ techniques [176]. Jet energy resolution (JER) uncertainties arise from the smearing procedure applied to MC events in order to match the energy resolution measured in data [177]. Finally, there is an uncertainty in the calibration of the Jet vertex tagger (JVT) algorithm, used to suppress pileup jets [149].

f) Flavour-tagging In most of the regions in the analysis a b-jet veto is applied, where b-jets are tagged as described in Section 5.2.1. The uncertainties arise from the b-tagging efficiency corrections parametrised over the jet p_{T} and flavour, which are applied to MC events [178].

g) Missing transverse momentum $E_{\mathrm{T}}^{\mathrm{miss}}$ is computed as described in Section 5.5 using the reconstructed physics objects and an additional track-based soft term comprising all remaining unmatched tracks. Uncertainties from the reconstructed particles that enter the $E_{\mathrm{T}}^{\mathrm{miss}}$ and the track-based soft term make up the uncertainty.

Theoretical uncertainties

When producing estimates of physical processes using MC, as described in Section 7.1, an uncertainty in the cross-section of the process has to be taken into account, as well as uncertainties reflecting the choices made for the matrix element generator, renormalisation and factorisation scale and the PDF. The choices made will have an impact on the result. For all of the backgrounds a theoretical uncertainty is considered to account for the uncertainty in the cross-section. For the three largest backgrounds, which are WZ, ZZ and $t\bar{t}$, more detailed theoretical uncertainties have been derived which will be discussed in this section.

1) WZ and ZZ theoretical uncertainties

Several sources of theoretical uncertainties on the modelling of the WZ and ZZ background have been considered. The theoretical uncertainties are provided by the generator of the WZ and ZZ samples, which is Sherpa. Each theoretical variation comes in the form of a weight in the nominal sample or in the form of an alternative generated sample. The weight in the nominal sample or the alternative sample is evaluated in the different regions of the analysis to obtain the variation in that region, and from there obtain the systematic uncertainty.

The nominal sample is passed through the full ATLAS detector simulation, it is thus possible when using the weights in the nominal sample to estimate the systematic uncertainty

after the full detector simulation. For the alternative samples the detector simulation has not been run, as it is computationally intensive and it has a minimal impact on the theoretical variation. The systematic uncertainty is thus only estimated at generator level when using the variations in the alternative samples. The uncertainties can be divided into several groups.

a) Scale variations Uncertainties arising from variations in the renormalisation and factorisation scales (μ_{R}, μ_{F}, μ_{R}+μ_{F}) of a factor $1/2$ and 2 have been evaluated. The scale variations are the leading diboson modelling uncertainties, with the largest contributions coming from the μ_R and $\mu_R + \mu_F$ variations. The uncertainty has been evaluated after full ATLAS detector simulation.

b) PDF + α_s variations The impact of the PDF choice was evaluated by using different PDF sets MMHT2014 [179], CT14 [180], and NNPDF [168], and taking the envelope as the uncertainty. The value of the strong coupling constant α_s is varied within its uncertainty. Both uncertainties have been evaluated after full ATLAS detector simulation.

c) Re-summation The uncertainty related to the re-summation scale QSF, for example the upper cut-off of perturbative calculations for parton shower evolution, has been evaluated. The nominal QSF value of 2 GeV is varied by a factor $1/4$ and 4. The uncertainty has been evaluated at generator level.

d) Merging scale variations The CKKW merging scale [181] determines the lower limit in p_{T} of the additional partons added in the matrix element. Below this threshold additional partons are added by the parton shower. The uncertainty related to the choice of the CKKW merging scale, at 20 GeV, has been evaluated, considering the alternative values of 15 GeV and 30 GeV. The uncertainty has been evaluated at generator level.

e) Recoil scheme variation The impact of using an alternative recoil scheme [182] for single particle emission in the parton shower has been evaluated. The uncertainty has been evaluated at generator level.

2) $t\bar{t}$ theoretical uncertainties

Several sources of theoretical uncertainties on the modelling of the $t\bar{t}$ background have been considered. The nominal sample used for $t\bar{t}$ is POWHEG + Pythia 8. Theoretical uncertainties are provided by variations in the nominal POWHEG + Pythia 8 sample itself, an aMC@NLO + Pythia 8 sample and a POWHEG + HERWIG7 sample. And a POWHEG + Pythia 8 sample

where the hdamp parameter is varied.[2] The nominal sample has hdamp set to $1.5 \times m_t$ and the alternative sample has hdamp set to $3 \times m_t$.

Each theoretical variation comes in the form of a weight in the nominal sample or in the form of an alternative generated sample. The weight in the nominal sample or the alternative sample is evaluated in the different regions of the analysis to obtain the variation in that region, and from there obtain the systematic uncertainty. On all the samples the full ATLAS detector simulation is run.

a) Matrix element generator The modelling at the matrix element level is checked by comparing the POWHEG + Pythia 8 sample with the aMC@NLO + Pythia 8 sample.

b) PDF + α_s variations PDF $+ \alpha_S$ uncertainties are estimated using weights provided by POWHEG in the nominal samples following the PDF4LHC [183] prescription.

c) ISR + FSR uncertainties Pythia contains a separate initial state radiation (ISR) parton shower scale α_S^{ISR} [184]. ISR uncertainties are derived by varying α_S^{ISR}, the renormalisation and factorisation scales (μ_{R}, μ_{F}, μ_{R}+μ_{F}) and the hdamp parameter. For the up variation α_S^{ISR} is varied up, a factor $1/2$ has been evaluated for the renormalisation and factorisation scales and the alternative hdamp sample is used. For the down variation α_S^{ISR} is varied down, a factor 2 has been evaluated for the renormalisation and factorisation scales and the nominal hdamp sample is used.

Pythia also contains a separate final state radiation (FSR) parton shower scale α_S^{FSR}. For the up variation α_S^{FSR} is varied up and a factor $1/2$ has been evaluated for the renormalisation and factorisation scales. For the down variation α_S^{FSR} is varied down and a factor 2 has been evaluated for the renormalisation and factorisation scales.

d) Showering The modelling at the matrix element level is checked by comparing the POWHEG + Pythia 8 sample with the POWHEG + HERWIG7 sample.

7.1.2 Control regions

The goal of the MC background estimation described in 7.1 is to provide a correct estimation of the SM backgrounds in the Signal Regions (SRs) described in Table 6.2. The correctness of the estimation of the MC background can be checked by comparing it with the measured data in a region pure in that MC background. If the MC background estimation agrees with

[2] The hdamp parameter controls the p_{T} of the first additional emission beyond the Born approximation and it regulates the high p_{T} emission against which the $t\bar{t}$ system can recoil.

the observed data it means a good estimation of that background is provided. However, the MC generators are not perfect, and especially when zooming in on extreme corners of phase space there is the possibility that the background is not properly normalised to the data or that the shape of the background is incorrect. For our main background derived using MC, the WZ background, it is important that both the normalisation and shape are correct. Control Regions (CRs) have been designed to adjust the normalisation of the WZ background.

The normalisation of the WZ background can be adjusted by comparing it with the measured data in a region pure in WZ events with high statistics, a WZ CR. In the CR a normalisation factor for WZ can be extracted such that,

$$\mu_{WZ} = \frac{\text{data} - \text{MC}_{\text{other}}}{\text{MC}_{WZ}}, \tag{7.1}$$

where $\text{MC}_{\text{other}} = \text{MC}_{\text{total}} - \text{MC}_{WZ}$. The normalisation factor is then applied in the SRs such that,

$$\text{MC}_{WZ,\text{normalised}} = \text{MC}_{WZ} \cdot \mu_{WZ}. \tag{7.2}$$

A CR should have high purity in the WZ background, ensuring that the normalisation is as little dependent on the contributions from other SM backgrounds as possible. Also a CR should be high in event statistics to not bias the correction with statistical fluctuations. It is also beneficial to have a CR kinematically close to the SRs, as the normalisation factor will then account for the mismodelling in that same phase space.

The CRs for the WZ background are designed to correct mismodelling observed in the $N_{\text{jets}}^{30\,\text{GeV}}$ distribution. In Figure 7.1 it is observed that the background estimation has a downward trend in the data/MC agreement with increasing jet multiplicity. To correct for the mismodelling the WZ CRs are divided into a jet-veto region, CRWZ-0j, and a region with jets, where at least one jet is required, CRWZ-nj. In each WZ CR a normalisation factor for WZ is extracted, thus obtaining normalisation factors μ_{WZ0j} and μ_{WZnj}.

The WZ CRs are defined in regions where the W and Z are on-shell. Ideally, it would be best to correct in an off-shell WZ phase space like the SRs, where $m_{\ell\ell} < 75$ GeV, however no orthogonal, sufficiently pure regions were found where this is possible. In order to select the on-shell Z the $m_{\ell\ell}$ window is $[81, 101]$ GeV, and to select the on-shell W a cut is placed of $m_{\text{T}} > 50$ GeV. An $E_{\text{T}}^{\text{miss}}$ cut is applied in order to be orthogonal with the on-shell $\tilde{\chi}_1^{\pm}\tilde{\chi}_2^0 \to W^{\pm}Z\tilde{\chi}_1^0\tilde{\chi}_1^0$ signal regions [15], of which the result is summarised in Section 11.5. The WZ CRs are defined in Table 7.4.

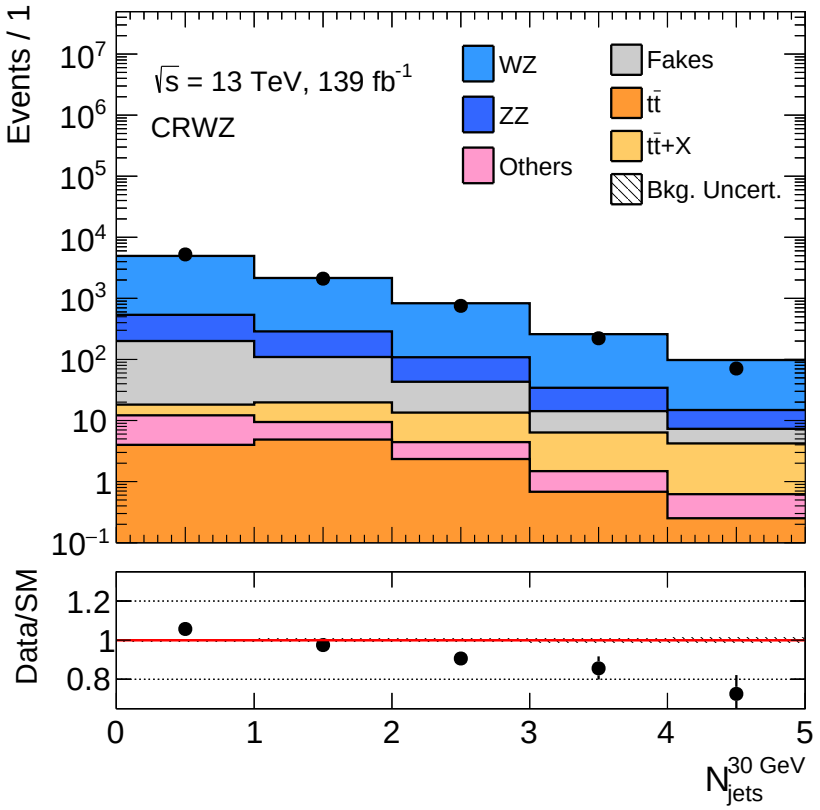

Fig. 7.1: Distribution for $N_{\text{jets}}^{30\text{ GeV}}$ in the CRWZ before the fit. $N_{\text{jets}}^{30\text{ GeV}}$ is defined as the number of jets with $p_{\text{T}} > 30$ GeV. Only statistical uncertainties are included.

Table 7.4: *WZ* control region (CRWZ) definitions.

	$m_{\ell\ell}$ [GeV]	$N_{\text{jets}}^{30\text{ GeV}}$	$E_{\text{T}}^{\text{miss}}$ [GeV]	lepton p_{T} [GeV]	m_{T} [GeV]
CRWZ-0j	$\in [81, 101]$	0	$<$50	all 3 $>$ 10	$>$50
CRWZ-nj	$\in [81, 101]$	$\geq$1	$<$50	all 3 $>$ 10	$>$50

Background-only fit

In order to determine μ_{WZ0j} and μ_{WZnj}, including the systematics uncertainties described in Section 7.1.1, a maximum likelihood method is used instead of Equation 7.1. All systematic uncertainties are implemented in the fit as nuisance parameters $\vec{\theta}$. The likelihood for measuring the observed data in the CRs is given by

$$L(\vec{n}|\mu_{WZ0j},\mu_{WZnj},\vec{\theta}) = \prod_{i\in CR} P(n_i|N_i(\mu_{WZ0j},\mu_{WZnj},\vec{\theta})) \times C_{syst}(\vec{\theta}), \tag{7.3}$$

where P is a poisson distribution and C is typically a gauss, poisson or log-normal distribution. The likelihood depends on the number of measured events, n_i, and the number of expected events N_i, where N_i is given by

$$N_i(\mu_{WZ0j},\mu_{WZnj},\theta) = \mu_{WZ0j}\cdot b_{WZ0j}(\vec{\theta}) + \mu_{WZnj}\cdot b_{WZnj}(\vec{\theta}) + \sum_{j\notin WZ} b_{j,i}(\vec{\theta}). \tag{7.4}$$

N_i is a function of normalisation scale factors μ_{WZ0j} and μ_{WZnj}, number of expected background events $\vec{b}$ and nuisance parameters $\vec{\theta}$. The profile likelihood ratio, λ, is then used to obtain the normalisation factors and uncertainty for μ_{WZ0j} and μ_{WZnj},

$$\lambda(\mu_{WZ0j},\mu_{WZnj}) = \frac{L(\vec{n}|\mu_{WZ0j},\mu_{WZnj},\hat{\hat{\vec{\theta}}}(\mu_{WZ0j},\mu_{WZnj}))}{L(\vec{n}|\hat{\mu}_{WZ0j},\hat{\mu}_{WZnj},\hat{\vec{\theta}})}. \tag{7.5}$$

In this notation a single hat corresponds to values that maximise the likelihood overall and a double hat corresponds to values that maximise the likelihood for a fixed μ_{WZ0j} and μ_{WZnj}.

The normalisation factors obtained are $\mu_{WZ0j} = 1.064 \pm 0.027$ and $\mu_{WZnj} = 0.932 \pm 0.030$. The yields before and after the fit are presented in Table 7.5. The determination of the normalisation is barely affected by the systematic uncertainties, retaining only statistical uncertainties gives $\mu^{\text{stat.}}_{WZ0j} = 1.064 \pm 0.017$ and $\mu^{\text{stat.}}_{WZnj} = 0.932 \pm 0.026$. The outcome of the fit is propagated to the *WZ* validation regions described in Section 9.1. The normalisation factors are also applied in the rest of the validation regions in Chapter 9 and when optimising the signal selection in Chapter 8. In Chapter 10, where the unblinded results will be shown, the outcome of the fit is propagated to the SRlow and SRhigh. The agreement after the fit between the estimation and the data can be seen in Figure 7.2 for CRWZ-0j and in Figure 7.3 for CRWZ-nj.

Table 7.5: Yields for CRWZ-0j and CRWZ-nj. The purity in the WZ background before the fit is 89% in the CRWZ-0j and 87% in the CRWZ-nj. The normalisation factor μ_{WZ} estimates the scale factor that should be applied to the WZ background to obtain a data/prediction ratio of 1. Statistical and systematic uncertainties are included.

Region	CRWZ-0j	CRWZ-nj
Observed	5237	3149
Post-fit	5237 ± 72	3149 ± 56
WZ	4699 ± 80	2703 ± 69
ZZ	337 ± 25	271 ± 35
Fakes	182 ± 19	130 ± 17
$t\bar{t}$	4.0 ± 1.4	8.2 ± 1.5
$t\bar{t}\,X$	4.6 ± 0.6	26.5 ± 3.2
Others	9.6 ± 1.9	9.2 ± 2.0
Pre-fit	4954 ± 90	3345 ± 69
WZ	4416 ± 75	2900 ± 49
ZZ	337 ± 26	271 ± 35
Fakes	182 ± 19	130 ± 17
$t\bar{t}$	4.0 ± 1.4	8.2 ± 1.5
$t\bar{t}\,X$	4.6 ± 0.6	26.5 ± 3.2
Others	9.6 ± 1.9	9.2 ± 2.1

Table 7.6: Breakdown of the systematic uncertainties on background prediction in the CRWZ. The sources of uncertainty considered in the fit have been grouped into categories taking into account their correlations. Because of these correlations, the total background uncertainty is not necessarily the sum in quadrature of the individual uncertainties. The fake systematic uncertainties are explained in Section 7.2.5.

Uncertainty of channel	CRWZ-0j	CRWZ-nj
Total background expectation	4954	3345
Total statistical ($\sqrt{N_{\text{exp}}}$)	± 70	± 58
Total background systematic	± 90 [1.8%]	± 69 [2.1%]
Theoretical	± 20	± 34
Fake	± 19	± 17
Experimental	± 15	± 9.2
MC stats	± 0.77	± 0.95
Normalisation	± 0.44	± 0.29

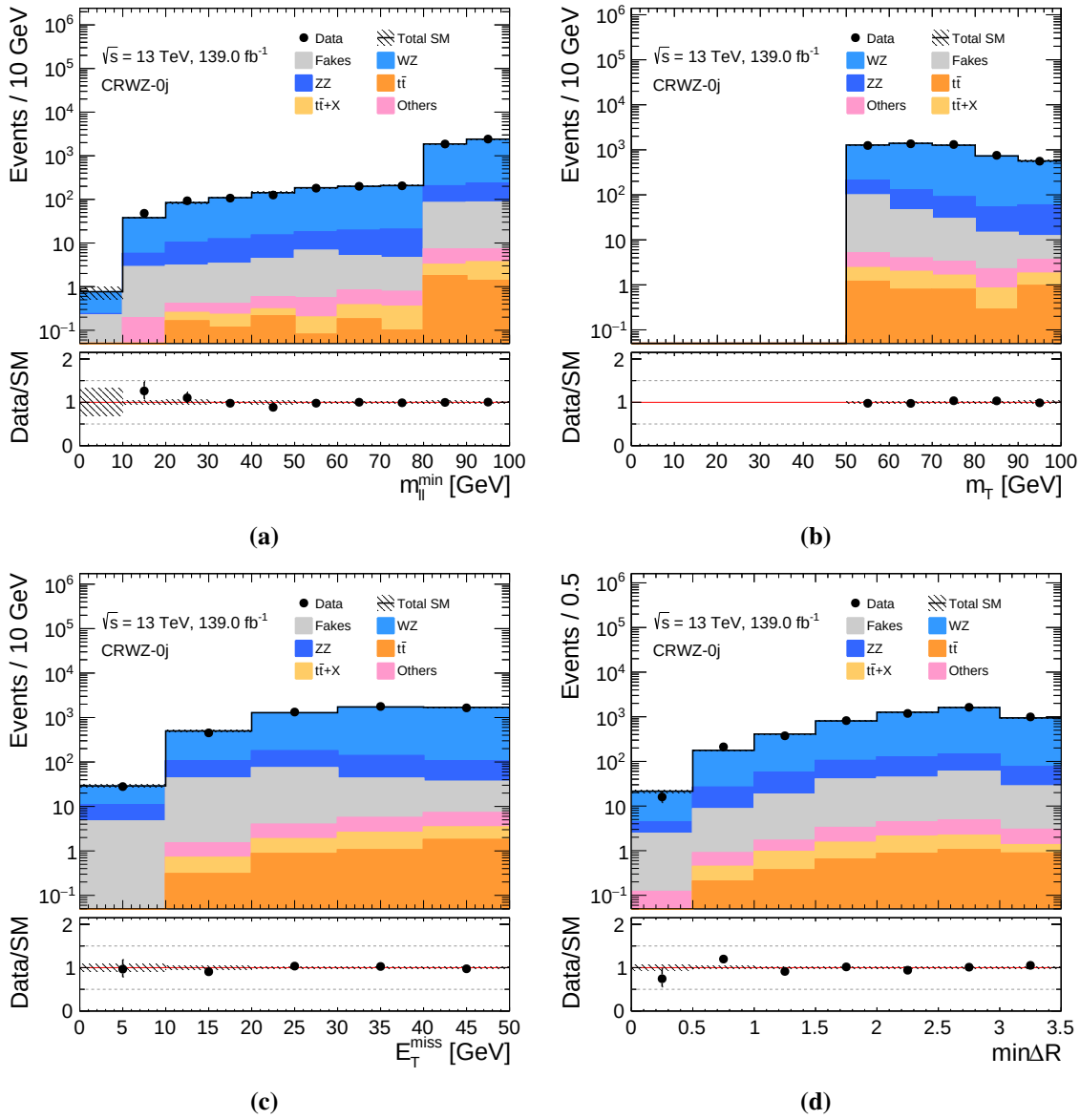

Fig. 7.2: Distributions for CRWZ-0j showing **(a)** $m_{\ell\ell}^{\text{min}}$, **(b)** m_{T}, **(c)** $E_{\text{T}}^{\text{miss}}$ and **(d)** $\min\Delta R$. The μ_{WZ0j} scale factor is applied to the *WZ* background. Statistical and systematic uncertainties are included. The last bin includes overflow.

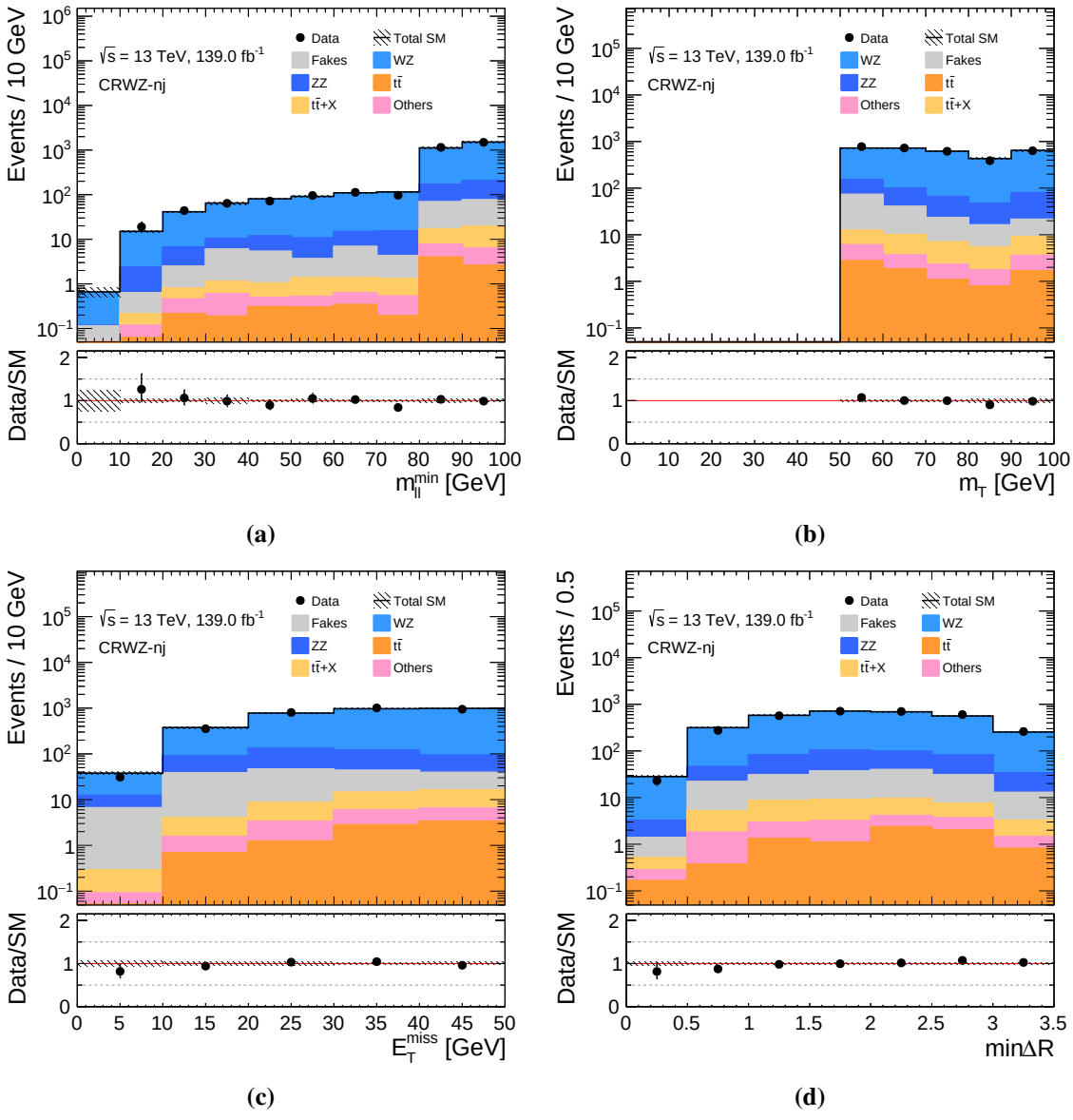

Fig. 7.3: Distributions for CRWZ-nj showing **(a)** $m_{\ell\ell}^{\text{min}}$, **(b)** m_{T}, **(c)** $E_{\text{T}}^{\text{miss}}$ and **(d)** $\min \Delta R$. The μ_{WZnj} scale factor is applied to the *WZ* background. Statistical and systematic uncertainties are included. The last bin includes overflow.

7.2 Data-driven background samples

The Z+jets/Z+γ background is estimated enacting a data-driven technique. The background has a 2-lepton final state and one misidentified (fake) lepton, and a data-driven technique is used because fake leptons are usually poorly described by MC simulation. A solid estimate for this background is needed in the region with low $E_{\mathrm{T}}^{\mathrm{miss}}$ and low p_{T}, as it is expected to be the dominant background.

A fake lepton can originate from different sources, such as when a light flavour jet is improperly identified as a lepton, when a heavy flavour hadron decays semi-leptonically, or when a photon converts into a pair of leptons. While heavy flavour decays and photon-conversions actually result in a non-prompt but real lepton, collectively all of these will be referred to as fake leptons for simplicity.

Fake leptons in the 3-lepton final state arise from two types of processes: Z+jets/Z+γ and top-like backgrounds. Z+jets/Z+γ refers to the process where a Z decays to two real leptons while a jet or photon fakes an electron or muon. Top-like backgrounds are the collection of $t\bar{t}$, singleTop (Wt), and diboson2ℓ (WW) backgrounds, and are treated simultaneously because they have similar kinematics. The primary distinction between the different top-like backgrounds is the number of b-jets in the final state. As $t\bar{t}$ has the largest cross-section it is typically the dominant process contributing to the top-like background.

There are three main reasons why Z+jets/Z+γ is estimated using a data-driven technique and the top-like fake backgrounds are estimated using MC. The first reason is that in the t decay there is a well modelled heavy-flavour decay, which originates from a real b-meson and will thus produce real leptons in the detector. In Z+jets/Z+γ there are also light-flavour decays containing pions and there are electrons that arise from photon-conversion, which are both harder to model in the detector simulation. The second reason that Z+jets/Z+γ is harder to model by a generator because it contains higher order corrections, whilst the top-like backgrounds are at leading order. The third reason is that the available Z+jets/Z+γ MC sample is low in statistics in the off-shell Z selection and thus gives a large statistical uncertainty. For these reasons a data-driven approach called the Fake Factor method is used to estimate the contribution of Z+jets/Z+γ.

7.2.1 Fake Factor method

The Fake Factor method relies on two sets of lepton identification criteria. The first is the standard lepton identification used in the analysis, referred to as ID lepton criteria. The second is an orthogonal criteria, referred to as anti-ID lepton criteria, which is designed to be enriched in fake leptons by relaxing or inverting various lepton identification criteria. The

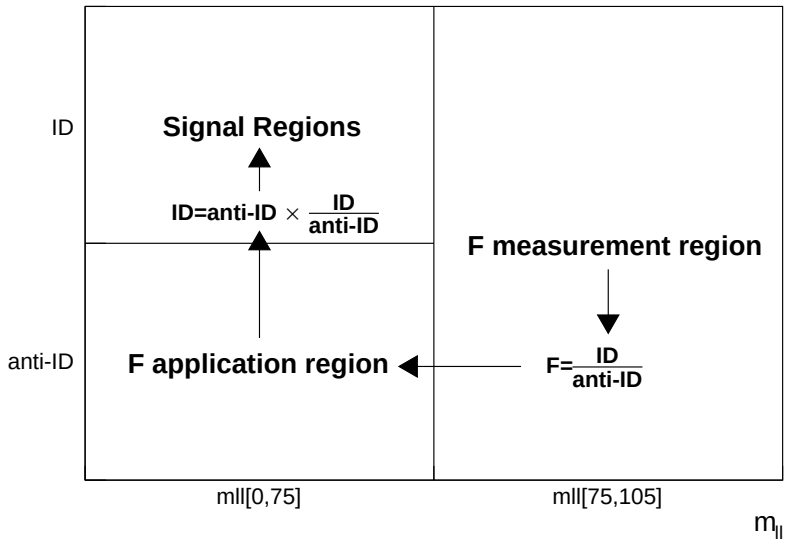

Fig. 7.4: Schematic representation of the fake factor method. F is measured in a region enriched in fakes, called the measurement region, and is then applied to the application region in order to estimate the amount of fake ID leptons in the signal regions.

fake factor, F, is defined as the ratio of ID to anti-ID leptons, as measured in a kinematic region in the data primarily consisting of fake leptons. To ensure that only the background that needs to be modelled, Z+jets/$Z+\gamma$, is considered in the measurement of F, MC is used to remove contamination from other backgrounds. The fake factor then takes the form,

$$F(i) = \frac{N_{\text{ID, data}}(i) - N_{\text{ID, other MC}}(i)}{N_{\text{anti-ID, data}}(i) - N_{\text{anti-ID, other MC}}(i)}, \tag{7.6}$$

where N is the number of events and other MC refers to backgrounds not estimated from F. F is binned on kinematic quantities such as the lepton p_{T}, so i refers to the i^{th} bin, for example p_{T} bin.

Once F has been measured in the fake dominated region, it can then be used to obtain the background estimate in the SRs. To do so, an application region identical to the SRs, except for the anti-ID requirement, is used. The number of fake ID leptons in the SR is estimated from anti-ID leptons applying F, such that

$$\text{ID}_{\text{lepton}}(i) = \text{anti-ID}_{\text{lepton}}(i) \cdot F(i). \tag{7.7}$$

The fake estimate for three lepton events containing at least one fake lepton is given by

$$\begin{aligned} N_{\uparrow\uparrow\uparrow}(i) - N^{\mathrm{RRR}}_{\uparrow\uparrow\uparrow}(i) = \\ F(i)(N_{\downarrow\uparrow\uparrow}(i) - N^{\mathrm{RRR}}_{\downarrow\uparrow\uparrow}(i)) + F(i)(N_{\uparrow\downarrow\uparrow}(i) - N^{\mathrm{RRR}}_{\uparrow\downarrow\uparrow}(i)) + F(i)(N_{\uparrow\uparrow\downarrow}(i) - N^{\mathrm{RRR}}_{\uparrow\uparrow\downarrow}(i)) \\ -F(i)F(i)(N_{\downarrow\downarrow\uparrow}(i) - N^{\mathrm{RRR}}_{\downarrow\downarrow\uparrow}(i)) - F(i)F(i)(N_{\downarrow\uparrow\downarrow}(i) - N^{\mathrm{RRR}}_{\downarrow\uparrow\downarrow}(i)) - F(i)F(i)(N_{\uparrow\downarrow\downarrow}(i) - N^{\mathrm{RRR}}_{\uparrow\downarrow\downarrow}(i)) \\ +F(i)F(i)F(i)(N_{\downarrow\downarrow\downarrow}(i) - N^{\mathrm{RRR}}_{\downarrow\downarrow\downarrow}(i)), \end{aligned} \tag{7.8}$$

where "RRR" indicates events with three real leptons as determined using MC, $\uparrow$ corresponds to ID leptons, and $\downarrow$ corresponds to anti-ID leptons.

In order for the Fake Factor method to estimate the Z+jets/Z+γ background as illustrated in Figure 7.4 it is needed to:

1. Define ID and anti-ID criteria and a measurement region.
2. Check the fake composition for the ID and anti-ID criteria between the measurement and application region, such that F is valid to be used in the application region.
3. Perform a measurement of F.
4. Perform the application of F using the application region.

7.2.2 Measurement region

The Fake Factor method relies on inverted lepton identification and isolation criteria to estimate the fake lepton background in data. In the analysis two different fake factors are measured for leptons, since the first two leptons leading in p_{T} have different ID criteria from the third leading lepton. The ID criteria of the third leading lepton include the Prompt Lepton Veto (PLV), which is defined is Section 5.4. The PLV is applied to reduce the amount of fakes, the use of which will be explained further in Section 8.3. As a consequence F is used for the first two leading leptons and F_{PLV} for the third leading lepton. The definitions of the ID and anti-ID criteria for electrons and muons are described in Table 7.7 for F and in Table 7.8 for F_{PLV}.

The fake factors in the analysis are derived in a region dominated by Z+jets/Z+γ. The region requires events to have three baseline leptons with at least one opposite-sign same-flavour (OSSF) pair of leptons. The OSSF pair should have $|m_{\ell\ell} - m_Z| < 15$ GeV, where in cases of ambiguity the $m_{\ell\ell}$ pairing is chosen to be the one that minimises $|m_{\ell\ell} - m_Z|$. The remaining unpaired lepton is the fake candidate since the other two leptons belong to the Z. The leptons paired with the Z are required to pass the ID criteria, while the remaining fake

Table 7.7: ID and anti-ID electron and muon definitions used for the measurement of F. The baseline and signal selection definitions for electrons from Table 6.3 and for muons from Table 6.4 are used to define anti-ID criteria, where anti-ID leptons are defined as leptons that pass the baseline selection but fail the signal (ID) selection. Overlap removal is not applied to muons to improve the amount of anti-ID muons at $p_{\mathrm{T}} > 30$ GeV.

	Electrons	**Muons**
ID	`Medium` identification `Gradient` isolation $\lvert d_0/\sigma_{d_0}\rvert < 5$ $\lvert \Delta z_0 \sin\theta\rvert < 0.5$ Pass overlap removal	`Medium` identification `FCLoose` isolation $\lvert d_0/\sigma_{d_0}\rvert < 3$ $\lvert \Delta z_0 \sin\theta\rvert < 0.5$ -
Anti-ID	`Loose` identification + hit in the innermost pixel layer $\lvert \Delta z_0 \sin\theta\rvert < 0.5$ Pass overlap removal !ID	`Medium` identification $\lvert \Delta z_0 \sin\theta\rvert < 0.5$ - !ID

Table 7.8: ID and anti-ID electron and muon definitions used for the measurement of F_{PLV} where `PLVTight` is applied to the lepton 3$^{\mathrm{rd}}$ leading in p_{T}. The baseline and signal selection definitions for electrons from Table 6.3 and for muons from Table 6.4 are used to define anti-ID criteria, where anti-ID leptons are defined as leptons that pass the baseline selection but fail the signal (ID) selection. Overlap removal is not applied to muons to improve the amount of anti-ID muons at $p_{\mathrm{T}} > 30$ GeV.

	Electrons	**Muons**
ID	`Medium` identification `Gradient` isolation $\lvert d_0/\sigma_{d_0}\rvert < 5$ $\lvert \Delta z_0 \sin\theta\rvert < 0.5$ Pass overlap removal `PLVTight`	`Medium` identification `FCLoose` isolation $\lvert d_0/\sigma_{d_0}\rvert < 3$ $\lvert \Delta z_0 \sin\theta\rvert < 0.5$ - `PLVTight`
Anti-ID	`Loose` identification + hit in the innermost pixel layer $\lvert \Delta z_0 \sin\theta\rvert < 0.5$ Pass overlap removal !ID	`Medium` identification $\lvert \Delta z_0 \sin\theta\rvert < 0.5$ - !ID

Table 7.9: Fake factor measurement region definition.

variable	cut
	Dilepton triggers from Table 8.4 matched to leptons from Z
	No overlap removal applied for the "unpaired" muons
N_{jets}	≤ 1 for events with a $p_{\text{T}} > 30$ GeV muon, and $N_{\text{jets}}^{30\text{ GeV}} == 0$ for all other events
$N_{\text{b-jets}}^{20\text{ GeV}}$	$== 0$
$E_{\text{T}}^{\text{miss}}$	<40 GeV
$m_{\ell\ell}$	$\in [m_Z - 15, m_Z + 15]$ GeV
m_{T}	<30 GeV
$m_{3\ell}$	>105 GeV

Table 7.10: Expected yields in the fake factor measurement region using MC. Z+jets/Z+γ MC simulations are generated using Sherpa 2.2.1. Only statistical uncertainties are included.

sample	Fake factor measurement region
Z+jets/Z+γ MC	36040 ± 540
WZ	1338 ± 12
ZZ	1122 ± 14
$t\bar{t}$	10.72 ± 0.71
$t\bar{t}$ +X	4.32 ± 0.16
Others	33.9 ± 1.5

candidate lepton must satisfy either the ID or the anti-ID criteria. In order not to obtain a trigger bias on the measurement of F, paired leptons from the Z are required to match the di-lepton trigger, such that the event is not triggered by the fake candidate.

The selection criteria for the fake factor measurement region are summarised in Table 7.9. The expected yields of all the backgrounds in the measurement region are displayed in Table 7.10. To suppress WZ, cuts on $E_{\text{T}}^{\text{miss}} < 40$ GeV and $m_T < 30$ GeV are imposed. A b-jet veto is imposed to suppress $t\bar{t}$. In order to primarily look at Z+jets events with exactly one fake, a jet-veto is applied, since the removed jet fakes the lepton, eliminating the need for additional jets in the event. A jet-veto is also applied for kinematic reasons, such that the event is a Z balanced against a fake from a jet or photon. $Z + \gamma$ events where the photon radiates off of a lepton have $m_{3\ell}$ consistent with m_Z. To reduce this contribution a requirement of $m_{3\ell} > 105$ GeV is imposed; this cut is further explained in Section 7.2.3.

Muons have a high reconstruction efficiency at high p_{T}, so in that p_{T} range there are few anti-ID muons. Having low statistics samples of anti-ID muons at high p_{T} will cause a large statistical uncertainty on F. In order to allow for more statistics of fake muons, no overlap

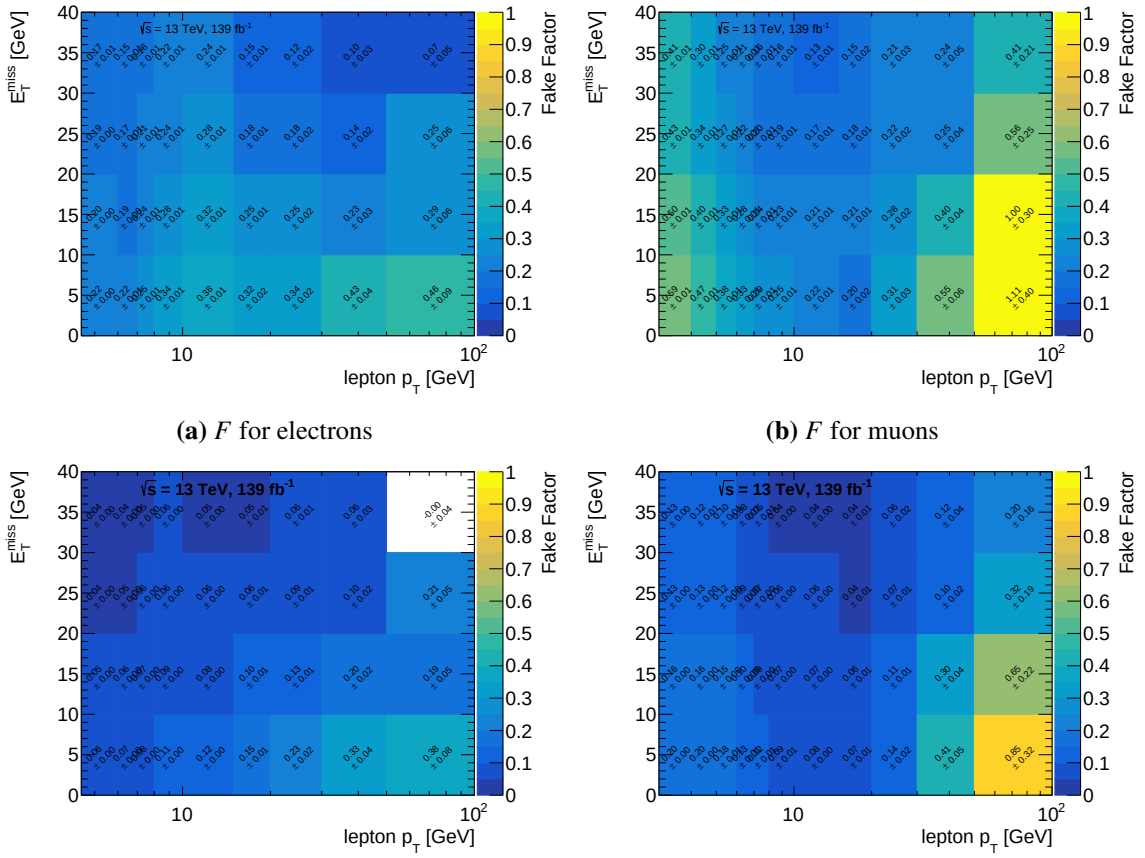

(a) F for electrons

(b) F for muons

(c) F_{PLV} for electrons

(d) F_{PLV} for muons

Fig. 7.5: (a-b) Fake factor F to be assigned to the first and second leading leptons in the fake-lepton background estimation. **(c-d)** Fake factor F_{PLV}, to be assigned to the third leading leptons in the fake-lepton background estimation.

removal (OR) is applied for the unpaired muons considered in the measurement region. This is done for both ID and anti-ID events. With no OR applied, a jet-veto requirement would also veto most muons. To allow for a jet-veto in spite of the relaxed muon OR, events are required to either have no reconstructed jets with $p_{\mathrm{T}} > 30$ GeV or no more than one $p_{\mathrm{T}} > 30$ GeV jet for events with a $p_{\mathrm{T}} > 30$ GeV muon.

Fake factors obtained from the measurement region are presented as a function of p_{T} and $E_{\mathrm{T}}^{\mathrm{miss}}$ in Figure 7.5. Since the goal is to obtain a fake factor to estimate Z+jets/Z+γ, the contribution from all the other backgrounds to the fake factor is removed using MC as defined in Equation 7.6. The percentage of the backgrounds other than Z+jets/Z+γ in the measurement region is highlighted in Table 7.11.

Table 7.11: Percentage of the backgrounds other than Z+jets/Z+γ in the measurement region. These backgrounds are subtracted using MC during the measurement of the fake factor in order to only estimate F for the Z+jets/Z+γ background.

Subtracted backgrounds	percentage in measurement region
WZ	3%
ZZ	3%
$t\bar{t}$	0%
$t\bar{t}+X$	0%
Others	0%

7.2.3 Fake composition

F depends on the composition of fake leptons sources (light flavour jets, heavy flavour jets and photon-conversions) and thus the composition of fake leptons in the measurement region should be as close as possible to the composition of fake leptons in the signal region. It is expected that the composition of fake leptons sources changes with certain kinematic variables such as p_{T}, $E_{\mathrm{T}}^{\mathrm{miss}}$ and η. Correct modelling of the fake background can be accounted for by binning F in these variables.

For electrons, Figure 7.6(a) demonstrates that photon-conversion fakes also depend on $m_{\ell\ell}^{\mathrm{min}}$ in SRlow. Since F is measured in $m_{\ell\ell} \in [75,105]$ GeV and applied in $m_{\ell\ell} < 75$ GeV, it is not possible to bin F in $m_{\ell\ell}^{\mathrm{min}} \in [0,75]$ GeV to capture this dependence. When the composition has such a difference, large systematic uncertainties have to be assigned which account for the mismatch. Another option is to reduce the photon-conversion fakes in the SRs. Photon-conversion fakes are reduced using cuts on $m_{3\ell}$ and $\min\Delta R$ and are derived on the basis of studies in the SRs presented in Figure 7.6. Events with eee or $\mu\mu$e (where the fake candidate is an electron and thus where there can be photon-conversion), are required to satisfy $m_{3\ell} \notin [m_Z - 20, m_Z + 20]$ GeV, and $\min\Delta R \in [0.6, 2.4]$. The former requirement suppresses Z+γ where the photon radiates off of a lepton, the latter reduces conversion from jets (< 2.4) and from electrons (> 0.6).

After having reduced the photon-conversion dependence on $m_{\ell\ell}^{\mathrm{min}}$ it is needed to decide in which variables to bin F. The fake lepton composition dependence on p_{T} and $E_{\mathrm{T}}^{\mathrm{miss}}$, in the measurement region and low $E_{\mathrm{T}}^{\mathrm{miss}}$ signal regions, for both ID and anti-ID leptons, is displayed in Figures 7.7 and 7.8. It is observed that for a two dimensional binning in p_{T} and $E_{\mathrm{T}}^{\mathrm{miss}}$ the fake composition is similar between the measurement region and SRlow. The binning used for the fake factor is defined in Table 7.12.

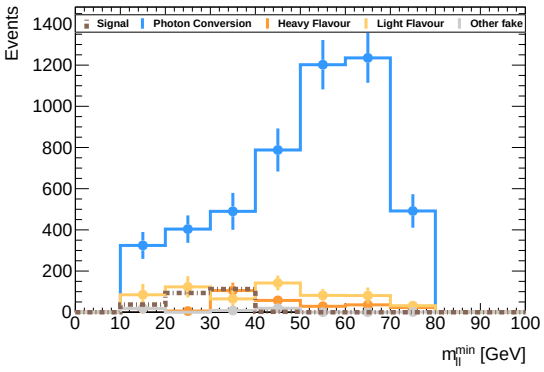

(a) SRlow.

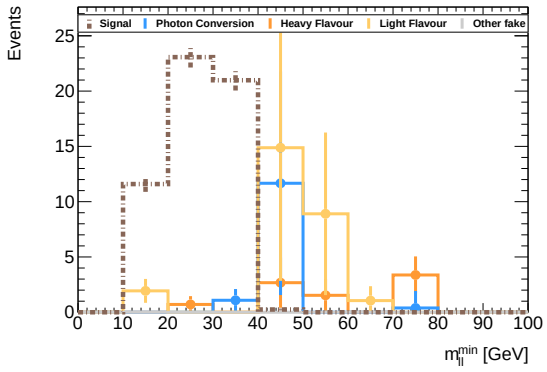

(b) SRhigh.

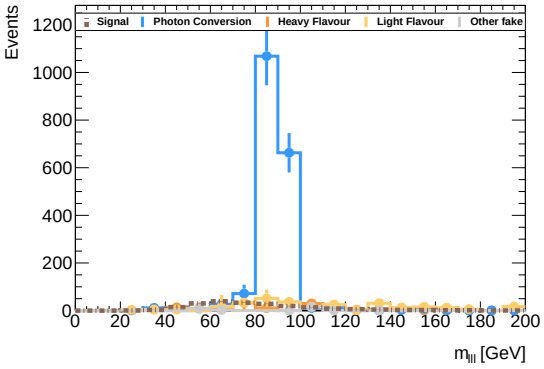

(c) SRlow with $\min\Delta R \in [0.6, 2.4]$.

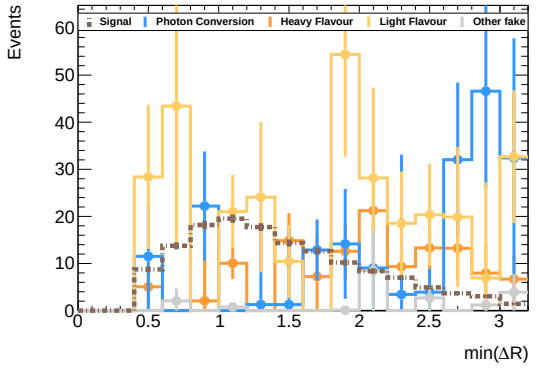

(d) SRlow with $m_{3\ell} \notin [m_Z - 20, m_Z + 20]$ GeV.

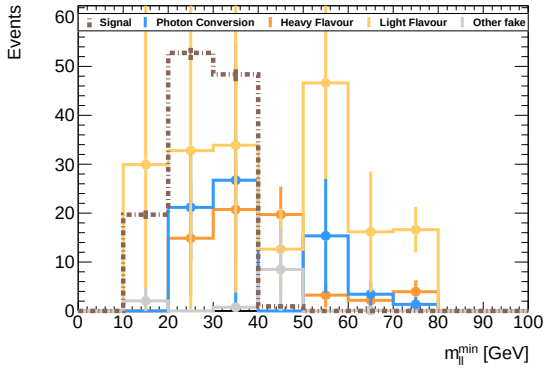

(e) SRlow with $m_{3\ell} \notin [m_Z - 20, m_Z + 20]$ GeV and $\min\Delta R \in [0.6, 2.4]$.

Fig. 7.6: Distributions showing the fake composition for electrons in the SRs. **(a)** Distribution of $m_{\ell\ell}^{\min}$ in SRlow. The $m_{\ell\ell}^{\min}$ distibution shows a dependence on photon-conversion fakes. **(b)** Distribution of $m_{\ell\ell}^{\min}$ in SRhigh. The distribution demonstrates that photon-conversion fakes are negligible at higher $E_{\mathrm{T}}^{\mathrm{miss}}$ as can also be concluded from Figure 7.8(d). **(c)** Distribution of $m_{3\ell}$ in the SRlow region. **(d)** Distribution of $\min\Delta R$ in the SRlow region. **(e)** Distribution of $m_{\ell\ell}^{\min}$ in SRlow after the $m_{3\ell}$ and $\min\Delta R$ cuts. The dependence on $m_{\ell\ell}^{\min}$ of the photon-conversion fakes in SRlow has been reduced. The distributions are obtained from Z+jets/Z+γ MC simulations generated using Sherpa 2.2.1. A distribution for $\tilde{\chi}_1^{\pm}\tilde{\chi}_2^0 \to WZ\tilde{\chi}_1^0\tilde{\chi}_1^0$ signal is overlaid, with mass values $\mathrm{m}(\tilde{\chi}_1^{\pm}) = 200$ GeV and $\mathrm{m}(\tilde{\chi}_1^0) = 160$ GeV. The signal is generated as described in Section 8.1.

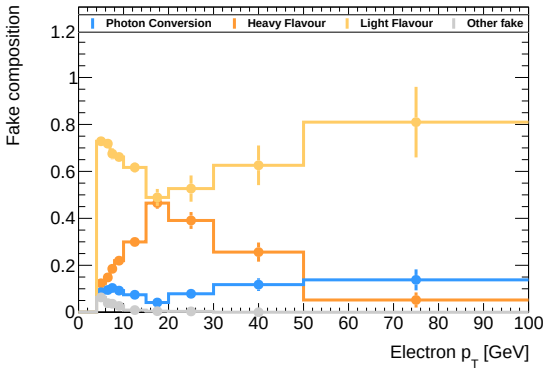

(a) Anti-ID electron F measurement region.

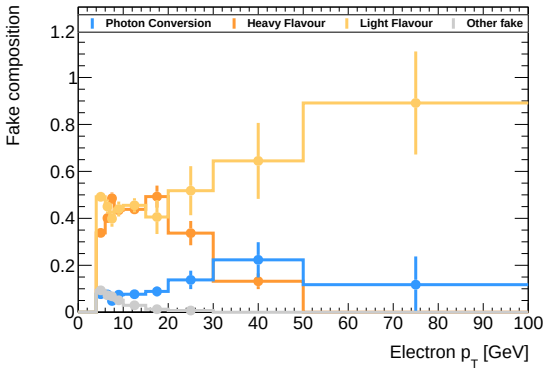

(b) ID electron F measurement region.

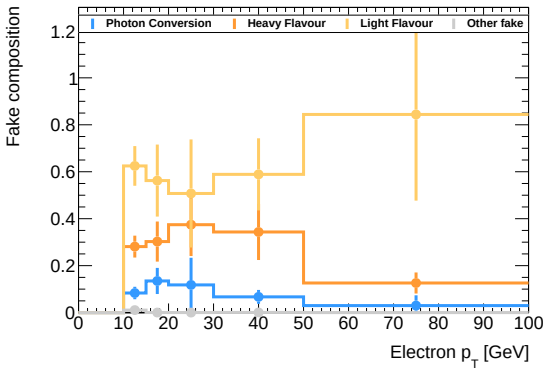

(c) Anti-ID electron SRlow.

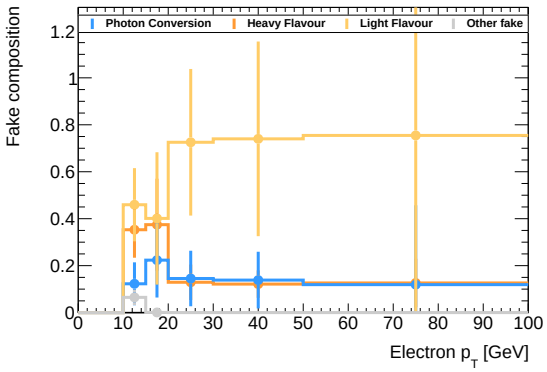

(d) ID electron SRlow.

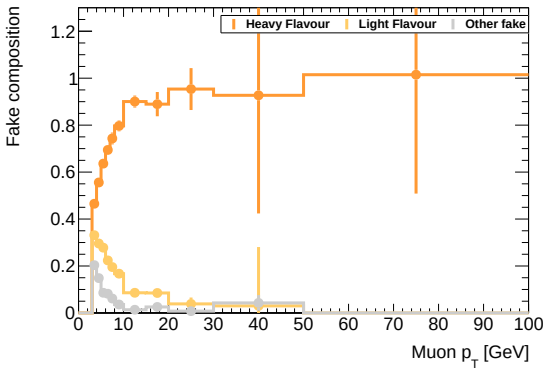

(e) Anti-ID muon F measurement region.

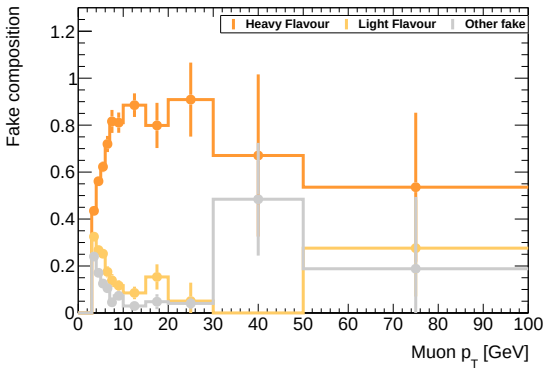

(f) ID muon F measurement region.

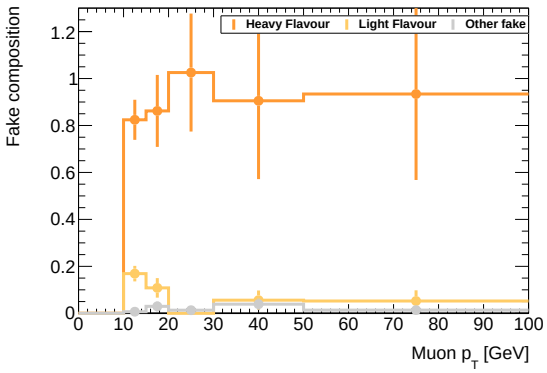

(g) Anti-ID muon SRlow.

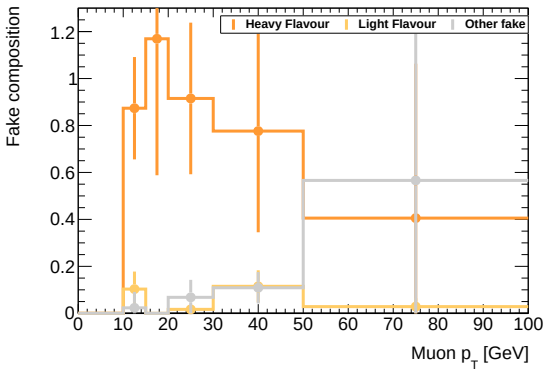

(h) ID muon SRlow.

Fig. 7.7: Fake composition versus p_{T} for electrons and muons. The distributions are obtained from Z+jets/Z+γ MC simulations generated using Sherpa 2.2.1.

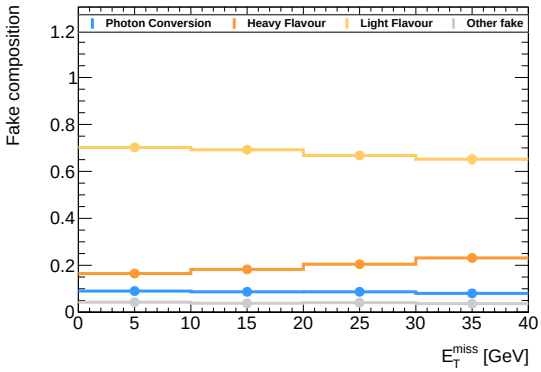

(a) anti-ID electron F measurement region.

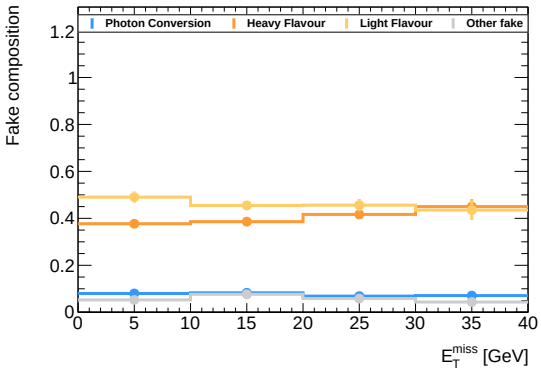

(b) ID electron F measurement region.

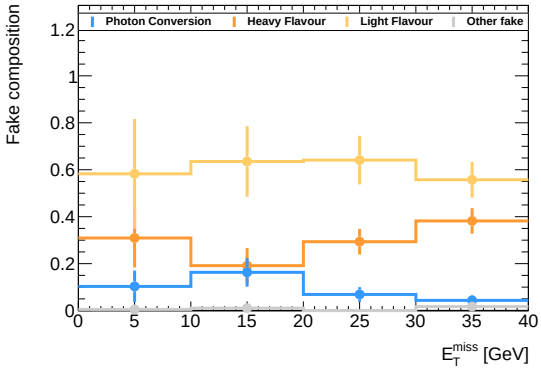

(c) anti-ID electron SRlow.

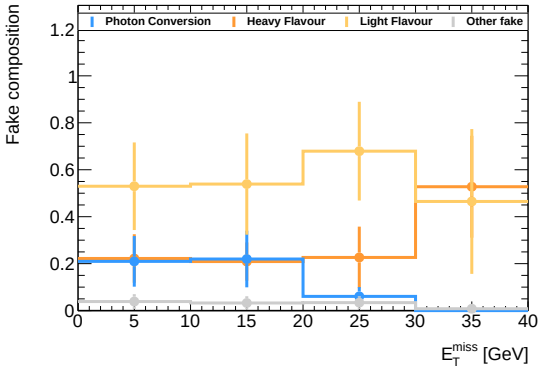

(d) ID electron SRlow.

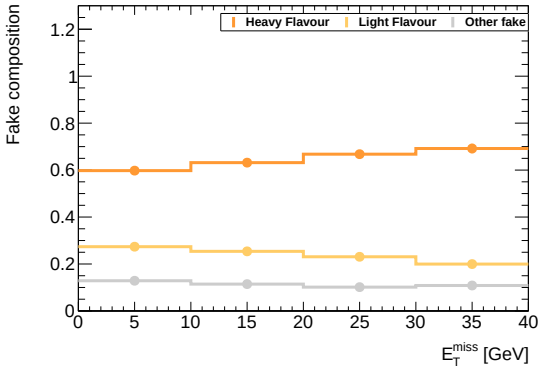

(e) anti-ID muon F measurement region.

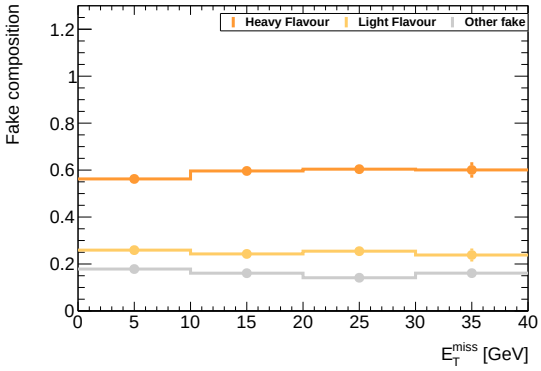

(f) ID muon F measurement region.

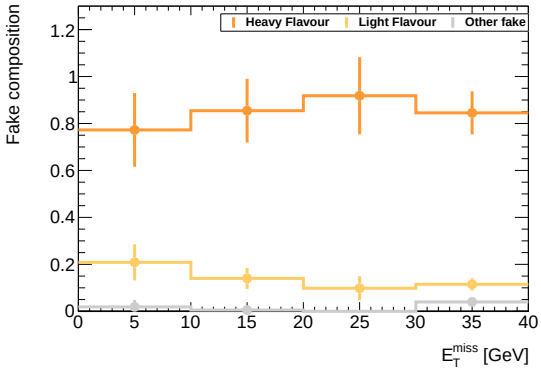

(g) anti-ID muon SRlow.

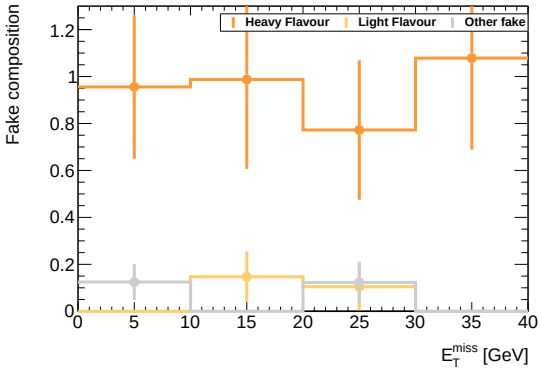

(h) ID muon SRlow.

Fig. 7.8: Fake composition versus $E_{\mathrm{T}}^{\mathrm{miss}}$ for electrons and muons. The distributions are obtained from Z+jets/Z+γ MC simulations generated using Sherpa 2.2.1.

Table 7.12: The fake factor F is binned in p_{T} and $E_{\mathrm{T}}^{\mathrm{miss}}$.

	Lepton	binning
p_{T} [GeV]	Electron	[0, 4.5, 6, 7, 8, 10, 15, 20, 30, 50, 100]
	Muon	[0, 3, 4, 5, 6, 7, 8, 10, 15, 20, 30, 50, 100]
$E_{\mathrm{T}}^{\mathrm{miss}}$ [GeV]	-	[0, 10, 20, 30, >40]

7.2.4 Application of F

Once the fake factor has been measured in the measurement region, it can be used to obtain the background estimate in the signal regions (or control/validation regions). To do so, an application region is used which is identical to the signal region except that one or more of the ID leptons is replaced with an anti-ID lepton. The anti-ID leptons from the application region then get transferred to ID leptons by applying Equation 7.8, using F for the two leptons leading in p_{T}, and F_{PLV} for the third leading lepton. In Equation 7.8, i now denotes the binning in lepton p_{T} and $E_{\mathrm{T}}^{\mathrm{miss}}$, such that F($p_{\mathrm{T}}$, $E_{\mathrm{T}}^{\mathrm{miss}}$).

The goal is to obtain a Z+jets/Z+γ background estimate, as a consequence all backgrounds other than Z+jets/Z+γ have to be subtracted. The backgrounds with three real leptons, indicated with "RRR" in Equation 7.8, get subtracted using MC. And also the top-like fake backgrounds get subtracted using MC. Since a large part of $t\bar{t}$ background is subtracted in the application to the signal region, it is necessary to have a correct estimate of the number of anti-ID $t\bar{t}$. To make sure that $t\bar{t}$ anti-ID normalisation is correct, a fit is performed on an anti-ID region pure in $t\bar{t}$ to calculate a normalisation factor for $t\bar{t}$ anti-ID.

$t\bar{t}$ anti-ID normalisation

The anti-ID events of the $t\bar{t}$ background are normalised to allow for improvement of the top-like background subtraction in the Z+jets/Z+γ estimate. For the top-like fake background ($t\bar{t}$, Wt, and WW), an anti-ID control region, called anti-ID CR$t\bar{t}$, is constructed using different-flavour, opposite-sign three lepton events. In other words, events must be of the form $e^{\pm}e^{\pm}\mu^{\mp}$ or $\mu^{\pm}\mu^{\pm}e^{\mp}$, where the two same-flavour leptons must have the same-sign and the different flavour lepton must have the opposite-sign. This is advantageous because it guarantees that one of the two same-flavour leptons is the fake lepton. Using the control region allowing for the presence of an anti-ID lepton results in high purity in top-like fakes. In addition to the different-flavour, opposite-sign requirement, an $E_{\mathrm{T}}^{\mathrm{miss}} > 50$ GeV cut is applied for $t\bar{t}$ purity. The selection criteria defining this top-like control region are summarised in Table 7.13. Normalisation factors are derived separately for electron and muon fake events,

Table 7.13: Anti-ID $t\bar{t}$ control region (anti-ID CR$t\bar{t}$) definition.

anti-ID CR$t\bar{t}$			
Trigger scheme as described in Section 8.2 Events with two ID leptons and one anti-ID lepton Only $e^{\pm}e^{\pm}\mu^{\mp}$ and $\mu^{\pm}\mu^{\pm}e^{\mp}$ events When measuring the normalisation factors for events with an anti-ID lepton, the anti-ID lepton must be one of the same-flavour, same-sign leptons $E_{\mathrm{T}}^{\mathrm{miss}} > 50$ GeV $p_{\mathrm{T}}^{\ell_3} > 10$ GeV			
Four normalisation factors are obtained from the CR			
$N_{\text{b-jets}}^{20\text{ GeV}} = 0$		$N_{\text{b-jets}}^{20\text{ GeV}} > 0$	
anti-ID = electron	anti-ID = muon	anti-ID = electron	anti-ID = muon

Table 7.14: Obtained normalisation factors from anti-ID CR$t\bar{t}$.

	electron	muon
$N_{\text{b-jets}}^{20\text{ GeV}} = 0$	0.953 ± 0.034	0.882 ± 0.045
$N_{\text{b-jets}}^{20\text{ GeV}} > 0$	0.924 ± 0.024	0.960 ± 0.028

as well as for events with $N_{\text{b-jets}} = 0$ and $N_{\text{b-jets}} > 0$ (to avoid extrapolating over $N_{\text{b-jets}}$). The distributions for this region are shown in Figure 7.9.

7.2.5 Treatment of uncertainties

After having established the Z+jets/$Z+\gamma$ estimation, an uncertainty has to be assigned to the estimation. The Z+jets/$Z+\gamma$ estimation is subject to a number of systematic uncertainties. The systematics uncertainties reflect statistical uncertainty in the measurement of F and choices in our strategy for the measurement of F. These systematic uncertainties are summarised as follows:

- Statistical uncertainty on measurement of F.
- Different choice of parametrisation of F.
- Different $E_{\mathrm{T}}^{\mathrm{miss}}$ binning of F.

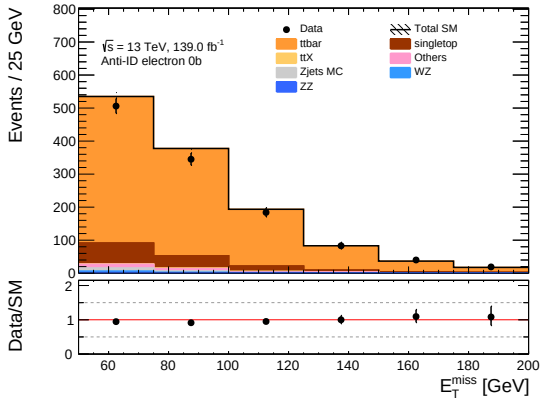

(a) Before fit electron $N_{\text{b-jets}}^{20\text{ GeV}} = 0$

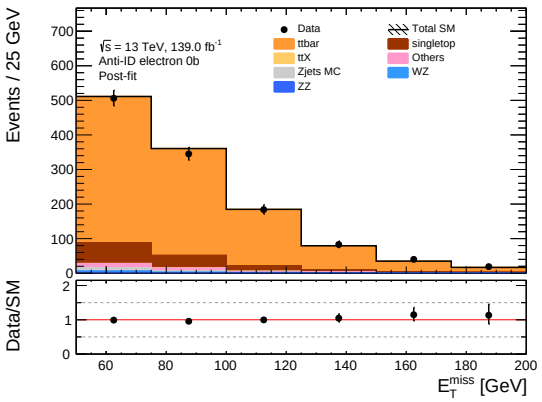

(b) After fit electron $N_{\text{b-jets}}^{20\text{ GeV}} = 0$

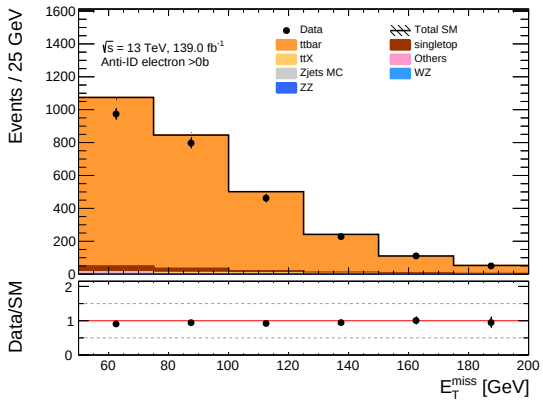

(c) Before fit electron $N_{\text{b-jets}}^{20\text{ GeV}} > 0$

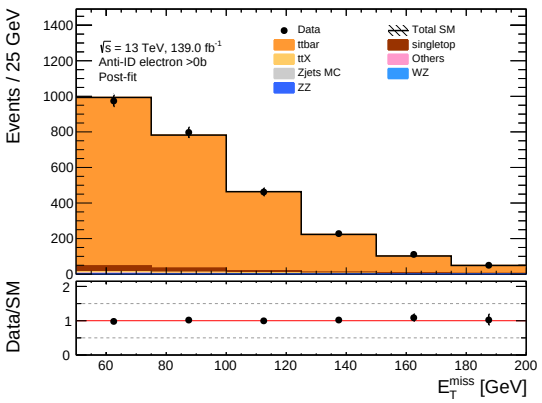

(d) After fit electron $N_{\text{b-jets}}^{20\text{ GeV}} > 0$

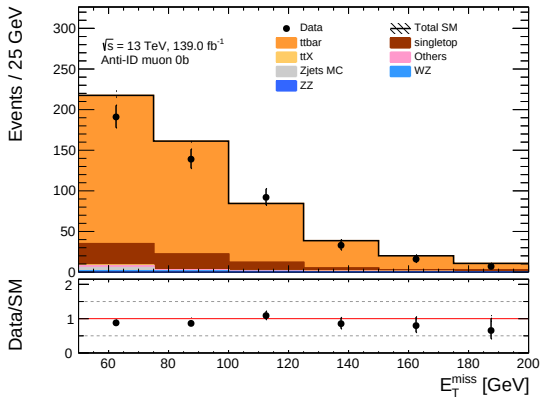

(e) Before fit muon $N_{\text{b-jets}}^{20\text{ GeV}} = 0$

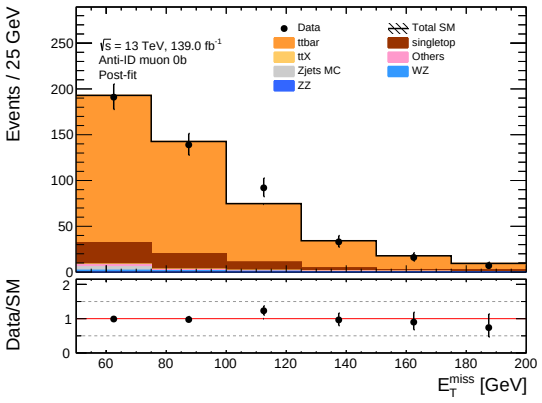

(f) After fit muon $N_{\text{b-jets}}^{20\text{ GeV}} = 0$

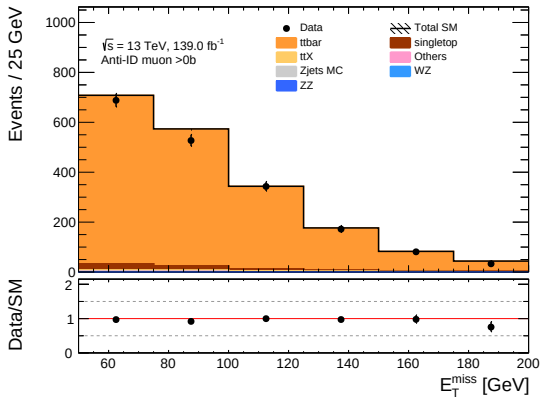

(g) Before fit muon $N_{\text{b-jets}}^{20\text{ GeV}} > 0$

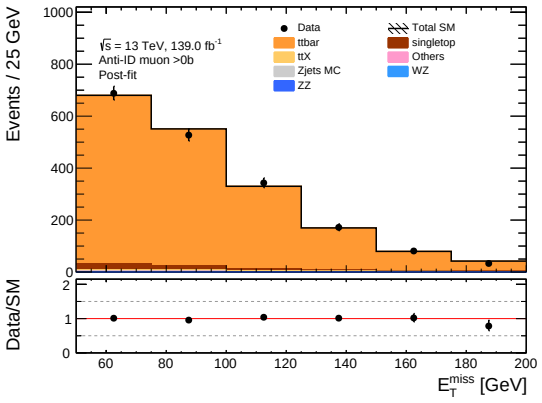

(h) After fit muon $N_{\text{b-jets}}^{20\text{ GeV}} > 0$

Fig. 7.9: Distributions of the $E_{\text{T}}^{\text{miss}}$ in anti-ID CR$t\bar{t}$. Only statistical uncertainties are included.

- *WZ* cross-section for MC subtraction in measurement of F.
- Muon overlap removal in measurement of F.

Statistical uncertainties

There is a limited amount of ID and anti-ID events present in the measurement region, which means there is a statistical uncertainty on the measurement of F. The statistical uncertainty can be kept to a minimum by increasing the amount of ID or anti-ID events, by for example turning off the OR for muons to increase the amount of anti-ID muons.

The statistical uncertainties on F are accounted for by error propagation obtaining the variations $F(p_{\mathrm{T}}, E_{\mathrm{T}}^{\mathrm{miss}}) \pm 1\sigma$ taken from Figure 7.5. All the p_{T} and $E_{\mathrm{T}}^{\mathrm{miss}}$ bins are independent measurements each with their own $F(p_{\mathrm{T}}, E_{\mathrm{T}}^{\mathrm{miss}})$ and their own σ accordingly, and as a result all the statistical uncertainties have to be treated separately. For each event the variation for 1σ up or down is stored together with which p_{T} and $E_{\mathrm{T}}^{\mathrm{miss}}$ bin the variation belongs to. Storing the variation for each p_{T} and $E_{\mathrm{T}}^{\mathrm{miss}}$ bin separately allows the fit to pull on each independent measurement of $F(p_{\mathrm{T}}, E_{\mathrm{T}}^{\mathrm{miss}})$.

In case of an event with two or more anti-ID leptons where the two leptons fall into the same p_{T} and $E_{\mathrm{T}}^{\mathrm{miss}}$ bin, their F is fully correlated. The uncertainty propagated in that case is $(F(p_{\mathrm{T}}, E_{\mathrm{T}}^{\mathrm{miss}}) \pm 1\sigma)^2$. At most two anti-ID leptons can be correlated since the third lepton uses F_{PLV}.

Different parametrisation

The fake factor, F, can depend on different variables, meaning that for the measurement of F a choice has to be made as to which variables to parametrise. Certain variables are sensitive to the composition of the different fake sources and binning in these variables allows for correct modelling of Z+jets/Z+γ. Section 7.2.3 elaborates on the choice to parametrise F on the lepton p_{T} and $E_{\mathrm{T}}^{\mathrm{miss}}$. While the p_{T} and $E_{\mathrm{T}}^{\mathrm{miss}}$ parametrisation is chosen for the better modelling, it does not capture the variations of F in η.

Since F can also depend on η, an alternative choice would be parametrising also on the lepton η. The choice of η binning is presented in Table 7.15. The fake factors, F and F_{PLV}, parametrised in p_{T}, $E_{\mathrm{T}}^{\mathrm{miss}}$ and $|\eta|$ are shown in Figure A.1 and Figure A.2, respectively, of appendix A. The three dimensional p_{T}, $E_{\mathrm{T}}^{\mathrm{miss}}$ and $|\eta|$ parametrisation is used to introduce a systematic variation, as an alternative to the two dimensional p_{T} and $E_{\mathrm{T}}^{\mathrm{miss}}$ parametrisation. The fake factors that account for the different parametrisation are propagated as an uncertainty on the Z+jets/Z+γ estimation.

Table 7.15: Variation of the fake factor F binning in η.

Lepton	η
Electron	[0, 1.37, 1.52, 2.47]
Muon	[0, 0.1, 1.3, 2.5]

Different $E_{\mathrm{T}}^{\mathrm{miss}}$ binning

A variation in the $E_{\mathrm{T}}^{\mathrm{miss}}$ binning takes into account the potential composition change at high $E_{\mathrm{T}}^{\mathrm{miss}}$ (>40 GeV), although the MC composition study as presented in Figure 7.10 demonstrates that the variation is almost saturated at 40 GeV. The alternative choice of $E_{\mathrm{T}}^{\mathrm{miss}}$ binning appears in Table 7.16. In order to incorporate the change in binning, the $E_{\mathrm{T}}^{\mathrm{miss}}$ cut in the measurement region is moved to < 50 GeV. The obtained F and F_{PLV} are shown in Figure A.3 of appendix A. The fake factors that account for the different parametrisation are propagated as an uncertainty on the Z+jets/$Z+\gamma$ estimation.

Table 7.16: Variation of the fake factor F binning in $E_{\mathrm{T}}^{\mathrm{miss}}$.

Nominal	$E_{\mathrm{T}}^{\mathrm{miss}}$ (GeV)	[0, 10, 20, 30, >40]
Variation	$E_{\mathrm{T}}^{\mathrm{miss}}$ (GeV)	[0, 15, 35, >50]

WZ cross-section in MC subtraction

The measurement of F is used to estimate only Z+jets/$Z+\gamma$, but there is contamination from other backgrounds in the measurement region as described in Table 7.11, therefore it is required to subtract these other backgrounds. The largest background that is subtracted in the measurement region is WZ. The uncertainty on the cross-section of WZ is 5% [185]. The WZ background subtraction is shifted up and down by the cross-section uncertainty to derive F and F_{PLV}. The resulting fake factors can be seen in Figure A.4 of appendix A. The fake factors that account for the uncertainty of the cross-section of WZ are propagated to the uncertainty on the Z+jets/$Z+\gamma$ estimation.

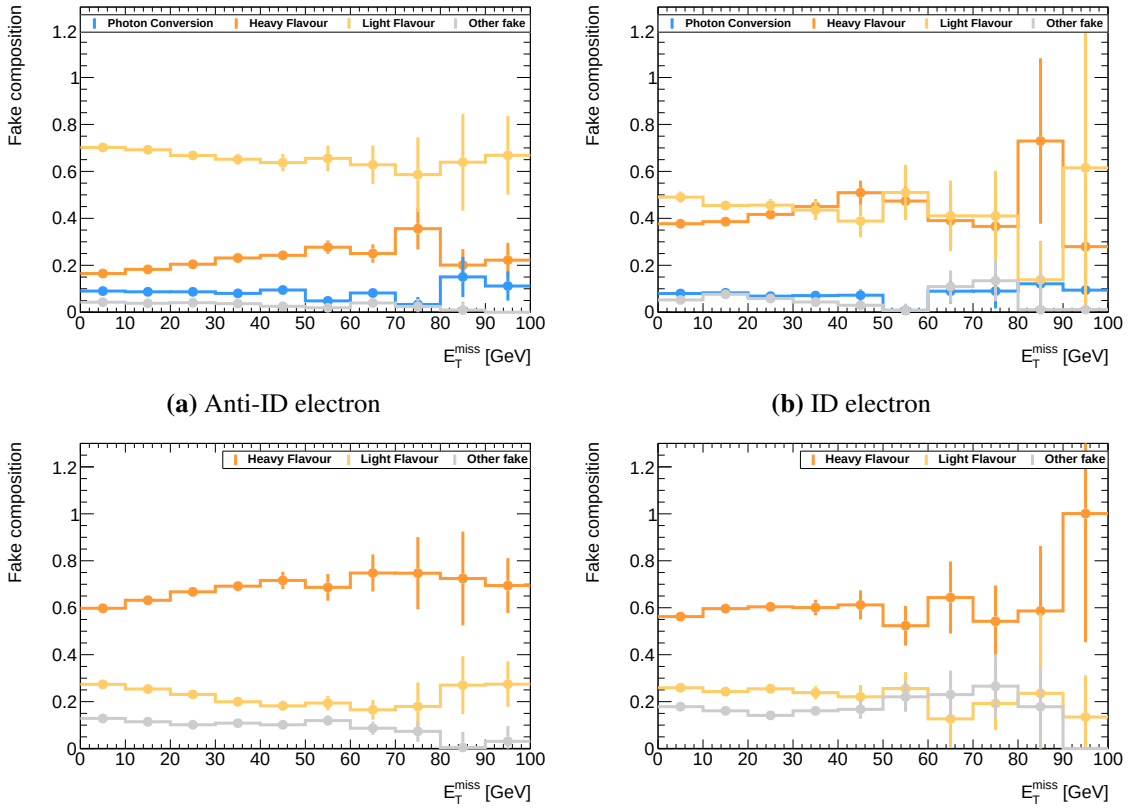

(a) Anti-ID electron

(b) ID electron

(c) Anti-ID muon

(d) ID muon

Fig. 7.10: Fake factor measurement region with extrapolated $E_{\mathrm{T}}^{\mathrm{miss}}$. The variation is almost saturated at 40 GeV. The distributions are obtained from Z+jets/Z+γ MC simulations generated using Sherpa 2.2.1.

Muon overlap removal

When the measurement region of F and application region of F are exactly the same, they have the same fake source composition. So when having measured F in the measurement region, it is expected that this is reflected in an accurate description of Z+jets/Z+γ in that same measurement region. However, for muons there is a difference in the way that F is measured and the way that F is applied. For the measurement of F the OR for muons has been turned off, whilst for the application of F the OR of muons has been turned on. For this reason the closure in the measurement region needs to be checked and this is shown in Table 7.17 for $\mu\mu\mu$, eeμ, eee and $\mu\mu$e. It can be seen from these tables there is a non-closure in the measurement region for muon faking channels, $\mu\mu\mu$ and eeμ. Since the only place disagreement is observed is in the muons, the hypothesis is that this is due to the muon overlap removal which is not applied when deriving F.

Table 7.17: The closure in the fake factor measurement region using the nominal fake factor. The channels shown are $\mu\mu\mu$, eeμ, eee and $\mu\mu$e. For the fakes background all the fakes systematics are implemented, except for a systematic covering the muon OR. The rest of the backgrounds only show the statistical uncertainty. It can be seen that there is non-closure in the $\mu\mu\mu$ and eeμ channels.

sample	$\mu\mu\mu$	eeμ	eee	$\mu\mu$e
Others	9.81 ± 0.82	8.73 ± 0.78	5.23 ± 0.61	10.17 ± 0.87
Fakes	13750 ± 230	10520 ± 180	5930 ± 100	7820 ± 130
$t\bar{t}$	1.82 ± 0.29	3.02 ± 0.38	1.65 ± 0.28	4.23 ± 0.44
$t\bar{t}$ +X	1.18 ± 0.09	0.95 ± 0.08	0.87 ± 0.07	1.33 ± 0.09
WZ	417.2 ± 7.2	289.3 ± 5.1	300.4 ± 5.0	330.9 ± 6.6
ZZ	329.4 ± 9.5	313.9 ± 8.4	255.1 ± 5.5	223.2 ± 3.2
Total	14510 ± 230	11140 ± 180	6490 ± 100	8390 ± 130
data	15940 ± 130	12010 ± 110	6649 ± 82	8316 ± 91

In order to validate the non-closure is due to the muon OR, the closure test can be repeated when F is measured with the muon OR turned on. The measurement of F when the muon OR is turned on can be seen in Figure A.5. The muon OR is only turned on for muon $p_{\mathrm{T}} <$ 30 GeV due to the high statistical uncertainty if the muon OR were also turned on at higher muon p_{T}. The resulting closure in the measurement region with F where muon OR is turned on is shown in Table 7.18 for $\mu\mu\mu$, eeμ, eee and $\mu\mu$e. As can be seen the closure in the measurement region is now within the statistical uncertainty for the muon faking channels, and from this it can be concluded that this systematic is indeed due to the muon OR. The F and F_{PLV} with the muon OR turned on, shown in Figure A.5 of appendix A, are propagated as an uncertainty on the Z+jets/Z+γ estimation.

Final systematics

After having derived the contribution due to the different systematics sources, which are statistical uncertainties, different parametrisation, different $E_{\mathrm{T}}^{\mathrm{miss}}$ binning, WZ cross-section in MC subtraction and muon overlap removal, the effect of the systematics can be checked in the SRs as presented in Table 7.19.

Table 7.18: The closure in the fake factor measurement region using the fake factor with muon OR turned on. The channels shown are $\mu\mu\mu$, eeμ, eee and $\mu\mu$e. For the fakes background only the statistical error is shown, since the fakes systematic uncertainties are derived with respect to the nominal fake factor. The rest of the backgrounds also only show the statistical uncertainty. It can be seen that there is closure in all the channels.

sample	$\mu\mu\mu$	eeμ	eee	$\mu\mu$e
Others	9.81 ± 0.82	8.73 ± 0.78	5.23 ± 0.61	10.17 ± 0.87
Fakes	15159 ± 51	11549 ± 47	5929 ± 25	7822 ± 28
$t\bar{t}$	1.82 ± 0.29	3.02 ± 0.38	1.65 ± 0.28	4.23 ± 0.44
$t\bar{t}$ +X	1.18 ± 0.09	0.95 ± 0.08	0.87 ± 0.07	1.33 ± 0.09
WZ	417.2 ± 7.2	289.3 ± 5.1	300.4 ± 5.0	330.9 ± 6.6
ZZ	329.4 ± 9.5	313.9 ± 8.4	255.1 ± 5.5	223.2 ± 3.2
Total	15918 ± 52	12165 ± 48	6492 ± 27	8392 ± 29
data	15940 ± 130	12010 ± 110	6649 ± 82	8316 ± 91

Table 7.19: Breakdown of the fakes systematics in the SRlow-0j, SRlow-nj, SRhigh-0j and SRhigh-nj regions. The regions are the combination of the regions defined in Section 8.4.

Region	SRlow-0j	SRlow-nj	SRhigh-0j	SRhigh-nj
Fake background expectation	122	16.0	14.1	3.03
Fake background systematic	$\pm$13 [11.0%]	$\pm$2.1 [13.2%]	$\pm$1.6 [11.5%]	$\pm$0.68 [22.4%]
Muon overlap removal	$\pm$13	$\pm$1.3	$\pm$0.80	$\pm$0.05
Different parametrisation	$\pm$1.1	$\pm$0.09	$\pm$0.10	$\pm$0.44
Different $E_{\mathrm{T}}^{\mathrm{miss}}$ binning	$\pm$0.71	$\pm$1.3	$\pm$0.93	$\pm$0.33
WZ cross-section	$\pm$0.00	$\pm$0.21	$\pm$0.00	$\pm$0.10
Statistical uncertainties	$\pm$0.00	$\pm$0.81	$\pm$0.94	$\pm$0.32

Chapter 8

Optimisation of the signal search

Once the Standard Model (SM) background has been modelled, the supersymmetry signal searched for needs to be modelled. Samples of signal events have been simulated in a grid of masses of the supersymmetric particles $\tilde{\chi}_1^{\pm}/\tilde{\chi}_2^0$ and $\tilde{\chi}_1^0$. Using the simulated signal points, the expected yield can be used to optimise the selection for the signal regions (SRs), whilst keeping the data in the regions blinded. First the trigger acceptance and efficiency for triggering on the signal is determined. Then the SRs described in Table 6.2 are further refined: by finding the optimal Prompt Lepton Veto (PLV) working point, and placing cuts on the kinematic variables described in Section 6.3 that select the signal and/or reduce the SM background.

8.1 Signal modelling

The supersymmetry signal samples are created using Monte Carlo (MC) simulations. In the chosen model all of the supersymmetry parameters described in Chapter 2 are kept fixed except for the mass of $\tilde{\chi}_1^0$ and $\tilde{\chi}_1^{\pm}/\tilde{\chi}_2^0$. By keeping these mass parameters as free parameters, a parameter space $(\tilde{\chi}_1^{\pm}/\tilde{\chi}_2^0, \tilde{\chi}_1^0)$ of possible supersymmetry models is scanned. In order to visualise the parameter space a grid has been created and is shown in Figure 8.1. The dashed lines indicate the semi-compressed region where $m_{\tilde{\chi}_1^{\pm}/\tilde{\chi}_2^0} - m_{\tilde{\chi}_1^0} < m_Z$. The points indicate the mass parameters of $\tilde{\chi}_1^0$ and $\tilde{\chi}_1^{\pm}/\tilde{\chi}_2^0$ for which signal samples have been created. The signal grid has been created in such a way that there are more samples at lower $\tilde{\chi}_1^{\pm}/\tilde{\chi}_2^0$ mass, where most sensitivity is expected.

Madgraph [166] is used to calculate the matrix element for each signal point on the grid. The matrix element is generated at leading-order (LO) with up to two extra partons. Since $m_{\tilde{\chi}_1^{\pm}/\tilde{\chi}_2^0} - m_{\tilde{\chi}_1^0} < m_Z$, the decay of the $\tilde{\chi}_1^{\pm}$ and $\tilde{\chi}_2^0$ produces off-shell $W^{\pm}$ and Z bosons; to better model these MadSpin [187, 188] is used, which takes into account angular correlations

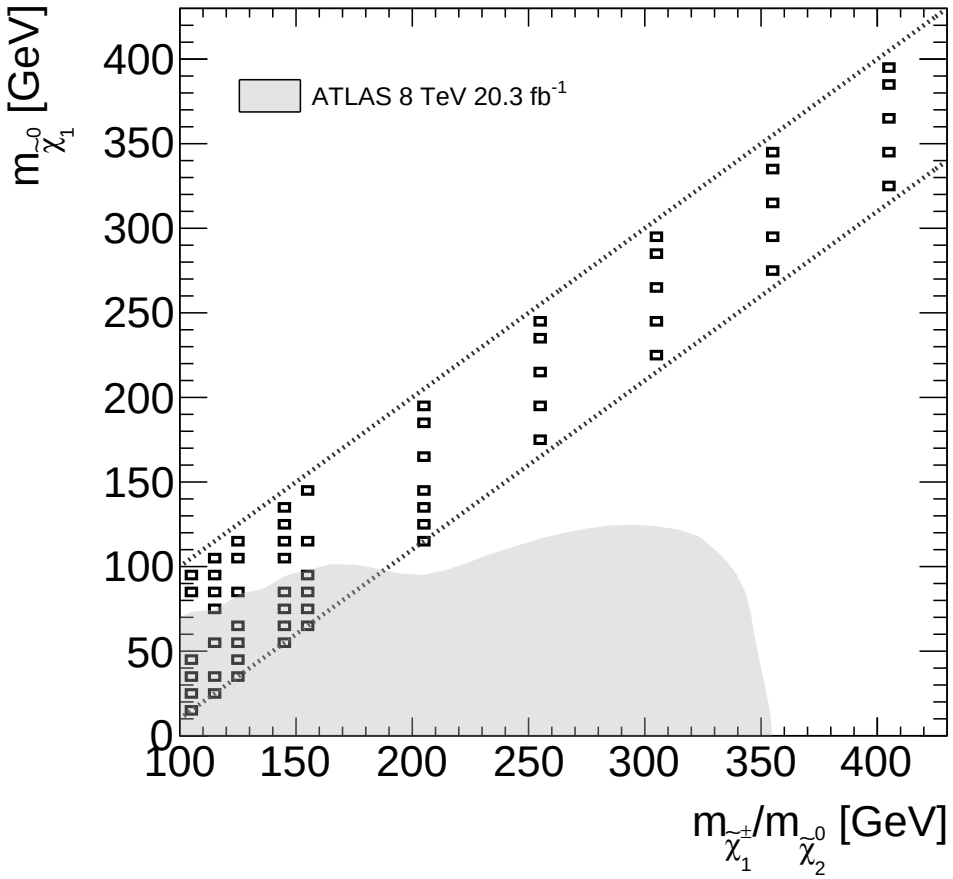

Fig. 8.1: Signal grid of possible supersymmetry models parametrised in $\tilde{\chi}_1^0$ and $\tilde{\chi}_1^\pm/\tilde{\chi}_2^0$ mass. The boxes show the generated signal points. The dashed line indicates the region where $m_{\tilde{\chi}_1^\pm/\tilde{\chi}_2^0} - m_{\tilde{\chi}_1^0} < m_Z$ and $m_{\tilde{\chi}_1^\pm/\tilde{\chi}_2^0} - m_{\tilde{\chi}_1^0} > 0$ GeV. The grey shade shows the previous exclusion limits with the ATLAS experiment, corresponding to the off-shell and on-shell WZ Run-1 result using 20.3 fb^{-1} at $\sqrt{s} = 8$ TeV [186].

Table 8.1: The signal samples MC generation and the choice of generator and parton shower.

Signal	Generator	Parton Shower
$\tilde{\chi}_1^{\pm}\tilde{\chi}_2^0 \rightarrow W^{\pm}Z\tilde{\chi}_1^0\tilde{\chi}_1^0$	MadGraph + MadSpin	Pythia8

of lepton pairs from the $W^{\pm}$ and Z boson decay. Madgraph and MadSpin are then interfaced with Pythia [169] with the A14 tune. Pythia takes care of the parton shower, hadronisation and the underlying event as described in Section 7.1. The choices of generator and parton shower are summarised in Table 8.1. The detector simulation is performed using GEANT4, not with the Full ATLAS simulation but with the fast simulation called ATLAS Fast II [189]. The fast detector simulation does a more coarse simulation of the electromagnetic and hadronic calorimeter response.

8.2 Trigger Selection

During data-taking there is a collision every 25 ns in which an interesting signal might be produced, but since the collisions happen so frequent, not all collisions can be processed and stored. In order to reduce the rate at which the data is stored, a trigger is in place selecting only the interesting events as described in Section 3.3. For this analysis a study has been performed to select good triggers to discover the signal.

Signals with a small mass difference (Δm) between the $\tilde{\chi}_1^0$ and $\tilde{\chi}_1^{\pm}/\tilde{\chi}_2^0$ mass decay into off-shell $W^{\pm}$ and Z bosons, which then decay into low p_{T} leptons. Since from the collisions there is a high rate of low p_{T} leptons (< 15 GeV), triggers have a p_{T} threshold in order to have an operable trigger rate, which is the lowest p_{T} possible. The threshold is still at too high p_{T} to be able to select all the supersymmetry signals with a small Δm. For this reason the signals with a small Δm have low acceptance from lepton triggers. However, using $E_{\mathrm{T}}^{\mathrm{miss}}$ triggers, sensitivity for the signals with a small Δm can be recovered at high $E_{\mathrm{T}}^{\mathrm{miss}}$. For this reason cuts to combine the lepton and $E_{\mathrm{T}}^{\mathrm{miss}}$ triggers are established, which are applied after the trigger selection and offline trigger cuts. The strategy is as described in Table 8.2.

For the lepton trigger events are selected from a combination of lepton triggers shown in Table 8.4. The choice of lepton trigger depends on the lepton's p_{T}, multiplicity, and flavour. The analysis requires exactly three leptons, so the trigger selection is a combination of electron and muons up to three leptons. The lepton trigger acceptance for signals with a small Δm depends on how low the p_{T} threshold for the trigger is. The selection contains

Table 8.2: The lepton and $E_{\mathrm{T}}^{\mathrm{miss}}$ triggers are combined depending on the lepton p_{T} and $E_{\mathrm{T}}^{\mathrm{miss}}$ in an event. The cuts are applied after the trigger selection and offline trigger cuts.

Trigger	Lepton trigger[1]	$E_{\mathrm{T}}^{\mathrm{miss}}$ trigger
$E_{\mathrm{T}}^{\mathrm{miss}}$ [GeV]	-	> 200
Lepton p_{T} [GeV]	$p_{\mathrm{T}}^{\ell 1}, p_{\mathrm{T}}^{\ell 2} > 10$	$p_{\mathrm{T}}^{\mathrm{electron}} > 4.5,\ p_{\mathrm{T}}^{\mathrm{muon}} > 3$

all the lowest p_{T} single muon, di-lepton and tri-muon triggers available. Single-electron triggers are disregarded because of too tight identification (ID) requirements included in the trigger.[2] Also the tri-electron trigger is not used, since it has low unique acceptance.[3] The lowest $E_{\mathrm{T}}^{\mathrm{miss}}$ triggers are chosen over the data taking periods as listed in Table 8.3. The trigger acceptance with all triggers used in the analysis, and without the trigger combination cuts presented in Table 8.2, is found to be $25\% - 70\%$ depending on the Δm of the signals as shown in Figure 8.2. The acceptance of 25% is for the signals with a small Δm ($\sim$ 10GeV), which results into the lowest p_{T} leptons. To select these the analysis relies for a large part on the $E_{\mathrm{T}}^{\mathrm{miss}}$ triggers. The acceptance for events of the supersymmetry signal that have $E_{\mathrm{T}}^{\mathrm{miss}} > 200$ GeV using the $E_{\mathrm{T}}^{\mathrm{miss}}$ triggers is found to be $> 98\%$.

8.2.1 Trigger efficiency

The lepton triggers are not yet fully efficient at the p_{T} threshold mentioned in Table 8.4, called the online p_{T} threshold. Triggers have a turn-on curve in their efficiency before they reach a plateau at which they are fully efficient. The turn-on curve of a trigger selecting on p_{T}, shows the efficiency of that trigger, with respect to the p_{T} of the lowest p_{T} lepton that fired that trigger. In Figure 8.3 the turn-on curve for the single muon trigger, the tri-muon trigger and the di-lepton triggers are shown. The efficiency for the $3\mu > 6$ GeV trigger is lower, 60%, since higher multiplicity triggers are generally less efficient due to the multiplication of the efficiency from each leg. All other triggers have a higher efficiency of 75%-90%. The signals with a small Δm ($\sim$ 10 GeV), besides having a low acceptance, typically rely on higher lepton multiplicity triggers such as the $3\mu > 6$ GeV trigger, and thus also have a low efficiency from the trigger.

Since there is a relatively high systematic uncertainty on the trigger efficiency attached to a lepton with a p_{T} at the start of the turn-on curve, a p_{T} cut is applied on top of the online

[1] There are cases where limitations from the trigger on the leading and subleading lepton p_{T} are higher than 10 GeV.

[2] The electron ID working point used for the analysis is medium, whilst the ID working point used by the single electron trigger is tight.

[3] The trigger p_{T} threshold is too high to be providing extra acceptance; 22, 8 and 8 GeV for the three leptons.

Table 8.3: Summary of the included $E_{\mathrm{T}}^{\mathrm{miss}}$ triggers.

Online p_{T} threshold	Year
$\boldsymbol{E_{\mathrm{T}}^{\mathrm{miss}}}$	
$E_{\mathrm{T}}^{\mathrm{miss}} > 70$ GeV	2015
$E_{\mathrm{T}}^{\mathrm{miss}} > 90$ GeV	2016 A-D1
$E_{\mathrm{T}}^{\mathrm{miss}} > 100$ GeV	2016 D1-F1
$E_{\mathrm{T}}^{\mathrm{miss}} > 110$ GeV	2016 F2-H
$E_{\mathrm{T}}^{\mathrm{miss}} > 110$ GeV	2017
$E_{\mathrm{T}}^{\mathrm{miss}} > 110$ GeV	2018

Table 8.4: Summary of included lepton triggers. There is a difference in the p_{T} threshold between 2015 and the years after. When in 2015 the LHC ran for the first time with 13 TeV, it started with a relative low instantaneous luminosity, which was ramped up the years after. Due to the higher instantaneous luminosity after 2015, trigger thresholds needed to be increased to maintain an acceptable trigger rate, since the bandwidth stayed the same.

Online p_{T} threshold	Identification (ID) requirement	Year
1μ		
$\mu > 20$ GeV	loose	2015
$\mu > 26$ GeV	medium	2016-2018
2μ		
$2\mu > 10$ GeV	-	2015
$2\mu > 14$ GeV	-	2016-2018
2e		
2e > 12 GeV	loose	2015
2e > 17 GeV	loose	2016-2018
1e1μ		
e > 17 GeV, $\mu > 14$ GeV	loose	2015
e > 17 GeV, $\mu > 14$ GeV	loose	2016-2018
3μ		
$3\mu > 6$ GeV	-	2015-2018

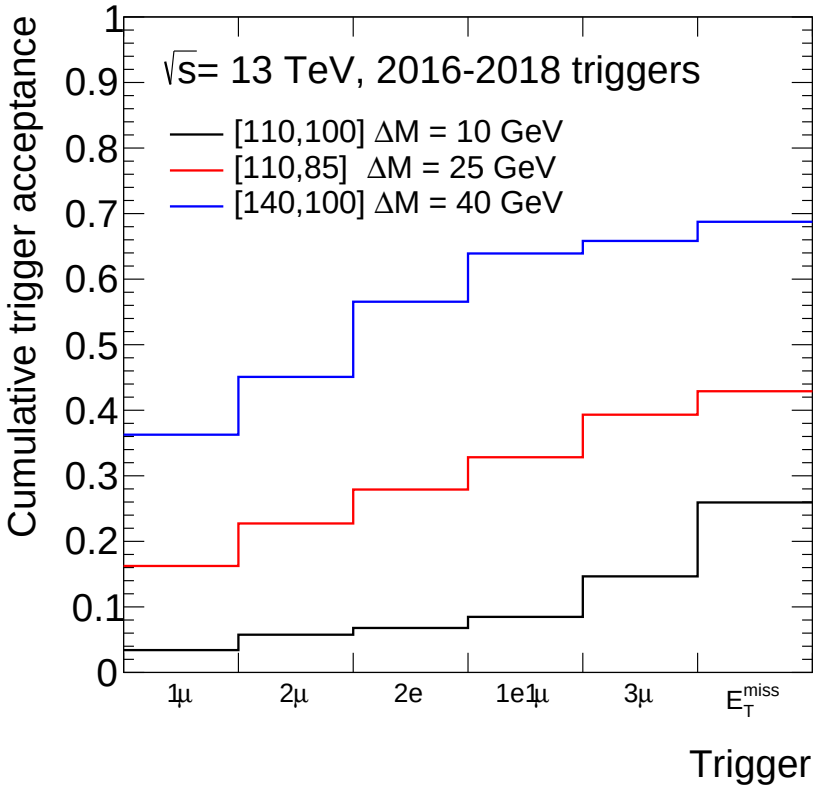

Fig. 8.2: Acceptance plotted as a function of the used triggers in the analysis. Distributions for $\tilde{\chi}_1^{\pm}\tilde{\chi}_2^0 \rightarrow WZ\tilde{\chi}_1^0\tilde{\chi}_1^0$ signals are presented, with mass values given as [m($\tilde{\chi}_1^{\pm}$,m($\tilde{\chi}_1^0$)] GeV. The trigger acceptance found is $25\% - 70\%$ depending on the Δm of the signals. The combination cuts for the lepton and $E_{\mathrm{T}}^{\mathrm{miss}}$ triggers demonstrated in Table 8.2 are not applied.

trigger p_{T} threshold, called the offline p_{T} cut. The p_{T} cut applied on top of the online trigger threshold is, +1.0 GeV for electrons, and +5% for muons. The offline p_{T} cuts are shown in Table 8.5 and a scheme combining single-, di- and tri-lepton triggers is shown in Figure 8.4. If an event passes the online p_{T} threshold, but not the corresponding offline p_{T} cut, it is not considered to pass that trigger.

From the plots it can be seen that after the offline p_{T} cut the muon triggers have reached their plateau and are efficient, however the electrons have a longer turn-on. The difference in turn-on with muons is not because reconstructing electrons is harder, there is just more background when reconstructing electrons from the electromagnetic (EM) calorimeters as opposed to reconstructing muons in the clean environment of the muon spectrometer (MS). During online reconstruction, at the trigger level, there is not much time to reconstruct the event, during offline reconstruction there is more time available. Due to the higher rate when reconstructing electrons and due to the limited time available during online reconstruction,

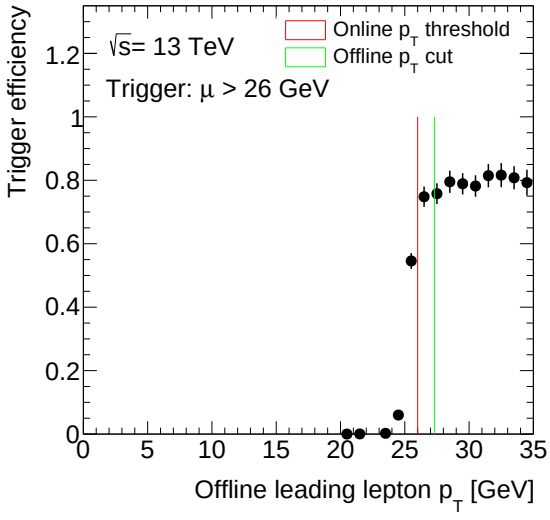

(a) $\mu > 26$ GeV trigger.

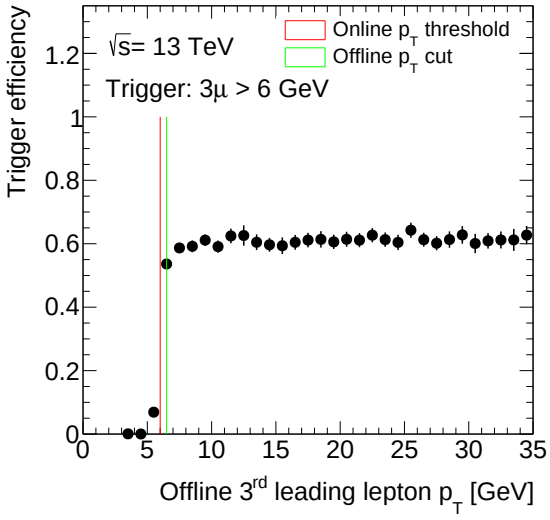

(b) $3\mu > 6$ GeV trigger.

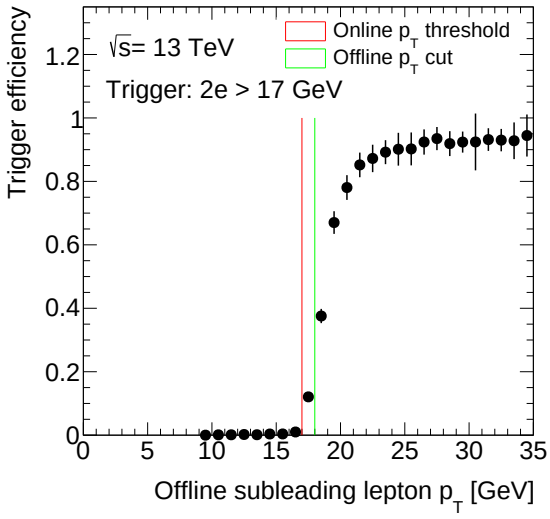

(c) 2e > 17 GeV trigger.

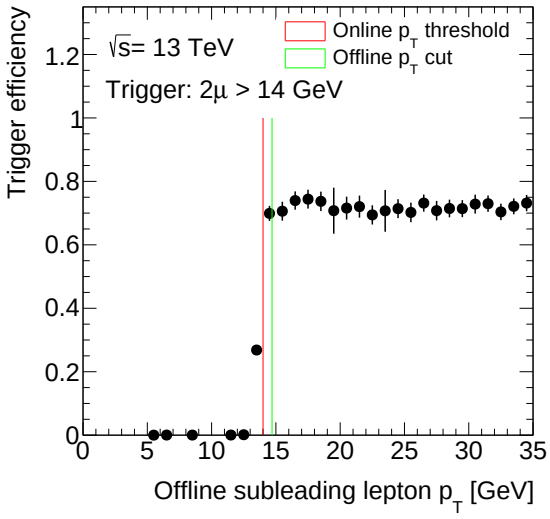

(d) $2\mu > 14$ GeV trigger.

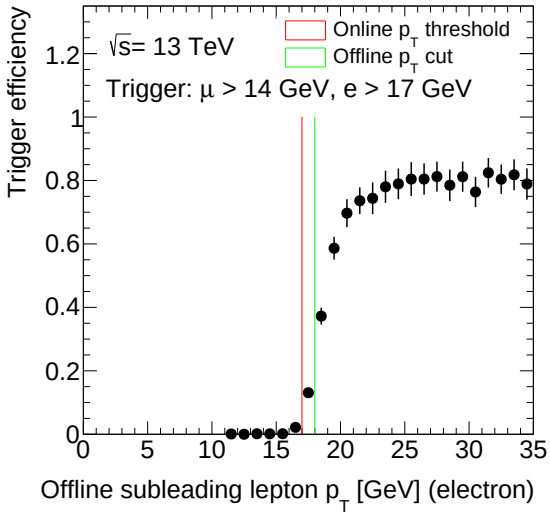

(e) e > 17 GeV, $\mu > 14$ GeV trigger (leading μ and subleading e).

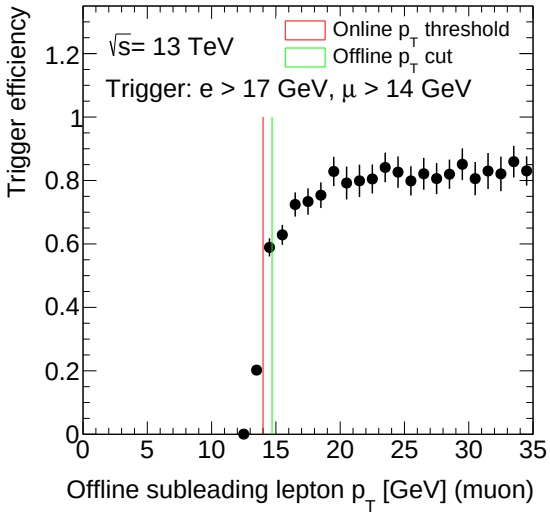

(f) e > 17 GeV, $\mu > 14$ GeV trigger (leading e and subleading μ).

Fig. 8.3: Efficiencies showing the turn on for offline lepton p_{T} using the *WZ* MC sample.

the electrons have a longer turn-on. For the muon triggers the turn-on does not fully reach the plateau with an efficiency of 100%. This is due to the L1 inefficiency. In the barrel of the MS the RPCs do not have full coverage due to holes in each sector, which are mostly structure-wise inevitable, causing an efficiency of around 70%. The muon L1 efficiency from the TGCs is much higher, the efficiency at the plateau in the end-cap is around 90%. For electrons the plateau efficiency is around 95%.

There is also a turn-on in the efficiency for the $E_{\mathrm{T}}^{\mathrm{miss}}$ triggers. As can be seen in Table 8.3, the online threshold for the $E_{\mathrm{T}}^{\mathrm{miss}}$ triggers is below 200 GeV. The decision for the offline threshold of $E_{\mathrm{T}}^{\mathrm{miss}} > 200$ GeV for the $E_{\mathrm{T}}^{\mathrm{miss}}$ triggers is driven by the turn-on in the efficiency as well.

8.3 Prompt Lepton Veto

The Prompt Lepton Veto (PLV) is described in Section 5.4 and is applied as a type of isolation. The PLV is used to reduce the amount of fake backgrounds that enter the analysis. The PLV is applied to the 3$^{\mathrm{rd}}$ leading (in p_{T}) lepton, which is at least 70% of the time the fake lepton for a $p_{\mathrm{T}} < 15$ GeV in Z+jets/Z+γ as can be seen in Figure 8.5(a). This is important since at low p_{T} the highest amount of fakes are expected. In Figure 8.5(b) it is shown that with increasing $m_{\ell\ell}^{\mathrm{min}}$ it becomes more likely for the 3$^{\mathrm{rd}}$ lepton to be the fake for Z+jets/Z+γ. The reason is that real leptons are expected to be low p_{T} in the low $m_{\ell\ell}^{\mathrm{min}}$ phase space due to the off-shell Z. It then becomes more likely for the fake lepton, a photon or jet, to be higher in p_{T}. The performance of the PLV working points in the SRlow-0j SR, the low $E_{\mathrm{T}}^{\mathrm{miss}}$ SR where Z+jets/Z+γ is expected to be the largest background, is shown in Table 8.6. It can be seen that the `PLVLoose` working point reduces the Z+jets/Z+γ fakes by 28%, while decreasing the signal by only 3%. The `PLVTight` working point reduces the Z+jets/Z+γ fakes by 50%, while reducing the signal by 10%. The `PLVTight` working point is chosen to be used in the analysis for its better Z+jets/Z+γ rejection, and is found to improve the final significance described in Section 8.4.

Besides the 3$^{\mathrm{rd}}$ leading lepton being the fake lepton most of the time, a second reason for only applying the PLV to the 3$^{\mathrm{rd}}$ lepton is to avoid biasing the scale factor applied to the PLV as derived in Section 5.4.1. The scale factor from the PLV can be biased when also a trigger scale factor, scaling MC to data, is applied, if that trigger for example also contains an isolation requirement on the lepton. As mentioned the leading and subleading leptons fire the single and di-lepton triggers, and only in case of the $3\mu > 6$ GeV trigger the 3$^{\mathrm{rd}}$ leading lepton is able to fire the trigger, thus causing a potential bias to the PLV scale factor. However, in past studies in the ttH multi-lepton final state [190], the PLV is shown to have

Table 8.5: Summary of offline p_{T} cut for the 2016 lepton triggers included in the analysis.

Trigger	$p_{\mathrm{T}}^{\ell 1}$ [GeV]	$p_{\mathrm{T}}^{\ell 2}$ [GeV]	$p_{\mathrm{T}}^{\ell 3}$ [GeV]
1μ	> 27.3	-	-
2e	> 18	> 18	-
1e1μ	> 18 (e)	> 14.7 (μ)	-
2μ	> 14.7	> 14.7	-
3μ	> 6.5	> 6.5	> 6.5

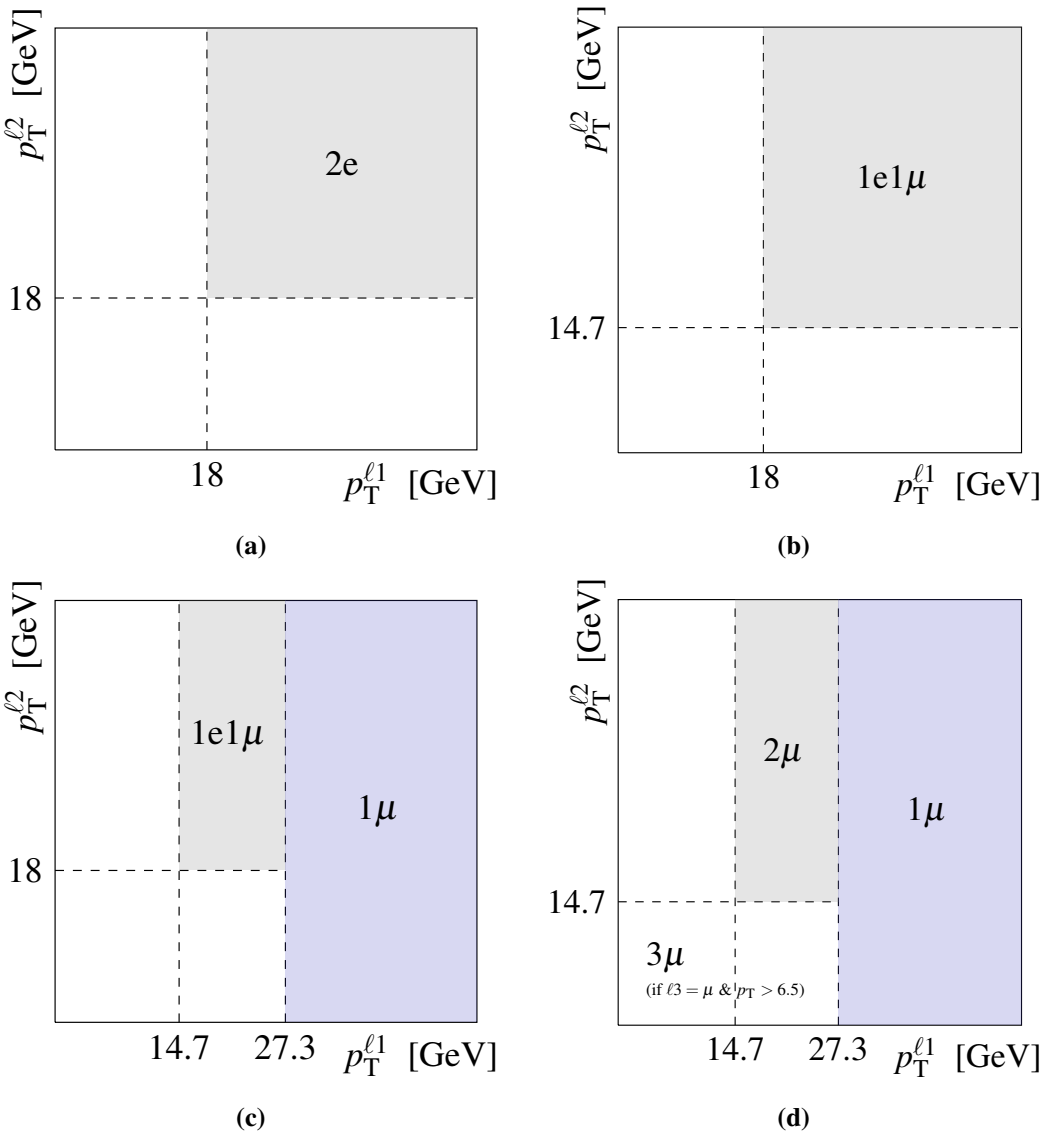

Fig. 8.4: The lepton trigger selection and offline lepton p_{T} cut causes different thresholds per case of lepton multiplicity. The p_{T} thresholds are shown for **(a)** the e/e case, **(b)** the e/μ case, **(c)** the μ/e case and **(d)** the μ/μ case.

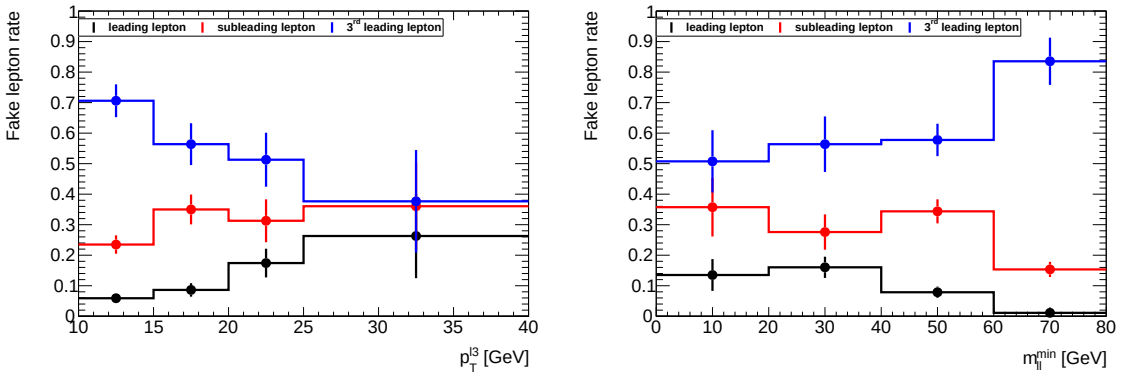

(a) **(b)**

Fig. 8.5: Fraction of events in which leading, subleading or 3rd leading lepton is the fake as a function of **(a)** $p_{\mathrm{T}}^{\ell_3}$ and **(b)** $m_{\ell\ell}^{\mathrm{min}}$, before applying the PLV. The preselection cuts include a b-jet veto and lepton $p_{\mathrm{T}} > 10$ GeV. The distributions are obtained from Z+jets/Z+γ MC simulations generated using Sherpa 2.2.1.

no correlation with the muon triggers without isolation requirement. In case of the $3\mu > 6$ GeV trigger there is no isolation requirement and thus no bias with respect to the PLV scale factor is expected. Since in our trigger strategy electron triggers are always matched with the leading and subleading lepton, and only muon triggers without an isolation requirement are used for the 3rd leading lepton, the bias on the PLV scale factor is avoided.

8.4 Signal regions

Signal regions (SRs) are defined by cuts on kinematic variables, such as the invariant mass of the leptons. The SRs are designed in such a way that they select the process from the Feynman diagram shown in Figure 6.1. Optimisation is performed for the $\tilde{\chi}_1^{\pm}/\tilde{\chi}_2^0$ and $\tilde{\chi}_1^0$ points which make up the signal grid shown in Figure 8.1. SRs are optimised by how many standard deviations the expected observation of the signal would be away from the SM background-only hypothesis. The number of standard deviations away from the background-only hypothesis is given by the significance, called the Zn. For signal points with $\mathrm{Zn} = 5$ there is sensitivity to discover the signal, if it is present in the data. For signal points with $\mathrm{Zn} = 1.64$ the signal can be excluded at 95% confidence level (CL), if it is not present in the data.

For the optimisation procedure, Zn is calculated starting from a likelihood consisting of two poisson distributions where a 30% flat (i.e. constant) systematic uncertainty is assumed

Table 8.6: Expected yields in the SRlow-0j SR in 139 fb^{-1} when applying different PLV working points. The `PLVLoose` working point reduces the Z+jets/Z+γ fakes by 28%, while it reduces the signal by only 3%. The `PLVTight` working point reduces the Z+jets/Z+γ fakes by 50%, while reducing the signal by 10%. Only statistical uncertainties are included.

sample	SRlow-0j	purity	SRlow-0j `PLVLoose`	purity	SRlow-0j `PLVTight`	purity
WZ	333.3 ± 5.2	12%	322.0 ± 5.2	13%	294.7 ± 5.0	14%
ZZ	1404 ± 15	49%	1352 ± 15	54%	1190 ± 14	58%
Fakes MC	1070 ± 180	37%	770 ± 160	31%	540 ± 140	26%
$t\bar{t}$	40.9 ± 1.4	1%	18.6 ± 0.9	1%	13.1 ± 0.8	1%
$t\bar{t}\,X$	2.7 ± 0.1	0%	2.4 ± 0.1	0%	2.1 ± 0.1	0%
Others	26.5 ± 1.7	1%	16.7 ± 1.1	1%	14.1 ± 1.0	1%
Total bg predicted	2880±180	-	2480±160	-	2060±140	-
125,110 [Δm=15]	15.8 ± 1.3	1%	15.3 ± 1.3	1%	14.6 ± 1.3	1%
125,100 [Δm=25]	183.0 ± 5.3	6%	177.9 ± 5.3	7%	160.5 ± 5.0	8%
140,100 [Δm=40]	351.1 ± 6.5	12%	338.9 ± 6.4	14%	308.5 ± 6.1	15%
150,60 [Δm=90]	57.5 ± 2.3	2%	56.0 ± 2.3	2%	53.7 ± 2.2	3%

on the background,

$$L(S,B) = P(n_{SR}|s+b) \cdot P(n_{CR}|b \cdot \tau(=30\%)), \tag{8.1}$$

where s is the expected number of signal events, b is the expected number of background events and τ is the flat systematic uncertainty. From a likelihood of two poisson distributions a p-value can be calculated analytically, which is converted into a Zn.

The signal region phase space is divided into four parts as previously shown in Table 6.2, SRlow-0j, SRlow-nj, SRhigh-0j and SRhigh-nj. SRlow-0j corresponds to $N_{\text{jets}}^{30\text{ GeV}} = 0$ and $E_{\text{T}}^{\text{miss}} < 50$ GeV, and SRlow-nj corresponds to $N_{\text{jets}}^{30\text{ GeV}} \geq 1$ and $E_{\text{T}}^{\text{miss}} < 200$ GeV, SRhigh-0j corresponds to $N_{\text{jets}}^{30\text{ GeV}} = 0$ and $E_{\text{T}}^{\text{miss}} > 50$ GeV and SRhigh-nj corresponds to $N_{\text{jets}}^{30\text{ GeV}} \geq 1$ and $E_{\text{T}}^{\text{miss}} > 200$ GeV.

The first step in the signal selection is to select an off-shell Z. Since the leptonic decay of a Z is to an opposite-sign same-flavour (OSSF) pair, OSSF leptons are assigned to the Z boson. In case there are two OSSF pairs in the event there are multiple ways to assign the leptons to the Z. As explained in Section 6.3 the invariant mass of the OSSF lepton pair closest to m_Z is called $m_{\ell\ell}$, $m_{\ell\ell}^{\text{min}}$ minimises the invariant mass of the OSSF lepton pair and $m_{\ell\ell}^{\text{max}}$ maximises the invariant mass of the OSSF lepton pair. After two leptons have been assigned to the Z boson, the remaining lepton is assigned to the W boson. The transverse mass of the W boson reconstructed with the W-lepton assigned according to $m_{\ell\ell}$ and $m_{\ell\ell}^{\text{min}}$ are labeled m_{T} and $m_{\text{T}}^{\text{minmll}}$ respectively.

Table 8.7: Binning in $m_{\ell\ell}^{\text{min}}$ used in the SRs.

	a	b	c	d	e	f	g
$m_{\ell\ell}^{\text{min}}$ (GeV)	[0,10]	[10,15]	[15,20]	[20,30]	[30,40]	[40,60]	[60,75]

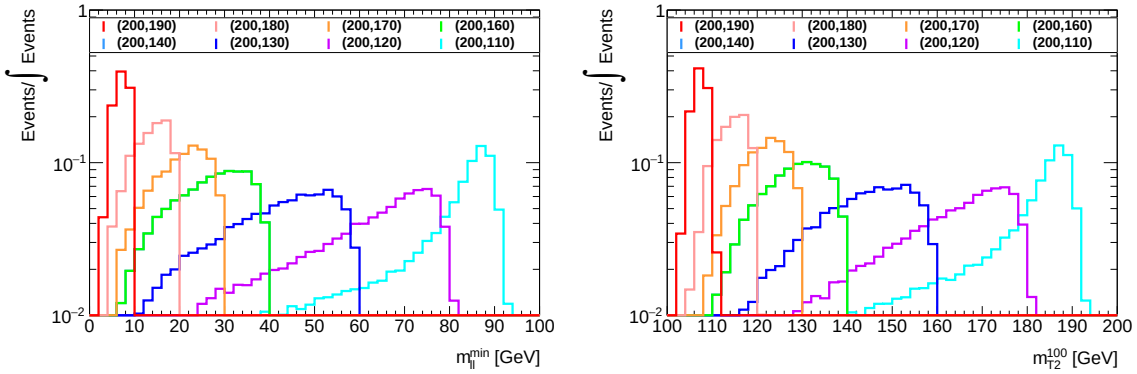

(a) **(b)**

Fig. 8.6: **(a)** The distribution of $m_{\ell\ell}^{\text{min}}$ for different signal samples after applying preselection cuts. The SRs are binned in $m_{\ell\ell}^{\text{min}}$ in order to target different Δm points in the signal grid. **(b)** The distribution of m_{T2}^{100} for different signal samples after applying preselection cuts. The signals also have a kinematic edge in m_{T2}^{100} which can also be used in order to target different Δm points.

The first event selection cuts are to select an off-shell Z and to reduce the background that comes from $t\bar{t}$. These cuts are used throughout the whole analysis:

- at least 1 opposite-sign same-flavour (OSSF) lepton pair to select the Z.
- $N_{\text{b-jets}}^{20\,\text{GeV}} = 0$ to reduce $t\bar{t}$ contamination.
- $m_{\ell\ell}^{\text{min}} < 75$ GeV to select off-shell Z events.
- $m_{\ell\ell}^{\text{max}} < 75$ GeV to reduce on-shell Z contamination from WZ background.
- veto $m_{\ell\ell}^{\text{min}}$ in the intervals [3,3.2] and [9,12] GeV to remove the J/ψ and Υ resonances.

In order to create specific SRs that target different mass difference (Δm) $m_{\tilde{\chi}_1^\pm/\tilde{\chi}_2^0} - m_{\tilde{\chi}_1^0}$ points from the signal grid a discriminating variable needs to be found for the Δm points. The variable $m_{\ell\ell}^{\text{min}}$ is found to be most accurate in reconstructing the Z boson in the signal process. The signal has a kinematic edge at $m_{\ell\ell}^{\text{min}} = m_{\tilde{\chi}_1^\pm/\tilde{\chi}_2^0} - m_{\tilde{\chi}_1^0}$ as shown in Figure 8.6. The SR phase space is further split into regions of $m_{\ell\ell}^{\text{min}}$, to target the points in the signal grid with a specific Δm. The $m_{\ell\ell}^{\text{min}}$ regions are defined in Table 8.7.

Each of the defined SRs will have a different background composition, so in each SR the background needs to be reduced to optimise the Zn for the signal in that region. In the

low $E_{\mathrm{T}}^{\mathrm{miss}}$ SRs, SRlow-0j and SRlow-nj, the Z+jets background will be dominant, whereas in the high $E_{\mathrm{T}}^{\mathrm{miss}}$ SRs, SRhigh-0j and SRhigh-nj, WZ and $t\bar{t}$ will be dominant. For this reason different strategies have been undertaken to optimise the low and high $E_{\mathrm{T}}^{\mathrm{miss}}$ SRs. After the divisions in bins of $N_{\mathrm{jets}}^{30\ \mathrm{GeV}}$, $E_{\mathrm{T}}^{\mathrm{miss}}$ and $m_{\ell\ell}^{\mathrm{min}}$ as described in Table 6.2 and 8.7, each of the SRs is further optimised using the following additional discriminating variables described in Section 6.3.

8.4.1 SRlow signal regions

The SRlow regions are optimised in a similar way since they share a common background composition, where the Z+jets background is dominant. There are two main changes with respect to the strategy of defining the SRs described in the Section 8.4:

- $m_{\ell\ell}^{\mathrm{min}}$ region a, where $m_{\ell\ell}^{\mathrm{min}} \in [0, 12]$, is dropped because of low trigger acceptance and due to large backgrounds from the J/ψ and Υ resonances.
- $m_{\ell\ell}^{\mathrm{min}}$ regions f and g are split into low $m_{\mathrm{T}}^{\mathrm{minmll}} < 60$ GeV regions, f1 and g1, and high $m_{\mathrm{T}}^{\mathrm{minmll}} > 90$ GeV regions, f2 and g2, in order to be able to design the WZ validation regions as described in Section 9.1.

The cuts for the low $E_{\mathrm{T}}^{\mathrm{miss}}$ SRs, both SRlow-0j and SRlow-nj, for all the $m_{\ell\ell}^{\mathrm{min}}$ regions are summarised in Table 8.8. Additional $m_{3\ell}$ and $\min\Delta R$ cuts are included in the channel where an electron is the fake candidate ($e^+e^-e^\pm$ or $\mu^+\mu^-e^\pm$) to reduce electron fakes due to photon-conversion. The cuts are applied in order to match the fake composition in the Z+jets estimation described in Section 7.2.3, where $\min\Delta R \in [0.6, 2.4]$ and $|m_{3\ell} - m_Z| > 20$ GeV.

- A cut on lepton p_{T} is applied to reduce the fake Z+jets background as illustrated in Figure 8.7.
- A cut on $m_{\mathrm{T}}^{\mathrm{minmll}}$ is applied to reduce on-shell WZ background. $m_{\mathrm{T}}^{\mathrm{minmll}}$ is the W reconstructed transverse mass, where the W-lepton is assigned according to $m_{\ell\ell}^{\mathrm{min}}$. As shown in Figure 8.8 the cuts on $m_{\mathrm{T}}^{\mathrm{minmll}}$ are applied in such a way to maximally increase the Zn.
- A cut on $E_{\mathrm{T}}^{\mathrm{miss}}$ significance is applied to reduce the fake Z+jets background. The $E_{\mathrm{T}}^{\mathrm{miss}}$ significance variable indicates the degree to which $E_{\mathrm{T}}^{\mathrm{miss}}$ corresponds to an actual particle escaping the detector as described in Section 5.5.2. As shown in Figure 8.9 $E_{\mathrm{T}}^{\mathrm{miss}}$ significance reduces the Z+jets background.

Table 8.8: Signal region definitions for SRlow-0j and SRlow-nj, with SRlow-0j corresponding to $N_{\text{jets}}^{30\text{ GeV}} = 0$ and $E_{\text{T}}^{\text{miss}} < 50$ GeV and SRlow-nj corresponding to $N_{\text{jets}}^{30\text{ GeV}} \geq 1$ and $E_{\text{T}}^{\text{miss}} < 200$ GeV.

	$m_{\ell\ell}^{\text{min}}$ [GeV]	$m_{\ell\ell}^{\text{max}}$ [GeV]	m_{T2}^{100} [GeV]	lepton p_{T} [GeV]	$m_{\text{T}}^{\text{minmll}}$ [GeV]	$E_{\text{T}}^{\text{miss}}$ significance	$p_{\text{T}}^{\text{leptons}}/E_{\text{T}}^{\text{miss}}$	min ΔR	$m_{3\ell}$ [GeV]
SRlow-0jb	[12,15]	<60	<115	all 3 > 10	<50	>1.5	<1.1	<1.6	-
SRlow-0jc	[15,20]	<60	<120	all 3 > 10	<50	>1.5	<1.1	<1.6	-
SRlow-0jd	[20,30]	<60	<130	all 3 > 10	<50	>1.5	<1.1	<1.6	-
SRlow-0je	[30,40]	<60	-	all 3 > 10	<60	>1.5	<1.3	-	-
SRlow-0jf1	[40,60]	<75	-	all 3 > 15	<60	>1.5	<1.4	-	>100
SRlow-0jf2	[40,60]	<75	-	all 3 > 15	>90	>1.5	<1.4	-	>100
SRlow-0jg1	[60,75]	<75	-	all 3 > 15	<60	>1.5	<1.4	-	>100
SRlow-0jg2	[60,75]	<75	-	all 3 > 15	>90	>1.5	<1.4	-	>100
SRlow-njb	[12,15]	<60	<115	all 3 > 10	<50	>3	<1.0	<1.6	-
SRlow-njc	[15,20]	<60	<120	all 3 > 10	<50	>3	<1.0	<1.6	-
SRlow-njd	[20,30]	<60	<130	all 3 > 10	<50	>3	<1.0	<1.6	-
SRlow-nje	[30,40]	<60	-	all 3 > 10	<60	>3	<1.0	-	-
SRlow-njf1	[40,60]	<75	-	all 3 > 15	<60	>3	<1.2	-	-
SRlow-njf2	[40,60]	<75	-	all 3 > 15	>90	>3	<1.2	-	-
SRlow-njg1	[60,75]	<75	-	all 3 > 15	<60	>3	<1.2	-	-
SRlow-njg2	[60,75]	<75	-	all 3 > 15	>90	>3	<1.2	-	-

- A cut on $m_{3\ell}$ is applied to reduce the ZZ background. As shown in Figure 8.10 for SRlow-0jf1 and SRlow-0jg1 there is a ZZ peak around $m_{3\ell} \sim 90$ GeV. The peak around m_Z in $m_{3\ell}$ is the contribution of $Z \to \ell\ell$, where a ℓ emits a virtual Z, which decays to $\ell\ell$. A cut is applied requiring $m_{3\ell} > 100$ GeV to remove the ZZ peak and improve the Zn.

- A cut on minΔR is applied to reduce the fake Z+jets background. The variable minΔR is the minimum ΔR between all OSSF lepton pairs in the event. Leptons from Z are expected to be close together and are expected to have the smallest ΔR of the OSSF leptons. As shown in Figure 8.11 a cut on minΔR improves the Zn.

- A cut on $p_{\text{T}}^{\text{leptons}}/E_{\text{T}}^{\text{miss}}$ is applied to select the signal. The variable $p_{\text{T}}^{\text{leptons}}/E_{\text{T}}^{\text{miss}}$ contains the ratio of the vector sum p_{T} of the lepton system and the $E_{\text{T}}^{\text{miss}}$, and is applied to SRlow-0j and SRlow-nj. This variable shows to have discrimination between signal and background in the SRhigh-nj region, as it can be interpreted as the fraction of $E_{\text{T}}^{\text{miss}}$ coming from ISR. However, also in the SRlow-0j and SRlow-nj it is found to be discriminating between signal and background. The cuts placed on $p_{\text{T}}^{\text{leptons}}/E_{\text{T}}^{\text{miss}}$ are shown in Figure 8.12.

After having illustrated that the cuts for SRlow-0j and SRlow-nj improve the Zn of the signal in each region individually, the combination of the 16 SRlow SRs will determine the total significance of the search in the lower $E_{\text{T}}^{\text{miss}}$ region. An estimate of the expected

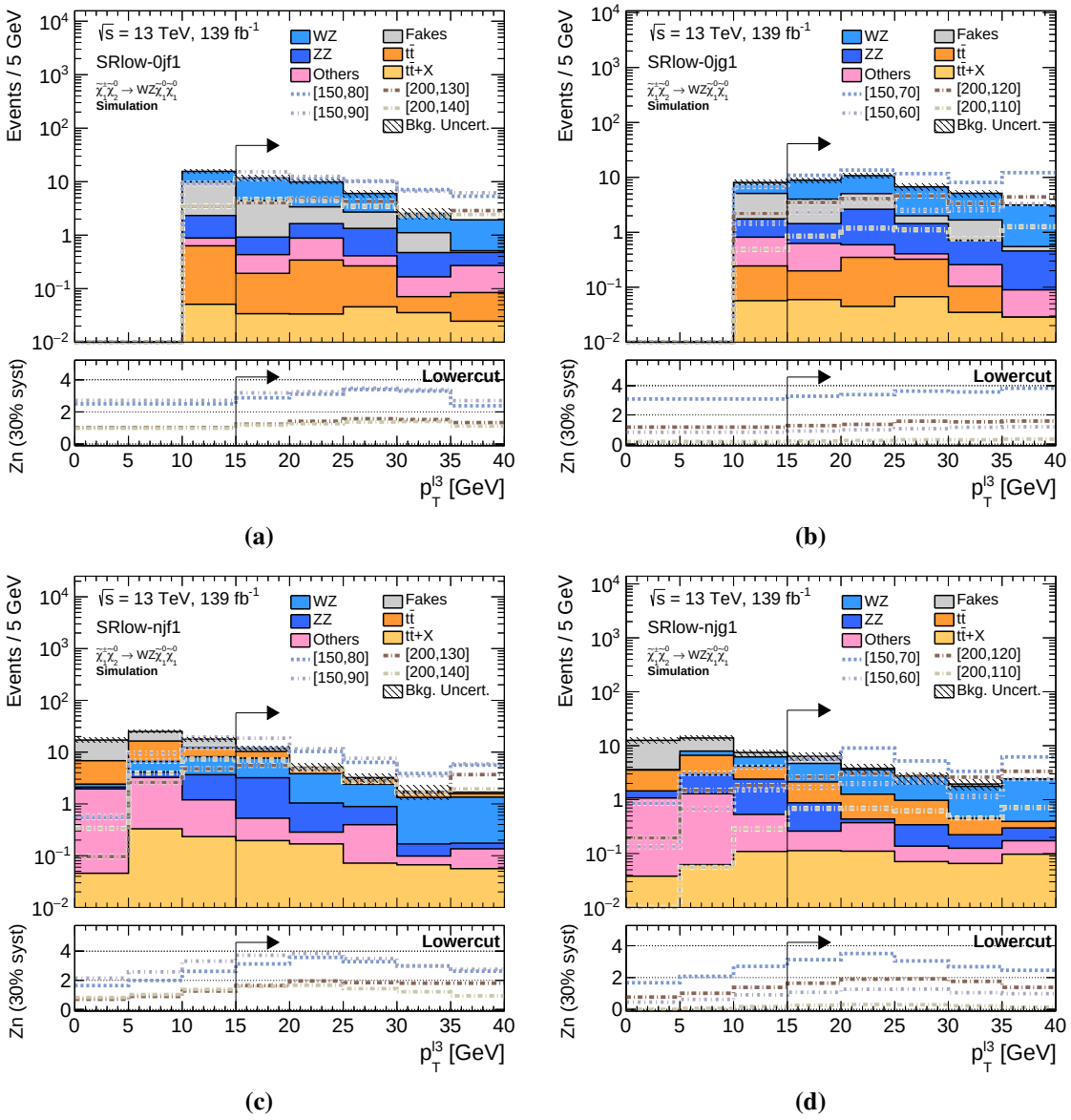

Fig. 8.7: Distributions of the $p_{\mathrm{T}}^{\ell_3}$ for **(a)** SRlow-0jf1, **(b)** SRlow-0jg1, **(c)** SRlow-njf1 and **(d)** SRlow-njg1. A cut on lepton p_{T} is applied to reduce the fake Z+jets background. A cut on lepton $p_{\mathrm{T}} > 10$ GeV is applied for the $m_{\ell\ell}^{\mathrm{min}} < 40$ GeV regions (SRlow-0jb −SRlow-0je) and a cut on lepton $p_{\mathrm{T}} > 15$ GeV is applied for the $m_{\ell\ell}^{\mathrm{min}} > 40$ GeV regions (SRlow-0jf −SRlow-0jg) . The reason for a higher p_{T} cut is that the targeted signal samples peak at higher p_{T} in the $m_{\ell\ell}^{\mathrm{min}} > 40$ GeV regions. Only statistical uncertainties are included in the top panel. The last bin includes overflow. Distributions for $\tilde{\chi}_1^{\pm}\tilde{\chi}_2^0 \to WZ\tilde{\chi}_1^0\tilde{\chi}_1^0$ signals are overlaid, with mass values given as [m($\tilde{\chi}_1^{\pm}$),m($\tilde{\chi}_1^0$)] GeV. In the bottom panel the Zn for the signals is calculated using a 30% flat systematic uncertainty. In the Zn calculation a lowercut integrates the yields from right to left, and an uppercut integrates the yields from left to right.

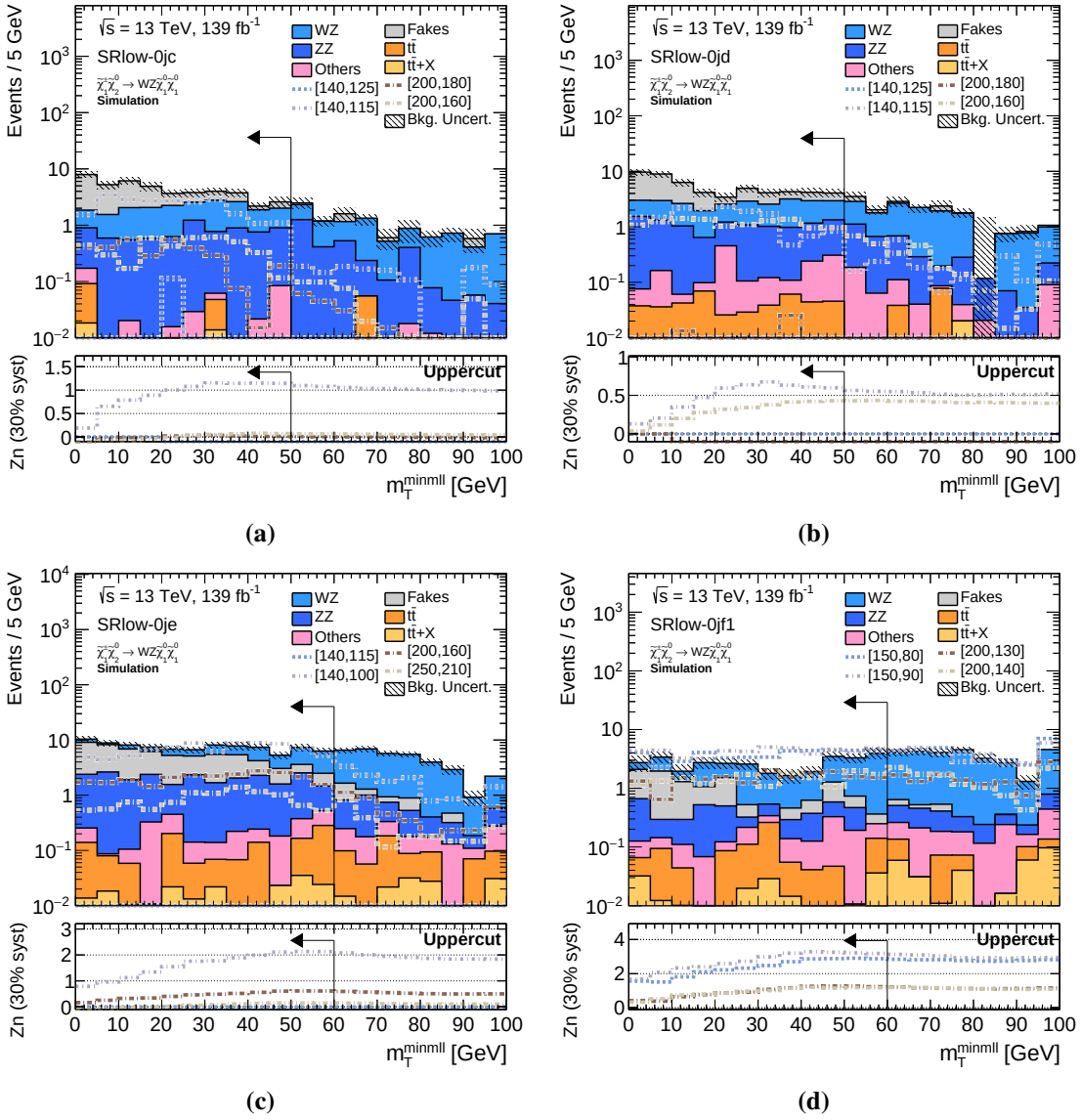

Fig. 8.8: Distributions of the $m_{\mathrm{T}}^{\mathrm{minmll}}$ for **(a)** SRlow-0jc, **(b)** SRlow-0jd, **(c)** SRlow-0je and **(d)** SRlow-0jf1. In the distribution for SRlow-0jf1 a cut on $m_{\mathrm{T}}^{\mathrm{minmll}} > 90$ GeV is placed to create the SRlow-0jf2 region. The $m_{\mathrm{T}}^{\mathrm{minmll}}$ distribution is expected to have an edge around the W mass at 80 GeV for the on-shell WZ background, so applying an upper cut below $m_{\mathrm{T}}^{\mathrm{minmll}} \sim 80$ GeV will reduce the on-shell WZ background. Also this cut will select the off-shell W expected from the signal. More explanation of the figure is given in the caption of Figure 8.7.

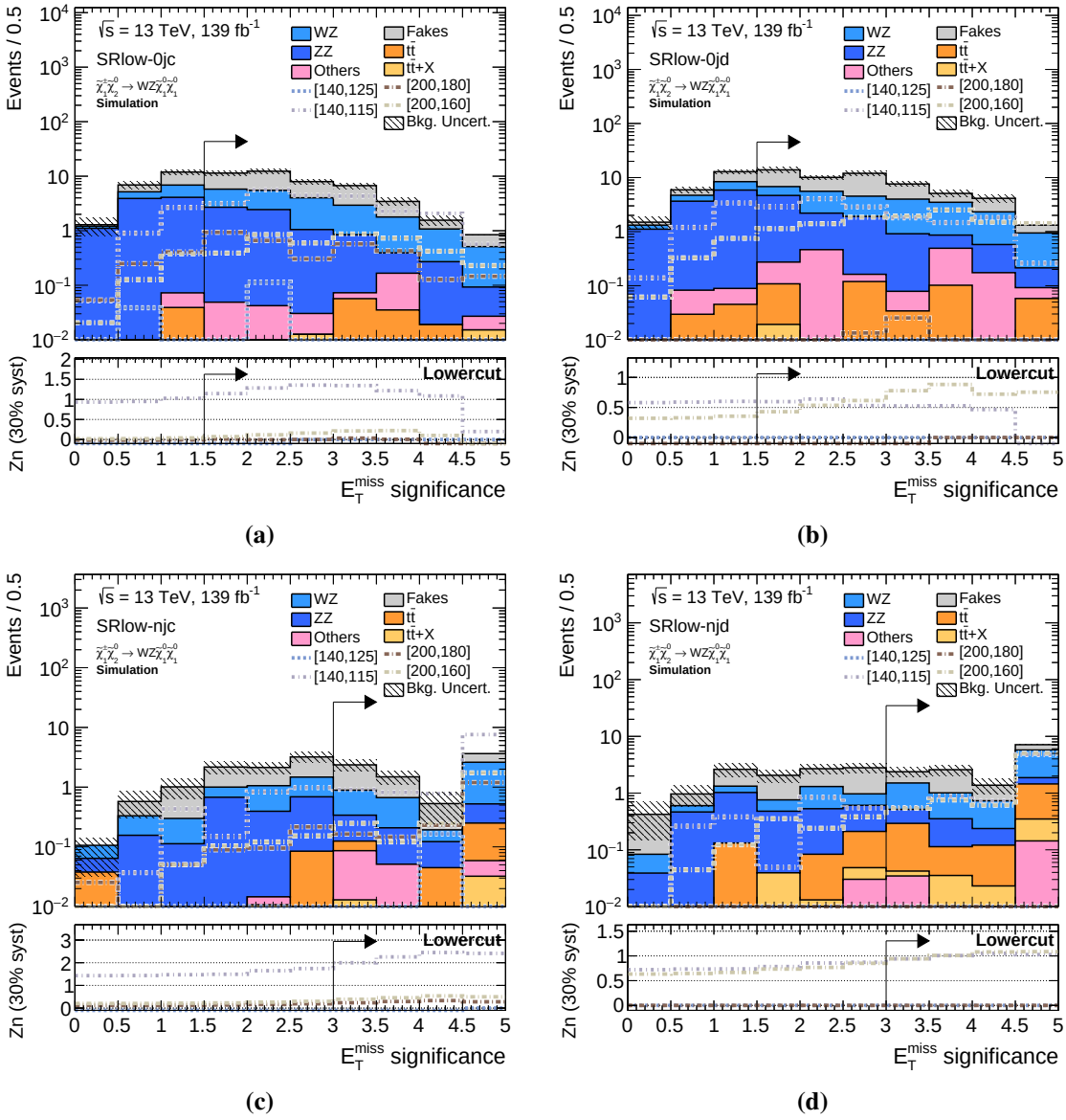

Fig. 8.9: Distributions of the $E_{\mathrm{T}}^{\mathrm{miss}}$ significance for **(a)** SRlow-0jc, **(b)** SRlow-0jd, **(c)** SRlow-njc and **(d)** SRlow-njd. Z+jets is a background which is expected to have fake $E_{\mathrm{T}}^{\mathrm{miss}}$, since a jet or photon may be inaccurately reconstructed as a lepton. The largest part of fake $E_{\mathrm{T}}^{\mathrm{miss}}$, up to $E_{\mathrm{T}}^{\mathrm{miss}} < 20$ GeV ($E_{\mathrm{T}}^{\mathrm{miss}}$ significance $= 2$ corresponds to $E_{\mathrm{T}}^{\mathrm{miss}} = 20$ GeV), is mainly due to jet energy resolution and the soft unreconstructed jets that are only counted partially as track soft-term. At higher $E_{\mathrm{T}}^{\mathrm{miss}}$, above 20 GeV, the tail is due to either the missing jets (out-of-acceptance, or removed in overlap removal) or the real $E_{\mathrm{T}}^{\mathrm{miss}}$ from heavy flavour decays. More explanation of the figure is given in the caption of Figure 8.7.

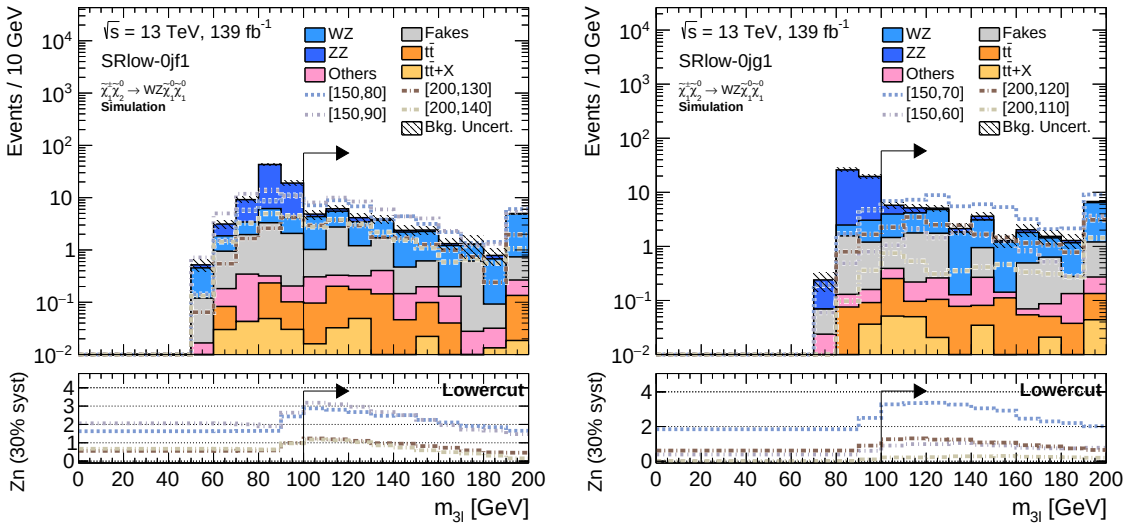

(a) (b)

Fig. 8.10: Distributions of the $m_{3\ell}$ for **(a)** SRlow-0jf1 and **(b)** SRlow-0jg1. As can be seen there is a ZZ peak around $m_{3\ell} \sim 90$ GeV. A cut is applied requiring $m_{3\ell} > 100$ GeV to remove the ZZ peak. More explanation of the figure is given in the caption of Figure 8.7.

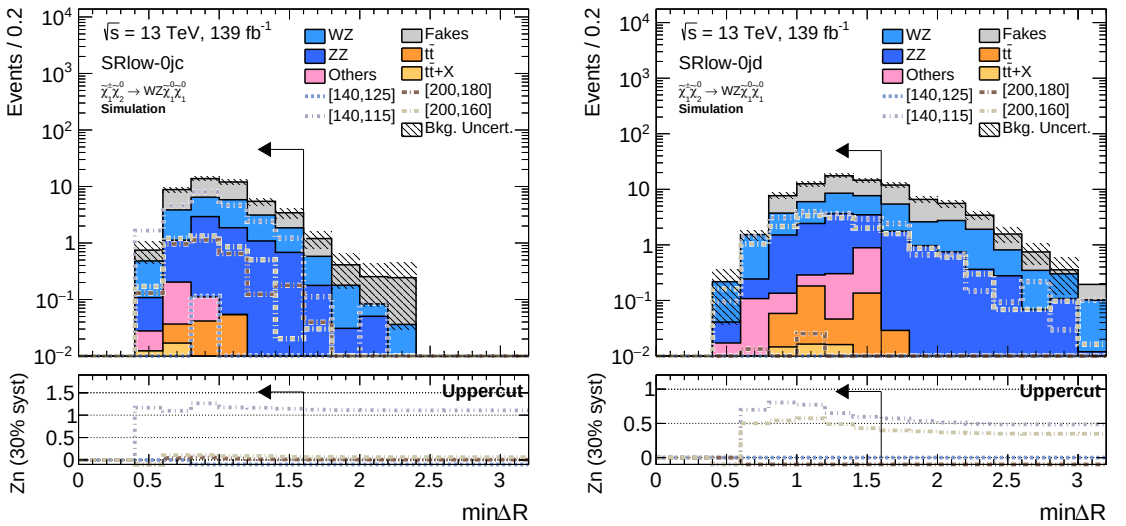

(a) (b)

Fig. 8.11: Distributions of the minΔR for **(a)** SRlow-0jc and **(b)** SRlow-0jd. For the low Δm signals the ΔR between the OSSF leptons is expected to be small. The low Δm signals correspond to the low $m_{\ell\ell}^{\text{min}}$ regions. For this reason a cut of min$\Delta R < 1.6$ is applied to the lower $m_{\ell\ell}^{\text{min}} < 30$ GeV regions. More explanation of the figure is given in the caption of Figure 8.7.

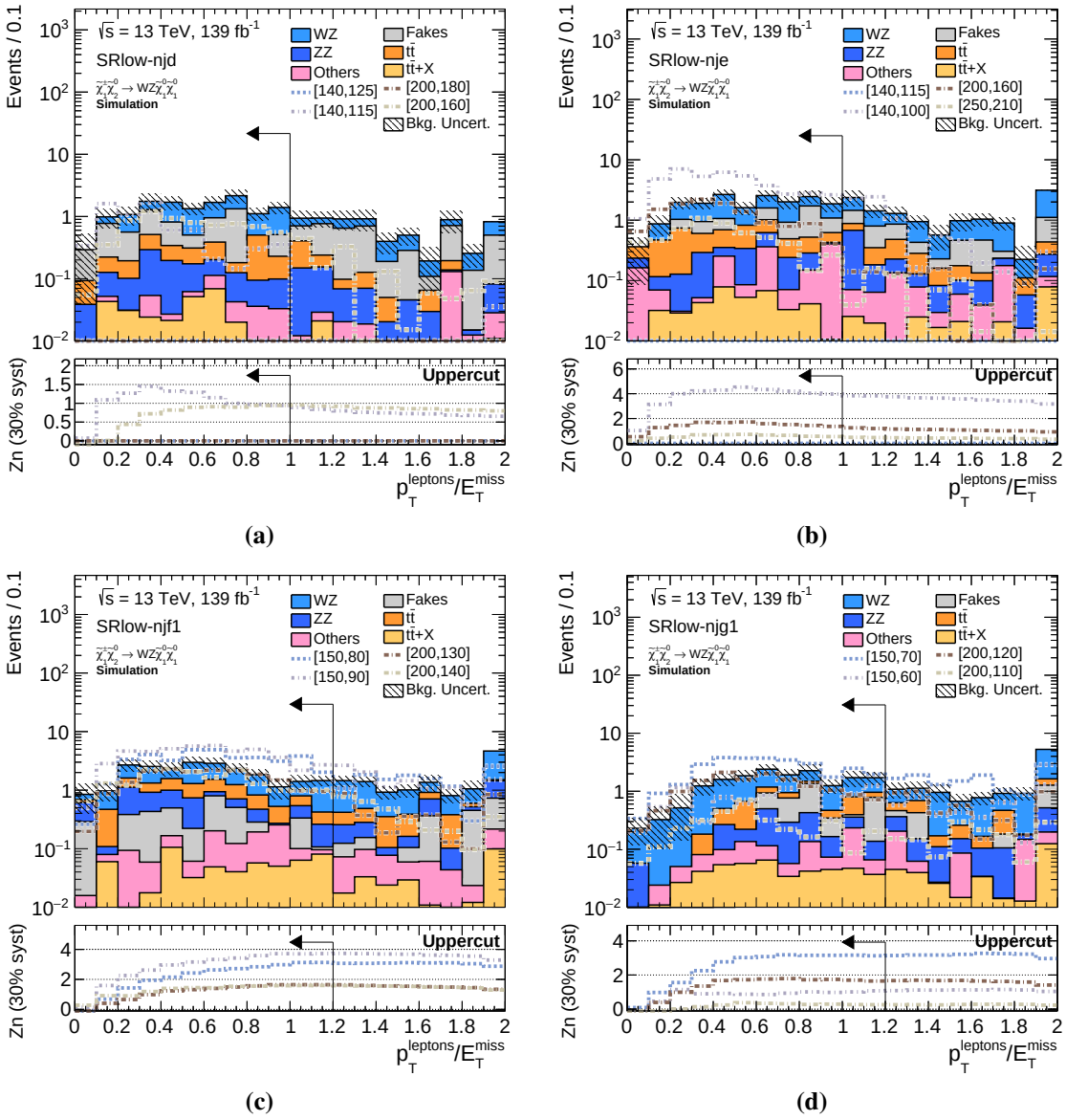

Fig. 8.12: Distributions of the $p_{\mathrm{T}}^{\mathrm{leptons}}/E_{\mathrm{T}}^{\mathrm{miss}}$ for **(a)** SRlow-njc, **(b)** SRlow-nje, **(c)** SRlow-njf1 and **(d)** SRlow-njg1. The variable $p_{\mathrm{T}}^{\mathrm{leptons}}/E_{\mathrm{T}}^{\mathrm{miss}}$ in the SRlow-0j and SRlow-nj is found to be discriminating between signal and background. More explanation of the figure is given in the caption of Figure 8.7.

significance can be calculated by quadratically adding the significances Zn from all the SRs for each signal point, such that

$$\mathrm{Zn}_{\mathrm{total}} = \sqrt{\mathrm{Zn}(\mathrm{SRlow\text{-}0jb})^2 + \ldots + \mathrm{Zn}(\mathrm{SRlow\text{-}njg2})^2}. \tag{8.2}$$

The yields and $\mathrm{Zn}_{\mathrm{total}}$ for the SRlow-0j regions are shown for a few selected Δm signal points in Table 8.9 and for the SRlow-nj regions in Table 8.10. A projection of the low $E_{\mathrm{T}}^{\mathrm{miss}}$ SRs signal significance with the assumption of a 30% flat systematic uncertainty is presented in Figure 8.13.

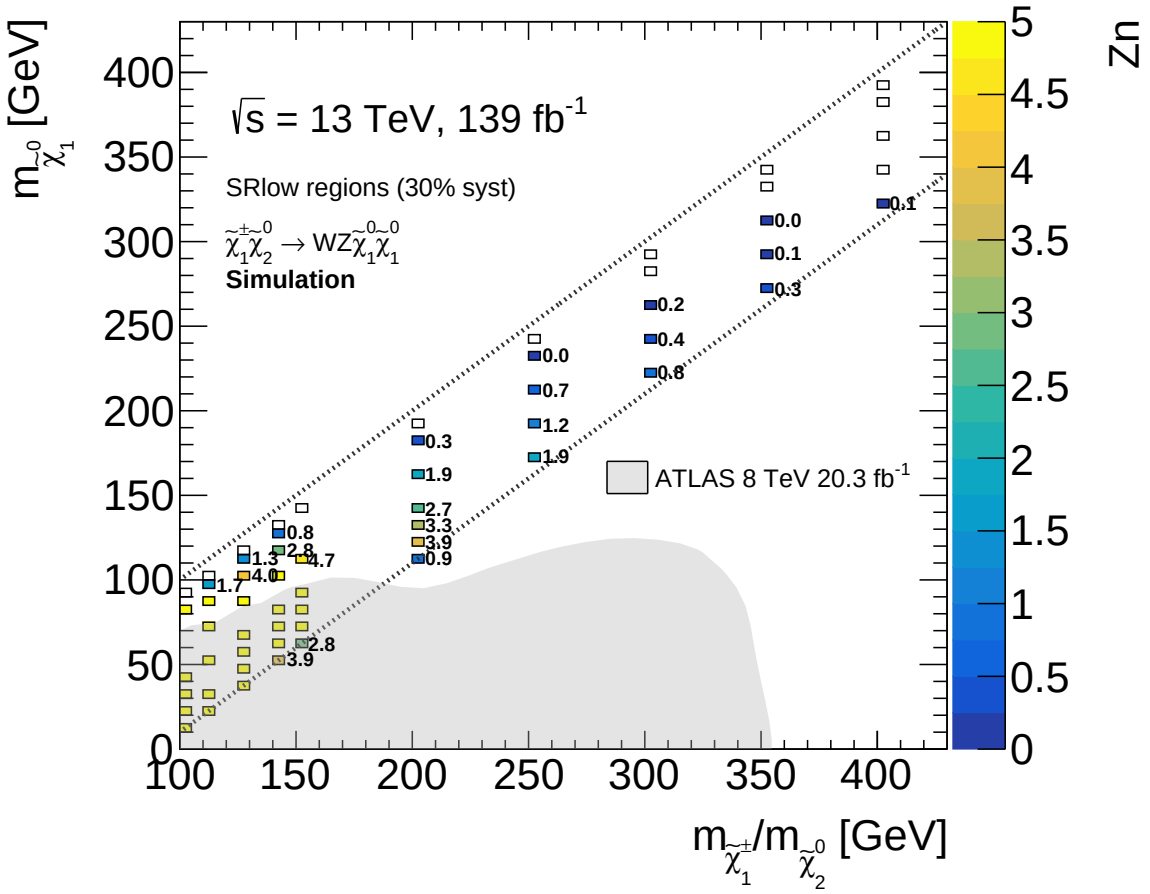

Fig. 8.13: Significance for the SRlow regions after adding the significances for the 16 individual SRlow regions in quadrature. A 30% flat systematic uncertainty is applied. The dashed line indicates the region where $m_{\tilde{\chi}_1^\pm/\tilde{\chi}_2^0} - m_{\tilde{\chi}_1^0} < m_Z$ and $m_{\tilde{\chi}_1^\pm/\tilde{\chi}_2^0} - m_{\tilde{\chi}_1^0} > 0$ GeV. The grey shade shows the previous exclusion limits with the ATLAS experiment, corresponding to the off-shell and on-shell WZ Run-1 result using 20.3 fb^{-1} at $\sqrt{s} = 8$ TeV [186].

Table 8.9: Expected yields for SRlow-0j in 139 fb^{-1}. Only statistical uncertainties are included. For the Zn calculation a 30% flat systematic uncertainty is applied.

sample	SRlow-0jb	purity	SRlow-0jc	purity	SRlow-0jd	purity	SRlow-0je	purity	SRlow-0jf1	purity	SRlow-0jf2	purity	SRlow-0jg1	purity	SRlow-0jg2	purity	
WZ	7.62 ± 0.68	24%	13.82 ± 0.90	31%	16.32 ± 0.97	30%	25.6 ± 1.4	28%	20.1 ± 1.1	62%	4.92 ± 0.54	83%	21.4 ± 1.2	62%	5.18 ± 0.48	83%	
ZZ	5.50 ± 0.80	17%	7.39 ± 0.63	17%	9.61 ± 0.89	18%	21.8 ± 1.4	24%	2.69 ± 0.74	8%	0.43 ± 0.07	7%	4.71 ± 0.65	14%	0.45 ± 0.06	7%	
Fakes	19.2 ± 1.8	59%	22.7 ± 1.9	51%	26.5 ± 2.1	49%	40.2 ± 2.7	44%	7.3 ± 1.4	23%	0.00 ± 0.38	0%	6.6 ± 1.2	19%	0.00 ± 0.15	0%	
$t\bar{t}$	0.05 ± 0.05	0%	0.11 ± 0.07	0%	0.38 ± 0.13	1%	1.09 ± 0.23	1%	0.78 ± 0.16	2%	0.08 ± 0.06	1%	0.77 ± 0.18	2%	0.36 ± 0.12	6%	
$t\bar{t}\,X$	0.03 ± 0.02	0%	0.04 ± 0.02	0%	0.05 ± 0.02	0%	0.21 ± 0.04	0%	0.17 ± 0.04	1%	0.16 ± 0.03	3%	0.23 ± 0.04	1%	0.11 ± 0.02	2%	
Others	0.02 ± 0.02	0%	0.26 ± 0.10	1%	1.31 ± 0.38	2%	1.75 ± 0.30	2%	1.20 ± 0.23	4%	0.37 ± 0.10	6%	0.97 ± 0.15	3%	0.16 ± 0.03	3%	
Total bg predicted	32.4 ± 2.1	-	44.3 ± 2.2	-	54.1 ± 2.5	-	90.6 ± 3.3	-	32.2 ± 2.0	-	5.95 ± 0.67	-	34.7 ± 1.9	-	6.27 ± 0.52	-	Total Zn
125,110 [Δm=15]	6.79 ± 0.91	21%	0.00 ± 0.00	0%	0.00 ± 0.00	0%	0.00 ± 0.00	0%	0.00 ± 0.00	0%	0.00 ± 0.00	0%	0.00 ± 0.00	0%	0.00 ± 0.00	0%	
Zn (30% syst)	0.38	-	0.00	-	0.00	-	0.00	-	0.00	-	0.00	-	0.00	-	0.00	-	**0.38**
125,100 [Δm=25]	13.3 ± 1.4	41%	29.1 ± 2.1	66%	25.5 ± 1.9	47%	0.00 ± 0.00	0%	0.00 ± 0.00	0%	0.00 ± 0.00	0%	0.00 ± 0.00	0%	0.00 ± 0.00	0%	
Zn (30% syst)	0.88	-	1.49	-	1.08	-	0.00	-	0.00	-	0.00	-	0.00	-	0.00	-	**2.04**
140,100 [Δm=40]	3.92 ± 0.64	12%	12.4 ± 1.2	28%	43.5 ± 2.2	80%	82.5 ± 3.1	91%	0.08 ± 0.08	0%	0.00 ± 0.00	0%	0.10 ± 0.10	0%	0.00 ± 0.00	0%	
Zn (30% syst)	0.14	-	0.58	-	1.84	-	2.13	-	0.00	-	0.00	-	0.00	-	0.00	-	**2.88**
150,60 [Δm=90]	0.00 ± 0.00	0%	0.27 ± 0.14	1%	0.79 ± 0.24	1%	1.97 ± 0.39	2%	6.86 ± 0.82	21%	2.51 ± 0.43	42%	14.5 ± 1.2	42%	4.54 ± 0.54	72%	
Zn (30% syst)	0.00	-	0.00	-	0.00	-	0.00	-	0.38	-	0.55	-	0.90	-	1.07	-	**1.55**

Table 8.10: Expected yields for SRlow-nj in 139 fb^{-1}. Only statistical uncertainties are included. For the Zn calculation a 30% flat systematic uncertainty is applied.

sample	SRlow-njb	purity	SRlow-njc	purity	SRlow-njd	purity	SRlow-nje	purity	SRlow-njf1	purity	SRlow-njf2	purity	SRlow-njg1	purity	SRlow-njg2	purity	
WZ	1.62 ± 0.24	47%	3.17 ± 0.35	39%	6.02 ± 0.50	45%	8.60 ± 0.53	47%	11.12 ± 0.65	47%	9.42 ± 0.58	53%	10.02 ± 0.61	59%	7.27 ± 0.49	59%	
ZZ	0.45 ± 0.08	13%	0.72 ± 0.10	9%	1.00 ± 0.11	7%	1.40 ± 0.14	8%	4.03 ± 0.78	17%	0.66 ± 0.12	4%	1.10 ± 0.52	6%	0.34 ± 0.06	3%	
Fakes	1.20 ± 0.42	35%	3.66 ± 0.78	46%	4.5 ± 1.0	33%	3.3 ± 1.1	18%	2.2 ± 1.3	9%	0.00 ± 1.2	0%	1.78 ± 1.1	10%	0.04 ± 0.80	0%	
$t\bar{t}$	0.15 ± 0.08	4%	0.28 ± 0.11	3%	1.53 ± 0.27	11%	3.31 ± 0.38	18%	4.61 ± 0.44	20%	5.69 ± 0.45	32%	3.03 ± 0.36	18%	2.86 ± 0.32	23%	
$t\bar{t}\,X$	0.03 ± 0.01	1%	0.05 ± 0.02	1%	0.27 ± 0.04	2%	0.38 ± 0.05	2%	0.56 ± 0.06	2%	0.81 ± 0.06	5%	0.46 ± 0.05	3%	0.59 ± 0.06	5%	
Others	0.01 ± 0.00	0%	0.14 ± 0.08	2%	0.18 ± 0.05	1%	1.26 ± 0.34	7%	0.89 ± 0.20	4%	1.27 ± 0.11	7%	0.61 ± 0.15	4%	1.29 ± 0.29	10%	
Total bg predicted	3.46 ± 0.49	-	8.02 ± 0.87	-	13.5 ± 1.2	-	18.2 ± 1.4	-	23.4 ± 1.7	-	17.9 ± 1.4	-	17.0 ± 1.4	-	12.4 ± 1.0	-	Total Zn
125,110 [Δm=15]	3.59 ± 0.80	104%	0.26 ± 0.15	3%	0.00 ± 0.00	0%	0.00 ± 0.00	0%	0.00 ± 0.00	0%	0.00 ± 0.00	0%	0.00 ± 0.00	0%	0.00 ± 0.00	0%	
Zn (30% syst)	1.22	-	0.00	-	0.00	-	0.00	-	0.00	-	0.00	-	0.00	-	0.00	-	**1.22**
125,100 [Δm=25]	4.76 ± 0.92	138%	12.3 ± 1.5	154%	13.9 ± 1.7	103%	0.00 ± 0.00	0%	0.00 ± 0.00	0%	0.00 ± 0.00	0%	0.00 ± 0.00	0%	0.00 ± 0.00	0%	
Zn (30% syst)	1.61	-	2.39	-	1.90	-	0.00	-	0.00	-	0.00	-	0.00	-	0.00	-	**3.45**
140,100 [Δm=40]	2.48 ± 0.61	72%	7.33 ± 0.99	91%	21.9 ± 1.9	163%	41.7 ± 2.5	229%	0.30 ± 0.18	1%	0.00 ± 0.00	0%	0.00 ± 0.00	0%	0.00 ± 0.00	0%	
Zn (30% syst)	0.81	-	1.47	-	2.84	-	3.97	-	0.00	-	0.00	-	0.00	-	0.00	-	**5.17**
150,60 [Δm=90]	0.00 ± 0.00	0%	0.33 ± 0.07	4%	0.12 ± 0.09	1%	0.90 ± 0.42	5%	4.21 ± 0.79	18%	9.5 ± 1.0	53%	9.40 ± 0.91	55%	12.3 ± 1.1	99%	
Zn (30% syst)	0.00	-	0.00	-	0.00	-	0.00	-	0.27	-	1.04	-	1.08	-	1.80	-	**2.35**

8.4.2 SRhigh signal regions

In analogy with the SRlow, the SRhigh regions are optimised for the best Zn. The SRhigh regions are optimised in a similar way since they share a common background composition, where the WZ and $t\bar{t}$ background are dominant. There are two main changes with respect to the global strategy of defining the SRs described in Section 8.4:

- The region SRhigh-0ja, where $m_{\ell\ell}^{\text{min}} \in [0, 12]$, is dropped due to backgrounds from the J/ψ and Υ resonances. In SRhigh-nja this background is negligible so the region is maintained.

- The regions SRhigh-0jf and SRhigh-0jg are split into low $m_{\text{T}}^{\text{minmll}} < 60$ GeV regions, SRhigh-0jf1 and SRhigh-0jg1, and high $m_{\text{T}}^{\text{minmll}} > 90$ GeV regions, SRhigh-0jf2 and SRhigh-0jg2. The SRhigh-nj regions are inclusive in $m_{\text{T}}^{\text{minmll}}$.

The cuts for the high $E_{\text{T}}^{\text{miss}}$ SRs are summarised in Table 8.11, for all the $m_{\ell\ell}^{\text{min}}$ regions of both SRhigh-0j and SRhigh-nj.

- A cut on $m_{\text{T}}^{\text{minmll}}$ is applied to reduce on-shell WZ background in the SRhigh-0j regions. The cut on $m_{\text{T}}^{\text{minmll}}$ is not applied in the SRhigh-nj regions as it was found to be ineffective at reducing the WZ background. As shown in Figure 8.14 for SRhigh-0j, the cuts are applied on $m_{\text{T}}^{\text{minmll}}$ in such a way to maximally increase the Zn.

Table 8.11: Signal region definitions for SRhigh-0j and SRhigh-nj. With SRhigh-0j corresponding to $N_{\text{jets}}^{30\text{ GeV}} = 0$ and $E_{\text{T}}^{\text{miss}} > 50$ GeV and SRhigh-nj corresponding to $N_{\text{jets}}^{30\text{ GeV}} \geq 1$ and $E_{\text{T}}^{\text{miss}} > 200$ GeV.

	$m_{\ell\ell}^{\text{min}}$ [GeV]	$m_{\ell\ell}^{\text{max}}$ [GeV]	m_{T2}^{100} [GeV]	lepton p_{T} [GeV]	$m_{\text{T}}^{\text{minmll}}$ [GeV]	$E_{\text{T}}^{\text{miss}}$ significance	$p_{\text{T}}^{\text{leptons}}/E_{\text{T}}^{\text{miss}}$
SRhigh-0jb	[12,15]	<75	<115	>25,15,10	<50	>3	-
SRhigh-0jc	[15,20]	<75	<120	>25,15,10	<50	>3	-
SRhigh-0jd	[20,30]	<75	<130	>25,15,10	<60	>3	-
SRhigh-0je	[30,40]	<75	<140	>25,15,10	<60	>3	-
SRhigh-0jf1	[40,60]	<75	<160	>25,15,10	<70	>3	-
SRhigh-0jf2	[40,60]	<75	<160	>25,15,10	>90	>3	-
SRhigh-0jg1	[60,75]	<75	<175	>25,15,10	<70	>3	-
SRhigh-0jg2	[60,75]	<75	<175	>25,15,10	>90	>3	-
SRhigh-nja	[1,12]	<75	<110	all 3 e(μ)>4.5(3.0)	-	>3	<0.2
SRhigh-njb	[12,15]	<75	<115	all 3 e(μ)>4.5(3.0)	-	>3	<0.2
SRhigh-njc	[15,20]	<75	<120	all 3 e(μ)>4.5(3.0)	-	>3	<0.3
SRhigh-njd	[20,30]	<75	<130	all 3 e(μ)>4.5(3.0)	-	>3	<0.3
SRhigh-nje	[30,40]	<75	<140	all 3 e(μ)>4.5(3.0)	-	>3	<0.3
SRhigh-njf	[40,60]	<75	<160	all 3 e(μ)>4.5(3.0)	-	>3	<1.0
SRhigh-njg	[60,75]	<75	<175	all 3 e(μ)>4.5(3.0)	-	>3	<1.0

- A cut on $p_{\mathrm{T}}^{\mathrm{leptons}}/E_{\mathrm{T}}^{\mathrm{miss}}$ is applied to select the signal. The variable provides signal-to-background discrimination which improves for smaller Δm in the signals. The cuts placed on $p_{\mathrm{T}}^{\mathrm{leptons}}/E_{\mathrm{T}}^{\mathrm{miss}}$ for SRhigh-nj are shown in Figure 8.15.

- A cut on m_{T2}^{100} as described in Section 6.3 is applied to select the signal. As shown in Figure 8.6(b) m_{T2}^{100} gives a sharp cut-off for the supersymmetry signals. The kinematic edge from m_{T2}^{100} can be optimised by choosing a corresponding cut in each $m_{\ell\ell}^{\mathrm{min}}$ bin, creating a double kinematic edge. This variable is shown for each $m_{\ell\ell}^{\mathrm{min}}$ bin for SRhigh-nj in Figure 8.16.

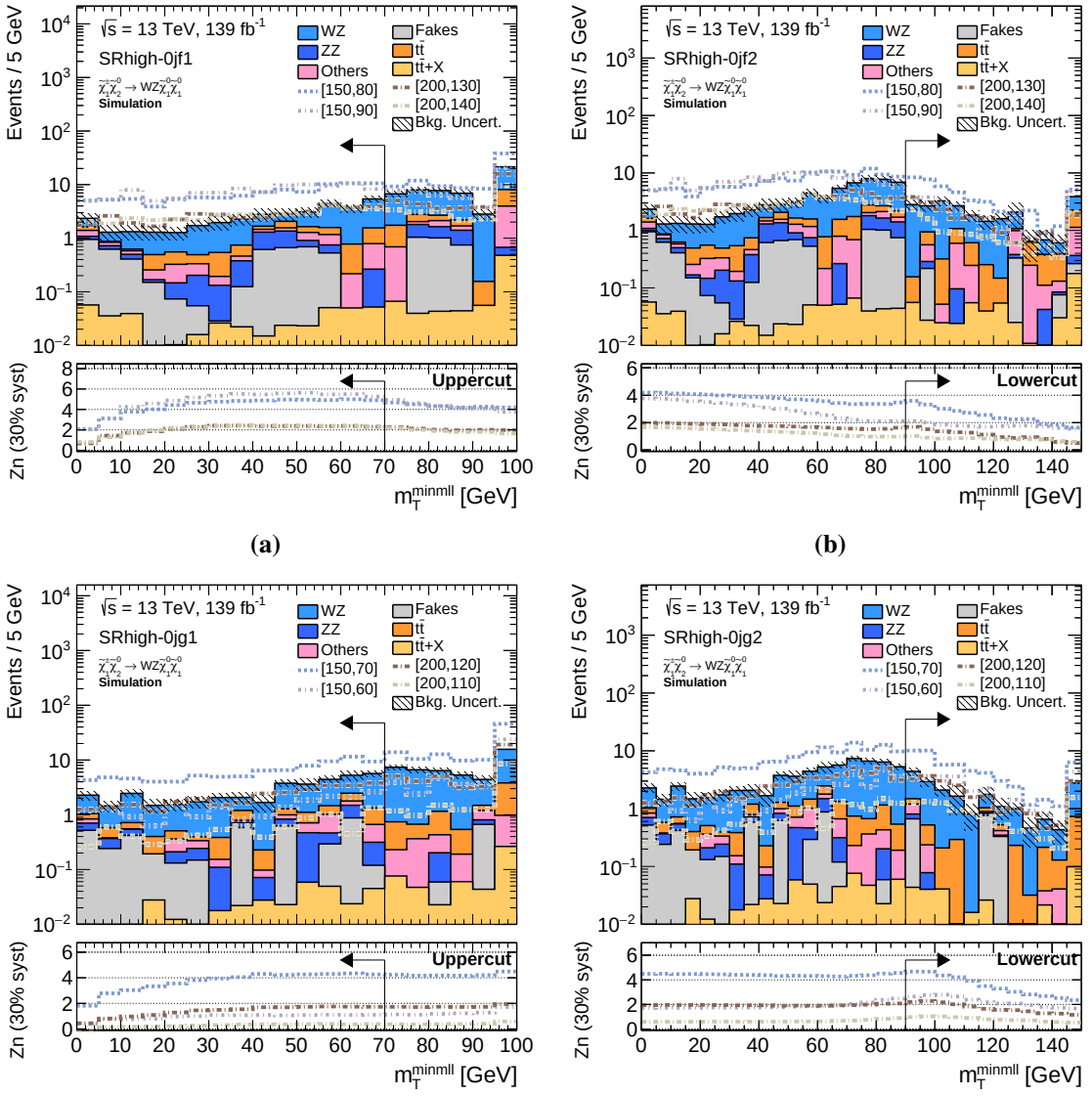

Fig. 8.14: Distributions of the $m_{\mathrm{T}}^{\mathrm{minmll}}$ for **(a)** SRhigh-0jf1, **(b)** SRhigh-0jf2, **(c)** SRhigh-0jg1 and **(d)** SRhigh-0jg2. The split into low $m_{\mathrm{T}}^{\mathrm{minmll}} < 60$ GeV regions, SRhigh-0jf1 and SRhigh-0jg1, and high $m_{\mathrm{T}}^{\mathrm{minmll}} > 90$ GeV regions, SRhigh-0jf2 and SRhigh-0jg2 is shown. More explanation of the figure is given in the caption of Figure 8.7.

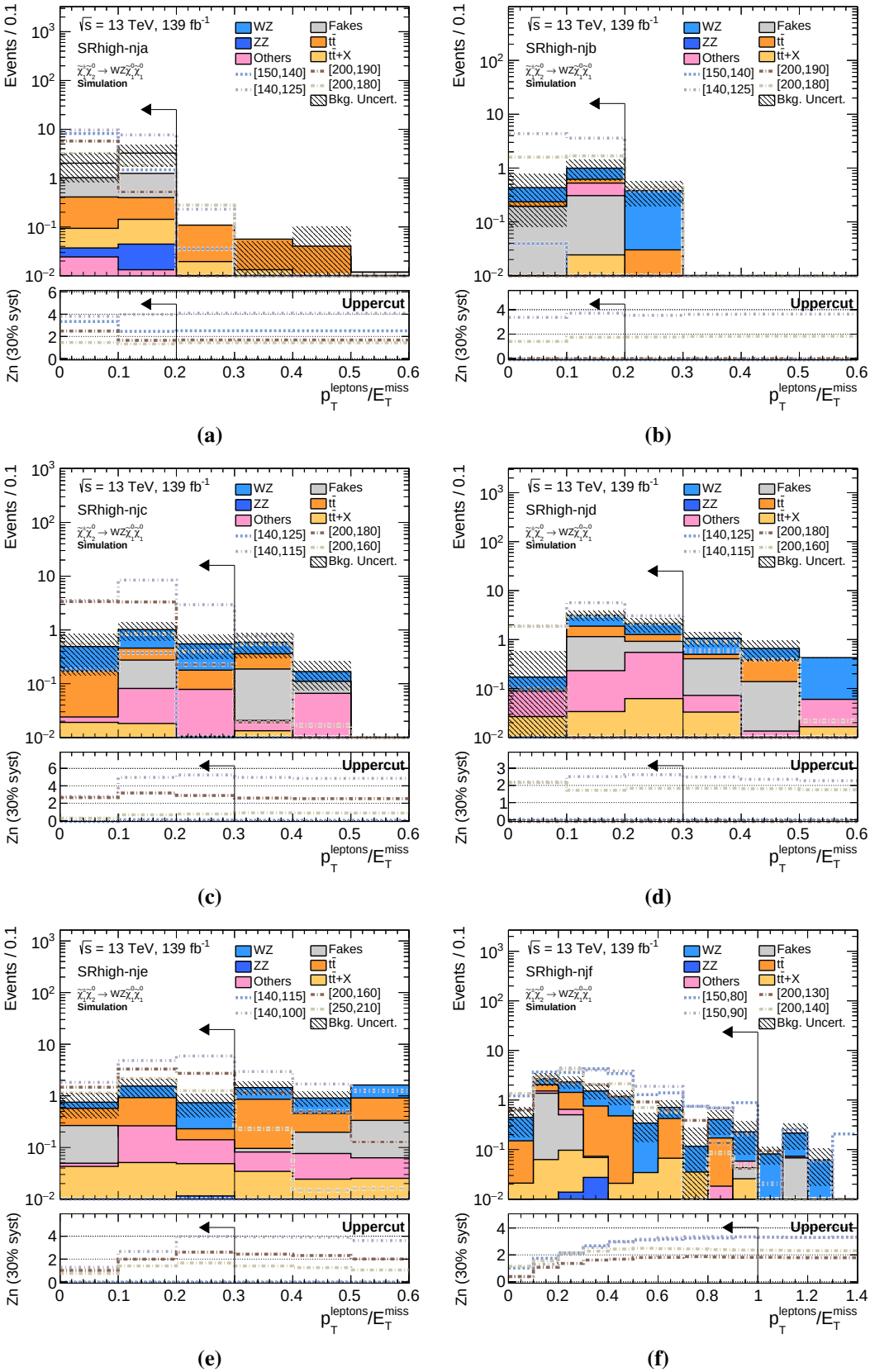

Fig. 8.15: Distributions of the $p_{\mathrm{T}}^{\mathrm{leptons}}/E_{\mathrm{T}}^{\mathrm{miss}}$ for **(a)** SRhigh-nja, **(b)** SRhigh-njb, **(c)** SRhigh-njc, **(d)** SRhigh-njd, **(e)** SRhigh-nje and **(f)** SRhigh-njf. In the SRhigh-nj region a cut on $p_{\mathrm{T}}^{\mathrm{leptons}}/E_{\mathrm{T}}^{\mathrm{miss}}$ is shown to have discrimination between signal and background. More explanation of the figure is given in the caption of Figure 8.7.

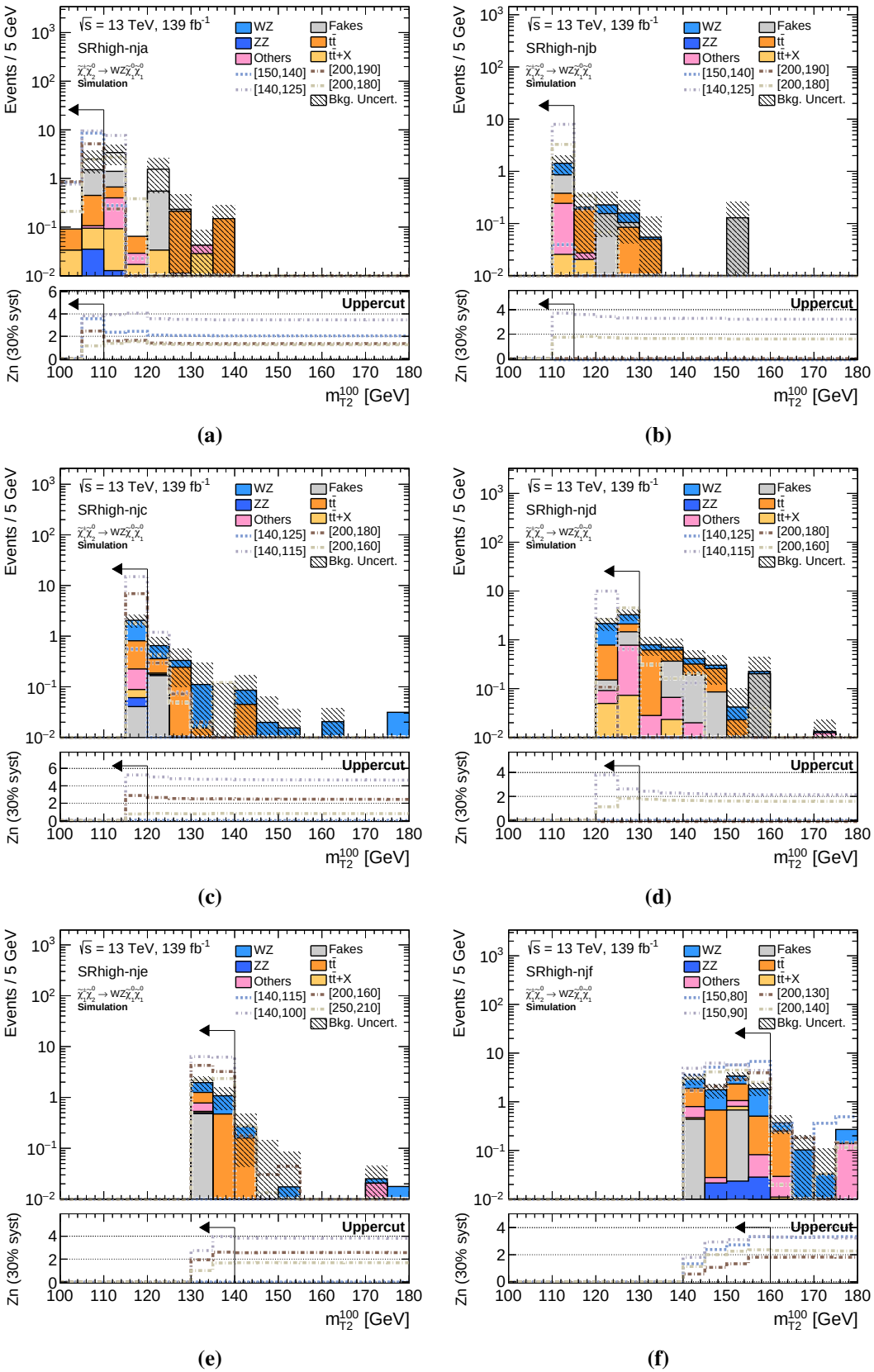

Fig. 8.16: Distributions of the m_{T2}^{100} for **(a)** SRhigh-nja, **(b)** SRhigh-njb, **(c)** SRhigh-njc, **(d)** SRhigh-njd, **(e)** SRhigh-nje and **(f)** SRhigh-njf. The kinematic edge for the signals from m_{T2}^{100} can be seen. More explanation of the figure is given in the caption of Figure 8.7.

Again the combination of the 15 SRhigh individual SRs will determine the total significance of the search in the higher $E_{\mathrm{T}}^{\mathrm{miss}}$ region, such that

$$\mathrm{Zn}_{\mathrm{total}} = \sqrt{\mathrm{Zn}(\text{SRhigh-0jb})^2 + \ldots + \mathrm{Zn}(\text{SRhigh-njg})^2}. \tag{8.3}$$

The yields and $\mathrm{Zn}_{\mathrm{total}}$ for the SRhigh-0j regions are captured for a few selected Δm signal points in Table 8.12 and for the SRhigh-nj regions in Table 8.13. A projection of the high $E_{\mathrm{T}}^{\mathrm{miss}}$ SRs signal significance with the assumption of a 30% flat systematic uncertainty is shown in Figure 8.17.

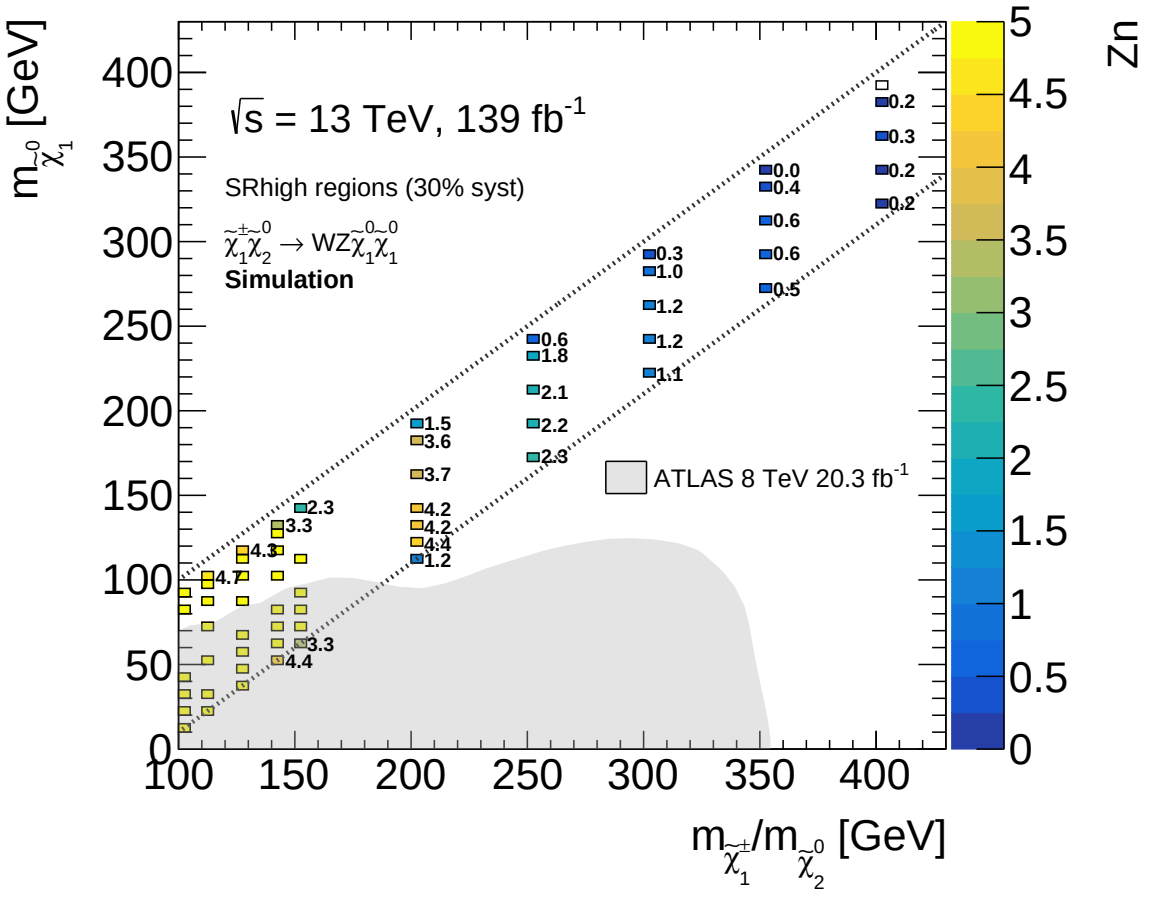

Fig. 8.17: Significance for the SRhigh regions after adding all the significances for the 15 regions in SRhigh regions in quadrature. A 30% flat systematic uncertainty is applied. The dashed line indicates the region where $m_{\tilde{\chi}_1^\pm/\tilde{\chi}_2^0} - m_{\tilde{\chi}_1^0} < m_Z$ and $m_{\tilde{\chi}_1^\pm/\tilde{\chi}_2^0} - m_{\tilde{\chi}_1^0} > 0$ GeV. The grey shade shows the previous exclusion limits with the ATLAS experiment, corresponding to the off-shell and on-shell WZ Run-1 result using 20.3 fb^{-1} at $\sqrt{s} = 8$ TeV [186].

Table 8.12: Expected yields for SRhigh-0j in 139 fb^{-1}. Only statistical uncertainties are included. For the Zn calculation a 30% flat systematic uncertainty is applied.

sample	SRhigh-0jb	purity	SRhigh-0jc	purity	SRhigh-0jd	purity	SRhigh-0je	purity	SRhigh-0jf1	purity	SRhigh-0jf2	purity	SRhigh-0jg1	purity	SRhigh-0jg2	purity	
WZ	0.20 ± 0.13	13%	1.47 ± 0.33	34%	6.00 ± 0.65	43%	6.09 ± 0.68	53%	20.5 ± 1.3	57%	16.0 ± 1.4	63%	26.4 ± 1.4	67%	14.8 ± 1.3	72%	
ZZ	0.47 ± 0.34	30%	0.31 ± 0.08	7%	1.77 ± 0.45	13%	0.89 ± 0.11	8%	3.15 ± 0.57	9%	0.95 ± 0.11	4%	2.99 ± 0.70	8%	0.58 ± 0.09	3%	
Fakes	0.81 ± 0.29	52%	1.73 ± 0.42	41%	4.45 ± 0.78	32%	1.08 ± 0.70	9%	4.3 ± 1.2	12%	0.00 ± 0.92	0%	3.4 ± 1.1	9%	0.00 ± 0.79	0%	
$t\bar{t}$	0.05 ± 0.05	3%	0.45 ± 0.14	11%	0.64 ± 0.15	5%	1.79 ± 0.27	15%	4.37 ± 0.40	12%	4.42 ± 0.42	17%	4.26 ± 0.41	11%	3.12 ± 0.34	15%	
$t\bar{t}\,X$	0.00 ± 0.00	0%	0.01 ± 0.01	0%	0.08 ± 0.02	1%	0.18 ± 0.03	2%	0.43 ± 0.06	1%	0.54 ± 0.06	2%	0.33 ± 0.05	1%	0.31 ± 0.05	1%	
Others	0.01 ± 0.01	1%	0.30 ± 0.16	7%	1.06 ± 0.25	8%	1.52 ± 0.21	13%	2.96 ± 0.34	8%	3.60 ± 0.35	14%	2.17 ± 0.39	6%	1.74 ± 0.24	8%	
Total bg predicted	1.55 ± 0.47	-	4.27 ± 0.58	-	14.0 ± 1.2	-	11.5 ± 1.0	-	35.8 ± 2.0	-	25.5 ± 1.7	-	39.5 ± 2.0	-	20.6 ± 1.5	-	Total Zn
125,110 [Δm=15]	0.53 ± 0.24	34%	0.04 ± 0.04	1%	0.00 ± 0.00	0%	0.00 ± 0.00	0%	0.00 ± 0.00	0%	0.00 ± 0.00	0%	0.00 ± 0.00	0%	0.00 ± 0.00	0%	
Zn (30% syst)	0.09	-	0.00	-	0.00	-	0.00	-	0.00	-	0.00	-	0.00	-	0.00	-	**0.09**
125,100 [Δm=25]	2.07 ± 0.64	134%	9.5 ± 1.3	223%	5.82 ± 0.85	42%	0.00 ± 0.00	0%	0.00 ± 0.00	0%	0.00 ± 0.00	0%	0.00 ± 0.00	0%	0.00 ± 0.00	0%	
Zn (30% syst)	1.05	-	2.71	-	0.75	-	0.00	-	0.00	-	0.00	-	0.00	-	0.00	-	**3.00**
140,100 [Δm=40]	1.29 ± 0.39	84%	6.14 ± 0.90	144%	33.5 ± 1.9	239%	35.1 ± 2.0	304%	0.66 ± 0.30	2%	0.00 ± 0.00	0%	0.00 ± 0.00	0%	0.00 ± 0.00	0%	
Zn (30% syst)	0.60	-	1.83	-	3.93	-	4.56	-	0.00	-	0.00	-	0.00	-	0.00	-	**6.31**
150,60 [Δm=90]	0.12 ± 0.12	8%	0.19 ± 0.10	4%	1.90 ± 0.44	14%	2.85 ± 0.51	25%	14.3 ± 1.1	40%	13.9 ± 1.2	54%	19.6 ± 1.1	50%	27.5 ± 1.5	134%	
Zn (30% syst)	0.00	-	0.00	-	0.12	-	0.35	-	0.86	-	1.14	-	1.11	-	2.60	-	**3.19**

Table 8.13: Expected yields for SRhigh-nj in 139 fb^{-1}. Only statistical uncertainties are included. For the Zn calculation a 30% flat systematic uncertainty is applied.

sample	SRhigh-nja	purity	SRhigh-njb	purity	SRhigh-njc	purity	SRhigh-njd	purity	SRhigh-nje	purity	SRhigh-njf	purity	SRhigh-njg	purity	
WZ	3.76 ± 0.28	62%	0.57 ± 0.09	40%	1.25 ± 0.11	61%	2.52 ± 0.20	47%	1.31 ± 0.13	43%	4.54 ± 0.18	46%	3.65 ± 0.16	54%	
ZZ	0.04 ± 0.01	1%	0.01 ± 0.00	1%	0.02 ± 0.00	1%	0.01 ± 0.01	0%	0.03 ± 0.01	1%	0.08 ± 0.02	1%	0.05 ± 0.01	1%	
Fakes	1.46 ± 0.81	24%	0.48 ± 0.48	33%	0.04 ± 0.49	2%	0.74 ± 0.81	14%	0.05 ± 0.65	2%	0.6 ± 1.0	6%	0.00 ± 0.45	0%	
$t\bar{t}$	0.57 ± 0.28	9%	0.14 ± 0.09	10%	0.59 ± 0.27	28%	1.28 ± 0.38	24%	1.23 ± 0.34	40%	3.43 ± 0.43	35%	2.54 ± 0.45	37%	
$t\bar{t}\,X$	0.16 ± 0.04	3%	0.02 ± 0.01	1%	0.03 ± 0.02	1%	0.11 ± 0.03	2%	0.11 ± 0.03	4%	0.35 ± 0.04	4%	0.22 ± 0.03	3%	
Others	0.04 ± 0.02	1%	0.22 ± 0.19	15%	0.14 ± 0.05	7%	0.74 ± 0.48	14%	0.31 ± 0.12	10%	0.91 ± 0.13	9%	0.33 ± 0.04	5%	
Total bg predicted	6.03 ± 0.90	-	1.43 ± 0.53	-	2.06 ± 0.57	-	5.4 ± 1.0	-	3.04 ± 0.76	-	9.9 ± 1.1	-	6.79 ± 0.66	-	Total Zn
125,110 [Δm=15]	17.9 ± 1.6	297%	9.1 ± 1.2	637%	0.44 ± 0.24	21%	0.00 ± 0.00	0%	0.00 ± 0.00	0%	0.00 ± 0.00	0%	0.00 ± 0.00	0%	
Zn (30% syst)	3.82	-	4.12	-	0.00	-	0.00	-	0.00	-	0.00	-	0.00	-	**5.61**
125,100 [Δm=25]	5.6 ± 1.2	92%	5.9 ± 1.1	414%	14.9 ± 1.6	724%	13.8 ± 1.7	256%	0.00 ± 0.00	0%	0.00 ± 0.00	0%	0.00 ± 0.00	0%	
Zn (30% syst)	1.35	-	2.93	-	5.23	-	3.28	-	0.00	-	0.00	-	0.00	-	**6.96**
140,100 [Δm=40]	1.21 ± 0.45	20%	1.13 ± 0.40	79%	3.70 ± 0.81	180%	11.6 ± 1.3	214%	12.6 ± 1.4	414%	0.11 ± 0.04	1%	0.16 ± 0.11	2%	
Zn (30% syst)	0.16	-	0.52	-	1.65	-	2.83	-	3.97	-	0.00	-	0.00	-	**5.17**
150,60 [Δm=90]	0.00 ± 0.00	0%	0.00 ± 0.00	0%	0.00 ± 0.00	0%	0.28 ± 0.15	5%	0.66 ± 0.34	22%	2.43 ± 0.42	24%	3.17 ± 0.52	47%	
Zn (30% syst)	0.00	-	0.00	-	0.00	-	0.00	-	0.07	-	0.33	-	0.67	-	**0.75**

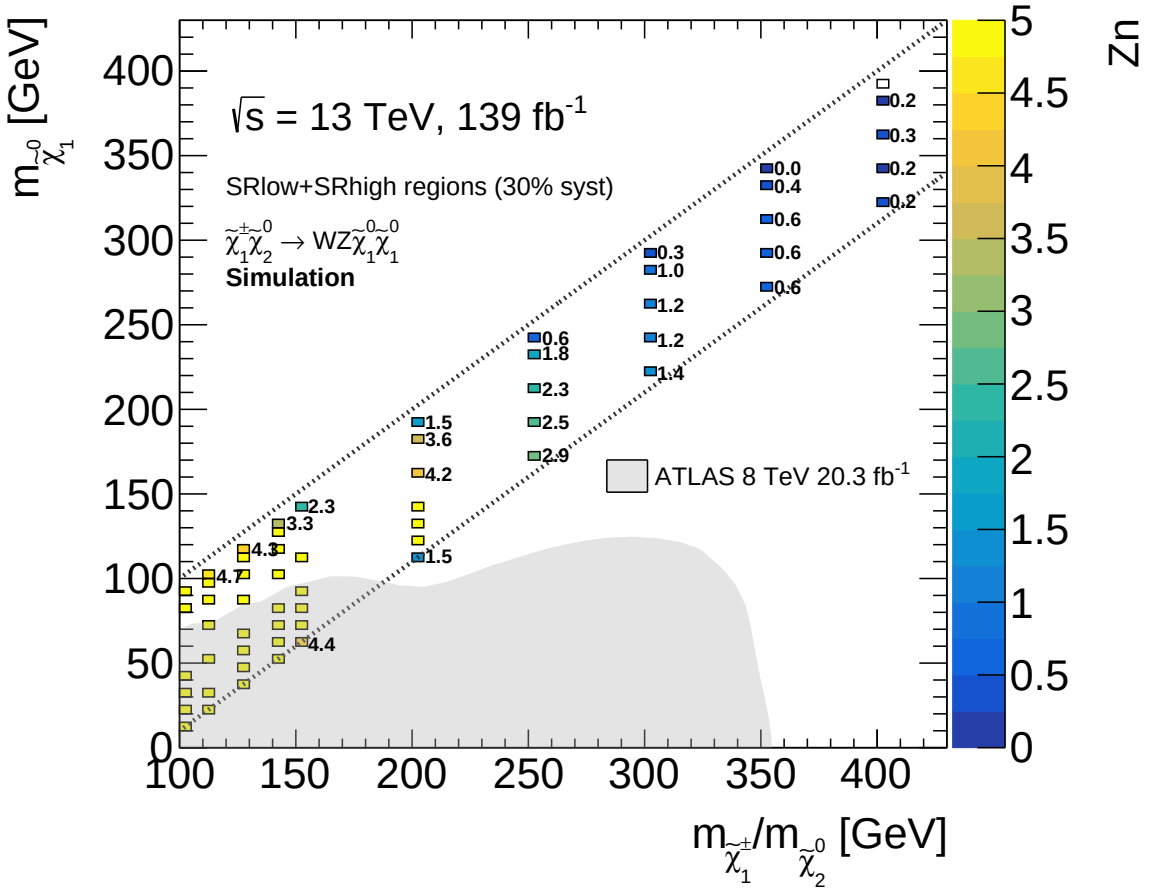

Fig. 8.18: Significance for the SRlow and SRhigh regions after adding the significances for the 16 SRlow regions and 15 SRhigh regions in quadrature. A 30% flat systematic uncertainty is applied. The dashed line indicates the region where $m_{\tilde{\chi}_1^\pm/\tilde{\chi}_2^0} - m_{\tilde{\chi}_1^0} < m_Z$ and $m_{\tilde{\chi}_1^\pm/\tilde{\chi}_2^0} - m_{\tilde{\chi}_1^0} > 0$ GeV. The grey shade shows the previous exclusion limits with the ATLAS experiment, corresponding to the off-shell and on-shell WZ Run-1 result using 20.3 fb^{-1} at $\sqrt{s} = 8$ TeV [186].

8.4.3 Combination of the SRlow and SRhigh signal regions

After having illustrated the significance for for SRlow in Figure 8.13 and for SRhigh in Figure 8.17 individually, an estimate of the total expected significance from both sets of SRs can be calculated. Again this is done by quadratically adding the significances Zn from all the SRs for each signal point, such that

$$\mathrm{Zn}_{\mathrm{total}} = \sqrt{\mathrm{Zn}(\text{SRlow-0jb})^2 + ... + \mathrm{Zn}(\text{SRlow-njg2})^2 + \text{SRhigh-0jb})^2 + ... + \mathrm{Zn}(\text{SRhigh-njg2})^2}. \tag{8.4}$$

A projection of the combination of the SRlow and SRhigh SRs signal significance with the assumption of a 30% flat systematic uncertainty is presented in Figure 8.18.

8.5 Model-independent discovery regions

The SRs described in Section 8.4 have been optimised for the studied supersymmetry model points. By optimising on the selected model points the search is made model dependent. However, besides the selected model there may be many more beyond-the-Standard-Model (BSM) theories that could provide a signal. There is a possibility that these other BSM theories show similar signatures in the detector as the Feynman diagram shown in Figure 6.1 in the studied region of $\tilde{\chi}_1^{\pm}/\tilde{\chi}_2^0$ and $\tilde{\chi}_1^0$ masses. In order to obtain more sensitivity to different BSM models, model-independent SRs have been defined from a combination of the SRs defined in the previous section. At the same time it has been verified that with the model-independent discovery regions it is still possible to discover the targeted simplified supersymmetry models.

A BSM signal different from the studied supersymmetry models might have a different signal width or shape in $m_{\ell\ell}^{\text{min}}$. In the model-independent case it is thus unknown how broad a signal will be in $m_{\ell\ell}^{\text{min}}$. For this reason a combination of the different $m_{\ell\ell}^{\text{min}}$ regions has been made to give sensitivity to more BSM scenarios. The existing $m_{\ell\ell}^{\text{min}}$ regions have been combined to recover sensitivity for the other BSM signals that might be spread over multiple neighbouring $m_{\ell\ell}^{\text{min}}$ regions. The choice is made for a combination of existing SRs and not to tighten or loosen the kinematic selections described in Section 8.4.

The strategy for the combination of existing signal regions to form discovery regions is described in Table 8.14. A few choices are made when combining the existing SRs:

- The $m_{\ell\ell}^{\text{min}}$ shape of the signal is not expected to depend on $N_{\text{jets}}^{30\,\text{GeV}}$, for this reason the 0j regions have been added to their respective nj regions.
- SRlow and SRhigh regions are kept separate in the low $m_{\ell\ell}^{\text{min}} < 20$ GeV regions, but are added together for the $m_{\ell\ell}^{\text{min}} > 20$ GeV regions. This is done because the sensitivity for the targeted simplified supersymmetry models decreases when adding the SRlow and SRhigh regions for low $m_{\ell\ell}^{\text{min}} < 20$ GeV.
- The best sensitivity to models with a small Δm is from the SRhigh-nj regions where $m_{\ell\ell}^{\text{min}} < 20$ GeV; as a consequence these regions are kept.

The yields for the discovery regions are shown in Table 8.15 and 8.16.

Table 8.14: Model-independent discovery regions definitions.

Name	$m_{\ell\ell}^{\min}$	Regions
disc-SRhigh-nJa	[1,12]	SRhigh-nja
disc-SRhigh-nJb	[12,15]	SRhigh-njb
disc-SRhigh-nJc1	[1,20]	SRhigh-nja, SRhigh-njb, SRhigh-njc
disc-SRhigh-nJc2	[15,20]	SRhigh-njc
disc-SRlow-b	[12,15]	SRlow-(0jb,njb)
disc-SRhigh-b	[12,15]	SRhigh-(0jb,njb)
disc-SRlow-c	[12,20]	SRlow-(0jb,njb,0jc,njc)
disc-SRhigh-c	[12,20]	SRhigh-(0jb,njb,0jc,njc)
disc-SR-d	[12,30]	SRlow-(0jb,njb,0jc,njc,0jd,njd), SRhigh-(0jb,njb,0jc,njc,0jd,njd)
disc-SR-e1	[12,40]	SRlow-(0jb,njb,0jc,njc,0jd,njd,0je,nje), SRhigh-(0jb,njb,0jc,njc,0jd,njd,0je,nje)
disc-SR-e2	[20,40]	SRlow-(0jc,njc,0jd,njd,0je,nje), SRhigh-(0jc,njc,0jd,njd,0je,nje)
disc-SR-f1	[12,60]	SRlow-(0jb,njb,0jc,njc,0jd,njd,0je,nje,0jf1,njf1,0jf2,njf2), SRhigh-(0jb,njb,0jc,njc,0jd,njd,0je,nje,0jf1,0jf2,njf)
disc-SR-f2	[30,60]	SRlow-(0je,nje,0jf1,njf1,0jf2,njf2), SRhigh-(0je,nje,0jf1,0jf2,njf)
disc-SR-g1	[12,75]	SRlow-(0jb,njb,0jc,njc,0jd,njd,0je,nje,0jf1,njf1,0jf2,njf2,0jg1,njg1,0jg2,njg2), SRhigh-(0jb,njb,0jc,njc,0jd,njd,0je,nje,0jf1,0jf2,njf,0jg1,0jg2,njg)
disc-SR-g2	[30,75]	SRlow-(0je,nje,0jf1,njf1,0jf2,njf2,0jg1,njg1,0jg2,njg2), SRhigh-(0je,nje,0jf1,0jf2,njf,0jg1,0jg2,njg)
disc-SR-g3	[40,75]	SRlow-(0jf1,njf1,0jf2,njf2,0jg1,njg1,0jg2,njg2), SRhigh-(0jf1,0jf2,njf,0jg1,0jg2,njg)
disc-SR-g4	[60,75]	SRlow-(0jg1,njg1,0jg2,njg2), SRhigh-(0jg1,0jg2,njg)

Table 8.15: Expected yields for the model-independent discovery regions in 139 fb^{-1}. Only statistical uncertainties are included. For the Zn calculation a 30% flat systematic uncertainty is applied.

sample	disc-SRhigh-nJa	purity	disc-SRhigh-nJb	purity	disc-SRhigh-nJc1	purity	disc-SRhigh-nJc2	purity	disc-SRlow-b	purity	disc-SRhigh-b	purity	disc-SRlow-c	purity	disc-SRhigh-c	purity
WZ	3.71 ± 0.27	62%	0.56 ± 0.09	40%	5.53 ± 0.31	58%	1.26 ± 0.12	61%	9.30 ± 0.73	26%	0.76 ± 0.16	26%	26.7 ± 1.2	30%	3.54 ± 0.39	38%
ZZ	0.05 ± 0.01	1%	0.01 ± 0.00	1%	0.08 ± 0.01	1%	0.02 ± 0.01	1%	6.32 ± 0.85	17%	0.49 ± 0.35	17%	14.8 ± 1.1	17%	0.83 ± 0.36	9%
Fakes	1.43 ± 0.81	24%	0.47 ± 0.48	33%	1.9 ± 1.1	20%	0.01 ± 0.49	0%	20.3 ± 1.8	56%	1.27 ± 0.56	43%	46.5 ± 2.8	52%	2.99 ± 0.86	32%
$t\bar{t}$	0.60 ± 0.29	10%	0.14 ± 0.09	10%	1.34 ± 0.41	14%	0.60 ± 0.27	29%	0.22 ± 0.10	1%	0.19 ± 0.11	6%	0.63 ± 0.17	1%	1.26 ± 0.33	13%
$t\bar{t}X$	0.16 ± 0.04	3%	0.02 ± 0.01	1%	0.20 ± 0.05	2%	0.03 ± 0.02	1%	0.06 ± 0.03	0%	0.02 ± 0.01	1%	0.16 ± 0.04	0%	0.06 ± 0.02	1%
Others	0.04 ± 0.02	1%	0.22 ± 0.19	15%	0.40 ± 0.20	4%	0.14 ± 0.05	7%	0.03 ± 0.02	0%	0.23 ± 0.19	8%	0.46 ± 0.13	1%	0.75 ± 0.29	8%
Total	5.98 ± 0.91	-	1.41 ± 0.53	-	9.5 ± 1.2	-	2.06 ± 0.58	-	36.2 ± 2.2	-	2.97 ± 0.72	-	89.2 ± 3.2	-	9.4 ± 1.1	-
125,110 [dM=15]	18.3 ± 1.6	305%	9.4 ± 1.3	667%	28.2 ± 2.1	298%	0.46 ± 0.26	23%	10.7 ± 1.3	30%	10.0 ± 1.3	336%	11.0 ± 1.3	12%	10.5 ± 1.3	111%
Zn (30% syst)	3.89	-	4.25	-	4.29	-	0.01	-	0.61	-	3.34	-	0.18	-	1.87	-
125,100 [dM=25]	5.8 ± 1.2	96%	6.1 ± 1.1	429%	27.4 ± 2.4	289%	15.5 ± 1.7	755%	19.2 ± 1.8	53%	8.2 ± 1.3	275%	62.7 ± 3.2	70%	33.8 ± 2.5	359%
Zn (30% syst)	1.41	-	3.00	-	4.20	-	5.39	-	1.17	-	2.83	-	1.67	-	4.94	-
140,100 [dM=40]	1.22 ± 0.45	20%	1.15 ± 0.40	82%	6.1 ± 1.0	65%	3.76 ± 0.82	183%	6.64 ± 0.91	18%	2.48 ± 0.57	84%	27.2 ± 1.9	30%	12.8 ± 1.4	136%
Zn (30% syst)	0.17	-	0.54	-	1.09	-	1.68	-	0.31	-	0.89	-	0.69	-	2.24	-
150,60 [dM=90]	0.00 ± 0.00	0%	0.00 ± 0.00	0%	0.00 ± 0.00	0%	0.00 ± 0.00	0%	0.00 ± 0.00	0%	0.12 ± 0.12	4%	0.64 ± 0.17	1%	0.33 ± 0.16	3%
Zn (30% syst)	0.00	-	0.00	-	0.00	-	0.00	-	0.00	-	0.00	-	0.00	-	0.00	-

Table 8.16: Expected yields for the model-independent discovery regions in 139 fb^{-1}. Only statistical uncertainties are included. For the Zn calculation a 30% flat systematic uncertainty is applied.

sample	disc-SR-d	purity	disc-SR-e1	purity	disc-SR-e2	purity	disc-SR-f1	purity	disc-SR-f2	purity	disc-SR-g1	purity	disc-SR-g2	purity	disc-SR-g3	purity	disc-SR-g4	purity
WZ	61.6 ± 1.8	33%	104.0 ± 2.4	33%	93.9 ± 2.3	34%	191.3 ± 3.5	41%	129.8 ± 2.9	47%	281.1 ± 4.2	47%	219.6 ± 3.8	53%	177.1 ± 3.5	62%	89.8 ± 2.5	66%
ZZ	28.6 ± 1.5	15%	54.2 ± 2.2	17%	47.4 ± 2.0	17%	67.0 ± 2.5	15%	38.4 ± 2.0	14%	77.7 ± 2.8	13%	49.1 ± 2.3	12%	23.5 ± 1.7	8%	10.7 ± 1.1	8%
Fakes	85.0 ± 3.9	46%	128.4 ± 4.9	41%	106.8 ± 4.6	39%	137.7 ± 5.8	30%	52.7 ± 4.2	19%	146.1 ± 6.2	24%	61.2 ± 4.8	15%	17.8 ± 3.8	6%	8.4 ± 2.3	6%
$t\bar{t}$	5.96 ± 0.65	3%	13.91 ± 0.93	4%	13.50 ± 0.92	5%	38.8 ± 1.4	8%	32.8 ± 1.2	12%	56.6 ± 1.7	9%	50.6 ± 1.5	12%	42.7 ± 1.4	15%	17.78 ± 0.91	13%
$t\bar{t}X$	0.76 ± 0.08	0%	1.69 ± 0.11	1%	1.61 ± 0.11	1%	4.84 ± 0.18	1%	4.07 ± 0.16	1%	7.21 ± 0.21	1%	6.44 ± 0.20	2%	5.52 ± 0.18	2%	2.37 ± 0.12	2%
Others	4.61 ± 0.73	2%	9.69 ± 0.91	3%	9.43 ± 0.89	3%	21.5 ± 1.1	5%	16.89 ± 0.85	6%	29.2 ± 1.3	5%	24.6 ± 1.1	6%	19.50 ± 0.90	7%	7.69 ± 0.62	6%
Total	186.4 ± 4.7	-	311.8 ± 6.1	-	272.7 ± 5.6	-	461.1 ± 7.4	-	274.7 ± 5.7	-	597.9 ± 8.3	-	411.4 ± 6.8	-	286.0 ± 5.6	-	136.8 ± 3.7	-
125,110 [dM=15]	21.5 ± 1.8	12%	21.5 ± 1.8	7%	0.78 ± 0.31	0%	21.5 ± 1.8	5%	0.00 ± 0.00	0%	21.5 ± 1.8	4%	0.00 ± 0.00	0%	0.00 ± 0.00	0%	0.00 ± 0.00	0%
Zn (30% syst)	0.17	-	0.02	-	0.00	-	0.00	-	0.00	-	0.00	-	0.00	-	0.00	-	0.00	-
125,100 [dM=25]	159.2 ± 5.3	85%	159.2 ± 5.3	51%	131.9 ± 4.8	48%	159.2 ± 5.3	35%	0.00 ± 0.00	0%	159.2 ± 5.3	27%	0.00 ± 0.00	0%	0.00 ± 0.00	0%	0.00 ± 0.00	0%
Zn (30% syst)	2.06	-	1.27	-	1.20	-	0.84	-	0.00	-	0.62	-	0.00	-	0.00	-	0.00	-
140,100 [dM=40]	156.5 ± 4.5	84%	337.1 ± 6.6	108%	327.9 ± 6.6	120%	338.4 ± 6.7	73%	181.9 ± 4.9	66%	338.6 ± 6.7	57%	182.2 ± 4.9	44%	1.57 ± 0.44	1%	0.27 ± 0.16	0%
Zn (30% syst)	2.03	-	2.57	-	2.81	-	1.82	-	1.64	-	1.42	-	1.10	-	0.00	-	0.00	-
150,60 [dM=90]	4.19 ± 0.60	2%	10.9 ± 1.1	3%	10.8 ± 1.1	4%	66.6 ± 2.6	14%	62.4 ± 2.5	23%	162.0 ± 3.8	27%	157.8 ± 3.8	38%	151.1 ± 3.7	53%	95.4 ± 2.8	70%
Zn (30% syst)	0.00	-	0.00	-	0.00	-	0.26	-	0.50	-	0.64	-	0.94	-	1.31	-	1.69	-

Chapter 9

Validation of the background

Before unblinding the Signal Regions (SRs) it is important to validate that the Standard Model (SM) background is modelled properly in the SRs. Validation Regions (VRs) are created in a region of phase space close to the SRs to test that the background is modelled properly. If it is shown that the SM background is understood, any deviation from the SM seen in the SRs is likely to be a real effect, such as expected from a supersymmetry or any other beyond-the-Standard-Model signal. VRs have been designed for the largest backgrounds in the analysis: WZ, $t\bar{t}$ and Z+jets/Z+γ.

9.1 WZ validation region

The control regions (CRs) for the WZ background as described in Section 7.1.2 are designed to normalise the Monte Carlo (MC) to data in a controlled WZ dominated phase space. In order to correct for the slope in the $N_{\text{jets}}^{30\,\text{GeV}}$ distribution the WZ CRs are split into a jet-veto (0j) region and a region with at least one jet (nj). The two normalisation factors μ_{WZ0j} and μ_{WZnj} from the WZ CRs are validated in the WZ VRs, which are kinematically closer to the SRs. For this reason, like the WZ CR, the WZ VR is divided into a jet-veto region, VRWZ-0j, and a region where at least one jet is required, VRWZ-nj. An additional validation region VRWZ-nj-lowmll is added to validate the low $m_{\ell\ell}^{\text{min}}$ phase space, which is relevant for validating the background of SRhigh-nja where $m_{\ell\ell}^{\text{min}} \in [0, 12]$ GeV.

The goal is to design WZ VRs close to SR phase space. The SR phase space is designed in such a way that it selects off-shell W and Z bosons. In order to select an off-shell Z boson in the WZ VRs, the $m_{\ell\ell}^{\text{min}}$ window is placed at $[12, 75]$ GeV. The next step would be to select an off-shell W boson, however, the VRs also need to be orthogonal to the SRs. In order to be orthogonal to the SRs, the WZ VRs select an on-shell W, with the m_{T} window placed at $[60, 90]$ GeV. An $E_{\text{T}}^{\text{miss}} < 80$ GeV cut is applied in the VRWZ-nj region in order

Table 9.1: Validation region *WZ* (VRWZ) definitions. A jet-veto is applied in the VRWZ-0j, $N_{\text{jets}}^{30\text{ GeV}} = 0$, and in the VRWZ-nj and VRWZ-nj-lowmll regions at least one jet is required, $N_{\text{jets}}^{30\text{ GeV}} \geq 1$. In all the regions a b-jet veto is applied, such that $N_{\text{b-jets}}^{20\text{ GeV}} = 0$.

	$m_{\ell\ell}$ [GeV]	$m_{\ell\ell}^{\text{min}}$ [GeV]	$E_{\text{T}}^{\text{miss}}$ [GeV]	lepton p_{T} [GeV]	$m_{\text{T}}^{\text{minmll}}$ [GeV]	$E_{\text{T}}^{\text{miss}}$ significance	$p_{\text{T}}^{\text{leptons}}/E_{\text{T}}^{\text{miss}}$	$m_{\text{W}}^{p_{\text{Z}}^{\text{balance}}}$ [GeV]	ΔR(Wlep,$E_{\text{T}}^{\text{miss}}$)
VRWZ-0j	<75	$\in [12,75]$	<50	all 3 > 10	$\in [60,90]$	>1.5	-	>75	>2.6
VRWZ-nj	<75	$\in [12,75]$	<80	all 3 > 10	$\in [60,90]$	>1.5	> 0.5	-	-
VRWZ-nj-lowmll	<75	$\in [1,3],[3.2,9]$	>80	all 3 e(μ)>4.5(3.0)	> 30	>1.5	> 0.3	-	-

to be orthogonal with SRs of the $\tilde{\chi}_1^{\pm}\tilde{\chi}_2^0 \to W^{\pm}h\tilde{\chi}_1^0\tilde{\chi}_1^0$ analysis [15], of which the result is summarised in Section 11.5. The region VRWZ-nj-lowmll is orthogonal to the SRhigh-nja region through $p_{\text{T}}^{\text{leptons}}/E_{\text{T}}^{\text{miss}} > 0.3$. The *WZ* VRs are summarised in Table 9.1. Additional $m_{3\ell}$ and $\min\Delta R$ cuts are included in the channel where an electron is the fake candidate ($e^+e^-e^{\pm}$ or $\mu^+\mu^-e^{\pm}$) to reduce electron fakes due to photon-conversion. The cuts are applied in order to match the fake composition in the *Z*+jets estimation described in Section 7.2.3, where $\min\Delta R \in [0.6, 2.4]$ and $|m_{3\ell} - m_Z| > 20$ GeV.

Since the VRs are designed close to the phase space of the SRs, there might be supersymmetry signal that enters the VRs. However, as the purpose is to validate the SM background it is important to keep the amount of signal contamination in VRs to a minimum. In a *WZ* VR, with only cuts on $m_{\ell\ell}^{\text{min}}$ and m_{T}, the signal contamination exceeds 20% for some unexcluded supersymmetry scenarios. In order to reduce the signal contamination extra cuts have been added on variables $p_{\text{T}}^{\text{leptons}}/E_{\text{T}}^{\text{miss}}$, $m_{\text{W}}^{p_{\text{Z}}^{\text{balance}}}$ and ΔR(Wlep,$E_{\text{T}}^{\text{miss}}$); these cuts are explained in Section 6.3. After these cuts, signal contamination drops below 12% for unexcluded scenarios, as shown in Figure 9.1.

The *WZ* background is validated in binned distributions of variables. For the distributions it has been checked whether within each bin the signal contamination is less than the expected error. The expected error is set to the statistical error plus a 20% flat systematic error. It was found that the $m_{\ell\ell}^{\text{min}}$ distribution is the most sensitive to signal contamination exceeding this criterion. In order for the signal contamination to fall within the expected error the $m_{\ell\ell}^{\text{min}}$ binning has been adjusted to [12,30], [30,50], [50,75] GeV for VRWZ-0j and VRWZ-nj. As shown in Figure 9.2 the signal contamination does not exceed the error with the adjusted binning. For VRWZ-nj-lowmll the $m_{\ell\ell}^{\text{min}}$ binning has been set to [1,9] GeV.

The agreement between the estimation and the data is shown in Figure 9.3 for VRWZ-0j, in Figure 9.4 for VRWZ-nj and in Figure 9.5 for VRWZ-nj-lowmll. Good modelling is observed in VRWZ-nj and VRWZ-nj-lowmll, however in VRWZ-0j there is an excess in the data. The significance of the excess in VRWZ-0j is above 2σ as can be seen in the summary of the VRs, which is shown in Figure 9.10. To correct for this excess of the data in VRWZ-0j the *WZ* background would need to be normalised with a normalisation factor

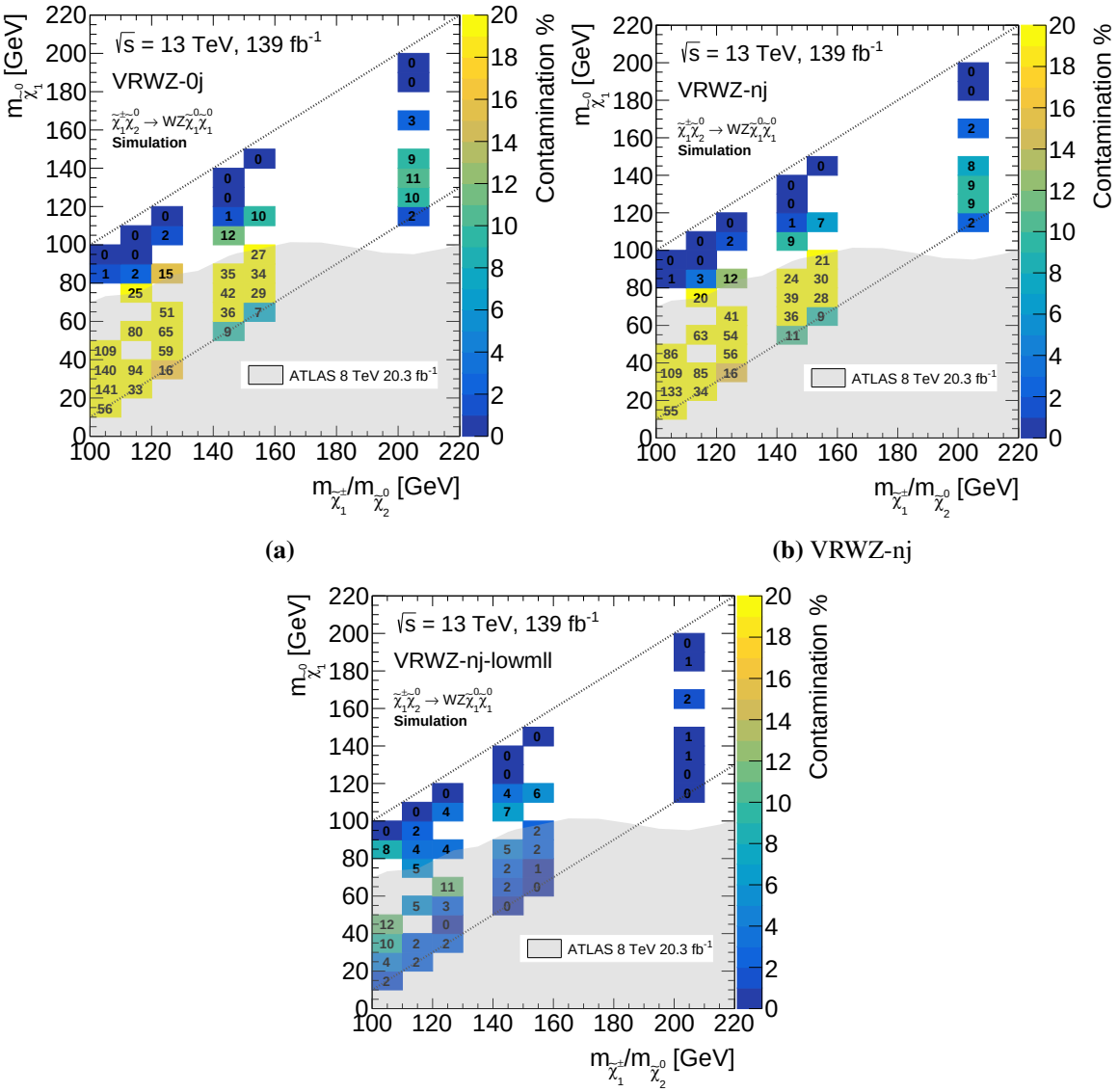

Fig. 9.1: Signal contamination of possible supersymmetry models, parametrised in $\tilde{\chi}_1^0$ and $\tilde{\chi}_2^0/\tilde{\chi}_1^\pm$ mass, shown as a % for **(a)** VRWZ-0j, **(b)** VRWZ-nj and **(c)** VRWZ-nj-lowmll. The dashed line indicates the region where $m_{\tilde{\chi}_1^\pm/\tilde{\chi}_2^0} - m_{\tilde{\chi}_1^0} < m_Z$ and $m_{\tilde{\chi}_1^\pm/\tilde{\chi}_2^0} - m_{\tilde{\chi}_1^0} > 0$ GeV. The grey shade shows the previous exclusion limits with the ATLAS experiment, corresponding to the off-shell and on-shell WZ Run-1 result using 20.3 fb^{-1} at $\sqrt{s} = 8$ TeV [186].

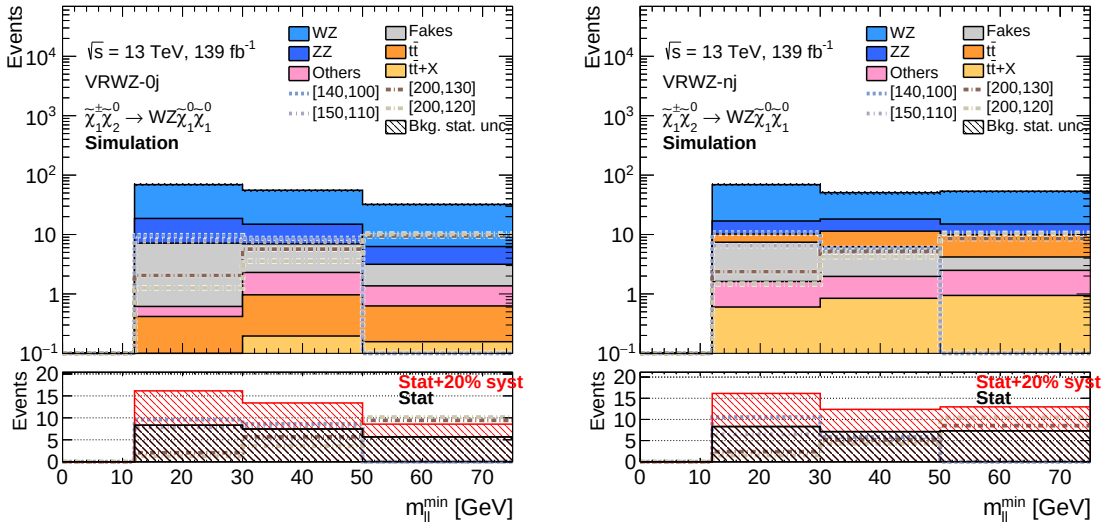

Fig. 9.2: The $m_{\ell\ell}^{\text{min}}$ distribution showing the contamination per bin for the most contaminating signals for **(a)** VRWZ-0j and **(b)** VRWZ-nj. Only statistical uncertainties are included in the top panel. Distributions for $\tilde{\chi}_1^{\pm}\tilde{\chi}_2^0 \rightarrow WZ\tilde{\chi}_1^0\tilde{\chi}_1^0$ signals are overlaid, with mass values given as [m($\tilde{\chi}_1^{\pm}$,m($\tilde{\chi}_1^0$)] GeV. In the bottom panel the numbers of expected signal events are shown. The $m_{\ell\ell}^{\text{min}}$ binning is chosen such that that the number of signal events does not exceed the total error; where the total error is the statistical error plus a flat systematic uncertainty of 20%.

around $\mu_{WZ0j} = 1.3$, instead of $\mu_{WZ0j} = 1.06$ as has been derived in Section 7.1.2. Such a change will adjust the normalisation factor μ_{WZ0j} by about 20%. A study has been done, presented in Section 11.2.1, to see how the measurement of μ_{WZ0j} can be improved for a next round of the analysis using a different type of CR. For this analysis the original CR strategy, yielding a normalisation factor of $\mu_{WZ0j} = 1.06$ is kept.

Another cause for the significance of the excess in the VRWZ-0j to be above 2σ is the systematic uncertainty on the WZ background. As can be seen from Table 9.2 the systematic uncertainty on the WZ background in VRWZ-0j is only 5% (where a conservative flat uncertainty of 20% was applied in Figure 9.2). The off-shell WZ phase space seems to be not perfectly predicted by the MC generator and tune, and thus an extra uncertainty could have been applied for the extrapolation from the on-shell WZ CRs, which has not been done.

9.2 $t\bar{t}$ validation region

In the SRhigh regions $t\bar{t}$ is one of the largest backgrounds and it is important to validate that $t\bar{t}$ is estimated correctly. The $t\bar{t}$ background is a fake lepton background just like Z+jets/$Z+\gamma$. However, the difference between the estimation of $t\bar{t}$ and Z+jets/$Z+\gamma$ is that the $t\bar{t}$ estimation

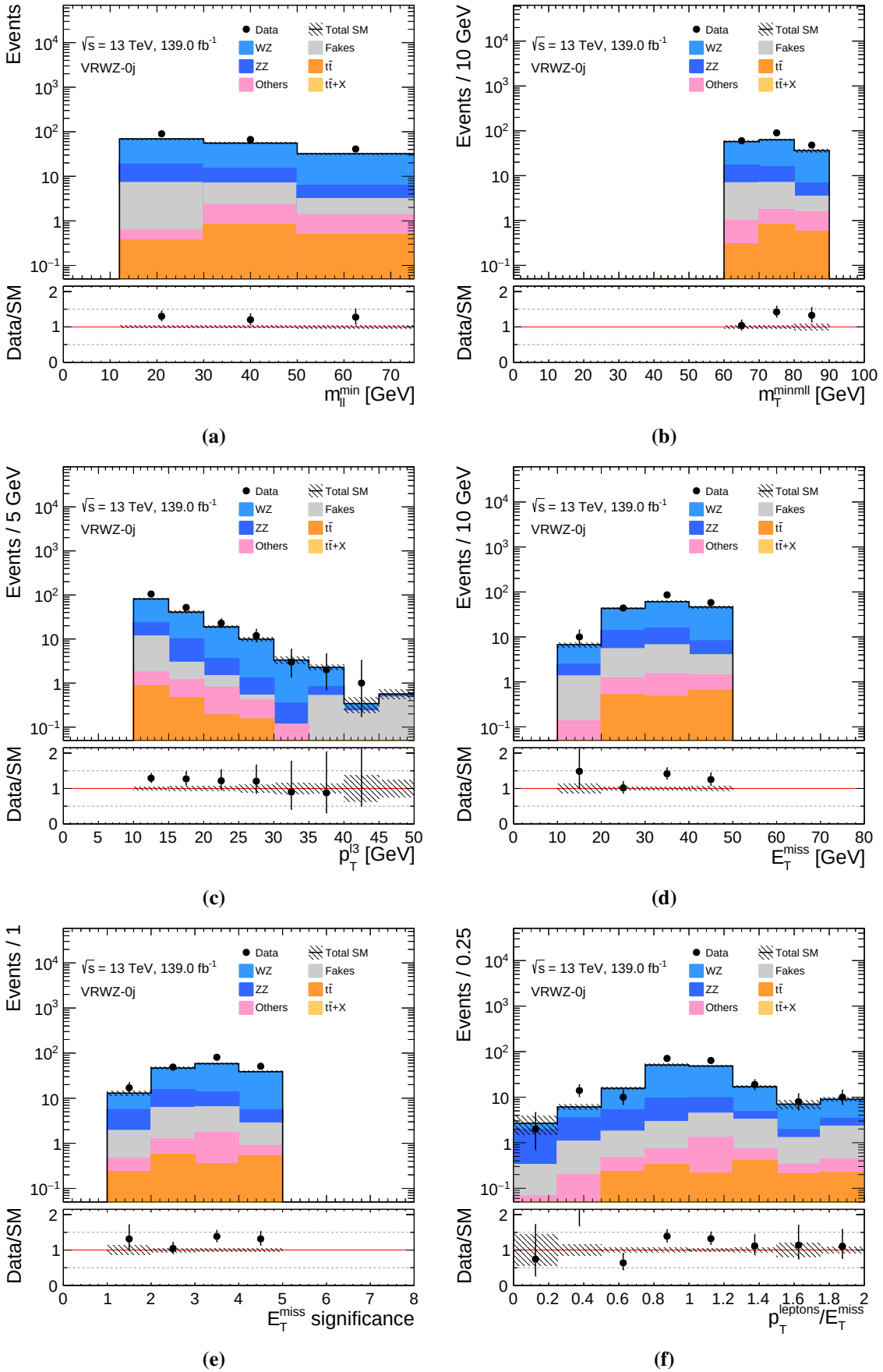

Fig. 9.3: Distributions for VRWZ-0j. Statistical and systematic uncertainties are included. The last bin includes overflow.

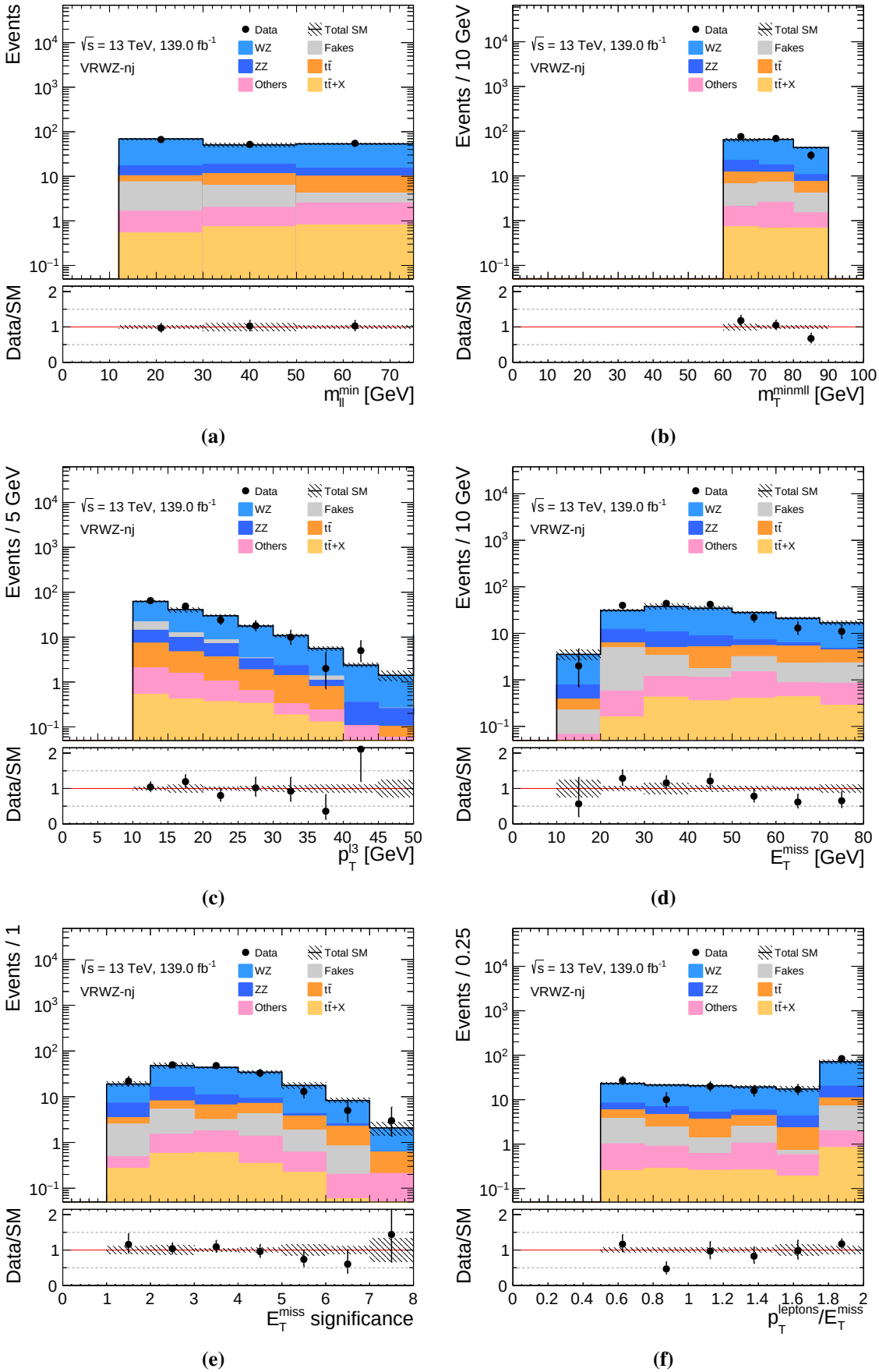

Fig. 9.4: Distributions for VRWZ-nj. Statistical and systematic uncertainties are included. The last bin includes overflow.

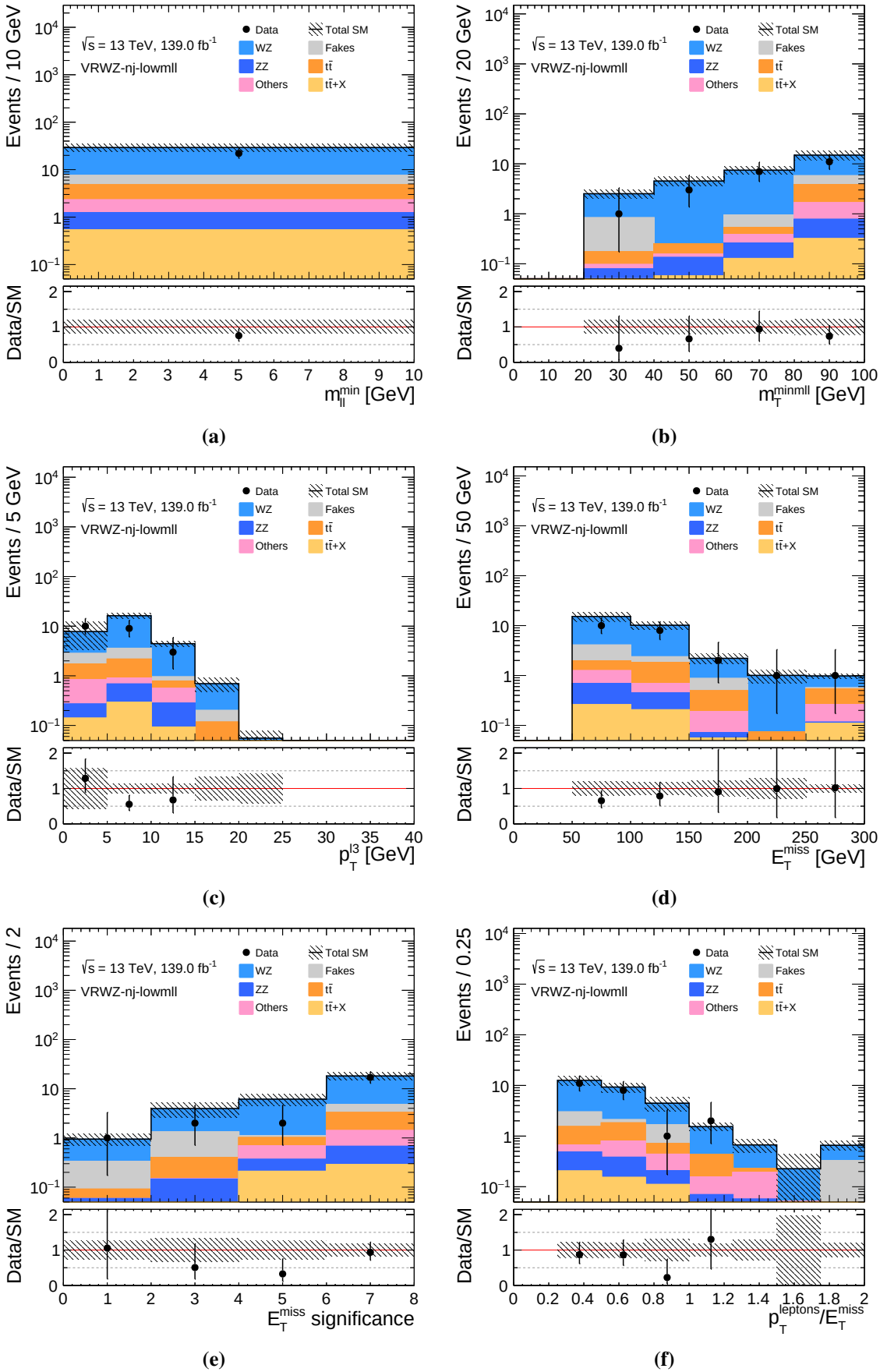

Fig. 9.5: Distributions for VRWZ-nj-lowmll. Statistical and systematic uncertainties are included. The last bin includes overflow.

Table 9.2: Yields for VRWZ-0j, VRWZ-nj and VRWZ-nj-lowmll. Statistical and systematic uncertainties are included.

Region	VRWZ-0j	VRWZ-nj	VRWZ-nj-lowmll
Observed	198	174	22
Bg predicted	157.0 ± 7.7	173 ± 12	29.2 ± 5.9
WZ	117.1 ± 4.9	123.2 ± 9.0	21.7 ± 4.5
ZZ	22.6 ± 6.0	18.6 ± 6.3	0.7 ± 0.4
Fakes	13.0 ± 2.8	11.8 ± 2.8	2.7 ± 1.2
$t\bar{t}$	1.60 ± 0.79	13.7 ± 2.7	2.5 ± 1.0
$t\bar{t}\,X$	0.08 ± 0.06	2.06 ± 0.30	0.53 ± 0.14
Others	2.6 ± 1.0	4.0 ± 1.3	1.06 ± 0.84

is done using MC. The Fake Factor method, described in Chapter 7.2, estimates the fake lepton background by assigning a fake factor to all events containing anti-ID leptons and this method can also be used to estimate $t\bar{t}$. However, since $t\bar{t}$ is estimated using MC, $t\bar{t}$ is subtracted from the fake estimation as described in Section 7.2.4. In order to validate the $t\bar{t}$ MC and the subtraction of $t\bar{t}$ from the Z+jets/$Z+\gamma$ sample, a validation region VR$t\bar{t}$ has been defined.

VR$t\bar{t}$ has been designed by removing the b-jet veto with respect to the SR selections. The region is defined in the off-shell $m_{\ell\ell}^{\text{min}}$ window $[1,75]$ GeV and has a $N_{\text{b-jets}}^{20\text{ GeV}} > 0$ requirement to be high in $t\bar{t}$ purity. The $N_{\text{b-jets}}^{20\text{ GeV}} > 0$ cut also ensures orthogonality to the SRlow and SRhigh regions. A $E_{\text{T}}^{\text{miss}} > 50$ GeV cut is placed to reduce the Z+jets fake background contribution. The cuts are summarised in Table 9.3.

It can be seen from Table 9.4 that the purity of $t\bar{t}$ is found to be 63%. The agreement between the estimation and the data is shown in Figure 9.6. Good modelling for the $t\bar{t}$ MC is observed in all distributions.

Table 9.3: VR$t\bar{t}$ definition.

	$m_{\ell\ell}$ [GeV]	$m_{\ell\ell}^{\text{min}}$ [GeV]	$N_{\text{b-jets}}^{20\text{ GeV}}$	$E_{\text{T}}^{\text{miss}}$ [GeV]	lepton p_{T} [GeV]
VR$t\bar{t}$	<75	[1,3], [3.2,9], >12	>0	>50	all 3 e(μ)>4.5(3.0)

9.3 Z+jets/$Z+\gamma$ validation region

After having established the Z+jets/$Z+\gamma$ background estimation and its uncertainties in Section 7.2, it needs to be validated. Three validation regions are defined, VRFF-0j, VRFF-nj

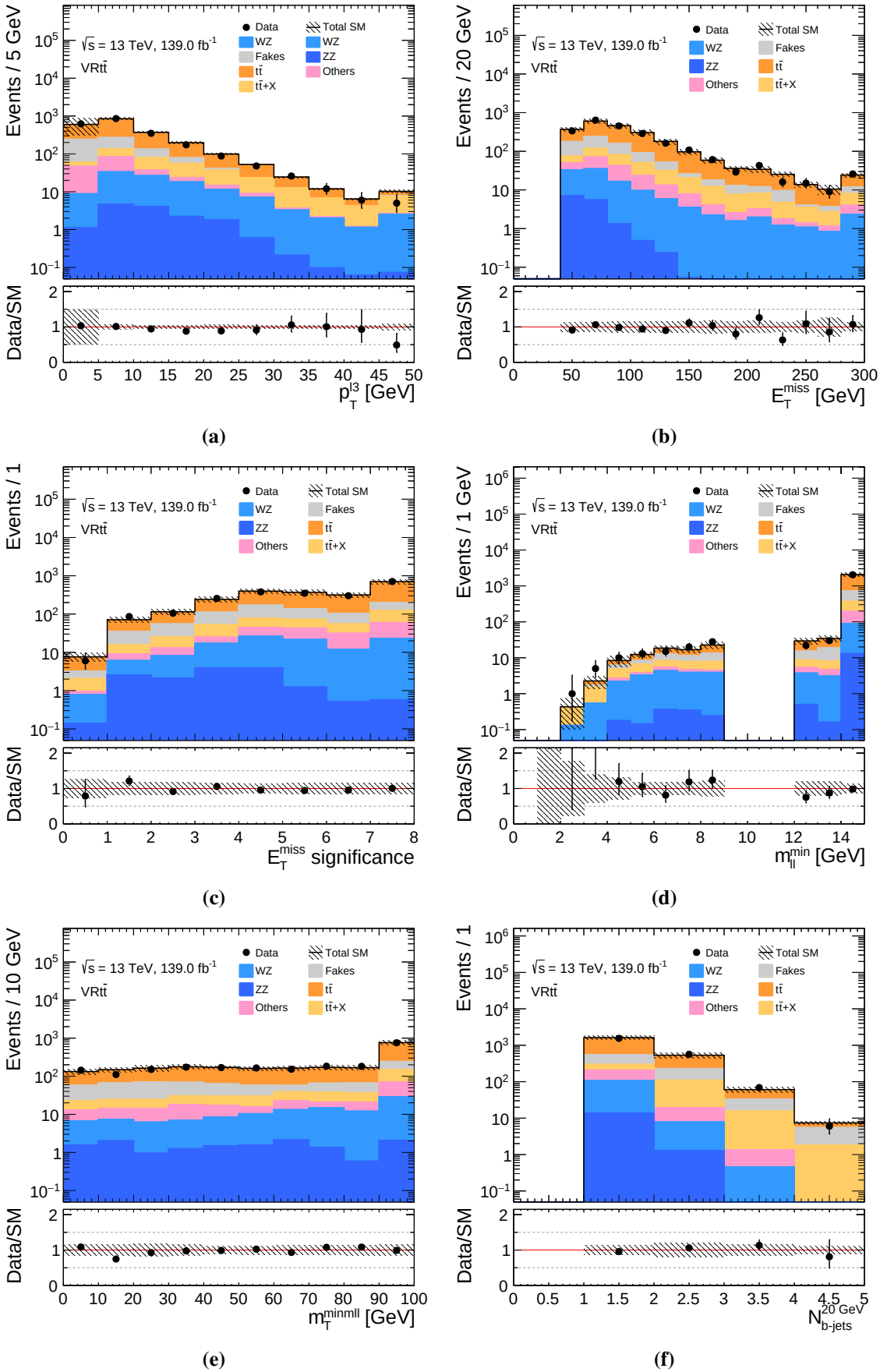

Fig. 9.6: Distributions for VRtt̄. Statistical and systematic uncertainties are included. The last bin includes overflow.

Table 9.4: Yields for VR$t\bar{t}$. Statistical and systematic uncertainties are included.

Region	VR$t\bar{t}$
Observed	2189
Bg predicted	2220 ± 370
WZ	8.0 ± 1.6
WZ	92 ± 11
ZZ	15.0 ± 2.8
Fakes	395 ± 42
$t\bar{t}$	1400 ± 330
$t\bar{t}\,X$	200 ± 15
Others	111 ± 61

Table 9.5: VRFF definitions. A jet-veto is applied in the VRFF-0j, $N_{\text{jets}}^{30\text{ GeV}} = 0$, and in the VRFF-nj and VRFF-nj-lowpt regions at least one jet is required, $N_{\text{jets}}^{30\text{ GeV}} \geq 1$. In all the regions a b-jet veto is applied, such that $N_{\text{b-jets}}^{20\text{ GeV}} = 0$.

	$m_{\ell\ell}$ [GeV]	$m_{\ell\ell}^{\text{min}}$ [GeV]	$E_{\text{T}}^{\text{miss}}$ [GeV]	$p_{\text{T}}^{\ell_3}$ [GeV]	$m_{\text{T}}^{\text{minmll}}$ [GeV]	$E_{\text{T}}^{\text{miss}}$ significance
VRFF-0j	<75	$\in [12,75]$	<50	>10	<50	$\in [0.5,1.5]$
VRFF-nj	<75	$\in [12,75]$	<200	>10	<50	$\in [0.5,3]$
VRFF-nj-lowpt	<75	$\in [1,75]$	<200	<10, all 3 e(μ)$>$4.5(3.0)	<50	$\in [0.5,3]$

and VRFF-nj-lowpt. The latter differs from VRFF-nj by having an inverted lepton p_{T} requirement. To make these validation regions pure in fake leptons and orthogonal to the SRs, the $E_{\text{T}}^{\text{miss}}$ significance cut is inverted with respect to the SRs. The cuts on $E_{\text{T}}^{\text{miss}}$ and $m_{\text{T}}^{\text{minmll}}$ are the same as those applied to the SRs. A more stringent selection on $m_{3\ell}$ reduces the ZZ background. The definition of the VRFF regions is shown in Table 9.5. Additional $m_{3\ell}$ and $\min\Delta R$ cuts are included in the channel where an electron is the fake candidate ($e^+e^-e^\pm$ or $\mu^+\mu^-e^\pm$) to reduce electron fakes due to photon-conversion. The cuts are applied in order to match the fake composition in the Z+jets estimation described in Section 7.2.3, where $\min\Delta R \in [0.6, 2.4]$ and $|m_{3\ell} - m_Z| > 20$ GeV.

The agreement between the estimation and the data in the validation regions VRFF-0j, VRFF-nj, VRFF-nj-lowpt is shown in Figures 9.7, 9.8 and 9.9. The yields are reported in Table 9.6. All the Z+jets/Z+γ estimation systematic uncertainties, discussed in Section 7.2.5, have been included. The unconstrained uncertainties before the fit in the WZ CRs, described in section 7.1.2, are shown. The normalisation factor for the WZ background is applied. Good modelling is observed in all the regions. In appendix B the figures and yield tables for the validation regions are shown split up into flavour components eee, $\mu\mu$e, eeμ and $\mu\mu\mu$. Also when splitting up into flavour components good modelling is observed in all the regions.

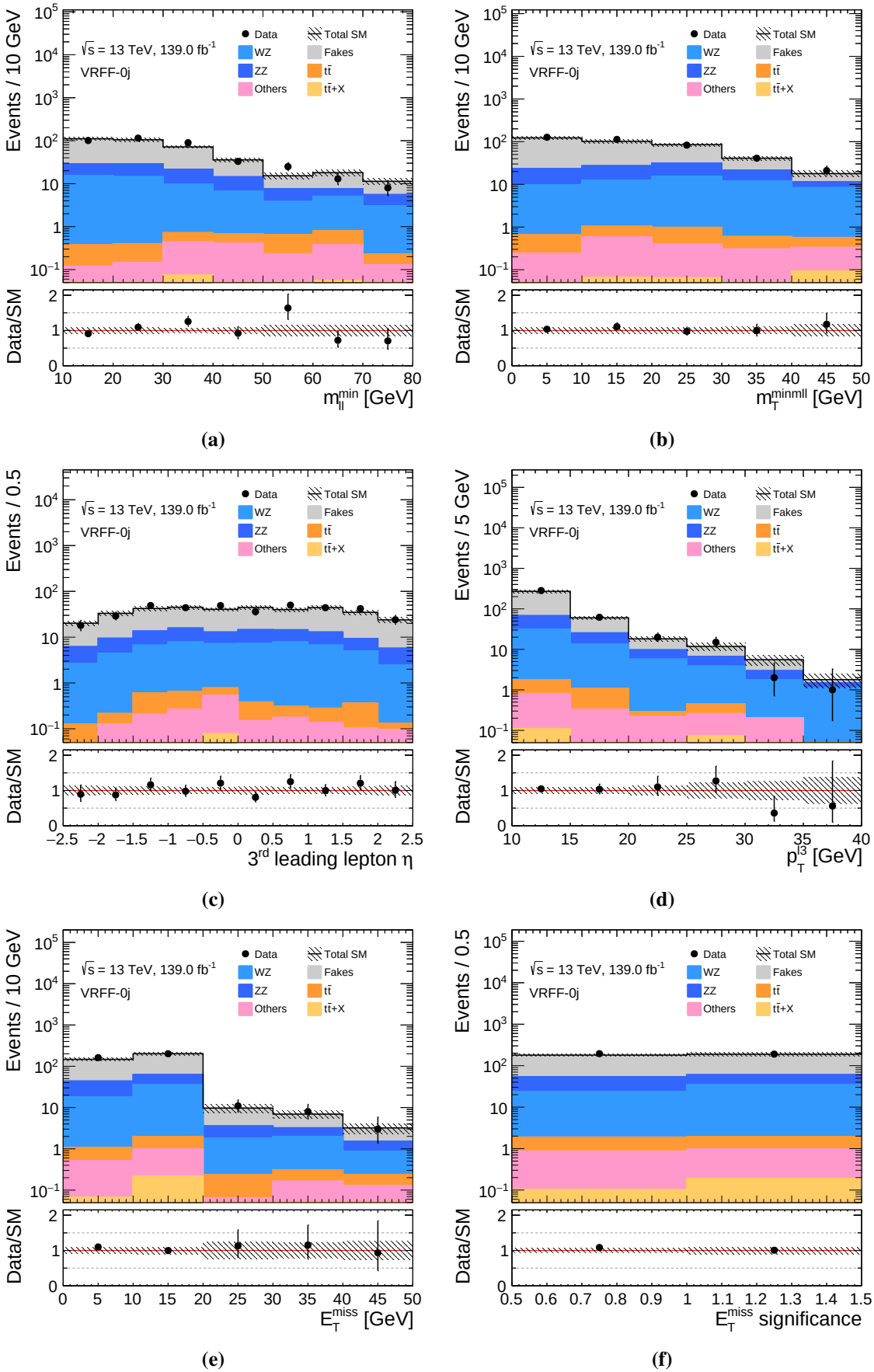

Fig. 9.7: Distributions for VRFF-0j. Statistical and systematic uncertainties are included. The last bin includes overflow.

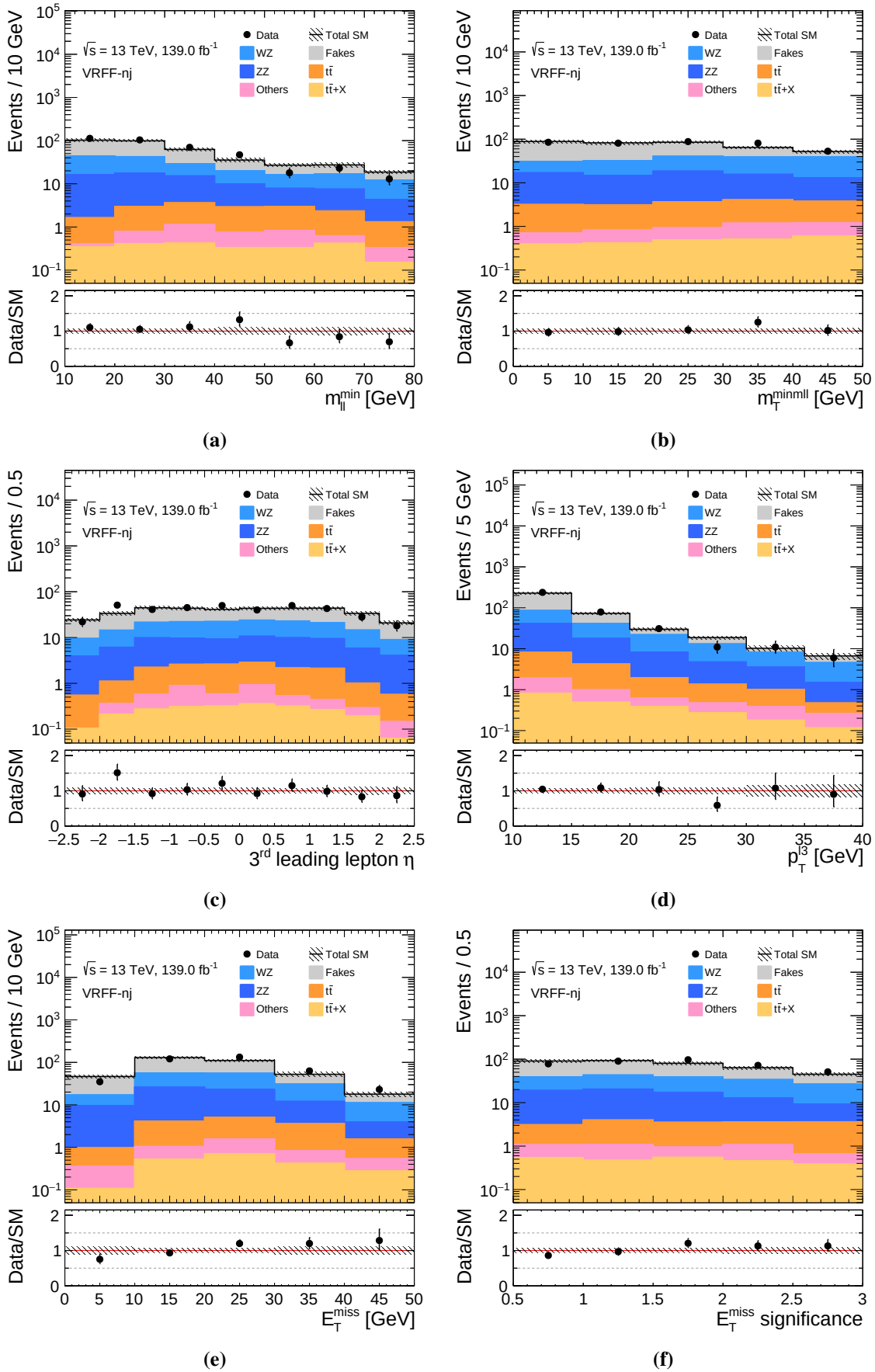

Fig. 9.8: Distributions for VRFF-nj. Statistical and systematic uncertainties are included. The last bin includes overflow.

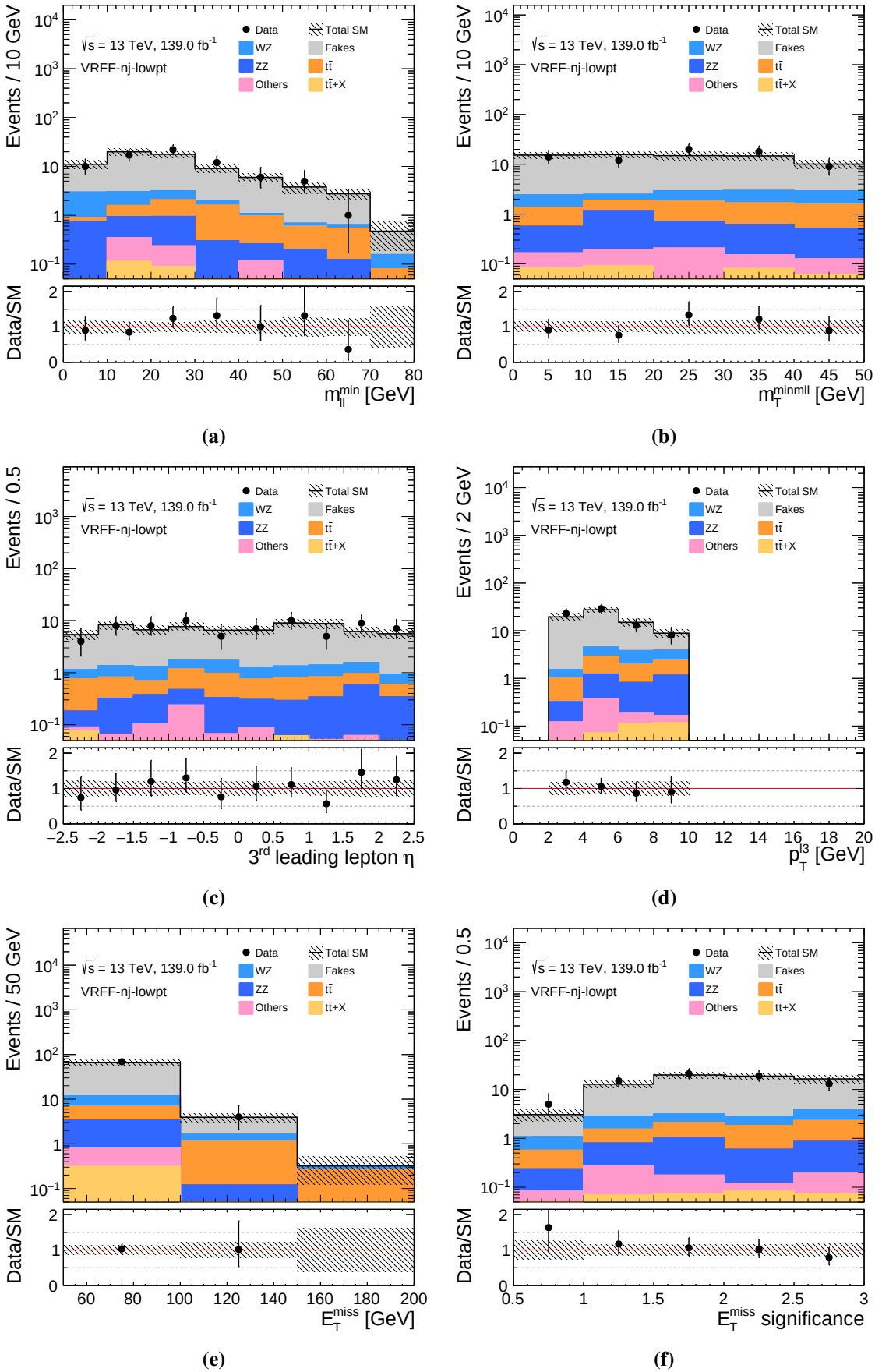

Fig. 9.9: Distributions for VRFF-nj-lowpt. Statistical and systematic uncertainties are included. The last bin includes overflow.

Table 9.6: Yields for VRFF-0J, VRFF-nJ and VRFF-nJ-lowpt. Statistical and systematic uncertainties are included.

Region	VRFF-0J	VRFF-nJ	VRFF-nJ-lowpt
Observed	385	388	73
Bg predicted	369 ± 25	373 ± 19	71 ± 9
WZ	54.3 ± 2.9	103 ± 5	5.4 ± 2.4
ZZ	57 ± 4	61 ± 5	2.7 ± 2.0
Fakes	254 ± 24	191 ± 16	57 ± 7
$t\bar{t}$	2.0 ± 0.5	13.0 ± 1.5	4.8 ± 1.5
$t\bar{t}\,X$	0.29 ± 0.10	2.41 ± 0.30	0.34 ± 0.10
Others	1.6 ± 0.6	2.4 ± 0.8	$0.5 \pm^{0.7}_{0.5}$

9.4 Summary plot of the validation regions

In Figure 9.10 the summary of the validation regions is shown. It can be observed that there is good agreement in all of the VRs, except for the 2σ deviation in the VRWZ-0j which has been discussed in Section 9.1.

The breakdown of the systematic uncertainties for the VRs is demonstrated in Figure 9.11. For the VRWZ-0j and VRWZ-nj regions the dominant systematic are theoretical uncertainties. In the VRWZ-nj-lowmll region the dominant systematic is from the experimental uncertainties, due to leptons which need to be reconstructed for $p_{\mathrm{T}} < 10$ GeV. The dominant systematic in the VR$t\bar{t}$ region are also experimental uncertainties because of leptons reconstructed for $p_{\mathrm{T}} < 10$ GeV. In the Z+jets/$Z+\gamma$ VRs the dominant systematic are fakes systematics, as is expected. In the VRFF-nj-lowpt the experimental uncertainties are also sizeable, again due to the leptons reconstructed for $p_{\mathrm{T}} < 10$ GeV.

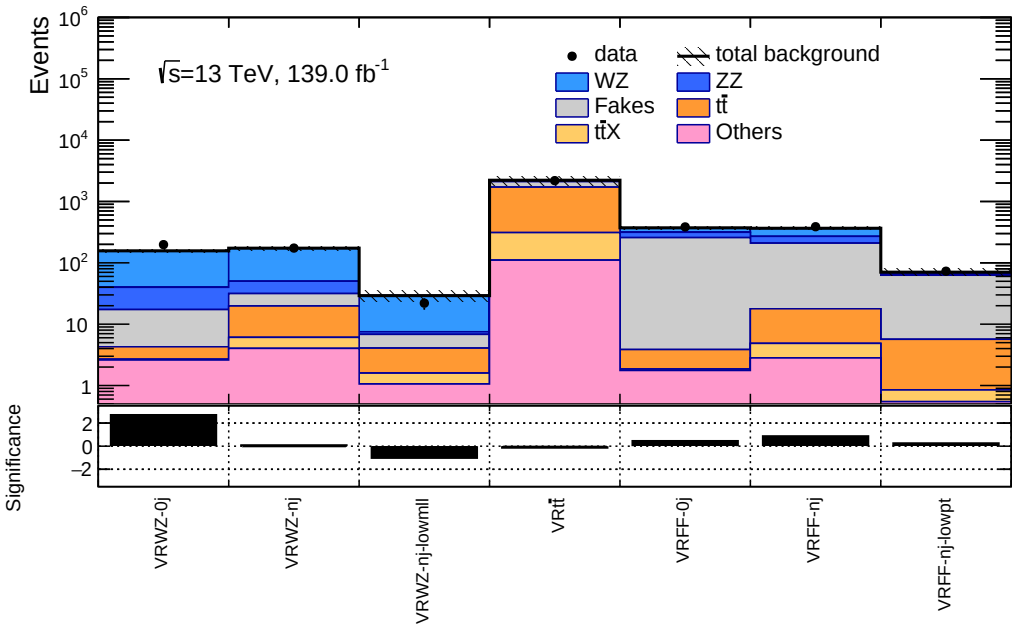

Fig. 9.10: Summary plot showing the number of events in all VRs and the expected background. The bottom panel shows the significance of the difference between the observed and the expected yields, calculated with the profile likelihood method from [191], adding a minus sign if the yield is below the prediction. Statistical and systematic uncertainties are included.

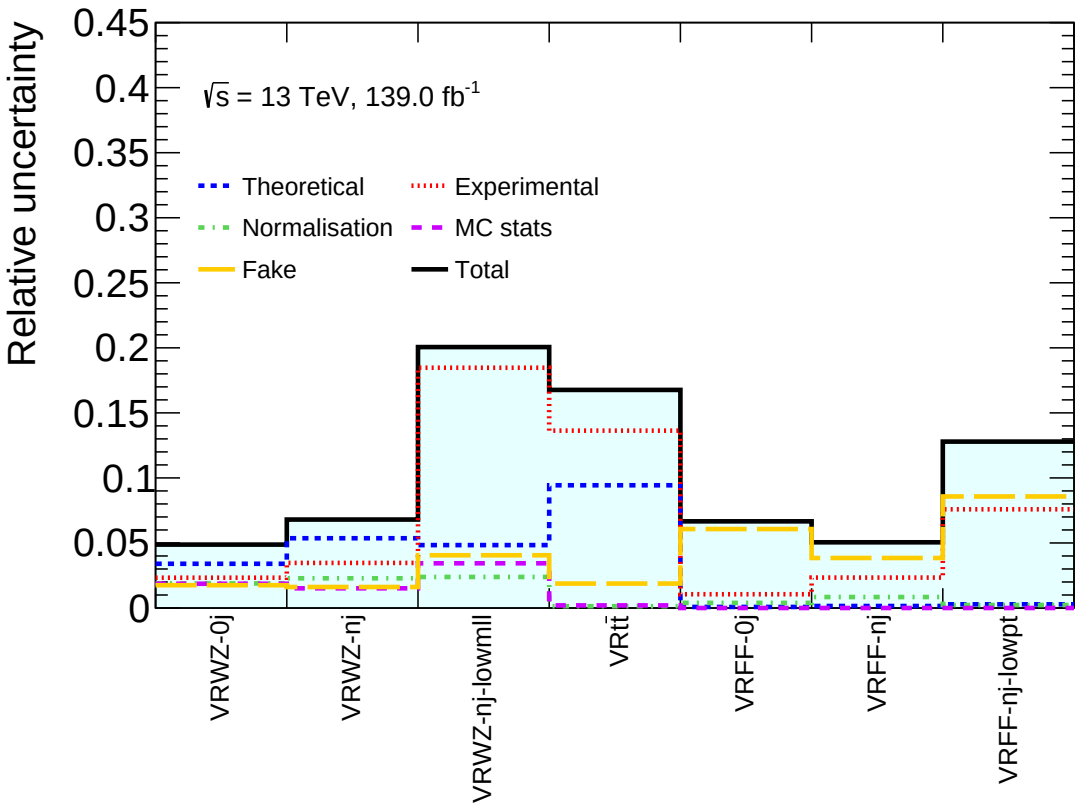

Fig. 9.11: Breakdown of the systematic uncertainties in the event yields in the VRs.

Chapter 10

Results

After the Signal Regions (SRs) have been optimised in Section 8.4, the discovery SRs have been defined in Section 8.5, and the predictions of the Standard Model (SM) backgrounds have been validated in Validation Regions (VRs) in Chapter 9, it is time to look at the data in the SRs. However, before the SRs can be looked at, the statistical procedure for signal discovery or signal exclusion needs to be outlined in order to avoid introducing a bias in the statistical inference procedure. It needs to be decided beforehand which conclusions are to be drawn from the measurement in the SRs and which hypothesis is assigned to the possible outcomes. It is important to determine both the test statistic and the level of significance for rejecting a hypothesis. After the statistical procedure has been introduced, the SRs can be unblinded.

10.1 Statistical procedure

The statistical procedure is implemented using Histfitter [192, 193], which is a framework capable of likelihood fits and hypothesis tests. Histfitter is based on RooFit [194] and RooStats [195]. Histfitter takes as input a likelihood function, a test statistic, the hypotheses to test and the level of significance for hypothesis rejection.

The likelihood used when optimising the signal in Section 8.4, given by Equation 8.1, used a flat systematic uncertainty of $\tau = 30\%$. For the final fit result, distributions for each nuisance parameter $\vec{\theta}$ are implemented. The likelihood for the data measured in the signal regions is then given by,

$$L(\vec{n}|\mu_s, \vec{\theta}) = \prod_{i \in SR} P(n_i|N_i(\mu_s, \vec{\theta})) \times \prod_{i \in CR} P(n_i|N_i(\mu_s, \vec{\theta})) \times C_{syst}(\vec{\theta}), \tag{10.1}$$

where P is a poisson distribution and C is typically a gauss, poisson or log-normal distribution, depending on the type of uncertainty. The likelihood depends on the number of measured events, n_i, and the number of expected events N_i, where N_i is given by

$$N_i(\mu_s, \theta) = \mu_S \cdot s_i(\vec{\theta}) + b_i(\vec{\theta}), \tag{10.2}$$

which is a function of the normalisation scale factor μ_s for the signal, the number of expected signal events s_i and background events b_i, and the nuisance parameters $\vec{\theta}$. The included nuisance parameters describe experimental and systematic uncertainties. Normalisation of the WZ background as described in Section 7.1.2 is included in the fit using additional nuisance parameters. The normalisation scale factor μ_s for the signal scales the expected signal. Scaling the signal allows to look at different scenarios, where $\mu_S = 0$ corresponds to no signal, $\mu_S = 1$ corresponds to the expected signal and $\mu_S > 1$ corresponds to more than the expected signal.

A hypothesis test will be done to evaluate whether the observed data is compatible with SM background only, the background-only hypothesis, or with SM background and supersymmetry signal, the signal-plus-background hypothesis. A composite hypothesis is used where μ_s is not fixed. A test statistic is used to determine the level of agreement of a hypothesis with the observation. In counting experiments the test statistic is chosen to be a function of the number of events. At the LHC the standard test statistic is the one-sided profile likelihood which in our case is given by

$$q(\mu_s) = -2\ln\left(\frac{L(n|\mu_s, \hat{\hat{b}}(\mu_s), \hat{\hat{\theta}}(\mu_s))}{L(n|\hat{\mu}_s, \hat{b}, \hat{\theta})}\right). \tag{10.3}$$

In this notation a single hat corresponds to values that maximise the likelihood overall and a double hat corresponds to values that maximise the likelihood for a fixed μ_s.

The probability density function of the test statistic $q(\mu_s)$ needs to be known,

$$f(q(\mu_s)|\mu_s). \tag{10.4}$$

The used test statistic has the advantage that the true test statistic distribution can be approximated. In the asymptotic limit the test statistic distribution will follow a χ^2 distribution [196]. Another option is to use toy experiments to obtain the test statistic distribution. In all the fits shown in this chapter the asymptotic approach is used. After the test statistic has been determined for the hypothesis, the observed value for the test statistic, q^{obs}, is determined

from the data sample. The p-value is then given by

$$p(\mu_s) = \int_{q_{\mu_s}^{obs}}^{\infty} f(q(\mu_s)|\mu_s) dq_{\mu_s}. \tag{10.5}$$

As a final step the level of significance or critical region where to reject the background-only or signal hypothesis needs to be decided. If the background-only hypothesis of $\mu_s = 0$ is rejected at 3σ, corresponding to a p-value of 0.013, there is evidence for the supersymmetry signal. A rejection of the background-only hypothesis at 5σ, corresponding to a p-value of $3 \cdot 10^{-7}$ will lead to a discovery. If the supersymmetry signal is not discovered, the supersymmetry signal hypothesis with $\mu_s = 1$ can be rejected at 1.64σ, corresponding to a p-value of 0.05, leading to an exclusion of the supersymmetry signal at a 95% confidence level (CL).

10.2 Unblinding of signal regions

After having defined the statistical inference procedure the SRs can be unblinded. Since the discovery SRs, defined in Section 8.5, are a combination of the exclusion SRs, defined in Section 8.4, all exclusion SRs are unblinded in order to validate the behaviour in the SRs before performing the discovery fit.

The yield tables are shown for the SRlow-0j regions in Table 10.1, for SRlow-nj in Table 10.2, for SRhigh-0j in Table 10.3 and for SRhigh-nj in Table 10.4. From the summary plot shown in Figure 10.1 it can be seen that the data in the SRs follows the background expectation and that no significant excess is observed in the SRs. There are two SRs, SRlow-0jd and SRhigh-0jf2, which show a 2σ tension with the data. However, observing two SRs with a 2σ tension is expected with 31 SRs. Since no significant excess has been observed in the exclusion SRs, the combination of the SRs to discovery SRs will unfortunately not lead to evidence or discovery of the supersymmetry signal.

The relative uncertainties, which have been described in sections 7.1.1 and 7.2.5, in the SRs are shown in Figure 10.2. The sources of uncertainty considered in the fit have been grouped into categories taking into account their correlations. It can be seen that the largest systematic uncertainties arise from the fakes in the fake dominated regions. In the SRhigh-nj regions the theoretical uncertainties dominate.

Table 10.1: Yields in SRlow-0j. Statistical and systematic uncertainties are included.

Region	SRlow-0jb	SRlow-0jc	SRlow-0jd	SRlow-0je	SRlow-0jf1	SRlow-0jf2	SRlow-0jg1	SRlow-0jg2
Observed	25	42	77	101	33	7	34	9
Bg predicted	32 ± 4	44 ± 4	54 ± 4	91 ± 6	32.2 ± 2.5	5.9 ± 1.1	34.7 ± 2.8	6.3 ± 1.1
WZ	7.6 ± 0.9	13.8 ± 1.3	16.3 ± 1.9	25.6 ± 1.8	20.1 ± 1.5	4.9 ± 1.0	21.4 ± 2.1	5.2 ± 1.0
ZZ	5.5 ± 1.3	7.4 ± 1.2	9.6 ± 1.6	21.8 ± 3.2	2.7 ± 1.1	0.43 ± 0.14	4.7 ± 1.4	0.45 ± 0.14
Fakes	19.1 ± 3.2	22.7 ± 3.4	26.5 ± 3.5	40 ± 5	7.2 ± 1.7	$0.00 \pm {}^{0.04}_{0.00}$	6.6 ± 1.6	$0.001 \pm {}^{0.029}_{0.001}$
$t\bar{t}$	$0.05 \pm {}^{0.18}_{0.05}$	$0.11 \pm {}^{0.17}_{0.11}$	0.38 ± 0.22	1.1 ± 0.4	0.78 ± 0.29	$0.08 \pm {}^{0.10}_{0.08}$	0.8 ± 0.4	0.36 ± 0.21
$t\bar{t}\,X$	$0.007 \pm {}^{0.019}_{0.007}$	$0.002 \pm {}^{0.008}_{0.002}$	$0.009 \pm {}^{0.019}_{0.009}$	$0.019 \pm {}^{0.026}_{0.019}$	$0.026 \pm {}^{0.026}_{0.026}$	$0.010 \pm {}^{0.015}_{0.010}$	0.039 ± 0.025	$0.003 \pm {}^{0.008}_{0.003}$
Others	0.045 ± 0.031	0.30 ± 0.12	1.3 ± 0.6	1.9 ± 0.6	1.4 ± 0.4	0.51 ± 0.18	1.16 ± 0.27	0.27 ± 0.09

Table 10.2: Yields in SRlow-nj. Statistical and systematic uncertainties are included.

Region	SRlow-njb	SRlow-njc	SRlow-njd	SRlow-nje	SRlow-njf1	SRlow-njf2	SRlow-njg1	SRlow-njg2
Observed	6	13	17	14	25	20	22	12
Bg predicted	3.5 ± 0.6	8.0 ± 1.2	13.5 ± 1.5	18.2 ± 3.4	23.4 ± 2.5	17.9 ± 1.9	17.0 ± 3.5	12.4 ± 1.9
WZ	1.62 ± 0.30	3.2 ± 0.6	6.0 ± 0.8	8.6 ± 1.3	11.1 ± 1.2	9.4 ± 1.1	10.0 ± 1.2	7.3 ± 1.3
ZZ	0.45 ± 0.13	0.72 ± 0.22	1.00 ± 0.28	1.4 ± 0.9	4.0 ± 1.6	0.66 ± 0.25	$1.1 \pm {}^{2.6}_{1.1}$	0.34 ± 0.11
Fakes	1.2 ± 0.5	3.7 ± 0.9	4.5 ± 1.2	3.3 ± 1.3	2.2 ± 1.4	$0.00 \pm {}^{0.14}_{0.00}$	1.8 ± 1.1	$0.0 \pm {}^{0.6}_{0.0}$
$t\bar{t}$	0.15 ± 0.13	0.28 ± 0.14	1.5 ± 0.4	3.3 ± 0.9	4.6 ± 1.1	5.7 ± 1.2	3.0 ± 0.8	2.9 ± 0.7
$t\bar{t}\,X$	0.030 ± 0.013	0.052 ± 0.019	0.24 ± 0.06	0.33 ± 0.07	0.44 ± 0.09	0.72 ± 0.11	0.36 ± 0.08	0.44 ± 0.09
Others	0.006 ± 0.004	$0.14 \pm {}^{0.34}_{0.14}$	0.21 ± 0.06	$1.3 \pm {}^{1.8}_{1.3}$	1.0 ± 0.4	1.4 ± 0.9	0.71 ± 0.21	1.4 ± 0.6

Table 10.3: Yields in SRhigh-0j. Statistical and systematic uncertainties are included.

Region	SRhigh-0jb	SRhigh-0jc	SRhigh-0jd	SRhigh-0je	SRhigh-0jf1	SRhigh-0jf2	SRhigh-0jg1	SRhigh-0jg2
Observed	1	4	11	13	37	14	43	17
Bg predicted	1.5 ± 0.7	4.3 ± 0.8	14.0 ± 1.6	11.5 ± 1.6	35.7 ± 3.2	25.5 ± 2.4	39.5 ± 3.0	21 ± 7
WZ	$0.20 \pm {}^{0.27}_{0.20}$	1.5 ± 0.5	6.0 ± 0.9	6.1 ± 1.1	20.5 ± 2.1	16.0 ± 2.3	26.4 ± 2.2	15 ± 7
ZZ	$0.5 \pm {}^{0.5}_{0.5}$	0.31 ± 0.12	1.8 ± 0.8	0.89 ± 0.24	3.1 ± 1.0	0.95 ± 0.35	3.0 ± 0.9	0.58 ± 0.17
Fakes	0.81 ± 0.31	1.7 ± 0.4	4.4 ± 1.0	1.1 ± 0.8	4.3 ± 1.4	$0.00 \pm {}^{0.15}_{0.00}$	3.4 ± 1.3	$0.00 \pm {}^{0.11}_{0.00}$
$t\bar{t}$	$0.05 \pm {}^{0.05}_{0.05}$	0.45 ± 0.17	0.64 ± 0.28	1.8 ± 0.6	4.4 ± 1.0	4.4 ± 1.0	4.3 ± 0.9	3.1 ± 0.7
$t\bar{t}\,X$	$0.003 \pm {}^{0.014}_{0.003}$	$0.009 \pm {}^{0.013}_{0.009}$	0.029 ± 0.015	0.08 ± 0.04	0.11 ± 0.05	0.109 ± 0.030	0.16 ± 0.05	0.09 ± 0.04
Others	$0.014 \pm {}^{0.018}_{0.014}$	$0.3 \pm {}^{0.4}_{0.3}$	1.1 ± 0.4	1.6 ± 0.4	3.3 ± 0.8	4.0 ± 1.0	2.3 ± 0.8	2.0 ± 0.5

Table 10.4: Yields in SRhigh-nj. Statistical and systematic uncertainties are included.

Region	SRhigh-nja	SRhigh-njb	SRhigh-njc	SRhigh-njd	SRhigh-nje	SRhigh-njf	SRhigh-njg
Observed	3	2	2	2	2	11	4
Bg predicted	6.0 ± 1.6	1.4 ± 0.6	2.1 ± 0.8	5.4 ± 1.4	3.0 ± 1.1	9.9 ± 2.5	6.8 ± 1.8
WZ	3.8 ± 1.2	0.57 ± 0.18	1.25 ± 0.25	2.5 ± 0.4	1.31 ± 0.25	4.5 ± 0.7	3.7 ± 0.6
ZZ	0.044 ± 0.023	0.009 ± 0.005	0.020 ± 0.011	0.014 ± 0.013	0.029 ± 0.014	0.081 ± 0.033	0.050 ± 0.020
Fakes	1.5 ± 0.8	$0.5 \pm {}^{0.5}_{0.5}$	$0.04 \pm {}^{0.28}_{0.04}$	$0.7 \pm {}^{0.8}_{0.7}$	$0.0 \pm {}^{0.4}_{0.0}$	$0.6 \pm {}^{0.9}_{0.6}$	$0.00 \pm {}^{0.19}_{0.00}$
$t\bar{t}$	0.6 ± 0.5	$0.14 \pm {}^{0.15}_{0.14}$	0.6 ± 0.5	1.3 ± 0.8	1.2 ± 1.0	3.4 ± 2.0	2.5 ± 1.6
$t\bar{t}\,X$	0.16 ± 0.06	$0.014 \pm {}^{0.025}_{0.014}$	0.027 ± 0.023	$0.08 \pm {}^{0.08}_{0.08}$	0.09 ± 0.04	0.31 ± 0.08	0.21 ± 0.07
Others	0.038 ± 0.030	$0.22 \pm {}^{0.22}_{0.22}$	$0.14 \pm {}^{0.36}_{0.14}$	0.8 ± 0.6	0.33 ± 0.21	1.0 ± 0.4	$0.3 \pm {}^{0.4}_{0.3}$

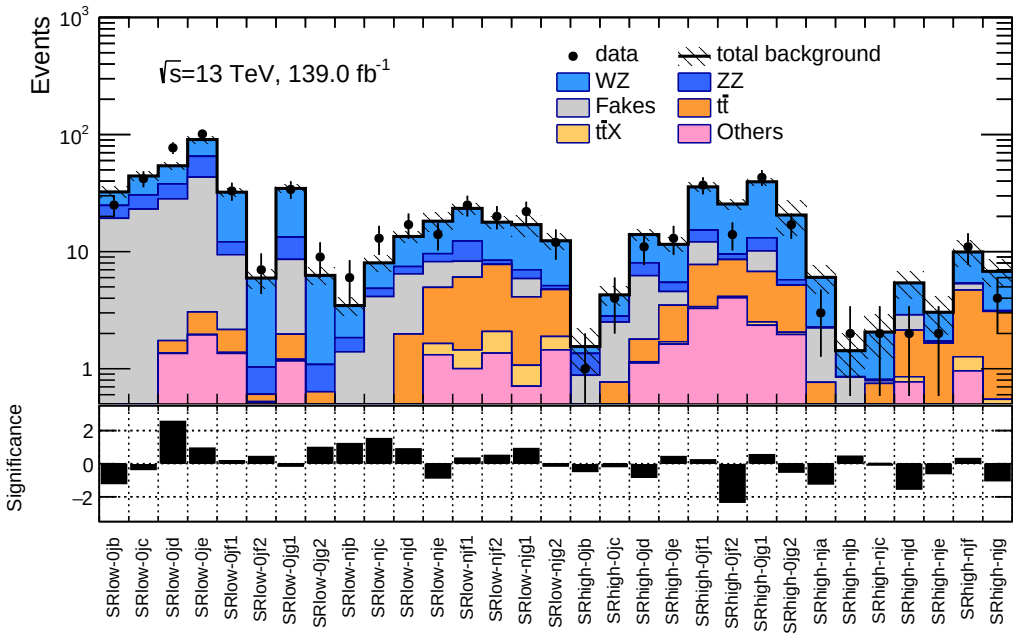

Fig. 10.1: Summary plot showing the number of events in all SRs and the expected background. The bottom panel shows the significance of the difference between the observed and the expected yields, calculated with the profile likelihood method from [191], adding a minus sign if the yield is below the prediction. Statistical and systematic uncertainties are included.

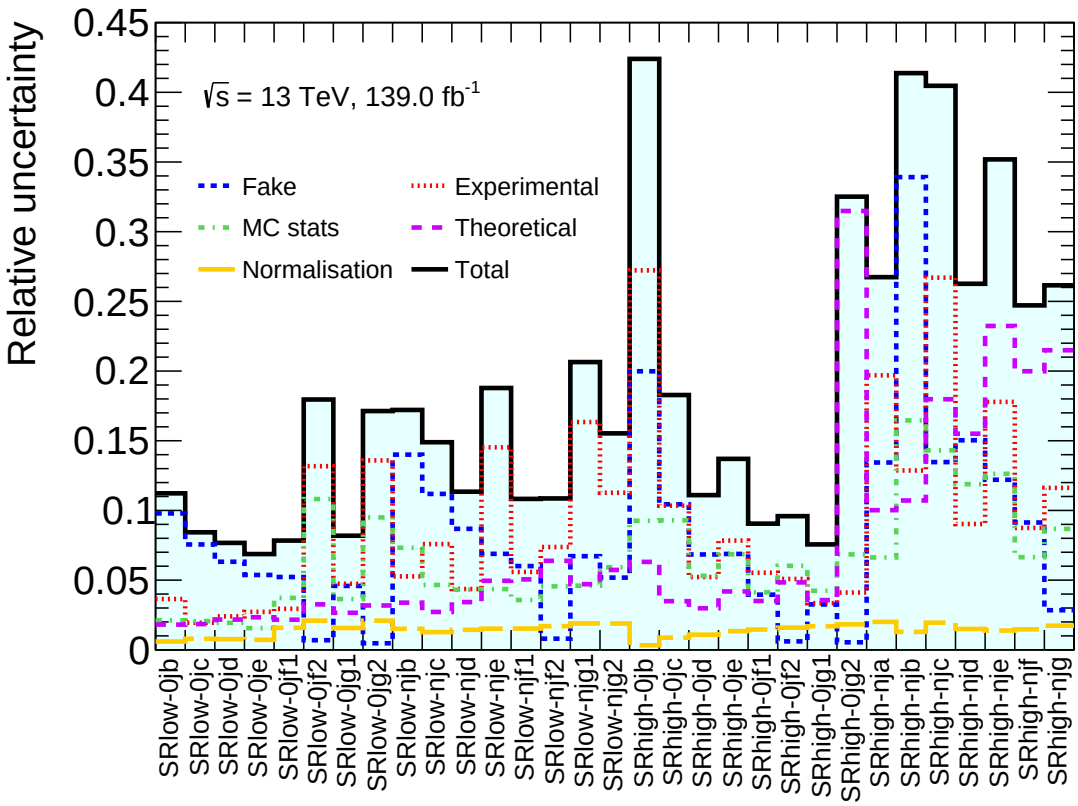

Fig. 10.2: Breakdown of the systematic uncertainties in the event yields in the SRs.

10.3 Discovery fit

The discovery fit is set up to reject the background-only hypothesis. For the discovery fit the model-independent SRs are used as defined in Section 8.5. The normalisation factor for the signal is set to zero, $\mu_S = 0$, in order to formulate the background-only hypothesis. The test statistic from Equation 10.3 is then modified such that it takes the form of

$$q_0 = \begin{cases} q(\mu_S = 0), & \text{if } \hat{\mu}_s > 0 \\ 0, & \text{if } \hat{\mu}_s < 0, \end{cases} \tag{10.6}$$

where in case of $\hat{\mu}_s < 0$ it is declared that the data is maximally compatible with the background-only hypothesis $\mu_S = 0$. Each discovery SR is fit independently together with the CRs.

For each signal region the discovery fit also produces a model-independent 95 % CL_S upper limit on the number of events of a generic beyond-the-Standard-Model process. The limit can be equivalently expressed as a limit on the visible cross-section of such process. From Table 10.5 it can be seen that the maximum significance of rejecting the background-only hypothesis is 1.28σ. It can thus be concluded that in none of the discovery regions the background-only hypothesis can be rejected.

10.4 Exclusion fit

For the exclusion fit the regular SRs are used as defined in Section 8.4. In the previous section it has been shown that the discovery fit has failed to reject the background-only hypothesis. The next step is to do an exclusion fit to reject the signal-plus-background hypothesis and derive exclusion contours. The exclusion fit measures the level of agreement of the observed data with the signal-plus-background hypothesis, with a signal strength of $\mu_S = 1$. In this case the test statistic from Equation 10.3 is modified such that it takes the form,

$$q_{\mu_s=1} = \begin{cases} q(\mu_s = 1), & \text{if } \hat{\mu}_s \leq \mu_s = 1 \\ 0, & \text{if } \hat{\mu}_s > \mu_s = 1, \end{cases} \tag{10.7}$$

where in case of $\hat{\mu}_s > \mu_s = 1$ the data is maximally compatible with the signal-plus-background hypothesis $\mu_S = 1$. All the SRs and CRs are fit simultaneously for each signal

Table 10.5: Summary of the expected background and data yields in the discovery signal regions. The second and third columns show the data and total expected background. Statistical and systematic uncertainties are included. The fourth column gives the model-independent upper limits at 95% CL on the visible cross-section (σ_{vis}). The fifth and sixth columns give the visible number of observed (S^{95}) and expected (S^{95}) events of a generic beyond-the-Standard-Model process. The last column shows the discovery p-value and expected Gaussian significance Z assuming the background-only hypothesis. A one sided p-value is used causing the maximum p-value to be at 0.5, which corresponds to a significance (Z) of zero.

Signal channel	N_{obs}	N_{exp}	σ^{95}_{vis}[fb]	S^{95}_{obs}	S^{95}_{exp}	CL_B	$p(s=0)$ (Z)
disc-SRhigh-nJa	3	6.0 ± 1.6	0.03	4.3	$6.3^{+3.1}_{-2.0}$	0.16	0.50 (0.00)
disc-SRhigh-nJb	2	1.43 ± 0.58	0.03	4.6	$4.0^{+1.0}_{-1.4}$	0.62	0.34 (0.41)
disc-SRhigh-nJc1	7	9.5 ± 2.2	0.05	6.3	$8.0^{+3.7}_{-2.4}$	0.26	0.50 (0.00)
disc-SRhigh-nJc2	2	2.06 ± 0.77	0.03	4.4	$4.4^{+2.5}_{-1.5}$	0.49	0.50 (0.00)
disc-SRlow-b	31	35.8 ± 3.8	0.08	11.5	$14.6^{+6.3}_{-4.3}$	0.25	0.50 (0.00)
disc-SRhigh-b	3	2.97 ± 0.89	0.04	5.0	$5.0^{+2.7}_{-1.7}$	0.50	0.50 (0.00)
disc-SRlow-c	86	88.1 ± 7.1	0.16	22.4	$23.8^{+9.8}_{-6.8}$	0.43	0.50 (0.00)
disc-SRhigh-c	9	9.3 ± 1.6	0.05	7.5	$7.8^{+3.7}_{-2.4}$	0.47	0.50 (0.00)
disc-SR-d	202	184 ± 12	0.36	49.9	$36.2^{+14.5}_{-10.3}$	0.83	0.17 (0.97)
disc-SR-e1	332	308 ± 17	0.49	68.4	$49.8^{+19.8}_{-14.0}$	0.83	0.17 (0.96)
disc-SR-e2	298	269 ± 15	0.49	68.3	$45.2^{+17.9}_{-12.6}$	0.90	0.10 (1.28)
disc-SR-f1	479	457 ± 22	0.57	79.1	$62.1^{+25.0}_{-17.8}$	0.76	0.23 (0.72)
disc-SR-f2	277	272 ± 13	0.34	47.1	$43.6^{+17.6}_{-12.6}$	0.59	0.41 (0.23)
disc-SR-g1	620	593 ± 28	0.69	96.0	$75.9^{+30.1}_{-21.9}$	0.76	0.23 (0.73)
disc-SR-g2	418	408 ± 20	0.47	65.9	$59.1^{+23.3}_{-17.1}$	0.63	0.37 (0.34)
disc-SR-g3	288	285 ± 16	0.36	50.5	$48.0^{+18.9}_{-13.4}$	0.55	0.45 (0.14)
disc-SR-g4	141	136 ± 10	0.25	34.9	$31.4^{+12.6}_{-8.7}$	0.62	0.38 (0.31)

point. In order to exclude a signal a confidence level is defined,

$$CL_s = \frac{p_{s+b}}{1 - p_b}, \tag{10.8}$$

where p_{s+b} corresponds to $\mu_s = 1$ and p_b corresponds to $\mu_s = 0$. The supersymmetry signals, depending on the $\tilde{\chi}^0_1$ and $\tilde{\chi}^0_2/\tilde{\chi}^\pm_1$ mass, are excluded at 95% Confidence Level (CL) if $CL_s < 0.05$.

The exclusion contours are shown in Figure 10.3 for the combination of the SRlow and SRhigh regions, as well as for each of the regions separately. It can be seen that the simplified models used in this thesis are excluded up to a $\tilde{\chi}^0_1$ mass of 250 GeV. As expected most of the exclusion power at low Δm between the $\tilde{\chi}^0_2/\tilde{\chi}^\pm_1$ and $\tilde{\chi}^0_1$ is driven by the SRhigh regions.

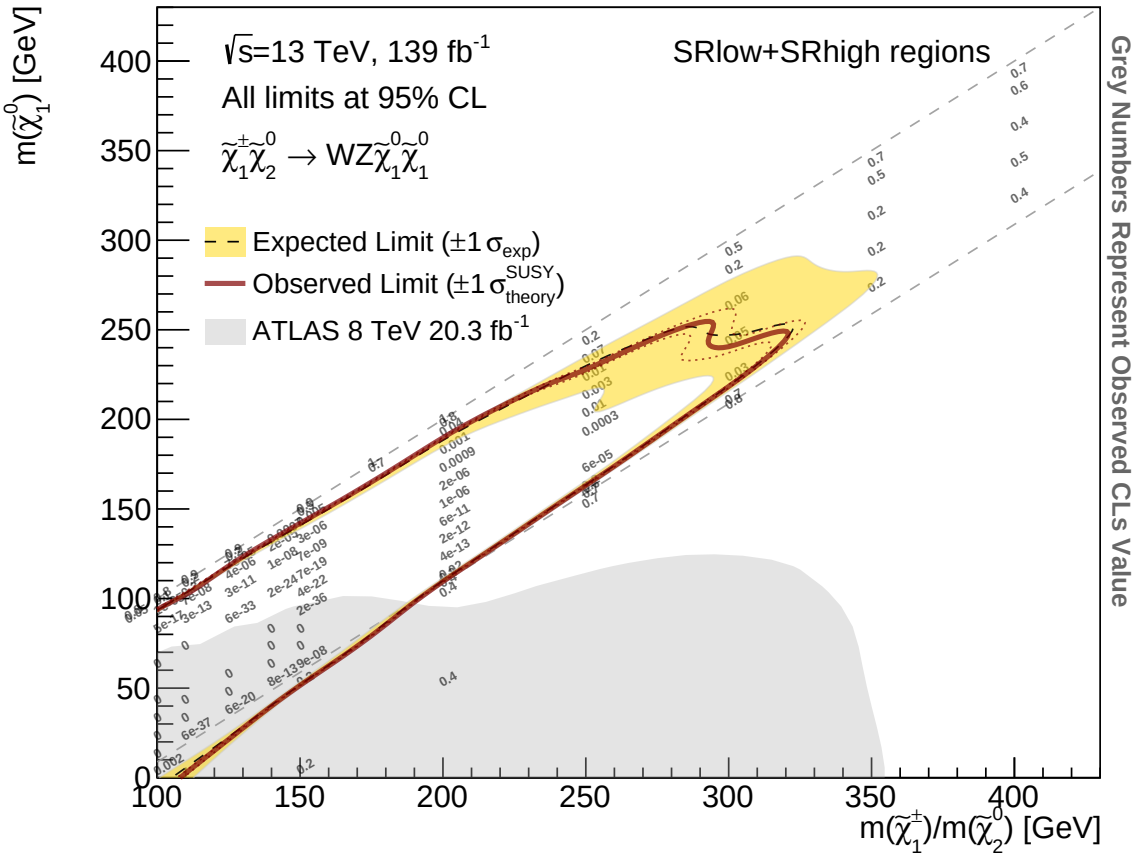

(a)

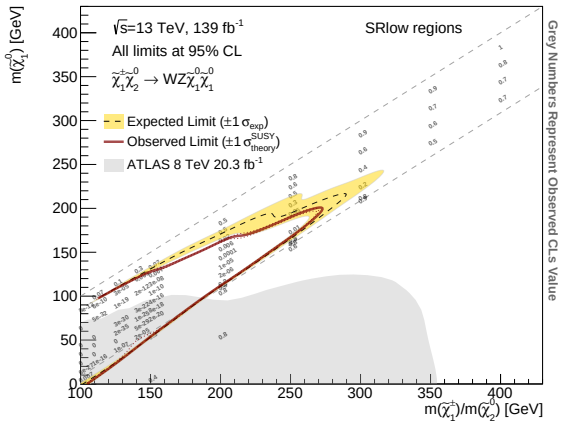

(b)

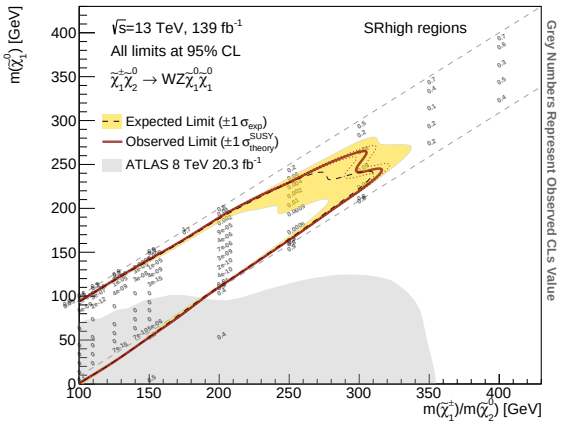

(c)

Fig. 10.3: Exclusion contours parametrised in $\tilde{\chi}_1^0$ and $\tilde{\chi}_1^{\pm}/\tilde{\chi}_2^0$ mass for **(a)** the combination of the SRlow and SRhigh regions, **(b)** the SRlow regions and **(c)** the SRhigh regions. The expected 95% confidence level (CL) sensitivity (dashed black line) is shown with $\pm 1\sigma_{\text{exp}}$ (yellow band) from experimental systematic uncertainties and statistical uncertainties on the data yields, the observed limit (red solid line) is shown with $\pm 1\sigma_{\text{theory}}$ (dotted red lines) from signal cross-section uncertainties. The grey shade are the constraints obtained by the off-shell and on-shell WZ Run-1 result using 20.3 fb^{-1} at $\sqrt{s} = 8$ TeV [186].

Chapter 11

Discussion

The supersymmetry signal motivated by global fits, described in Section 2.4, has not been found by the analysis performed in this thesis, described in Part III. This could be due to a number of reasons which will be discussed in this chapter. Also possible improvements to the analysis are mentioned which could increase the sensitivity to higher $\tilde{\chi}_1^{\pm}/\tilde{\chi}_2^0$ mass or in the more compressed regions, where the mass difference (Δm = $m_{\tilde{\chi}_1^{\pm}/\tilde{\chi}_2^0} - m_{\tilde{\chi}_1^0}$) is small.

11.1 Different models

In the Signal Regions (SRs) considered and under the assumptions made, supersymmetry has not been found by this analysis. However, if there is new physics in the phase space described in this thesis, at the mass scale accessible by the LHC, it is possible to question why it has not been observed. There are a number of reasons why this might happen:

- New physics has too small couplings and/or a branching ratio (BR) to three leptons less than 100%, which causes a much lower sensitivity than the simplified scenario considered in this analysis.
- The kinematics of the new physics lead to final states that are difficult to detect, as is the case for the compressed signal points.

11.1.1 Smaller couplings

In the typical supersymmetry analysis done by ATLAS simplified models are used which include certain assumptions, for example that supersymmetry particles not considered in the analysis are heavy and decoupled. As an advantage this provides good sensitivity and the ability to exclude regions in the supersymmetry phase space. The simplified models used to

describe the supersymmetry signal assume gaugino mixing, as described in Section 2.1.1, such that the $\tilde{\chi}_1^{\pm}/\tilde{\chi}_2^0$ are wino-like and the $\tilde{\chi}_1^0$ is bino-like, which results in a high production cross-section. Also the BR for the decay of $\tilde{\chi}_1^{\pm}\tilde{\chi}_2^0$ to the final state under consideration,

$$\tilde{\chi}_1^{\pm}\tilde{\chi}_2^0 \rightarrow W^{\pm}Z\tilde{\chi}_1^0\tilde{\chi}_1^0, \tag{11.1}$$

is assumed to be 100%. However, in scenarios with different gaugino mixing the production cross-section needs to be multiplied with about $\sim \frac{3}{4}$. If one then further assumes a branching ratio of about 50% instead of a 100% to the WZ final state, the visible cross-section of the process needs to be multiplied by $\sim \frac{1}{4}$. It is interesting, under the assumption that the shape of the supersymmetry kinematic distributions stay the same, to consider what the exclusion would look like in case of such a different scenario. As can be seen in Figure 11.1, when reducing the cross-section of the supersymmetry signal by a factor of four, the supersymmetry models are only excluded up to a $\tilde{\chi}_1^0$ mass of 150 GeV.

11.1.2 Difficult kinematics: go more compressed

In the compressed regime, where $m_{\tilde{\chi}_1^{\pm}/\tilde{\chi}_2^0} - m_{\tilde{\chi}_1^0} < 15$ GeV, the kinematics are a limiting factor to obtain good sensitivity with the ATLAS detector as the signature of the process results in low p_{T} leptons and low $E_{\mathrm{T}}^{\mathrm{miss}}$. At an e^+e^- collider, such as the Large Electron-Positron Collider (LEP), low p_{T} and low $E_{\mathrm{T}}^{\mathrm{miss}}$ is not as much of a problem, which is why there always have been strong limits in the compressed regime from LEP. However, at a hadron collider doing a search with low p_{T} leptons and low $E_{\mathrm{T}}^{\mathrm{miss}}$ is hard, due to the large SM background and trigger restrictions. The strategy used to search for $\tilde{\chi}_1^{\pm}\tilde{\chi}_2^0$ in the analysis described in this thesis is through the Drell-Yan (DY) production process involving a W boson. In order to gain sensitivity for the more compressed signals an ISR jet to boost the system is used in the SRhigh-nj regions. A different analysis strategy can be considered as has been done by CMS where Vector Boson Fusion (VBF) production is studied [197].

When looking for $\tilde{\chi}_1^{\pm}\tilde{\chi}_2^0$ through DY production, the cross-section is of the order of α_{EW}^2. When looking at production through VBF, the cross-section is of the order of α_{EW}^4, decreasing the cross-section with a factor 10^{-4}. However, as can be seen in Figure 11.2, in VBF production the $\tilde{\chi}_1^{\pm}\tilde{\chi}_2^0$ are produced in association with two high p_{T} jets. Due to the kinematics of the process the two jets will be in opposite direction and close to the beam axis, which will result in a large di-jet invariant mass. The specific signature of the two high p_{T} VBF jets suppresses the SM background, but more importantly it boosts the $E_{\mathrm{T}}^{\mathrm{miss}}$ and p_{T} of the leptons. As a result from the boost the compressed regime will then become more accessible. Even the extreme compressed case where the $\tilde{\chi}_1^{\pm}\tilde{\chi}_2^0$ and $\tilde{\chi}_1^0$ are degenerate is

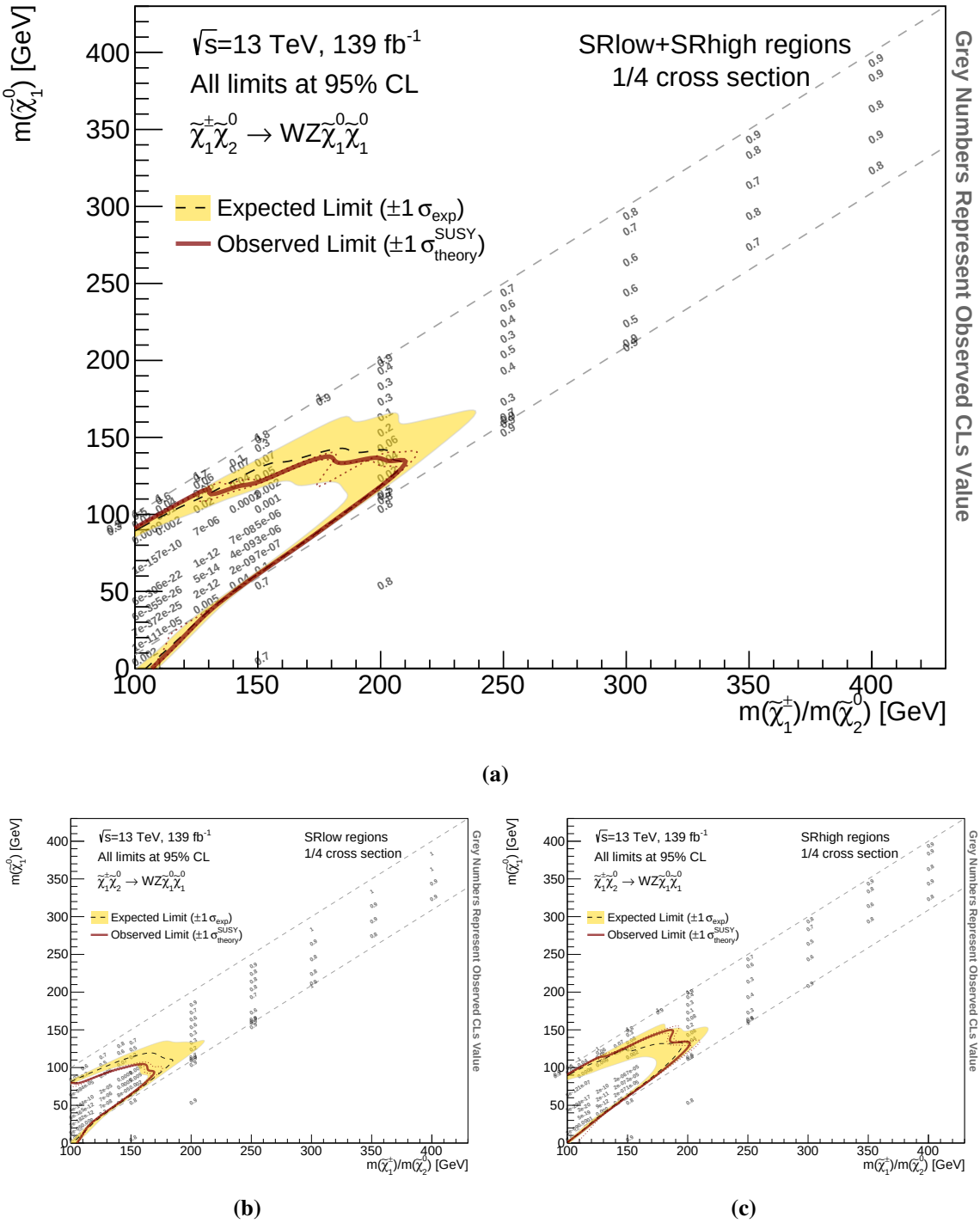

Fig. 11.1: Exclusion contours when reducing the cross-section of the supersymmetry signal by a factor four, parametrised in $\tilde{\chi}_1^0$ and $\tilde{\chi}_1^{\pm}/\tilde{\chi}_2^0$ mass for **(a)** the combination of the SRlow and SRhigh regions, **(b)** the SRlow regions and **(c)** the SRhigh regions. The expected 95% confidence level (CL) sensitivity (dashed black line) is shown with $\pm 1\sigma_{\text{exp}}$ (yellow band) from experimental systematic uncertainties and statistical uncertainties on the data yields, the observed limit (red solid line) is shown with $\pm 1\sigma_{\text{theory}}$ (dotted red lines) from signal cross-section uncertainties.

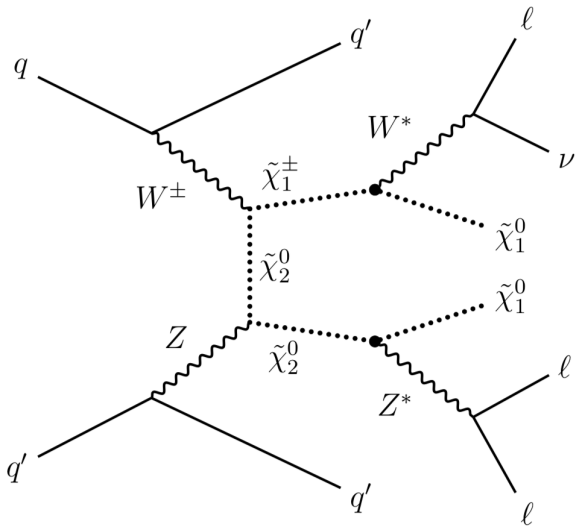

Fig. 11.2: Feynman diagram showing $\tilde{\chi}_1^\pm \tilde{\chi}_2^0$ production through the vector boson fusion (VBF) process.

accessible through a zero lepton search, in a two jet and $E_{\mathrm{T}}^{\mathrm{miss}}$ final state. It will be interesting to use such a technique to gain more sensitivity for the compressed signals, especially with the High Luminosity LHC where the low production cross-section of the VBF process can be compensated with a large luminosity.

11.2 Improvements to the analysis technique

Considering the analysis strategy discussed in this thesis, there are some improvements that will be interesting to implement in a next round of the analysis. Most of these improvements have not yet been implemented because of the timeline of the analysis and the fact that the new techniques described have to be further developed.

11.2.1 WZ control region

In validation region (VR) VRWZ-0j there is a 2σ tension with the data, as can be seen from the yields in Table 9.2. In an ideal case such a tension with the data is not present in a VR, assuming the background under validation is properly normalised through the use of a control region (CR). In order to properly normalise a background and to correct mismodelling it is important that the phase space of the CRs is close to the phase space of the VRs and SRs. However, in the current analysis, due to orthogonality restrictions and limited possibilities in terms of phase space, instead of selecting off-shell WZ as used in the VR, a CR has been used

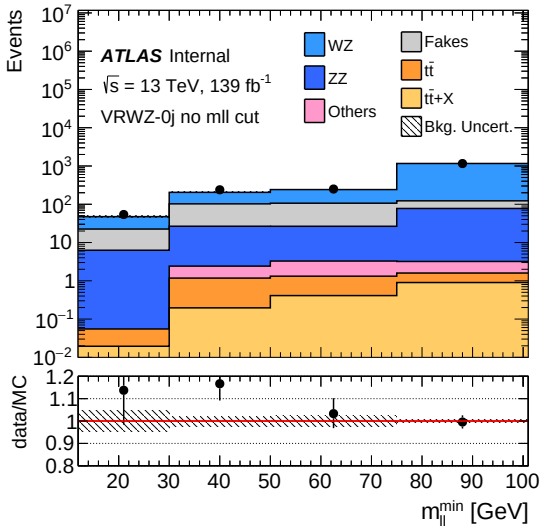

Fig. 11.3: Distribution of the $m_{\ell\ell}^{\text{min}}$ for VRWZ-0j. The VRWZ-0j is shown without $m_{\ell\ell}$ cut to study the extrapolation from CRWZ-0j to VRWZ-0j. As can be seen the modelling in the on-shell region $m_{\ell\ell}^{\text{min}}$ >75 GeV is different from the modelling in the off-shell region $m_{\ell\ell}^{\text{min}}$ <75 GeV. Only statistical uncertainties are included.

which selects on-shell WZ, as defined in Section 7.1.2. The $m_{\ell\ell}$ window in the CRWZ-0j is [81,101] GeV, while in the VRWZ-0j the cut is placed at $m_{\ell\ell} < 75$ GeV. The variable $m_{\ell\ell}$ is thus extrapolated from the CR to the VR. One of the most relevant checks is to examine the VRWZ-0j with the $m_{\ell\ell}$ cut moved up to < 101 GeV, to study the modelling in the $m_{\ell\ell}$ variable.

In Figure 11.3 the VRWZ-0j is shown with the moved $m_{\ell\ell}$ cut. It can be seen that the data/MC agreement in the CRWZ-0j phase space, $m_{\ell\ell}$ range [81,101] GeV, is better than in the VRWZ-0j phase space, where the $m_{\ell\ell} < 75$ GeV. It can be concluded that in order to correct for the mismodelling in the the VRWZ-0j, a different normalisation factor would be needed than the one obtained from the on-shell WZ CR, to adjust the data/MC agreement.

In order to improve the CRWZ-0j, to correct the mismodelling in the off-shell WZ phase space, there are limited possibilities in the three lepton phase space. However, there is the possibility of using a four lepton phase space and normalise using the ZZ background. A CRZZ-0j, as defined in Table 11.1, can be used to normalise the WZ background because both backgrounds represent a similar process and both are generated using Sherpa. As can be seen in Figure 11.4 the mismodelling observed in the off-shell VRWZ-0j region is similar to the CRZZ-0j. The yields are shown in Table 11.2, where a normalisation factor of 1.29 is obtained from the CRZZ-0j, which can be used to correct for the mismodelling in the VRWZ-0j. If this strategy is to be used, it is important to study that the same kinematic

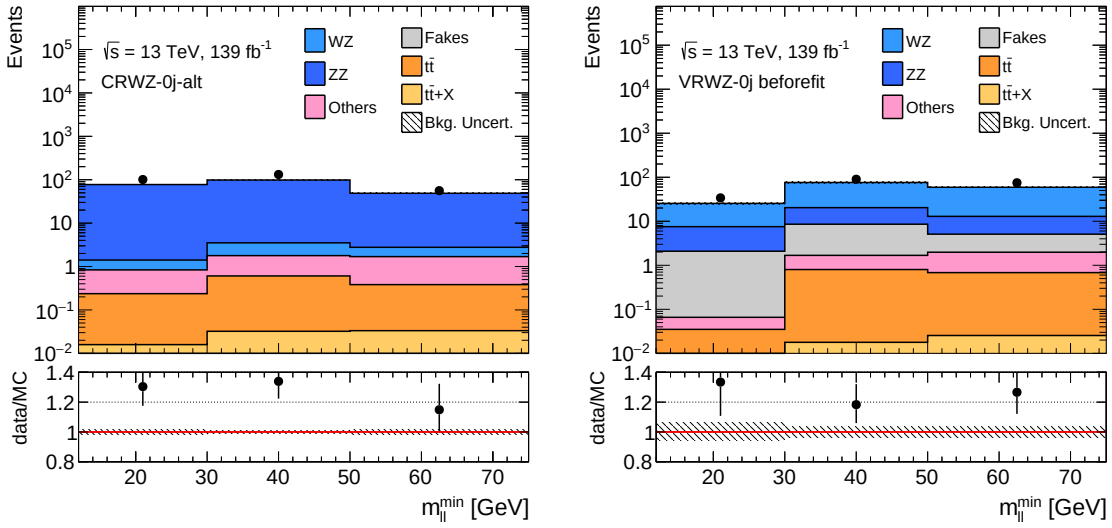

Fig. 11.4: Distributions of the $m_{\ell\ell}^{\text{min}}$ for **(a)** CRZZ-0j and **(b)** VRWZ-0j. As can be seen the mis-modelling in $m_{\ell\ell}^{\text{min}}$ for the off-shell region is similar for CRZZ-0j and VRWZ-0j, and thus it may be interesting to use CRZZ-0j as a CR to normalise the WZ and ZZ. Only statistical uncertainties are included.

selection for ZZ means the same phase-space for WZ and extra systematic uncertainties need to be derived that describe the uncertainties that belong to such an extrapolation.

Table 11.1: Off-shell CRZZ-0j definition. A jet-veto is applied, $N_{\text{jets}}^{30\text{ GeV}} = 0$, and a b-jet veto, such that $N_{\text{b-jets}}^{20\text{ GeV}} = 0$.

	n_{lep}	$m_{\ell\ell}$ [GeV]	$m_{\ell\ell}^{\text{min}}$ [GeV]	$E_{\text{T}}^{\text{miss}}$ [GeV]	lepton p_{T} [GeV]	$m_{\text{T}}^{\text{minmll}}$ [GeV]	$E_{\text{T}}^{\text{miss}}$ significance
CRZZ-0j	4	<75	>12	<50	all 3 > 10	-	>1.5

11.2.2 Different binning of the fake factor F

In order to obtain correct modelling for the fake leptons it is important to measure the fake factor F in bins where the fake composition is the same between the measurement region and the application region. When extrapolating between the on-shell Z fake lepton background measurement region of F and the off-shell WZ SRs, which is the application region, it was found that correctly modelling conversion fakes was not possible, since the conversion fakes have a different composition depending on $m_{\ell\ell}^{\text{min}}$, as can be seen in Figure 11.5. In the analysis this is dealt with by cutting away the conversion fake component in the SRs as described in

Table 11.2: Yields of CRZZ-0j and VRWZ-0j and the obtained scale factor μ_{ZZ0j}. Only statistical uncertainties are included.

sample	CRZZ-0j	purity	VRWZ-0j	purity	VRWZ-0j (μ_{ZZ0j} applied)	purity
Others	3.1 ± 0.3	1%	2.2 ± 0.5	1%	2.2 ± 0.5	1%
Fakes	0.0 ± 0.0	0%	12.0 ± 1.7	7%	12.0 ± 1.7	6%
$t\bar{t}$	1.1 ± 0.2	1%	1.5 ± 0.3	1%	1.5 ± 0.3	1%
$t\bar{t}$ +X	0.1 ± 0.0	0%	0.0 ± 0.0	0%	0.0 ± 0.0	0%
WZ	3.4 ± 0.4	2%	119.9 ± 2.8	75%	151.07 ± 3.5	76%
ZZ	217.1 ± 1.9	97%	25.1 ± 2.0	16%	31.6 ± 2.0	16%
Total	224.7 ± 2.0	-	160.8 ± 3.9	-	198.4 ± 4.4	-
data	289.0 ± 17.0	-	199.0 ± 14.1	-	199.0 ± 14.1	-
μ_{ZZ0j}	1.29	-	-	-	-	-

Section 7.2.3. For a new round of the analysis, correct modelling for the conversion fakes in the SRs would require not cutting away the conversion fake component.

In order to model the conversion fake component it needs to be measured depending on $m_{\ell\ell}^{\text{min}}$ in the off-shell Z fake lepton background measurement region. Construction of such a measurement region, with a good amount of statistics, to measure the F dependence on $m_{\ell\ell}^{\text{min}}$ has been tried but was unsuccessful. Instead a proxy can be used to measure this dependence. For each fake component a specific measurement region can be made to obtain the F for that fake source. For example a cut on the d_0 significance can be used as a discriminant to select heavy-flavour fakes, and photon-related variables that depend on the shower shape can be used to select conversion fakes. Once having obtained separate F for each of the fake sources these have to be combined to correctly mimic the dependence of the fake sources on $m_{\ell\ell}^{\text{min}}$. The easiest method would be to use the distribution in Figure 11.5 to determine the fake composition from each of the fake components as a function of $m_{\ell\ell}^{\text{min}}$ from Z+jets/Z+γ MC. However, since Z+jets/Z+γ MC has been found to be unreliable, it would be better to use a data-driven method to obtain the dependence of the fake composition on $m_{\ell\ell}^{\text{min}}$. Such a data-driven method could consist of fitting templates, for each fake source, of the d_0 significance distribution, which contains information on the sources of fake components, in the application region to determine the composition. Such a method of fitting templates is also used by the b-tagging efficiency measurement [178]. A method like this would be the most robust fully data-driven method to estimate the fakes in the off-shell region.

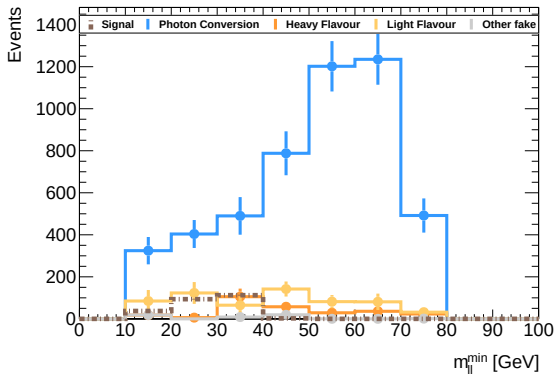

Fig. 11.5: Distribution showing the dependence of different fake sources on $m_{\ell\ell}^{\text{min}}$ in the SRlow-0j region.

11.2.3 Improved Prompt Lepton Veto

The Prompt Lepton Veto (PLV) is described in Section 5.4 and the performance of the two working points, `PLVLoose` and `PLVTight`, in a preselection region of the SRs is described in Section 8.3. Improvements to the `PLVLoose` and `PLVTight` working points have been made in parallel with this analysis and can be used in the next round of the analysis. The nominal PLV used in the analysis is trained at $p_{\text{T}} > 10$ GeV. To improve the PLV at low p_{T} a separate low p_{T} PLV is trained. The new PLV working point would then be a combination of the two PLVs, the nominal and low p_{T} working point, by using an interpolation function. The interpolation function uses a smooth cut on the BDT score, instead of the binned approach shown in Table 5.4. The interpolation function takes the form of

$$PLV < \begin{cases} ap_{\text{T}}^3 + bp_{\text{T}}^2 + cp_{\text{T}} + d & (p_{\text{T}} < p_{\text{T}}^{int}), \quad \text{low } p_{\text{T}} \text{ PLV (trained at } p_{\text{T}} < 6 \text{ GeV)} \\ max(-0.88, A + Be^{\frac{p_{\text{T}}}{C}}) & (p_{\text{T}} > p_{\text{T}}^{int}), \quad \text{nominal PLV (trained at } p_{\text{T}} > 10 \text{ GeV)}, \end{cases} \tag{11.2}$$

where p_{T}^{int} is the intersection between the nominal and the low p_{T} PLV. The optimal working point found is described in Table 11.3. With the low lepton p_{T} working point added, the fake rejection improves by 20-30% at low p_{T}.

11.2.4 Specialised trigger

As can be seen in Figure 8.2 trigger acceptance is a bottle neck for the compressed supersymmetry signal grid points with $m_{\tilde{\chi}_1^\pm/\tilde{\chi}_2^0} - m_{\tilde{\chi}_1^0} < 25$ GeV. In order to trigger signals with such low Δm the analysis now mostly relies on the SRhigh-nj regions where the $E_{\text{T}}^{\text{miss}}$ triggers can be used. To increase the sensitivity for these mass points in the other SRs, SRlow and

Table 11.3: Definition of the new PLV working point where a smooth cut on the BDT score is applied using an interpolation function. Two working points have been defined with the same names as before, `PLVLoose` and `PLVTight`. The variable p_{T}^{int} is the intersection between the nominal and the low p_{T} PLV. The function for the cut value on the BDT for the low p_{T} PLV depends on variables a, b, c and d. The function of the cut value on the BDT for the nominal PLV depends on A, B and C.

	a [GeV^{-3}]	b [GeV^{-2}]	c [GeV^{-1}]	d	A	B	C [GeV]	p_{T}^{int} [GeV]
	Electrons							
`PLVLoose`	0	-0.000106967	-0.0160896	0.960105	-0.94386	3.03257	28.0508	18.457
`PLVTight`	0	-0.000722487	-0.0750674	1.13016	-0.881497	2.29469	11.5776	16.967
	Muons							
`PLVLoose`	-0.000186	0.0058481	-0.0788936	1.05942	-0.958651	3.54785	19.6155	18.452
`PLVTight`	0	-0.000992265	-0.0597252	0.998203	-0.929774	2.9159	10.2339	18.603

SRhigh-0j, a specialised trigger can be developed. For example a topological trigger that uses a ΔR requirement between the leptons would be an option.

11.3 High luminosity LHC

The expected exclusion contour for this analysis with the High Luminosity LHC, with an expected luminosity of 3000 fb^{-1}, is shown in Figure 11.6. The expected result is obtained using the analysis as described in this thesis, assuming the trigger acceptance stays the same, as well as the reconstruction and identification efficiencies, and the regions used. The sensitivity is shown for the simplified models used in the analysis, as well as the case where the cross-section is reduced by a factor four. When adding new analysis techniques as described in Section 11.2 further improvements are expected: an improved μ_{WZ}, better fakes modelling, improved fake background rejection from the PLV, and improved acceptance from the triggers for the compressed grid points. Also it will be interesting to include a VBF SR for the almost degenerate compressed scenarios.

11.4 Comparison with CMS

A similar analysis as described in this thesis has been performed by CMS during Run-1. The simplified model is used, where for $\tilde{\chi}_1^{\pm}\tilde{\chi}_2^0$ production the $\tilde{\chi}_1^{\pm}$ and $\tilde{\chi}_2^0$ are assumed to be mass-degenerate and wino-like, and the $\tilde{\chi}_1^0$ is set to be bino-like. The result with 35.9 fb^{-1} is shown in Figure 11.7 [76]. Due to the smaller dataset used for the analysis the limit obtained

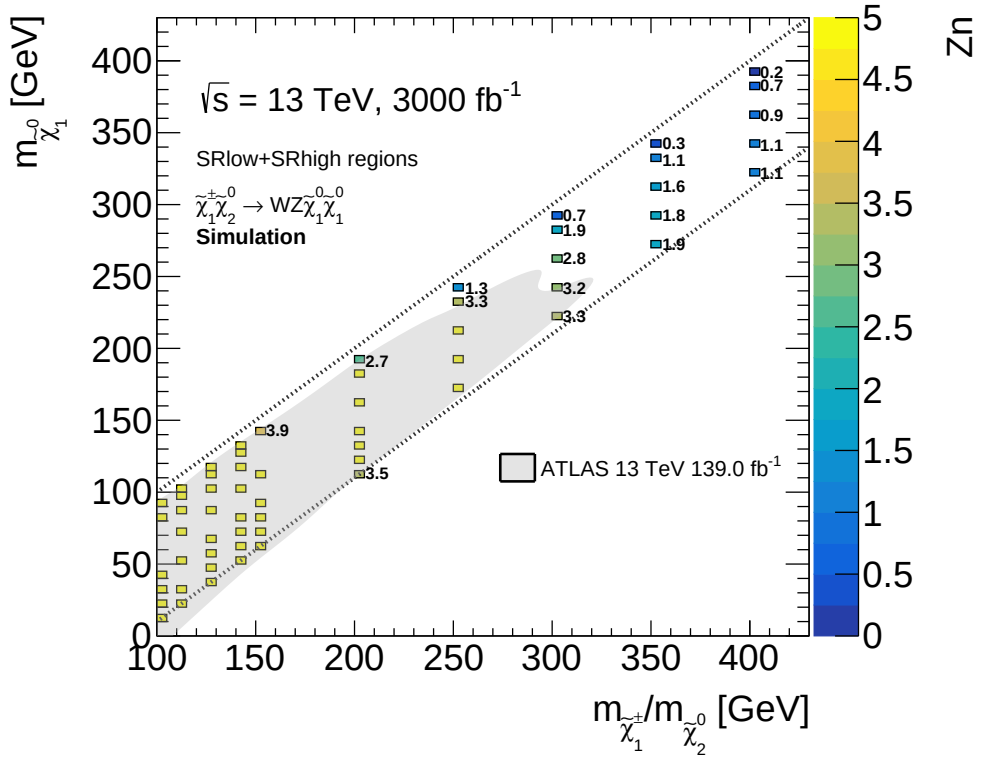

(a)

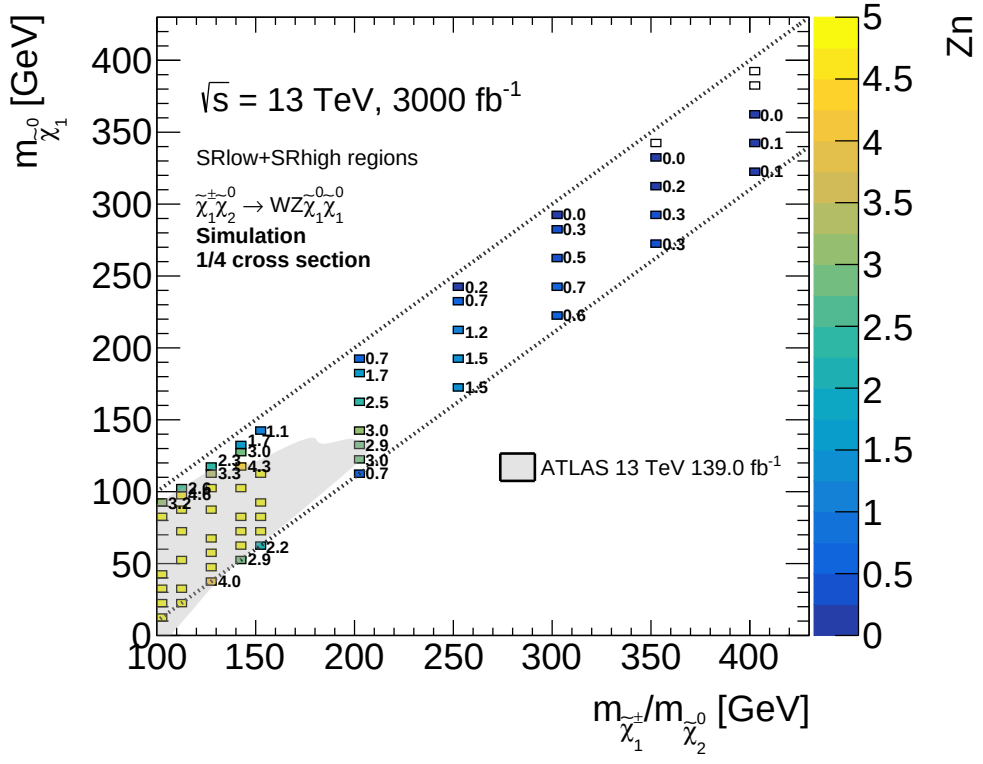

(b)

Fig. 11.6: Expected significance with the High Luminosity LHC in the SRlow and SRhigh signal regions for **(a)** the nominal simplified models and **(b)** the simplified models with the cross-section reduced by a factor four. Flat systematics per SR are implemented corresponding to Figure 10.2. The dashed line indicates the region where $m_{\tilde{\chi}_1^\pm/\tilde{\chi}_2^0} - m_{\tilde{\chi}_1^0} < m_Z$ and $m_{\tilde{\chi}_1^\pm/\tilde{\chi}_2^0} - m_{\tilde{\chi}_1^0} > 0$ GeV. The grey shade shows the obtained exclusion limits from the analysis described in this thesis, corresponding to the off-shell WZ Run-2 result using 139.0 fb^{-1} at $\sqrt{s} = 13$ TeV.

with the CMS analysis is weaker than the limit obtained by the ATLAS analysis described in this thesis. A new result from CMS with the full Run-2 dataset is expected in the near future.

A comparison can still be made with the analysis presented in this thesis. Figure 11.8 shows a comparison of the Run-1 CMS exclusion contour, and the expected sensitivity of the analysis described in this thesis with 35.9 fb^{-1}. It can be seen that the CMS search has a similar sensitivity, although at the smaller Δm between the $\tilde{\chi}_1^{\pm}/\tilde{\chi}_2^0$ and $\tilde{\chi}_1^0$ the presented analysis in this thesis outperforms the CMS search.

11.5 Combination with other gaugino analyses

The result presented in this thesis is made public as a conference proceeding [15]. The public result is a combination of several analyses assuming $\tilde{\chi}_1^{\pm}\tilde{\chi}_2^0$ production: the off-shell WZ analysis ($\tilde{\chi}_1^{\pm}\tilde{\chi}_2^0 \rightarrow W^*Z^*\tilde{\chi}_1^0\tilde{\chi}_1^0$) presented in this thesis, an on-shell WZ analysis ($\tilde{\chi}_1^{\pm}\tilde{\chi}_2^0 \rightarrow WZ\tilde{\chi}_1^0\tilde{\chi}_1^0$) and a Wh analysis ($\tilde{\chi}_1^{\pm}\tilde{\chi}_2^0 \rightarrow Wh\tilde{\chi}_1^0\tilde{\chi}_1^0$).

In Figure 11.9 the exclusion contour for the off-shell WZ analysis, the same as Figure 10.3 in Chapter 10, is shown in the Δm($\tilde{\chi}_1^{\pm}/\tilde{\chi}_2^0$,$\tilde{\chi}_1^0$) plane. The result is compared to the Higgsino analysis [198] shown in dark grey, where the Higgsino-like $\tilde{\chi}_1^0$ simplified model is reinterpreted as a bino-like $\tilde{\chi}_1^0$ simplified model. It can be seen that the Higgsino analysis is capable of excluding signals with a compressed Δm of below 10 GeV up to a $\tilde{\chi}_1^{\pm}\tilde{\chi}_2^0$ mass of almost 250 GeV. For the semi-compressed signals, with Δm larger than 10 GeV, the off-shell WZ analysis takes over the exclusion limit. The simplified models that are capable of reproducing the observed dark matter relic density, Ωh^2, are illustrated in the figure through a blue line, with a thickness corresponding to its uncertainty. Above the line corresponds to simplified models that produce a higher than observed dark matter relic density and below the line corresponds to simplified models that produce a lower dark matter relic density. It can be seen that the analysis presented in this thesis is capable of excluding the simplified models that correspond to the observed dark matter relic density up to a $\tilde{\chi}_1^{\pm}/\tilde{\chi}_2^0$ mass of around 200 GeV.

In Figure 11.10(a) the off-shell WZ result is combined with the on-shell WZ analysis. It can be seen that the on-shell WZ analysis is able to exclude signals up to a $\tilde{\chi}_1^{\pm}\tilde{\chi}_2^0$ mass of 640 GeV for signals with a Δm larger than 90 GeV. From the figure also the improvement with respect to the previous Run-1 combination of off-shell WZ and on-shell WZ analyses, shown in light grey, can be seen. In Figure 11.10(b) the Wh analysis is shown. Similar to the WZ analyses, the Wh analysis focuses on the pair production of $\tilde{\chi}_1^{\pm}$ and $\tilde{\chi}_2^0$, but with subsequent decay into $W^{\pm}\tilde{\chi}_1^0$ and $h\tilde{\chi}_1^0$, respectively. The h can then decay into WW, ZZ or

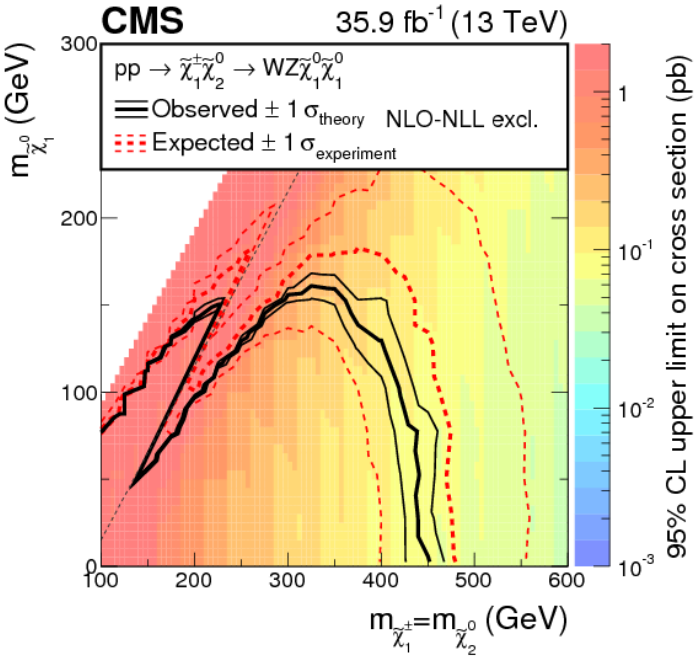

Fig. 11.7: Exclusion contours obtained by CMS using 35.9 fb^{-1} at $\sqrt{s} = 13$ TeV, parametrised in $\tilde{\chi}_1^0$ and $\tilde{\chi}_1^{\pm}/\tilde{\chi}_2^0$ mass. The shading indicates the 95% CL upper limit on the $\tilde{\chi}_1^{\pm}\tilde{\chi}_2^0$ production cross section. The contours bound the mass regions excluded at 95% CL assuming the NLO+NLL cross sections. The observed, $\pm 1\sigma_{\text{theory}}$ (± 1 standard deviation of the theoretical cross section) observed, median expected, and $\pm 1\sigma_{\text{experiment}}$ expected bounds are shown [76].

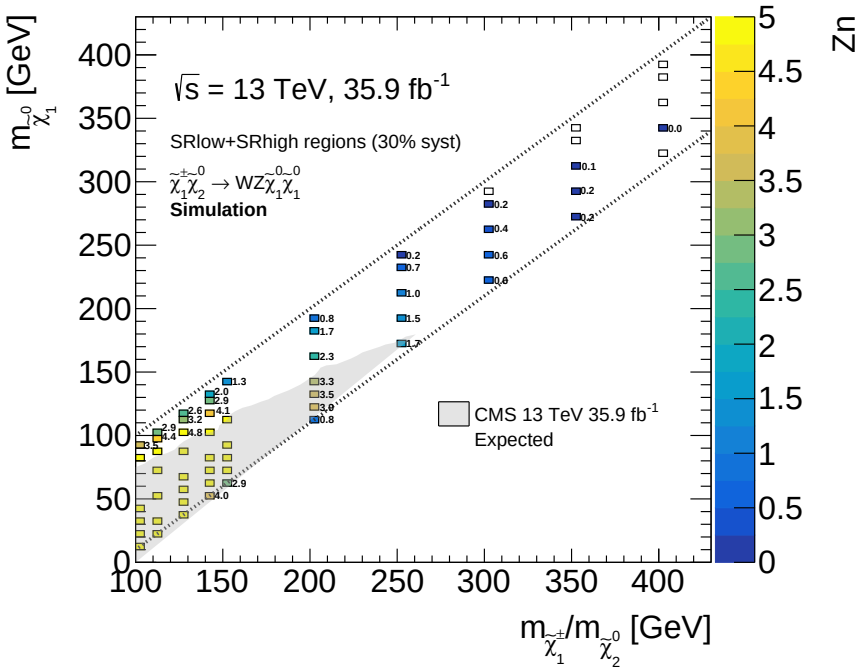

Fig. 11.8: Expected significance using 35.9 fb^{-1} at $\sqrt{s} = 13$ TeV in the SRlow and SRhigh signal regions. A 30% flat systematic uncertainty is applied. The dashed line indicates the region where $m_{\tilde{\chi}_1^{\pm}/\tilde{\chi}_2^0} - m_{\tilde{\chi}_1^0} < m_Z$ and $m_{\tilde{\chi}_1^{\pm}/\tilde{\chi}_2^0} - m_{\tilde{\chi}_1^0} > 0$ GeV. The grey shade shows the expected limits using the same simplified models with the CMS experiment, corresponding to the off-shell Run-2 result using 35.9 fb^{-1} at $\sqrt{s} = 13$ TeV [76].

$\tau\tau$ corresponding to multiple three lepton final states. It can be seen that the analysis is able to exclude up to a $\tilde{\chi}_1^{\pm}\tilde{\chi}_2^0$ mass of around 180 GeV for a $\tilde{\chi}_1^0$ mass up to 20 GeV.

In Figure 11.11 the summary plot is shown before and after addition of the analysis. It can be concluded that although the analysis was not able to find evidence for supersymmetry, it was able to exclude a large part of before uncovered phase space.

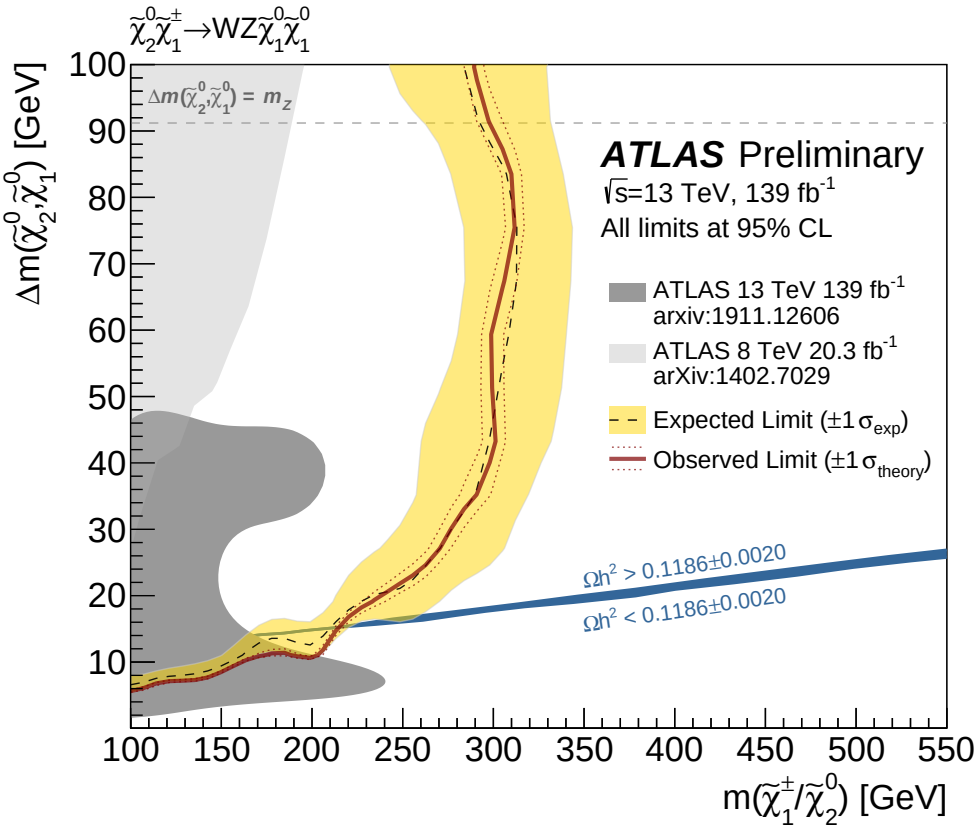

Fig. 11.9: Exclusion contour of the off-shell WZ analysis in the $\Delta m(\tilde{\chi}_1^{\pm}/\tilde{\chi}_2^0,\tilde{\chi}_1^0)$ plane. The expected 95% confidence level (CL) sensitivity (dashed black line) is shown with $\pm1\sigma_{\text{exp}}$ (yellow band) from experimental systematic uncertainties and statistical uncertainties on the data yields, the observed limit (red solid line) is shown with $\pm1\sigma_{\text{theory}}$ (dotted red lines) from signal cross-section uncertainties. The light and dark grey shade are the constraints obtained by the previous equivalent analysis in ATLAS using the 8 TeV 20.3 fb^{-1} dataset [186] and the compressed spectra search using the 13 TeV 139 fb^{-1} dataset [198] respectively. The dark blue line in the top right panel represents the mass splitting range that yields a dark-matter relic density equal to the observed relic density, $\Omega h^2 = 0.1186 \pm 0.0020$ [199], when the mass parameters of all the decoupled SUSY partners are set to 5 TeV and $\tan\beta$ is chosen such that the SM-like Higgs boson mass is consistent with the observed value [200]. The area above (below) the blue line represents a dark-matter relic density larger (smaller) than the observed [15].

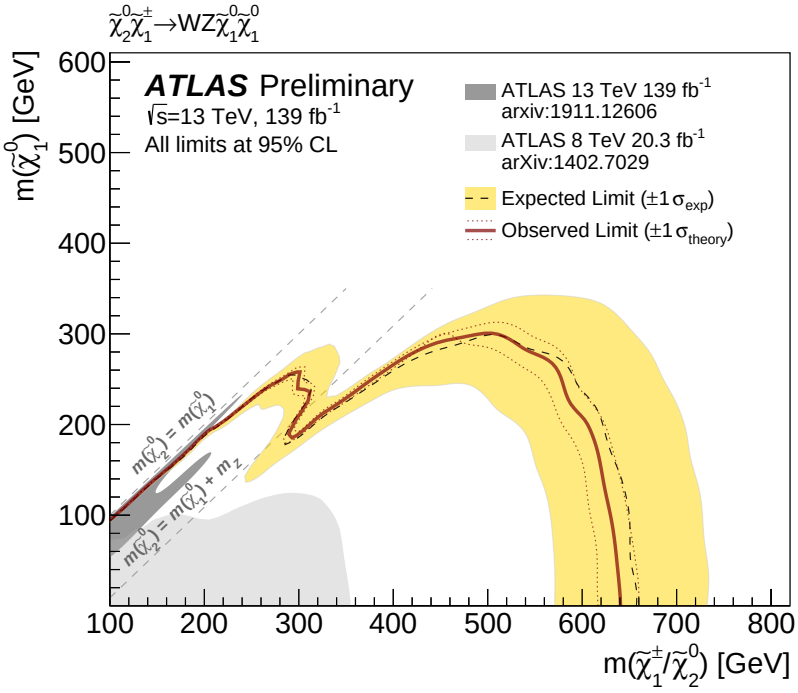

(a)

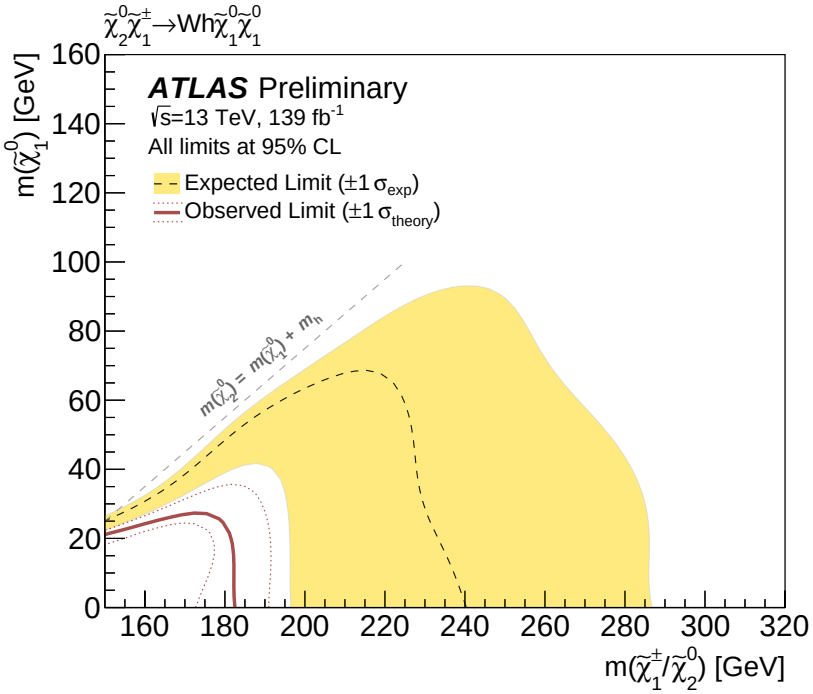

(b)

Fig. 11.10: **(a)** Exclusion contour of combination of the off-shell and on-shell WZ analyses parametrised in $\tilde{\chi}_1^0$ and $\tilde{\chi}_1^\pm/\tilde{\chi}_2^0$ mass. The light and dark grey shade are the constraints obtained by the previous equivalent analysis in ATLAS using the 8 TeV 20.3 fb^{-1} dataset [186] and the compressed spectra search using the 13 TeV 139 fb^{-1} dataset [198] respectively. **(b)** Exclusion contour of combination of the Wh analysis parametrised in $\tilde{\chi}_1^0$ and $\tilde{\chi}_1^\pm/\tilde{\chi}_2^0$ mass. In both figures the expected 95% confidence level (CL) sensitivity (dashed black line) is shown with $\pm 1\sigma_{\text{exp}}$ (yellow band) from experimental systematic uncertainties and statistical uncertainties on the data yields, the observed limit (red solid line) is shown with $\pm 1\sigma_{\text{theory}}$ (dotted red lines) from signal cross-section uncertainties [15].

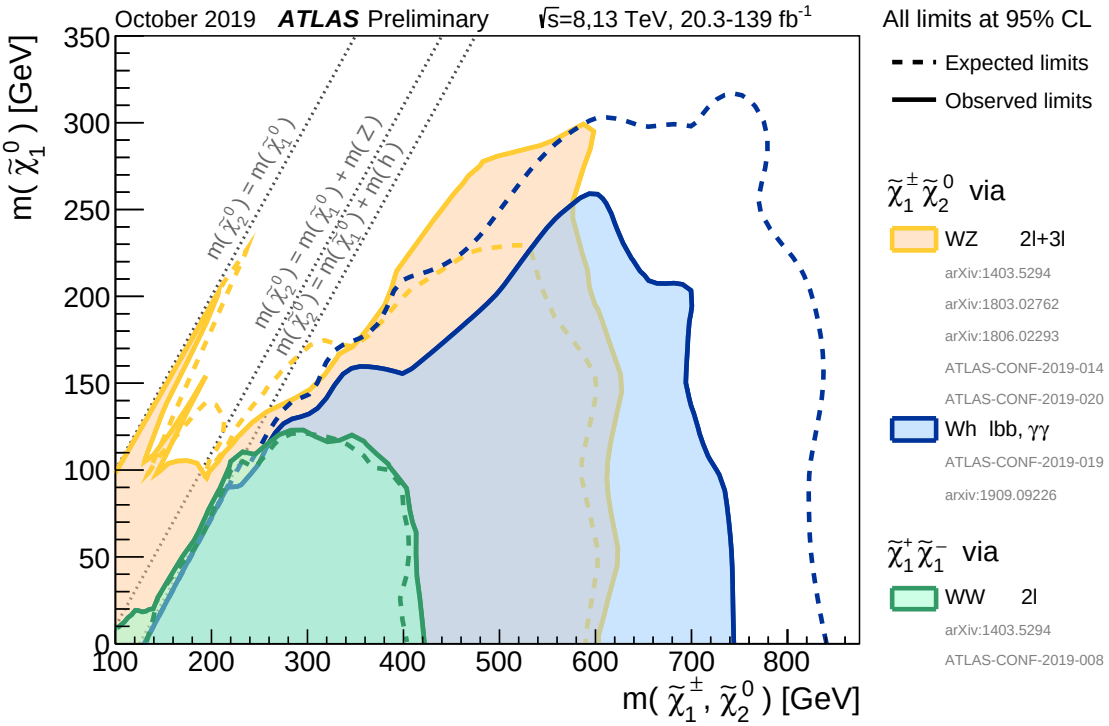

(a)

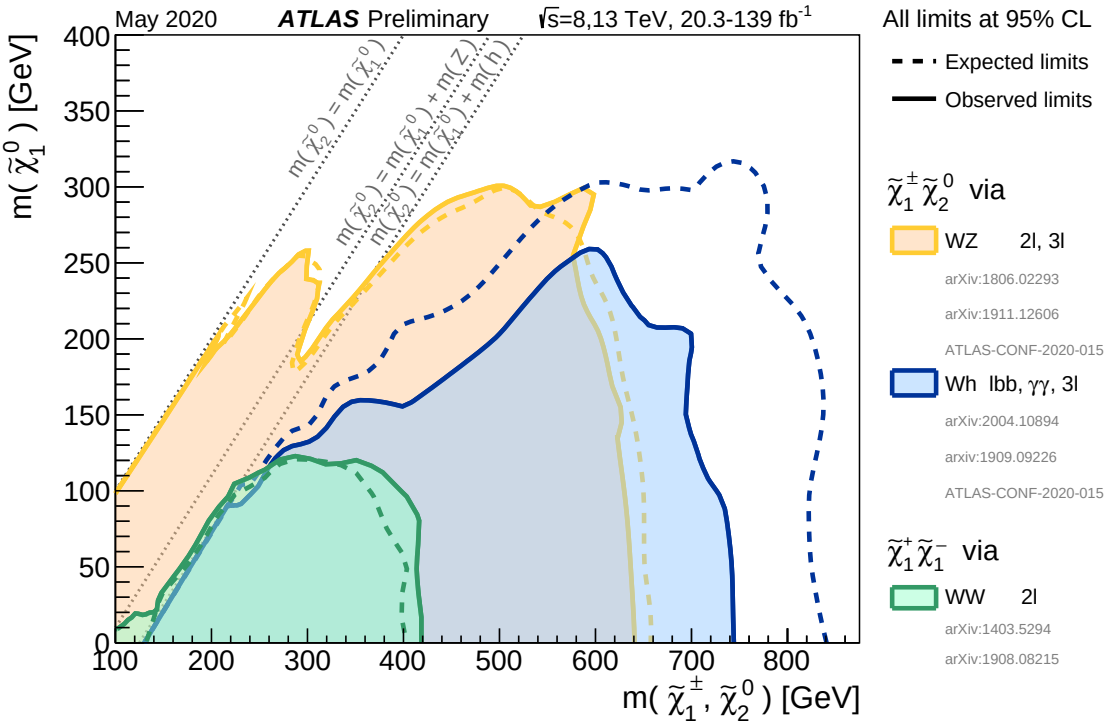

(b)

Fig. 11.11: Summary plots of the 95% CL exclusion limits **(a)** before and **(b)** after the analysis described in [15]. The exclusion limits on $\tilde{\chi}_1^\pm\tilde{\chi}_2^0$ and $\tilde{\chi}_1^+\tilde{\chi}_1^-$ production with SM-boson-mediated decays are shown as a function of the $\tilde{\chi}_1^0$ and $\tilde{\chi}_1^\pm/\tilde{\chi}_2^0$ masses. The production cross-section is for pure wino $\tilde{\chi}_1^+\tilde{\chi}_1^-$ and $\tilde{\chi}_1^\pm\tilde{\chi}_2^0$. Each individual exclusion contour represents a union of the excluded regions of one or more analyses [201, 202].

Appendix A

Fake factor systematic uncertainty variations

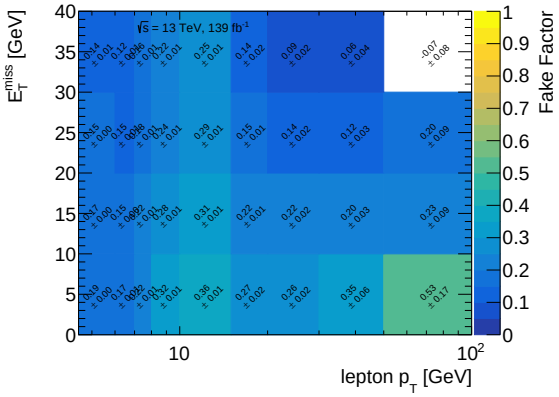

(a) F for electrons - $\eta \in [0,1.37]$

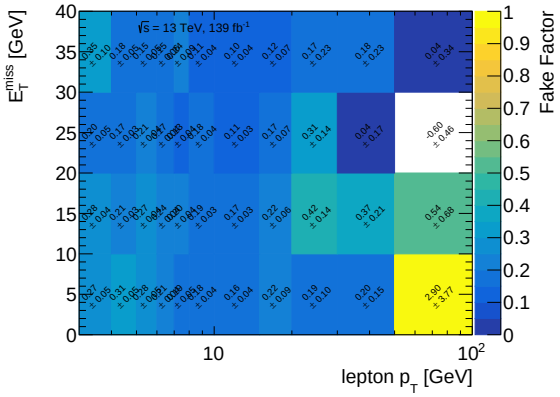

(b) F for muons - $\eta \in [0,0.1]$

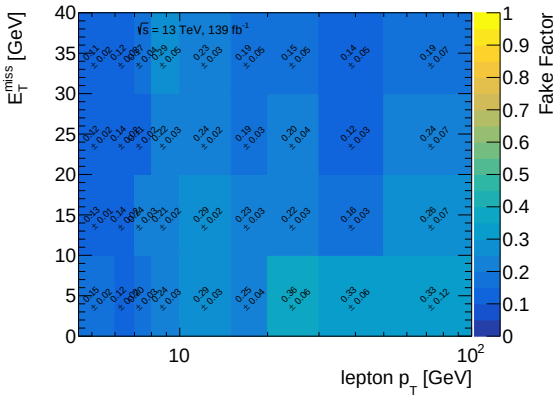

(c) F for electrons - $\eta \in [1.37,1.52]$

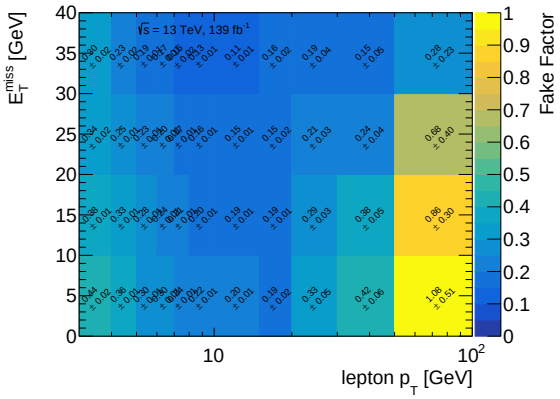

(d) F for muons - $\eta \in [0.1,1.3]$

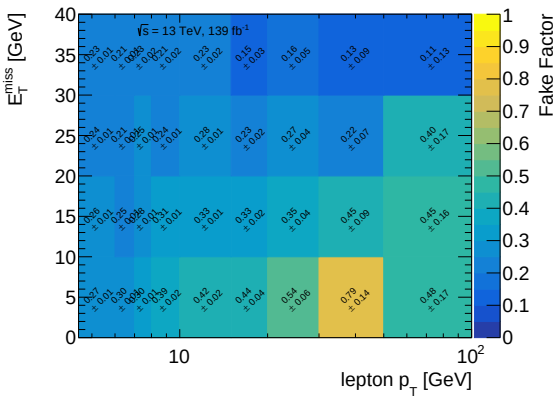

(e) F for electrons - $\eta \in [1.52,2.47]$

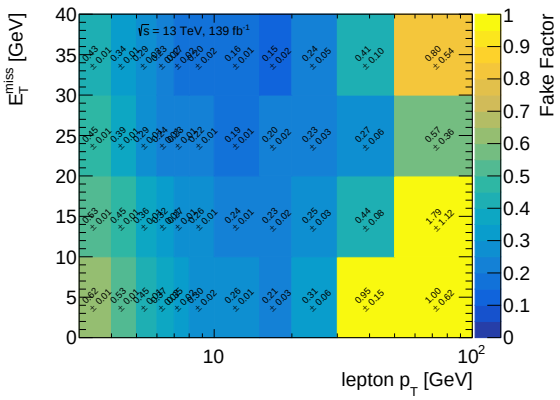

(f) F for muons - $\eta \in [1.3,2.5]$

Fig. A.1: Fake factor F with different parametrisation, binned in p_{T}, $E_{\mathrm{T}}^{\mathrm{miss}}$ and $|\eta|$.

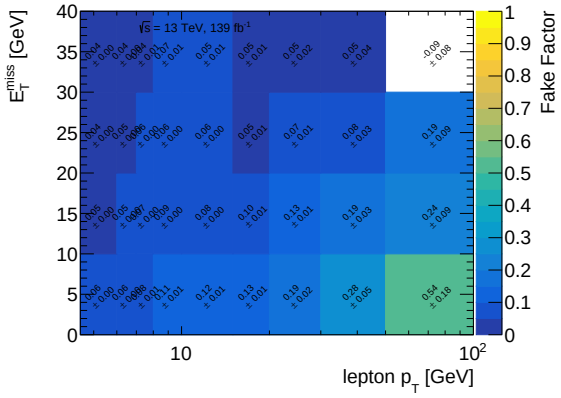

(a) F_{PLV} for electrons - $\eta \in [0,1.37]$

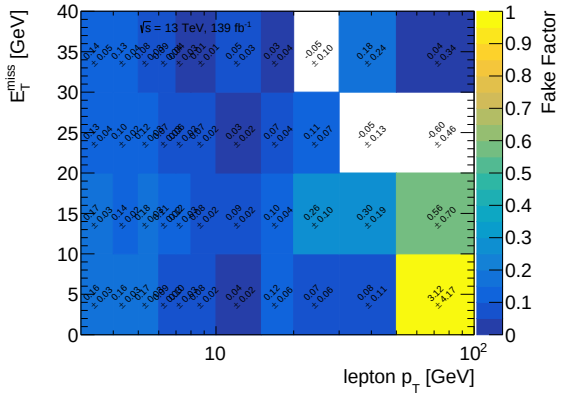

(b) F_{PLV} for muons - $\eta \in [0,0.1]$

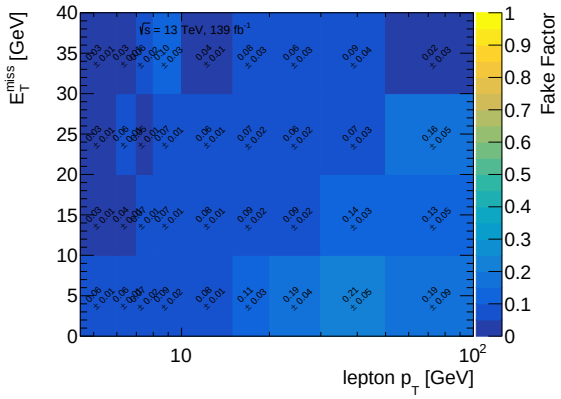

(c) F_{PLV} for electrons - $\eta \in [1.37,1.52]$

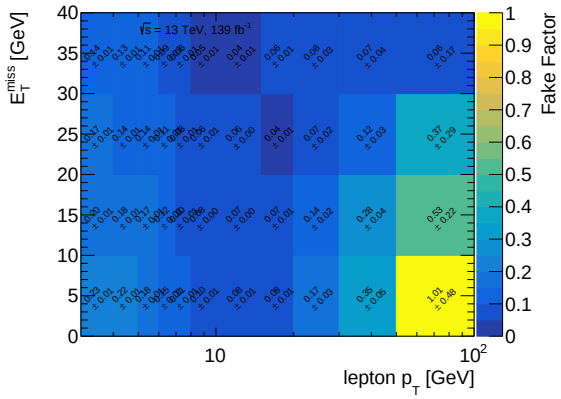

(d) F_{PLV} for muons - $\eta \in [0.1,1.3]$

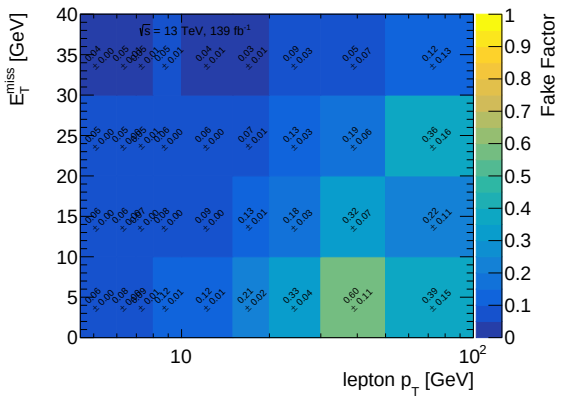

(e) F_{PLV} for electrons - $\eta \in [1.52,2.47]$

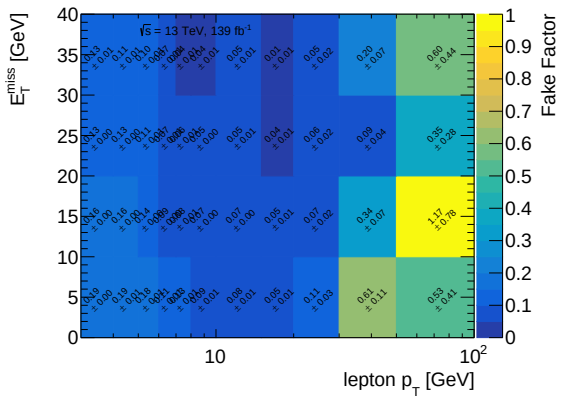

(f) F_{PLV} for muons - $\eta \in [1.3,2.5]$

Fig. A.2: Fake factor F_{PLV} with different parametrisation, binned in p_{T}, $E_{\mathrm{T}}^{\mathrm{miss}}$ and $|\eta|$.

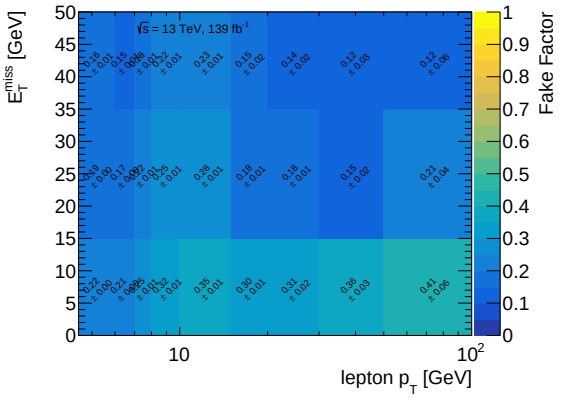

(a) F for electrons

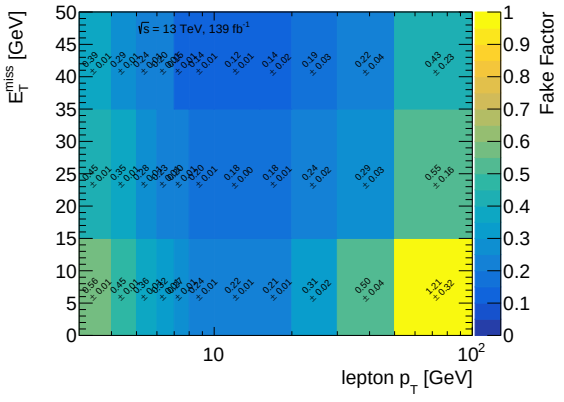

(b) F for muons

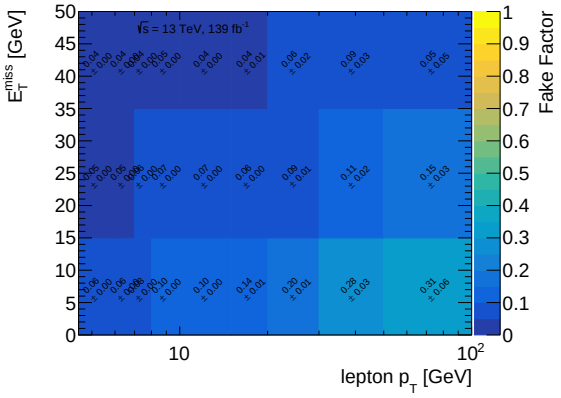

(c) F_{PLV} for electrons

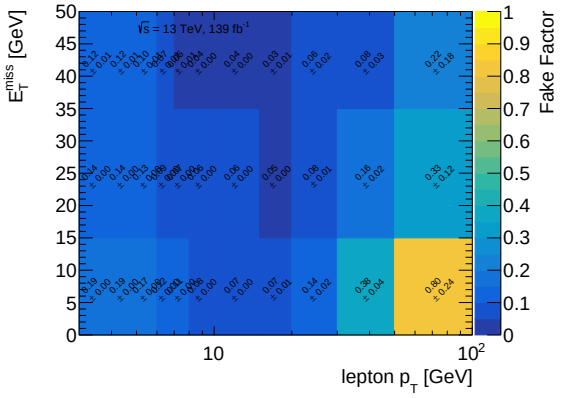

(d) F_{PLV} for muons

Fig. A.3: Fake factor F and F_{PLV} with different $E_{\mathrm{T}}^{\mathrm{miss}}$ binning.

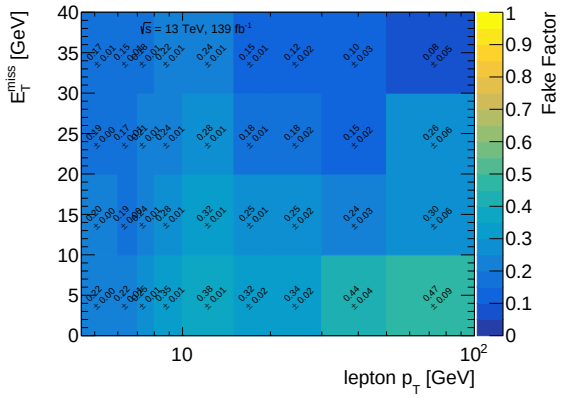

(a) F for electrons SystDown

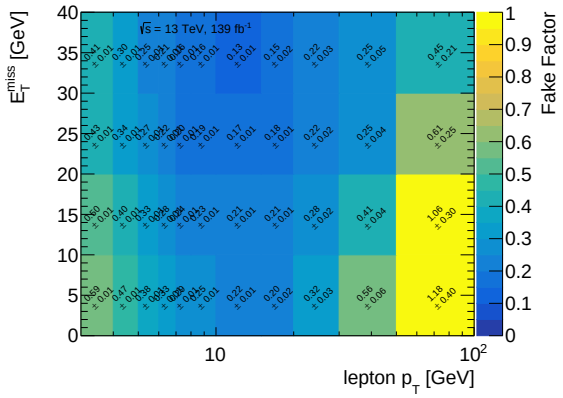

(b) F for muons SystDown

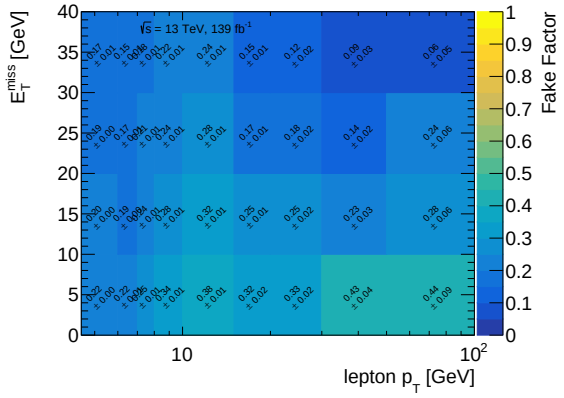

(c) F for electrons SystUp

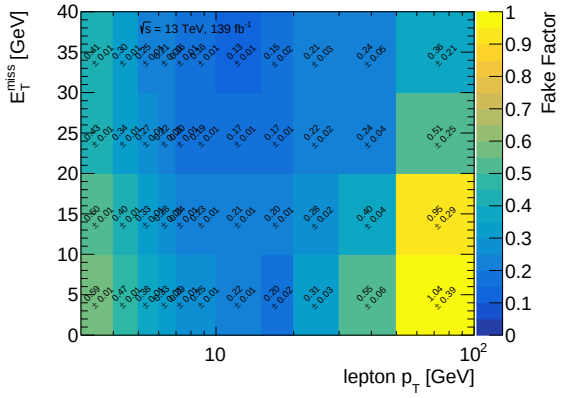

(d) F for muons SystUp

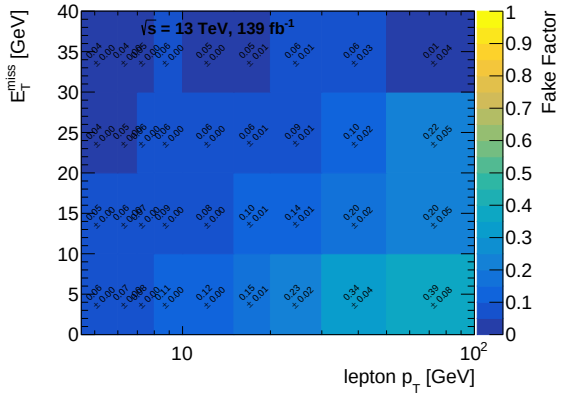

(e) F_{PLV} for electrons SystDown

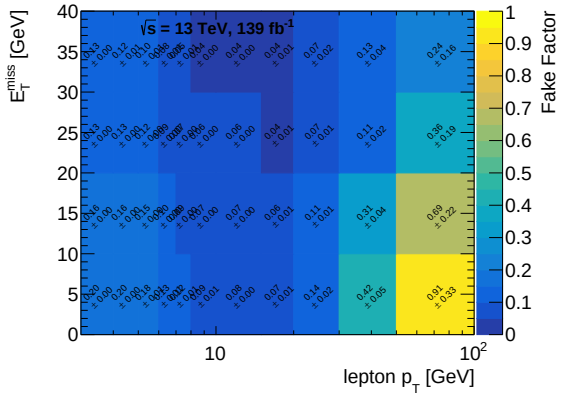

(f) F_{PLV} for muons SystDown

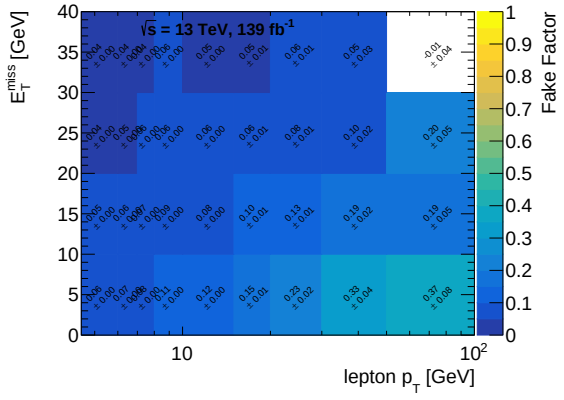

(g) F_{PLV} for electrons SystUp

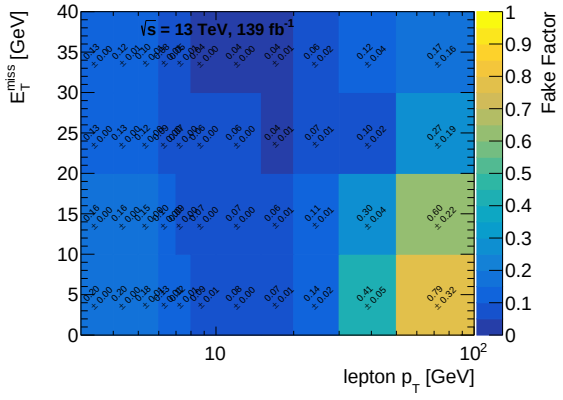

(h) F_{PLV} for muons SystUp

Fig. A.4: Fake factor F and F_{PLV} with the WZ cross-section varied up and down.

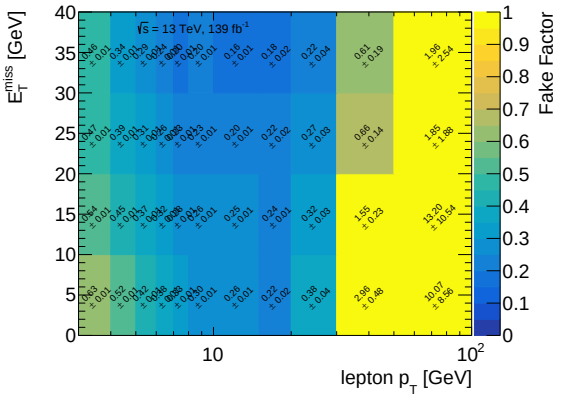

(a) F for muons

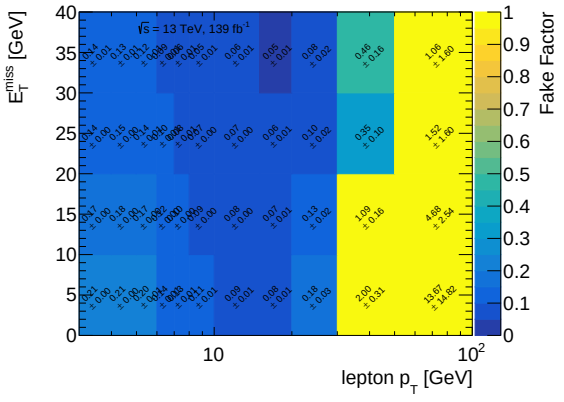

(b) F_{PLV} for muons

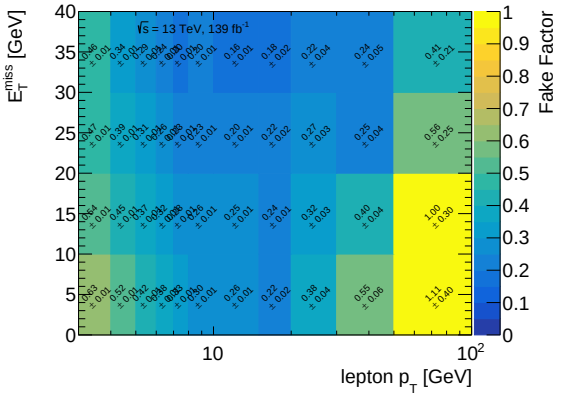

(c) F hybrid for muons

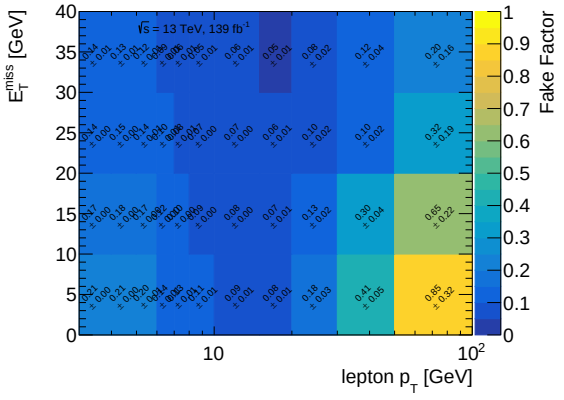

(d) F_{PLV} hybrid for muons

Fig. A.5: Fake factor F and F_{PLV} for muons when overlap removal (OR) is turned on.

Appendix B

Fake factor validation

Table B.1: Yields for the 3e, 2e1μ, 3μ and 2μ1e selection of VRFF-0J. Statistical and systematic uncertainties are included.

Region	VRFF-0J-eee	VRFF-0J-eeμ	VRFF-0J-$\mu\mu\mu$	VRFF-0J-$\mu\mu$e
Observed	36	57	170	122
Bg predicted	33.2 ± 3.4	56 ± 6	146 ± 18	134 ± 8
WZ	4.2 ± 1.0	14.2 ± 2.4	19.3 ± 1.6	16.6 ± 1.8
ZZ	7.6 ± 1.5	12.5 ± 1.8	24.3 ± 2.3	12.5 ± 1.7
Fakes	21.0 ± 2.5	27 ± 5	102 ± 18	103 ± 8
$t\bar{t}$	0.14 ± 0.09	0.98 ± 0.33	$0.08 \pm^{0.22}_{0.08}$	0.80 ± 0.30
$t\bar{t}\,X$	$0.03 \pm^{0.04}_{0.03}$	0.14 ± 0.06	0.052 ± 0.028	0.07 ± 0.05
Others	$0.21 \pm^{0.32}_{0.21}$	0.63 ± 0.28	$0.10 \pm^{0.24}_{0.10}$	0.6 ± 0.5

Table B.2: Yields for the 3e, 2e1μ, 3μ and 2μ1e selection of VRFF-nJ. Statistical and systematic uncertainties are included.

Region	VRFF-nJ-eee	VRFF-nJ-eeμ	VRFF-nJ-$\mu\mu\mu$	VRFF-nJ-$\mu\mu$e
Observed	48	75	107	158
Bg predicted	35.7 ± 3.0	80 ± 6	100 ± 11	157 ± 7
WZ	8.4 ± 1.0	32.9 ± 2.2	28.1 ± 2.3	33.5 ± 2.5
ZZ	9.4 ± 1.4	12.2 ± 1.5	17.6 ± 1.7	21.7 ± 2.7
Fakes	17.2 ± 2.0	27 ± 5	52 ± 10	96 ± 5
$t\bar{t}$	0.37 ± 0.16	6.3 ± 0.9	1.8 ± 0.5	4.5 ± 0.7
$t\bar{t}\,X$	0.18 ± 0.06	0.88 ± 0.14	0.47 ± 0.10	0.88 ± 0.15
Others	0.11 ± 0.06	1.0 ± 0.5	0.22 ± 0.10	1.1 ± 0.5

Table B.3: Yields for the 3e, 2e1μ, 3μ and 2μ1e selection of VRFF-nJ-lowpt. Statistical and systematic uncertainties are included.

Region	VRFF-nJ-lowpt-eee	VRFF-nJ-lowpt-eeμ	VRFF-nJ-lowpt-$\mu\mu\mu$	VRFF-nJ-lowpt-$\mu\mu$e
Observed	0	24	32	17
Bg predicted	1.6 ± 0.4	14.8 ± 2.6	37 ± 5	17.6 ± 2.9
WZ	0.26 ± 0.17	1.0 ± 0.5	3.1 ± 1.4	1.0 ± 0.6
ZZ	0.18 ± 0.12	$0.4 \pm^{0.4}_{0.4}$	1.5 ± 0.9	$0.6 \pm^{1.0}_{0.6}$
Fakes	0.93 ± 0.27	11.1 ± 2.0	31 ± 5	14.2 ± 1.7
$t\bar{t}$	0.20 ± 0.10	2.1 ± 0.8	0.8 ± 0.4	1.7 ± 0.8
$t\bar{t}\,X$	$0.011 \pm^{0.016}_{0.011}$	0.09 ± 0.05	0.11 ± 0.06	0.13 ± 0.05
Others	$0.01 \pm^{0.11}_{0.01}$	$0.15 \pm^{0.22}_{0.15}$	$0.29 \pm^{0.31}_{0.29}$	$0.05 \pm^{0.22}_{0.05}$

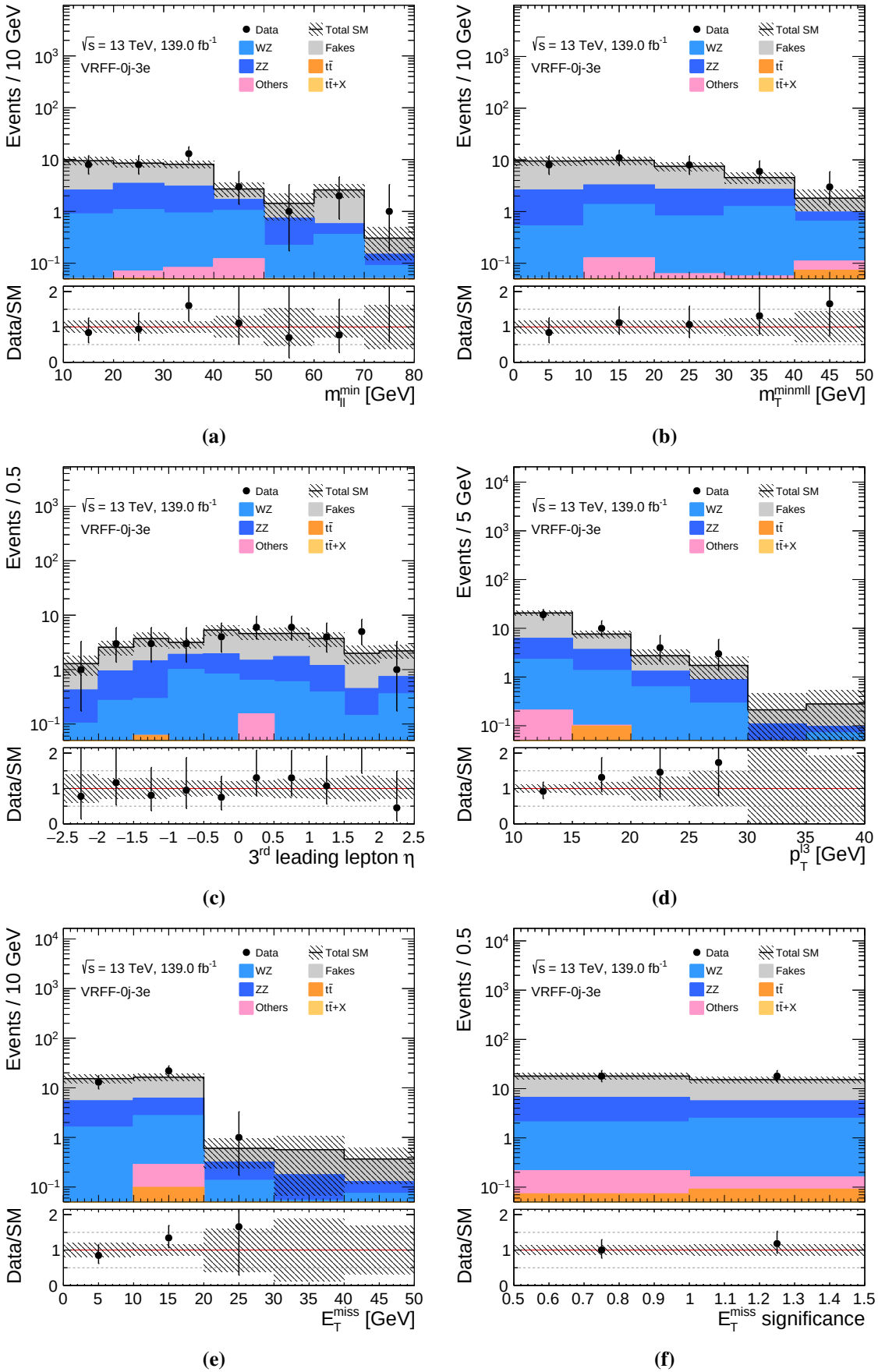

Fig. B.1: Distributions for the 3e selection of VRFF-0j. Statistical and systematic uncertainties are included. The last bin includes overflow.

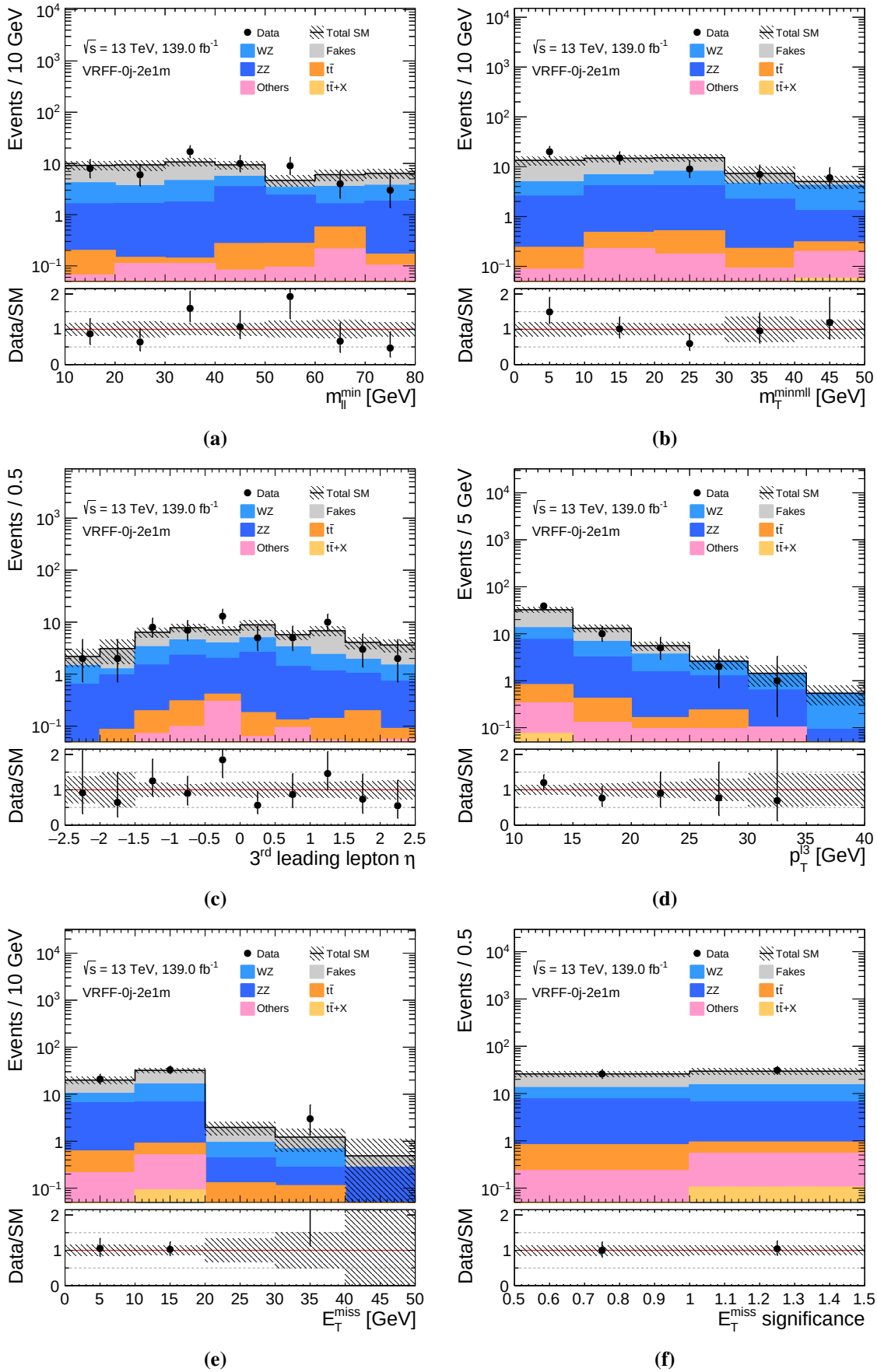

Fig. B.2: Distributions for the 2e1μ selection of VRFF-0j. Statistical and systematic uncertainties are included. The last bin includes overflow.

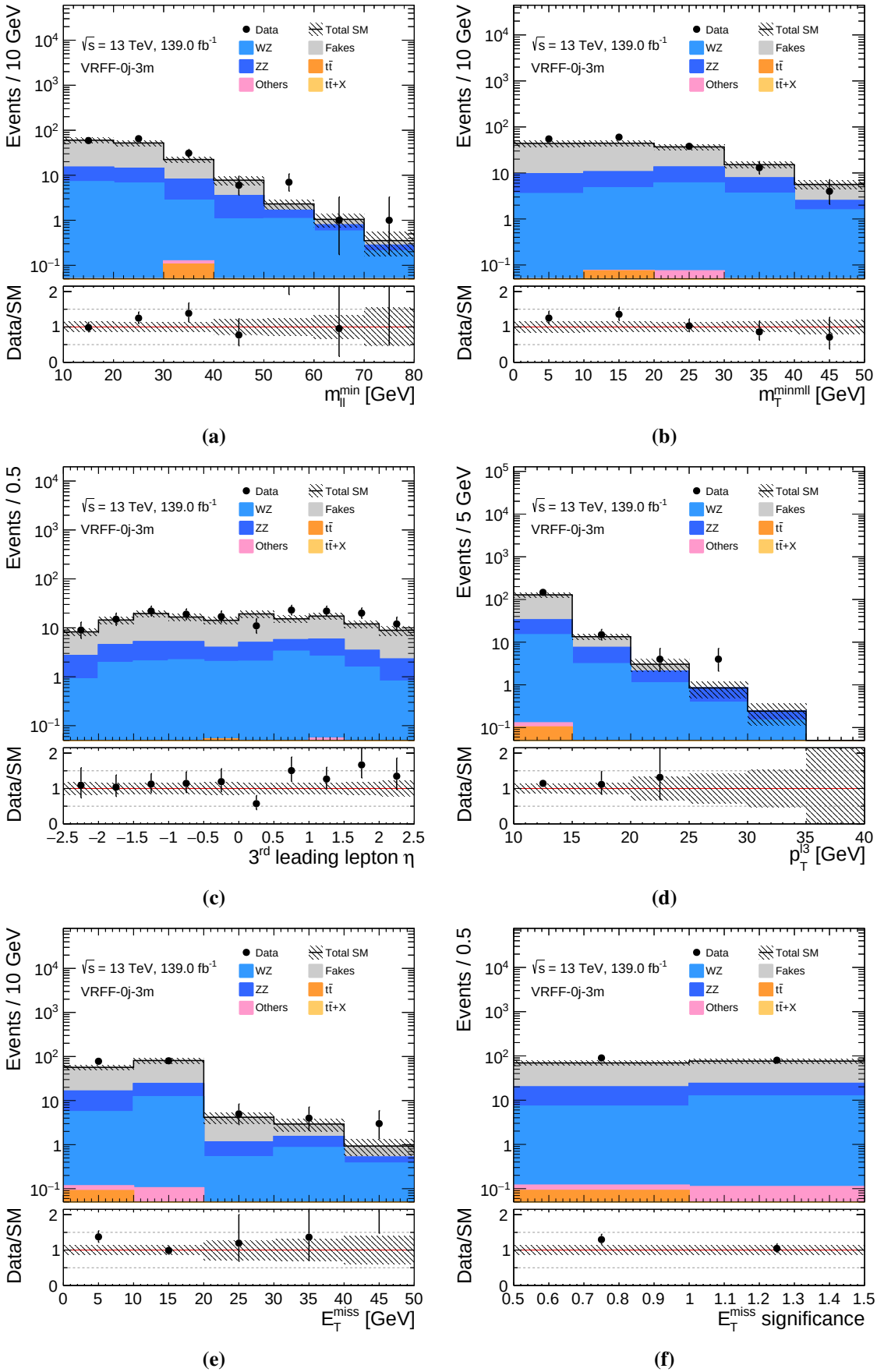

Fig. B.3: Distributions for the 3μ selection of VRFF-0j. Statistical and systematic uncertainties are included. The last bin includes overflow.

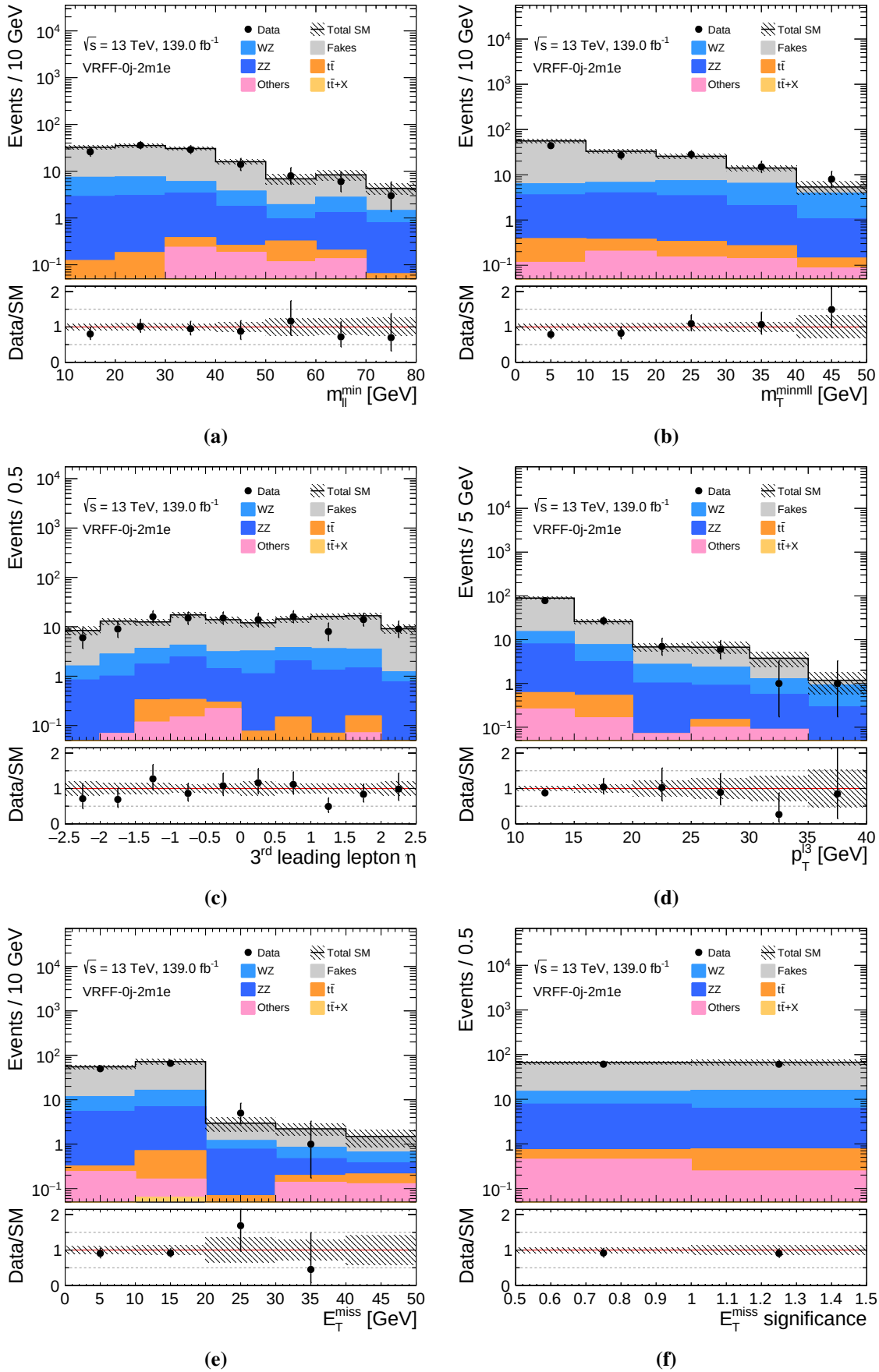

Fig. B.4: Distributions for the $2\mu 1e$ selection of VRFF-0j. Statistical and systematic uncertainties are included. The last bin includes overflow.

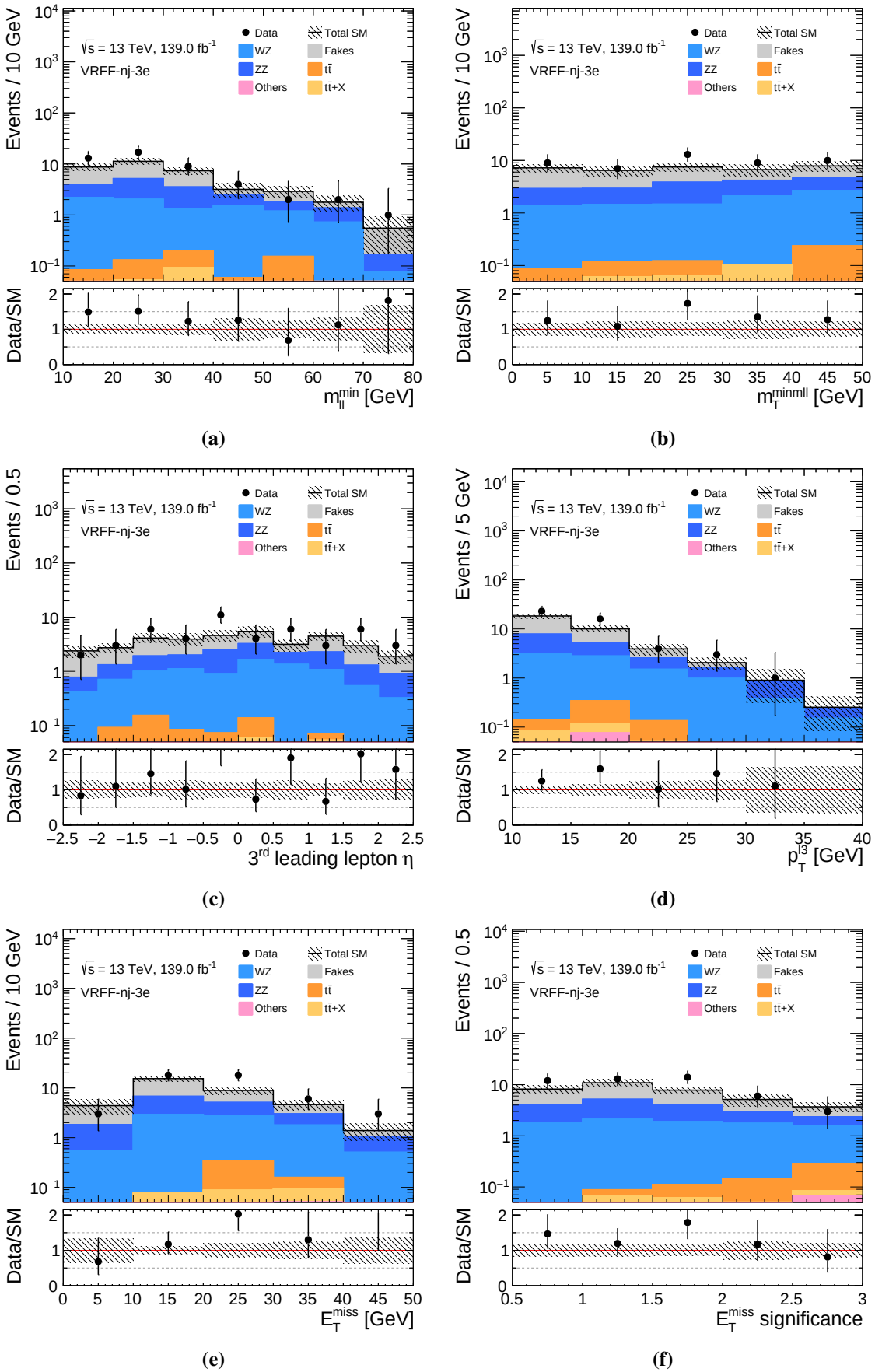

Fig. B.5: Distributions for the 3e selection of VRFF-nj. Statistical and systematic uncertainties are included. The last bin includes overflow.

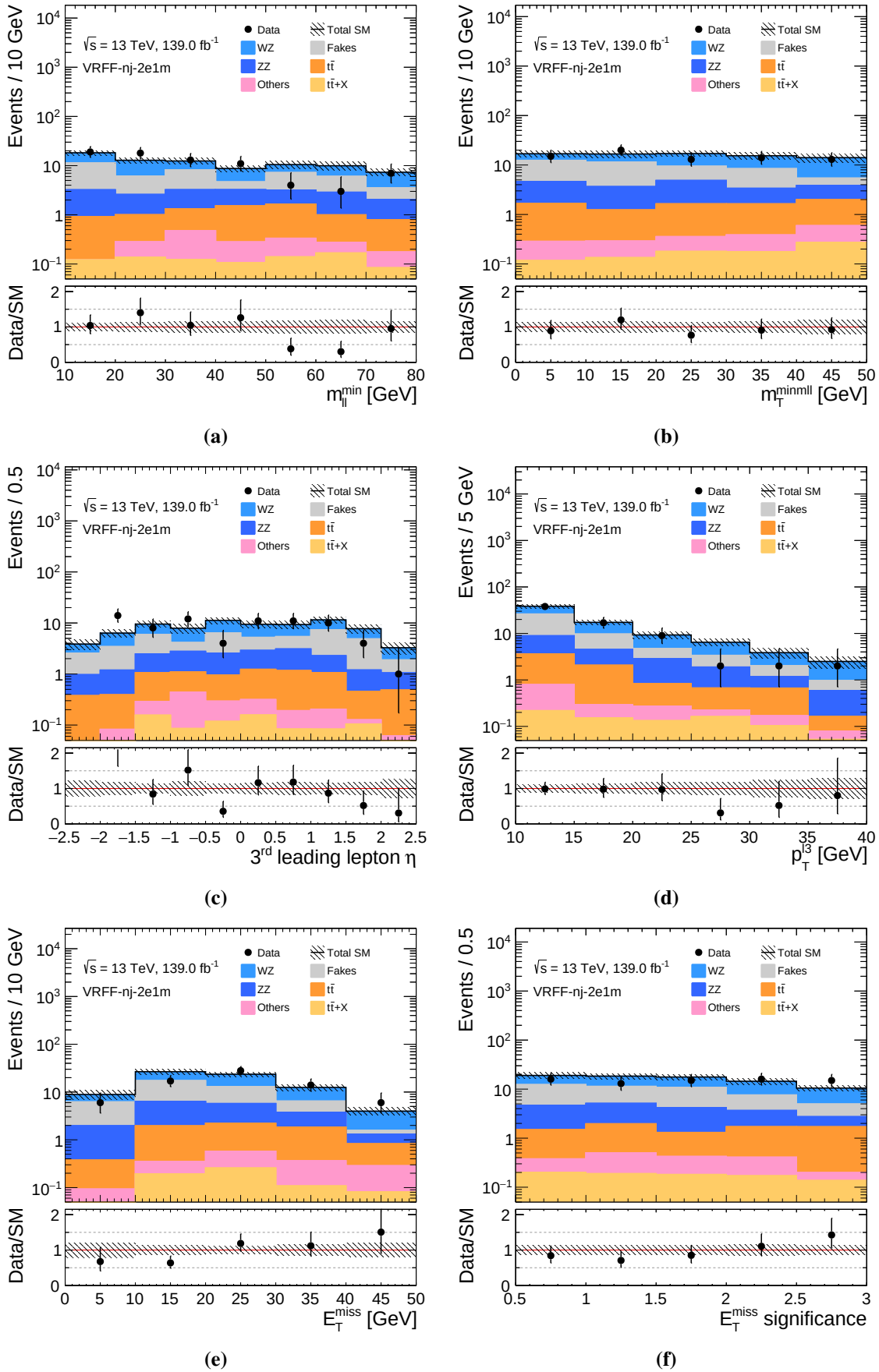

Fig. B.6: Distributions for the 2e1μ selection of VRFF-nj. Statistical and systematic uncertainties are included. The last bin includes overflow.

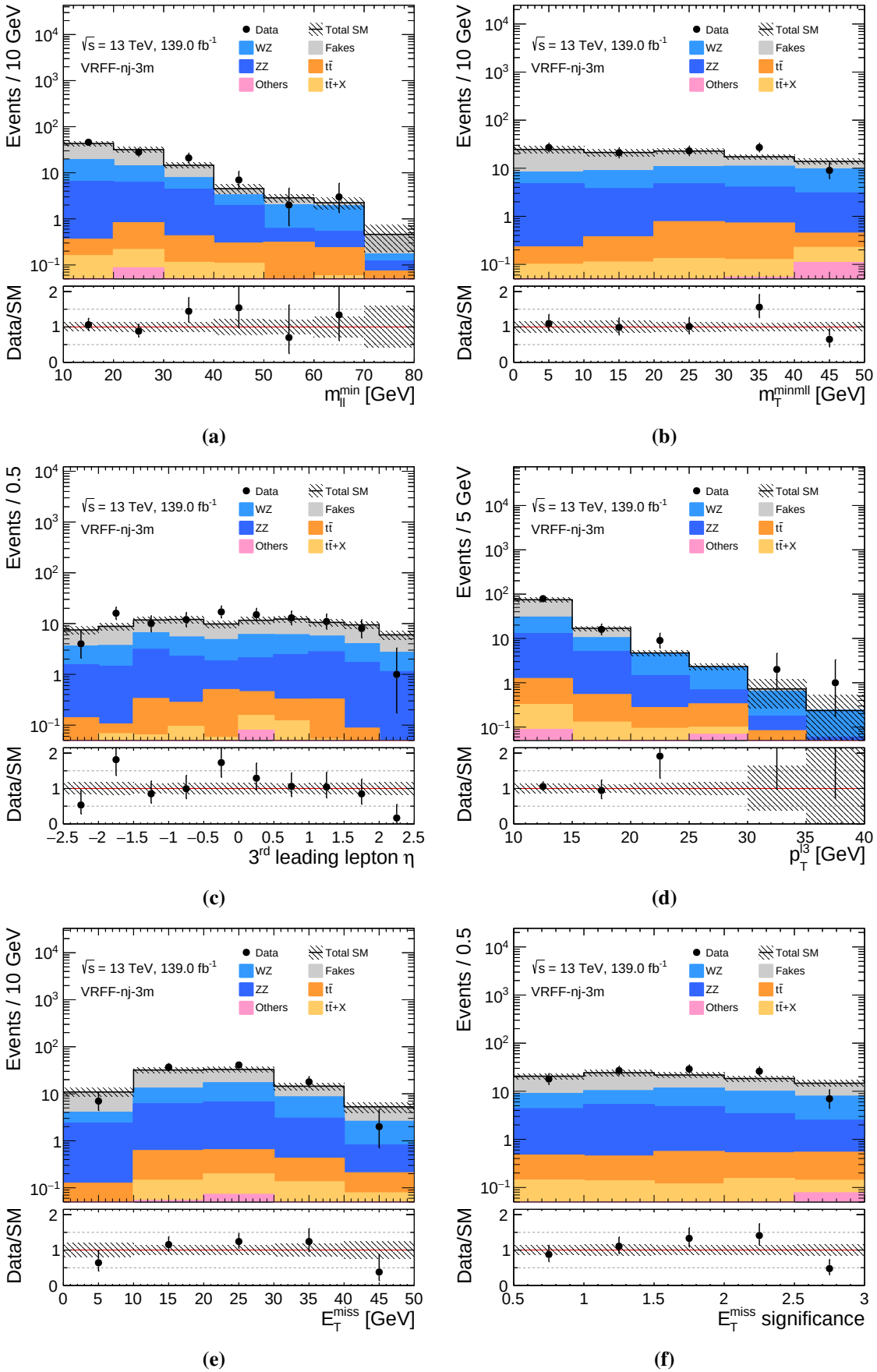

Fig. B.7: Distributions for the 3μ selection of VRFF-nj. Statistical and systematic uncertainties are included. The last bin includes overflow.

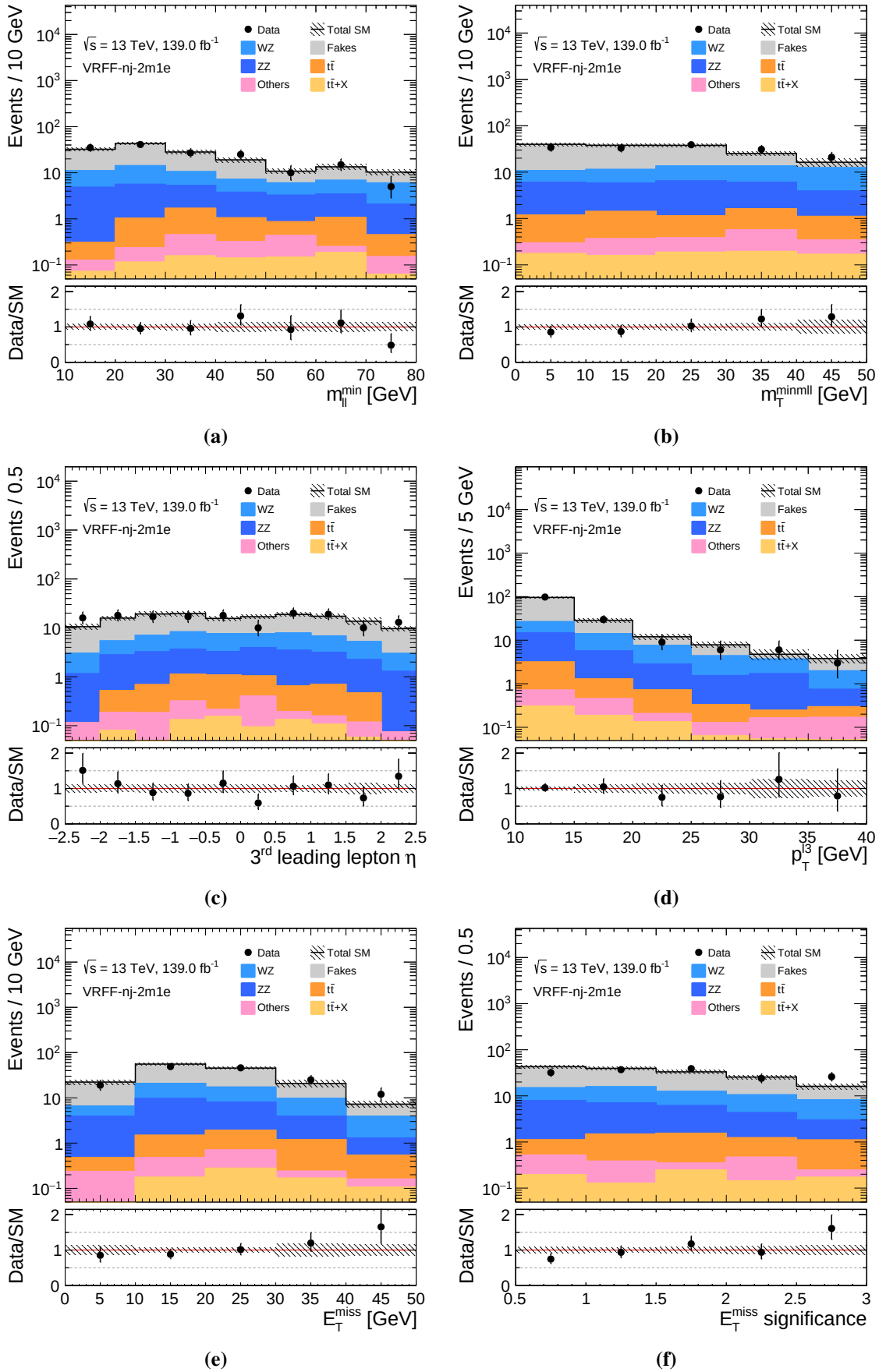

Fig. B.8: Distributions for the $2\mu 1e$ selection of VRFF-nj. Statistical and systematic uncertainties are included. The last bin includes overflow.

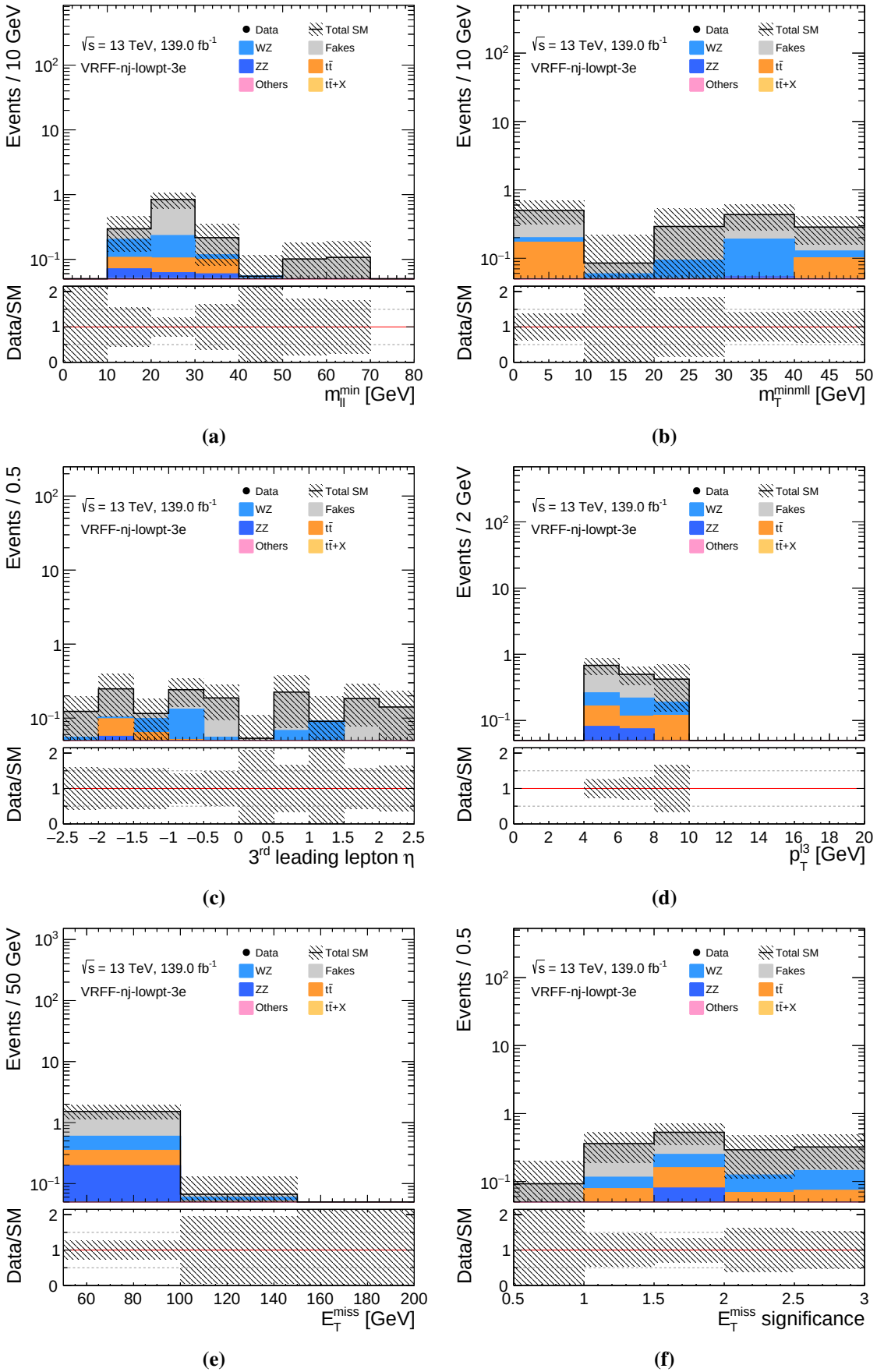

Fig. B.9: Distributions for the 3e selection of VRFF-nj-lowpt. Statistical and systematic uncertainties are included. The last bin includes overflow.

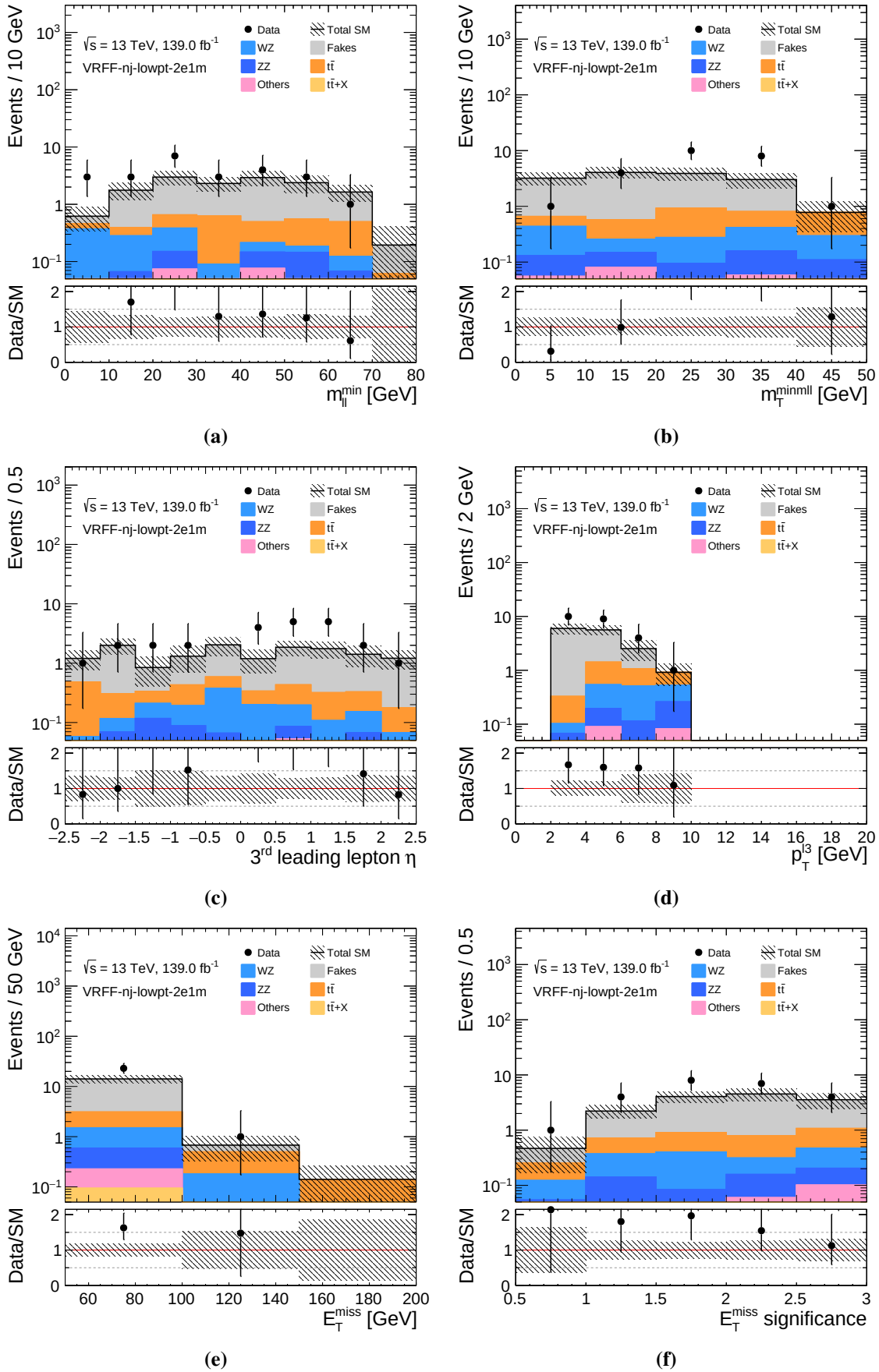

Fig. B.10: Distributions for the 2e1μ selection of VRFF-nj-lowpt. Statistical and systematic uncertainties are included. The last bin includes overflow.

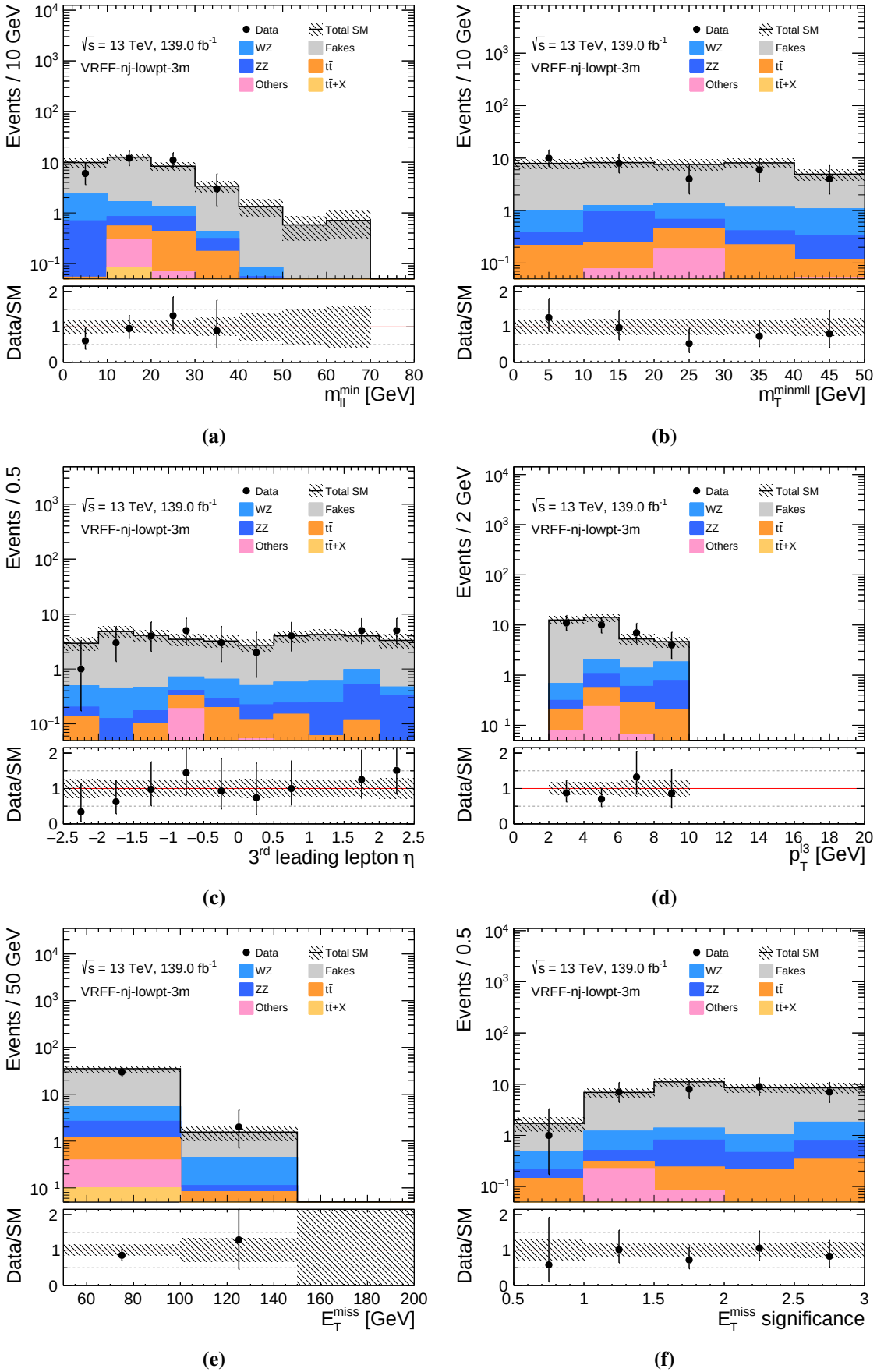

Fig. B.11: Distributions for the 3μ selection of VRFF-nj-lowpt. Statistical and systematic uncertainties are included. The last bin includes overflow.

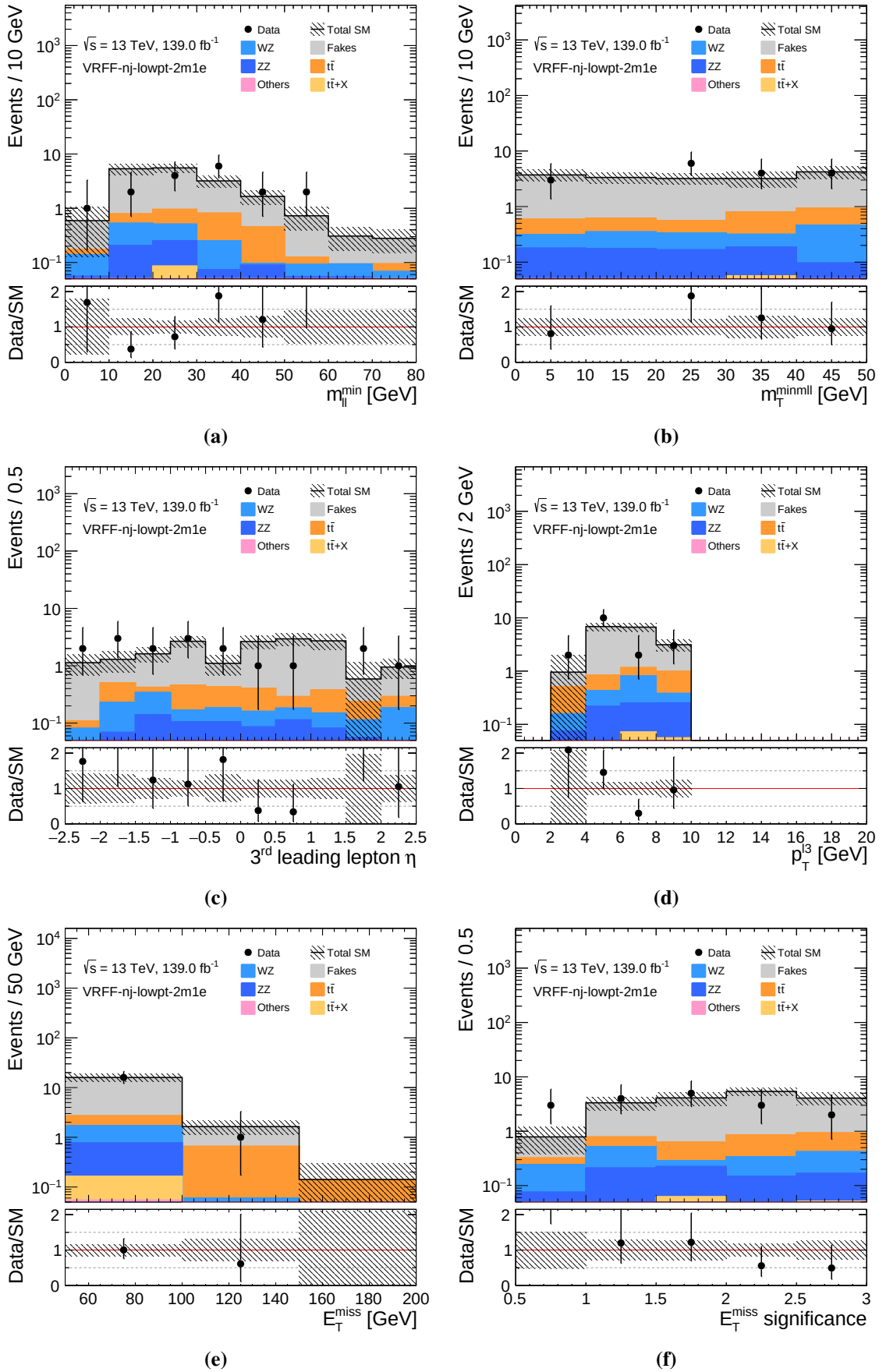

Fig. B.12: Distributions for the $2\mu 1e$ selection of VRFF-nj-lowpt. Statistical and systematic uncertainties are included. The last bin includes overflow.

Bibliography

[1] S. L. Glashow. Partial Symmetries of Weak Interactions. *Nucl. Phys.*, 22:579, 1961.

[2] S. Weinberg. A Model of Leptons. *Phys. Rev. Lett.*, 19:1264, 1967.

[3] A. Salam. Weak and Electromagnetic Interactions. *Conf. Proc. C*, 680519:367, 1968.

[4] S. L. Glashow, J. Iliopoulos, and L. Maiani. Weak Interactions with Lepton-Hadron Symmetry. *Phys. Rev. D*, 2:1285, 1970.

[5] G. 't Hooft and M. J. G. Veltman. Regularization and Renormalization of Gauge Fields. *Nucl. Phys. B*, 44:189, 1972.

[6] E. D. Bloom, D. H. Coward, H. DeStaebler, J. Drees, G. Miller, L. W. Mo, R. E. Taylor, M. Breidenbach, J. I. Friedman, G. C. Hartmann, and H. W. Kendall. High-Energy Inelastic $e-p$ Scattering at 6° and 10°. *Phys. Rev. Lett.*, 23:930, Oct 1969.

[7] M. Breidenbach, J. I. Friedman, H. W. Kendall, E. D. Bloom, D. H. Coward, H. DeStaebler, J. Drees, L. W. Mo, and R. E. Taylor. Observed Behavior of Highly Inelastic Electron-Proton Scattering. *Phys. Rev. Lett.*, 23:935, Oct 1969.

[8] CDF Collaboration. Observation of Top Quark Production in $\overline{p}p$ Collisions with the Collider Detector at Fermilab. *Phys. Rev. Lett.*, 74:2626, Apr 1995.

[9] D0 Collaboration. Search for High Mass Top Quark Production in $p\overline{p}$ Collisions at $\sqrt{s} =$ 1.8 TeV. *Phys. Rev. Lett.*, 74:2422, Mar 1995.

[10] DONUT Collaboration. Observation of tau neutrino interactions. *Phys. Lett. B*, 504 (3):218, 2001.

[11] ATLAS Collaboration. Observation of a new particle in the search for the Standard Model Higgs boson with the ATLAS detector at the LHC. *Phys. Lett. B*, 716(1):1, 2012.

[12] CMS Collaboration. Observation of a new boson at a mass of 125 GeV with the CMS experiment at the LHC. *Phys. Lett. B*, 716(1):30, 2012.

[13] P. W. Higgs. Broken Symmetries and the Masses of Gauge Bosons. *Phys. Rev. Lett.*, 13:508, Oct 1964.

[14] F. Englert and R. Brout. Broken Symmetry and the Mass of Gauge Vector Mesons. *Phys. Rev. Lett.*, 13:321, Aug 1964.

[15] ATLAS Collaboration. Search for chargino-neutralino pair production in final states with three leptons and missing transverse momentum in $\sqrt{s}$ = 13 TeV p-p collisions with the ATLAS detector. Technical Report ATLAS-CONF-2020-015, CERN, Geneva, Jun 2020. URL https://cds.cern.ch/record/2719521.

[16] Glashow's Snake. http://physics.bu.edu/cc104/chapters10and11.html, viewed Jun 2020.

[17] M. Gell-Mann. The Eightfold Way: A Theory of strong interaction symmetry. California Inst. of Technol. Synchrotron Lab Report No. 20, 1961.

[18] Y. Ne'eman. Derivation of strong interactions from a gauge invariance. *Nucl. Phys.*, 26(2):222, 1961.

[19] C.N. Yang and R.L. Mills. Conservation of Isotopic Spin and Isotopic Gauge Invariance. *Phys. Rev.*, 96:191, 1954.

[20] J. Ellis. Higgs physics, 2013. arXiv:1312.5672.

[21] N. Cabibbo. Unitary Symmetry and Leptonic Decays. *Phys. Rev. Lett.*, 10:531, 1963.

[22] M. Kobayashi and T. Maskawa. CP-Violation in the renormalizable theory of weak interaction. *Prog. Theor. Phys.*, 49:652, 1973.

[23] M. Thomson. *Modern Particle Physics*. Cambridge, 2013.

[24] D.J. Gross and F. Wilczek. Ultraviolet Behavior of Nonabelian Gauge Theories. *Phys. Rev. Lett.*, 30:1343, 1973.

[25] Y. Fukuda, T. Hayakawa, E. Ichihara, K. Inoue, K. Ishihara, H. Ishino, Y. Itow, T. Kajita, J. Kameda, S. Kasuga, et al. Evidence for Oscillation of Atmospheric Neutrinos. *Phys. Rev. Lett.*, 81(8):1562, Aug 1998.

[26] K. Abe, Y. Hayato, T. Iida, K. Iyogi, J. Kameda, Y. Koshio, Y. Kozuma, Ll. Marti, M. Miura, S. Moriyama, et al. Evidence for the Appearance of Atmospheric Tau Neutrinos in Super-Kamiokande. *Phys. Rev. Lett.*, 110(18):181802, May 2013.

[27] Q. R. Ahmad, R. C. Allen, T. C. Andersen, J. D.Anglin, J. C. Barton, E. W. Beier, M. Bercovitch, J. Bigu, S. D. Biller, R. A. Black, et al. Direct Evidence for Neutrino Flavor Transformation from Neutral-Current Interactions in the Sudbury Neutrino Observatory. *Phys. Rev. Lett.*, 89(1):011301, Jun 2002.

[28] K. Eguchi, S. Enomoto, K. Furuno, J. Goldman, H. Hanada, H. Ikeda, K. Ikeda, K. Inoue, K. Ishihara, W. Itoh, et al. First Results from KamLAND: Evidence for Reactor Antineutrino Disappearance. *Phys. Rev. Lett.*, 90(2):021802, Jan 2003.

[29] M. Aker, K. Altenmüller, M. Arenz, M. Babutzka, J. Barrett, S. Bauer, M. Beck, A. Beglarian, J. Behrens, T. Bergmann, et al. Improved Upper Limit on the Neutrino Mass from a Direct Kinematic Method by KATRIN. *Phys. Rev. Lett.*, 123(22):221802, Nov 2019.

[30] Planck Collaboration. Planck 2018 results. VI. Cosmological parameters, 2018. arXiv:1807.06209.

[31] G. Senjanovic. Proton decay and grand unification. *AIP Conf. Proc.*, 1200(1):131, 2010.

[32] C. Deffayet, P. Peter, B. Wandelt, M. Zaldarriaga, and L. F. Cugliandolo. Proceedings, 100th Les Houches Summer School: Post-Planck Cosmology. *Les Houches Lect. Notes*, 100, 2015.

[33] F. Zwicky. Die Rotverschiebung von extragalaktischen Nebeln. *Helv. Phys. Acta*, 6: 110, 1933.

[34] G. Bertone and D. Hooper. History of dark matter. *Rev. Mod. Phys.*, 90(4):45002, Oct 2018.

[35] V. C. Rubin and W. K. Ford, Jr. Rotation of the Andromeda Nebula from a Spectroscopic Survey of Emission Regions. *Astrophys. J.*, 159:379, 1970.

[36] D. Clowe, M. Bradač, A. H. Gonzalez, M. Markevitch, S. W. Randall, C. Jones, and D. Zaritsky. A Direct Empirical Proof of the Existence of Dark Matter. *The Astrophysical Journal*, 648(2):L109, Aug 2006.

[37] J. P. Ostriker and P. J. E. Peebles. A Numerical Study of the Stability of Flattened Galaxies: or, can Cold Galaxies Survive? *Astrophys. J.*, 186:467, Dec 1973.

[38] V. Springel, R. Pakmor, A. Pillepich, R. Weinberger, D. Nelson, L. Hernquist, M. Vogelsberger, S. Genel, P. Torrey, F. Marinacci, et al. First results from the IllustrisTNG simulations: matter and galaxy clustering. *Monthly Notices of the Royal Astronomical Society*, 475(1):676, Dec 2017.

[39] A. Pillepich, D. Nelson, L. Hernquist, V. Springel, R. Pakmor, P. Torrey, R. Weinberger, S. Genel, J. P Naiman, F. Marinacci, et al. First results from the IllustrisTNG simulations: the stellar mass content of groups and clusters of galaxies. *Monthly Notices of the Royal Astronomical Society*, 475(1):648, Dec 2017.

[40] J. R. Bond, G. Efstathiou, and J. Silk. Massive Neutrinos and the Large-Scale Structure of the Universe. *Phys. Rev. Lett.*, 45:1980, Dec 1980.

[41] J. R. Bond and A. S. Szalay. The collisionless damping of density fluctuations in an expanding universe. *Astrophys. J.*, 274:443, Nov 1983.

[42] A. G. Doroshkevich, Y. B. Zeldovich, R. A. Sunyaev, and M. Khlopov. Astrophysical implications of the neutrino rest mass. II. The density-perturbation spectrum and small-scale fluctuations in the microwave background. *Sov. Astron. Lett.*, 6:252, 1980.

[43] P. J. E. Peebles. Primeval adiabatic perturbations - Effect of massive neutrinos. *Astrophys. J.*, 258:415, Jul 1982.

[44] D. N. Schramm and G. Steigman. Relic Neutrinos and the Density of the Universe. *Astrophys. J.*, 243:1, Jan 1981.

[45] M. Davis, J. Huchra, D. W. Latham, and J. Tonry. A survey of galaxy redshifts. II. The large scale space distribution. *Astrophys. J.*, 253:423, Feb 1982.

[46] J. Huchra and M. Geller. Mapping the Universe. *Science*, 246(4932):897, 1989.

[47] J. K. Adelman-McCarthy et al. The Sixth Data Release of the Sloan Digital Sky Survey. *Astrophys. J.*, 175(2):297, Apr 2008.

[48] J. Ellis. Beyond the standard model for hill walkers. In *1998 European School of High-Energy Physics*, page 133, Aug 1998.

[49] S. Coleman and J. Mandula. All Possible Symmetries of the *S* Matrix. *Phys. Rev.*, 159:1251, Jul 1967.

[50] Yu.A. Golfand and E.P. Likhtman. Extension of the Algebra of Poincare Group Generators and Violation of p Invariance. *JETP Lett.*, 13:323, 1971.

[51] P. Ramond. Dual Theory for Free Fermions. *Phys. Rev. D*, 3:2415, May 1971.

[52] A. Neveu and J. H. Schwarz. Quark Model of Dual Pions. *Phys. Rev. D*, 4:1109, Aug 1971.

[53] D.V. Volkov and V.P. Akulov. Is the Neutrino a Goldstone Particle? *Phys. Lett. B*, 46: 109, 1973.

[54] J. Wess and B. Zumino. Supergauge Transformations in Four-Dimensions. *Nucl. Phys. B*, 70:39, 1974.

[55] S. Dimopoulos and H. Georgi. Softly Broken Supersymmetry and SU(5). *Nucl. Phys. B*, 193:150, 1981.

[56] J. Ellis and S. Rudaz. Search for supersymmetry in toponium decays. *Phys. Lett. B*, 128(3):248, 1983.

[57] J. Ellis and D.V. Nanopoulos. Flavour-changing neutral interactions in broken supersymmetric theories. *Phys. Lett. B*, 110(1):44, 1982.

[58] T.G. Rizzo. The Zoo of BSM Physics at the LHC. 40th SLAC Summer Institute, 2012.

[59] ALEPH Collaboration. Search for charginos and neutralinos in e^+e^- collisions at centre-of-mass energies near 183 GeV and constraints on the MSSM parameter space. *Eur. Phys. J. C*, 11(2):193, 1999.

[60] J. Ellis, S. Kelley, and D.V. Nanopoulos. Probing the desert using gauge coupling unification. *Phys. Lett. B*, 260(1):131, 1991.

[61] P. Langacker and N. Polonsky. Uncertainties in coupling constant unification. *Phys. Rev. D*, 47:4028, May 1993.

[62] Prospino sparticle production cross-sections at $\sqrt{s} = 8$ TeV. https://www.thphys.uni-heidelberg.de/~plehn/includes/prospino/prospino_lhc8.eps, viewed Apr 2020.

[63] CERN Twiki for SUSY cross section at $\sqrt{s} = 13$ TeV. https://twiki.cern.ch/twiki/pub/LHCPhysics/SUSYCrossSections/SUSY_xsecs_20190729.png, viewed Apr 2020.

[64] M. Krämer, A. Kulesza, R. van der Leeuw, M. Mangano, S. Padhi, T. Plehn, and X. Portell. Supersymmetry production cross sections in pp collisions at $\sqrt{s}$ = 7 TeV, 2012. arXiv:1206.2892.

[65] ATLAS Collaboration. Search for new phenomena in final states with large jet multiplicities and missing transverse momentum at $\sqrt{s} = 8$ TeV proton-proton collisions using the ATLAS experiment. *J. High Energ. Phys.*, 10:130, 2013.

[66] A. Arvanitaki, M. Baryakhtar, X. Huang, K. Van Tilburg, and G. Villadoro. The last vestiges of naturalness. *J. High Energ. Phys.*, 3:022, Mar 2014.

[67] ATLAS Collaboration. ATLAS Run 1 searches for direct pair production of third-generation squarks at the Large Hadron Collider. *Eur. Phys. J. C*, 75(10):510, Oct 2015. [Erratum: Eur.Phys.J.C 76, 153 (2016)].

[68] I. Melzer-Pellmann and P. Pralavorio. Lessons for SUSY from the LHC after the first run. *Eur. Phys. J. C*, 74:2801, 2014.

[69] ATLAS Collaboration. Search for direct production of charginos, neutralinos and sleptons in final states with two leptons and missing transverse momentum in pp collisions at $\sqrt{s}$ = 8 TeV with the ATLAS detector. *J. High Energ. Phys.*, 5:71, May 2014.

[70] ATLAS Collaboration. Search for an additional, heavy Higgs boson in the $H \to ZZ$ decay channel at $\sqrt{s} = 8$TeV in pp collision data with the ATLAS detector. *Eur. Phys. J. C*, 76(1):45, Jan 2016.

[71] A. Djouadi, L. Maiani, G. Moreau, A. Polosa, J. Quevillon, and V. Riquer. The post-Higgs MSSM scenario: habemus MSSM? *Eur. Phys. J. C*, 73(12):2650, Nov 2013.

[72] M. W. Goodman and E. Witten. Detectability of certain dark-matter candidates. *Phys. Rev. D*, 31:3059, Jun 1985.

[73] XENON Collaboration. Dark Matter Search Results from a One Ton-Year Exposure of XENON1T. *Phys. Rev. Lett.*, 121(11):111302, Sep 2018.

[74] S. Profumo, T. Stefaniak, and L. Stephenson-Haskins. The Not-So-Well Tempered Neutralino. *Phys. Rev. D*, 96(5):055018, Sep 2017.

[75] ALEPH, DELPHI, L3, and OPAL Experiments. The LEP2 SUSY Working Group. LEPSUSYWG/01-03.1, 2001.

[76] CMS Collaboration. Search for electroweak production of charginos and neutralinos in multilepton final states in proton-proton collisions at $\sqrt{s} = 13$ TeV. *J. High Energ. Phys.*, 3:166, Mar 2018.

[77] S. Hoof, A. Geringer-Sameth, and R. Trotta. A global analysis of dark matter signals from 27 dwarf spheroidal galaxies using 11 years of Fermi-LAT observations. *Journal of Cosmology and Astroparticle Physics*, 2:012, Feb 2020.

[78] P. Salati, F. Donato, and N. Fornengo. Indirect Dark Matter Detection with Cosmic Antimatter, 2010. arXiv:1003.4124.

[79] M. Ackermann, M. Ajello, A. Albert, W. B. Atwood, L. Baldini, J. Ballet, G. Barbiellini, D. Bastieri, R. Bellazzini, E. Bissaldi, et al. The Fermi Galactic Center GeV Excess and Implications for Dark Matter. *The Astrophysical Journal*, 840(1):43, May 2017.

[80] C. Johnson, R. Caputo, C. Karwin, S. Murgia, S. Ritz, and J. Shelton. Search for gamma-ray emission from p-wave dark matter annihilation in the Galactic Center. *Phys. Rev. D*, 99(10):103007, May 2019.

[81] M. Di Mauro, X. Hou, C. Eckner, G. Zaharijas, and E. Charles. Search for γ-ray emission from dark matter particle interactions from the Andromeda and Triangulum galaxies with the Fermi Large Area Telescope. *Phys. Rev. D*, 99(12):123027, Jun 2019.

[82] J. Coronado-Blázquez, M. A. Sánchez-Conde, M. D. Mauro, A. Aguirre-Santaella, I. Ciucă, A. Domínguez, D. Kawata, and N. Mirabal. Spectral and spatial analysis of the dark matter subhalo candidates among Fermi Large Area Telescope unidentified sources. *Journal of Cosmology and Astroparticle Physics*, 11:045, Nov 2019.

[83] O. Adriani et al. Ten years of PAMELA in space. *Riv. Nuovo Cim.*, 40(10):1, 2017.

[84] L. Accardo et al. High Statistics Measurement of the Positron Fraction in Primary Cosmic Rays of 0.5–500 GeV with the Alpha Magnetic Spectrometer on the International Space Station. *Phys. Rev. Lett.*, 113:121101, 2014.

[85] M. G. Aartsen, R. Abbasi, Y. Abdou, M. Ackermann, J. Adams, J. A. Aguilar, M. Ahlers, D. Altmann, J. Auffenberg, X. Bai, et al. Search for Dark Matter Annihilations in the Sun with the 79-String IceCube Detector. *Phys. Rev. Lett.*, 110(13): 131302, Mar 2013.

[86] M.G. Aartsen, K. Abraham, M. Ackermann, J. Adams, J.A. Aguilar, M. Ahlers, M. Ahrens, D. Altmann, T. Anderson, I. Ansseau, et al. Improved limits on dark matter annihilation in the Sun with the 79-string IceCube detector and implications for supersymmetry. *Journal of Cosmology and Astroparticle Physics*, 4:022, Apr 2016.

[87] S. Adrián-Martínez, A. Albert, M. André, G. Anton, M. Ardid, J.-J. Aubert, T. Avgitas, B. Baret, J. Barrios-Martí, S. Basa, et al. Limits on dark matter annihilation in the sun using the ANTARES neutrino telescope. *Phys. Lett. B*, 759:69, Aug 2016.

[88] K. J. de Vries, E. A. Bagnaschi, O. Buchmueller, R. Cavanaugh, M. Citron, A. De Roeck, M. J. Dolan, J. R. Ellis, H. Flächer, S. Heinemeyer, et al. The pMSSM10 after LHC run 1. *Eur. Phys. J. C*, 75(9):422, Sep 2015.

[89] E.A. Bagnaschi et al. Supersymmetric Dark Matter after LHC Run 1. *Eur. Phys. J. C*, 75:500, 2015.

[90] P. Athron, C. Balázs, T. Bringmann, A. Buckley, M. Chrząszcz, J. Conrad, J. M. Cornell, L. A. Dal, J. Edsjö, et al. A global fit of the MSSM with GAMBIT. *Eur. Phys. J. C*, 77(12):879, Dec 2017.

[91] C. Strege, G. Bertone, G. J. Besjes, S. Caron, R. Ruiz de Austri, A. Strubig, and R. Trotta. Profile likelihood maps of a 15-dimensional MSSM. *J. High Energ. Phys.*, 9:81, Sep 2014.

[92] A. Achterberg, S. Amoroso, S. Caron, L. Hendriks, R. R. de Austri, and C. Weniger. A description of the Galactic Center excess in the Minimal Supersymmetric Standard Model. *Journal of Cosmology and Astroparticle Physics*, 8:006, Aug 2015.

[93] G. Bertone, F. Calore, S. Caron, R. Ruiz, J. S. Kim, R. Trotta, and C. Weniger. Global analysis of the pMSSM in light of the Fermi GeV excess: prospects for the LHC Run-II and astroparticle experiments. *Journal of Cosmology and Astroparticle Physics*, 4:037, Apr 2016.

[94] HL-LHC Project Schedule. https://project-hl-lhc-industry.web.cern.ch/content/project-schedule, viewed Jun 2020.

[95] ATLAS Collaboration. The ATLAS Experiment at the CERN Large Hadron Collider. *JINST*, 3:S08003, 2008.

[96] CMS Collaboration. The CMS Experiment at the CERN LHC. *JINST*, 3:S08004, 2008.

[97] LHCb Collaboration. The LHCb Detector at the LHC. *JINST*, 3:S08005, 2008.

[98] ALICE Collaboration. The ALICE experiment at the CERN LHC. *JINST*, 3:S08002, 2008.

[99] R. E. Allen. The Higgs Bridge. *Phys. Scripta*, 89:018001, 2013.

[100] L. Evans and P. Bryant. LHC Machine. *JINST*, 3:S08001, 2008.

[101] LHC beampipe section. https://cds.cern.ch/record/2290375, viewed Mar 2020.

[102] The Large Hadron Collider. https://home.cern/science/accelerators/large-hadron-collider, viewed Mar 2020.

[103] Powering CERN. https://home.cern/science/engineering/powering-cern, viewed Mar 2020.

[104] Cryogenics: Low temperatures, high performance. https://home.cern/science/engineering/cryogenics-low-temperatures-high-performance, viewed Mar 2020.

[105] The CERN accelerator complex. https://cds.cern.ch/record/2197559, viewed Mar 2020.

[106] Accelerating: Radiofrequency cavities. https://home.cern/science/engineering/accelerating-radiofrequency-cavities, viewed Mar 2020.

[107] Pulling together: Superconducting electromagnets. https://home.cern/science/engineering/pulling-together-superconducting-electromagnets, viewed Mar 2020.

[108] ATLAS Luminosity Run 2. https://twiki.cern.ch/twiki/bin/view/AtlasPublic/LuminosityPublicResultsRun2, viewed Mar 2020.

[109] ATLAS Collaboration. Luminosity determination in pp collisions at $\sqrt{s} = 7$ TeV using the ATLAS detector at the LHC. *Eur. Phys. J. C*, 71(4):1630, Apr 2011.

[110] J. Pequenao and P. Schaffner. How ATLAS detects particles: diagram of particle paths in the detector. Jan 2013. URL https://cds.cern.ch/record/1505342.

[111] Particle Data Group. Review of particle physics. *Phys. Rev. D*, 98(3):1, Aug 2018.

[112] M. Capeans, G. Darbo, K. Einsweiller, M. Elsing, T. Flick, M. Garcia-Sciveres, C. Gemme, H. Pernegger, O. Rohne, and R. Vuillermet. ATLAS Insertable B-Layer Technical Design Report. Technical Report CERN-LHCC-2010-013. ATLAS-TDR-19, CERN, Geneva, Sep 2010. URL https://cds.cern.ch/record/1291633.

[113] ATLAS Collaboration. ATLAS Inner Detector Alignment Performance with February 2015 Cosmic Rays Data. Technical Report ATL-PHYS-PUB-2015-009, CERN, Geneva, Apr 2015. URL https://cds.cern.ch/record/2008724.

[114] ATLAS Collaboration. Alignment of the ATLAS Inner Detector. Technical Report ATL-COM-PHYS-2019-953, CERN, Geneva, Jul 2019. URL https://cds.cern.ch/record/2684129.

[115] ATLAS Collaboration. Resolution of the ATLAS muon spectrometer monitored drift tubes in LHC Run 2. *JINST*, 14:P09011, Sep 2019.

[116] T. Argyropoulos et al. Cathode strip chambers in ATLAS: Installation, commissioning and in situ performance. *IEEE Trans. Nucl. Sci.*, 56:1568, 2009.

[117] Giordano C. and the RPC group. The Resistive Plate Chambers of the ATLAS experiment: performance studies. *Journal of Physics: Conference Series*, 280:12001, Feb 2011.

[118] S. Majewski, G. Charpak, A. Breskin, and G. Mikenberg. A thin multiwire chamber operating in the high multiplication mode. *Nuclear Instruments and Methods in Physics Research*, 217(1):265, 1983.

[119] E. Etzion, Y. Benhammou, J. Ginzburg, M. Ishino, L. Levinson, G. Mikenberg, N. Panikashvili, D. Primor, and V. P. Smakhtin. The Certification of ATLAS thin gap chambers produced in Israel and China. In *2004 IEEE Nuclear Science Symposium and Medical Imaging Conference*, volume 1, page 236, 2004.

[120] A. Ruiz-Martinez and ATLAS Collaboration. The Run-2 ATLAS Trigger System. Technical Report ATL-DAQ-PROC-2016-003, CERN, Geneva, Feb 2016. URL https://cds.cern.ch/record/2133909.

[121] ATLAS Collaboration. The ATLAS Data Acquisition and High Level Trigger system. *JINST*, 11:P06008, Jun 2016.

[122] K. Stoerig, J. Grosse-Knetter, K. Kroeninger, A. Quadt, and T. Goettfert. Alignment Studies of the ATLAS Silicon Trackers with Overlap Residuals. Technical Report ATL-INDET-INT-2009-001. ATL-COM-INDET-2008-012, CERN, Geneva, Aug 2008. URL https://cds.cern.ch/record/1121595.

[123] P. Brückman, A. Hicheur, and S. J. Haywood. Global χ^2 approach to the Alignment of the ATLAS Silicon Tracking Detectors. Technical Report ATL-INDET-PUB-2005-002. ATL-COM-INDET-2005-004. CERN-ATL-INDET-PUB-2005-002, CERN, Geneva, 2005. URL https://cds.cern.ch/record/835270.

[124] A. Bocci and W. Hulsbergen. TRT Alignment For SR1 Cosmics and Beyond. Technical Report ATL-INDET-PUB-2007-009. ATL-COM-INDET-2007-011. CERN-ATL-COM-INDET-2007-011, CERN, Geneva, Jun 2007. URL https://cds.cern.ch/record/1039585.

[125] T.G. Cornelissen, M. Elsing, I. Gavrilenko, J.F. Laporte, W. Liebig, M. Limper, K. Nikolopoulos, A. Poppleton, and A. Salzburger. The global χ^2 track fitter in ATLAS. *J. Phys. Conf. Ser.*, 119:32013, 2008.

[126] ATLAS Collaboration. Study of alignment-related systematic effects on the ATLAS Inner Detector tracking. Technical Report ATLAS-CONF-2012-141, CERN, Geneva, Oct 2012. URL https://cds.cern.ch/record/1483518.

[127] J. Boudreau and V. Tsulaia. The GeoModel toolkit for detector description. In *14th International Conference on Computing in High-Energy and Nuclear Physics*, page 353, 2005.

[128] ATLAS Collaboration. Alignment of the ATLAS Inner Detector with the initial LHC data at $\sqrt{s}$ = 13 TeV. Technical Report ATL-PHYS-PUB-2015-031, CERN, Geneva, Jul 2015. URL https://cds.cern.ch/record/2038139.

[129] ATLAS Collaboration. Time dependent alignment corrections to IBL distortions. https://atlas.web.cern.ch/Atlas/GROUPS/PHYSICS/PLOTS/IDTR-2015-011/, Dec 2015.

[130] P. Butti. *Search for scalar top quarks decaying into scalar tau leptons with ATLAS at* $\sqrt{s} = 8$ *TeV*. PhD thesis, University of Amsterdam, 2017.

[131] T Golling. Alignment of the Silicon Tracking Detector using Survey Constraints. Technical Report ATL-INDET-PUB-2006-001. ATL-COM-INDET-2006-002. CERN-ATL-INDET-PUB-2006-001, CERN, Geneva, Mar 2006. URL https://cds.cern.ch/record/941076.

[132] A. Morley. Transverse impact parameter biases in 8 TeV data. Private communication, Aug 2015.

[133] T. Cornelissen, M. Elsing, S. Fleischmann, W. Liebig, E. Moyse, and A. Salzburger. Concepts, Design and Implementation of the ATLAS New Tracking (NEWT). Technical Report ATL-SOFT-PUB-2007-007. ATL-COM-SOFT-2007-002, CERN, Geneva, Mar 2007. URL https://cds.cern.ch/record/1020106.

[134] R. Kalman. A New Approach to Linear Filtering and Prediction Problems. *Journal of Basic Engineering*, 82(1):35, 1960.

[135] R. Frühwirth. Application of Kalman filtering to track and vertex fitting. *Nucl. Instrum. Meth. A*, 262:444, 1987.

[136] D. Wicke. A New Algorithm for Solving Tracking Ambiguities, Nov 1998. DELPHI-98-163 PROG 236 TRACK 92.

[137] ATLAS Collaboration. Early Inner Detector Tracking Performance in the 2015 data at $\sqrt{s}$ = 13 TeV. Technical Report ATL-PHYS-PUB-2015-051, CERN, Geneva, Dec 2015. URL https://cds.cern.ch/record/2110140.

[138] ATLAS Collaboration. Performance of the ATLAS Inner Detector Track and Vertex Reconstruction in the High Pile-Up LHC Environment. Technical Report ATLAS-CONF-2012-042, CERN, Geneva, Mar 2012. URL https://cds.cern.ch/record/1435196.

[139] R. Frühwirth, W. Waltenberger, and P. Vanlaer. Adaptive vertex fitting. *J. Phys. G*, 34 (12):N343, 2007.

[140] ATLAS Collaboration. Event display showing a Z boson decaying into two muons with 11 reconstructed vertices. http://opendata.atlas.cern/books/current/openatlasdatatools/_book/atlas_events.html, Apr 2011.

[141] ATLAS Collaboration. Vertex Reconstruction Performance of the ATLAS Detector at $\sqrt{s} = 13$ TeV. Technical Report ATL-PHYS-PUB-2015-026, CERN, Geneva, Jul 2015. URL https://cds.cern.ch/record/2037717.

[142] ATLAS Collaboration. Performance of primary vertex reconstruction in proton-proton collisions at $\sqrt{s}$ =7 TeV in the ATLAS experiment. Technical Report ATLAS-CONF-2010-069, CERN, Geneva, Jul 2010. URL https://cds.cern.ch/record/1281344.

[143] ATLAS Collaboration. Reconstruction of primary vertices at the ATLAS experiment in Run 1 proton-proton collisions at the LHC. *Eur. Phys. J. C*, 77(5):332, May 2017.

[144] ATLAS Collaboration. Jet energy scale measurements and their systematic uncertainties in proton-proton collisions at $\sqrt{s}$ = 13 TeV with the ATLAS detector. *Phys. Rev. D*, 96(7):72002, Oct 2017.

[145] M. Cacciari, G. Salam, and G. Soyez. The anti-k_t jet clustering algorithm. *J. High Energ. Phys.*, 4:63, Apr 2008.

[146] S. D. Ellis and D. E. Soper. Successive combination jet algorithm for hadron collisions. *Phys. Rev. D*, 48(7):3160, Oct 1993.

[147] ATLAS Collaboration. A neural network clustering algorithm for the ATLAS silicon pixel detector. *JINST*, 9:P09009, Sep 2014.

[148] ATLAS Collaboration. Jet energy scale and uncertainties in 2015-2017 data and simulation. https://atlas.web.cern.ch/Atlas/GROUPS/PHYSICS/PLOTS/JETM-2018-006/, Nov 2018.

[149] ATLAS Collaboration. Tagging and suppression of pileup jets with the ATLAS detector. Technical Report ATLAS-CONF-2014-018, CERN, Geneva, May 2014. URL https://cds.cern.ch/record/1700870.

[150] B-tagging sketch. http://bartosik.pp.ua/hep_sketches/btagging, viewed Jan 2020.

[151] ATLAS Collaboration. Optimisation of the ATLAS *b*-tagging performance for the 2016 LHC Run. Technical Report ATL-PHYS-PUB-2016-012, CERN, Geneva, Jun 2016. URL https://cds.cern.ch/record/2160731.

[152] ATLAS Collaboration. Improved electron reconstruction in ATLAS using the Gaussian Sum Filter-based model for bremsstrahlung. Technical Report ATLAS-CONF-2012-047, CERN, Geneva, May 2012. URL https://cds.cern.ch/record/1449796.

[153] ATLAS Collaboration. Electron reconstruction and identification in the ATLAS experiment using the 2015 and 2016 LHC proton-proton collision data at $\sqrt{s}$ = 13 TeV. *Eur. Phys. J. C*, 79(8):639, 2019.

[154] ATLAS Collaboration. Electron efficiency measurements with the ATLAS detector using the 2015 LHC proton-proton collision data. Technical Report ATLAS-CONF-2016-024, CERN, Geneva, Jun 2016. URL https://cds.cern.ch/record/2157687.

[155] ATLAS Collaboration. Electron reconstruction and identification efficiency measurements in 2016 Data. https://atlas.web.cern.ch/Atlas/GROUPS/PHYSICS/PLOTS/EGAM-2017-003/, Mar 2017.

[156] F. He, J. Liu, R. Ospanov, and R. T. Roberts. Tagging non-prompt electrons and muons using lifetime and isolation information. Technical Report ATL-COM-PHYS-2018-1083, CERN, Geneva, Jul 2018. URL https://cds.cern.ch/record/2632152.

[157] ATLAS Collaboration. Muon reconstruction performance of the ATLAS detector in proton-proton collision data at $\sqrt{s} = 13$ TeV. *Eur. Phys. J. C*, 76(5):292, May 2016.

[158] ATLAS Collaboration. Low-pT Muon Selection: Preliminary Public Plots. https://atlas.web.cern.ch/Atlas/GROUPS/PHYSICS/PLOTS/MUON-2018-005/, July 2018.

[159] ATLAS Collaboration. Performance of missing transverse momentum reconstruction with the ATLAS detector using proton-proton collisions at $\sqrt{s}$ = 13 TeV. *Eur. Phys. J. C*, 78(11):903, Nov 2018.

[160] ATLAS Collaboration. Measurement of the photon identification efficiencies with the ATLAS detector using LHC Run 2 data collected in 2015 and 2016. *Eur. Phys. J. C*, 79(3):205, Mar 2019.

[161] A. Vermeulen on behalf of the ATLAS Collaboration. Reconstruction techniques in Supersymmetry searches with the ATLAS detector. *Journal of Physics: Conference Series*, 1390(1):12037, 2019.

[162] ATLAS Collaboration. Object-based missing transverse momentum significance in the ATLAS detector. Technical Report ATLAS-CONF-2018-038, CERN, Geneva, Jul 2018. URL https://cds.cern.ch/record/2630948.

[163] A. Barr, C. Lester, and P. Stephens. A variable for measuring masses at hadron colliders when missing energy is expected; mT2: the truth behind the glamour. *Journal of Physics G: Nuclear and Particle Physics*, 29(10):2343, Sep 2003.

[164] E. Bothmann, G. Singh Chahal, S. Höche, J. Krause, F. Krauss, S. Kuttimalai, S. Liebschner, D. Napoletano, M. Schönherr, H. Schulz, et al. Event generation with Sherpa 2.2. *SciPost Physics*, 7(3):34, Sep 2019.

[165] C. Oleari. The POWHEG BOX. *Nucl. Phys. B - Proceedings Supplements*, 205-206: 36, Aug 2010.

[166] J. Alwall, R. Frederix, S. Frixione, V. Hirschi, F. Maltoni, O. Mattelaer, H.-S. Shao, T. Stelzer, P. Torrielli, and M. Zaro. The automated computation of tree-level and next-to-leading order differential cross sections, and their matching to parton shower simulations. *J. High Energ. Phys.*, 7:79, Jul 2014.

[167] A. Buckley, J. Butterworth, S. Gieseke, D. Grellscheid, S. Höche, H. Hoeth, F. Krauss, L. Lönnblad, E. Nurse, P. Richardson, et al. General-purpose event generators for LHC physics. *Physics Reports*, 504(5):145, Jul 2011.

[168] R. D. Ball, V. Bertone, S. Carrazza, C. S. Deans, L. Del Debbio, S. Forte, A. Guffanti, N. P. Hartland, J. I. Latorre, et al. Parton distributions for the LHC run II. *J. High Energ. Phys.*, 4:40, Apr 2015.

[169] T. Sjostrand, S. Mrenna, and P. Z. Skands. A Brief Introduction to PYTHIA 8.1. *Comput. Phys. Commun.*, 178:852, 2008.

[170] ATLAS Collaboration. ATLAS Run 1 Pythia8 tunes. Technical Report ATL-PHYS-PUB-2014-021, CERN, Geneva, Nov 2014. URL http://cds.cern.ch/record/1966419.

[171] S. Agostinelli et al. GEANT4: A Simulation toolkit. *Nucl. Instrum. Meth.*, A506:250, 2003.

[172] ATLAS Collaboration. The ATLAS Simulation Infrastructure. *Eur. Phys. J. C*, 70(3): 823, Sep 2010.

[173] S. van der Meer. Calibration of the effective beam height in the ISR. Technical Report CERN-ISR-PO-68-31. ISR-PO-68-31, CERN, Geneva, 1968. URL https://cds.cern.ch/record/296752.

[174] ATLAS Collaboration. Luminosity determination in pp collisions at $\sqrt{s} = 13$ TeV using the ATLAS detector at the LHC. Technical Report ATLAS-CONF-2019-021, CERN, Geneva, Jun 2019. URL https://cds.cern.ch/record/2677054.

[175] ATLAS Collaboration. Electron and photon energy calibration with the ATLAS detector using 2015-2016 LHC proton-proton collision data. *JINST*, 14:P03017, 2019.

[176] ATLAS Collaboration. Jet energy scale measurements and their systematic uncertainties in proton–proton collisions at $\sqrt{s} = 13\,\text{TeV}$ with the ATLAS detector. *Phys. Rev. D*, 96:72002, 2017.

[177] ATLAS Collaboration. Jet energy measurement and its systematic uncertainty in proton–proton collisions at $\sqrt{s} = 7\,\text{TeV}$ with the ATLAS detector. *Eur. Phys. J. C*, 75: 17, 2015.

[178] ATLAS Collaboration. ATLAS b-jet identification performance and efficiency measurement with $t\bar{t}$ events in pp collisions at $\sqrt{s} = 13$ TeV. *Eur. Phys. J. C*, 79:970, Jul 2019.

[179] L. A. Harland-Lang, A. D. Martin, P. Motylinski, and R. S. Thorne. Parton distributions in the LHC era: MMHT 2014 PDFs. *Eur. Phys. J. C*, 75(5):204, May 2015.

[180] S. Dulat, T. Hou, J. Gao, M. Guzzi, J. Huston, P. Nadolsky, J. Pumplin, C. Schmidt, D. Stump, and C. P. Yuan. New parton distribution functions from a global analysis of quantum chromodynamics. *Phys. Rev. D*, 93(3):33006, Feb 2016.

[181] S. Catani, F. Krauss, B. R. Webber, and R. Kuhn. QCD Matrix Elements + Parton Showers. *J. High Energ. Phys.*, 11:63, Nov 2001.

[182] S. Schumann and F. Krauss. A parton shower algorithm based on Catani-Seymour dipole factorisation. *J. High Energ. Phys.*, 3:38, Mar 2008.

[183] J. Butterworth et al. PDF4LHC recommendations for LHC Run II. *J. Phys. G*, 43: 23001, 2016.

[184] T. Sjöstrand, S. Ask, J. R. Christiansen, R. Corke, N. Desai, P. Ilten, S. Mrenna, S. Prestel, C. O. Rasmussen, and P. Z. Skands. An introduction to PYTHIA 8.2. *Computer Physics Communications*, 191:159, Jun 2015.

[185] ATLAS Collaboration. Measurement of $W^{\pm}Z$ production cross sections and gauge boson polarisation in pp collisions at $\sqrt{s} = 13$ TeV with the ATLAS detector. Technical Report ATLAS-CONF-2018-034, CERN, Geneva, Jul 2018. URL https://cds.cern.ch/record/2630187.

[186] ATLAS Collaboration. Search for direct production of charginos, neutralinos and sleptons in final states with two leptons and missing transverse momentum in pp collisions at $\sqrt{s} = 8$ TeV with the ATLAS detector. *J. High Energ. Phys.*, 5:71, 2014.

[187] S. Frixione, E. Laenen, P. Motylinski, and B. R. Webber. Angular correlations of lepton pairs from vector boson and top quark decays in Monte Carlo simulations. *J. High Energ. Phys.*, 4:81, Apr 2007.

[188] P. Artoisenet, R. Frederix, O. Mattelaer, and R. Rietkerk. Automatic spin-entangled decays of heavy resonances in Monte Carlo simulations. *J. High Energ. Phys.*, 3:15, Mar 2013.

[189] ATLAS Collaboration. The simulation principle and performance of the ATLAS fast calorimeter simulation FastCaloSim. Technical Report ATL-PHYS-PUB-2010-013, CERN, Geneva, Oct 2010. URL https://cds.cern.ch/record/1300517.

[190] ATLAS Collaboration. Evidence for the associated production of the Higgs boson and a top quark pair with the ATLAS detector. *Phys. Rev. D*, 97:72003, 2018.

[191] R. D. Cousins, J. T. Linnemann, and J. Tucker. Evaluation of three methods for calculating statistical significance when incorporating a systematic uncertainty into a test of the background-only hypothesis for a Poisson process. *Nucl. Instrum. Meth. A*, 595(2):480, 2008.

[192] K. Cranmer, G. Lewis, L. Moneta, A. Shibata, and W. Verkerke. HistFactory: A tool for creating statistical models for use with RooFit and RooStats. Technical Report CERN-OPEN-2012-016, New York U., New York, Jan 2012. URL https://cds.cern.ch/record/1456844.

[193] M. Baak, G. J. Besjes, D. Côté, A. Koutsman, J. Lorenz, and D. Short. HistFitter software framework for statistical data analysis. *Eur. Phys. J. C*, 75(4):153, Apr 2015.

[194] W. Verkerke and D. Kirkby. The RooFit toolkit for data modeling, 2003. arXiv:physics/0306116.

[195] L. Moneta, K. Belasco, K. Cranmer, S. Kreiss, A. Lazzaro, D. Piparo, G. Schott, W. Verkerke, and M. Wolf. The RooStats Project, 2010. arXiv:1009.1003.

[196] G. Cowan, K. Cranmer, E. Gross, and O. Vitells. Asymptotic formulae for likelihood-based tests of new physics. *Eur. Phys. J. C*, 71:1554, 2011. [Erratum: Eur.Phys.J.C 73, 2501 (2013)].

[197] CMS Collaboration. Search for supersymmetry with a compressed mass spectrum in the vector boson fusion topology with 1-lepton and 0-lepton final states in proton-proton collisions at $\sqrt{s}$ = 13 TeV. *J. High Energ. Phys.*, 8:150, Aug 2019.

[198] ATLAS Collaboration. Searches for electroweak production of supersymmetric particles with compressed mass spectra in $\sqrt{s}$ = 13 TeV pp collisions with the ATLAS detector. *Phys. Rev. D*, 101(5):52005, Mar 2020.

[199] P. A. R. Ade, N. Aghanim, M. Arnaud, M. Ashdown, J. Aumont, C. Baccigalupi, A. J. Banday, R. B. Barreiro, J. G. Bartlett, et al. Planck 2015 results. XIII. Cosmological parameters. *Astronomy & Astrophysics*, 594:A13, Sep 2016.

[200] G. H. Duan, K. Hikasa, J. Ren, L. Wu, and J. M. Yang. Probing bino-wino coannihilation dark matter below the neutrino floor at the LHC. *Phys. Rev. D*, 98(1):15010, Jul 2018.

[201] ATLAS Collaboration. SUSY October 2019 Summary Plot Update. Technical Report ATL-PHYS-PUB-2019-044, CERN, Geneva, 2020. URL http://cds.cern.ch/record/2697155.

[202] ATLAS Collaboration. SUSY May 2020 Summary Plot Update. Technical Report ATL-PHYS-PUB-2020-013, CERN, Geneva, May 2020. URL http://cds.cern.ch/record/2718947.

[203] L. Lapikás M.W. van de Heijden and H. de Vries. *Elektronenversnellers in Amsterdam*. NIKHEF, 1999.

[204] AMPS The Amsterdam Pulse Stretcher. https://www.nikhef.nl/~pieth/mea_amps/, viewed Aug 2019.

[205] The Large Electron-Positron Collider. https://home.cern/science/accelerators/large-electron-positron-collider, viewed Aug 2019.

[206] Llewellyn Smith C. Genesis of the Large Hadron Collider. *Phil. Trans. R. Soc. A*, 373: 20140037, 2015.

Summary

Through physics we try to understand the world. And we do understand a lot about it. Especially when we consider the matter around us. As is the case with what the air that we breathe is made of or what the table we sit at is made of. Most people are aware that matter is made up out of atoms. But one could then ask the subsequent question: what are atoms made of? As with a lot of questions, one could go deeper and deeper into an explanation for why something happens. When describing what atoms are made of we enter the field of particle physics. The theory that describes particle physics is called the Standard Model (SM). The SM is successful at describing the complexity of matter that we observe at particle accelerators, where the building blocks of atoms are revealed.

Particle accelerators have come a long way since they were first blown into existence, with the Large Hadron Collider (LHC) being the pinnacle of its technique. The first particle accelerator, the cyclotron created by Ernest Lawrence in 1930, fitted in the palm of your hand as exemplified in Figure 1(a). With the start of the new field of particle physics, bigger and more powerful accelerators came into existence. There were also particle accelerators operational at Nikhef in Amsterdam. These electron accelerators started in the 1950s with energies of 100 MeV and before the year 2000 the energy increased to almost 1000 MeV, with the Amsterdam Pulse Stretcher (AmPS) [203]. Already the AmPS storage ring had a circumference of 212 m, which received its electrons from a linear accelerator called the Medium Energy Accelerator (MEA), a 180 m long. A setup like this no longer fits into your hand, let alone stand in your back garden. At the start of 1999 AmPS and MEA were decommissioned due to budgetary constraints [204]. If we want higher energies the costs and size increases by a lot. The size increase of accelerators is demonstrated in Figure 1. With higher energies it becomes possible to study the building blocks of matter with higher degrees of precision. This is why big international collaborations such as CERN are needed, which set the stage for different countries to bundle their efforts. By gathering all the capacities of tens of countries the Large Electron-Positron Collider (LEP) was able to reach an energy of 209 GeV [205]. A two times higher order of magnitude than we were able to achieve in Amsterdam. The current energy frontier in particle physics is the LHC. The LHC is the

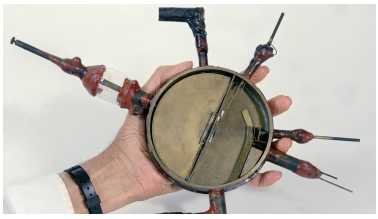

(a) First cyclotron

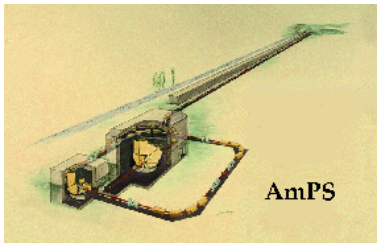

(b) AmPS and MEA

(c) LEP and the LHC

Fig. 1: Size increase of particle accelerators over less than a century.

particle accelerator with the highest collision energy of 13 TeV and it is built inside the old LEP tunnels. To get an idea of its size, it is situated on average 100 m underground and has a circumference of 26.7 km. The first studies for the LHC already started in 1983, the installation started in 2004, the first time it could be used to study physics was in 2010 and it is supposed to run until around 2040 [206]. This gives a feeling for the timescale of the initial idea to a working accelerator in such a huge international project. It is the machine that delivered the collisions to two experiments, ATLAS and CMS, leading to the Higgs discovery.

The SM and the confirmation of the Higgs particle, with its associated mechanism of electroweak symmetry breaking giving mass to particles, are a great triumph for the field of particle physics. However, is it capable of describing all the matter around us? The main motivation for the research performed in this thesis is that the SM does not provide a complete picture of the fundamental building blocks of nature and the laws governing their interactions. On earth the SM is capable of describing matter, however the problem arrises when we start to look at large objects in the universe, like the rotation of galaxies or light coming from very far away, where observations do not match the predictions from the SM. We see stars rotating faster than they should. We see light getting bended by gravitational fields that we do not see. What if we do not know all that much about the matter that surrounds us? Certain experiments conclude that the world we know of, including all the atoms, only makes up 5% of the matter-energy density in the universe, where the dark energy density makes up 68.5% and the remaining 26.5% is contributed to Dark Matter (DM) [30]. Luckily, with the addition of DM we can explain the behaviour of the stars and light in the universe. But how can we explain DM?

DM can be described using supersymmetry. Supersymmetry is a symmetry that relates fermions, particles that make up the matter content of the universe, and bosons, the particles that carry the forces. Supersymmetry predicts many new particles, among which a possible candidate for DM. Besides providing a DM candidate, it solves the mass hierarchy problem

of the SM if supersymmetry is found at the TeV scale. Quantum corrections from the new particles can stabilise the electroweak scale. Supersymmetry also naturally achieves the unification of the electroweak and the strong force, which has been a long-held ideal for particle physics. Furthermore, if supersymmetry is imposed locally, general relativity is automatically included, thus including the fourth fundamental force, gravity, and making supersymmetry a fundamental ingredient for string theory. As a consequence supersymmetry is well motivated by theory, but unfortunately there has not been any experimental confirmation. Without experimental confirmation, a theory, no matter how many problems it solves, stays just a theory. Experiments at LEP, the Tevatron and at Run-1 of the LHC ruled out a large number of supersymmetric models. After Run-1 of the LHC there are stringent constraints on the masses of the strongly produced supersymmetric particles called squarks and gluinos. On the other hand, the values of the masses of the weakly produced supersymmetric charginos and neutralinos are less constrained, since these particles have much smaller production cross-sections. The weakly produced charginos and neutralinos play an important role in establishing a connection between supersymmetric models and DM, where the lightest supersymmetric particle, the lightest neutralino, $\tilde{\chi}_1^0$, is the DM candidate. Since supersymmetry predicts a DM candidate, constraints from astrophysical observations can help motivate which supersymmetric models to look for. In this thesis supersymmetric models are being looked for which are motivated by the thermal relic abundance of DM in the universe. Also supersymmetric models must be coherent with the SM, and agree with measurements from b-physics, Higgs measurements and electroweak precision measurements.

The search performed in this thesis is for the process $\tilde{\chi}_1^{\pm}\tilde{\chi}_2^0 \rightarrow WZ\tilde{\chi}_1^0\tilde{\chi}_1^0$. The process is well-motivated through global fits and is not excluded yet in the case where the mass gap between the $\tilde{\chi}_1^{\pm}\tilde{\chi}_2^0$ and the $\tilde{\chi}_1^0$ is small. The process decays into a final state of three leptons and missing energy ($E_{\mathrm{T}}^{\mathrm{miss}}$). An illustration of the Feynman diagram is introduced in Figure 2, as well as an explanation of how the signal results in a signature of three leptons and $E_{\mathrm{T}}^{\mathrm{miss}}$. The signal is arduous to detect when there is a small mass gap between the supersymmetric particles, as this will result in low p_{T} leptons and low $E_{\mathrm{T}}^{\mathrm{miss}}$. Reconstruction and triggering become difficult in this scenario because there are a lot of different background processes that have similar signatures in the detector. For this reason new identification techniques are used in this thesis to reconstruct leptons that can be classified to result from the signal process. The technique is called the Prompt Lepton Veto (PLV) and it employs a Boosted Decision Tree, which has been tuned for optimal performance in the analysis.

In order to search for the process a choice has to be made what the mass of the supersymmetric particles is expected to be. The possible choices of mass for the supersymmetric particles, $\tilde{\chi}_1^{\pm}\tilde{\chi}_2^0$ and the $\tilde{\chi}_1^0$, all correspond to different supersymmetric models. Multiple

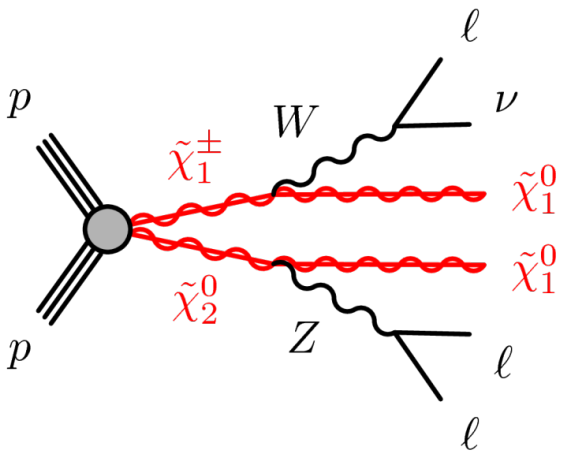

Fig. 2: Feynman diagram showing the process searched for in this thesis. The diagram can be read from left to right and the red lines signify supersymmetric particles. First the two incoming protons (p) from the LHC collide to form the supersymmetric particles $\tilde{\chi}_1^{\pm}$ and $\tilde{\chi}_2^0$. Consequently these hypothetical supersymmetrical particles decay into the Standard Model (SM) particles W and Z, and two of the Dark Matter (DM) candidates, $\tilde{\chi}_1^0$. The W and Z subsequently decay into three leptons and a neutrino. Both the neutrino and the DM candidates end up as missing energy ($E_{\mathrm{T}}^{\mathrm{miss}}$) in the detector. The signature to be measured in the detector is thus three leptons and $E_{\mathrm{T}}^{\mathrm{miss}}$.

Signal Regions (SRs) have been created to target the different possible values the mass of the supersymmetric particles could have. Specifically, the SRs are constructed for different values of the mass gap between the $\tilde{\chi}_2^0/\tilde{\chi}_1^{\pm}$ and $\tilde{\chi}_1^0$ particles. These SRs are optimised to maximise the probability to find supersymmetric particles in them. In order to do so background processes that could have a similar signature are reduced, and the number of supersymmetric particles that could end up in the SRs are maximised. In Figure 3 the result of the search is presented. The different bins correspond to all the SRs that have been created to target the supersymmetric models. In order to evaluate if there were actually supersymmetric particles in the SRs, the expected background from the SM has been computed and has been compared to what is observed in the data. In case supersymmetry is present an excess over the SM prediction is expected. The bottom panel quantifies the significance of the disagreement of the expected background from the SM with the data. A significance of 3σ is evidence for supersymmetry and of 5σ would have been a discovery. In view of the fact that the significance in two of the bins only barely exceeds 2σ, it can be concluded that the SM is able to account for the observations in the SRs. Unfortunately this also means that supersymmetric particles are not found.

The sought for supersymmetric models have not been found, making it possible to exclude them. In order to do so a grid is created representing possible values for the mass of the supersymmetric particles. The grid demonstrating the exclusion of the parameter space is

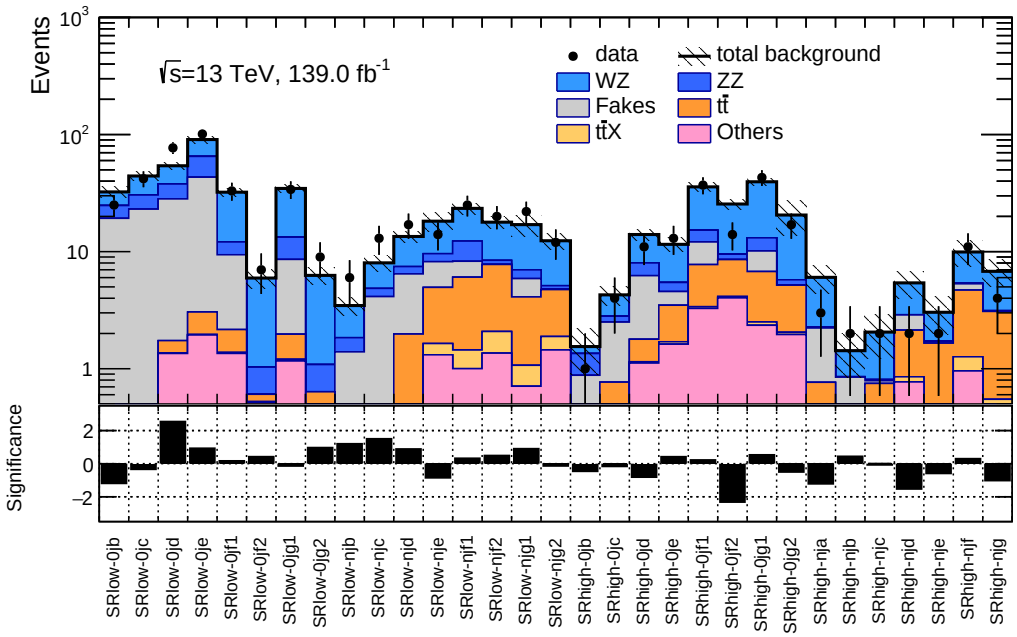

Fig. 3: Summary plot showing the number of events in all SRs and the expected background. The bottom panel shows the significance of the difference between the observed and the expected Standard Model (SM) yields, calculated with the profile likelihood method from [191], adding a minus sign if the yield is below the prediction.

presented in Figure 4. Within the grid all the different SRs provide exclusion power for different values of the mass gap between the $\tilde{\chi}_2^0/\tilde{\chi}_1^{\pm}$ and $\tilde{\chi}_1^0$ particles, resulting in strong exclusion power throughout the grid. The region that falls within the red line has been excluded. It can be concluded that the following models are excluded: the ones which are enclosed in the region where the mass of the $\tilde{\chi}_1^0$ is 250 GeV and the mass of the $\tilde{\chi}_1^{\pm}/\tilde{\chi}_2^0$ is 300 GeV. Although the analysis was not able to find evidence or a discovery of supersymmetry, it was able to exclude a large part of before uncovered phase space.

In closing, the evolution of the field of particle physics, with its increase in the size of the accelerators and of the complexity of the theories, has promoted it into an advanced field. A field that is capable of predicting the behaviour of particles with great precision. However, despite all of its success there are still challenges for particle physics that lie ahead, such as explaining DM or the desire to unify all forces into a single theory. The search presented in this thesis has been one of the attempts to shed light on questions like this. Although the breakthrough is still keeping us waiting, it is what makes this mature field both challenging and exciting at the moment. It will be with great pleasure when we finally arrive at this breakthrough.

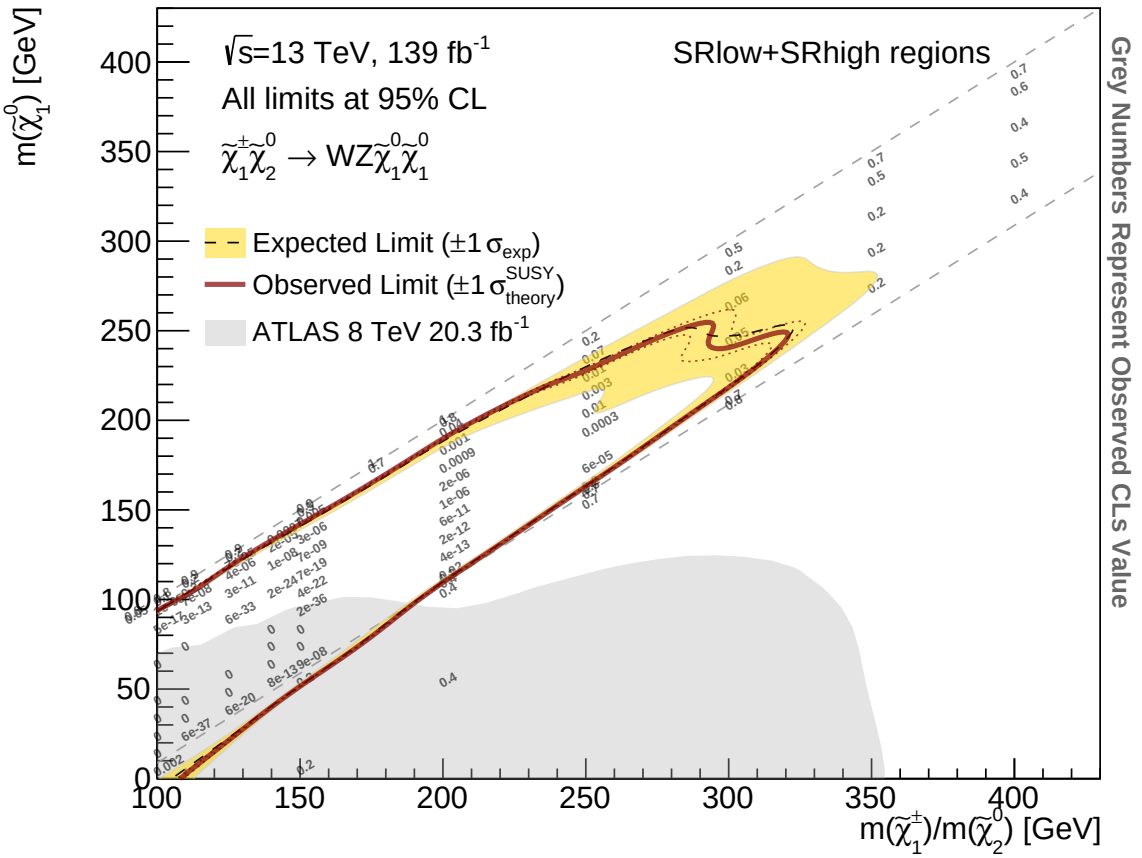

Fig. 4: Exclusion contours parametrised in $\tilde{\chi}_1^0$ and $\tilde{\chi}_1^{\pm}/\tilde{\chi}_2^0$ mass for the combination of all the Signal Regions (SRs). The region within the yellow band defines the limit that was expected within $\pm 1\sigma$. The solid red line demonstrates the observed limit, and the dotted red lines represents the limit within $\pm 1\sigma$. All limits are calculated at a 95% confidence level. The grey shade is the limit obtained by the previous result from ATLAS during Run-1 [186].

Samenvatting

Door de lens van natuurkunde proberen we de wereld te begrijpen. En we begrijpen veel. Zeker als we de materie om ons heen bekijken. Of het nu gaat om de samenstelling van de lucht die we inademen of die van de tafel waar we aan zitten. De meeste mensen zijn zich ervan bewust dat materie bestaat uit atomen. Maar je zou altijd de vervolgvraag kunnen stellen: waar zijn atomen van gemaakt? Zoals met veel vragen kan men dieper en dieper graven naar de verklaring waarom iets gebeurt. Als we willen beschrijven waaruit atomen zijn opgemaakt, komen we in het vakgebied van de deeltjesfysica. De theorie die de deeltjesfysica beschrijft, is het Standaard Model (SM). Het SM kan de complexiteit van materie succesvol beschrijven in deeltjesversnellers, waar de bouwstenen van atomen worden onthuld.

Deeltjesversnellers hebben een lange weg afgelegd sinds ze voor het eerst het daglicht zagen en op dit moment is de Large Hadron Collider (LHC) het toppunt van ons kunnen. De eerste deeltjesversneller, de cyclotron van Ernest Lawrence uit 1930, paste nog in de palm van je hand zoals te zien is in Figuur 1(a). In het nieuwe vakgebied van de deeltjesfysica werden steeds grotere en krachtigere versnellers ontwikkeld. Er waren ook deeltjesversnellers operationeel bij het Nikhef in Amsterdam. Waar deze electronenversnellers in de jaren 50 nog een energie van 100 MeV hadden, nam dit al voor het jaar 2000 toe tot 1000 MeV, door middel van de Amsterdam Pulse Stretcher (AmPS) [203]. De AmPS opslagring had een omtrek van 212 m en kreeg zijn electronen van een lineaire versneller genaamd de Medium Energy Accelerator (MEA), met een lengte van 180 m. Een opstelling als deze past niet in je achtertuin, en al helemaal niet meer in de palm van je hand. Aan het begin van 1999 werden AmPS and MEA stopgezet vanwege budgettaire beperkingen [204]. Als we een hogere botsingsenergie willen bereiken, gaan de grootte en dus kosten enorm omhoog. De toename van de grootte van versnellers in de loop der jaren is te zien in Figuur 1. Met een hogere botsingsenergie wordt het mogelijk om de bouwstenen van materie met grotere precisie te bestuderen. Dit is waarom grote samenwerkingsverbanden zoals CERN nodig zijn, want deze bieden een platform voor verschillende landen om hun krachten te bundelen. Door de inspanningen van tientallen landen samen te voegen was het voor de Large Electron-Positron Collider (LEP) mogelijk om een energie van 209 GeV te bereiken [205]. Een energie die

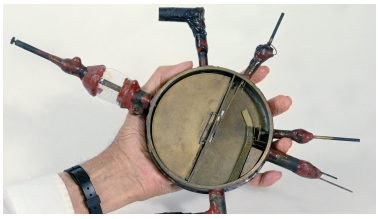

(a) Eerste cyclotron

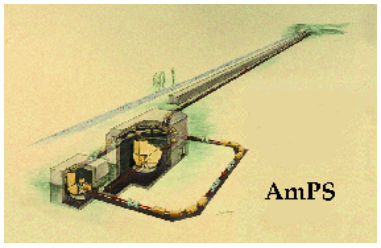

(b) AmPS en MEA

(c) LEP en de LHC

Fig. 1: De toename in grootte van deeltjesversnellers in minder dan een eeuw.

twee ordes van grootte hoger ligt dan wat mogelijk was in Amsterdam. De versneller met de huidig hoogste botsingsenergie is de LHC. De LHC, gebouwd in de oude LEP tunnels, bereikt een maximale botsingsenergie van 13 TeV. Om een idee van de grootte te krijgen: de LHC ligt gemiddeld 100 m ondergronds en heeft een omtrek van 26.7 km. De eerste studies voor de LHC begonnen al in 1983, de installatie begon in 2004, de eerste keer dat er botsingen bestudeerd konden worden was in 2010 en het plan is om de LHC draaiende te houden tot rond 2040 [206]. Dit geeft een idee van de tijd die nodig is om van het initiële concept naar een werkende versneller te gaan in zo'n groot internationaal project. Het is de machine die de botsingen geleverd heeft voor de twee experimenten, ATLAS en CMS, die hebben geleid tot de ontdekking van het Higgsdeeltje.

Het SM en de bevestiging van het bestaan van het Higgsdeeltje met daarbij het mechanisme van electrozwakke symmetriebreking waardoor deeltjes massa krijgen, zijn grote mijlpalen in de deeltjesfysica. Is het SM echter in staat om alle materie rondom ons te beschrijven? De belangrijkste motivatie voor het onderzoek in dit proefschrift bestaat hierin, dat het SM niet de complete beschrijving geeft van de fundamentele bouwstenen van materie en de onderlinge krachten. Op aarde is het SM in staat om materie te beschrijven, het probleem ontstaat echter als we naar grote objecten in het universum gaan kijken, zoals de rotaties van sterrenstelsels en licht dat van ver komt. Onze observaties stroken dan niet met de voorspellingen van het SM. We zien sterren die sneller draaien dan het volgens ons zou moeten. We zien licht dat gebogen wordt door gravitatievelden die we niet kunnen zien. Wat nu als we niet zoveel weten van de materie rondom ons als we denken? Bepaalde experimenten concluderen, dat de wereld zoals wij die kennen, met daarbij alle atomen, slechts 5% uitmaakt van de totale massa-energiedichtheid van het universum, waarbij de donkere energie dichtheid 68.5% inneemt en de overige 26.5% kan worden toegeschreven aan Donkere Materie (DM) [30]. Gelukkig kunnen we met de toevoeging van DM het gedrag van sterren en licht in het universum beschrijven. Maar hoe zouden we DM kunnen verklaren?

DM kan worden beschreven door supersymmetrie. Supersymmetrie is een symmetrie die fermionen, de deeltjes die materie vormen, aan bosonen, de deeltjes die de onderlinge krachten dragen, relateert. Supersymmetrie voorspelt vele nieuwe deeltjes, waaronder een mogelijke kandidaat voor DM. Buiten het feit dat supersymmetrie een kandidaat voor DM levert, lost het ook het massahiërarchieprobleem van het SM op als supersymmetrie zich op de TeV-schaal bevindt. Ook kunnen quantumcorrecties van de nieuwe deeltjes de electrozwakke schaal stabiliseren. Supersymmetrie kan ook op natuurlijke wijze de electrozwakke en de sterke kracht verenigen, wat al lang een ideaal is voor de deeltjesfysica. Bovendien, als supersymmetrie lokaal wordt opgelegd, wordt de algemene relativiteitstheorie automatisch ook beschreven. Hiermee wordt dus ook de vierde fundamentele kracht, de zwaartekracht, meegerekend in de theorie, hetgeen supersymmetrie een fundamenteel ingrediënt maakt voor de snaartheorie. Als gevolg van deze eigenschappen is supersymmetrie goed gemotiveerd door de theorie, maar helaas ontbreekt de experimentele bevestiging. Zonder experimentele bevestiging blijft een theorie, ongeacht hoeveel problemen ermee worden opgelost, slechts een theorie. Experimenten bij LEP, de Tevatron en Run-1 van de LHC hebben een groot aantal supersymmetrische modellen uitgesloten. Na Run-1 van de LHC zijn er strenge limieten aan de massa's van de sterk geproduceerde supersymmetrische deeltjes, de squarks en gluinos. Aan de andere kant zijn de massa's van de zwak geproduceerde supersymmetrische chargino's en neutrino's minder beperkt aangezien deze deeltjes veel kleinere productiedoorsneden hebben. De zwak geproduceerde chargino's en neutralino's spelen een belangrijke rol bij het tot stand brengen van een verband tussen supersymmetrische modellen en DM, waarbij het lichtste supersymmetrische deeltje, de lichtste neutralino, $\tilde{\chi}_1^0$, de DM kandidaat is. Aangezien supersymmetrie een DM kandidaat voorspelt, kunnen beperkingen van astrofysische waarnemingen helpen bij het motiveren naar welke supersymmetrische modellen moet worden gezocht. In dit proefschrift wordt gezocht naar supersymmetrische modellen die worden gemotiveerd door de thermische overblijfselen van DM in het universum. Ook moeten de supersymmetrische modellen coherent zijn met het SM, en overeenkomen met metingen uit b-fysica, Higgs metingen en elektrozwakke precisiemetingen.

De zoektocht die in dit proefschrift is uitgevoerd, geldt voor het proces $\tilde{\chi}_1^{\pm}\tilde{\chi}_2^0 \rightarrow WZ\tilde{\chi}_1^0\tilde{\chi}_1^0$. Dit proces is goed gemotiveerd door globale fits en is nog niet uitgesloten in het geval dat het verschil in massa tussen de $\tilde{\chi}_1^{\pm}\tilde{\chi}_2^0$ en de $\tilde{\chi}_1^0$ klein is. Het proces vervalt naar een eindtoestand van drie leptonen en missende energie ($E_{\mathrm{T}}^{\mathrm{miss}}$). Een illustratie van het Feynman-diagram wordt geïntroduceerd in Figuur 2, evenals een uitleg van hoe het signaal resulteert in een signatuur van drie leptonen en $E_{\mathrm{T}}^{\mathrm{miss}}$. Het signaal is moeilijk te detecteren wanneer er een klein verschil in massa is tussen de supersymmetrische deeltjes, aangezien dit zal resulteren in lage p_{T} leptonen en lage $E_{\mathrm{T}}^{\mathrm{miss}}$. Reconstructie en triggering worden in dit scenario lastig, omdat er

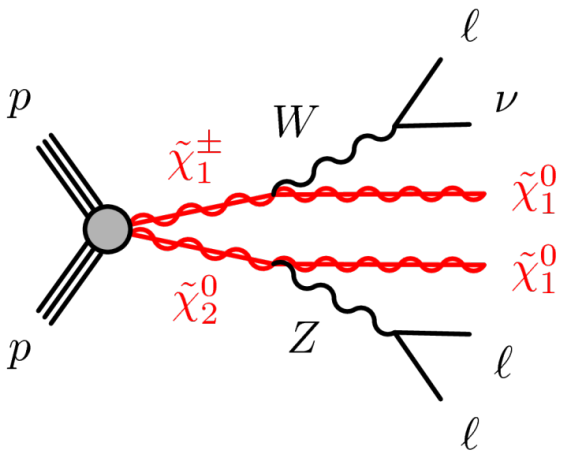

Fig. 2: Feynmandiagram dat het proces laat zien waarnaar gezocht wordt in dit proefschrift. Het diagram is van links naar rechts te lezen en de rode lijnen duiden supersymmetrische deeltjes aan. Eerst botsen de twee inkomende protonen (p) van de LHC om de supersymmetrische deeltjes $\tilde{\chi}_1^{\pm}$ en $\tilde{\chi}_2^0$ te vormen. Vervolgens vervallen deze hypothetische supersymmetrische deeltjes in de Standaard Model (SM) deeltjes W en Z, en twee van de Dark Matter (DM) kandidaten, $\tilde{\chi}_1^0$. De W en Z vervallen vervolgens in drie leptonen en een neutrino. Zowel de neutrino als de DM kandidaten eindigen als missende energie ($E_{\mathrm{T}}^{\mathrm{miss}}$) in de detector. De signatuur die gemeten moet worden in de detector is dus drie leptonen en $E_{\mathrm{T}}^{\mathrm{miss}}$.

veel verschillende achtergrondprocessen zijn met vergelijkbare signaturen in de detector. Om deze reden worden in dit proefschrift nieuwe identificatietechnieken gebruikt om leptonen te reconstrueren die kunnen worden geclassificeerd als resultaat van het signaalproces. De techniek heet de Prompt Lepton Veto (PLV) en maakt gebruik van een Boosted Decision Tree die is afgesteld voor optimale prestaties bij de analyse.

Om naar het proces te kunnen zoeken moet een keuze gemaakt worden wat de massa's van de supersymmetrische deeltjes zullen zijn. De verschillende keuzes voor de massa's van de supersymmetrische deeltjes, $\tilde{\chi}_1^{\pm}\tilde{\chi}_2^0$ en de $\tilde{\chi}_1^0$, komen allemaal overeen met verschillende supersymmetrische modellen. Meerdere Signaal Regio's (SR's) zijn gemaakt, die zich kunnen richten op de verschillende mogelijke waardes van de massa's van de supersymmetrische deeltjes. In het bijzonder zijn de SR's geconstrueerd voor verschillende waardes van het verschil in massa tussen de $\tilde{\chi}_2^0/\tilde{\chi}_1^{\pm}$ and $\tilde{\chi}_1^0$ deeltjes. Deze SR's zijn geoptimaliseerd om de kans te maximaliseren om supersymmetrische deeltjes te vinden. Om dit te realiseren worden achtergrondprocessen die een vergelijkbare signatuur hebben geminimaliseerd en wordt het aantal supersymmetrische deeltjes dat in de SR's zou kunnen belanden gemaximaliseerd. In Figuur 3 wordt het resultaat van de zoekopdracht gepresenteerd. De verschillende kolommen komen overeen met alle SR's die zijn gemaakt om de supersymmetrische modellen te verkennen. Om te evalueren of er daadwerkelijk supersymmetrische deeltjes in de SR's

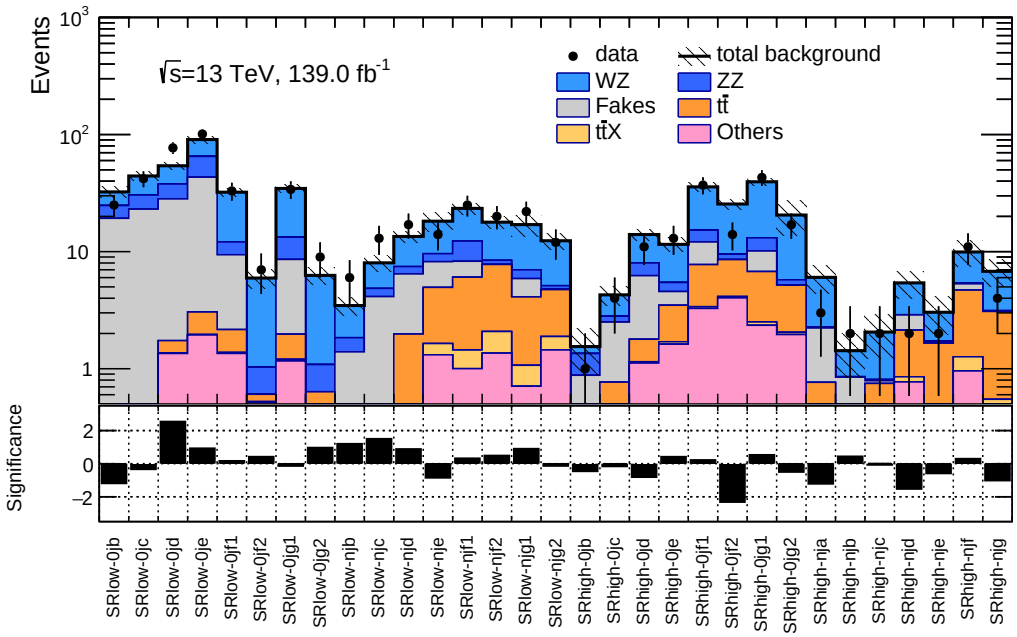

Fig. 3: Een samenvatting van de metingen in alle SR's met daarbij de verwachte achtergrond. Het onderste paneel toont de significantie van het verschil tussen de waargenomen metingen en de verwachting vanuit het Standaard Model (SM), berekend met de profile likelihood methode uit [191], waarbij een minteken wordt toegevoegd als de meting onder de verwachte voorspelling ligt.

waren, is de verwachte achtergrond van de SM berekend en vergeleken met de waarnemingen in de data. Als supersymmetrie aanwezig is, wordt een overschrijding van de SM voorspelling verwacht. Het onderste paneel kwantificeert de significantie van de afwijking van de verwachte achtergrond van de SM met de data. Een significantie van 3σ levert bewijs voor supersymmetrie en die met een waarde van 5σ zou een ontdekking hebben betekend. Gezien het feit dat de significantie in twee van de kolommen 2σ nauwelijks overschrijdt, kan worden geconcludeerd dat de SM in staat is om de waarnemingen in de SR's te verklaren. Helaas betekent dit ook dat de supersymmetrische deeltjes niet zijn gevonden.

De supersymmetrische modellen waarnaar gezocht is, zijn niet aangetroffen, waardoor het mogelijk is de supersymmetrische modellen uit te sluiten. Om dit te bereiken wordt een raster gemaakt van de mogelijke waarden voor de massa's van de supersymmetrische deeltjes. Het raster met de uitsluiting van de supersymmetrische parameterruimte wordt weergegeven in Figuur 4. Binnen het raster bieden alle verschillende SR's uitsluitingsvermogen voor verschillende waarden van het verschil in massa tussen de $\tilde{\chi}_2^0/\tilde{\chi}_1^\pm$ en de $\tilde{\chi}_1^0$ deeltjes, wat resulteert in een sterke uitsluitingskracht over het gehele raster. Het gebied dat binnen de rode lijn valt, is uitgesloten. Er kan worden geconcludeerd dat de volgende modellen zijn uitgesloten: de modellen zijn ingesloten in het gebied waar de massa van $\tilde{\chi}_1^0$ een waarde heeft

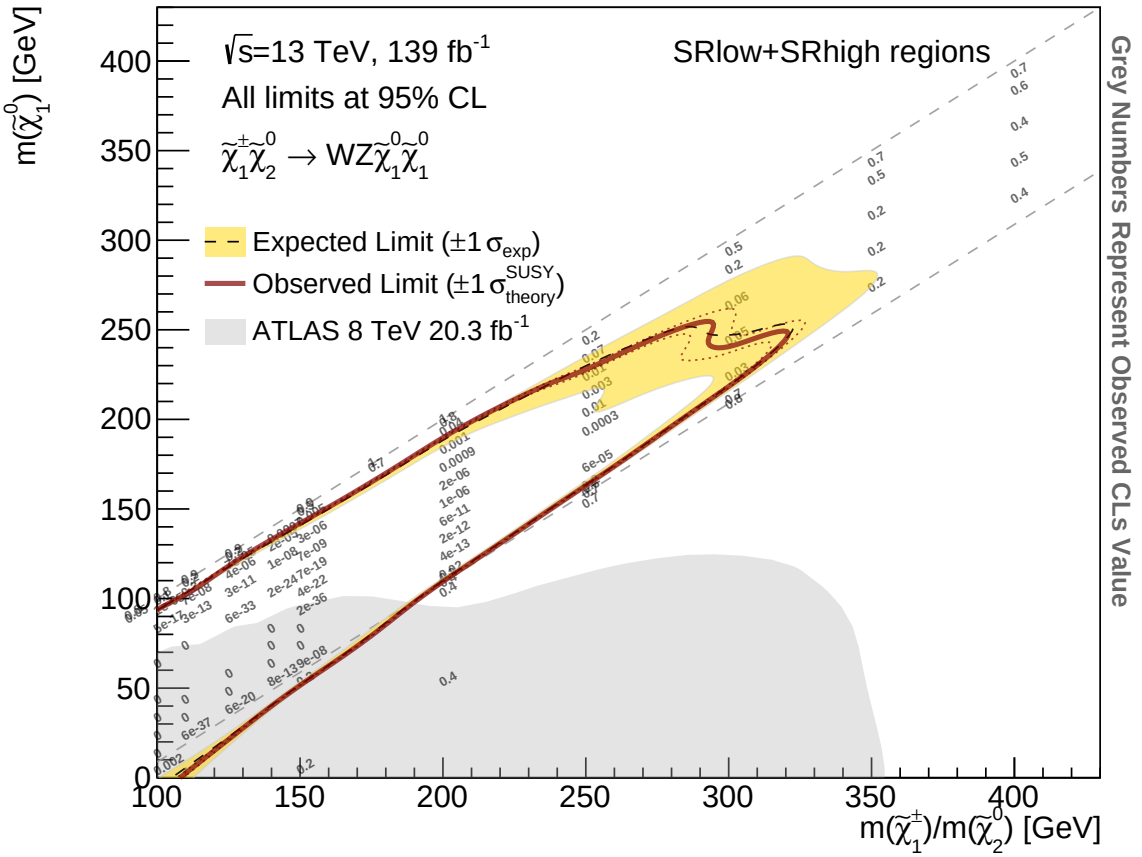

Fig. 4: Uitsluitings contouren geparametriseerd in de massa van de $\tilde{\chi}_1^0$ en $\tilde{\chi}_1^{\pm}/\tilde{\chi}_2^0$ deeltjes voor de combinatie van alle Signaal Regio's (SR's). Het gebied binnen de gele band definieert de verwachte limiet binnen $\pm 1\sigma$. De rode lijn geeft de waargenomen limiet aan en de gestippelde rode lijn geeft de waargenomen limiet binnen $\pm 1\sigma$ weer. Alle limieten zijn berekend op een betrouwbaarheidsinterval van 95 %. Het grijs-getinte gebied is de limiet die verkregen is door het vorige resultaat van ATLAS tijdens Run-1 [186].

van 250 GeV en de massa van $\tilde{\chi}_1^{\pm}/\tilde{\chi}_2^0$ een waarde heeft van 300 GeV. Hoewel de analyse geen bewijs levert of een ontdekking van supersymmetrie kon aantonen, was deze wel in staat om een groot deel van de eerder ongedekte parameterruimte uit te sluiten.

Tot slot, heeft de evolutie van de deeltjesfysica met zijn toename in de omvang van de versnellers en de complexiteit van de theorieën, het vakgebied in hoge mate geavanceerd, resulterend in een werkveld dat het gedrag van deeltjes met grote precisie kan voorspellen. Ondanks alle successen zijn er echter nog uitdagingen voor de deeltjesfysica die in het verschiet liggen, zoals het verklaren van DM of de wens om alle krachten te verenigen in een enkele theorie. De zoektocht die in dit proefschrift wordt gepresenteerd, was een van de pogingen om licht te doen schijnen op dit soort vragen. Hoewel de doorbraak nog steeds op

zich laat wachten, maakt het dit ver ontwikkelde veld op het moment zowel spannend als uitdagend. Het zal een groot genoegen zijn als we uiteindelijk deze doorbraak bereiken.

Acknowledgements

Thrilled to go on with research at the next level, I started a PhD without too much contemplation, right after my masters, or actually while my masters thesis was yet to be completed. It has been an amazing four and a half years with unique memories, where I was able to see more of the world and understand how the scientific world operates. Being part of a big collaboration such as the ATLAS experiment at CERN has been a privilege I will never forget.

For this I would like to thank first and foremost my promotor and supervisor prof. dr. ir. Paul de Jong for bringing me aboard at Nikhef. Coming from a different field of research during my masters, which was on quantum optics, Paul has helped me find my way in Particle Physics. He has helped to find the right books to read, projects to start out with and has connected me with the right people. But primarily he has challenged me to do good research and learned me how to operate in a large collaboration, to make sure the Nikhef plans are aligned with the other groups at CERN. All the way until the final stage, during the process of writing the thesis, where he has taught me how to formulate more precisely. All of these lessons have been learned with a large amount of freedom, where I was able to find my own path and overcome the different obstacles that one meets during a PhD.

I would like to thank dr. Sara Alderweireldt, with whom I had the pleasure to work with throughout the analysis. Sara joined Nikhef as a postdoc, while we were in the process of setting up the analysis, and later she became convener of the analysis. After accepting a fellowship at CERN, while we were ramping up the analysis efforts, Sara still offered to mentor me throughout the procedure of finalising the analysis. When arriving at the point where a copromotor had to be chosen, I am thankful that Sara was willing to fulfil this position. We have worked together a lot on a daily basis and whilst she had to juggle a lot of different responsibilities at CERN, such as the operations of the ATLAS trigger, she always made time to help me out with problems I encountered. I would like to thank Sara as well as dr. Jeff Dandoy for their enthusiastic leadership of the analysis group and making sure we would arrive at such a meticulous result.

I would especially like to thank dr. Shion Chen, who has guided me throughout almost all the projects within the analysis group, such as deriving the estimate for the fakes and designing a working point for the Prompt Lepton Veto. I have learned from him how to utilise the techniques and how to implement them in such a way that they would be optimal for our analysis. Whenever I was stuck in solving a problem along the way he has pointed me in the right direction. Where I initially would perform a more "trial and error" approach until it worked, Shion has taught me to investigate the problem more in depth in order to gain clues on the possible solution. This approach usually led to loads of diagnostic figures, but we could in the end pinpoint where our approach was inadequate. Together we managed to solve all the puzzles and I think the additions we included really made the analysis stand out with new techniques.

Within the analysis group I would also like to thank dr. Elodie Resseguie for developing the signal regions with me, as well as her advise and useful reviews on our analysis techniques. Also, I would like to thank dr. Joey Reichert for setting up the framework for deriving the fake factors. It has been a great pleasure to work with the Penn group! Also, I would like to thank dr. Carlo Gottardo and Lucia Pedraza who worked on the analysis and limit setting from the Nikhef group. As well as dr. Marcus Morgenstern who helped with the trigger studies and explained me the fake factor method.

During my qualification task I worked on the ATLAS alignment. While a qualification task can be an obstacle to many, it was not the case for me due to dr. Pierfrancesco Butti. He got me up to speed with the alignment framework and the task I had to do within no time, due to his "if you get stuck for 15 minutes come to me" rule. I think this took time in the beginning, but definitely saved time in the end. Within just a few weeks I could run the alignment and was able to make contributions to the group. In my first three months I could already give a talk in one of the performance weeks at CERN. Thank you for getting me up to speed so fast and introducing me to how ATLAS works.

After the analysis was finished, it was time to think about the cover of the thesis. I did not have to think twice about whom to ask to help me with this, for which I would like to thank Rolf Weijburg. Rolf is an artist and a friend of my parents, who has known me since I was little. Rolf has also visited Geneva, where I could show him the ATLAS detector. The fact that he designed the cover of this thesis is the ultimate personal touch to this work. The drawing is one of a kind. I have framed it and will keep it for the rest of my life.

Besides all the work that had to be done, there has been also a lot of time for unwinding with colleagues for which I would like to thank the whole of the ATLAS group at Nikhef, the rest of the students and staff I have met at Nikhef, and the members of the ondernemingsraad. Especially, I would like to thank Marc, Marko and Karel, a group I ended up spending quite

a bit of time with. Besides discussions about physics, it was also pleasant to talk about the difficulties in the PhD and our different approaches to these problems. Also, I would like to thank Matthew and Shuvay whom I met at CERN in Geneva. You made my time in Geneva a lot of fun! I am sure we will keep seeing each other. Our trip together with Marc to South Africa has been a great sealing of our friendship and undoubtedly we will head out there again! Also, I would like to thank Milo for the enjoyable time we had in our apartment in Ferney-Voltaire. It has been a pleasure to be your roommate and to get to know you better.

I would also like to thank my friends in Amsterdam who supported me a lot in the final year, especially my paranymphs Ludo and Jan. I would also like to thank them, as well as Rogier, for the good time we had exploring Amsterdam when we first moved here. Also, I would like to thank Edzard, Joris, Jan and Ruben for their visit to Geneva. It was a memorable weekend and for me the last moments I had with Joris, for which I am grateful. We have been a great support for each other in the time afterwards. Also, I would like to thank Ludo, Stijn en Coen for their visit and support, as well as Maurice and Rooj. Also, Walter for the great motorcycle trips we have made. In my final years of the PhD in Amsterdam, I would also like to thank my roommates at the Singel: Smits, Cas, Rogier and Remmert. Especially in the final moments, where through all the chaos, I relied more on you than I wanted in terms of cleaning out the dishwasher. We made sure we had a good time throughout the lockdown.

Finally, I would like to thank my family who have been the biggest support of all. I am grateful for the foundation that my parents instilled in me, giving me the curiosity to look around, to have an open mind and to question my surroundings. Attributes which have helped me during the PhD and might have even made me start one. As well as how they have helped throughout the process. Moving all my stuff back and forth between Geneva and visiting me many times while I was there. It has been rewarding to see the interest they had in the work I was doing. My father read the whole thesis in just two days after I had finished. I was astonished that he was able to grasp the structure of the analysis. He has provided comments and improvements to the thesis. I would also like to thank my sisters for their support and their visit. I would like to thank Sara and Leon for the fun evenings we had at their place during the lockdown. My sister is lucky to have such a good cook, and so am I!


Palazzani